PORE-SCALE MICROSTRUCTURE, MECHANISMS, AND MODELS FOR SUBSURFACE FLOW AND TRANSPORT

EDITED BY: James E. McClure, Charlotte Garing, Anna L. Herring and Carl Fredrik Berg

PUBLISHED IN: Frontiers in Water

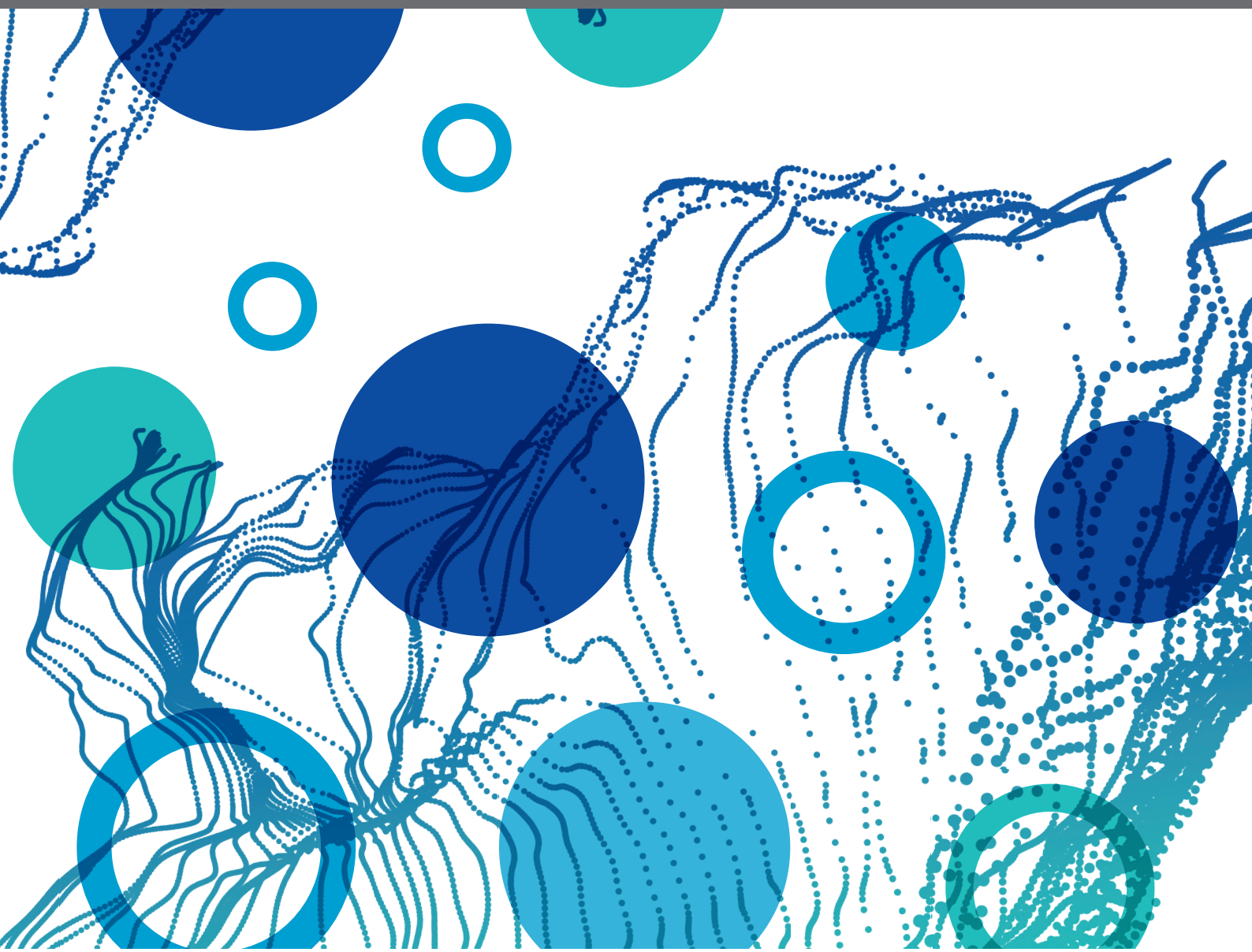

frontiers Research Topics

frontiers

ISSN 1664-8714
ISBN 978-2-83250-747-6
DOI 10.3389/978-2-83250-747-6

About Frontiers

Frontiers is more than just an open-access publisher of scholarly articles: it is a pioneering approach to the world of academia, radically improving the way scholarly research is managed. The grand vision of Frontiers is a world where all people have an equal opportunity to seek, share and generate knowledge. Frontiers provides immediate and permanent online open access to all its publications, but this alone is not enough to realize our grand goals.

Frontiers Journal Series

The Frontiers Journal Series is a multi-tier and interdisciplinary set of open-access, online journals, promising a paradigm shift from the current review, selection and dissemination processes in academic publishing. All Frontiers journals are driven by researchers for researchers; therefore, they constitute a service to the scholarly community. At the same time, the Frontiers Journal Series operates on a revolutionary invention, the tiered publishing system, initially addressing specific communities of scholars, and gradually climbing up to broader public understanding, thus serving the interests of the lay society, too.

Dedication to Quality

Each Frontiers article is a landmark of the highest quality, thanks to genuinely collaborative interactions between authors and review editors, who include some of the world's best academicians. Research must be certified by peers before entering a stream of knowledge that may eventually reach the public - and shape society; therefore, Frontiers only applies the most rigorous and unbiased reviews.
Frontiers revolutionizes research publishing by freely delivering the most outstanding research, evaluated with no bias from both the academic and social point of view. By applying the most advanced information technologies, Frontiers is catapulting scholarly publishing into a new generation.

What are Frontiers Research Topics?

Frontiers Research Topics are very popular trademarks of the Frontiers Journals Series: they are collections of at least ten articles, all centered on a particular subject. With their unique mix of varied contributions from Original Research to Review Articles, Frontiers Research Topics unify the most influential researchers, the latest key findings and historical advances in a hot research area! Find out more on how to host your own Frontiers Research Topic or contribute to one as an author by contacting the Frontiers Editorial Office: frontiersin.org/about/contact

PORE-SCALE MICROSTRUCTURE, MECHANISMS, AND MODELS FOR SUBSURFACE FLOW AND TRANSPORT

Topic Editors:
James E. McClure, Virginia Tech, United States
Charlotte Garing, University of Georgia, United States
Anna L. Herring, Australian National University, Australia
Carl Fredrik Berg, Norwegian University of Science and Technology, Norway

Citation: McClure, J. E., Garing, C., Herring, A. L., Berg, C. F., eds. (2022). Pore-Scale Microstructure, Mechanisms, and Models for Subsurface Flow and Transport. Lausanne: Frontiers Media SA. doi: 10.3389/978-2-83250-747-6

Table of Contents

frontiers | Frontiers in Water

EDITORIAL
published: 25 May 2022
doi: 10.3389/frwa.2022.935404

Editorial: Pore-Scale Microstructure, Mechanisms, and Models for Subsurface Flow and Transport

James E. McClure[1]*, *Charlotte Garing*[2], *Anna L. Herring*[3] and *Carl Fredrik Berg*[4]

[1] Aerospace and Ocean Systems Division, National Security Institute, Virginia Tech, Blacksburg, VA, United States, [2] Department of Geology, University of Georgia, Athens, GA, United States, [3] Department of Materials Physics, Research School of Physics, The Australian National University, Canberra, ACT, Australia, [4] PoreLab, Department of Geoscience and Petroleum, Norwegian University of Technology and Science (NTNU), Trondheim, Norway

Keywords: porous media, carbon sequestration, digital rock, pore-scale model, hydrology

Editorial on the Research Topic

Pore-Scale Microstructure, Mechanisms, and Models for Subsurface Flow and Transport

The microscopic structure of soil, rock and other geological material strongly influences the behavior of groundwater systems, geologic carbon sequestration, and other applications in subsurface flow and transport. Experimental and computational advancements now support a wide range of studies that explicitly link the microscopic structure of materials with both physical mechanisms and larger scale flow and transport behaviors. Predictive pore-scale studies to understand and model displacement and transport rely on geometric information obtained from experimental imaging. As new capabilities are developed, quantitative measurements can be made to inform understanding in a variety of ways. Pore-scale studies can provide insight into the operative mechanisms for particular processes, as well as serving as a tool to directly upscale results from the smaller scale to a larger one. Direct exploration of pore-scale processes have lead to significant contributions toward our understanding of the fundamental physics of flow and transport through porous media. This collection highlights key active research areas and identifies new opportunities to advance the state-of-the art, with representative spectrum of theoretical, experimental and computational contributions.

At the most basic level, high-quality experimental image data is indispensable for pore-scale studies.In recent years, artificial intelligence and machine learning techniques have grown as new tools to improve image data quality. Tawfik et al. compare traditional de-noising technique with a variety of artificial neural networks in the context of application to digital rock physics. This touchstone work assesses the performance for several machine learning approaches and identifies promising avenues for future exploration. Efforts to enhance the fidelity of experimental observations underpin theoretical and computational studies that expand our understanding in many different ways. Soulaine et al. review the state-of-the-art computational microfluidics for geosciences, a emerging modeling approach leveraging microfluidic experiments and high-resolution imaging. After introducing the governing equations and numerical methods used in computational microfluidics, the paper highlights recent success and unsolved challenges in modeling multiphase flow and reactive transport at the pore-scale.

Microscopic imaging techniques provide important opportunities to better understand the energy dynamics of immiscible displacement. Li et al. use microscopic particle image velocimetry (μPIV) to experimentally resolve the dynamics of pore-scale events. This approach provides important information that can help to characterize the bursty dynamics that are typical of two-fluid flow through porous media. Their analysis suggests that as much as 90% of the

OPEN ACCESS

Edited and reviewed by:
Carl i Steefel,
Berkeley Lab (DOE), United States

***Correspondence:**
James E. McClure
mcclurej@vt.edu

Specialty section:
This article was submitted to Water and Critical Zone, a section of the journal Frontiers in Water

Received: *03 May 2022*
Accepted: *09 May 2022*
Published: *25 May 2022*

Citation:
McClure JE, Garing C, Herring AL and Berg CF (2022) Editorial: Pore-Scale Microstructure, Mechanisms, and Models for Subsurface Flow and Transport. Front. Water 4:935404. doi: 10.3389/frwa.2022.935404

energy of a pore-scale event is reversibly transferred to surface energy, and finding that has important consequences for larger-scale model development. At the macroscopic level, Darcy-scale descriptions of two-fluid through porous media have typically ignored the fluctuations caused by pore-scale events. Rücker et al. consider pressure fluctuations that arise during two-fluid fractional flow experiments. The characteristic energy and time scales are determined and shown to be associated with capillary events that occur within the microstructure. Deeper mechanistic understanding of these phenomena are linked to many possible avenues for research, including as a way to infer wetting phenomena and to formulate a more complete understanding of multiphase flow instabilities and their consequences.

When two-phase flow is capillary or viscous dominated, the relation between total flow rate and pressure drop is linear, similar to the single phase description of Darcy. There is an ongoing effort to classify and describe the transition between these two regimes, a third regime where both capillary and viscous forces are of importance. In Roy et al. the authors use network models to simulate multiphase flow at different flow rates, pore size distributions and fluid saturation fractions. In accordance with earlier research, they observe a power law between flow rate and pressure drop in the transition regime. The authors show how this power law exponent is dependent on pore size distribution and saturation, and obtain a wide range of exponents for different network and saturation settings.

Microscopic insight into CO_2 sequestration is an important application area for microscale studies. Kohanpur et al. present an approach to integrate direct numerical simulation results of pore-scale events into larger domain pore-network models. The modified pore-network model provides better agreement with experimental results of residual trapping of CO_2. Trapping is a key mechanism to reduce the mobility of sequestered CO_2 over short timescales, providing an opportunity for longer-term mechanisms to act. Since the dominant mechanisms for trapping are due to capillary forces subject to the influence of confinement based on the solid microstructure, first-principles studies can provide very important insight into the behavior of real systems.

At even smaller length scales, boundary slip can play a significant role in transport behavior. In the theoretical work of Valdés-Parada and Lasseux, volume averaging techniques are used to derive a generalized model that accounts for the consequences of both Knudsen and diffusive slip contributions in the context of macroscopic dispersion. There are many situations where the length scale for solid microstructure is small enough to constitute an essential contribution to the system behavior. This work is also relevant to cases where solid heterogeneity leads to mass fluxes between sub-micron structures and larger scale structures such as fractions and larger pores. Gouze et al. investigates dispersion processes in porous media. The authors create two sets of porous media samples, both following the same porosity-permeability trends, but with different pore structure evolution and thus dispersion evolution. These two sets allows the authors to investigate how dispersion is affected by micro-structure relative to changes in porosity and permeability. Mass transfer processes also play an important role in surface reactions that can alter the pore structure and cause corresponding changes to macroscopic transport coefficients. Starchenko constructs a first-principles model to study the role played by nucleation in mineral precipitation and growth. The constructed numerical model is used to demonstrate how this mechanism influences the formation of heterogeneous microstructures within a porous material.

The vibrant pore-scale research community fosters essential connections between first-principles physics, high quality experimental data and practical applications. Scientific advancements have always relied on new data sources as a way to substantiate theo retical models and inform engineering applications that benefit society as a whole. As the volume and quality of pore-scale experimental data continue to grow, associated opportunities to learn from theory and computation will grow as well. Insights that result from these developments will be essential to formulate strategic responses to a wide range of challenges that face global society, particularly those related to climate change, water resources management and energy.

AUTHOR CONTRIBUTIONS

All authors listed have made a substantial, direct, and intellectual contribution to the work and approved it for publication.

Conflict of Interest: The authors declare that the research was conducted in the absence of any commercial or financial relationships that could be construed as a potential conflict of interest.

Publisher's Note: All claims expressed in this article are solely those of the authors and do not necessarily represent those of their affiliated organizations, or those of the publisher, the editors and the reviewers. Any product that may be evaluated in this article, or claim that may be made by its manufacturer, is not guaranteed or endorsed by the publisher.

frontiers in Water

REVIEW
published: 02 March 2021
doi: 10.3389/frwa.2021.643714

Computational Microfluidics for Geosciences

Cyprien Soulaine[1]*, *Julien Maes*[2] *and Sophie Roman*[1]

[1] *Earth Sciences Institute of Orléans, University of Orléans-CNRS-BRGM, Orléans, France,* [2] *Institute of GeoEnergy Engineering, Heriot-Watt University, Edinburgh, United Kingdom*

Computational microfluidics for geosciences is the third leg of the scientific strategy that includes microfluidic experiments and high-resolution imaging for deciphering coupled processes in geological porous media. This modeling approach solves the fundamental equations of continuum mechanics in the exact geometry of porous materials. Computational microfluidics intends to complement and augment laboratory experiments. Although the field is still in its infancy, the recent progress in modeling multiphase flow and reactive transport at the pore-scale has shed new light on the coupled mechanisms occurring in geological porous media already. In this paper, we review the state-of-the-art computational microfluidics for geosciences, the open challenges, and the future trends.

Keywords: pore-scale analysis, microfluidics, computational fluid dynamics, reactive transport modeling, depth-averaged 2D model, porous media, multiphase flow

OPEN ACCESS

Edited by:
Charlotte Garing,
University of Georgia, United States

Reviewed by:
Albert J. Valocchi,
University of Illinois at Urbana-Champaign, United States
Steffen Berg,
Shell, Netherlands

***Correspondence:**
Cyprien Soulaine
cyprien.soulaine@cnrs-orleans.fr

Specialty section:
This article was submitted to Water and Critical Zone, a section of the journal Frontiers in Water

Received: *18 December 2020*
Accepted: *25 January 2021*
Published: *02 March 2021*

Citation:
Soulaine C, Maes J and Roman S (2021) Computational Microfluidics for Geosciences. Front. Water 3:643714. doi: 10.3389/frwa.2021.643714

1. INTRODUCTION

Since their appearance in the early eighties, microfluidic experiments have revolutionized the knowledge in porous media research. They brought new insights into the debates that drive the community for decades including the controversial use of Darcy's law for modeling multiphase flow and the understanding of the complex feedback between hydro-bio-chemical systems. The most famous example is the work of Lenormand et al. (1988) who identified different flow instabilities in unsaturated porous systems according to the fluid pair and the flow rates using micromodels. These microfluidic devices enable direct visualization of the flow, transport, and chemical processes in rock microstructure replica sandwiched between two parallel plates separated by a small distance (Jahanbakhsh et al., 2020; Morais et al., 2020). Classically, a representation of the pore space is etched on a substrate made of silicon, glass or polymeric materials and covered by a transparent material. Recently, 3D printing has been used for fast and robust micromodel fabrication (Watson et al., 2019), allowing to conduct many flow experiments at lower cost for 2D to complex 3D geometry, although for now resolution is not as accurate as etched 2D micromodels. Coupled with high-resolution imaging both in space and time, microfluidic experiments have shed new light on the key mechanisms controlling subsurface flow. For example, particle image velocimetry has highlighted internal fluid eddies within droplets trapped by capillary forces whose large scale impact is not included in multiphase Darcy's law (Kazemifar et al., 2016; Roman et al., 2016, 2020; Zarikos et al., 2018). Microfluidics also led to substantial advancements in the understanding of reactive systems as the most recent microchips involve reactive materials to investigate dissolution and precipitation of solid minerals in fractured porous media (Zhang et al., 2013; Song et al., 2014; Porter et al., 2015; Osselin et al., 2016; Soulaine et al., 2017, 2018; Yoon et al., 2019; Agrawal et al., 2020; Poonoosamy et al., 2020; Yun et al., 2020). In just a few decades, microfluidics has become an indispensable tool in geosciences to decipher the complex mechanisms that occur in porous systems and the discipline keeps improving.

Computational microfluidics is the digital counterpart of microfluidic experiments. Like any modeling approach, it is a natural companion of laboratory experiments as it can be used to perform sensitivity analysis for identifying the key parameters of the underlying processes or to explore ranges of conditions including pressure and temperature that are difficult to reach in the laboratory without dedicated equipment. Moreover, computational microfluidics can also assist in the design of micromodels. Unlike pore-network modeling—a widely used approach for describing pore-scale physics (Fatt, 1956)—that relies on an approximation of the pore geometries and on pore-averaged physical laws, computational microfluidics solves the fundamental equations of continuum mechanics in the exact microstructure geometry. Historically, this kind of simulations was considered computationally expensive and almost impossible to run on complex and large domains. The enormous progress in high-resolution numerical simulation of complex flow and high-performance computing techniques, however, makes it possible to perform routinely computational microfluidics for single-phase flows on domains that reach the size of a Representative Elementary Volume (Roman et al., 2016). Although it heavily relies on advanced and modern approaches for simulating fluid dynamics, computational microfluidics for geosciences has its own challenges related to the complexity of natural systems including the heterogeneity of geological porous media, the evolving porous microstructure along with geochemical processes, and the complex description of interfacial phenomena at the mineral surfaces (Meakin and Tartakovsky, 2009).

The recent improvements in computational microfluidics for geosciences enable the modeling of multiphase flow and reactive transport. Current capabilities capture many of the mechanisms observed experimentally. For example, two-phase flow simulations in micromodels describe the complex interplay between viscous, capillary, and gravity forces leading to viscous fingerings if a fluid drains another fluid (Ferrari and Lunati, 2013; Alpak et al., 2016; Chen et al., 2019; Zhao et al., 2019), or to the trapping of carbon dioxide droplets in the pore space (Chen et al., 2015; Hu et al., 2017). Computational microfluidics allows the understanding of subsurface processes by identifying key mechanisms. Hence, the integrated usage of computational and experimental microfluidics led (Roman et al., 2017) to highlight that snap-off events, i.e., the break-up of the invading fluid at the entrance of a pore-throat, can be followed by a reconnection to the flowing phase. They observed and characterized cycles of snap-off and reconnection events that contradict the criteria that are generally used to assess the storage capacity by capillary trapping. Another example is the study of Ferrari and Lunati (2014) which establishes that inertial forces arise during pore invasion—a statement also supported by glass bead experiments (Moebius and Or, 2012) and interface tracking in micromodels (Roman et al., 2016)—suggesting that creeping flow assumption for the derivation of multiphase Darcy's law is erroneous. Moreover, as computational microfluidics provides a mapping of pressure, velocity, species concentration, and mineral distribution, the characterization of constitutive laws using volume averaging is straightforward. For instance, Soulaine et al. (2017) used computational microfluidics to compute the accessible reactive surface area of a rock sample. A more comprehensive review of the state-of-the-art including the authors' contributions, as well as the remaining challenges that need to be solved for being truly predictive, are presented in section 3.

Our definition of computational microfluidics goes beyond the modeling of flow and geochemical processes in micromodels as it can also be applied to complex 3D structures. In this sense, computational microfluidics for geosciences is intimately linked to Digital Rock Physics, an emerging technology concerned with the estimation of effective upscaled parameters (e.g., permeability, dispersion tensor) in three-dimensional images of rock samples (Blunt et al., 2013). In Digital Rock Physics, these properties can be calculated using different techniques, such as pore network analysis (Andre et al., 2013a,b) or closure problem approaches (Whitaker, 1999; Soulaine et al., 2013). Alternatively, computational microfluidics can be used to directly solve the flow and transport equations within the pore-space and compute the desired upscaled properties. Although it is often restricted to small micro-CT images ($<300^3$ voxels) or to single-phase flow due to high computing cost, computational microfluidics is also well-suited to investigate pore-to-pore physics (Ferrari and Lunati, 2014; Pavuluri et al., 2020) with the objective of improving upscaling techniques (e.g., pore entry pressure for pore network modeling). A major asset of microfluidics is the ability to design well-controlled experiments and obtain high-resolution measurements—both in space and time—of the velocity fields (Roman et al., 2016), phase distribution, film thickness (Roman et al., 2017), aqueous species concentrations (Chang et al., 2017), and mapping in mineral changes (Poonoosamy et al., 2020). Microfluidics is inestimable to verify the numerical models using direct comparison with microfluidic experiments (Willingham et al., 2008; Yoon et al., 2012; Chapman et al., 2013; Oostrom et al., 2016; Roman et al., 2017; Soulaine et al., 2018). Therefore, the combination of computational and experimental microfluidics promotes the development of robust and validated numerical models for pore-scale modeling.

Exposing simulation results to experimental data, however, is not always an easy task as it raises questions regarding the measurement resolution and also questions on the modeling spatial description. Micromodels are often referred to as "two-dimensional" objects by opposition to real geological objects or their reproduction using 3D printing. This qualification is somewhat imprecise as the micromodels are made of the assembly of two parallel plates and that important physical phenomena occur in the confined space between the plates. This confusion leads many scientists to use two-dimensional models for representing their microfluidic experiments numerically. In most cases, however, 2D simulations are not able to reproduce the experiments. Even in cases for which the micromodel depth is much larger than the smallest pore-throat diameter the two-dimensional hypothesis breaks down because physical events are not uniform in the thickness. For example, reactive particles can nucleate in the mid-plane or at the solid walls (Beuvier et al., 2015) and instabilities in the liquid films that wet the top and

bottom plates can lead to the formation of bubbles in the bulk (Hansen and Toong, 1971; Zhao et al., 2018). The systematic usage of 3D models, however, is computationally intensive. To reduce the computational efforts, 2D depth-integrated models are an interesting alternative for solving flow in microfluidic chips. These approaches, however, can have strong limitations. In section 2, we present depth-integrated models for single-phase, two-phase, and species transport, and we discuss their range of validity.

This paper aims at reviewing the modeling approaches in computational microfluidics for geosciences and their open challenges, as well as the authors' contributions to this emerging scientific discipline. It is organized as follows. First, we introduce the fundamental equations used in computational microfluidics (section 2.1) and the common numerical approaches to solve them (section 2.2). We also present models that solve directly for the depth-averaged variables at a reduced simulation cost (section 2.3). Then, we summarize the main advances in modeling multiphase flow (section 3.1) and reactive transport (section 3.2), and we discuss future lines of research.

2. MATHEMATICAL MODELS AND NUMERICAL SOLUTIONS

In this section, we introduce the fundamental equations used in computational microfluidics for solving flow and transport. We also discuss the standard numerical approaches for solving these equations.

2.1. Fundamental Governing Equations

Computational microfluidics relies on the fundamental equations of continuum mechanics for fluid flow, namely the Navier-Stokes equations, solved in the exact geometry of the pore space. They are composed of a set of mass and momentum balance equations combined with boundary conditions at the solid surface.

2.1.1. Flow Equations

For single-phase flow, the conservation of mass reads,

$$\frac{\partial \rho}{\partial t} + \nabla.\left(\rho \boldsymbol{v}\right) = 0, \tag{1}$$

where ρ and $\boldsymbol{v}$ are the fluid density and velocity, respectively. For liquids, it is common to assume that the fluid is incompressible, and the mass balance equation (Equation 1) reduces to the divergence-free velocity,

$$\nabla.\boldsymbol{v} = 0. \tag{2}$$

In an Eulerian frame, the momentum balance writes,

$$\frac{\partial \rho \boldsymbol{v}}{\partial t} + \nabla.\left(\rho \boldsymbol{v}\boldsymbol{v}\right) = -\nabla p + \rho \boldsymbol{g} + \nabla.\mu\left(\nabla \boldsymbol{v} + \nabla^t \boldsymbol{v}\right), \tag{3}$$

where p is the pressure field, $\boldsymbol{g}$ is the gravity, and μ is the fluid viscosity. The left-hand side corresponds to the inertial effects. As mass flow rates in the soils and the subsurface are usually low, it is common to neglect this term and to use Stokes instead of the Navier-Stokes momentum equation. On the right-hand side, the first term is the pressure gradient, the second is the gravity acceleration and the third term is the viscous dissipation. The latter characterizes the internal friction of the fluid particles with each other. The higher the viscosity, the larger the pressure gradient has to be to initiate the fluid movement. At the pore-scale, it is also common to neglect the gravity term.

For multiphase flow, the mass and momentum equations, Equations (1)–(3) apply to each fluid phase. Alternative forms of the Navier-Stokes equations including non-Newtonian and compressible fluids as well as descriptions of the equations in a Lagrangian frame are found in any fluid mechanics textbook (e.g., Landau and Lifshitz, 1987; Caltagirone, 2013).

2.1.2. Boundary Conditions at the Solid Walls

The flow equations are supplemented with boundary conditions at the solid surface that arise from particle/solid molecular interactions. Because the fluid molecules cannot penetrate into the impermeable boundary, the mass flux at the solid surface is null and the normal component of the velocity is zero, i.e., $\boldsymbol{n}.\boldsymbol{v} = 0$. For viscous flow, it is common to consider that the fluid molecules adhere to the surface due to molecular interactions including van der Waals or Coulombic forces. Because of this adherence, the fluid particles at the solid wall cannot slide on the surface and the tangential component of the velocity is null, leading to the *no-slip* condition,

$$\boldsymbol{v} = 0. \tag{4}$$

The no-slip boundary condition is valid for most of the Newtonian liquids flowing through porous media with pore-throats larger than 100 nm. Although widely used in fluid dynamics, the no-slip condition is not always valid in geological systems. In particular, in complex fluids involving colloids or polymers, the fluid elements adjacent to the surface can travel along the surface by rolling or sliding. In such cases, the fluid in contact with the solid surface slide over it with a finite value. Moreover, the no-slip condition poses a problem in viscous flow theory at the place where an interface between two fluids meets a solid boundary. Instead, the so-called *partial slip* condition,

$$\boldsymbol{v} = \beta\left(\mathrm{I} - \boldsymbol{n}\boldsymbol{n}\right).\left(\boldsymbol{n}.\left(\nabla \boldsymbol{v} + \nabla^t \boldsymbol{v}\right)\right), \tag{5}$$

proposed by Navier (1823) and later revisited by Maxwell (1879), relates the tangential velocity to the strain rate. In this relation, $\boldsymbol{n}$ is the normal vector at the solid surface and β is called the slip length and is typically of the order of ten nanometers.

The description of boundary conditions at the solid walls for multiphase flow is discussed in section 3.1.

2.1.3. Interfacial Conditions Between Two Fluids

The interface between two fluid phases (labeled fluid 1 and fluid 2, respectively) is a discontinuity on which boundary conditions are applied. The interface deforms with the fluid motion and moves at the *interface velocity*, $\boldsymbol{w}$. The latter is obtained using the conservation of mass at the vicinity of the interface,

$$\boldsymbol{n}_{12}.\rho_1\left(\boldsymbol{v}_1 - \boldsymbol{w}\right) = \boldsymbol{n}_{12}.\rho_2\left(\boldsymbol{v}_2 - \boldsymbol{w}\right), \tag{6}$$

where $\boldsymbol{n}_{12}$ is the normal at the interface separating the two fluids, and ρ_i and $\boldsymbol{v}_i$ are the density and velocity of phase i, respectively. If there is no phase change, the interface velocity and the fluid velocity balance each other at the interface and $\boldsymbol{n}_{12}.\boldsymbol{v}_1 = \boldsymbol{n}_{12}.\boldsymbol{v}_2$.

The normal stress balance at the interface gives (Landau and Lifshitz, 1987),

$$\begin{aligned}\boldsymbol{n}_{12}.\left[-p_1\mathbf{I} + \left(\mu_1\nabla\boldsymbol{v}_1 + \nabla^t\boldsymbol{v}_1\right)\right] \\ = \boldsymbol{n}_{12}.\left[-p_2\mathbf{I} + \left(\mu_2\nabla\boldsymbol{v}_2 + \nabla^t\boldsymbol{v}_2\right)\right] + \sigma\kappa,\end{aligned} \tag{7}$$

where p_i is the fluid pressure in fluid i, σ is the surface tension, and κ is the interface curvature. At equilibrium, this condition becomes Laplace law.

An overview of the simulation techniques used in computational microfluidics to solve Navier-Stokes equations along with the interfacial conditions is given in section 3.1.

2.1.4. Solute Transport

In its simplest form, the transport of a species i in a fluid phase is modeled by an advection-diffusion equation:

$$\frac{\partial C_i}{\partial t} + \nabla.\left(\boldsymbol{v}C_i\right) = \nabla.\left(D_i\nabla C_i\right), \tag{8}$$

where the first term is the accumulation term, the second term is the advection term and the right-hand side corresponds to diffusion effects where D_i is the diffusion coefficient of species i into the fluid phase. More complex forms of the solute transport includes multi-component diffusion, thermal diffusion and electrostatic gradients (Bird et al., 2002).

As for flow equations, the solute balance equation is supplemented by boundary conditions at the solid walls. For a passive tracer the *no flux* condition writes,

$$\boldsymbol{n}.D_i\nabla C_i = 0. \tag{9}$$

If the species reacts with the solid surface the *reactive flux* condition is,

$$\boldsymbol{n}.D_i\nabla C_i = r_m\left(C_i\right), \tag{10}$$

where r_m is a source or sink term that describes kinetic reactions or adsorption phenomena (Molins et al., 2014).

It is also common to consider that the species satisfies *thermodynamics equilibrium condition* with the solid wall using,

$$C_i = C_i^{eq}, \tag{11}$$

where C_i^{eq} is a fixed value imposed by thermodynamics equilibrium.

2.2. Numerical Engines for Solving Navier-Stokes Equations

Solving Navier-Stokes equations in complex geometries is not trivial, and except in very few situations, there are no analytical solutions. Computational microfluidics uses numerical approximations to solve the flow within the pore space. Complexities include the pressure-velocity coupling and the non-linearity due to the inertial term in the momentum equation.

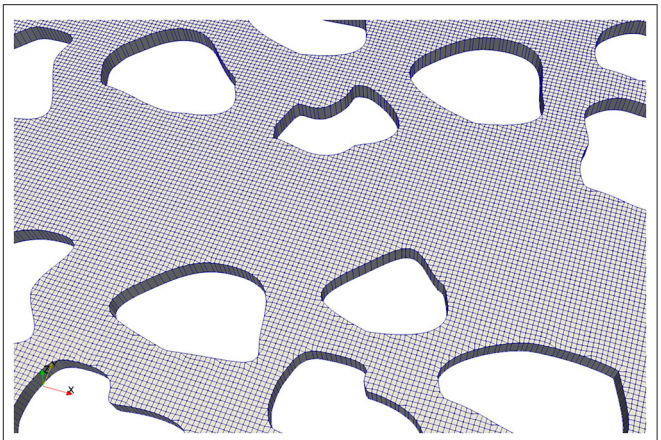

FIGURE 1 | Example of finite-volume grid used in computational microfluidics.

In this section, we introduce some of the standard approaches for solving Navier-Stokes equations. Specific techniques for multiphase flow and reactive transport are introduced and discussed in section 3.

2.2.1. Computational Fluid Dynamics

In Computational Fluid Dynamics (CFD), the Navier-Stokes equations are solved by discretizing the spatial differential operators on an Eulerian grid using techniques such as the finite difference method (FDM), the finite volume method (FVM), or the finite element method (FEM) (Ferziger and Peric, 2002). In principle, the three families of techniques yield the same solution if the computational grid is fine enough. For fluid flow, however, FVM is usually preferred as it is locally conservative and deals with unstructured grids by construction. In FVM, the domain is subdivided into a finite number of contiguous control volumes whereby the integral form of the conservation laws is applied. Modern gridders generate meshes that follow the complex boundaries of the microstructure (see **Figure 1**). Nowadays, all the commercial or open-source CFD simulators embed very efficient Navier-Stokes solvers that can deal with very large grids and complex geometries using multigrid strategies and High-Performance Computing. Solution algorithms usually rely on predictor-corrector methods to solve for the pressure-velocity coupling. The Pressure-Implicit with Splitting of Operators (PISO) algorithm is one of the most popular for solving transient flow (Issa, 1985). Algorithms such as Semi-Implicit Method for Pressure Linked Equations (SIMPLE) solve directly for steady-state flow (Patankar, 1980).

2.2.2. Lattice Boltzmann Method

The lattice Boltzmann method (LBM) is an alternative CFD technique to solve fluid flow at the pore-scale. The popularity of LBM comes from the ease to program massively parallel codes. Unlike traditional CFD approaches that solve for Navier-Stokes equations, LBM is based on the Boltzmann equation that describes the probability of finding a given particle at a given position with a given velocity. This is a statistical approach and

the averaged behavior approximates the continuum mechanics described by the Navier-Stokes equations. In LBM, a discrete Boltzmann equation is solved on a lattice where the particles can only move along a finite number of directions. The degree of freedom is determined by the nature of the lattice classified with the nomenclature $DnQm$ where n corresponds to the dimension of the lattice ($n = 2$ for two-dimensional simulations, $n = 3$ for three-dimensional simulations) and m stands for the number of directions. The Boltzmann equation involves a collision operator that describes the change in the probability distribution function induced by the collisions between particles. In the Lattice Boltzmann method, the boundary conditions are described in terms of probability distribution functions. The description of the wall conditions corresponds actually to the physical model of boundary events proposed by Maxwell (1879). For a no-slip, the bounce-back condition is used where the particles are reflected at the wall. Hence, the net average flow rate at the solid surface is zero. Slip conditions can be obtained using specular reflections (Succi, 2002). Partial slip is modeled with a mix of bounceback and specular reflections. The implementation of boundary conditions in LBM can become very complex when the solid surface is not aligned with the lattice.

2.2.3. Smoothed-Particle Hydrodynamics

Smoothed-Particle Hydrodynamics (SPH) is a mesh-free modeling technique that describes fluids as a set of discrete moving particles in a Lagrangian framework. The method was initially developed to model the interaction of stars in astrophysics (Gingold and Monaghan, 1977; Lucy, 1977) and is now being used increasingly in real-time animation and video games. The particles have a spatial distance over which their properties are smoothed by a kernel function centered on the particles. This distance defines the sphere of influence for each particle and is used to reconstruct continuous variables such as fluid density. The SPH particles are then used as interpolation points to discretize and solve the governing equations. SPH has several benefits over traditional grid-based methods. First, it is meshless and there is no need to go through complex gridding processes. Second, it explicitly conserves mass and momentum. Because the method is Lagrangian, there is no non-linear term in the momentum equation and that allows an accurate description of the advection terms when dealing with high flow rates. Third, the SPH Lagrangian framework allows for the modeling of moving and deformable boundaries without using complex tracking algorithms. SPH has also important drawbacks. Although the SPH algorithms due to their simplicity and structure are easy to program, the implementation of boundary conditions can be tricky. Moreover, for the same accuracy, SPH is more computationally intensive than FVM or FEM because it requires much more neighboring particles than the tensile of grid-based methods. Nevertheless, because SPH can be easily paralleled, the rise of parallel computing including Graphical Processing Units makes SPH a promising technique (Vacondio et al., 2020).

2.3. Depth-Averaged Models: 2D vs. 3D

Most of the time, measurements in microfluidic experiments relate to depth-averaged values. For example, even though micro-Particle Image Velocimetry that uses confocal microscopy or laser pretends to measure the velocity profiles in a cross-section, these techniques do measure values averaged in a thickness of the order of few micrometers that corresponds to the laser thickness or the close surrounding of the focal plan (Roman et al., 2016). Likewise, microfluidic experiments using optical luminescence for measuring a concentration profile (Watson et al., 2019) or mapping the water distribution (Zhao et al., 2016; Roman et al., 2017) provides values that are averaged along the micromodel depth, h, without information of the depth profile of the species concentration or water saturation. The depth-averaged variables are defined as the vertical integration of the 3D fields,

$$\bar{\boldsymbol{v}}^{2D} = \frac{1}{h}\int_0^h \boldsymbol{v}\left(x, y, z\right) dz. \tag{12}$$

In this section, we present depth-averaged models that directly provide the solution for the depth-averaged velocity, $\bar{\boldsymbol{v}}^{2D}$, pressure, $\bar{p}^{2D}$, and concentration, $\overline{C_i}^{2D}$, fields without solving 3D problems. These models result from the integration of the fundamental equations described in section 2.1 along the depth axis and can significantly reduce the simulation costs. They have, however, ranges of validity that are discussed below.

2.3.1. Single-Phase Flow

The integration of Navier-Stokes momentum equation over the micromodel depth along with the assumption that a parabolic profile approximates the flow in the thickness gives,

$$\frac{\partial \rho \bar{\boldsymbol{v}}^{2D}}{\partial t} + \nabla.\left(\rho \bar{\boldsymbol{v}}^{2D}\bar{\boldsymbol{v}}^{2D}\right) = -\nabla \bar{p}^{2D} + \nabla.\mu\left(\nabla \bar{\boldsymbol{v}}^{2D} + \nabla^t \bar{\boldsymbol{v}}^{2D}\right) - \mu\frac{12}{h^2}\bar{\boldsymbol{v}}^{2D}, \tag{13}$$

where the last term of the right-hand side, $\mu\frac{12}{h^2}\bar{\boldsymbol{v}}^{2D}$, is the Hele-Shaw correction (Lamb, 1906), i.e., a drag force related to the friction of the fluid along the micromodel top and bottom plates. Numerical implementation of Equation (13) has been reported using CFD (Roman et al., 2016) and LBM (Venturoli and Boek, 2006; Laleian et al., 2015). The Hele-Shaw correction is similar to a Darcy law for which the permeability is $k = \frac{h^2}{12}$ and the porosity is $\phi = 1$. This simple depth-integration was historically the first step toward the derivation of Darcy's law from Stokes equation (Vasil'ev, 2009). Actually, for micromodels with a low aspect ratio between the cell thickness and the pore-throat size, $h/d \ll 1$, the drag force is the dominant force and Equation 13 can be replaced by Darcy's law for Hele-Shaw cells,

$$\bar{\boldsymbol{v}}^{2D} = -\frac{h^2}{12\mu}\nabla \bar{p}^{2D}. \tag{14}$$

Theoretically, the hypothesis that flow sandwiched in between two parallel plates obey a parabolic profile is only valid for infinite plates—their dimensions are much larger than the space

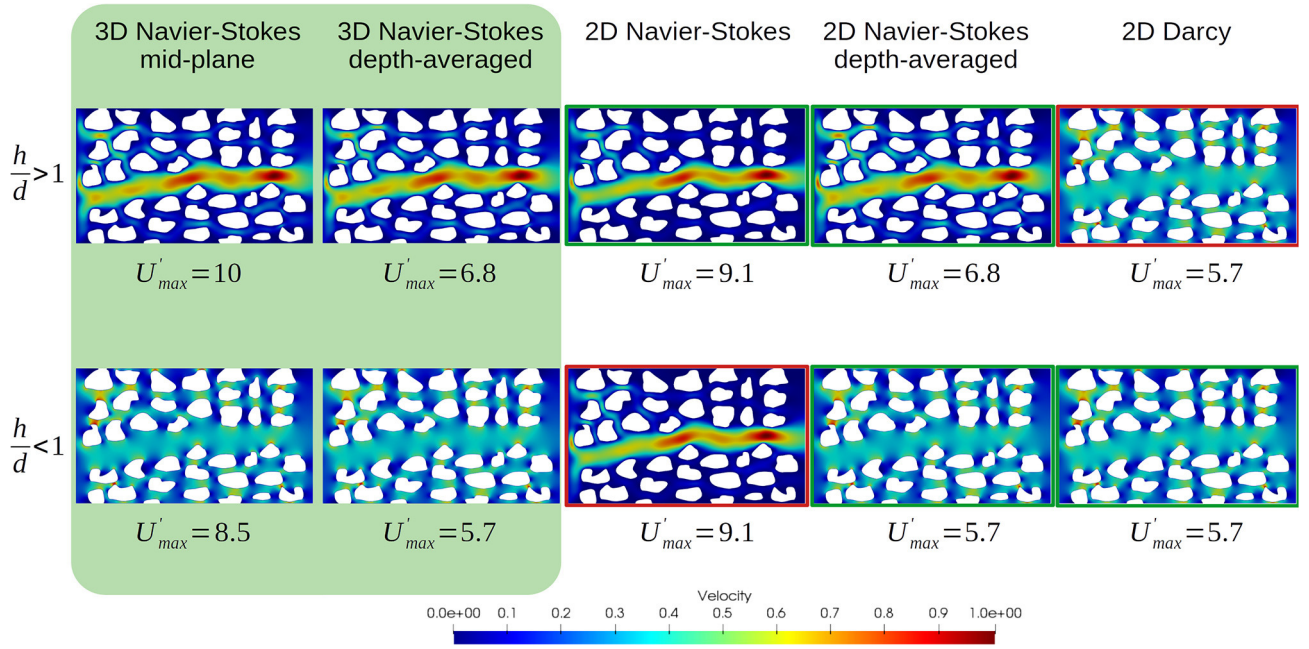

FIGURE 2 | Single-phase flow simulations using 3D, 2D, and 2D-depth-averaged models for different aspect ratio between the micromodel thickness, h and the smallest pore-throat, d. The computational domain is gridded with 1.4×10^5 cells for the 2D cases and $11.4 \times 10^5 \times 10$ for the 3D cases. The typical pore-throat size is $d_{typ} = 4 \times 10^{-3}$ m, the largest is $d_{large} = 12 \times 10^{-3}$ m and the smallest is $d = 0.5 \times 10^{-3}$ m. We used two different depth thickness, namely $h = 10^{-2}$ m and $h = 10^{-4}$ m. Simulations are performed with OpenFOAM. For each simulation, the velocity profile is normalized by the maximum value, and we indicate the maximum value normalized by the inlet velocity. If $\frac{h}{d} > 1$, 2D Navier-Stokes simulations tend toward the mid-plane 3D Navier-Stokes solution and 2D Darcy is far from the reference solution. If $\frac{h}{d} < 1$, 2D Darcy captures the 3D reference solution whereas 2D Navier-Stokes breaks down. The 2D depth-integrated Navier-Stokes model captures the 3D flow behavior regardless the micromodel thickness.

between them. Micromodels mimicking rock porous structures, however, contain pillars that violate this assumption with three-dimensional flowlines at the vicinity of the corner formed by the pillars and the top and bottom plates. Nonetheless, in practice, Equation (13) is a very good approximation of the flow behavior in Hele-Shaw cells. In Roman et al. (2016), the very good agreement in the comparison of the velocity profiles obtained experimentally with micro-PIV and numerically solving Equation (13) illustrates that the depth-averaged flow model is relevant for micromodels. This statement is verified numerically in the simulation results presented in **Figure 2** for which the velocity profile in a micromodel was computed based on 2D, 2D depth-integrated, or 3D simulations for different micromodel thickness. For 3D simulations, the 2/3 factor in the velocity magnitude of the 3D depth-integrated profile with respect to the mid-plane value is representative of a parabolic profile in the third dimension. The 2D Navier-Stokes model only tends to the 3D solution if $h/d > 1$ and corresponds to the 3D mid-plane profile. In this case, the scales separation hypothesis leading to Darcy's law is not satisfied and the 2D Darcy solution cannot describe the flow through the micromodel. If $h/d < 1$, the friction of the fluid along the top and bottom plates are the dominant resistance to the flow. In such a case, the 3D flow tends to the 2D Darcy solution whereas the 2D Navier-Stokes solution—that corresponds to an infinite thickness—is completely off the reference data. The 2D depth-averaged simulations remain consistent with the 3D solution regardless of the aspect ratio.

2.3.2. Single-Phase Scalar Transport

The integration of an advection-diffusion equation for the transport of a scalar—e.g., species concentration or temperature–across the micromodel thickness gives,

$$\frac{\partial \overline{C}^{2D}}{\partial t} + \nabla.\left(\overline{\boldsymbol{v}}^{2D}\overline{C}^{2D}\right) = \nabla.\left(\mathsf{D}(t).\nabla\overline{C}^{2D}\right), \tag{15}$$

where $\overline{\boldsymbol{v}}^{2D}$ is obtained using Equation (13), and $\mathsf{D}(t)$ is a time-dependent dispersion tensor. Because of the parabolic velocity profile in the micromodel depth, there are hydrodynamic dispersion effects that must be considered even if the aspect ratio between the pore-throat size and micromodel thickness is lower than one, $h/d > 1$. For transport in between two parallel plates, the dispersion tensor exactly writes (Dentz and Carrera, 2007),

$$\mathsf{D}(t) = D_i\mathsf{I} + \frac{h^2}{4D_i}\overline{\boldsymbol{v}}^{2D}\overline{\boldsymbol{v}}^{2D}\left(\frac{2}{105} - \sum_{n=1}^{\infty}\frac{18}{(n\pi)^6}\exp\left(-4\left(\frac{n\pi}{h}\right)^2 D_i t\right)\right), \tag{16}$$

where the first term is the molecular diffusion and the second term corresponds to Taylor-Aris dispersion in the direction of the flow (Taylor, 1953; Aris, 1956)—notes that $\overline{\boldsymbol{v}}^{2D}\overline{\boldsymbol{v}}^{2D}$ is a tensor. The

FIGURE 3 | Transport of a scalar in a micromodel with aspect ratio $h/d > 1$. We use 3D, 2D, and 2D-depth-averaged models for different Péclet number by varying the diffusion. The results correspond to isocontour of the concentration for $C = 0.2$ (blue), $C = 0.5$ (green), $C = 0.8$ (orange) at $t = 42$ s. 2D models without dispersion break down for $Pe_h > 10$.

time-dependent infinite series accounts for the pre-asymptotic regime at early time and tends toward zero at long time. In practice, only the two first terms of the series are necessary.

Hydrodynamic dispersion effects are characterized by the Peclet number, $Pe_h = \frac{hU}{D}$, that compares the transport by advection and the transport by diffusion. They are illustrated in the simulation results of **Figure 3** that solve the transport of a scalar using 3D, 2D, and 2D depth-averaged models for Peclet numbers ranging from 0.1 to 10^4. The deviations between mid-plane and depth-averaged values of the 3D simulations illustrate the hydrodynamic dispersion when advection is the dominant transport mechanism. Experimentally, the measurement of species concentration using optical index corresponds to depth-averaged values (Watson et al., 2019). Confusion regarding the nature of measured value may lead to misinterpretations of the comparison between experiments and 3D simulations. For transport dominated by diffusion, $Pe_h < 1$, the concentration profile is flat over the micromodel depth. Therefore, there are no dispersion effects and the 2D models are in good agreement with 3D simulations. If the advection takes over, $Pe_h > 1$, hydrodynamic dispersion becomes important and 2D model breaks down. The two-dimensional depth-averaged simulations using the time-dependant dispersion tensor approximate well the depth-integrated solution of the 3D simulations, regardless the Peclet number. **Figure 4** highlights the importance of considering the pre-asymptotic regime. Neglecting the dispersion (i.e., $\mathsf{D}(t) = D_i\mathsf{I}$) or considering only the asymptotic Taylor-Aris dispersion (i.e., $\mathsf{D}(t) = D_i\mathsf{I} + \frac{h^2\overline{\boldsymbol{v}}^{2D}\overline{\boldsymbol{v}}^{2D}}{210D_i}$) tends to overdisperse the solute. Likewise, it is crucial to consider the product $\overline{\boldsymbol{v}}^{2D}\overline{\boldsymbol{v}}^{2D}$ as a

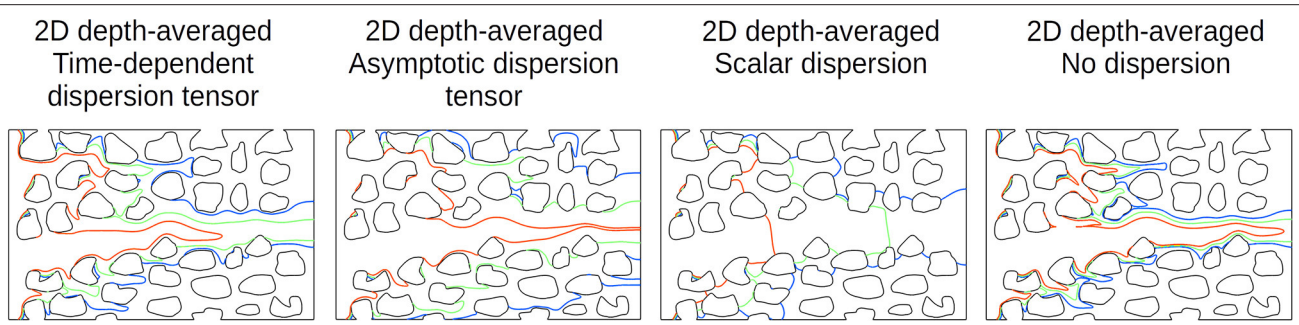

FIGURE 4 | Comparison of the transport of a scalar at $Pe = 10^3$ in a micromodel with aspect ratio $h/d > 1$ using 2D depth-averaged models including time-dependent dispersion tensor, the asymptotic dispersion tensor, isotropic dispersion, and no dispersion. The results correspond to isocontour of the concentration for $C = 0.2$ (blue), $C = 0.5$ (green), $C = 0.8$ (orange) at $t = 42$ s. Neglecting the dispersion [i.e., $\mathrm{D}(t) = D_i\mathrm{I}$] or considering only the asymptotic Taylor-Aris dispersion [i.e., $\mathrm{D}(t) = D_i\mathrm{I} + \frac{h^2\overline{\boldsymbol{v}}^{2D}\overline{\boldsymbol{v}}^{2D}}{210D_i}$] tends to overdisperse the solute. Isotropic dispersion cannot capture the transport of scalars in micromodels.

tensor and not as a scalar $\left|\overline{\boldsymbol{v}}^{2D}\right|^2$ because Taylor-Aris dispersion in microfluidic devices is not isotropic and occurs in the direction of the flow.

2.3.3. Two-Phase Flow

Simulation of two-phase flow processes in microfluidic cells using 2D depth-averaged models is challenging as the fluid-fluid interface has two curvature radii: one in the micromodel plane, another in the micromodel thickness. Horgue et al. (2013) proposes 2D depth-averaged equations in which they integrated the interface curvature along the micromodel thickness in addition to the Hele-Shaw correction. Their model, however, is limited to cases for which no liquid films are flowing on the top and bottom plates, and cannot capture phenomena such as snap-off. Alternatively, Cueto-Felgueroso and Juanes (2014) proposes a Darcy-like model to simulate two-phase flow in Hele-Shaw cells that accounts for water films flowing on the top and bottom plates using relative permeabilities. The applicability of their model, however, is restricted to aspect ratios between the micromodel thickness and the pore-throat size smaller than one, $h/d \ll 1$. In absence of reliable 2D depth-integrated models for two-phase flow, it is recommended to use 3D rather than 2D simulations since the former can capture the impact of wetting films along the top and bottom plates as well as corner flows (Zhao et al., 2019). Moreover, phenomena such as snap-off can only be captured if the two curvature radii are considered (Roman et al., 2017).

2.4. Multi-Scale Approach

Multi-modal pore-size distributions are quite common in geological porous media. This special feature appears, for example, in porous fractured media for which the width of a fracture is orders of magnitude larger than the typical pore throat diameter in the porous matrix. In such a case, a full Navier-Stokes modeling approach requires to resolve all the porosity explicitly and leads to tremendous computational grid size. Alternative approaches including micro-continuum models propose to model only the flow in the fracture using Navier-Stokes while the flow in the matrix is described by Darcy's law (Soulaine and Tchelepi, 2016). Micro-continuum approach relies on a hybrid-scale flow model based on the Darcy-Brinkman-Stokes equation (Brinkman, 1947; Neale and Nader, 1974) discretized with the Finite-Volume Method. All the geometric structures below a threshold that corresponds to the spatial resolution of the simulation is filtered and modeled as a porous medium. The momentum equation reads

$$\frac{1}{\phi}\left(\frac{\partial\rho\overline{\boldsymbol{v}}}{\partial t} + \nabla.\left(\frac{\rho}{\phi}\overline{\boldsymbol{v}}\overline{\boldsymbol{v}}\right)\right) = -\nabla\overline{p} + \nabla.\frac{\mu}{\phi}\left(\nabla\overline{\boldsymbol{v}} + \nabla^t\overline{\boldsymbol{v}}\right) - \mu k^{-1}\overline{\boldsymbol{v}}, \tag{17}$$

where the overline notation denotes filtered variables, ϕ is porosity field, and k is the local permeability of the porous regions. Recent studies show that the micro-continuum framework is well-suited to solve problems involving two characteristic length-scales (e.g., fractured media, micro-porous rocks) (Arns et al., 2005; Scheibe et al., 2015; Soulaine et al., 2016, 2021; Carrillo et al., 2020; Menke et al., 2020; Poonoosamy et al., 2020) and also to describe the movement of fluid/solid interfaces caused by dissolution/erosion and precipitation/deposition (Soulaine and Tchelepi, 2016; Soulaine et al., 2017; Molins et al., 2020) or by solid deformation due to swelling or fracturing (Carrillo and Bourg, 2019). Micro-continuum models are also able to simulate two-phase flow processes (Soulaine et al., 2018, 2019; Carrillo et al., 2020).

3. APPLICATION TO GEOSCIENCES AND OPEN CHALLENGES

In this section, we review the main advances in computational microfluidics involving multiphase flow and reactive transport including the authors' own contributions. We also discuss the open-challenges and the current and future lines of research in this area.

3.1. Modeling of Immiscible Two-Phase Flow

Modeling immiscible multi-phase flow is one the biggest challenge in the porous media community. Despite a very large usage in subsurface engineering, many studies have

emphasized the limits of Darcy's law for two or more fluids (Danis and Quintard, 1984; Rose, 2000; Cinar et al., 2009). An accurate description of the flow mechanisms in porous media is challenged by the complex interplay between capillary, viscous, and gravitational forces that may lead to highly unstable flow and trapping mechanisms. The heterogeneous nature of geological formations further complicates the development of predictive models.

Computational microfluidics for multiphase flow offers an appealing framework to probe the underlying mechanisms in unsaturated porous media. Despite enormous improvements, however, the numerical modeling of multi-phase flow remains challenging. The difficulties are twofold: on the one hand, numeric must be improved (for calculating the interface curvature dynamically, for tracking the composition of the fluids, for speeding-up the simulation times); on the other hand, the physical description of interfacial properties is still not well-established (e.g., wettability conditions, thin films). Current research intends to address these open-challenges by developing reliable and efficient multi-phase flow simulators at the pore-scale.

3.1.1. Efficient Numerical Solvers for Capillary-Dominated Flow

The standard approaches for tracking the interface movement of two immiscible fluids rely on solving single-field equations for the single-field variables, i.e., variables that includes the contribution of each phase. Whether the modeling is grid-based or particle-based, a phase indicator function maps the distribution of the fluids within the pore-space and evolves as the fluid-fluid interface propagates along with hydrodynamic forces. This function denotes either the fluid volume fraction in every grid cells for the Volume-of-Fluid (VOF, Hirt and Nichols, 1981) and phase-field (PF, Jacqmin, 1999) approaches, a distance to the fluid interface for Level-Set (LS, Sussman et al., 1994) approaches, or a color function for Smooth Particles Hydrodynamics (SPH, Tartakovsky and Meakin, 2005) and Lattice Boltzmann Methods (LBM, Gunstensen et al., 1991). The literature also reports on modeling based on the Density Functional Theory for hydrodynamics (Demianov et al., 2014). A review of approaches is found in Wörner (2012). The phase indicator function is used to define single-field variables by weighting the fluid properties (e.g., viscosity, density) according to the distribution of fluid phases. Its gradient is also used to calculate the interface curvature. Today, none of the existing approaches can solve two-phase flow problems accurately and efficiently for a wide range of flow regimes (Abadie et al., 2015). One of the bottlenecks is the existence of spurious velocities near the interface attributed to inaccuracies in the calculation of the interface curvature, regardless of the computational approach. This problem acknowledged for more than 30 years (Brackbill et al., 1992), is particularly limiting for capillary-dominated flow (Scardovelli and Zaleski, 1999) that are the dominant regimes in many subsurface systems (Cinar and Riaz, 2014). An important part of the current research in computational microfluidics for two-phase flow consists in developing robust solvers that minimize these numerical issues (Pavuluri et al., 2018).

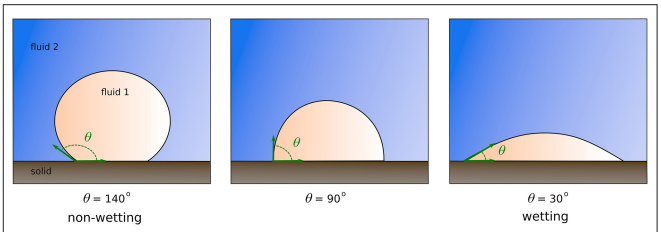

FIGURE 5 | The contact angle, θ, is the angle formed by the tangent to the solid surface and the tangent to the fluid-fluid interface. For values smaller than 90°, a droplet lying on a solid substrate tends to spread over the surface. The fluid within the droplet is the wetting fluid with respect to the other fluid and the solid surface. For values larger than 90°, the droplet is the non-wetting phase and tends to minimize its surface area in contact with the solid substrate.

One of the popular approach in computational microfluidics is the algebraic VOF approach. This is the technique used in the simulations that illustrate the application section. In this technique, the phase indicator functions, α_l and α_g, described the volume fraction of each fluid within each cell of the computational domain and the governing equations are obtained by volume averaging the Navier-Stokes equations over a control volume (Maes and Soulaine, 2020). For incompressible fluids, the continuity equation writes,

$$\nabla.\boldsymbol{v} = 0, \tag{18}$$

the mass balance equation for the liquid phase is

$$\frac{\partial \alpha_l}{\partial t} + \nabla.\left(\alpha_l \boldsymbol{v}\right) + \nabla.\left(\alpha_l \alpha_g \boldsymbol{v}_r\right) = 0, \tag{19}$$

and the momentum equation writes

$$\frac{\partial \rho \boldsymbol{v}}{\partial t} + \nabla.\left(\rho \boldsymbol{v}\boldsymbol{v}\right) = -\nabla p + \rho \boldsymbol{g} + \nabla.\left(\mu\left(\nabla \boldsymbol{v} + \nabla^t \boldsymbol{v}\right)\right) + \boldsymbol{F}_c, \tag{20}$$

where $\boldsymbol{v}_r$ and $\boldsymbol{F}_c$ are sub-grid models that describe the fluid-fluid interactions in cells that contain the interface. They represent the relative velocity and the surface tension force due to the curvature of the interface, respectively. Although other methods such as CFD with level-set (Sussman et al., 1994; Abu AlSaud et al., 2017, 2018) or combinations of LBM and level-set (McClure et al., 2016) can provide a more accurate description of the sharp interface, the VOF method is attractive due to its flexibility, robustness in terms of mass conservation, and adaptability to more complex physic (e.g., multi-component mass transfer). Because the derivation of the governing equations relies on volume averaging principles, algebraic VOF methods are the cornerstone of multi-scale solvers for two-phase flow using micro-continuum (Soulaine et al., 2018, 2019; Carrillo et al., 2020).

3.1.2. Modeling of Wettability and Interfacial Properties

Wettability plays a key role in multiphase flow in porous media (De Gennes, 1985; Singh et al., 2018). Accurate prediction

of multiphase flow in the soils and the subsurface for geo-environmental issues including Carbon Capture and geological Storage, water resources remediation, or Enhanced Oil Recovery requires an in-depth understanding at the pore-scale of the key mechanisms that influence the fluid displacements and dynamics including viscous and capillary forces but also the solid surface wettability. Recent studies have shown that the spatial distribution of wettability play a crucial role (AlRatrout et al., 2018; Yesufu-Rufai et al., 2020). The rock wettability and the resulting multiphase flow can be modified by a change in pore water composition (pH, salinity) and interfacial physicochemical properties. For example, an oil droplet trapped within a pore may be more easily remobilized using low salinity water (Jackson et al., 2016). Accurate modeling of wettability conditions at the mineral surface is therefore crucial to develop efficient and reliable computational microfluidics for two-phase flow.

Traditionally, wettability is described considering that the fluid-fluid interface and the solid surface form a contact angle (see **Figure 5**). The value of the contact angle is provided from static measurements that described the contact angle at the nanoscale. In computational microfluidics, the cell size near the solid surface is usually orders of magnitude larger than nanometers. Therefore, upscaled laws including the Cox-Voinov model estimates an apparent dynamic contact angle that depends on the interface velocity near the solid surface and accounts for viscous bending (Voinov, 1976; Cox, 1986). The alteration of interfacial and solid surface properties due to a change of pH and salinity requires constitutive laws for modifying the contact angle accordingly (Maes and Geiger, 2018). Moreover, flow models based on contact angles break down in the presence of thin water films on the mineral surface (Starov et al., 2007).

Alternative flow models including lubrication theory offer an appealing framework to account for physicochemical mechanisms controlling the wettability of rocks according to pore water chemistry and surface roughness for instance (Abu AlSaud et al., 2017, 2020). Instead of using a contact angle, lubrication theory provides a partial differential equation governing the evolution of the film thickness, δ, on the solid surface including molecular forces (Pahlavan et al., 2018). It reads,

$$\frac{\partial \delta}{\partial t} + \frac{1}{\mu_w} \nabla . \left[\left(\frac{\delta^3}{3} \nabla \left(\sigma \kappa - \Pi \left(\delta \right) \right) \right) + \frac{\delta^2 \tau}{2} \right] = 0, \qquad (21)$$

where μ_w is the water viscosity, σ is the surface tension, κ is the interface curvature, $\Pi(\delta)$ is the disjoining pressure term, and τ is the shear-stress exerted on the film surface. The disjoining – or Derjaguin– pressure includes attractive (e.g., van der Waals) and repulsive (e.g., electrostatic) forces that change with the ionic strength, i.e., pH and salinity. The film equation is solved on the solid surface and is coupled with the two-phase Navier-Stokes solver in the volume of the pore. By getting rid of the concept of contact angle, it is believed that simulators using lubrication models are more realistic and mechanistic for the description of multiphase systems in geological formations for energy and environmental issues. Applications include the modeling of wettability alteration measured in supercritical CO_2 stored in deep saline aquifers (Wan et al., 2014) and the detachment of crude oil from mineral surface observed when changing the brine from high to low salinity (Berg et al., 2010). The state-of-the-art computational microfluidics using lubrication theory, however, is limited to flat solid boundaries (Abu AlSaud et al., 2017, 2020). Recent work considers curvilinear surfaces on cylindrical solids (Qin et al., 2020). However, pore-scale multiphase flow solvers with lubrication models on generic solid geometries are still under development.

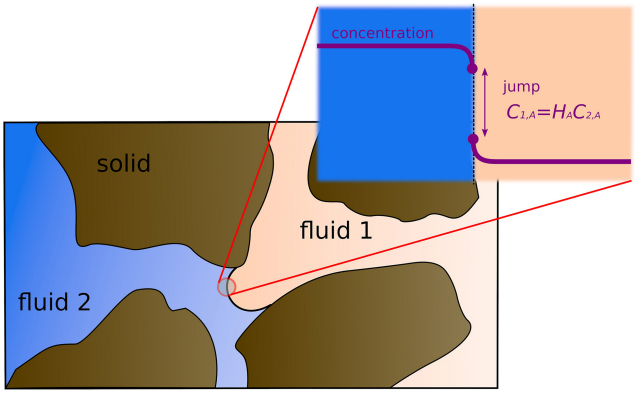

FIGURE 6 | Illustration of multicomponent mass transfer in two-phase flow at the pore-scale. Thermodynamic equilibrium at the fluid/fluid interface obeys a partitioning relationship such as Henry's law.

3.1.3. Modeling of Species Transfer Across Fluid-Fluid Interfaces

In many subsurface processes including the injection and sequestration of supercritical carbon dioxide (sCO_2) into deep geological formations, there is a transfer of species across the fluid-fluid interface. Moreover, the ability to track the composition of fluids in two-phase flow is crucial for modeling efficiently the change of wettability conditions with pH evolution (Maes and Geiger, 2018). The Continuous Species Transfer (CST) approach allows tracking multicomponent multiphase flow at the pore-scale (Haroun et al., 2010; Marschall et al., 2012). In this approach, the thermodynamic equilibrium at the interface is described by a partitioning relationship such as Henry's law (Henry, 1803) and the continuity of mass fluxes is guaranteed while the interface evolves in the pore-space due to fluid displacements including drainage and imbibition (see **Figure 6**).

CST is a single-field approach along the same lines as the Volume-Of-Fluid technique used for simulating immiscible two-phase flow, i.e., a unique partial differential equation solves for a single-field concentration regardless of the content of a grid block. It reads,

$$\frac{\partial C_A}{\partial t} + \nabla . \left(\boldsymbol{v} C_A \right) = \nabla . \left(D_A^* \left(\nabla C_A + \Phi_A \right) \right), \qquad (22)$$

where D_A^* is the weighted-average of the diffusion coefficients in both fluids and Φ_A is the CST flux enforcing the concentration discontinuity due to Henry's law. Graveleau et al. (2017) derived

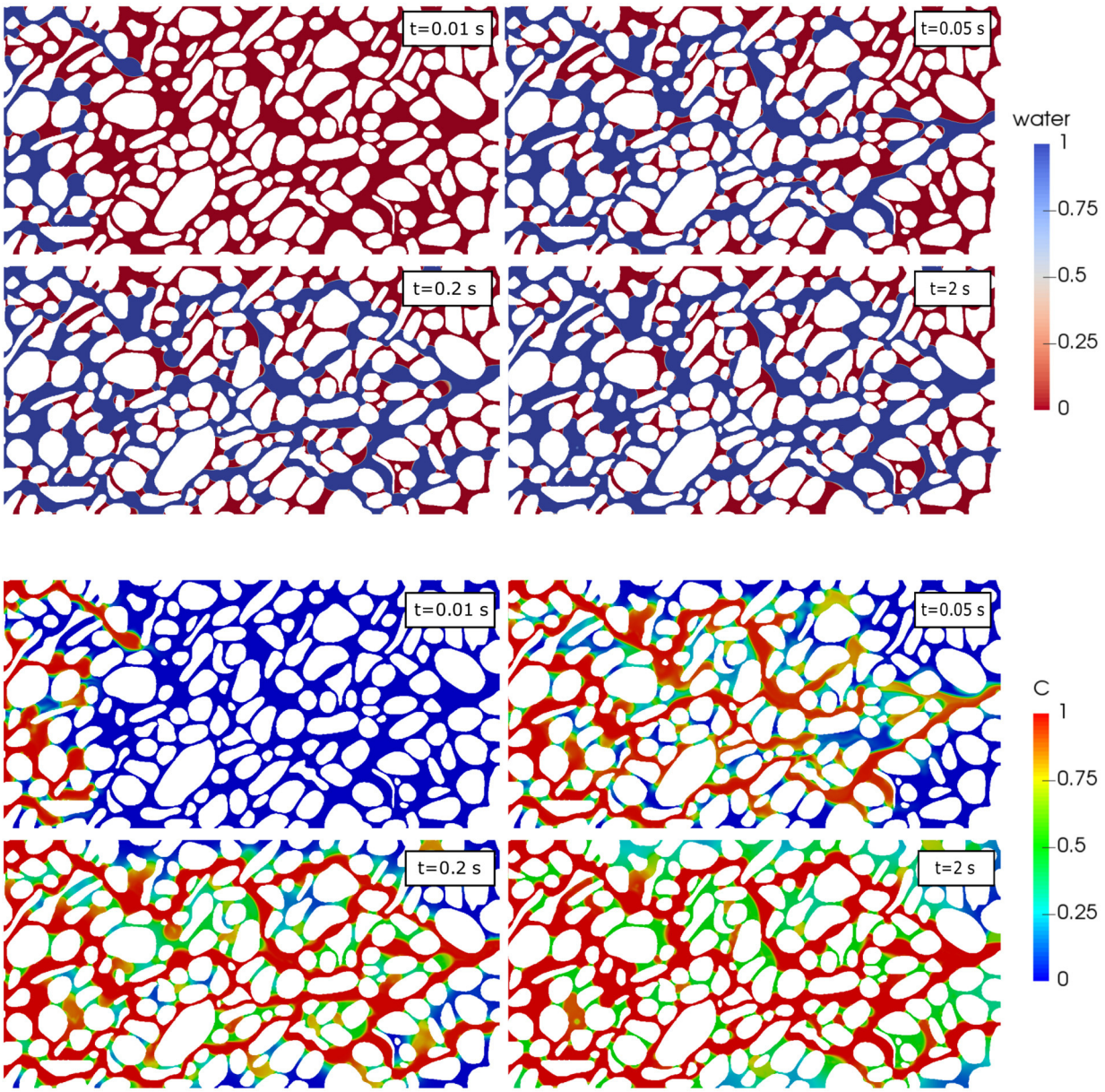

FIGURE 7 | Simulation results of drainage of oil (wetting phase) by water with multi-component mass transfer at the pore-scale. The white pillars correspond to the solid grains. **Top:** distribution of the fluid phases during the drainage at different timestep. **Bottom:** concentration profile in the system (adapted from Maes and Soulaine, 2018b).

a boundary condition on a wetted wall for the CST and used the modeling approach to upscale the rate of mass transfer in unsaturated porous media as a function of the flow rates. Yang et al. (2017), however, pointed out that when convection dominates diffusion locally near the interface, the CST method generates large numerical errors. They show that in order to capture the species concentration discontinuity accurately, the mesh should be extremely refined at the vicinity of the interface. This workaround, however, increases dramatically the computational cost, especially for advection-dominated systems. The CST derivation was carefully revisited using the method of volume averaging (Maes and Soulaine, 2018b) leading to a new approach without limitation on the transport regimes or the grid refinement level—referred to as Compressive-CST or simply C-CST—that is fully consistent with the phase advection scheme unlike the standard CST scheme that was causing unbalanced mass transfer. C-CST can simulate the mass transfer of a passive scalar in a dynamic system (see **Figure 7**), and therefore, enable the assessment of the mean rate of mass transfer in unsaturated porous media in terms of saturation, flow rates and interfacial

area. C-CST can be used to evaluate the role played on the mass transfer by the internal re-circulation within the trapped droplets that was observed experimentally using microfludics (Roman et al., 2016, 2020; Zarikos et al., 2018).

In more recent work, the C-CST has been extended for modeling cases for which the species transfer across the fluid-fluid interface is no longer passive but leads to local volume changes (Maes and Soulaine, 2020). Such situations happen, for example, when a soda can is opened, the pressure in the headspace falls abruptly and Henry's law is no longer satisfied. To re-establish equilibrium, the carbon dioxide concentration in water decreases by forming gas bubbles. During their travel toward the surface, gas bubbles grow because of the diffusive flux from the carbon dioxide dissolved in the liquid (Power et al., 2009). The other way around occurs in carbon sequestration processes when sCO_2 is stored in deep saline aquifers by capillary effects and trapped sCO_2 droplets dissolve into the surrounding brine (Kim et al., 2012). As a consequence, the volume of droplets decreases, and the equilibrium of hydrodynamic forces that was maintaining the sCO_2 trapped in the pore-space is displaced, eventually leading to a mobilization of the droplets. Computational microfluidics using C-CST for phase change can estimate the volume of CO_2 trapped in the porous structure and assess the timescale of potential remobilization.

3.1.4. Multi-Scale Two-Phase Flow

The micro-continuum approach for two-phase flow enables the simultaneous modeling of multiphase flow at two different length scales: *(i)* a Darcy-scale where sub-voxel fluid-fluid and fluid-solid interactions within a porous medium are modeled through relative permeability and capillary constitutive models, *(ii)* a pore-scale (or Navier-Stokes scale) where the solid material is non-porous and fluid-fluid interactions are described through a continuum representation of the Young-Laplace equation. The model combines the Volume-of-Fluid approach for tracking the fluid-fluid interface in regions free of solid and the Darcy-Brinkman-Stokes equation for modeling flow in porous regions (Soulaine et al., 2019). It includes classic concepts such as saturation, relative permeability, and capillary pressure curves in the porous matrix (Carrillo et al., 2020). This multiscale approach offers new possibilities in computational microfluidics to investigate multiphase flow in fractured porous media including the fracture-matrix interactions and to study the role played by microporosity in processes such as imbibition and drainage.

For example, the two-phase micro-continuum model was used to simulate the expulsion of methane stored in microporous matrix into a soaked fracture (see **Figure 8**). The results highlight two completely different expulsion flow regimes whether the fracture boundaries are hydrophobic or hydrophilic. On the one hand, there is a continuous gas production, and on the other hand a bubbly regime because the surface tension effects at the wet fracture boundary generate an energetic barrier that tends to form gas bubbles as far as the pressure in the microporous regions is sufficient to inflate them. This kind of simulations enables the assessment of the rate of hydrocarbon recovery in shale gas according to the spatial distribution of the kerogen

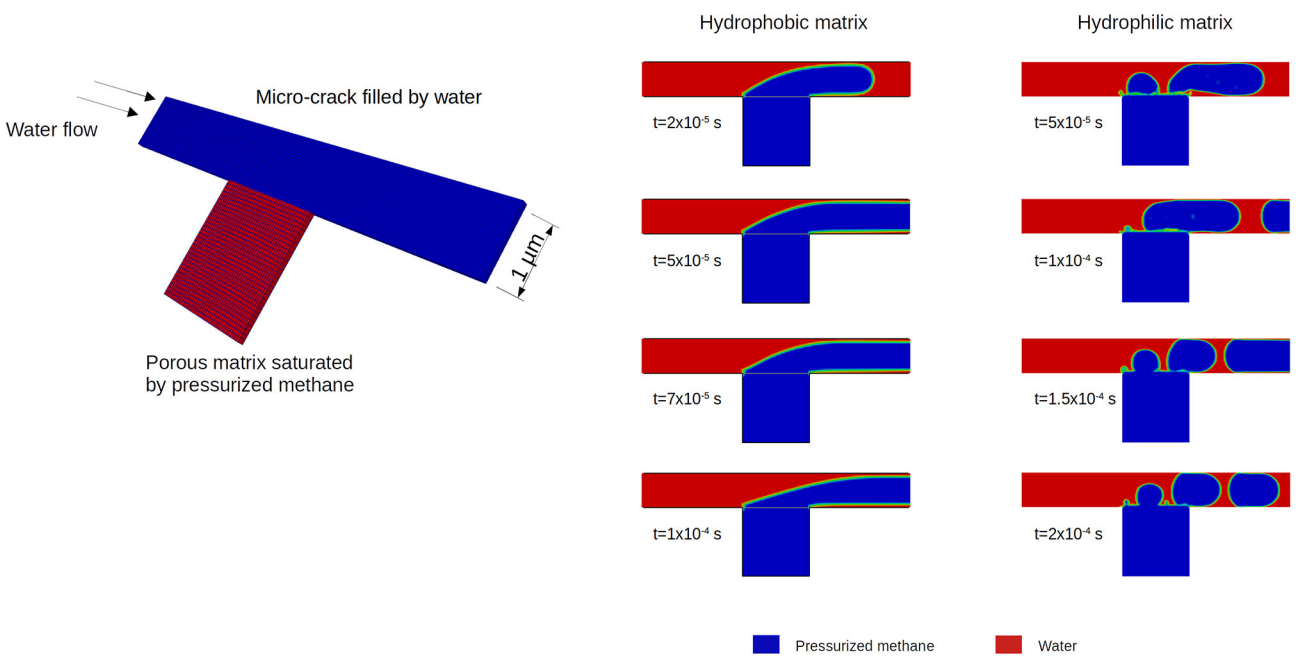

FIGURE 8 | Multi-scale simulations of the expulsion of methane stored in a microporous matrix into a soaked fracture. We investigated two scenarios: the fracture/matrix interface is non-wetting and the methane production is continuous, and the fracture/matrix interface is wetting and the gas is produced in a bubbly flow regime. The simulation setup is fully described in Soulaine et al. (2019).

(hydrophobic) and clay (hydrophilic) in the vicinity of the micro-cracks (Soulaine et al., 2019).

3.1.5. Three-Phase Flow

Computational microfluidics for three-phase flow (e.g., gas-water-oil) are still scarce in the literature because the community focuses mostly on two-phase flow simulators for which the open challenges discussed in previous sections are still limiting the predictive capabilities. Such a tool is crucial to understand fully the underlying mechanisms of non-aqueous phase liquid (e.g., hydrocarbon, chlorinated solvents) trapped in the unsaturated zone by capillary effects and to propose innovative remediation strategies. In the literature, Bayestehparvin et al. (2015) use a Volume-of-Fluid approach, Helland et al. (2017) and Mohammadmoradi and Kantzas (2017) use quasi-static displacement using a Level-Set method, Tartakovsky and Panchenko (2016) use Smooth Particle Hydrodynamics, Dinariev and Evseev (2016) use a phase-field method and van Kats and Egberts (1999) and Jiang and Tsuji (2017) use a lattice-Boltzmann method to investigate three-phase Navier-Stokes flow at pore scale. The development of efficient three-phase flow simulators at the pore-scale is still under development and microfluidic experiments will help to assess the robustness of the computational models.

3.2. Reactive Transport Modeling at the Pore-Scale

Most of computational microfluidics developments so far have been devoted to solve the Navier-Stokes equations under single (Spanne et al., 1994; Bijeljic et al., 2013; Guibert et al., 2015; Soulaine et al., 2016) and two-phase flow conditions (Horgue et al., 2013; Raeini et al., 2014; Graveleau et al., 2017; Maes and Soulaine, 2018a; Pavuluri et al., 2020). Flow in geological porous media, however, has the distinctive feature to interact chemically with the solid walls. The consideration of surface reactions in computational microfluidics requires inclusion of comprehensive reaction networks along with flow and transport, an approach known as Reactive Transport Modeling (Steefel et al., 2005). Despite the growing investment in the development of RTM at the pore-scale—pioneer simulators date back to the late 90s (Békri et al., 1995, 1997)—the field is still in its infancy. The main challenge consists in moving the fluid/solid boundary with respect to chemical reactions at the mineral surfaces. A large variety of methodologies has been proposed by the community to solve this problem and a comprehensive review can be found in Molins et al. (2020). They include Level-Set (Molins et al., 2014, 2017), or phase-field (Xu and Meakin, 2008, 2011) techniques in a Eulerian grid, LBM (Kang et al., 2003; Szymczak and Ladd, 2009; Prasianakis et al., 2013; Chen et al., 2014b; Yoon et al., 2015), SPH (Tartakovsky et al., 2007), and Arbitrary Lagrangian-Eulerian (Oltéan et al., 2013; Starchenko et al., 2016) frameworks. Another family of methods for displacing the mineral interface uses the micro-continuum approach (Soulaine and Tchelepi, 2016; Soulaine et al., 2017).

3.2.1. Modeling of Dissolution Processes

The modeling of pore-scale dissolution is the most advanced of the reactive transport processes using computational microfluidics. In this case, the solid mineral dissolves into the fluid phase according to thermodynamics and chemical reactions at the solid surface. High-resolution data of well-controlled microfluidic experiments have highlighted that the shape of a cylindrical crystal evolves into an elongated profile due to

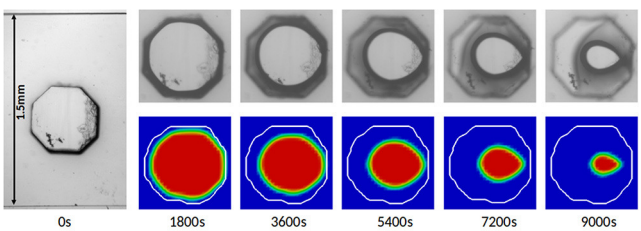

FIGURE 9 | Experimental **(top)** and computational **(bottom)** microfluidics images of calcite dissolution process at different time steps during the injection of 0.05% HCl at a mean velocity of 1.16×10^{-3} m/s flow rate from the left to the right (Reprinted with permission from Soulaine et al., 2017, Copyright Cambridge University Press 2017).

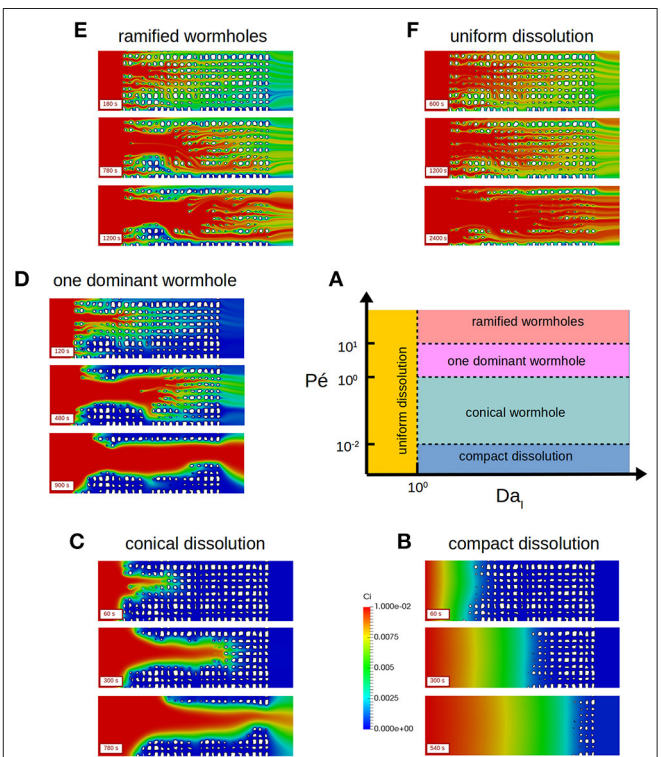

FIGURE 10 | Prediction of the evolution of the pore space of a micromodel for different values of the constant of reaction and of the diffusion coefficient. Five different dissolution regimes are identified **(A)** namely compact dissolution **(B)**, conical dissolution **(C)**, one dominant wormhole **(D)**, ramified wormholes **(E)**, and uniform dissolution **(F)** (Reprinted with permission from Soulaine et al., 2017, Copyright Cambridge University Press 2017).

non-uniform distribution of the solute along the solid surface leading to faster dissolution rates upstream than downstream (Soulaine et al., 2017; Dutka et al., 2020) as illustrated in **Figure 9**. The elongated profile of the crystal as it dissolved in the acid flowing solution illustrates well the complex coupling between streamlines, solute transport, and surface reaction. The state-of-the-art of computational microfluidics for reactive transport using different techniques including micro-continuum, Level-Set, LBM, moving grids with conformal mapping, and Vortex methods can reproduce the shape evolution of the dissolving crystal with great fidelity (Molins et al., 2020). This success leads to the strong conclusion that pore-scale technologies for moving fluid-solid boundaries along with geochemical reactions are now mature enough to be used as predictive tools. Current development uses computational microfluidics along with geochemical packages to model comprehensive reaction networks.

Computational microfluidics was used to investigate the dissolution of micro-model pore networks (Szymczak and Ladd, 2009; Kang et al., 2014; Molins et al., 2017; Soulaine et al., 2017). Five different dissolution regimes are observed according to the constant of reaction at the mineral surface and the injection mass flow rate as illustrated in **Figure 10**. For a given fluid, these two effects are characterized by the Damkohler number Da_I (i.e., ratio of the characteristic timescale of transport and surface reaction) and the Peclet number Pe (i.e., ratio of advection and diffusion), respectively. These regimes are: compact dissolution ($Pe < 10^{-2}$ and $Da_I > 1$), conical dissolution ($1 > Pe > 10^{-2}$ and $Da_I > 1$), dominant wormhole ($10 > Pe > 1$ and $Da_I > 1$), ramified wormholes ($Pe > 10$ and $Da_I > 1$) and uniform dissolution ($Da_I < 1$ and regardless the Peclet number). Because computational microfluidics provides a full mapping of the species and mineral evolution in the system, macroscopic properties can be obtained directly by averaging the simulation results, something that is barely achievable experimentally. For example, knowing the exact distribution of solute concentration including the local mass flux at the mineral surface (Soulaine et al., 2017) volume-averaged the pore-scale results and proposed a new law for quantifying the accessible reactive surface area, A, based on the transport and reactivity conditions. It reads

$$\frac{A}{A_0} = 1 - \exp\left(-Pe^{-n} Da_I^{-m}\right), \tag{23}$$

where A_0 is the geometric surface area of the porous sample and n and m are model parameters. Similar relations that reduce the accessible surface area based on hydrodynamics conditions were used to reconcile experimental or numerical data at the larger scales (Wen and Li, 2017; Deng et al., 2018).

3.2.2. Modeling of Precipitation Processes

Although computational microfluidics for simulating precipitation processes are reported in the literature (Tartakovsky et al., 2007; Li et al., 2008; Yoon et al., 2012; Huber et al., 2014; Chen et al., 2015; Prasianakis et al., 2017; Ray et al., 2019), the field is still scarce and more development and verification are required to reach predictive capabilities. Pore-scale precipitation cannot be treated simply as the reverse problem of dissolution. Indeed, the creation of the solid phase during the precipitation of minerals needs to consider the nucleation of mineral at the solid surface. Moreover, the development of depth-averaged model for precipitation is challenging because in microfluidic experiments it is possible that precipitate preferentially form either on the top and bottom plates or in the bulk (Beuvier et al., 2015; Yoon et al., 2019). Model verification will use the ability of microfluidics to design well-controlled experiments along with high-resolution imaging and chemical characterization (Poonoosamy et al., 2020).

3.2.3. Multi-Scale Reactive Transport Models

Hybrid-scale models have been proposed to describe reactive systems that include multiple characteristic length-scales for which some regions are described using pore-scale modeling while others are modeled with continuum approaches (Liu and Ortoleva, 1996; Liu et al., 1997). Two kinds of approaches solve hybrid-scale problems. On the one hand, the domain

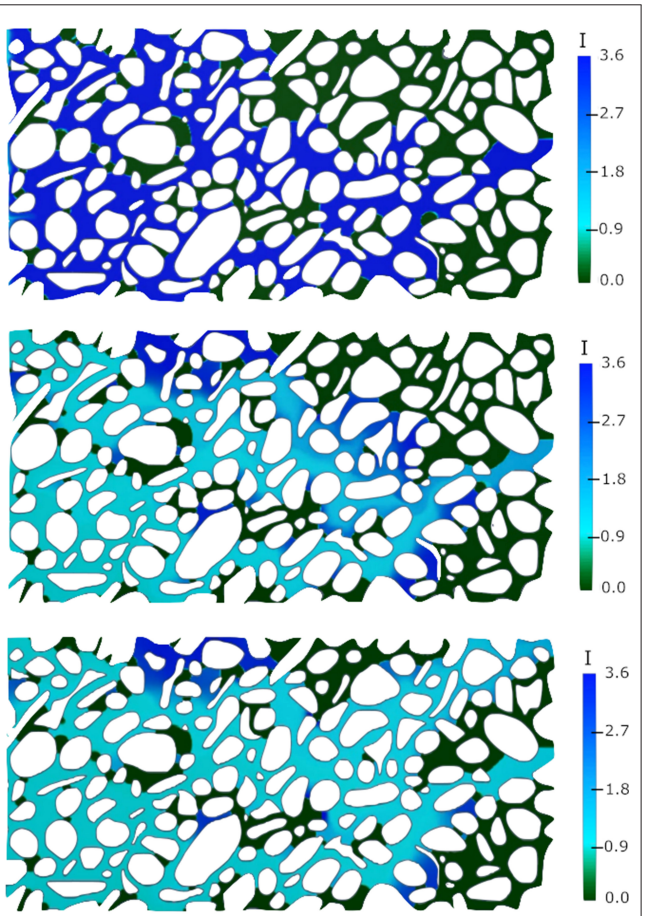

FIGURE 11 | Numerical simulation of tertiary low-salinity flooding in a micromodel. The colormap corresponds to the ionic strength (mol/l) in the domain. The non-aqueous phase appears in green (I = 0), the high salinity water appears in dark blue (I = 3.6) and the low-salinity water appears in light blue (I = 0.9). The simulation parameters are fully described in Maes and Geiger (2018).

decomposition technique solves different physics on separate domains—one for Darcy flow, another for Stokes flow—linked together through appropriate boundary conditions (Tartakovsky et al., 2008; Molins et al., 2019). On the other hand, micro-continuum models use a single set of partial differential equations throughout the computational domain regardless of the content of a grid block (Steefel et al., 2015; Soulaine and Tchelepi, 2016). The latter approach is particularly well-suited to capture the dynamic displacement of the interface between the porous and solid-free regions without involving complex re-meshing strategies. For example, micro-continuum models have been used successfully to simulate the formation and growth of wormholes in acidic environments (Ormond and Ortoleva, 2000; Golfier et al., 2002; Soulaine and Tchelepi, 2016; Faris et al., 2020).

3.2.4. Two-Phase Flow in Reactive Environments

The dynamics modeling of multiphase flow phenomena in reactive environments is quite complex because it involves tracking multiple interfaces that evolve as a function of the details of the reactive transport: on the one hand, the fluid/fluid interface is subject to surface tension forces, on the other hand, the fluid/solid interface moves with chemical reactions at the surface of the solid minerals. The modeling is complicated by the dynamics of the contact line or thin films along the solid walls, and by the transfer of mass across interfaces. Few research works have been devoted to the modeling of multiphase flow with solid boundaries that evolve with chemical reactions. Parmigiani et al. (2011) have proposed an LBM approach to study the evolution of capillary fingers in a porous medium that dynamically evolves with the melting of the solid phase. Later, LBM has been extended to multicomponent multiphase fluid flow and applied to reactive transport with dissolution and precipitation (Chen et al., 2013, 2015). LBM-based approaches, however, are unstable for high-density ratios between the liquid and the gas (Chen et al., 2014a), which, therefore, limits the predictive aspects of such modeling frameworks.

Alternatively, multicomponent multiphase reactive transport can be modeled using the Volume Of Fluid method to track the fluid/fluid interface and the C-CST approach to model the transport of reactive species in the system, including the effect of speciation and surface reactions (Maes and Menke, 2020). Maes and Geiger (2018) used this model to track pH, solid surface potential and contact angle alteration during injection of low-salinity water in micromodels and were able to observe and characterize for the first time the effect of secondary and tertiary low-salinity flooding at the pore-scale (**Figure 11**). Moreover, Soulaine et al. (2018) proposes new computational microfluidics

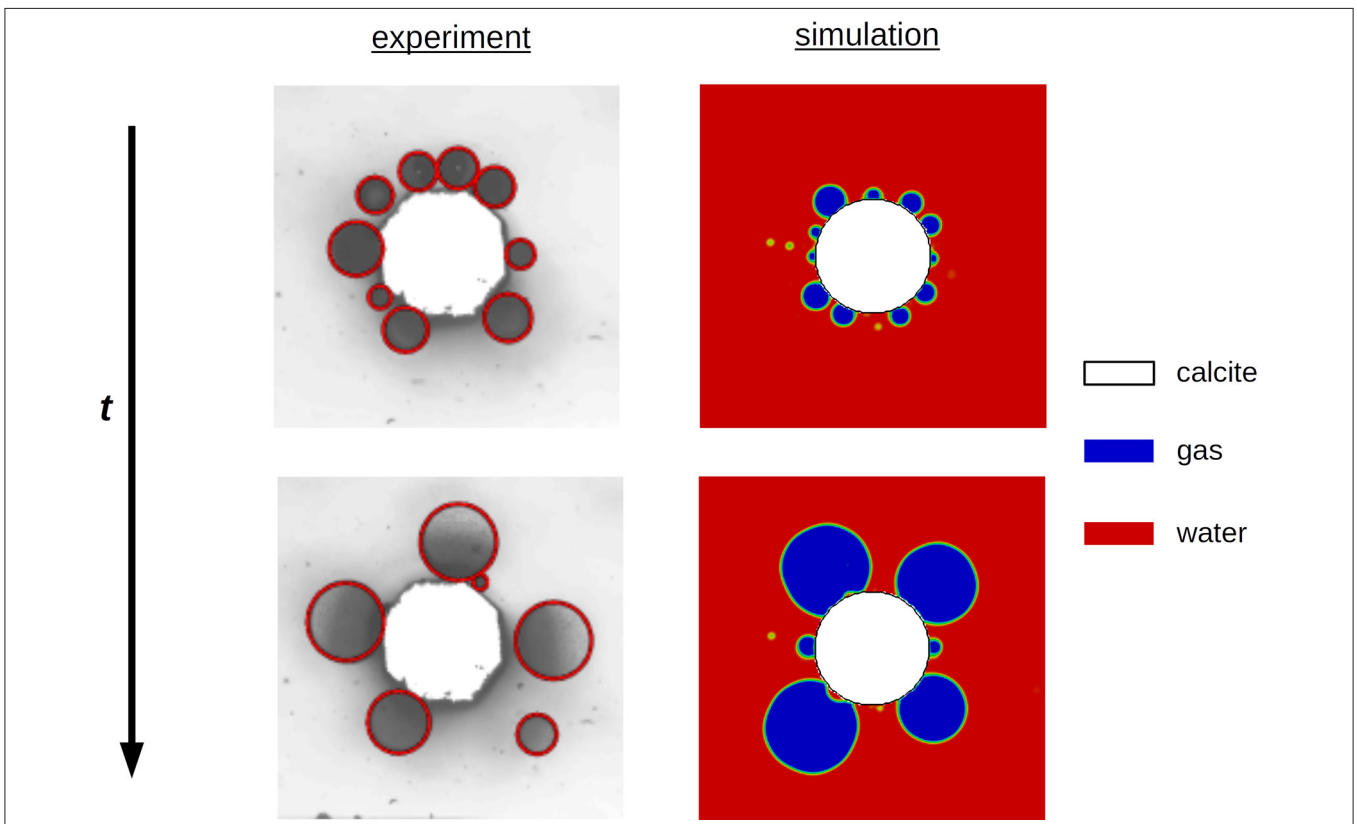

FIGURE 12 | Comparison between experimental and computational microfluidics. A calcite crystal is dissolved in a flow of hydrochloric acid at atmospheric conditions. Carbon dioxide gas bubbles nucleate at the mineral surface, grow, coalesce, and eventually detach. The micro-continuum model for two-phase flow in reactive environments can reproduce accurately the microfluidic experiments. The microfluidic experiment and simulation are fully described in Soulaine et al. (2018).

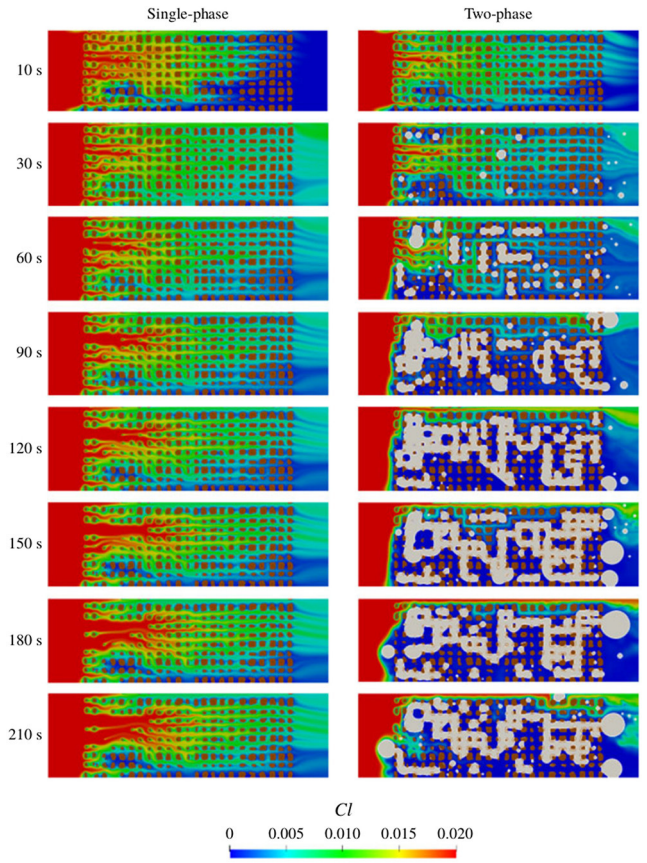

FIGURE 13 | Evolution of a porous medium during the injection of acid. The color map corresponds to the concentration of acid in the domain. Solid grains are depicted in brown. **(Left)** Under single-phase flow conditions, the acid penetrates the domain and dissolves the solid grains producing wormholes. **(Right)** The mineral dissolution generates CO_2 gas that occupies the pore space, limits the dissolution process and prevents the development of wormholes (Reprinted with permission from Soulaine et al., 2018, Copyright Cambridge University Press 2018).

to simulate mineral dissolution in unsaturated porous media. The model combines the reactive micro-continuum approach developed in Soulaine et al. (2017) with the VOF and C-CST methods. Chemical reactions and wettability conditions at the mineral surface are described as immersed boundaries that evolve with the dissolution of the solid phase. Microfluidic experiments that consist of a calcite crystal dissolving in a microchannel after the injection of an aqueous solution containing up to 1% of hydrochloric acid were used to verify the predictive aspect of the model (see **Figure 12**).

The model has been used to investigate the effect of carbon dioxide production during the acidizing of carbonate formations. Results show that under single-phase flow conditions, i.e., when the dissolution time of CO_2 into the aqueous phase is instantaneous, the solid structure dissolves forming wormholes. However, if the characteristic time scale of CO_2 dissolving in brine is much longer compared to the rate of gas production, then CO_2 bubbles grow, coalesce and form flow barriers that limit the transport of the acid in the domain (see **Figure 13**). These flow barriers prevent the emergence of wormholes and limit significantly the overall dissolution rate. This finding is of great interest in acid stimulation processes for which a gas phase can be produced (Prutton and Savage, 1945; Thompson and Gdanski, 1993). Hence, the presence of a second fluid phase under the same flow conditions may lead to very different dissolution regimes, and the common behavior diagrams that characterize the dissolution pattern based on the Peclet and Damkohler numbers (Golfier et al., 2002) have to be complemented, at a minimum, by a third dimension that quantifies the solubility of the CO_2 in the aqueous phase.

4. CONCLUSION AND PERSPECTIVES

Computational microfluidics for geosciences offers an appealing framework to investigate the coupled processes in geological porous media. The integrated usage of experimental and computational microfluidics is, therefore, a powerful approach to decipher the complex mechanisms that occur in the soils and the subsurface and to bring new insights into the open challenges associated with the continuum-scale modeling of flow and transport in geological systems. Microfluidic experiments provide valuable benchmark data sets, leading to more accurate and robust numerical solvers, while numerical simulations augment microfluidic experiments by providing high-resolution mapping of pressure and velocity profiles, solute concentration, and mineral distribution that are not easily measurable experimentally. Modern approaches can simulate pore-scale events over a wide range of conditions including multiphase flow and the microstructure evolution due to precipitation and dissolution. Combining experimental and computational microfluidics have led to new insights into complex subsurface processes, such as CO_2 geological storage, low salinity flooding and acid stimulation. The paper presents a snapshot of the current capabilities and discuss the validity of depth-averaged models.

The future of this emerging scientific discipline is guaranteed by the continuous improvements of numerical algorithms, modeling, and high-performance computing. The next generations of computational microfluidics will be able to simulate the transport of particles including the micro-dynamics of colloids, their aggregation and stability, the attachment/detachment from the solid walls, and pore-clogging mechanisms according to pH ad salinity conditions. This will necessitate handling the strong coupling between hydro-electro-chemical effects. Important efforts will be dedicated to the consideration of biological processes including the growth of biofilms.

AUTHOR CONTRIBUTIONS

All authors listed have made a substantial, direct and intellectual contribution to the work, and approved it for publication.

ACKNOWLEDGMENTS

We acknowledge the first reviewer for suggesting time-dependent dispersion. The research leading to these results has received support from the French Agency for Research (Agence Nationale de la Recherche, ANR) through the Equipex Planex ANR-11-EQPX-36, the Labex Voltaire ANR-10-LABX-100-01, the grant CATCH ANR-18-CE05-0035, and through the FraMatI project under contract ANR-19-CE05-0002. It has also received financial support from the CNRS through the MITI interdisciplinary programs, and from the UK EPSRC funded project on Direct Numerical Simulation for Additive Manufacturing in Porous Media (grant reference EP/P031307/1). Finally, SR and JM would like to thank ALLIANCE (Partenariat Hubert Curien) for the grant that enable the scholar exchange of scientists.

REFERENCES

Abadie, T., Aubin, J., and Legendre, D. (2015). On the combined effects of surface tension force calculation and interface advection on spurious currents within volume of fluid and level set frameworks. *J. Comput. Phys.* 297, 611–636. doi: 10.1016/j.jcp.2015.04.054

Abu AlSaud, M. O., Esmaeilzadeh, S., Riaz, A., and Tchelepi, H. A. (2020). Pore-scale study of water salinity effect on thin-film stability for a moving oil droplet. *J. Colloid Interface Sci.* 569, 366–377. doi: 10.1016/j.jcis.2020.02.044

Abu AlSaud, M. O., Popinet, S., and Tchelepi, H. A. (2018). A conservative and well-balanced17 surface tension model. *J. Comput. Phys.* 371, 896–913. doi: 10.1016/j.jcp.2018.02.022

Abu AlSaud, M. O., Soulaine, C., Riaz, A., and Tchelepi, H. A. (2017). Level-set method for accurate modeling of two-phase immiscible flow with moving contact lines. *arXiv[Preprint]. arXiv:1708.04771*.

Agrawal, P., Raoof, A., Iliev, O., and Wolthers, M. (2020). Evolution of pore-shape and its impact on pore conductivity during co2 injection in calcite: single pore simulations and microfluidic experiments. *Adv. Water Resour.* 136:103480. doi: 10.1016/j.advwatres.2019.103480

Alpak, F., Riviere, B., and Frank, F. (2016). A phase-field method for the direct simulation of two-phase flows in pore-scale media using a non-equilibrium wetting boundary condition. *Comput. Geosci.* 20, 881–908. doi: 10.1007/s10596-015-9551-2

AlRatrout, A., Blunt, M. J., and Bijeljic, B. (2018). Spatial correlation of contact angle and curvature in pore-space images. *Water Resour. Res.* 54, 6133–6152. doi: 10.1029/2017WR022124

Andre, H., Combaret, N., Dvorkin, J., Glatt, E., Han, J., Kabel, M., et al. (2013a). Digital rock physics benchmarks Part I: imaging and segmentation. *Comput. Geosci.* 50, 25–32. doi: 10.1016/j.cageo.2012.09.005

Andre, H., Combaret, N., Dvorkin, J., Glatt, E., Han, J., Kabel, M., et al. (2013b). Digital rock physics benchmarks Part II: computing effective properties. *Comput. Geosci.* 50, 33–43. doi: 10.1016/j.cageo.2012.09.008

Aris, R. (1956). On the dispersion of a solute in a fluid flowing through a tube. *Proc. R. Soc. A.* 235, 67–77. doi: 10.1098/rspa.1956.0065

Arns, C., Bauget, F., Limaye, A., Sakellariou, A., Senden, T., Sheppard, A., et al. (2005). Pore-scale characterization of carbonates using x-ray microtomography. *SPE J.* 10, 475–484. doi: 10.2118/90368-PA

Bayestehparvin, B., Abedi, J., and Ali, S. M. F. (2015). "Dissolution and mobilization of bitumen at pore scale," in *SPE Canada Heavy Oil Technical Conference* (Calgary, AL: Society of Petroleum Engineers). doi: 10.2118/174482-MS

Békri, S., Thovert, J., and Adler, P. (1995). Dissolution of porous media. *Chem. Eng. Sci.* 50, 2765–2791. doi: 10.1016/0009-2509(95)00121-K

Békri, S., Thovert, J.-F., and Adler, P. (1997). Dissolution and deposition in fractures. *Eng. Geol.* 48, 283–308. doi: 10.1016/S0013-7952(97)00044-6

Berg, S., Cense, A., Jansen, E., and Bakker, K. (2010). Direct experimental evidence of wettability modification by low salinity. *Petrophysics* 51, 314–322.

Beuvier, T., Panduro, E. A. C., Kwaśniewski, P., Marre, S., Lecoutre, C., Garrabos, Y., et al. (2015). Implementation of *in situ* saxs/waxs characterization into silicon/glass microreactors. *Lab Chip* 15, 2002–2008. doi: 10.1039/C5LC00115C

Bijeljic, B., Raeini, A., Mostaghimi, P., and Blunt, M. J. (2013). Predictions of non-fickian solute transport in different classes of porous media using direct simulation on pore-scale images. *Phys. Rev. E* 87:013011. doi: 10.1103/PhysRevE.87.013011

Bird, R. B., Stewart, W. E., and Lightfoot, E. N. (2002). *Transport Phenomena, 2nd Edn*. New York, NY: John Wiley Sons, Inc.

Blunt, M. J., Bijeljic, B., Dong, H., Gharbi, O., Iglauer, S., Mostaghimi, P., et al. (2013). Pore-scale imaging and modelling. *Adv. Water Resour.* 51, 197–216. doi: 10.1016/j.advwatres.2012.03.003

Brackbill, J. U., Kothe, D. B., and Zemach, C. (1992). A continuum method for modeling surface tension. *J. Comput. Phys.* 100, 335–354. doi: 10.1016/0021-9991(92)90240-Y

Brinkman, H. C. (1947). A calculation of the viscous force exerted by a flowing fluid on a dense swarm of particles. *Appl. Sci. Res. A* 1, 27–34. doi: 10.1007/BF02120313

Caltagirone, J.-P. (2013). *Physique Des écoulements Continus*. Berlin; Heidelberg: Springer. doi: 10.1007/978-3-642-39510-9

Carrillo, F. J., and Bourg, I. C. (2019). A Darcy-Brinkman-Biot approach to modeling the hydrology and mechanics of porous media containing macropores and deformable microporous regions. *Water Resour. Res.* 55, 8096–8121. doi: 10.1029/2019WR024712

Carrillo, F. J., Bourg, I. C., and Soulaine, C. (2020). Multiphase flow modeling in multiscale porous media: an open-source micro-continuum approach. *J. Comput. Phys. X* 8:100073. doi: 10.1016/j.jcpx.2020.100073

Chang, C., Zhou, Q., Oostrom, M., Kneafsey, T. J., and Mehta, H. (2017). Pore-scale supercritical co2 dissolution and mass transfer under drainage conditions. *Adv. Water Resour.* 100, 14–25. doi: 10.1016/j.advwatres.2016.12.003

Chapman, E., Yang, J., Crawshaw, J., and Boek, E. (2013). Pore scale models for imbibition of co2 analogue fluids in etched micro-fluidic junctions from micro-model experiments and direct lbm flow calculations. *Energy Proc.* 37, 3680–3686. doi: 10.1016/j.egypro.2013.06.262

Chen, L., Kang, Q., Mu, Y., He, Y.-L., and Tao, W.-Q. (2014a). A critical review of the pseudopotential multiphase lattice Boltzmann model: methods and applications. *Int. J. Heat Mass Transfer* 76, 210–236. doi: 10.1016/j.ijheatmasstransfer.2014.04.032

Chen, L., Kang, Q., Robinson, B. A., He, Y.-L., and Tao, W.-Q. (2013). Pore-scale modeling of multiphase reactive transport with phase transitions and dissolution-precipitation processes in closed systems. *Phys. Rev. E* 87:043306. doi: 10.1103/PhysRevE.87.043306

Chen, L., Kang, Q., Tang, Q., Robinson, B. A., He, Y.-L., and Tao, W.-Q. (2015). Pore-scale simulation of multicomponent multiphase reactive transport with dissolution and precipitation. *Int. J. Heat Mass Transfer* 85, 935–949. doi: 10.1016/j.ijheatmasstransfer.2015.02.035

Chen, L., Kang, Q., Viswanathan, H. S., and Tao, W.-Q. (2014b). Pore-scale study of dissolution-induced changes in hydrologic properties of rocks with binary minerals. *Water Resour. Res.* 50, 9343–9365. doi: 10.1002/2014WR015646

Chen, Y., Valocchi, A. J., Kang, Q., and Viswanathan, H. S. (2019). Inertial effects during the process of supercritical CO2 displacing brine in a sandstone: lattice Boltzmann simulations based on the continuum-surface-force and geometrical wetting models. *Water Resour. Res.* 55, 11144–11165. doi: 10.1029/2019WR025746

Cinar, Y., and Riaz, A. (2014). Carbon dioxide sequestration in saline formations: part 2-review of multiphase flow modeling. *J. Petrol. Sci. Eng.* 124, 381–398. doi: 10.1016/j.petrol.2014.07.023

Cinar, Y., Riaz, A., and Tchelepi, H. A. (2009). Experimental study of Co2 injection into saline formations. *SPE J.* 14, 588–594. doi: 10.2118/110628-PA

Cox, R. (1986). The dynamics of the spreading of liquids on a solid surface. Part 1. Viscous flow. *J. Fluid Mech.* 168, 169–194. doi: 10.1017/S0022112086000332

Cueto-Felgueroso, L., and Juanes, R. (2014). A phase-field model of two-phase hele-shaw flow. *J. Fluid Mech.* 758, 522–552. doi: 10.1017/jfm.2014.512

Danis, M., and Quintard, M. (1984). Modélisation d'un écoulement diphasique dans une succession de pores. *Oil Gas Sci. Technol.* 39, 37–46. doi: 10.2516/ogst:1984003

De Gennes, P. (1985). Wetting: statics and dynamics. *Rev. Mod. Phys.* 57, 827–863. doi: 10.1103/RevModPhys.57.827

Demianov, A., Dinariev, O., and Evseev, N. (2014). *Introduction to the Density Functional Method in Hydrodynamics*. Moscow: Fizmatlit.

Deng, H., Molins, S., Trebotich, D., Steefel, C., and DePaolo, D. (2018). Pore-scale numerical investigation of the impacts of surface roughness: Upscaling of reaction rates in rough fractures. *Geochim. Cosmochim. Acta* 239, 374–389. doi: 10.1016/j.gca.2018.08.005

Dentz, M., and Carrera, J. (2007). Mixing and spreading in stratified flow. *Phys. Fluids* 19:017107. doi: 10.1063/1.2427089

Dinariev, O., and Evseev, N. (2016). Multiphase flow modeling with density functional method. *Comput. Geosci.* 20, 835–856. doi: 10.1007/s10596-015-9527-2

Dutka, F., Starchenko, V., Osselin, F., Magni, S., Szymczak, P., and Ladd, A. J. (2020). Time-dependent shapes of a dissolving mineral grain: Comparisons of simulations with microfluidic experiments. *Chem. Geol.* 540:119459. doi: 10.1016/j.chemgeo.2019.119459

Faris, A., Maes, J., and Menke, H. P. (2020). "An investigation into the upscaling of mineral dissolution from the pore to the core scale," in *Proceedings of the 17th European Conference on the Mathematics of Oil Recovery* (Endinburgh) doi: 10.3997/2214-4609.202035250

Fatt, I. (1956). The network model of porous media. *Petrol. Trans. AIME* 207, 144–181. doi: 10.2118/574-G

Ferrari, A., and Lunati, I. (2013). Direct numerical simulations of interface dynamics to link capillary pressure and total surface energy. *Adv. Water Resour.* 57, 19–31. doi: 10.1016/j.advwatres.2013.03.005

Ferrari, A., and Lunati, I. (2014). Inertial effects during irreversible meniscus reconfiguration in angular pores. *Adv. Water Resour.* 74, 1–13. doi: 10.1016/j.advwatres.2014.07.009

Ferziger, J., and Peric, M. (2002). *Computational Methods for Fluid Dynamics, 3rd Edn*. Berlin; Heidelberg; New York, NY: Springer. doi: 10.1007/978-3-642-56026-2

Gingold, R. A., and Monaghan, J. J. (1977). Smoothed particle hydrodynamics: theory and application to non-spherical stars. *Mnthy Notices R. Astron. Soc.* 181, 375–389. doi: 10.1093/mnras/181.3.375

Golfier, F., Zarcone, C., Bazin, B., Lenormand, R., Lasseux, D., and Quintard, M. (2002). On the ability of a darcy-scale model to capture wormhole formation during the dissolution of a porous medium. *J. Fluid Mech.* 457, 213–254. doi: 10.1017/S0022112002007735

Graveleau, M., Soulaine, C., and Tchelepi, H. A. (2017). Pore-scale simulation of interphase multicomponent mass transfer for subsurface flow. *Transport Porous Media* 120, 287–308. doi: 10.1007/s11242-017-0921-1

Guibert, R., Nazarova, M., Horgue, P., Hamon, G., Creux, P., and Debenest, G. (2015). Computational permeability determination from pore-scale imaging: sample size, mesh and method sensitivities. *Transport Porous Media* 107, 641–656. doi: 10.1007/s11242-015-0458-0

Gunstensen, A. K., Rothman, D. H., Zaleski, S., and Zanetti, G. (1991). Lattice boltzmann model of immiscible fluids. *Phys. Rev. A* 43, 4320–4327. doi: 10.1103/PhysRevA.43.4320

Hansen, R. J., and Toong, T. Y. (1971). Interface behavior as one fluid completely displaces another from a small-diameter tube. *J. Colloid Interface Sci.* 36, 410–413. doi: 10.1016/0021-9797(71)90014-2

Haroun, Y., Legendre, D., and Raynal, L. (2010). Volume of fluid method for interfacial reactive mass transfer: application to stable liquid film. *Chem. Eng. Sci.* 65, 2896–2909. doi: 10.1016/j.ces.2010.01.012

Helland, J. O., Pedersen, J., and Jettestuen, E. (2017). "Pore-scale simulation of three-phase capillary pressure and trapping on 3D rock images," in *IOR NORWAY 2017-19th European Symposium on Improved Oil Recovery* (Stavanger).

Henry, W. (1803). Experiments on the quantity of gases absorbed by water, at different temperatures, and under different pressures. *Philos. Trans. R. Soc. Lond.* 93, 29–42, 274–276. doi: 10.1098/rstl.1803.0004

Hirt, C. W., and Nichols, B. D. (1981). Volume-Of-Fluid (VOF) method fior the dynamic of free boundaries. *J. Comput. Phys.* 39, 201–225. doi: 10.1016/0021-9991(81)90145-5

Horgue, P., Augier, F., Duru, P., Prat, M., and Quintard, M. (2013). Experimental and numerical study of two-phase flows in arrays of cylinders. *Chem. Eng. Sci.* 102, 335–345. doi: 10.1016/j.ces.2013.08.031

Hu, R., Wan, J., Kim, Y., and Tokunaga, T. K. (2017). Wettability effects on supercritical co2-brine immiscible displacement during drainage: pore-scale observation and 3d simulation. *Int. J. Greenhouse Gas Control* 60, 129–139. doi: 10.1016/j.ijggc.2017.03.011

Huber, C., Shafei, B., and Parmigiani, A. (2014). A new pore-scale model for linear and non-linear heterogeneous dissolution and precipitation. *Geochim. Cosmochim. Acta* 124, 109–130. doi: 10.1016/j.gca.2013.09.003

Issa, R. I. (1985). Solution of the implicitly discretised fluid flow equations by operator-splitting. *J. Comput. Phys.* 62, 40–65. doi: 10.1016/0021-9991(86)90099-9

Jackson, M. D., Al-Mahrouqi, D., and Vinogradov, J. (2016). Zeta potential in oil-water-carbonate systems and its impact on oil recovery during controlled salinity water-flooding. *Sci. Rep.* 6, 1–13. doi: 10.1038/srep37363

Jacqmin, D. (1999). Calculation of two-phase Navier-Stokes flows using phase-field modeling. *J. Comput. Phys.* 155, 96–127. doi: 10.1006/jcph.1999.6332

Jahanbakhsh, A., Wlodarczyk, K. L., Hand, D. P., Maier, R. R. J., and Maroto-Valer, M. M. (2020). Review of microfluidic devices and imaging techniques for fluid flow study in porous geomaterials. *Sensors* 20:4030. doi: 10.3390/s20144030

Jiang, F., and Tsuji, T. (2017). Estimation of three-phase relative permeability by simulating fluid dynamics directly on rock-microstructure images. *Water Resour. Res.* 53, 11–32. doi: 10.1002/2016WR019098

Kang, Q., Chen, L., Valocchi, A. J., and Viswanathan, H. S. (2014). Pore-scale study of dissolution-induced changes in permeability and porosity of porous media. *J. Hydrol.* 517, 1049–1055. doi: 10.1016/j.jhydrol.2014.06.045

Kang, Q., Zhang, D., and Chen, S. (2003). Simulation of dissolution and precipitation in porous media. *J. Geophys. Res. Solid Earth* 108, 1–5. doi: 10.1029/2003JB002504

Kazemifar, F., Blois, G., Kyritsis, D. C., and Christensen, K. T. (2016). Quantifying the flow dynamics of supercritical CO2-water displacement in a 2d porous micromodel using fluorescent microscopy and microscopic PIV. *Adv. Water Resour.* 95, 352–368. doi: 10.1016/j.advwatres.2015.05.011

Kim, Y., Wan, J., Kneafsey, T. J., and Tokunaga, T. K. (2012). Dewetting of silica surfaces upon reactions with supercritical CO2 and brine: pore-scale studies in micromodels. *Environ. Sci. Technol.* 46, 4228–4235. doi: 10.1021/es204096w

Laleian, A., Valocchi, A., and Werth, C. (2015). An incompressible, depth-averaged lattice boltzmann method for liquid flow in microfluidic devices with variable aperture. *Computation* 3, 600–615. doi: 10.3390/computation3040600

Lamb, H. (1906). *Hydrodynamics, 3rd Edn*. Cambridge: Cambridge University Press.

Landau, L., and Lifshitz, E. (1987). "Fluid mechanics," in *Course of Theoretical Physics, 2nd Edn*, Vol. 6 (Oxford: Pergamon Press Inc.).

Lenormand, R., Touboul, E., and Zarcone, C. (1988). Numerical models and experiments on immiscible displacements in porous media. *J. Fluid Mech.* 189, 165–187. doi: 10.1017/S0022112088000953

Li, X., Huang, H., and Meakin, P. (2008). Level set simulation of coupled advection-diffusion and pore structure evolution due to mineral precipitation in porous media. *Water Resour. Res.* 44, 1–17. doi: 10.1029/2007WR006742

Liu, X., Ormond, A., Bartko, K., Ying, L., and Ortoleva, P. (1997). A geochemical reaction-transport simulator for matrix acidizing analysis and design. *J. Petrol. Sci. Eng.* 17, 181–196. doi: 10.1016/S0920-4105(96)00064-2

Liu, X., and Ortoleva, P. (1996). "A general-purpose, geochemical reservoir simulator," in *SPE Annual Technical Conference and Exhibition* (Society of Petroleum Engineers). doi: 10.2118/36700-MS

Lucy, L. B. (1977). A numerical approach to the testing of the fission hypothesis. *Astron. J.* 82, 1013–1024. doi: 10.1086/112164

Maes, J., and Geiger, S. (2018). Direct pore-scale reactive transport modelling of dynamic wettability changes induced by surface complexation. *Adv. Water Resour.* 111, 6–19. doi: 10.1016/j.advwatres.2017.10.032

Maes, J., and Menke, H. P. (2020). "A bespoke openfoam toolbox for multiphysics flow simulations in pore structures," in *Proceedings of the 17th International Conference on Flow Dynamics (ICFD2020)* (Endinburgh).

Maes, J., and Soulaine, C. (2018a). "Direct pore-scale modelling of dissolution and trapping of supercritical CO2 in reservoir brine," in *Proceedings of the 16th European Conference on the Mathematics of Oil Recovery* (Barcelona). doi: 10.3997/2214-4609.201802238

Maes, J., and Soulaine, C. (2018b). A new compressive scheme to simulate species transfer across fluid interfaces using the volume-of-fluid method. *Chem. Eng. Sci.* 190, 405–418. doi: 10.1016/j.ces.2018.06.026

Maes, J., and Soulaine, C. (2020). A unified single-field volume-of-fluid-based formulation for multi-component interfacial transfer with local volume changes. *J. Comput. Phys.* 402:109024. doi: 10.1016/j.jcp.2019.109024

Marschall, H., Hinterberger, K., Schüler, C., Habla, F., and Hinrichsen, O. (2012). Numerical simulation of species transfer across fluid interfaces in free-surface flows using openfoam. *Chem. Eng. Sci.* 78, 111–127. doi: 10.1016/j.ces.2012.02.034

Maxwell, J. C. (1879). VII. On stresses in rarified gases arising from inequalities of temperature. *Philos. Trans. R. Soc. Lond.* 170, 231–256. doi: 10.1098/rstl.1879.0067

McClure, J. E., Berrill, M. A., Gray, W. G., and Miller, C. T. (2016). Tracking interface and common curve dynamics for two-fluid flow in porous media. *J. Fluid Mech.* 796, 211–232. doi: 10.1017/jfm.2016.212

Meakin, P., and Tartakovsky, A. M. (2009). Modeling and simulation of pore-scale multiphase fluid flow and reactive transport in fractured and porous media. *Rev. Geophys.* 47, 1–47. doi: 10.1029/2008RG000263

Menke, H. P., Maes, J., and Geiger, S. (2020). Upscaling the porosity-permeability relationship of a microporous carbonate to the darcy scale with machine learning. *Sci. Rep.* 11, 1–10. doi: 10.1038/s41598-021-82029-2

Moebius, F., and Or, D. (2012). Interfacial jumps and pressure bursts during fluid displacement in interacting irregular capillaries. *J. Colloid Interface Sci.* 377, 406–415. doi: 10.1016/j.jcis.2012.03.070

Mohammadmoradi, P., and Kantzas, A. (2017). Toward direct pore-scale modeling of three-phase displacements. *Adv. Water Resour.* 110, 120–135. doi: 10.1016/j.advwatres.2017.10.010

Molins, S., Soulaine, C., Prasianakis, N., Abbasi, A., Poncet, P., Ladd, A., et al. (2020). Simulation of mineral dissolution at the pore scale with evolving fluid-solid interfaces: review of approaches and benchmark problem set. *Comput. Geosci.* doi: 10.1007/s10596-019-09903-x

Molins, S., Trebotich, D., Arora, B., Steefel, C. I., and Deng, H. (2019). Multi-scale model of reactive transport in fractured media: diffusion limitations on rates. *Transport Porous Media* 128, 701–721. doi: 10.1007/s11242-019-01266-2

Molins, S., Trebotich, D., Miller, G. H., and Steefel, C. I. (2017). Mineralogical and transport controls on the evolution of porous media texture using direct numerical simulation. *Water Resour. Res.* 53, 3645–3661. doi: 10.1002/2016WR020323

Molins, S., Trebotich, D., Yang, L., Ajo-Franklin, J. B., Ligocki, T. J., Shen, C., et al. (2014). Pore-scale controls on calcite dissolution rates from flow-through laboratory and numerical experiments. *Environ. Sci. Technol.* 48, 7453–7460. doi: 10.1021/es5013438

Morais, S., Cario, A., Liu, N., Bernard, D., Lecoutre, C., Garrabos, Y., et al. (2020). Studying key processes related to CO_2 underground storage at the pore scale using high pressure micromodels. *React. Chem. Eng.* 5, 1156–1185. doi: 10.1039/D0RE00023J

Navier, C. (1823). Mémoire sur les lois du mouvement des fluides. *Mémoires de l'Académie Royale des Sciences de l'Institut de France* 6, 389–440.

Neale, G., and Nader, W. (1974). Practical significance of brinkman's extension of darcy's law: coupled parallel flows within a channel and a bounding porous medium. *Can. J. Chem. Eng.* 52, 475–478. doi: 10.1002/cjce.5450520407

Oltéan, C., Golfier, F., and Bués, M. A. (2013). Numerical and experimental investigation of buoyancy-driven dissolution in vertical fracture. *J. Geophys. Res. Solid Earth* 118, 2038–2048. doi: 10.1002/jgrb.50188

Oostrom, M., Mehmani, Y., Romero-Gomez, P., Tang, Y., Liu, H., Yoon, H., et al. (2016). Pore-scale and continuum simulations of solute transport micromodel benchmark experiments. *Comput. Geosci.* 20, 857–879. doi: 10.1007/s10596-014-9424-0

Ormond, A., and Ortoleva, P. (2000). Numerical modeling of reaction-induced cavities in a porous rock. *J. Geophys. Res. Solid Earth* 105, 16737–16747. doi: 10.1029/2000JB900116

Osselin, F., Kondratiuk, P., Budek, A., Cybulski, O., Garstecki, P., and Szymczak, P. (2016). Microfluidic observation of the onset of reactive-infitration instability in an analog fracture. *Geophys. Res. Lett.* 43, 6907–6915. doi: 10.1002/2016GL069261

Pahlavan, A. A., Cueto-Felgueroso, L., Hosoi, A. E., McKinley, G. H., and Juanes, R. (2018). Thin films in partial wetting: stability, dewetting and coarsening. *J. Fluid Mech.* 845, 642–681. doi: 10.1017/jfm.2018.255

Parmigiani, A., Huber, C., Bachmann, O., and Chopard, B. (2011). Pore-scale mass and reactant transport in multiphase porous media flows. *J. Fluid Mech.* 686:40. doi: 10.1017/jfm.2011.268

Patankar, S. V. (1980). *Numerical Heat Transfer and Fluid Flow*. Washington, DC: Taylor Francis.

Pavuluri, S., Maes, J., and Doster, F. (2018). Spontaneous imbibition in a microchannel: analytical solution and assessment of volume of fluid formulations. *Microfluid Nanofluid* 22, 1–18. doi: 10.1007/s10404-018-2106-9

Pavuluri, S., Maes, J., Yang, J., Regaieg, M., Moncorge, A., and Doster, F. (2020). Towards pore network modelling of spontaneous imbibition: contact angle dependent invasion patterns and the occurrence of dynamic capillary barriers. *Comput. Geosci.* 24, 951–969. doi: 10.1007/s10596-019-09842-7

Poonoosamy, J., Soulaine, C., Burmeister, A., Deissmann, G., Bosbach, D., and Roman, S. (2020). Microfluidic flow-through reactor and 3d raman imaging for *in situ* assessment of mineral reactivity in porous and fractured porous media. *Lab Chip.* 20, 2562–2571. doi: 10.1039/D0LC00360C

Porter, M. L., Jimnez-Martinez, J., Martinez, R., McCulloch, Q., Carey, J. W., and Viswanathan, H. S. (2015). Geo-material microfluidics at reservoir conditions for subsurface energy resource applications. *Lab Chip* 15, 4044–4053. doi: 10.1039/C5LC00704F

Power, O. A., Lee, W. T., Fowler, A. C., Dellar, P. J., Schwartz, L. W., Lukaschuk, S., et al. (2009). "The initiation of guinness," in *Proceedings of the Seventieth European Study Group with Industry*, (Limerick: Mathematics Applications Consortium for Science and Industry), 141–182.

Prasianakis, N. I., Curti, E., Kosakowski, G., Poonoosamy, J., and Churakov, S. V. (2017). Deciphering pore-level precipitation mechanisms. *Sci. Rep.* 7, 1–9. doi: 10.1038/s41598-017-14142-0

Prasianakis, N. I., Rosen, T., Kang, J., Eller, J., Mantzaras, J., and Bichi, F. N. (2013). Simulation of 3D porous media flows with application to polymer electrolyte fuel cells. *Commun. Comput. Phys.* 13, 851–866. doi: 10.4208/cicp.341011.310112s

Prutton, C., and Savage, R. (1945). The solubility of carbon dioxide in calcium chloride-water solutions at 75, 100, 120 and high pressures. *J. Am. Chem. Soc.* 67, 1550–1554. doi: 10.1021/ja01225a047

Qin, Z., Esmaeilzadeh, S., Riaz, A., and Tchelepi, H. A. (2020). Two-phase multiscale numerical framework for modeling thin films on curved solid surfaces in porous media. *J. Comput. Phys.* 413:109464. doi: 10.1016/j.jcp.2020.109464

Raeini, A. Q., Blunt, M. J., and Bijeljic, B. (2014). Direct simulations of two-phase flow on micro-CT images of porous media and upscaling of pore-scale forces. *Adv. Water Resour.* 74, 116–126. doi: 10.1016/j.advwatres.2014.08.012

Ray, N., Oberlander, J., and Frolkovic, P. (2019). Numerical investigation of a fully coupled micro-macro model for mineral dissolution and precipitation. *Comput. Geosci.* 23, 1173–1192. doi: 10.1007/s10596-019-09876-x

Roman, S., Abu-Al-Saud, M. O., Tokunaga, T., Wan, J., Kovscek, A. R., and Tchelepi, H. A. (2017). Measurements and simulation of liquid films during drainage displacements and snap-off in constricted capillary tubes. *J. Colloid Interface Sci.* 507, 279–289. doi: 10.1016/j.jcis.2017.07.092

Roman, S., Soulaine, C., AlSaud, M. A., Kovscek, A., and Tchelepi, H. (2016). Particle velocimetry analysis of immiscible two-phase flow in micromodels. *Adv. Water Resour.* 95, 199–211. doi: 10.1016/j.advwatres.2015.08.015

Roman, S., Soulaine, C., and Kovscek, A. (2020). Pore-scale visualization and characterization of viscous dissipation in porous media. *J. Colloid Interface Sci.* 558, 269–279. doi: 10.1016/j.jcis.2019.09.072

Rose, W. (2000). Myths about later-day extensions of Darcy's law. *J. Petrol. Sci. Eng.* 26, 187–198. doi: 10.1016/S0920-4105(00)00033-4

Scardovelli, R., and Zaleski, S. (1999). Direct numerical simulation of free-surface and interfacial flow. *Annu. Rev. Fluid Mech*. 31, 567–603. doi: 10.1146/annurev.fluid.31.1.567

Scheibe, T. D., Perkins, W. A., Richmond, M. C., McKinley, M. I., Romero-Gomez, P. D. J., Oostrom, M., et al. (2015). Pore-scale and multiscale numerical simulation of flow and transport in a laboratory-scale column. *Water Resour. Res*. 51, 1023–1035. doi: 10.1002/2014WR015959

Singh, K., Menke, H. P., Andrew, M., Rau, C., Bijeljic, B., and Blunt, M. J. (2018). Time-resolved synchrotron x-ray micro-tomography datasets of drainage and imbibition in carbonate rocks. *Sci. Data* 5:180265. doi: 10.1038/sdata.2018.265

Song, W., de Haas, T. W., Fadaei, H., and Sinton, D. (2014). Chip-off-the-old-rock: the study of reservoir-relevant geological processes with real-rock micromodels. *Lab Chip* 14, 4382–4390. doi: 10.1039/C4LC00608A

Soulaine, C., Creux, P., and Tchelepi, H. A. (2019). Micro-continuum framework for pore-scale multiphase fluid transport in shale formations. *Transport Porous Media* 127, 85–112 doi: 10.1007/s11242-018-1181-4

Soulaine, C., Davit, Y., and Quintard, M. (2013). A two-pressure model for slightly compressible single phase flow in bi-structured porous media. *Chem. Eng. Sci*. 96, 55–70. doi: 10.1016/j.ces.2013.03.060

Soulaine, C., Gjetvaj, F., Garing, C., Roman, S., Russian, A., Gouze, P., et al. (2016). The impact of sub-resolution porosity of x-ray microtomography images on the permeability. *Transport Porous Media* 113, 227–243. doi: 10.1007/s11242-016-0690-2

Soulaine, C., Pavuluri, S., Claret, F., and Tournassat, C. (2021). porousMedia4Foam: multi-scale open-source platform for hydro-geochemical simulations with OpenFOAM. *Earth Space Sci. Open Arch*. 1–23. doi: 10.1002/essoar.10505772.1

Soulaine, C., Roman, S., Kovscek, A., and Tchelepi, H. A. (2017). Mineral dissolution and wormholing from a pore-scale perspective. *J. Fluid Mech*. 827, 457–483. doi: 10.1017/jfm.2017.499

Soulaine, C., Roman, S., Kovscek, A., and Tchelepi, H. A. (2018). Pore-scale modelling of multiphase reactive flow. Application to mineral dissolution with production of CO_2. *J. Fluid Mech*. 855, 616–645. doi: 10.1017/jfm.2018.655

Soulaine, C., and Tchelepi, H. A. (2016). Micro-continuum approach for pore-scale simulation of subsurface processes. *Transport Porous Media* 113, 431–456. doi: 10.1007/s11242-016-0701-3

Spanne, P., Thovert, J., Jacquin, C., Lindquist, W., Jones, K., and Adler, P. (1994). Synchrotron computed microtomography of porous media: topology and transports. *Phys. Rev. Lett*. 73:2001. doi: 10.1103/PhysRevLett.73.2001

Starchenko, V., Marra, C. J., and Ladd, A. J. (2016). Three-dimensional simulations of fracture dissolution. *J. Geophys. Res. Solid Earth* 121, 6421–6444. doi: 10.1002/2016JB013321

Starov, V. M., Velarde, M. G., and Radke, C. J. (2007). *Wetting and Spreading Dynamics*. Boca Raton, FL: CRC Press. doi: 10.1201/9781420016178

Steefel, C. I., Beckingham, L. E., and Landrot, G. (2015). Micro-continuum approaches for modeling pore-scale geochemical processes. *Rev. Mineral Geochem*. 80, 217–246. doi: 10.1515/9781501502071

Steefel, C. I., DePaolo, D. J., and Lichtner, P. C. (2005). Reactive transport modeling: an essential tool and a new research approach for the earth sciences. *Earth Planet. Sci. Lett*. 240, 539–558. doi: 10.1016/j.epsl.2005.09.017

Succi, S. (2002). Mesoscopic modeling of slip motion at fluid-solid interfaces with heterogeneous catalysis. *Phys. Rev. Lett*. 89:064502. doi: 10.1103/PhysRevLett.89.064502

Sussman, M., Smereka, P., and Osher, S. (1994). A level-set approach for computing solutions to incompressible tow-phase flow. *J. Comput. Phys*. 114, 146–159. doi: 10.1006/jcph.1994.1155

Szymczak, P., and Ladd, A. (2009). Wormhole formation in dissolving fractures. *J. Geophys. Res. Solid Earth* 114, 1–22. doi: 10.1029/2008JB006122

Tartakovsky, A., and Meakin, P. (2005). Modeling of surface tension and contact angles with smoothed particle hydrodynamics. *Phys. Rev. E* 72:026301. doi: 10.1103/PhysRevE.72.026301

Tartakovsky, A. M., Meakin, P., Scheibe, T. D., and West, R. M. E. (2007). Simulations of reactive transport and precipitation with smoothed particle hydrodynamics. *J. Comput. Phys*. 222, 654–672. doi: 10.1016/j.jcp.2006.08.013

Tartakovsky, A. M., and Panchenko, A. (2016). Pairwise force smoothed particle hydrodynamics model for multiphase flow: surface tension and contact line dynamics. *J. Comput. Phys*. 305, 1119–1146. doi: 10.1016/j.jcp.2015.08.037

Tartakovsky, A. M., Tartakovsky, D. M., Scheibe, T. D., and Meakin, P. (2008). Hybrid simulations of reaction-diffusion systems in porous media. *SIAM J. Sci. Comput*. 30, 2799–2816. doi: 10.1137/070691097

Taylor, G. (1953). Dispersion of soluble matter in solvent flowing slowly through a tube. *Proc. R. Soc. Lond. Ser. A Math. Phys*. 219, 186–203. doi: 10.1098/rspa.1953.0139

Thompson, K., and Gdanski, R. (1993). Laboratory study provides guidelines for diverting acid with foam. *SPE Product. Facil*. 8, 285–290. doi: 10.2118/23436-PA

Vacondio, R., Altomare, C., Leffe, M. D., Hu, X., Touzé, D. L., Lind, S., et al. (2020). Grand challenges for smoothed particle hydrodynamics numerical schemes. *Comp. Part. Mech*. 1–14. doi: 10.1007/s40571-020-00354-1

van Kats, F. M., and Egberts, P. J. P. (1999). Simulation of three-phase displacement mechanisms using a 2d lattice-boltzmann model. *Transport Porous Media* 37, 55–68. doi: 10.1023/A:1006502831641

Vasil'ev, A. (2009). From the Hele-Shaw experiment to integrable systems: a historical overview. *Complex Anal. Operator Theory* 3, 551–585. doi: 10.1007/s11785-008-0104-8

Venturoli, M., and Boek, E. S. (2006). Two-dimensional lattice-boltzmann simulations of single phase flow in a pseudo two-dimensional micromodel. *Phys. A Stat. Mech. Appl*. 362, 23–29. doi: 10.1016/j.physa.2005.09.006

Voinov, O. (1976). Hydrodynamics of wetting. *Fluid Dyn*. 11, 714–721. doi: 10.1007/BF01012963

Wan, J., Kim, Y., and Tokunaga, T. K. (2014). Contact angle measurement ambiguity in supercritical CO2-water-mineral systems: mica as an example. *Int. J. Greenhouse Gas Control* 31, 128–137. doi: 10.1016/j.ijggc.2014.09.029

Watson, F., Maes, J., Geiger, S., Mackay, E., Singleton, M., McGravie, T., et al. (2019). Comparison of flow and transport experiments on 3d printed micromodels with direct numerical simulations. *Transport Porous media* 129, 449–466. doi: 10.1007/s11242-018-1136-9

Wen, H., and Li, L. (2017). An upscaled rate law for magnesite dissolution in heterogeneous porous media. *Geochim. Cosmochim. Acta* 210, 289–305. doi: 10.1016/j.gca.2017.04.019

Whitaker, S. (1999). *The Method of Volume Averaging, Theory and Applications of Transport in Porous Media*. Dorderecht: Kluwer Academic. doi: 10.1007/978-94-017-3389-2

Willingham, T. W., Werth, C. J., and Valocchi, A. J. (2008). Evaluation of the effects of porous media structure on mixing-controlled reactions using pore-scale modeling and micromodel experiments. *Environ. Sci. Technol*. 42, 3185–3193. doi: 10.1021/es7022835

Wörner, M. (2012). Numerical modeling of multiphase flows in microfluidics and micro process engineering: a review of methods and applications. *Microfluid. Nanofluid*. 12, 841–886. doi: 10.1007/s10404-012-0940-8

Xu, Z., and Meakin, P. (2008). Phase-field modeling of solute precipitation and dissolution. *J. Chem. Phys*. 129:014705. doi: 10.1063/1.2948949

Xu, Z., and Meakin, P. (2011). Phase-field modeling of two-dimensional solute precipitation/dissolution: solid fingers and diffusion-limited precipitation. *J. Chem. Phys*. 134:044137. doi: 10.1063/1.3537973

Yang, L., Nieves-Remacha, M. J., and Jensen, K. F. (2017). Simulations and analysis of multiphase transport and reaction in segmented flow microreactors. *Chem. Eng. Sci*. 169, 106–116. doi: 10.1016/j.ces.2016.12.003

Yesufu-Rufai, S., Rcker, M., Berg, S., Lowe, S. F., Marcelis, F., Georgiadis, A., et al. (2020). Assessing the wetting state of minerals in complex sandstone rock *in-situ* by atomic force microscopy (AFM). *Fuel* 273:117807. doi: 10.1016/j.fuel.2020.117807

Yoon, H., Chojnicki, K. N., and Martinez, M. J. (2019). Pore-scale analysis of calcium carbonate precipitation and dissolution kinetics in a microfluidic device. *Environ. Sci. Technol*. 53, 14233–14242. doi: 10.1021/acs.est.9b01634

Yoon, H., Kang, Q., and Valocchi, A. J. (2015). Lattice Boltzmann-based approaches for pore-scale reactive transport. *Rev. Mineral. Geochem*. 80, 393–431. doi: 10.2138/rmg.2015.80.12

Yoon, H., Valocchi, A. J., Werth, C. J., and Dewers, T. (2012). Pore-scale simulation of mixing-induced calcium carbonate precipitation and dissolution in a microfluidic pore network. *Water Resour. Res*. 48:W02524. doi: 10.1029/2011WR011192

Yun, W., Chang, S., Cogswell, D. A., Eichmann, S. L., Gizzatov, A., Thomas, G., et al. (2020). Toward reservoir-on-a-chip: rapid performance evaluation

of enhanced oil recovery surfactants for carbonate reservoirs using a calcite-coated micromodel. *Sci. Rep*. 10, 1–12. doi: 10.1038/s41598-020-57485-x

Zarikos, I., Terzis, A., Hassanizadeh, S. M., and Weigand, B. (2018). Velocity distributions in trapped and mobilized non-wetting phase ganglia in porous media. *Sci. Rep*. 8, 1–11. doi: 10.1038/s41598-018-31639-4

Zhang, C., Liu, C., and Shi, Z. (2013). Micromodel investigation of transport effect on the kinetics of reductive dissolution of hematite. *Environ. Sci. Technol*. 47, 4131–4139. doi: 10.1021/es304006w

Zhao, B., MacMinn, C. W., and Juanes, R. (2016). Wettability control on multiphase flow in patterned microfluidics. *Proc. Natl. Acad. Sci. U.S.A*. 113, 10251–10256. doi: 10.1073/pnas.1603387113

Zhao, B., MacMinn, C. W., Primkulov, B. K., Chen, Y., Valocchi, A. J., Zhao, J., et al. (2019). Comprehensive comparison of pore-scale models for multiphase flow in porous media. *Proc. Natl. Acad. Sci. U.S.A*. 116, 13799–13806. doi: 10.1073/pnas.1901619116

Zhao, B., Pahlavan, A. A., Cueto-Felgueroso, L., and Juanes, R. (2018). Forced wetting transition and bubble pinch-off in a capillary tube. *Phys. Rev. Lett*. 120, 1–9. doi: 10.1103/PhysRevLett.120.084501

Conflict of Interest: The authors declare that the research was conducted in the absence of any commercial or financial relationships that could be construed as a potential conflict of interest.

frontiers in Water

ORIGINAL RESEARCH
published: 01 June 2021
doi: 10.3389/frwa.2021.671399

The Origin of Non-thermal Fluctuations in Multiphase Flow in Porous Media

Maja Rücker[1,2], Apostolos Georgiadis[3], Ryan T. Armstrong[4], Holger Ott[5], Niels Brussee[3], Hilbert van der Linde[3], Ludwig Simon[6], Frieder Enzmann[6], Michael Kersten[6] and Steffen Berg[3,2,7]**

[1] Department of Mechanical Engineering, Technical University Eindhoven, Eindhoven, Netherlands, [2] Department of Chemical Engineering, Imperial College London, London, United Kingdom, [3] Shell Global Solutions International B.V., Amsterdam, Netherlands, [4] School of Minerals and Energy Resources Engineering, University of New South Wales, Sydney, NSW, Australia, [5] Department Petroleum Engineering, Montanuniversität Leoben, Leoben, Austria, [6] Hydrogeochemistry, Geosciences Institute, Johannes-Gutenberg University, Mainz, Germany, [7] Department of Earth Sciences and Engineering, Imperial College London, London, United Kingdom

Core flooding experiments to determine multiphase flow in properties of rock such as relative permeability can show significant fluctuations in terms of pressure, saturation, and electrical conductivity. That is typically not considered in the Darcy scale interpretation but treated as noise. However, in recent years, flow regimes that exhibit spatio-temporal variations in pore scale occupancy related to fluid phase pressure changes have been identified. They are associated with topological changes in the fluid configurations caused by pore-scale instabilities such as snap-off. The common understanding of Darcy-scale flow regimes is that pore-scale phenomena and their signature should have averaged out at the scale of representative elementary volumes (REV) and above. In this work, it is demonstrated that pressure fluctuations observed in centimeter-scale experiments commonly considered Darcy-scale at fractional flow conditions, where wetting and non-wetting phases are co-injected into porous rock at small ($<10^{-6}$) capillary numbers are ultimately caused by pore-scale processes, but there is also a Darcy-scale fractional flow theory aspect. We compare fluctuations in fractional flow experiments conducted on samples of few centimeters size with respective experiments and *in-situ* micro-CT imaging at pore-scale resolution using synchrotron-based X-ray computed micro-tomography. On that basis we can establish a systematic causality from pore to Darcy scale. At the pore scale, dynamic imaging allows to directly observe the associated breakup and coalescence processes of non-wetting phase clusters, which follow "trajectories" in a "phase diagram" defined by fractional flow and capillary number and can be used to categorize flow regimes. Connected pathway flow would be represented by a fixed point, whereas processes such as ganglion dynamics follow trajectories but are still overall capillary-dominated. That suggests that the origin of the pressure fluctuations observed in centimeter-sized fractional flow experiments are capillary effects. The energy scale of the pressure fluctuations corresponds to 10^5-10^6 times the thermal energy scale. This means the fluctuations are non-thermal. At the centimeter scale, there are non-monotonic and even oscillatory solutions permissible by the fractional flow theory, which allow the fluctuations to be visible and—depending

OPEN ACCESS

Edited by:
Charlotte Garing, University of Georgia, United States

Reviewed by:
Mohamed Regaieg, Total, France
Chi Zhang, University of Kansas, United States

***Correspondence:**
Maja Rücker
m.rucker@tue.nl
Steffen Berg
steffen.berg@shell.com

Specialty section:
This article was submitted to Water and Critical Zone, a section of the journal Frontiers in Water

Received: *23 February 2021*
Accepted: *22 April 2021*
Published: *01 June 2021*

Citation:
Rücker M, Georgiadis A, Armstrong RT, Ott H, Brussee N, van der Linde H, Simon L, Enzmann F, Kersten M and Berg S (2021) The Origin of Non-thermal Fluctuations in Multiphase Flow in Porous Media. Front. Water 3:671399. doi: 10.3389/frwa.2021.671399

on exact conditions—significant at centimeter scale, within the viscous limit of classical (Darcy scale) fractional flow theory. That also means that the phenomenon involves both capillary aspects from the pore or cluster scale and viscous aspects of fractional flow and occurs right at the transition, where the physical description concept changes from pore to Darcy scale.

Keywords: multiphase, pore scale, fractional flow analysis, fluctuations, displacement

INTRODUCTION

Multiphase flow in porous media is an integral part in many aspects of every-day life and plays a critical role in some of the most important processes and technologies from agriculture to energy. Examples range from the hydrology in the Vadose zone where the water table rises and falls and water and air occupy the pore space in soil, contaminant hydrology, hydrocarbon recovery, hydrogen storage, and carbon capture and sequestration (CCS) (Bui et al., 2018). Multiphase transport is also a rate-limiting step in gas diffusion layers in electrocatalytic devices such as fuel cells (Simon et al., 2017), electrolysis, and more novel concepts, where CO_2 is converted into base chemicals (Kondratenko et al., 2013).

In most applications, multiphase transport is described with the 2-phase Darcy equations, which are a continuum mechanic concept for relating transport, i.e., average phase fluxes to average pressure gradients applicable at the "Darcy scale." They are phenomenological extensions of Darcy's law from single to multiphase flow. One of the consequences of operating with a phenomenological transport equation is that it contains parameters, such as relative permeability, which cannot be predicted within the framework of the 2-phase Darcy equations. Since relative permeability is specific to the porous medium and its chemical interaction with the fluids present manifesting in characteristic wetting behavior of the system (Abdallah et al., 2007), they have to be determined for each situation individually. Common methods to experimentally determine relative permeability are core flooding experiments, which are typically conducted on porous media samples of few centimeters in size. For instance, in the petroleum industry, cylindrical rock samples from drilled cores are used, which are limited in size by the diameter of the core and are typically between 2.54 and 5.00 cm in length and diameter, which is commonly assumed to represent Darcy scale. The steady-state method is one of the most trusted methods as it provides a wide accessible saturation range and in combination with numerical simulation (Kokkedee et al., 1996; Masalmeh et al., 2014; Sorop et al., 2015) allows the correct treatment of experimental artifacts, such the capillary end-effect (Huang and Honarpour, 1998). In steady-state experiments, the two immiscible fluids phases, e.g., water or brine and oil or gas are co-injected at stepwise varied fractions of wetting phase flux over total flux, termed fractional flow f_w. At each fractional flow step, fluids are co-injected until a "steady-state" has been reached, which is defined by saturation, pressure-drop, and electrical resistivity becoming time-independent, i.e., $d\overline{S_w}/dt = 0$, where $\overline{S_w}$ is the space and time-averaged saturation. Relative permeability is then determined from the time-averaged pressure-drop and time-averaged saturation.

However, many of these fractional flow experiments show notable fluctuations (Datta et al., 2014a,b; Masalmeh et al., 2014; Reynolds and Krevor, 2015; Rücker et al., 2015a; Sorop et al., 2015; Gao et al., 2017, 2019, 2020; Lin Q. et al., 2018; Alcorn et al., 2019; Clennell et al., 2019; Lin et al., 2019a; Spurin et al., 2019; Wang and Masalmeh, 2019; Menke et al., 2021), for instance in pressure drop but also saturation. In some cases, the magnitude of these fluctuations is comparable or even larger than the average values of the respective property, e.g., pressure drop, between the previous or following fractional flow. Historically, such fluctuation have been considered as indicative for failed experiments and often led to dismissal of the experiment. That is potentially the reason why despite extensive literature on steady-state relative permeability in only relatively few cases the raw data is shown. Even in the cases where pressure drop as a function of time is shown, it is often not clear whether this data is filtered or smoothed, operating under the assumption that the fluctuations are caused by noise.

Also, pressure fluctuations are more prominent for water-wet rock and much less visible for intermediate or mixed-wet cases (Jung et al., 2016; Lin Q. et al., 2018; Lin et al., 2019a), where the magnitude of capillary pressure is much less or even near zero (Lin et al., 2019a). Experiments conducted on twin samples of the same rock to exclude all other factors show noticeable fluctuations in the water-wet case (Lin Q. et al., 2018) but much less in the intermediate-wet case (Lin et al., 2019a), which has been achieved by aging with crude oil. In the intermediate-wet case, capillary pressure is near zero, because the mean curvature is near zero, which has been established from imaging the liquid-liquid interfaces by micro-CT. But that does not mean the interfaces are flat, but rather form bi-continuous interfaces that allow both aqueous and oil phases to be continuous at the same time, i.e., fractional flow does not cause displacement events, which is the primary reason why pressure fluctuations are less. Wettability heterogeneity may also impact the magnitude of fluctuations due to the associated energy dissipation (Murison et al., 2014). Also, fluctuations are stronger for a gas-liquid system and more often reported explicitly (Alkan and Müller, 2008; Reynolds and Krevor, 2015; Xu et al., 2015; Spurin et al., 2020), which suggests that viscosity ratio may be an important factor, which has been also reported in (Spurin et al., 2019).

Pore scale experiments (DiCarlo et al., 2003; Moebius and Or, 2012; Berg et al., 2013, 2014; Armstrong et al., 2014a; Reynolds et al., 2017; Lin Q. et al., 2018; Lin et al., 2019a) and numerical simulations (Lenormand et al., 1983; Raeini et al., 2014; Armstrong et al., 2015; Guédon et al., 2017; Alpak

et al., 2019; Berg C. F. et al., 2020; Winkler et al., 2020) also exhibit fluctuations in pressure and saturation (Ramstad and Hansen, 2006; Pak et al., 2015), which are caused by pore scale displacement events, such as Haines jumps and coalescence (Rücker et al., 2015b), where the non-wetting phase replaces the wetting phase and snap-off and piston-like displacement (Lenormand et al., 1983; Dixit et al., 1998), where the wetting phase replaces the non-wetting phase. These events lead to interruption and rearrangement of the connected pathways the respective phases flow through (Tuller and Or, 2001) and are described by a rigorous theoretical framework of pore-scale thermodynamics (Morrow, 1970). Depending on flow rate and other conditions (Avraam and Payatakes, 1995a; Lenormand and Touboul, 1998), there are different regimes that can cause fluctuations in pressure and saturation that have been systematically investigated in Avraam and Payatakes (1995a), Tsakiroglou (2019). The main regimes identified were connected pathway flow, ganglion dynamics and drop traffic. While sequences of oil-filling and water filling events of different nature cause ganglion dynamics (Rücker et al., 2015b) already at capillary numbers below $Ca < 10^{-6}$, effects such as ganglion dynamics, where such events occur repeatedly at the same location (Lenormand et al., 1983; Datta et al., 2014a,b; Gao et al., 2017, 2019, 2020; Spurin et al., 2019), are often observed close to the critical capillary number for capillary de-saturation (Berg and Cense, 2009) and likely caused by viscous mobilization and associated breakup, which can in the extreme case lead to "drop traffic" (Avraam and Payatakes, 1995a,b). Note that in the porous media literature, the term "intermittency" is frequently used instead of ganglion dynamics. However, outside the porous media community, this term is commonly associated with turbulent flow, which could lead to misconceptions as in porous media, and this behavior is often observed already in the capillary dominated regime. Periodic pressure fluctuations can also be caused by snap-off of non-wetting phase bubbles at the outlet although this is a mechanism observed more in spontaneous imbibition (Unsal et al., 2007a,b; Unsal et al., 2009; Bartels et al., 2019). While the exact pore scale mechanism can differ, the pressure signature is typically caused by capillary effects in a capillary-dominated regime (Singh et al., 2019). A recent pore scale simulation study that shows such fluctuations caused by pore-scale displacement events introduced the term "athermal" to characterize the energy scale of these fluctuations (Winkler et al., 2020).

The referenced literature suggests that these non-thermal fluctuations are a relatively universal phenomenon occurring in a very wide range of rock types and are observable on different scales. The key step that has been missing so far is a direct link between pore-scale fluctuations and Darcy scale behavior, which is the focus of this paper. This link between fluctuations observed in core flooding experiments at a length scale of several centimeters and their origin from pore scale displacement events is important because from both a very fundamental perspective and also for practical reasons. It is important to understand whether fluctuations are caused by pore scale displacement events, because such events are always to some extent irreversible and associated with the dissipation of energy (Morrow, 1970; Seth and Morrow, 2007; Berg et al., 2013). The big question is whether this energy dissipation by pore scale events is correctly captured when using time-averaged pressure and saturation data. At this moment, we do not fully understand the consequence of the averaging in case that fluctuations are not just noise but indeed caused by pore scale displacement events. Also, for the interpretation of such experiments by inverse modeling to determine the relative permeability (Berg S. et al., 2020), for a correct assessment of the associated uncertainty, it is important to understand whether fluctuations are noise or have another cause, e.g., a physical mechanism.

In this work we address this question of the link between fluctuations and pore-scale displacement events by analyzing the magnitude and statistics of Darcy scale "steady-state" fractional flow experiments for different rocks and fluid/fluid/solid wetting and comparison with pore-scale fractional flow experiments with synchrotron beamline-based fast x-ray computed tomography. We will discuss the reason why fluctuations involve hundreds or more pores. From a pore scale perspective alone, this would not be very obvious, because fluctuations are mainly associated with individual pore scale displacement events and larger fluctuations are interpreted from the pore scale perspective as ganglion dynamics. The dominance of fluctuations involving hundreds to thousands of individual pores becomes understandable as in the transition to the Darcy scale fluctuations can only persist if a permissible (Darcy-scale) fractional flow solution exists, for which we will present supporting evidence. That emphasizes the need to presenting both the pore scale and the Darcy scale perspective on the *same* phenomenon. Each experiment has significant complexity, which cannot be fully covered in this work, which focuses very much on the link between pore and Darcy scale. Therefore, we largely rely on thoroughly conducted experiments on each scale using dedicated experimental setups that are designed to rule out instrumental artifacts, i.e., avoid back pressure controllers and other potential source of fluctuations other than the ones caused by the multiphase flow in porous media. We make use of the best experimental data that are unfortunately not conducted on exactly the same sample. We use Fontainebleau sandstone for Darcy scale experiments and sintered glass of comparable pore size at the pore scale. The phenomena found in the sandstone sample and the sintered glass are comparable, which is also established through consistency with other studies in the literature, which suggest that phenomena are actually generic and observed in many different rock types. The experiments we present here have the highest level of confidence to rule out such artifacts, which is why we gave priority over fully consistent samples. Ultimately, the pressure signature but also associated fluctuations in connectivity (McClure et al., 2016) (which in the Darcy scale experiments is represented by electrical resistivity) (Liu Z. et al., 2018) provides the connection between Darcy scale fluctuations and pore scale displacement events.

METHODS AND MATERIALS

Two different set-ups were used in this study to relate pore-scale mechanisms with Darcy-scale responses. The different set-ups, sample preparation and analysis are described below.

TABLE 1 | Fluid properties in pore-scale and Darcy-scale SCAL experiments.

Fluid	Density (20°C)	Viscosity (20°C)
Brine—pore scale	1,111 kgm^{-3}	Similar to Darcy scale
Brine—Darcy scale	1,037 kgm^{-3}	0.992 mPas
n-decane	731.9 kgm^{-3}	0.933 mPas
Crude 1	934.7 kgm^{-3}	88.43 mPas
Crude 2	833.9 kgm^{-3}	4.87 mPas
Crude 3	859.2 kgm^{-3}	9.47 mPas

TABLE 2 | Analysis of the 3 crude oils in terms of total acid number (TAN), total basic nitrogen (TBN), and the SARA analysis in terms of saturates (Sat), aromats (Aro), and resins (Res).

	TAN mg KOH/g	TBN mg/kg	Sat wt-%	Aro wt-%	Res wt-%
Crude 1	1.37	320	37.27	48.45	14.21
Crude 2	0.07	83.9	58.45	36.92	4.39
Crude 3	0.09	270.6	44.00	44.00	9.69

Rocks and Fluids

For the Darcy scale experiments, a cylindrical Fontainebleau sandstone sample with a diameter of $d = 2.54$ cm and a length of $L = 4.45$ cm was used. Fontainebleau sandstone is a fine-grained, well-sorted cretaceous sandstone outcropping in South France, well-known for its regular grain framework, the almost mono-mineral composition up to 99.5% quartz and for the absence of clay in it (Jacquin, 1964; Al Saadi et al., 2017). The rock sample had a porosity of $\phi = 0.13$ and a permeability of $K_{abs} = 5.32 \times 10^{-13}$ m^2 (539 mD). This permeability is particularly well-suited for special core analysis (SCAL) steady-state flow experiments, because it falls in the middle of the operating envelope of the setup, which has a maximum accessible permeability of about 2–3 Darcy. Before the experiment the rock sample was cleaned in a chloroform-methanol azeotrope in a Soxhlett extractor to complete water wetness. The sample was not aged with crude oil and only inert fluids were used, which means that the rock remained strongly water wet.

In a second series of Darcy scale experiments addressing the effect of wettability through variation of fluids, 3 cylindrical rock samples of Bentheimer sandstone rock (Lin et al., 2019a,b) with 5 cm length and 3.8 cm diameter were used. The porosity ranged between 0.246 and 0.248 and the permeability between 2,577 and 2,642 mD. The samples were cleaned with by Soxhlett extraction and then saturated with brine for permeability measurements. The three rock samples were then de-saturated with 3 crude oils (basic properties are listed in **Table 1** and analysis results of total acid number (TAN), total basic nitrogen (TBN) and SARA are listed in **Table 2**) and subsequently aged (Lin et al., 2019b) for 40 days. Based on an extensive analysis of the crude oils, the potential for wettability alteration is highest for crude 3, somewhat less for crude 2 and least for crude 1, i.e., it is expected that for crude 1 the Bentheimer rock remains more water wet, whereas for crude 3, the rock is expected to become more intermediate wet.

For the micro-CT (pore-scale) flow experiments, a sintered glass model purchased from Robuglass (Berg et al., 2014) was chosen because of its large pores that are particularly well-suited for imaging pore scale fluid distributions, i.e., much more suitable than the very narrow pores of Fontainebleau sandstone. The sample had a diameter of $\varnothing = 4$ mm and a length of $L = 2$ cm. The porosity determined from a segmented micro-CT image was $\phi = 0.36$. The permeability of $K_{abs} = 1.38 \times 10^{-11}$ m^2 (14 D) was obtained from numerical flow simulation with the Navier-Stokes solver from GeoDICT (Math2Market) (Berg and van Wunnik, 2017). This permeability is too high for the SCAL steady-state experimental setup (the associated pressure drops are too small for the range of the pressure transducers). The sample is naturally (from the sintering process) clean and strongly water wet.

The fluids used in both experiments was n-decane and brine doped for contrast with 14.3% CsCl in the pore-scale experiment and 5% in the Darcy scale experiment. Density ρ and viscosity μ of the fluids are listed in **Table 1**. The interfacial tension was around 40 mN/m. Decane and brine don't form any emulsions, which might hypothetically also cause pressure fluctuations (Cobos et al., 2009; Yu et al., 2019).

"Darcy Scale" Fractional Flow Experiments

The Darcy scale experiments were conducted in an experimental setup, which is routinely used for measuring relative permeability with the so-called "steady-state" method, where water and oil phases are co-injected at fractional flow:

$$f_w = \frac{q_w}{q_w + q_o} = \frac{\lambda_w}{\lambda_w + \lambda_n} = \frac{1}{1 + \frac{k_{r,n}/\mu_n}{k_{r,w}/\mu_w}} \quad (1)$$

where q_α are the fluxes and $\lambda_\alpha = k_{r,\alpha}/\mu_\alpha$ the mobility of phase α, with the relative permeability $k_{r,\alpha}$ and viscosity μ_α ($\alpha = w$ for wetting phase and $\alpha = n$ for the non-wetting phase). The co-injection at f_w is realized by two dual-piston Quizzix pumps (Chandler, Metek) that operate with zero-dead volume switching valves for smooth and pulse-free continuous flow (Vindum Engineering). Fluids are re-circulated (after separation) without any back-pressure controller that could cause artifacts such as pressure oscillations. The core is enclosed in an X-ray transparent Hassler-type core holder made from carbon fiber epoxy composite that allows *in-situ* saturation monitoring by a self-built X-ray transmission system that measures saturation at 22 positions along the core (Cense et al., 2014). During the experiment, the pressures drop dP_w is monitored at a 1 min time interval and saturation S_w and resistivity at a time interval of 8 min 30 s. The conceptual overview of the setup is displayed in **Figure 1A**.

At the inlet, the oil and water supplied by 1/16 inch tubing are first dispersed by a set of diffusor plates with two rings of concentric circular grooves followed by a metal mesh (both at same cross section as the core) before entering the core. A similar end piece construction is used at the outlet.

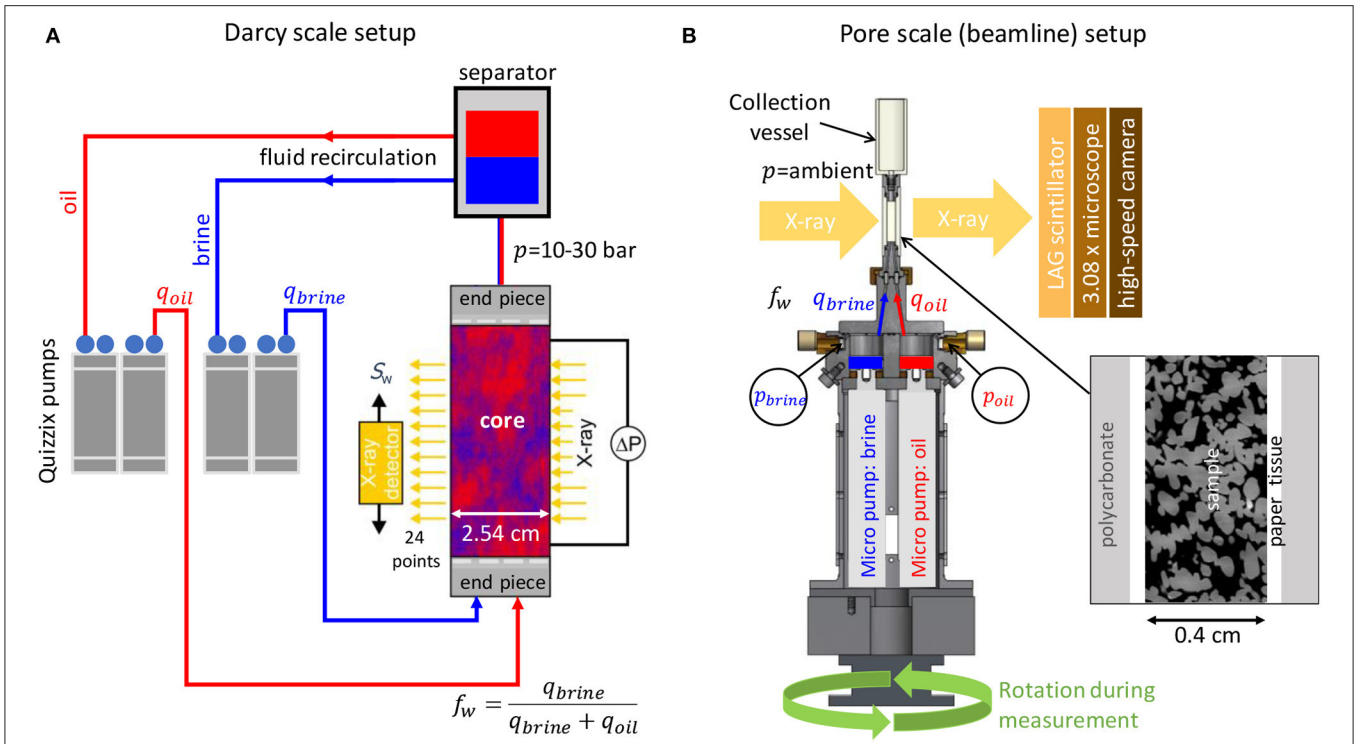

FIGURE 1 | Experimental setups for the Darcy-scale fractional flow "SCAL" experiments **(A)** and pore scale "beamline" experiments **(B)**. In the Darcy-scale experiments oil and brine are co-injected at varying flow rates and fractional flow f_w with 2 dual-piston Quizzix pumps that operate with zero-dead volume switching valves for smooth and pulse-free continuous flow. Fluids are re-circulated (after separation) without any back-pressure controller. Saturation is measured *in-situ* during the experiment using a linear X-ray scanner. The micro-CT setup **(B)** uses a core holder with 2 integrated micro-pumps (Berg et al., 2013) for water and oil co-injection at specified fractional flow f_w. At the outlet side the fluids are collected at ambient pressure, i.e., no back-pressure control system is used. The porous sample is wrapped with paper (for a hydrophilic boundary condition) and heat-shrunk into a poly-carbonate cylinder. The setup is self-contained as it is rotating during the micro-CT scans, i.e., no external flow lines are used. Power is supplied via slip rings and the pressure sensor readings are transmitted with a wireless system.

Starting with primary drainage, the fractional flow f_w was systematically changed from 100% brine ($f_w = 1$) to 100% oil ($f_w = 0$), followed by 1st imbibition cycle, where the fractional flow f_w was systematically changed from 100% oil ($f_w = 0$) to 100% brine ($f_w = 1$) in 10 saturation steps each. The total injection rate of $q_w + q_o$ was thereby kept constantly at 3 ml/min. That corresponds to a capillary number of $Ca = 10^{-5}$, which is still smaller than the onset of capillary de-saturation in imbibition and 1–2 orders below the onset of capillary de-saturation in drainage (Berg and Cense, 2009) but also high enough to suppress any capillary end-effect (Huang and Honarpour, 1998).

At each saturation step f_w, the saturation and phase pressures were recorded when, based on a constant pressure with a variation of the respective average being <1%, steady state was reached. The pressure readings were obtained with differential pressure transducers (Rosemount, type 3051 with an accuracy of ±0.15%) (Kokkedee et al., 1996). In addition, conductivity and saturation profiles at 30 positions along the rock sample were measured. The saturation profiles were obtained by X-ray transmission measurements calibrated to both 100% brine and oil saturation. The X-ray transmission is measured using a home-built linear X-ray scanner with a conventional X-ray tube and semiconductor-based detector, which makes individual point measurements (after an 8 min 30 s average to achieve sufficient signal-to-noise ratio). For details on the equipment, sample preparation, measurement procedures and analysis were published in previous studies (Kokkedee et al., 1996; Berg et al., 2016; Berg S. et al., 2020). For the particular case of the strongly water-wet Fontainebleau sandstone sample, the saturation profiles along the sample $S_w(x)$ (not shown) are flat as expected for a homogeneous sample and there is no noticeable capillary end-effect. The absence of saturation gradients allows us to directly compute the relative permeability-saturation relationships using the two-phase extension of Darcy's law for the phase fluxes

$$q_{w/o} = -\frac{k_{r,\alpha}}{\mu_\alpha} K \frac{\Delta p_{w/o}}{L} \quad (2)$$

where $k_{r,\alpha}$ is the relative permeability of phase α, K is the absolute permeability of the porous medium, μ_α is the viscosity and Δp_α the pressure of phase α over sample length L.

Resistivity is measured by a 4-point impedance measurement technique using (blackened platinum) electrodes embedded into the end pieces of the core holder.

Micro-CT Beamline Experiments (PS)

The experiments were performed in 2012 at the TOMCAT beamline of the Swiss-Light Source Synchrotron at the Paul-Scherrer Institute, Villigen, Switzerland. The flow cell was

specially designed for fractional flow experiments with two remotely controlled micro piston pumps (based on linear motors from Physics Instruments with a modified gear box for low-rate injection) enabling pulse-free continuous, low rate injection while performing 3D imaging (Berg et al., 2013; Rücker et al., 2015a). The pumps are built-into the core holder itself, which rotates continuously during the fast tomography in order to avoid any displacements caused by bending of flow lines. Flow lines of 0.8 mm diameter directly enter the bottom of the core, which has—because of lack of space—no extra diffusor plate. Since we only monitor the middle section of the core, the first section of the core acts as diffusor. The pressure of water and oil phases at injection side was monitored with 2 pressure sensors (Keller 2 MI), which transmitted the pressure data in real-time using a wireless method enabling a constant data acquisition in the field of view during the experiment. The conceptual overview of the setup is displayed in **Figure 1B**.

One full 3D image with a voxel size of 2.2 μm was recorded in 1 min. The reconstructed micro-CT images were further processed and segmented with the software package Avizo (ThermoFisher). Details on the flow cell, sample preparation, the experimental settings and image processing were described previously (Armstrong et al., 2014a; Rücker et al., 2015a). Further analysis was conducted with MatLab (MathWorks).

Even though at a resolution of 2.2 μm process such as film flow are not resolved anymore, such sub-resolution physics is effectively captured through the effective displacement events leading to filling of pores or changes in non-wetting phase connectivity, which is captured at this resolution.

The flow sequence included 3 fractional flow steps f_w ($f_w = 0.8$, $f_w = 0.5$ and $f_w = 0.2$), where at each f_w the total injection rate $q_{tot} = q_w + q_o$ was increased step-wise from 3 μl/min to 30 μl/min and 300 μl/min. The associated capillary numbers, which will be shown later in more detail in **Figure 13**, are in the capillary-dominated regime below the critical onset for viscous mobilization (Oughanem et al., 2015).

The permeability of the segmented pore space (in the imaged field of view) K_{abs} was computed by using a Stokes flow simulation conducted with GeoDICT (Math2Market). In addition, for selected time sequences of 2-phase flow experiments, the permeability of water K_w and oil phases K_o was computed in a similar fashion. The respective connected pathway relative permeability for water $k_{r,w}$ and oil $k_{r,o}$ was then obtained by dividing by the absolute permeability, i.e., $k_{r,w/o} = K_{w,o}/K_{abs}$.

RESULTS AND DISCUSSION

One of the main findings of the Darcy scale experiment is that the raw data contains fluctuations which—while varying in amplitude significantly from experiment to experiment—have often a systematic trend with fractional flow showing often maximum amplitudes at intermediate fractional flows.

In section Fluctuations in "Darcy scale" Fractional Flow Experiments, a detailed analysis of the noise structure in Darcy-scale steady-state core flooding experiments is presented. The focus is less the resulting relative permeability, which is also shown for completeness, but rather the raw data itself. We make a clear distinction between instrumental noise with Gaussian distribution (noise as a random process would result in a Gaussian probability distribution, fully described by its mean and standard deviation) and fluctuations with much larger amplitude than the instrumental noise for which we can largely rule out any instrumental artifacts. In section Dependency of the Fluctuations on Wettability the effect of wettability on the observed pressure fluctuation is discussed.

Finally, in section Energy Scale of Fluctuations, the energy scale of the large fluctuations observed in the Darcy scale flow experiments is analyzed and identified as a capillary energy scale, which is orders of magnitude larger than the thermal energies, i.e., fluctuations are non-thermal and of pore-scale origin. In section Time Scale of Fluctuations the time scale of the fluctuations is put into perspective with other characteristic times scales encountered in multiphase flow.

In sections Pressure and Saturation Fluctuations in Micro-CT fractional Flow Experiments, Pore Scale: Breakup and Coalescence Processes–Ganglion Dynamics, Identification of Pore Scale Flow Regimes by Collective Cluster Dynamics and the Pressure/Saturation Signature of Ganglion Dynamics the results from the synchrotron-beamline based micro-CT flow experiments are presented. The pore scale events presented in section Pressure and Saturation Fluctuations in Micro-CT Fractional Flow Experiments have similar amplitude as the significant fluctuations observed in the Darcy scale experiments in section Fluctuations in "Darcy scale" Fractional Flow Experiments. The pore-scale event observed under fractional flow conditions show transitions between two discrete states, which provides a further analogy to the oscillatory fluctuations shown in section Fluctuations in "Darcy scale" Fractional Flow Experiments. This is another piece of evidence that the significant fluctuations observed in SCAL experiments are de-facto caused by pore scale events. Using the insight of the *in-situ* 3D imaging, in section Pore Scale: Breakup and Coalescence Processes - Ganglion Dynamics the underlying fundamental pore-scale mechanism of breakup and coalescence that constitute ganglion dynamics and cause such events are discussed. In section Identification of Pore Scale Flow Regimes by Collective Cluster Dynamics and the Pressure/Saturation Signature of Ganglion Dynamics the effective flow regimes are characterized on the basis of saturation and macroscopic capillary number. The pore scale events discussed in section Pressure and Saturation Fluctuations in Micro-CT Fractional Flow Experiments suggest that ganglion dynamics events are initiated by an imbibition cycle followed by a drainage cycle.

Fluctuations in "Darcy Scale" Fractional Flow Experiments

Differentiation of Capillary Fluctuations From Gaussian Noise

Fractional flow experiments, often also referred as the steady-state method, are routinely used to determine relative permeability from cylindrical rock samples. Two immiscible fluids, such as oil and water are co-injected at fractional flow f_w

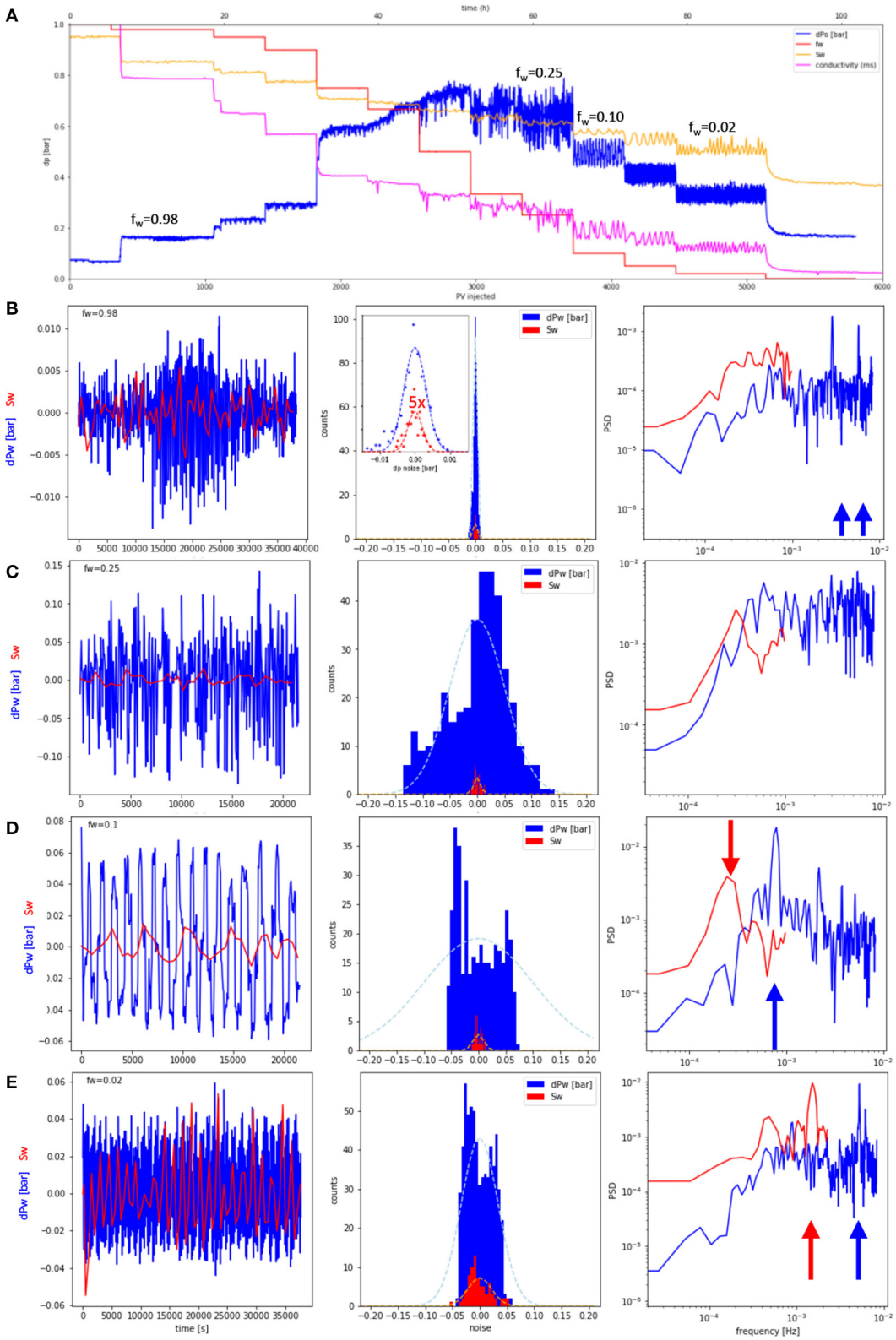

FIGURE 2 | Water pressure drop dP_w, water saturation S_w and electrical conductivity during a SCAL fractional flow experiment to determine relative permeability on a centimeter-sized Fontainebleau sandstone sample. Overview of the water pressure drop for all fractional flows f_w **(A)** and fluctuations (with base line subtracted) for

(Continued)

FIGURE 2 | selected fractional flow vs. time for pressure (blue) and saturation (red), fluctuation histogram and associated power law spectrum **(B–E)**. While the fractional flows $f_w \geq 0.75$, the fluctuation histogram follows a Gaussian shape (dotted light blue line in the middle in **B–E**) suggesting instrumental noise as cause. At $0.67 \geq f_w \geq 0.02$, the noise amplitude is significantly larger than instrumental noise and the histogram is clearly non-Gaussian and in most cases also non-symmetric and even bi-modal **(D,E)** suggesting other causes than instrumental noise. For some fractional flows, e.g., $f_w = 0.1$ the pressure fluctuations are almost perfectly periodic **(D)** with an oscillation period of $t \approx 21$ min, which is also reflected in a peak in the Fourier spectrum (marked with a blue arrow). Similarly, for S_w also perfectly periodic behavior can be observed, although at different frequencies (marked with red arrow), which could be potentially caused by the different sampling rates of dP (1 min intervals) and S_w (8 min 30 s intervals).

(Equation 1) following a sequence of fractional flow steps that starts at $f_w = 1$ (only brine) to $f_w = 0$ (only oil) for a drainage experiment and vice versa for imbibition. In **Figure 2** the raw data of the experiment, i.e., the pressure drop Δp, saturation S_w, and electrical conductivity are plotted for a drainage experiment in the Fontainebleau sandstone sample.

Figure 2A shows an overview of the whole experiment, where f_w, pressure drop $\mathrm{dP_w}$, saturation S_w, and resistivity are plotted for a constant flow rate drainage experiment as a function of injected pore volumes (bottom axis) and time (top axis). Pressure drop dP_w, saturation S_w, and resistivity show fluctuations that are very small for high fractional flows but increase for intermediate fractional flows significantly. For a more detailed view and analysis for each fractional flow, the fluctuations were isolated by subtracting the base line (using a moving average window). In the left panel of **Figures 2B–E** for 4 selected fractional flows, the isolated fluctuations for pressure drop $\mathrm{dP_w}$ and saturation S_w are displayed.

In the middle panel of **Figures 2B–E**, the fluctuation histogram is shown. For fractional flows $f_w \geq 0.75$ (which is not a hard cut-off but rather based on the observations in the fractional flow sequence that has been established over several years as standard protocol), the histogram is symmetric and in good approximation of Gaussian shape, see also **Figure 3**, where the respective histograms for pressure and saturation fluctuations are fitted with a Gaussian. That indeed suggests instrumental noise as cause for the fluctuations. However, for $0.67 \geq f_w \geq 0.02$ the fluctuation histogram is clearly non-Gaussian as the middle panel of **Figures 2C–E** show (a Gaussian fit is added for visual comparison as dotted line). The histogram is not symmetric and for $f_w = 0.1$ and $f_w = 0.02$ has even a bimodal distribution (middle panel of **Figures 2D,E**). Pressure fluctuations range up to $\delta dP_w = \pm 0.15\ bar$ and saturation fluctuations up to $\delta S_w = \pm 0.05$, i.e., ± 5 percent points.

For these cases, the fluctuations are highly periodic, which is also reflected in the peak in the Fourier transform of the fluctuation time signal in the right panel of **Figure 2**. The fluctuation spectra for saturation (and electrical conductivity data in **Figure 2A**) differ from the pressure fluctuations, which could be a consequence of the different sampling rates. The pressure is sampled at 1 min time intervals, which means that fluctuations at a 2 min time interval are resolved. Saturation and resistivity are only monitored at an 8 min 30 s time interval. Faster fluctuations are not explicitly resolved.

When performing time averages of the detected signal, a smoothening operation commonly applied during the analysis of multiphase flow experiments in porous media, the fluctuations, which are initially clearly non-Gaussian and even bi-modal as in **Figure 2E**, become increasingly symmetric as shown in **Figure 4**. Here, a rolling average over a window of 2, 4 and 16 individual data points was used. After sufficient averaging, the histogram (**Figure 4B**) becomes perfectly Gaussian (which is a consequence of the central limit theorem) and the information this signal may have originally contained get lost, which has implications for the interpretation of the energy dissipation (McClure et al., 2020a,b).

For $f_w < 0.67$, the pressure fluctuations $\delta \Delta p$ are much larger than what would be expected from the behavior of the pure noise from instrumentation, which has been established based on amplitude and Gaussian shape of the histogram in **Figure 3**. The pure instrumental noise can be established from $f_w = 1.0$, which corresponds to the injection of 100% brine into a fully brine-saturated rock without any oil, representing single-phase flow conditions. Nevertheless, the instrumental noise of the pressure transducer is proportional to the magnitude of the pressure. With $\delta \Delta p \propto \Delta p$ we can extrapolate a noise trend from the first 6 f_w, which is illustrated by the dotted line in **Figure 5A**. In **Figure 5B** a similar approach was applied to saturation S_w (Cense et al., 2014). This way the fluctuations can be separated from the noise. Fluctuations falling into the noise regime (below the dotted lines in **Figures 5A,B**) can be either instrument noise or pore-scale events. But for the events with standard deviation significantly above that line, instrumentation noise can be ruled out entirely.

Differentiation of Capillary Fluctuations From Experimental Artifacts

As **Figures 2–5** illustrate the strong pressure fluctuations do not occur for all fractional flows but primarily for fractional flows $0.5 < f_w \leq 0.02$ as shown in **Figure 5C**, where the presumably both fluid phases are mobile and ganglion dynamics (Rücker et al., 2015b) is possible.

In order to characterize the periodic aspect of the fluctuations, the three largest peaks in the Fourier spectrum are displayed in **Figures 5C,D**. Note that in order to separate dominant peaks with significant amplitude from insignificant peaks the dot size represents peak amplitude and color its prominence (ratio of peak amplitude to that of the next peak). The same representation is used in **Figures 5C,D**. Based on the magnitude of the periodic fraction one can divide the fluctuations into a periodic and non-periodic dominated regime as indicated in **Figures 5C,D**. While **Figure 5C** suggests that f_w is a control parameter for the magnitude of fluctuations in general, i.e., including periodic and non-periodic ones and also the magnitude of the periodic oscillations (PSD) initially scales with f_w, the frequency of the dominant peaks do not scale with f_w as shown in **Figure 5D**.

As already established in section Differentiation of Capillary Fluctuations From Gaussian Noise, the significant fluctuations

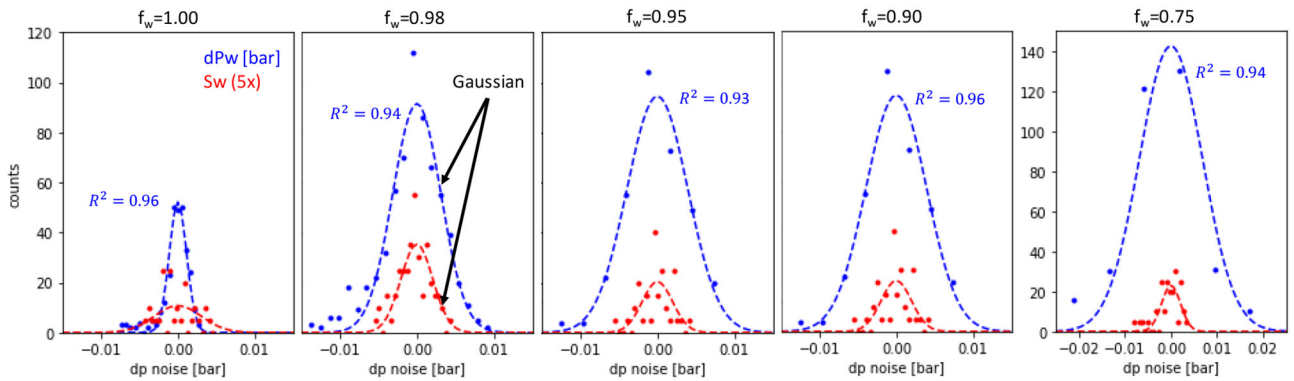

FIGURE 3 | Pressure drop *dp* and saturation S_w fluctuation (S_w fluctuations were magnified by factor 5 for better visibility) from **Figure 2** for fractional flows $1.0 \geq f_w \geq 0.75$ showing an almost perfectly Gaussian behavior (dotted lines represent a Gaussian fit to the respective data). For *dp* the correlation coefficient R^2 is 0.94–0.96. For S_w the correlation coefficient ranges between 0.41 and 0.69, which is likely because of the lower signal-to-noise of the S_w data.

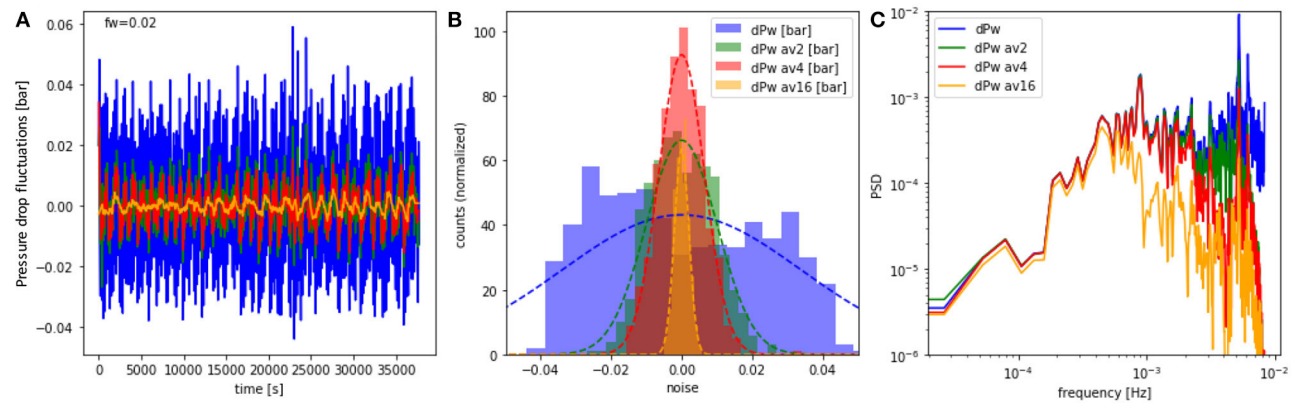

FIGURE 4 | Pressure fluctuations for $f_w = 0.02$ from **Figure 2E**, and rolling-averages over a window of 2, 4, and 16 data points **(A)**. While the histogram for the original data (blue) set is bi-modal and clearly distinct from a Gaussian (dotted line), the histograms of the averages become increasingly symmetric and can be fitted very well with Gaussians **(B)**. The Fourier spectrum **(C)** shows that smaller frequencies remain unaffected up to the frequency associated with the timer period of the averaging window.

occurring at intermediate fractional flows are not caused by instrumental noise. We can also largely rule out other artifacts from the experimental setup. These would manifest in a scaling of the periodicity with f_o, which is not observed. Also, common effects known from traditional experimental setups for fractional flow, can be ruled out due to the design chosen in the outlined work.

In traditional set-ups one likely cause of fluctuations is the back-pressure control system. Membrane-based back-pressure regulators may oscillate when two immiscible fluid phases pass through simultaneously, or pumps with a servo control system for back-pressure control could potentially cause oscillations as well. However, in this particular setup the fluids were internally circulated, and no back-pressure control system was used, see **Figure 1A**. The two Quizzix feed pumps do use a servo control system for maintaining a constant flow rate. But that servo control system is only reacting on feedback of the pump piston movement, which is independent of the flow dynamics within the rock sample. Furthermore, if this set-up would induce fluctuations, then these would be visible at all fractional flows including $f_w = 1.0$ and $f_w = 0.0$. But, at these fractional flows no oscillations were observed.

The frequency of the dominant Fourier peaks does not show any obvious systematic, e.g., linear dependency on oil fractional flow $f_o = 1 - f_w$. If—hypothetically speaking—the periodic oscillations were an instrumental artifact one would expect a dependency with the rate of oil injection, i.e., $q_o = f_o \cdot q_{tot}$ at constant q_{tot}. Doubling f_o would then double the oscillation frequency. That was not observed. The dark-gray dotted line in **Figure 5D** representing such scaling with $f_o = 1 - f_w$ made to pass (by choice of a suitable offset) the dominant peak in the Fourier spectrum at $f_w = 0.1$ (**Figure 2D**) does not pass the dominant peaks at $f_w = 0.05$ and $f_w = 0.02$ (**Figure 2E**). A more general linear model (light gray dotted line) does not describe the data either. It may pass through some of the dominant peaks but miss other dominant peaks of the Fourier spectrum. That clearly

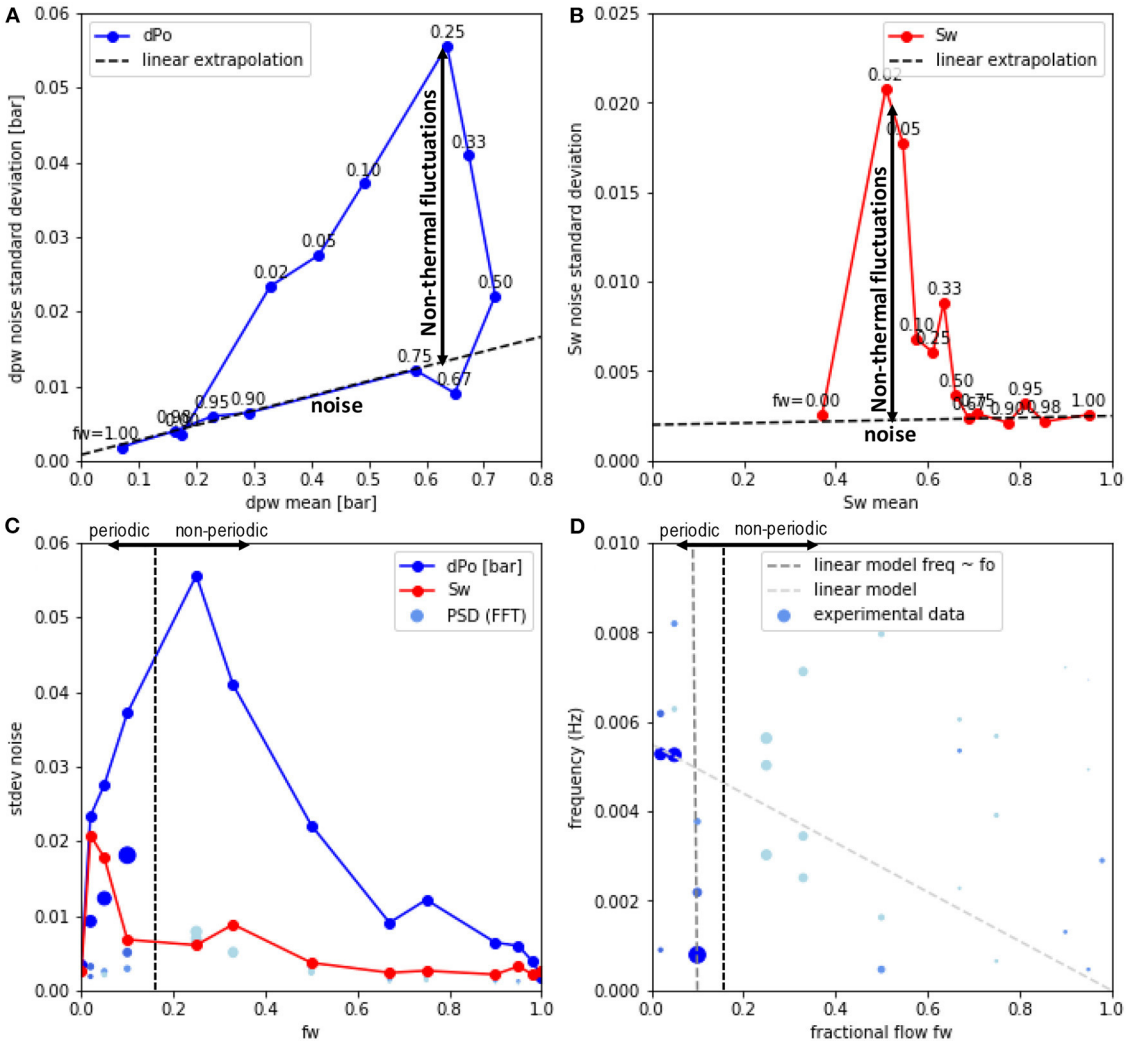

FIGURE 5 | Separating the non-thermal fluctuations from instrumental noise: Standard deviation of the noise for pressure drop **(A)** and saturation **(B)** for each f_w plateau (added as label for each point) in **Figure 2A** as a function of the respective mean values for each f_w plateau. For the pressure drop Δp **(A)**, for $f_w \geq 0.67$ an approximately linear increase is observed meaning that the pressure fluctuations are proportional to the mean pressure (dotted red line). But at $f_w < 0.67$ the fluctuations are up to more than 3 times the value above the noise. The saturation **(B)** follows a somewhat similar behavior in the sense that the fluctuations can be much larger than noise. But there is no direct proportionality between pressure and saturation fluctuations. The maximum in fluctuations is observed also for different f_w **(C)**. The periodic fraction of the fluctuations characterized by the PSD of the FFT from **Figures 2B–E** (dot size represents peak amplitude and color its prominence) shows a somewhat similar trend with f_w.Based on the magnitude of the periodic fraction one can divide the fluctuations into a periodic and non-periodic dominated regime. However, the frequency of the dominant peaks in the Fourier spectrum do not show any obvious systematic, e.g., linear dependency on fractional flow **(D)**.

rules out any instrumental artifacts related to the regulation of oil fractional flow, or also injection instabilities into the rock, as they would all be expected to scale with oil injection rate, i.e., f_o.

Analysis of Capillary Fluctuations at the Darcy-Scale

In order to gain deeper insight into the cause for the oscillations, which have also been observed in several independent pore scale experiments (Spurin et al., 2020; Menke et al., 2021), in **Figure 6** we show the saturation profiles for $f_w = 0.1$, which has the longest oscillation period and the sampling rate of saturation would be sufficient to resolve both pressure and saturation. A closeup of the pressure data from **Figure 2D** for the same time interval of saturation profiles is shown in **Figure 6A**. While the pressure data goes through 5 oscillations, the saturation shows only 2 full oscillations. The respective saturation profiles for the same time interval are shown in **Figure 6B**. For clarity, the saturation profiles have been vertically shifted. The wave structure is better visible in the space-time contour plot shown in **Figure 6C**.

The saturation profiles show a peak that travels from inlet to outlet at constant velocity. The dashed black lines in **Figure 6B** represent the wave, which is better visible in the space-time plot in **Figure 6C**. Even though **Figure 6C** may appear at first glance as a standing wave, a water saturation peak (red) moving

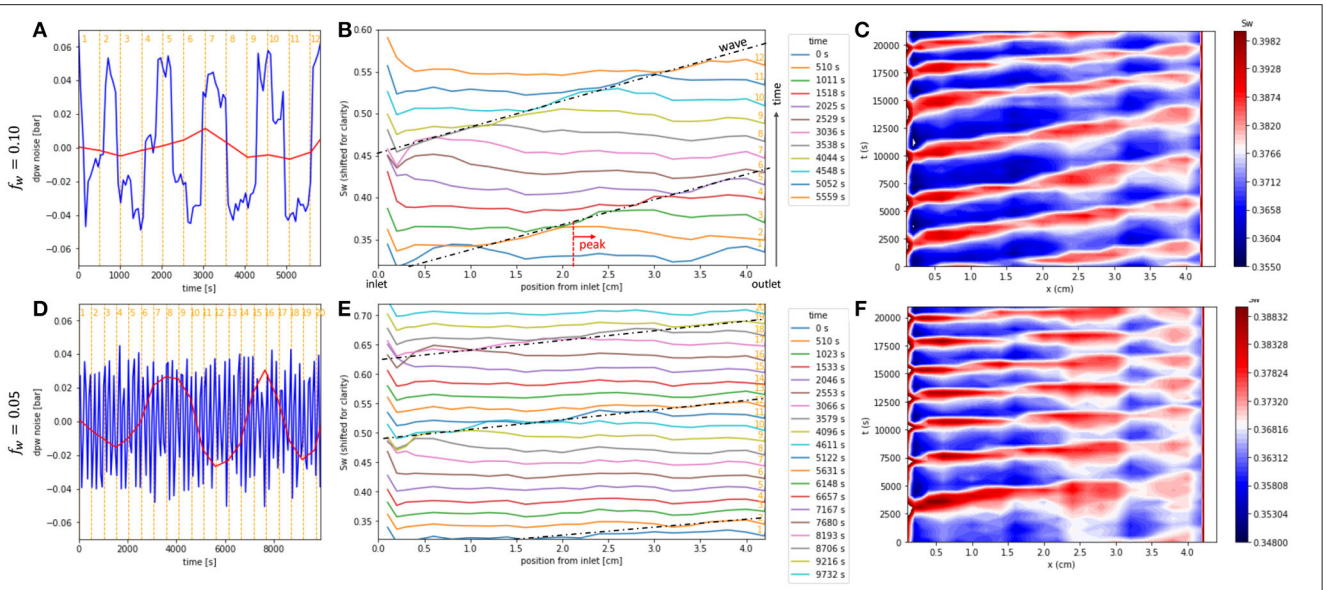

FIGURE 6 | Pressure and saturation fluctuations for $f_w = 0.10$ (limited range, 0–5700 s from **Figure 2D**) **(A)** and $f_w = 0.05$ **(D)** showing pressure data in blue and saturation data (sampled at much lower frequency) in red. Respective saturation profiles (**B,E**, which have been vertically shifted for clarity) exhibit a water saturation peak, which moves from inlet to outlet at constant velocity, forming a traveling wave, which repeats one the peak reaches the outlet. The wave structure in **(B,E)** has been emphasized by adding the dashed black lines. The wave structure is better visible in the space-time contour plots in **(C,F)**. For $f_w = 0.10$ the wave velocity is $v_{S_w} = 0.75\ mm/$ min and for $f_w = 0.05$ the wave velocity is between 1.7 and 2.1 mm/min.

horizontally from left to right at different times t (vertical coordinate). The fact that in the space-time plot in **Figure 6C** diagonal structures at constant angle and constant spacing are found suggests that the water saturation peak moves at constant velocity, which ultimately reveals a traveling wave structure, which through its repetitive pattern is emphasized in the space-time representation. A similar behavior is observed for $f_w = 0.05$ shown in **Figures 6D–F**.

In the experiment the behavior was reproducible. In total, 3 drainage and 3 imbibition cycles were performed. The experiment started with the 1st drainage cycle arriving at connate water saturation of ∼4%. It was followed by the 1st imbibition cycle arriving at a residual oil saturation of ∼48%, which is typical for a strongly water-wet rock sample such as the non-aged Fontainebleau sandstone. Then the rock was cleaned *in-situ* by flushing with iso-propanol without removing the sample. Then the 2nd drainage and 2nd imbibition cycle were performed, followed by *in-situ* cleaning and finally conducting the 3rd drainage and 3rd imbibition cycle. The respective relative permeability computed from the raw data (such as the 1st drainage cycle from **Figure 2**) are displayed in **Figure 7**. For all 3 cycles the relative permeability data overlaps indicating excellent repeatability of the experiment. We observe overall larger noise amplitudes in the drainage cycles than for the imbibition cycles (not shown), which suggests that hysteresis may play a role.

By comparing the speed of the traveling wave from the experiment with the prediction of fractional flow theory we can test whether the wave propagation is a simple fractional flow phenomenon. According to fractional flow theory, $v_D = x_D/t_D = df_w/dS_w$, which is shown as an inset in **Figure 8B**. $x_D = x/L$ is the dimension distance (L is the length of the core) and $t_D = PV_{injected}/PV$ the dimensionless time (PV =pore volume). For $f_w = 0.10$ the wave velocity in the experiment is $v = 0.76$ mm/min, which corresponds to a dimensionless velocity $v_D = 0.46$. For $f_w = 0.05$ the wave velocity v is between 1.7 and 2.1 mm/min, which corresponds to dimensionless velocity $v_D = 2.1 - 2.6$.

In **Figure 8B**, we show the fractional flow curves for the saturation range of interest, and in **Figure 8C**, the respective $v_D = df_w/dS_w$. For $f_w = 0.05$, the experimentally measured v_D is more compatible with the imbibition curve, whereas for $f_w = 0.10$ the wave velocity is more compatible with the drainage curve. At first glance that appears somewhat inconsistent. However, when taking a closer look at the fractional flow construction involving two fractional flow curves, which is analogous to a moving an oil bank known, e.g., from polymer flooding (Lake, 1984), we notice a somewhat subtle detail, which is an inflection point around $f_w^* \approx 0.12$ above which the water saturation of the bank (wave peak) increases compared with the initial saturation $S_{w,i}$ for the respective flow. An example is shown in **Figure 8A** for $f_w = 0.15$. If we consider the experimental uncertainties in terms of saturation measurements and instead of using dotted blue lines in **Figures 8D,E** as initial saturations but the lowest saturation observed, it is very well possible that in the experiment the inflection point is at $0.07 < f_w^* < 0.10$. That would imply that for $f_w = 0.10$ we have indeed a water bank pushed by oil (which is drainage) and for $f_w = 0.05$ we would have an oil peak pushed by water (imbibition). From the experiment, it is difficult to distinguish between the two

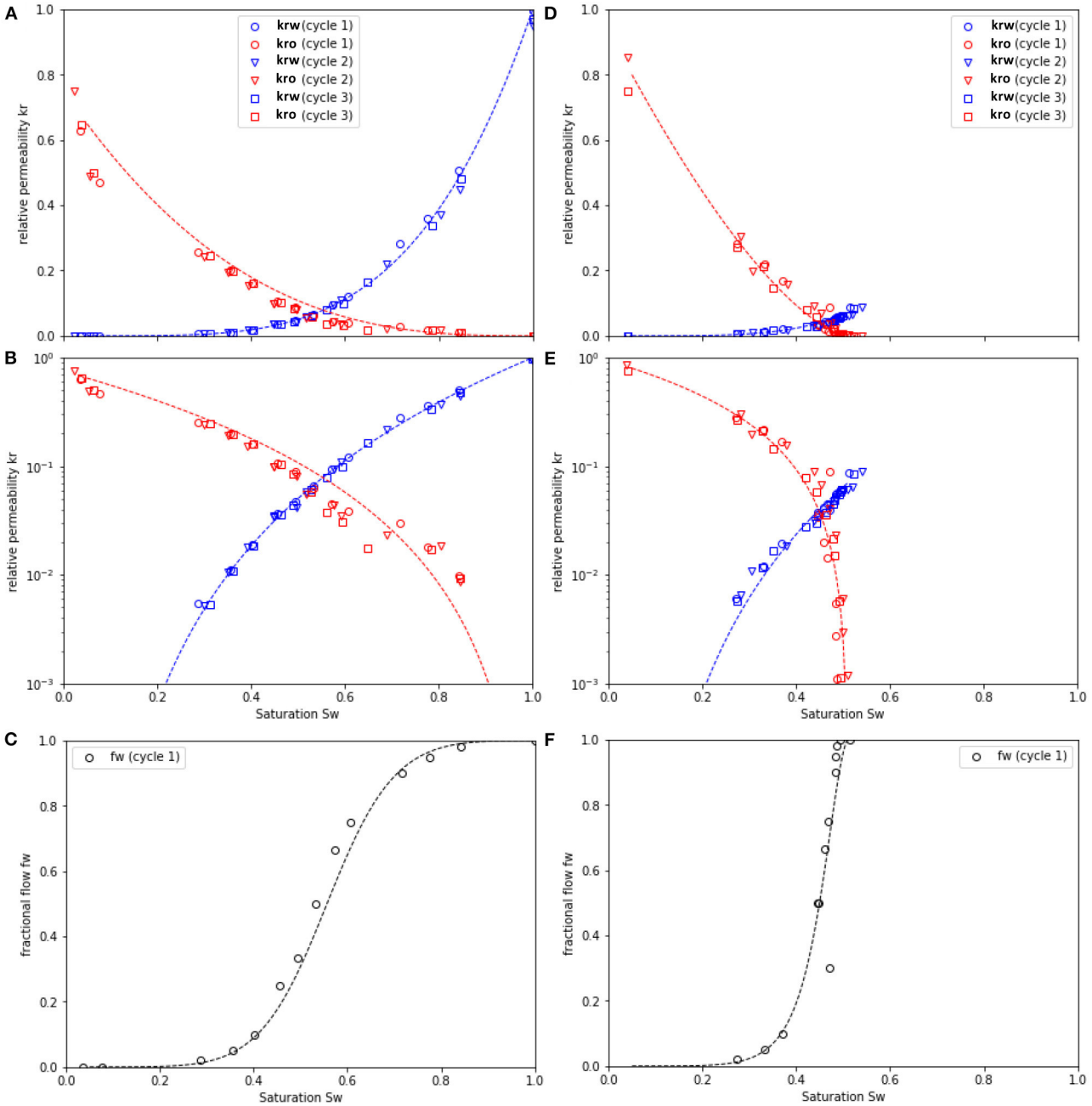

FIGURE 7 | Relative permeability for water (blue) and oil (red) for the SCAL experiment with the strongly water-wet Fontainebleau sandstone sample for the 1st, 2nd, and 3rd cycles for drainage **(A–C)** and imbibition **(D–F)**. Each cycle consisted of drainage, followed by imbibition, and sub-sequent *in-situ* cleaning of the sample with iso-propanol inside the setup without unmounting/remounting the sample. There is excellent repeatability between individual experiments. The dotted lines show a Corey fit of the data. The fractional flow functions $f_w(S_w)$ for the first drainage and imbibition cycle are shown in **(C,F)**, respectively.

situations based on saturation profiles because the phenomenon is repetitive, and it is not fully clear, which phase is displacing and which phase is displaced. Within the experimental uncertainties, it is very well possible that the $f_w = 0.10$ experiment is above f_w^*, whereas the $f_w = 0.05$ experiment is below the inflection point f_w^*. That would explain why the experimentally observed wave velocities follow the prediction from fractional flow theory $v_D = df_w/dS_w$ for drainage at $f_w = 0.10$ and imbibition for the $f_w = 0.05$ shown in **Figure 8C**.

The correct modeling of the traveling water peak involves hysteresis in the relative permeability-saturation functions. For the situation encountered in the experiment, the relative permeability would actually reflect a scanning curve, which needs to be considered in respective analysis (Plohr et al., 2001).

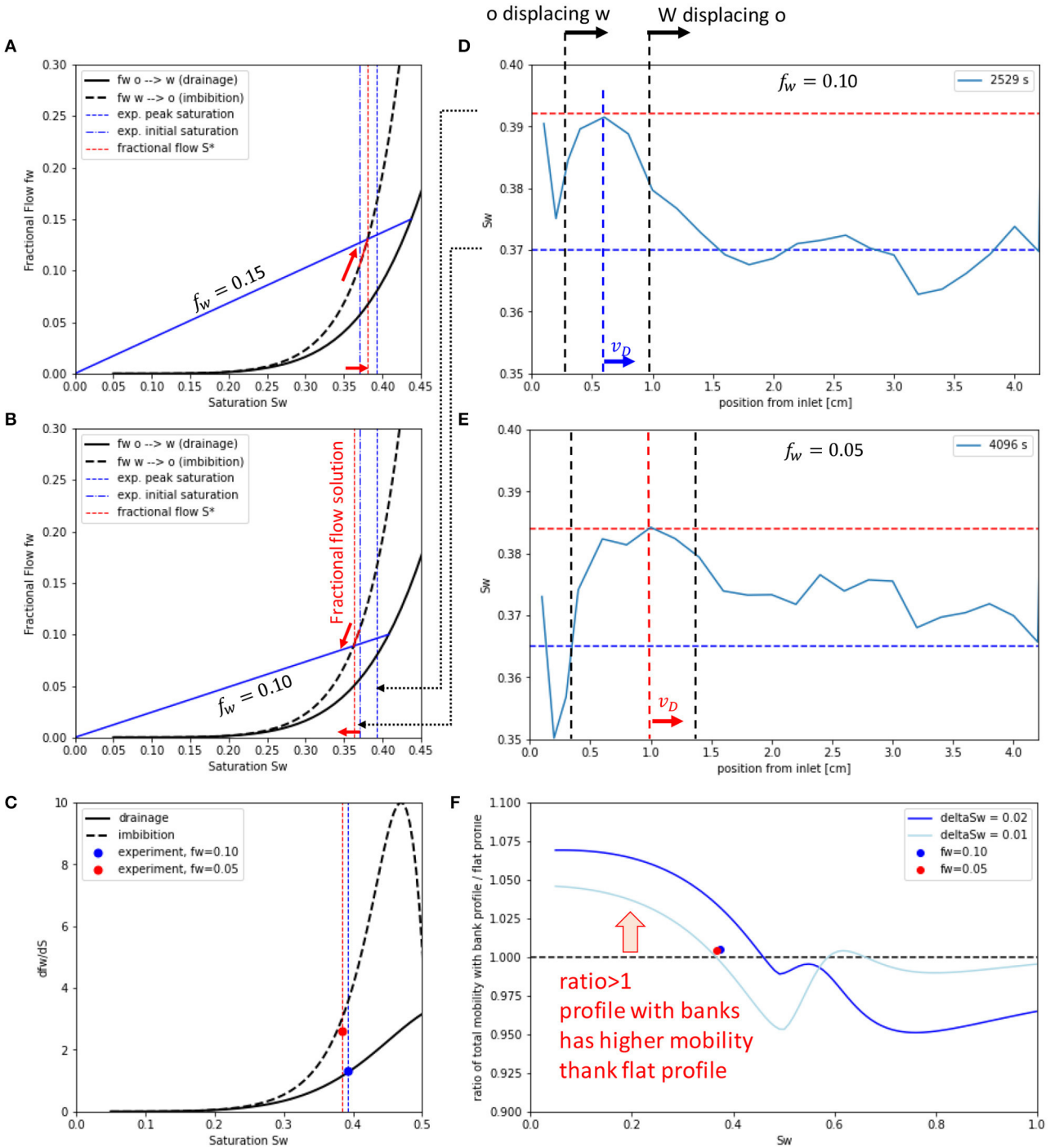

FIGURE 8 | Fractional flow $f_w(S_w)$ **(A,B)** and the derivative $v_D = df_w/dS_w$ **(C)** for $f_w = 0.15$ **(A)** and $f_w = 0.10$ **(B)** for the saturation interval corresponding to the top and bottom of the peak of the saturation waves **(D,E)**. Representative examples of the wave profile are shown for $f_w = 0.10$ **(D)** and $f_w = 0.05$ **(E)**. The wave for each fractional flow consists of a water peak moving from inlet to outlet, which has water displacing oil at the front and oil displacing water at the back. The respective fractional flow constructions are shown in **(B)**, where the flow line is constructed from the intersection of the drainage fractional flow curve at respective f_w step. The fractional flow solution is the intersection between the blue line with the imbibition fractional flow curve (Lake, 1984). Note that depending on the exact value of the initial saturations **(D,E)** there is an inflection point $0.07 < f_w^* < 0.12$ above which the water saturation from the fractional flow solution increases compared to the initial saturation **(A)**, while below f_w^* it decreases **(B)**. That would imply a change from oil pushing a water bank (drainage) at $f_w > f_w^*$ to water pushing an oil bank (imbibition) for $f_w < f_w^*$. That could explain why the experimentally observed wave velocities follow the prediction from fractional flow theory $v_D = df_w/dS_w$ for drainage at higher fractional flows and the imbibition line for smaller fractional flows. That transition is within the experimental uncertainty between $f_w = 0.10$ and $f_w = 0.05$. A saturation profile with moving banks has an overall higher total mobility than a flat saturation profile for the saturation range $S_{w,c} < S_w \leq 0.4 - 0.5$ **(F)**. The two experiments at $f_w = 0.10$ and $f_w = 0.05$ are added as points, where for the computation of mobility, respective bank saturations and lengths have been taken from **(D)** and **(E)**, respectively.

Such traveling waves with non-monotonic saturation profiles are known to form under specific conditions for instance for infiltration of water into dry soil (Schneider et al., 2018; Kmec et al., 2019; Mitra et al., 2020) and can be theoretically described with a range of models ranging from generalized Darcy-scale formalisms with dynamic capillary pressure (Schneider et al., 2018) to hybrid models combining Darcy physics and pore scale aspects (Kmec et al., 2019). Mitra et al. (2020) provides a mathematical model, where for specific choices of parameters, the solution forms spirals in the $S_w - p_c$ space. The hysteresis model by Plohr et al. (2001) demonstrates that for specific choices of parameter values "loop", i.e., recurring solutions can be found, which implies stable orbits in phase space (Strogatz, 1994). These consist of a sequence of water and oil bank, where the respective final saturation and fractional flow serves as an initial condition for the next wave sequence. In that way, the sequence becomes recurring. Although Corli and Fan (2018) raise questions around non-uniqueness, the principle does provide a reasonable working hypothesis about the origin of the periodic waves observed in the experiments.

Whether periodic wave structures are observed depends on the initial condition $S_{w,i}$ for each fractional flow f_w, the fractional flow f_w and the underlying relative permeability functions, and potentially also the domain size L. It cannot be excluded that the large but non-periodic oscillations in **Figure 2C** are in the end related to the same fractional flow effect, but cannot form a closed loop (Plohr et al., 2001). More generally, phenomena at the Darcy scale are only visible if a permissible fractional flow solution exists, otherwise they would be dampened and a periodic trigger from e.g., initial or boundary conditions would decay.

Physical Interpretation of the Wave Characteristics of the Observed Fluctuations

While mathematically the solutions are permissible by fractional flow theory, the question is now why from a physical perspective a bank solution would form. A solution with moving banks would be plausible if, for the same total pressure drop, more total flux was transported than for a flat saturation profile. Whether that is the case can be assessed by computing total mobility for a flat saturation profile and compare it with the respective total mobility for the situation with moving banks. For the flat saturation profile the total mobility of water and oil phases, weighted with the respective fractional flow

$$\lambda_{tot}^{flat} = f_w \frac{k_{r,w}^{drain}}{\mu_w} + \left(1 - f_w\right) \frac{k_{r,o}^{drain}}{\mu_o} \tag{3}$$

using drainage relative permeability (because overall it is a drainage experiment). Note that the definition in Equation (3) is different from standard fractional flow theory and in that sense represents a pseudo-mobility. The weighting with the respective fractional flow is done in order to estimate the total flux based on the contributions of drainage and imbibition waves from segregated flow. For the situation with a moving bank, we assume based on the experimental observation that the saturation profile is composed of one water and one oil bank and compute the total mobility each bank separately. In absence of a rigorous fractional flow solution, which would first require a very detailed treatment for hysteresis, we simply estimate the top and bottom saturations by adding a typical saturation fluctuation amplitude of $\delta S_w = \pm 0.1$ or $\delta S_w = \pm 0.2$. For the water bank we use imbibition relative permeability and for the oil bank drainage relative permeability. We then weight the contribution of water and oil bank by their respective length in the saturation profile, i.e., the water bank is about 10–20% in terms length of the total saturation profile $l_w = 0.1 - 0.2$ (see **Figures 6C,F**), i.e., $\lambda^{banks} = l_w \lambda^{water\ bank} + (1 - l_w)\lambda^{oil\ bank}$. In order to assess whether the bank solution has higher mobility we divide $\lambda^{banks}/\lambda^{flat}$, which is plotted in **Figure 8F**. We see that depending on the magnitude of δS_w the bank solution has a higher mobility for saturations below $S_w < 0.4 - 0.5$, corresponding to approximately $f_w < 0.4$, which is also the range in which the large fluctuations in pressure and saturation are observed (see **Figure 5C**). Note that the fractional flow picture does not capture the effects of capillarity, which can improve the microscopic sweep (Khorshidian et al., 2021).

The remaining question is what actually triggers the fluctuations in general and waves in particular. In the following sections, we will establish from pore scale fractional flow experiments conducted in a similar steady-state manner as the core flooding experiments in **Figures 2–5** that periodic variations of pressure and saturation already occur on the oil-cluster scale and ultimately caused by pore scale displacement events (Berg et al., 2013, 2014; Spurin et al., 2020; Menke et al., 2021). The pressure and connectivity signature and 3D imaging of respective pore scale fluid distributions observed in the fractional flow micro-CT experiment suggest that pore scale displacement events are the underlying cause of fluctuations that are still visible in experiments commonly assumed at Darcy scale. They also likely provide the trigger for the waves from **Figures 6C,F**.

Dependency of the Fluctuations on Wettability

In order to investigate the dependency on rock wettability, a systematic study was conducted using twin samples of Bentheimer outcrop rock taken from the same block and selected for homogeneity and similar properties in terms of porosity and permeability. The rock was then de-saturated and aged with 3 different crude oils ("crude 1," "crude 2," "crude 3") with properties listed in **Tables 1**, **2**. In **Figure 9** the raw data of the respective steady-state imbibition experiments (analogous to **Figure 2A**) are shown.

The pressure fluctuations are largest for the sample aged with crude 1 and become much smaller for Bentheimer samples aged with crude 2 and 3 (**Figure 9A**). Based on the trends of residual oil saturation $S_{o,r}$ and water endpoint relative permeability $k_{r,w}(S_{o,r})$ shown in **Figure 9B** the sample aged with crude 1 is the most water-wet case, whereas crude 2 and 3 become increasingly intermediate-wet. This confirms the experience in the SCAL community that significant fluctuations are mainly observed for water-wet cases.

When normalizing the standard deviations of the pressure fluctuations by the mean pressure along the lines of the learnings from **Figure 5** we find that over-proportionally-large pressure

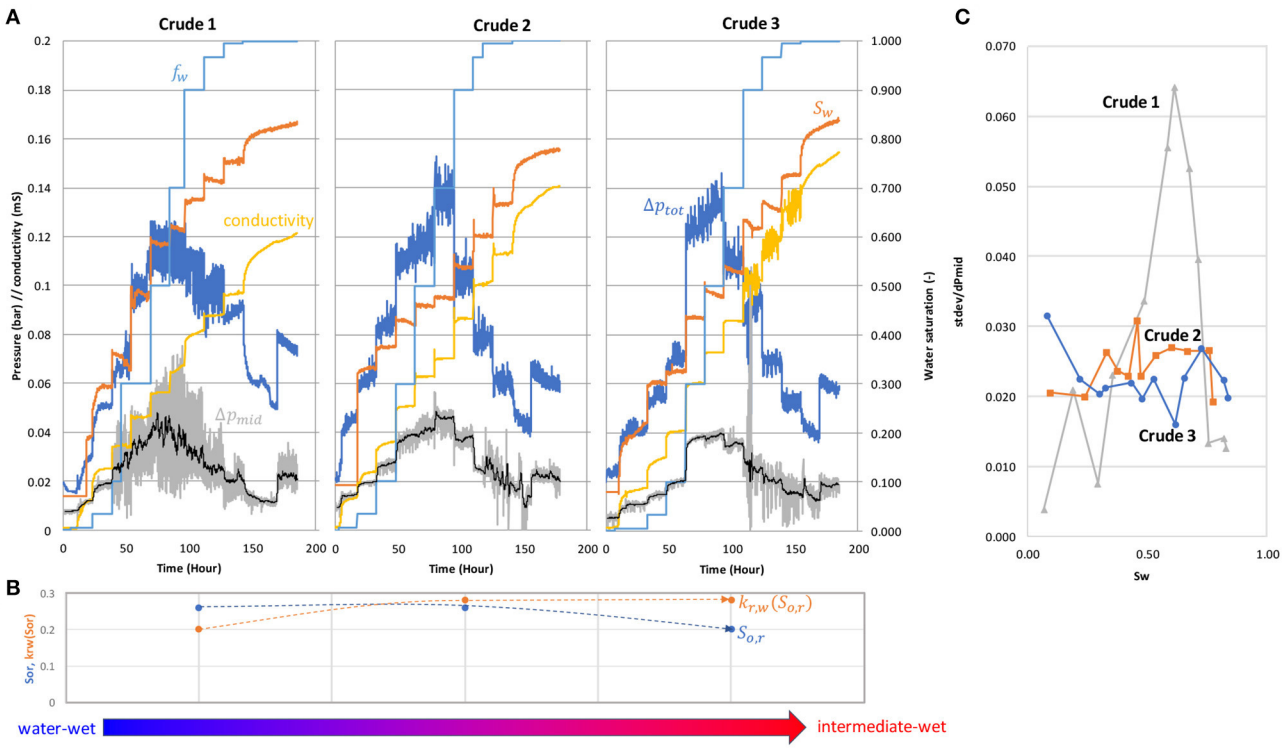

FIGURE 9 | Dependency of the fluctuations on the wetting state of the rock. Pressure fluctuations are largest for the Bentheimer rock sample aged with crude 1 and become much smaller for Bentheimer samples aged with crude 2 and 3 **(A)**. The trends for residual oil saturation $S_{o,r}$ and water endpoint relative permeability $k_{r,w}(S_{o,r})$ suggest that the wettability for the sample aged with crude 1 is more water-wet, whereas samples aged with crude 2 and crude 3 become increasingly intermediate-wet **(B)**. The standard deviation of the pressure fluctuations normalized by the mean pressure for each fractional flow f_w is largest for crude 1 (which is the most water-wet case) and becomes significantly less for crude 2 and 3 **(C)**.

fluctuations are only observed for the crude 1 case, i.e., the most water-wet sample. However, the trend toward crude 2 and 3 cases and respective wetting states seems highly non-linear and also not entirely consistent. For instance, in the crude 3 case we do observe fluctuations in electrical conductivity, which suggests that in intermediate cases fluctuations at the pore scale could still be present but due to the much smaller capillary pressure (Lin et al., 2019a) show a much smaller signature in the pressure but still are subject to ganglion dynamics. This is in line with pore-scale studies, in which fluid redistributions were still happening in mixed-wet scenarios, though much slower pace compared to water-wet situations (Rücker et al., 2019). At intermediate wetting states, the connectivity of the brine phase, which controls the electrical conductivity (Liu Z. et al., 2018), is perhaps also more sensitive to ganglion dynamics, because water-films may be overall less connected.

Energy Scale of Fluctuations

Figures 2–5 suggest that the pressure fluctuations not related to instrumental noise have amplitudes between 40 and 150 mbar and a standard deviation up to 55 mbar. Based on that magnitude we can identify the energy scale of the fluctuations.

We begin with a number of model calculations for typical pore body and throat sizes in sandstone rock of $d = 25\ \mu m$ diameter for pore throats and $d = 60\ \mu m$ for pore bodies (Berg et al., 2013). Assuming furthermore an interfacial tension of $\sigma = 25\ mN/m$ for a typical crude oil-brine system (water-decane with highest purity n-decane would be $\approx 50\ mN/m$ but polar components in crude oil can reduce interfacial tension below 1 mN/m, therefore 25 mN/m is a good average value) we can estimate capillary pressure

$$p_c = \frac{2\sigma\, cos(\theta)}{r} \tag{4}$$

(with contact angle $\theta \approx 0^\circ$ for a water-wet system and radius $r = d/2$) for a water-wet system as $p_c = 0.017$ bar for pore bodies and $p_c = 0.04$ bar for pore throats, which are also typical values for the pressure fluctuations in the steady-state experiment in **Figures 2–5** (the maximum fluctuations can be a factor 3–4 larger but for most f_w the range is very similar) (Berg C. F. et al., 2020). This suggests that the pressure fluctuations are likely caused by events on the capillary energy scale, which are typically pore scale events. Therefore, pore scale displacement events related to capillary instabilities (Singh et al., 2017, 2019; Primkulov et al., 2019) are the most likely cause for the significant fluctuations.

The associated pressure-volume work of displacing the wetting-phase by non-wetting phase fluid (Morrow, 1970).

$$\Delta W_{pressure-volume} = p_c \Delta V \quad (5)$$

In a pore body ($\Delta V \approx 1.1 \cdot 10^{-13} m^3$ for a spherical pore) is $4.5 \cdot 10^{-10}$ J and for a pore throat ($\Delta V \approx 1.2 \cdot 10^{-14} m^3$) $4.9 \cdot 10^{-11}$ J. This can be expressed in terms of thermal energy units k_BT, where $k_B = 1.38 \cdot 10^{-23} J/K$ is the Boltzmann constant and $T = 300K$ ($\approx 26.7^{\circ}C$) the temperature arriving at $1.1 \cdot 10^{11} k_BT$ and $1.2 \cdot 10^{10} k_BT$ for pore bodies and throats, respectively, which is also summarized in **Table 3**. Since the associated energy of the pressure fluctuations is many orders of magnitude larger than k_BT these fluctuations can be classified as non-thermal (Winkler et al., 2020).

To put this into perspective, we can also estimate the kinetic energy that is associated with laminar single-phase flow at a typical injection rate 1 $foot/day$, which is typical for a water flood in oil reservoirs far away from the well bore, which translates for a porosity $\phi = 0.25$ into a linear flow velocity of $v = 1.4 \cdot 10^{-5}$ ms^{-1} (Berg and van Wunnik, 2017).

The kinetic energy

$$E_{kinetic} = \frac{1}{2} \rho V v^2 \quad (6)$$

is for an aqueous phase fluid with density $\rho = 1000$ kg m^{-3} around $1.1 \cdot 10^{-20}$ $J \approx 2.63$ k_BT, which is roughly on the thermal energy scale.

The linear flow velocity during a Haines jump, which can be computed numerically with a phase-field type of method and validated with experimental data, is around $v = 1.0 \cdot 10^{-2}$ ms^{-1} (Armstrong et al., 2015). That translates into a kinetic energy of $5.7 \cdot 10^{-15}$ $J \approx 1.4 \cdot 10^{6}$ k_BT, which is again several orders of magnitude larger than the thermal energy scale.

Note that for pressure-volume work and kinetic energy of pore-scale displacement events there is always a range, which depends on the non-local nature of the Haines jumps, pore size, wetting conditions etc. The important point to make here is that the kinetic energy is orders of magnitude larger than the thermal energy scale, which is consistent with the classification as non-thermal fluctuations. Since the energy scale of these fluctuations is many orders of magnitude above the thermal energy scale, increasing temperature cannot trigger pore scale displacement events (unless phase changes or disintegration of material occur).

We observe pressure fluctuation amplitudes in the range of capillary pressure representative, typical pore throats of sandstone rock and indicative of pore scale displacement events as origin (**Figures 2–5**). However, the magnitude of the saturation change in relation to the volume of an individual pore suggests that many individual pores are involved in the phenomenon. The pore volume of the Fontainebleau rock sample is $V_{pore,tot} = 2.85$ cm^3, whereas the pore volume of a single pore of $d = 60$ μm diameter is $V_{pore,single} = 1.1 \cdot 10^{-7}$ cm^3, which means that a saturation change of 5% needs to involve thousands of individual pores. The associated energy scale can be estimated as $p_c \cdot V_{pore,tot} \cdot \delta dS_w$ with $p_c \approx \delta dP_w = 0.15$ bar resulting in 0.043 J or $10^{19} k_BT$, which is significantly larger than the energy scale of displacements involving individual pores.

That means that multiple individual pores are involved in these fluctuations. From a pore-scale perspective this is not too surprising as experiments have already shown that displacement events are not necessarily always isolated but can be cooperative causing avalanche-like cascading sequences of individual displacements adding up to an overall significant event, that involves many pores and lasts over a time period of between 0.5 and 2 s (Armstrong et al., 2014a). What is new is that the fluctuations measured at the Darcy-scale are periodic, which means that the respective pore-scale displacement events would also need to be repetitive under fractional flow conditions. In order to address that question, in the following sections time sequences of 3D imaging are presented, which give further insight into the pore-scale origin of the fluctuations.

Time Scale of Fluctuations

When comparing experiments of different scales, both, the magnitude of time and length differences need to be considered. The time series and frequency analysis of the pressure fluctuations shown in **Figures 2**, **4C**, **5D** suggest a frequency range of fluctuations between $10^{-3} - 10^{-2}$ Hz corresponding to a time period of $T = 1/f = 1 - 20$ $minutes$, which also reflects the dominant peaks in **Figure 5D**. The time scale of the saturation fluctuations is between 5 and 60 min, which is also about the time scale of the traveling waves from **Figure 6**.

In **Figure 10**, we put the time scale of pressure and saturation fluctuations and traveling waves into perspective with characteristic time scales encountered in multiphase flow in porous media. Displacement events in individual pores such as Haines jumps and snap-off are on the time scale around 1 ms (Armstrong et al., 2015). Cascading displacement events involving multiple pores show a relaxation time scale around one second (Armstrong et al., 2014a). The time scale of pressure fluctuations observed in this work, in particular the periodic oscillations in **Figures 2–4**, are on the order of 1–20 min, which is also the time scale of periodic pressure fluctuations reported in recent studies (Spurin et al., 2020; Menke et al., 2021) see also the supporting information of (Spurin et al., 2020). The time scale of the saturation fluctuations is 30–60 min, which is similar as the characteristic time of traveling waves from **Figure 6**, which is still faster than the slow relaxation behavior observed in (Schlüter et al., 2017).

Figure 10 suggests that in terms of time scale the pressure and saturation fluctuations observed in the SCAL experiments are a phenomenon ranging right between pore scale and Darcy scale flow physics (Khorshidian et al., 2021). Imaging at the Darcy length scale may not give further insights into the underlying mechanisms and pore scale imaging is required. Based on **Figure 10**, we can expect a time scale of the order of minutes, which means that imaging at the time scale of few seconds will be sufficient to resolve the phenomenon.

TABLE 3 | Pressure-volume work ($p_c \Delta V$) for model scenarios of immiscible displacement and kinetic energy for 1 ft/day flow in units of Joule (J) and thermal energy ($k_B T$).

	Diameter (μm)	Volume (m^3)	Pressure volume work (J)	Kinetic E (J)	Energy ($k_B T$)
$p_c \Delta V$ pore throat	25	$1.2 \cdot 10^{-14} m^3$	$4.9 \cdot 10^{-11}$		$1.2 \cdot 10^{10}$
$p_c \Delta V$ pore body	60	$1.1 \cdot 10^{-13} m^3$	$4.5 \cdot 10^{-10}$		$1.1 \cdot 10^{11}$
Kinetic energy laminar flow	60	$1.1 \cdot 10^{-13} m^3$		$1.1 \cdot 10^{-20}$	2.63
Kinetic energy Haines jump	60	$1.1 \cdot 10^{-13} m^3$		$5.7 \cdot 10^{-15}$	$1.4 \cdot 10^{6}$

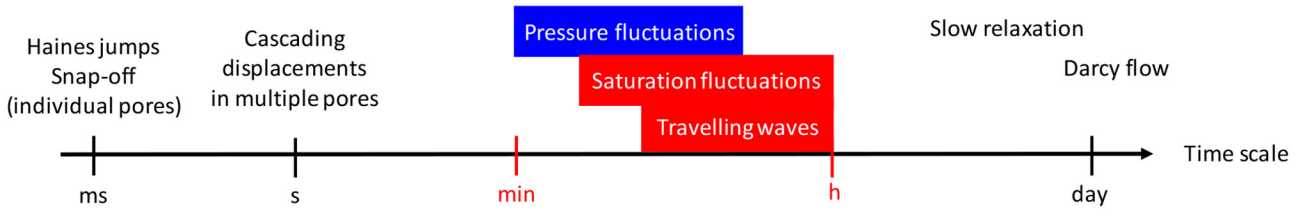

FIGURE 10 | Time scale of the fluctuations observed in this work (red) put into perspective with other characteristic times scales encountered in porous media. Displacement events in individual pores such as Haines jumps and snap-off are on the time scale around 1 ms (Armstrong et al., 2015). Cascading displacement events involving multiple pores show a relaxation time scale around one second (Armstrong et al., 2014a). The time scale of pressure fluctuations observed in this work and related studies (Spurin et al., 2020; Menke et al., 2021) are on the order of 1–20 min and the saturation fluctuations and traveling saturation waves from **Figure 6** are on the order of 30–60 min. That is still faster than the slow relaxation behavior observed in Schlüter et al. (2017). Darcy flow, e.g., at typical field rates of 1 ft/day over a characteristic length scale such as a capillary dispersion zone of 3–5 centimeters length occurs at 7–10 h.

Pressure and Saturation Fluctuations in Micro-CT Fractional Flow Experiments

In the steady-state micro-CT flow experiment conducted at a much smaller sample (4 mm diameter, 2 cm length) also fluctuations in pressure and saturation are observed as shown in the example in **Figure 11**. These events are re-occurring between periods of meta-stable and predominantly connected pathway flow (Rücker et al., 2015b). Associated changes in pressure in **Figure 11A** and saturation in **Figure 11B** have similar magnitude as the fluctuation amplitudes in the SCAL steady-state experiment conducted at a much larger sample shown in **Figures 2–5**. The pressure fluctuation event in **Figure 11** of 10–20 mbar amplitude is similar to the fluctuation amplitude in **Figure 2C**. The monitored fluctuations at the pore-scale are significantly larger than instrumental noise and are not caused by instrumental artifacts, which is evident from the larger scale analysis, the chosen experimental set-up as well as the additional information revealed by the imaging of the interior of the rock during flow (**Figure 11**).

Note that—as discussed in section Energy Scale of Fluctuations—pressure fluctuations are mainly caused by capillary effects. Therefore, even though the micro-CT sample has a significantly larger permeability, but pore throat size distribution is actually similar to that of sandstone rock of comparable porosity and permeability as in the SCAL experiments (see Figure 1 in Berg et al., 2014), the magnitude of pressure fluctuations is similar.

These observed fluctuations and associated pore-scale events are related to change in fluid connectivity as the Euler characteristic (Herring et al., 2013), a mathematical measure for connectivity displayed in **Figure 11G**, and the connected pathway relative permeability computed from the fluid phases imaged by micro-CT displayed in **Figure 11D** shows. Even though the sample is significantly smaller than in the SCAL experiment, the associated saturation change is much bigger than the volume of individual pores, which implies that these events involve multiple individual pores. The event statistics, which was obtained by comparing 3D images of water and oil phases of subsequent time steps (Rücker et al., 2015b) displayed in **Figure 11C** show that the events observed in pressure and saturation consist of hundreds of individual pore level displacements.

That is consistent with cooperative displacements of advancing fluids fronts (Jung et al., 2016; Singh et al., 2017; Primkulov et al., 2019) and the observation in Armstrong et al. (2014a) with avalanche-like cascades of individual pore filling events operating overall at the cluster scale. The repetitive sequence of oil and water filling events are indicative of waves passing through the field of view, although the domain size in micro-CT experiments does not permit to resolve the spatial extent of the wave but rather see repetitive behavior in the average S_w. The event statistics in **Figure 11C** shows that the macroscopically-visible events start with sequences of water filling events, which are then followed by sequences of capillary-driven oil filling events, which may provide the trigger for the Darcy scale observations, where traveling waves of water saturation peaks were observed (**Figure 6B**) and permissible by fractional flow solutions (**Figure 8**), which operate in the viscous limit. This draws a direct connection between Darcy-scale observable flow regimes (which have to be permissible by fractional flow solution, otherwise they would be damped and decay) and cooperative pore-scale

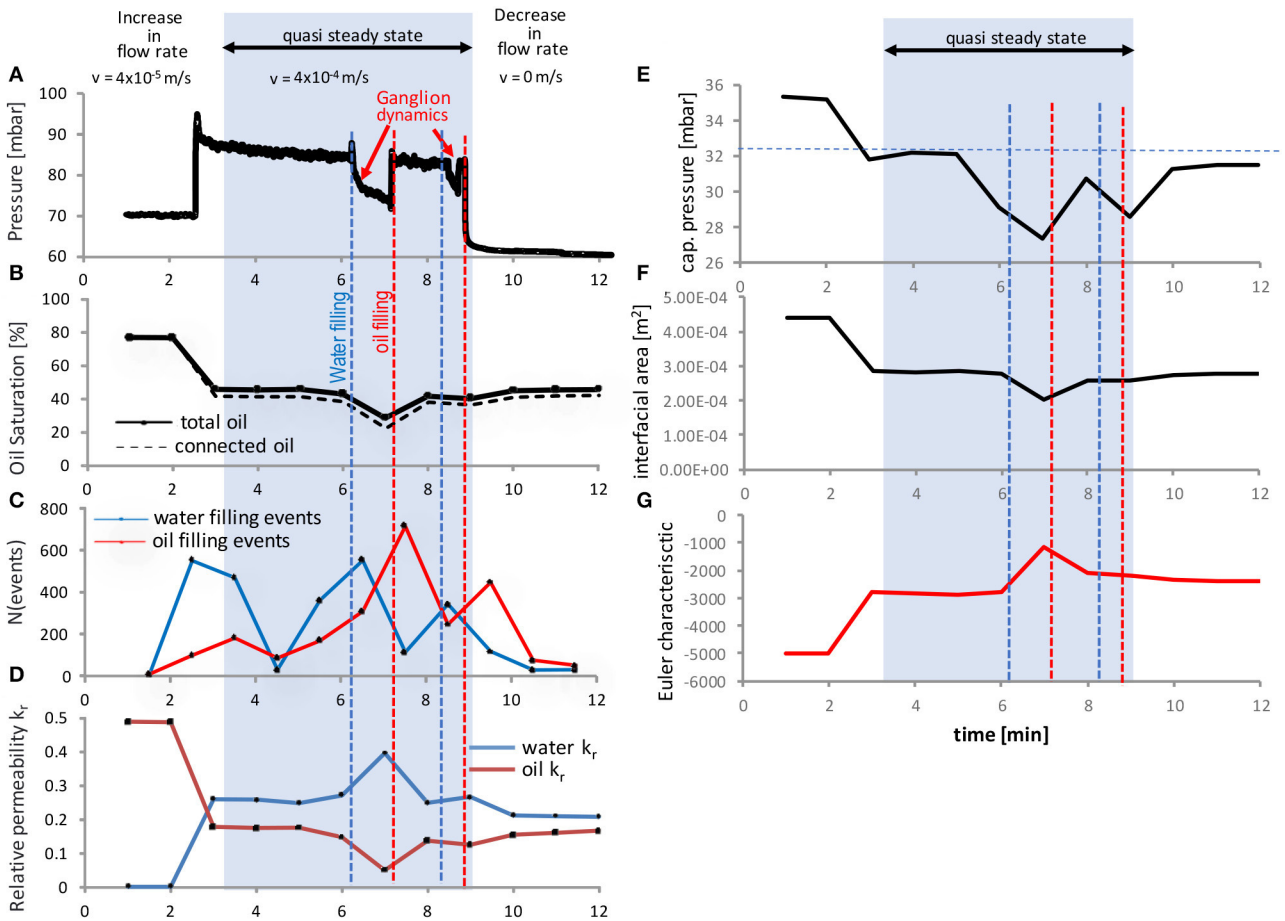

FIGURE 11 | Pressure drop **(A)**, water saturation **(B)**, event statistics **(C)** connected pathway relative permeability k_r of connected water and oil phases **(D)**, capillary pressure p_c obtained from the mean curvature **(E)**, interfacial area, **(F)** and the Euler characteristic for the oil phase **(G)** for the experiment at $f_w = 0.5$ and $v = 4 \cdot 10^{-4}\ m/s$. The fluctuation events with a clear pressure and saturation signature are caused by a sequence of water and oil filling events. They are causing changes in the connectivity of water and oil phases as visible in the connected pathway relative permeability, which was computed by Stokes flow simulations of the imaged water and oil phases in relation to the (analogous computed) permeability of the respective pore space. The capillary pressure largely follows the saturation and connectivity behavior, which all typically lag behind water or oil filing events, respectively. Note that capillary pressure shows a clear signature also for the 2nd filling event, which is much less visible in saturation, interfacial area (Joekar-Niasar and Hassanizadeh, 2011) and Euler characteristic (Herring et al., 2013).

displacement behavior. It furthermore suggests that analogous to ganglion dynamics (Rücker et al., 2015b) the dynamics is initiated by snap-off which is a capillary instability, where capillary energy is converted into kinetic energy, which can then drive event cascades. The pore-scale fluid configuration eventually reverts back to the original situation in terms of saturation, pressure drop and connectivity of each phase as suggested by **Figures 11A,B,D**. There is a range of possible reasons from the bubble instability (Unsal et al., 2007a,b; Unsal et al., 2009), which can in principle also occur in large pores inside of rock, relaxation time scales (Armstrong et al., 2014a) being longer than the re-supply of injected liquid at fractional flow f_w, questions about the energy efficiency of connected pathways (Spurin et al., 2021) and inertial effects during displacement events causing ganglion dynamics (Rücker et al., 2015b), which can all explain why established flow paths can become unstable and disconnection processes are followed by re-connection processes. The capillary pressure determined from the liquid-liquid curvature (see, e.g., Lin et al., 2019b) shown in **Figure 11D** largely follows the saturation and connectivity behavior, which typically lag behind water or oil filing events, respectively. The magnitude of the capillary pressure changes is about 10 mbar, which is significant and suggests that capillarity is involved in the process. The system can reduce its capillary energy by water filling events, but because of the flux and fractional flow boundary conditions, oil-filling events temporarily increase the capillary energy again. This suggests that the condition is not only viscous-unstable as the fractional flow assessment suggests, but also capillary unstable, based on the competition between minimizing potential energy (where capillary energy is a significant fraction) and fractional flow boundary conditions. Note that pore filling events in **Figure 11C** are computed from difference images, which is the reason why they may appear somewhat earlier than the capillary pressure response in **Figure 11E**, which are computed from only one image.

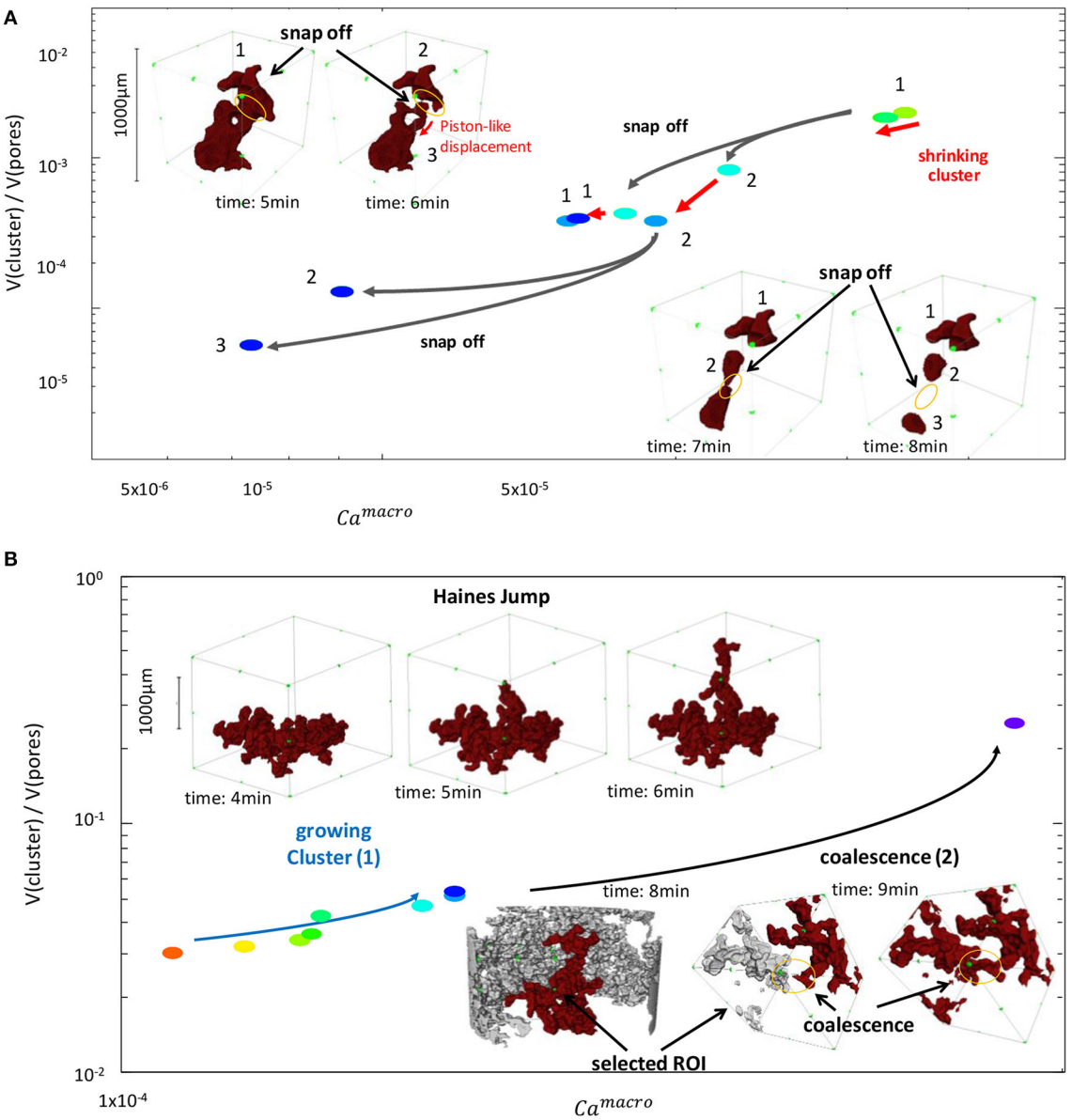

FIGURE 12 | Breakup of oil clusters **(A)** and coalescence **(B)** processes at the pore scale. Breakup occurs often by simultaneous snap-off processes in a cluster thereby preserving topological loop structures (see insets in **A**). Clusters can also grow by coalescence, which is overall more a frontal propagation, whereby connectivity is maintained, and formation of loops is largely avoided. Both breakup and coalescence events impact cluster volume, i.e., saturation and cluster length, i.e., the macroscopic capillary number, which is proportional to the viscous pressure drop over the cluster length.

The question is now how we can use 3D pore scale imaging to understand more about the origin of these repeating events with cascading pore-level event structure.

Pore Scale: Breakup and Coalescence Processes—Ganglion Dynamics

In order to characterize the processes at the pore scale, we first establish a general insight into the evolution of oil clusters under fractional flow conditions, which is more complex than the ganglion dynamics during imbibition alone (Rücker et al., 2015b), because both wetting and non-wetting phases are permanently co-injected. One of the questions is how that co-injection at fractional flow f_w is translating into the flow at pore scale, i.e., what the associated flow regimes are.

At the pore scale the fractional flow can be divided into time periods of connected pathway flow and time intervals with topological changes in the fluid configuration. These can be decomposed into a more imbibition-dominated regime with breakup of oil clusters by sequences of snap-off and piston-like displacement processes as shown in **Figure 12A**, and a more drainage-dominated regime with oil cluster growth by Haines-jumps and coalescence as shown in **Figure 12B**. Note that as clusters breakup /shrink or grow, also their length changes, which

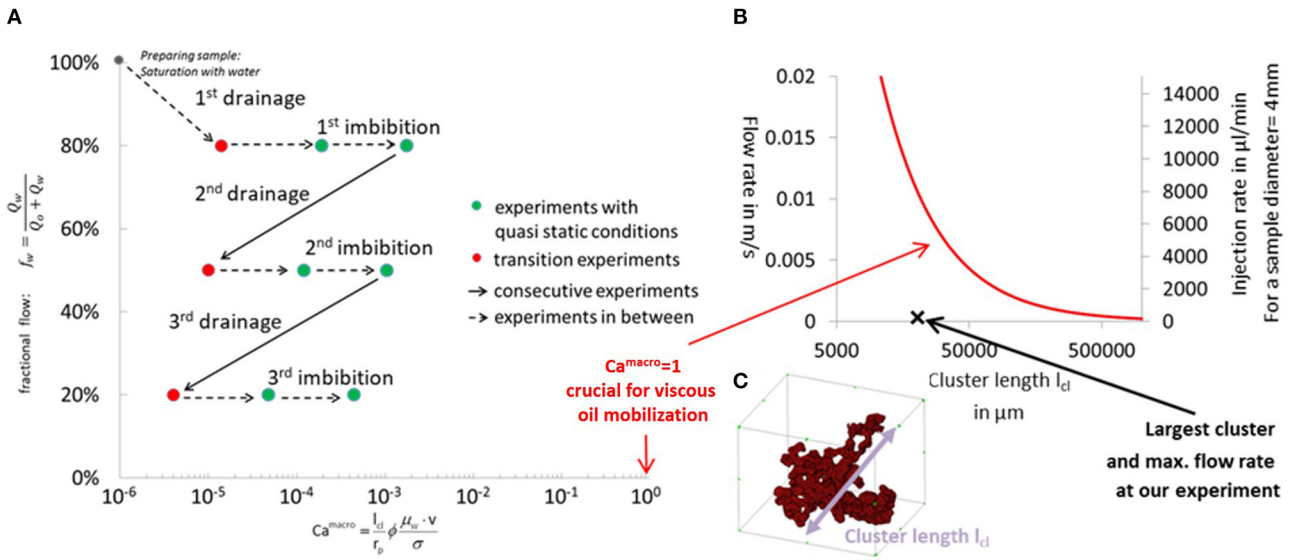

FIGURE 13 | Fractional flows f_w (0.8, 0.5, and 0.2) and cluster-based capillary number $Ca_{cluster}$ from Equation (7) for the micro-CT flow experiments conducted at flow rates of 3, 30, and 300 µl/min **(A)**. For all flow rates and fractional flows $Ca_{cluster} \ll 1$, which means that the flow regime is capillary dominated. The bounding line for $Ca_{macro} = 1$, which is the transition to the viscous-dominated regime is plotted as red line in **(B)** in the flow velocity (left axis) and injection rate (right axis) vs. cluster length **(C)** space. Also, the largest cluster falls below this line even at the highest flow rate, which means that the flow regime is capillary dominated.

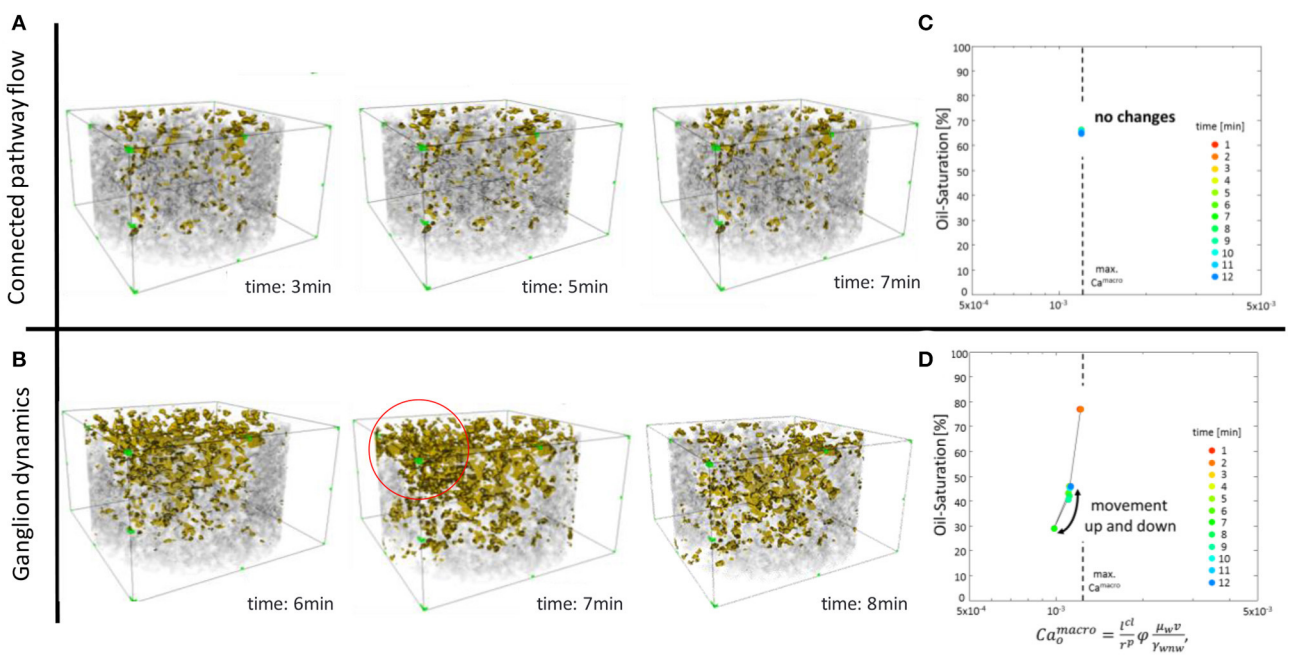

FIGURE 14 | Pressure drop and saturation from **Figure 11** show long time periods without any change but also time periods with discrete events. Based on the associated dynamics at the pore scale, respective pore scale flow regimes can be categorized into predominantly connected pathway **(A)** and ganglion dynamics **(B)**. A "phase diagram" can be developed in analogy to **Figure 12** but now for the whole field of view instead of individual clusters only, where connected pathway flow is characterized by a fixed point **(C)** and ganglion dynamics as trajectories **(D)** in the saturation-macroscopic capillary number space.

impacts the cluster-based capillary number (Hilfer and Oren, 1996; Armstrong et al., 2014b).

$$Ca_{macro} = \frac{\Delta p_{visc}}{\Delta p_{cap}} \approx \frac{L_{cluster} \mu_w v_w}{K \cdot p_c} \approx \frac{L_{cluster}}{r_{pore}} \frac{\mu_w v_w}{\sigma_{ow} \cos(\theta)} \quad (7)$$

where $L_{cluster}$ is the length of the respective oil cluster, μ_w the wetting phase viscosity, v_w the wetting phase Darcy velocity, σ_{ow} the wetting/non-wetting phase interfacial tension and θ the contact angle, and p_c the capillary pressure at breakthrough.

In that way, for each oil cluster an individual capillary number can be assigned, which is proportional to the cluster length $L_{cluster}$ and increases or decrease according to how the cluster grows by coalescence or shrinks by breakup.

Figure 12 is based on actual data from the micro-CT flow experiment conduced in the sintered glass sample. Conceptually similar behavior is expected also in other porous media but may change in terms of quantity, because of e.g., different scaling of permeability over capillary pressure.

Note that these examples characterize local flow regimes. These local regimes can also dominate the macroscopic flow regime in a macroscopic drainage or imbibition experiment, but they can also co-exist, or alternate in time, in fractional flow.

Identification of Pore Scale Flow Regimes by Collective Cluster Dynamics and the Pressure/Saturation Signature of Ganglion Dynamics

The micro-CT flow experiments involved three different fractional flows $f_w = 0.8,\ 0.5,\ 0.2$ and three different injection rates of $q_{tot} = 3,\ 30,\ 300\ \mu l/\text{min}$. Using the largest from the imaged cluster size distribution from Rücker et al. (2015a) these flow rates are then translated into the maximum cluster-based capillary number (Equation 7). The overview of all experiments is shown in **Figure 13A** in the fractional flow-macroscopic capillary number space.

All measurements obtained fall significantly below the $Ca_{macro} = 1$ bounding line, which is the transition to the viscous-dominated regime as shown in **Figure 13B**. This means that in every respect the flow regime is capillary dominated below the onset for viscous mobilization (Oughanem et al., 2015).

Nevertheless, at specific saturations and higher flow rates we observe ganglion dynamic behavior as shown in **Figure 11**. In **Figure 14** we show the respective pore scale fluid distributions. In **Figure 14A** shows an example for a connected pathway flow period without any significant fluctuations. In **Figure 14B** shows the pore scale fluid distributions for the fluctuating event from **Figure 11**.

Figures 14C,D are an extension of the concepts from **Figure 12** but now for the whole oil saturation in the imaged field of view and not only individual clusters, the capillary number is calculated using the a volume weighted average cluster length. The connected pathway flow regime is characterized by a single point in **Figure 14C**, whereas the fluctuating regime is characterized by a trajectory in **Figure 14D**. Based on that observation, the saturation-macroscopic capillary number space displayed in **Figures 14C,D** can be understood as "phase diagram", where connected pathway flow is characterized by a fixed point and ganglion dynamics as trajectories.

The ganglion dynamic events from **Figure 11** are characterized by a diagonal movement between two discrete states in the saturation-capillary number space as shown in **Figure 14C**. This repeated switch between two states is very similar as the pressure and saturation fluctuations between an maximum and a minimum saturation level, and a maximum and minimum pressure drop, observed in Darcy-scale SCAL experiments in **Figures 2–5**. From the change in saturation but also the associated 3D visualization of the respective pore scale fluid distribution shown in **Figure 14B** it is clear that such ganglion dynamics events involve cooperative displacement in a large number of individual pores.

SUMMARY AND CONCLUSION

In this work we establish that significant fluctuations in pressure and saturation well visible in multiphase flow experiments on centimeter-sized samples are not instrumental noise (or artifacts) but caused by cooperative pore scale displacement events. There is consistent evidence ranging from special core analysis (SCAL) core floods on samples few centimeter length and diameter and micro-CT flow experiments on few mm sized samples. Fluctuations are observed in several independent SCAL studies, show non-Gaussian statistics. Displacement events imaged by beamline based micro-CT flow experiments have similar characteristics in terms of amplitude and saturation change as the SCAL experiments.

Until now, the common view has been that porous media, e.g., rock samples of few centimeter in size are above the REV scale and therefore, pore-scale events should have averaged out. It is, however, not too surprising that pore-scale events do not average out at sample sizes of few centimeters since non-wetting phase cluster sizes can reach into the several mm to few centimeter range (Georgiadis et al., 2013; Armstrong et al., 2014b) and that the pressure signature of respective ganglion dynamics (Rücker et al., 2015b) remains visible. In order to average out, if at all, sample sizes that could enclose several free non-wetting phase clusters would be required.

By focusing on the specific case of steady-state experiments where wetting and non-wetting phases are co-injected at varying fractional flow, we can exclude transient effects. Even though in many cases of such fractional flow experiments, after injection of hundreds of pore volumes, pressure and saturation eventually stabilize, there are many other reported cases, where significant fluctuations in pressure and saturation persist in a wide range of different rock types, experimental conditions and scales investigated, which suggests that the phenomenon is somewhat universal and applicable to a wide range of rock types (Datta et al., 2014a,b; Masalmeh et al., 2014; Reynolds and Krevor, 2015; Sorop et al., 2015; Gao et al., 2017, 2019, 2020; Lin Q. et al., 2018; Alcorn et al., 2019; Clennell et al., 2019; Lin et al., 2019a; Spurin et al., 2019; Wang and Masalmeh, 2019). Based on capillary number and pore-scale mechanisms involved the cause of the fluctuations is of capillary nature. The magnitude of the fluctuations depends strongly on the wetting state and may be noticed only in more water-wet cases, which does not necessarily mean that ganglion dynamics is absent in mixed-wet cases (Rücker et al., 2019). It is still uncertain whether bi-continuous oil-water configurations and associated connected pathway flow regimes can be established for specific pore space morphologies and the spatial wettability distributions (Lin et al., 2019a).

In the analyzed experiments, the amplitude of the pressure fluctuations is at a capillary energy scale, which suggests that

pore-scale events are the most likely cause. The volume associated with the saturation fluctuations are many orders of magnitude larger than individual pores suggesting that the pore-scale displacement events are cooperative and involve many pores, which is also reflected in the hundreds of individual pore scale displacements observed in the changes of the pore scale fluid distributions imaged in the micro-CT flow experiments.

The root cause for fluctuations are discontinuities associated with pore scale displacement events. However, the involvement of hundreds to thousands of individual pores stretches the limits of what is explainable at pore scale just by cooperative displacements of advancing fluids fronts (Jung et al., 2016; Singh et al., 2017; Primkulov et al., 2019) and avalanche-like cascades of individual pore filling events (Armstrong et al., 2014a). Cooperative displacements with locally either more imbibition and drainage dominated behavior with associated breakup and coalescence processes is ultimately reminiscent of what we would describe as ganglion dynamics (Rücker et al., 2015b) although the necessity for ganglion dynamics has not been fully comprehended. Associated flow regimes can be identified in the capillary number—saturation space where during breakup and coalescence, oil clusters follow specific trajectories. In the transition to the Darcy scale, e.g., when averaged over all oil clusters to characterize the average macroscopic behavior, connected pathway flow without significant saturation changes is a fixed point and ganglion dynamics form trajectories. The observation of fluctuating flow where saturation, pressure drop, and fluid connectivity change repetitively between two different states is somewhat reminiscent of ganglion dynamics, which operates on a capillary energy scale many orders of magnitude above thermal fluctuations suggesting that these fluctuations are non-thermal.

Ganglion dynamics events can indeed involve many individual pores. However, a more statistical distribution would be expected, where filling events with hundreds to thousands of individual pores would be relatively rare, because the event size distribution follows a power law (Berg et al., 2014). Therefore, from the pore scale perspective alone it is not clear why these large events would become the dominant feature, in a sometimes perfectly repetitive oscillatory manner.

The Darcy scale experiments provide the missing piece of the puzzle. At the centimeter scale oscillatory regimes with traveling waves are observed. The characteristic feature is a saturation peak traveling at constant velocity from inlet to outlet. Once the outlet is reached, a saturation peak emerges at the inlet repeating the cycle. Such waves are compatible with fractional flow principles (based on Darcy scale physics) and can be explained by a "loop" fractional flow solution (Plohr et al., 2001). Darcy scale phenomena are only observable over larger length and time scales due to permissibility by fractional flow solutions (otherwise they would be damped and decay exponentially), meaning that they enter a viscous-dominated flow regime. The trigger mechanism for such waves, however, are provided by capillary-driven ganglion dynamics events observed on the cluster scale. In a respective micro-CT flow experiments imaged by fast X-ray computed micro-tomography such recurring events were observed, which are initiated by an increase in water-filling events. That is reminiscent to the ganglion dynamics observed in imbibition at low capillary numbers (Rücker et al., 2015b), where ganglion movement is only initiated after a sequence of snap-offs disconnecting an oil cluster, which then becomes mobile through a sequence of disconnection and coalescence processes, at a capillary energy scale, which upon snap-off is converted into kinetic energy. This may provide the trigger for Darcy-scale "loop" solutions, which consist of a moving water bank followed by an oil bank in a periodic "loop" between bounding drainage and imbibition fractional flow curves, potentially forming closed orbits in the phase space (Strogatz, 1994).

A possible physical explanation for the occurrence of fluctuations are indeed the underlying traveling waves which can transport more flux than a homogeneous saturation profile. In other words, the Darcy scale solution becomes unstable against fluctuations, because in this way, at the same pressure drop, more flux is transported, i.e., energy dissipation is minimized.

The phenomenon of the clearly visible fluctuations in core flooding experiments at the centimeter length scale involve both capillary driven dynamics at the cluster scale with pore scale origin, and aspects of fractional flow solutions in the viscous limit. In other words, these phenomena are bridging between pore and Darcy scale physics, and the complexity arises from the fact that between the two scales the physical description concept changes.

There are now several potential implications, ranging from the question on the rate of energy dissipation associated with the fluctuations (McClure et al., 2020a,b) to non-uniqueness of the "loop" fractional flow solutions of the periodic oscillations (Plohr et al., 2001; Corli and Fan, 2018) and implications for the relative permeability-saturation functions obtained from such experiments. Ultimately, we have to also ask ourselves from a practical application perspective how we can use the details of fluctuations and traveling waves revealed in this much more dedicated analysis to enrich the interpretation of the experiment, acknowledging that by averaging the information would be largely lost. For instance, fluctuations could be used as a wettability indicator. These questions are good starting points for future work on the subject.

DATA AVAILABILITY STATEMENT

The raw data supporting the conclusions of this article will be made available by the authors, without undue reservation.

AUTHOR CONTRIBUTIONS

SB, MR, AG, RA, HO, FE, and MK conceptualized the research. SB, AG, HO, MR, FE, and MK planned the research. AG, MR, SB, RA, HO, NB, HvdL, and LS performed the research. MR and SB performed the data analysis and wrote the manuscript. All authors contributed to the article and approved the submitted version.

ACKNOWLEDGMENTS

We would like to acknowledge Kevin Mader and Marco Stampanoni (Tomcat beamline at the Swiss Light Source of Paul Scherrer Institute, Villigen, Switzerland). We thank Alex Schwing and Rob Neiteler for the design of the flow set-up and instrumentation, Ab Coorn, Fons Marcelis for sample selection and preparation and Sebastiaan Pieterse for assisting with the steady-state relative permeability measurements. We thank Sander de With for helpful discussions and assisting with the single-phase flow simulations with GeoDICT and OpenFOAM. We gratefully acknowledge Shell Global Solutions International B.V. for permission to publish this work. Catherine Spurin is acknowledged for helpful discussions pointing out the importance of putting the time scale of the fluctuations into perspective of the wider range of characteristic time scales and making us aware of more relevant literature supporting our findings. Diederik van Batenburg, Harm Dijk, John van Wunnik, and Jasper de Reus are acknowledged for helpful discussion concerning the fractional flow analysis. μCT was performed on the TOMCAT beamline at the Swiss Light Source, Paul Scherrer Institute, Villigen, Switzerland. We are grateful to Kevin Mader at Swiss Light Source, whose outstanding efforts have made these experiments possible.

REFERENCES

Abdallah, W., Buckley, J., Carnegie, A., Edwards, J., Herold, B., Fordham, E., et al. (2007). Fundamentals of wettability. *Oilfield Rev.* 44–61. Available online at: https://www.slb.com/-/media/files/oilfield-review/p44-61-english

Al Saadi, F., Wolf, K., and Kruijsdijk, C. V. (2017). Characterization of Fontainebleau sandstone: quartz overgrowth and its impact on pore-throat framework. *J. Petrol. Environ. Biotechnol.* 7, 1–12. doi: 10.4172/2157-7463.1000328

Alcorn, Z. P., Fredriksen, S. B., Sharma, M., Føyen, T., Wergeland, C., Ferno, M. A., et al. (2019). "Core-scale sensitivity study of CO_2 foam injection strategies for mobility control, enhanced oil recovery and CO_2 storage," in *International Symposium of the Society of Core Analysts* (Pau). doi: 10.1051/e3sconf/202014602002

Alkan, H., and Müller, W. (2008). Approaches for modelling gas flow in clay formations as repository systems. *Phys. Chem. Earth* 33, S260–S268. doi: 10.1016/j.pce.2008.10.037

Alpak, F. O., Zacharoudiou, I., Berg, S., Dietderich, J., and Saxena, N. (2019). Direct simulation of pore-scale two-phase visco-capillary flow on large digital rock images using a phase-field lattice boltzmann method on general-purpose graphics processing units. *Comput. Geosci.* 23, 849–880. doi: 10.1007/s10596-019-9818-0

Armstrong, R. T., Evseev, N., Koroteev, D., and Berg, S. (2015). Modeling the velocity field during Haines jumps in porous media. *Adv. Water Resour.* 77, 57–68. doi: 10.1016/j.advwatres.2015.01.008

Armstrong, R. T., Georgiadis, A., Ott, H., Klemin, D., and Berg, S. (2014b). Pore-scale mobilization of non-wetting phase ganglia and critical capillary number for onset of macroscopic capillary desaturation. *Geophys. Res. Lett*. 41, 1–6. doi: 10.1002/2013GL058075

Armstrong, R. T., Ott, H., Georgiadis, A., Rücker, M., Schwing, A., and Berg, S. (2014a). Subsecond pore-scale displacement processes and relaxation dynamics in multiphase flow. *Water Resour. Res.* 50, 9162–9176. doi: 10.1002/2014WR015858

Avraam, D. G., and Payatakes, A. C. (1995a). Flow regimes and relative permeabilities during steady-state two-phase flow in porous media. *J. Fluid Mech*. 293, 207–236. doi: 10.1017/S0022112095001698

Avraam, D. G., and Payatakes, A. C. (1995b). Generalized relative permeability coefficients during steady-state two-phase flow in porous media, and correlation with the flow mechanisms. *Transport Porous Media* 20, 135–168. doi: 10.1007/978-94-017-2372-5_6

Bartels, W.-B., Rücker, M., Boone, M., Bultreys, T., Mahani, H., Berg, S., et al. (2019). Imaging spontaneous imbibition in full Darcy-scale samples at pore-scale resolution by fast X-ray tomography. *Water Resour. Res.* 55, 7072–7085. doi: 10.1029/2018WR024541

Berg, C. F., Slotte, P. A., and Khanamiri, H. H. (2020). Geometrically derived efficiency of slow immiscible displacement in porous media. *Phys. Rev. E* 102:033113. doi: 10.1103/PhysRevE.102.033113

Berg, S., Armstrong, R. T., Ott, H., Georgiadis, A., Klapp, S. A., Schwing, A., et al. (2014). Multiphase flow in porous rock imaged under dynamic flow conditions with fast X-ray computed microtomography. *Petrophysics* 55, 304–312. Available online at: https://onepetro.org/petrophysics/article-abstract/55/04/304/171378/Multiphase-Flow-in-Porous-Rock-Imaged-Under?redirectedFrom=fulltext

Berg, S., and Cense, A. W. (2009). "The viscous-capillary paradox in 2-phase flow in porous media," in *International Symposium of the Society of Core Analysts held in Noordwijk*.

Berg, S., Ott, H., Klapp, S. A., Schwing, A., Neiteler, R., Brussee, N., et al. (2013). Real-time 3D imaging of Haines jumps in porous media flow. *Proc. Natl. Acad. Sci. U.S.A.* 110, 3755–3759. doi: 10.1073/pnas.1221373110

Berg, S., Rücker, M., Ott, H., Georgiadis, A., Van der Linde, H., Enzmann, F., et al. (2016). Connected pathway relative permeability from pore-scale imaging of imbibition. *Adv. Water Resour.* 90, 24–35. doi: 10.1016/j.advwatres.2016.01.010

Berg, S., Unsal, E., and Dijk, H. (2020). Non-uniqueness and uncertainty quantification of relative permeability measurements by inverse modelling. *Comput. Geotech.* 132:103964. doi: 10.1016/j.compgeo.2020.103964

Berg, S., and van Wunnik, J. (2017). Shear rate determination from pore scale flow fields. *Transport Porous Media* 117, 229–246. doi: 10.1007/s11242-017-0830-3

Bui, M., Adjiman, C. S., Bardow, A., Anthony, E. J., Boston, A., Brown, S., et al. (2018). Carbon Capture and Storage (CCS): the way forward. *Energy Environ. Sci.* 11, 1062–1176. doi: 10.1039/C7EE02342A

Cense, A. W., van der Linde, H. A., Brussee, N., Beljaars, J., and Schwing, A. (2014). "How reliable is *in-situ* saturation monitoring (ISSM) using X-Ray?," *International Symposium of the Society of Core Analysts* (Avignon).

Clennell, M. B., White, C., Giwelli, A., Myers, M., Esteban, L., Cullingford, M., et al. (2019). "Improved method for complete gas-brine imbibition relative permeability curves," in *International Symposium of the Society of Core Analysts* (Pau).

Cobos, S., Carvalho, M. S., and Alvarado, V. (2009). Flow of oil-water emulsions through a constricted capillary. *Int. J. Multiphase Flow* 35, 507–515. doi: 10.1016/j.ijmultiphaseflow.2009.02.018

Corli, A., and Fan, H. (2018). Two-phase flow in porous media with hysteresis. *J. Differe. Equations* 265, 1156–1190. doi: 10.1016/j.jde.2018.03.021

Datta, S. S., Dupin, J.-B., and Weitz, D. A. (2014a). Fluid breakup during simultaneous two-phase flow through a three-dimensional porous medium. *Phys. Fluids* 26:62004. doi: 10.1063/1.4884955

Datta, S. S., Ramakrishnan, T. S., and Weitz, D. A. (2014b). Mobilization of a trapped non-wetting fluid from a three-dimensional porous medium. *Phys. Fluids* 26:22002. doi: 10.1063/1.4866641

DiCarlo, D. A., Cidoncha, J. I. G., and Hickey, C. (2003). Acoustic measurements of pore scale displacements. *Geophys. Res. Lett.* 30:1901. doi: 10.1029/2003GL017811

Dixit, A. B., McDougall, S. R., and Sorbie, K. S. (1998). A pore-level investigation of relative permeability hysteresis in water-wet systems. *SPE J.* 3, 115–123. doi: 10.2118/37233-PA

Gao, Y., Lin, Q., Bijeljic, B., and Blunt, M. J. (2017). X-ray microtomography of intermittency in multiphase flow at steady state using a differential imaging method. *Water Resour. Res.* 51, 10274–10292. doi: 10.1002/2017WR021736

Gao, Y., Lin, Q., Bijeljic, B., and Blunt, M. J. (2020). Pore-scale dynamics and the multiphase Darcy law. *Phys. Rev. Fluids* 5:013801. doi: 10.1103/PhysRevFluids.5.013801

Gao, Y., Raeini, A. Q., Blunt, M. J., and Bijeljic, B. (2019). Pore occupancy, relative permeability and flow intermittency measurements using X-ray micro-tomography in a complex carbonate. *Adv. Water Resour.* 129, 56–69. doi: 10.1016/j.advwatres.2019.04.007

Georgiadis, A., Berg, S., Maitland, G., Makurat, A., and Ott, H. (2013). Pore-Scale micro-CT imaging: non-wetting phase cluster size distribution during drainage and imbibition. *Phys. Rev. E* 88:033002. doi: 10.1103/PhysRevE.88.033002

Guédon, G. R., Hyman, J. D., Inzoli, F., Riva, M., and Guadagnini, A. (2017). Influence of capillary end effects on steady-state relative permeability estimates from direct pore-scale simulations. *Phy. Fluids* 29:123104. doi: 10.1063/1.5009075

Herring, A. L., Harper, E. J., Andersson, L., Sheppard, A., Bay, B. K., and Wildenschild, D. (2013). Effect of fluid topology on residual nonwetting phase trapping: Implications for geologic CO_2 sequestration. *Adv. Water Resour.* 62, 47–58. doi: 10.1016/j.advwatres.2013.09.015

Hilfer, R., and Oren, P. E. (1996). Dimensional analysis of pore scale and field scale immiscible displacement. *Transport Porous Media* 22, 53–72. doi: 10.1007/BF00974311

Huang, D. D., and Honarpour, M. M. (1998). Capillary end effects in coreflood calculations. *J. Petrol. Sci. Eng.* 19, 103–117. doi: 10.1016/S0920-4105(97)00040-5

Jacquin, C. (1964). Correlations between the permeability and the geometric characteristics of the Fontainebleau gres. *Rev. Inst. Fr. Pet.* 19, 921–937.

Joekar-Niasar, V., and Hassanizadeh, S. M. (2011). Specific interfacial area: the missing state variable in two-phase flow equation. *Water Resour. Res.* 47:W05513. doi: 10.1029/2010WR009291

Jung, M., Brinkmann, M., Seemann, R., Hiller, T., Sanchez de La Lama, M., and Herminghaus, S. (2016). Wettability controls slow immiscible displacement through local interfacial instabilities. *Phys. Rev. Fluids* 1:074202. doi: 10.1103/PhysRevFluids.1.074202

Khorshidian, H., Afshari, S., Bagherzadeh, H., and Hejazi, S. H. (2021). The effect of flow swing on waterflood under oil-wet conditions: a pore-level study. *Transp Porous Med.* 137, 109–130. doi: 10.1007/s11242-021-01549-7

Kmec, J., Fürst, T., Vodak, R., and Sir, M. (2019). A semi-continuum model of saturation overshoot in one dimensional unsaturated porous media flow. *Sci. Rep.* 9:8390. doi: 10.1038/s41598-019-44831-x

Kokkedee, J. A., Boom, W., Frens, A. M., and Maas, J. G. (1996). "Improved special core analysis: scope for a reduced residual oil saturation," in *Proceedings of Society of Core Analysis Conference Paper SCA-9601*, 1–13.

Kondratenko, E. V., Mul, G., Baltrusaitis, J., Larrazabal, G. O., and Perez-Ramirez, J. (2013). Status and perspectives of CO_2 conversion into fuels and chemicals by catalytic, photocatalytic and electrocatalytic processes. *Energy Environ. Sci.* 6, 3112–3135. doi: 10.1039/c3ee41272e

Lake, L. W. (1984). *Enhanced Oil Recovery*. Upper Saddle River, NJ: Prentice Hall.

Lenormand, R., and Touboul, E. (1998). Numerical models and experiments on immiscible displacements in porous media. *J. Fluid Mech.* 189, 165–187. doi: 10.1017/S0022112088000953

Lenormand, R., Zarcone, C., and Sarr, A. (1983). Mechanisms of the displacement of one fluid by another in a network of capillary ducts. *J. Fluid Mech.* 135, 337–353. doi: 10.1017/S0022112083003110

Lin, Q., Bijeljic, B., Berg, S., Pini, R., Blunt, M. J., and Krevor, S. (2019a). Minimal surfaces in porous media: Pore-scale imaging of multiphase flow in an altered-wettability Bentheimer Sandstone. *Phys. Rev. E* 99:063105. doi: 10.1103/PhysRevE.99.063105

Lin, Q., Bijeljic, B., Krevor, S. C., Blunt, M. J., Rücker, M., Berg, S., et al. (2019b). A new waterflood initialization protocol for pore-scale multiphase flow experiments. *Petrophysics* 60, 264–272. doi: 10.30632/PJV60N2-2019a4

Lin, Q., Bijeljic, B., Pini, R., Blunt, M. J., and Krevor, S. (2018). Imaging and measurement of pore-scale interfacial curvature to determine capillary pressure simultaneously with relative permeability. *Water Resour. Res.* 54, 7046–7060. doi: 10.1029/2018WR023214

Liu, Z., McClure, J. E., and Armstrong, R. T. (2018). Influence of wettability on phase connectivity and electrical resistivity. *Phys. Rev. E* 98:043102. doi: 10.1103/PhysRevE.98.043102

Masalmeh, S. K., Sorop, T. G., Suijkerbuijk, B. M. J. M., Vermolen, E. C. M., Douma, S., van der Linde, H. A., et al. (2014). "Low salinity flooding: experimental evaluation and numerical interpretation," in *IPTC 17558, Presented at the International Petroleum Technology Conference* (Doha). doi: 10.3997/2214-4609-pdb.395.IPTC-17558-MS

McClure, J. E., Berg, S., and Armstrong, R. T. (2020a). Capillary fluctuations and energy dynamics for flow in porous media. *arXiv*. arXiv:2012.09206.

McClure, J. E., Berg, S., and Armstrong, R. T. (2020b). Capillary fluctuations in non-equilibrium systems. *arXiv*. arXiv:2012.09139.

McClure, J. E., Berrill, M. A., Gray, W. G., and Miller, C. T. (2016). Influence of phase connectivity on the relationship among capillary pressure, fluid saturation, and interfacial area in two-phase porous medium systems. *Phys. Rev. E* 94:033102. doi: 10.1103/PhysRevE.94.033102

Menke, H. P., Gao, Y., Linden, S., and Andrew, M. G. (2021). Using nano-XRM and high-contrast imaging to inform micro-porosity permeability during Stokes-Brinkman single and two-phase flow simulations on micro-CT images. *Earth ArXiv [preprint]*. doi: 10.31223/osf.io/ubg6p

Mitra, K., Köppl, T., Pop, I. S., van Duijn, C. J., and Helmig, R. (2020). Fronts in two-phase porous media flow problems: The effects of hysteresis and dynamic capillarity. *Stud. Appl. Mathematics* 144, 449–492. doi: 10.1111/sapm.12304

Moebius, F., and Or, D. (2012). Interfacial jumps and pressure bursts during fluid displacement in interacting regular capillaries. *J. Colloid Interface Sci.* 377, 406–415. doi: 10.1016/j.jcis.2012.03.070

Morrow, N. R. (1970). Physics and thermodynamics of capillary action in porous media. *Ind. Eng. Chem.* 63, 32–56. doi: 10.1021/ie50726a006

Murison, J., Semin, B., Baret, J.-C., Herminghaus, S., Schröter, M., and Brinkmann, M. (2014). Wetting heterogeneities in porous media control flow dissipation. *Phys. Rev. Appl.* 2:034002. doi: 10.1103/PhysRevApplied.2.034002

Oughanem, R., Youssef, S., Bauer, D., Peysson, Y., Maire, E., and Vizika, O. (2015). A multi-scale investigation of pore structure impact on the mobilization of trapped oil by surfactant injection. *Transport Porous Media* 109, 673–692. doi: 10.1007/s11242-015-0542-5

Pak, T., Butler, I. B., Geiger, S., Van Dijke, M. I. J., and Sorbie, K. S. (2015). Droplet fragmentation: 3D imaging of a previously unidentified pore-scale process during multiphase flow in porous media. *Proc. Natl Acad. Sci. U.S.A.* 112, 1947–1952. doi: 10.1073/pnas.1420202112

Plohr, B., Marchesin, D., Bedrikovetsky, P., and Krause, P. (2001). Modeling hysteresis in porous media flow via relaxation. *Comput. Geosci.* 5, 225–256. doi: 10.1023/A:1013759420009

Primkulov, B. K., Pahlavan, A. A., Fu, X., Zhao, B., MacMinn, C. W., and Juanes, R. (2019). Signatures of fluid-fluid displacement in porous media: wettability, patterns and pressures. *J. Fluid Mech.* 875:R4. doi: 10.1017/jfm.2019.554

Raeini, A. Q., Blunt, M. J., and Bijeljic, B. (2014). Direct simulations of two-phase flow on micro-CT images of porous media and upscaling of pore-scale forces. *Adv. Water Resour.* 74, 116–126. doi: 10.1016/j.advwatres.2014.08.012

Ramstad, T., and Hansen, A. (2006). Cluster evolution in steady-state two-phase flow in porous media. *Phys. Rev. E* 73:026306. doi: 10.1103/PhysRevE.73.026306

Reynolds, C. A., and Krevor, S. (2015). Characterizing flow behavior for gas injection; relative permeability of CO_2-brine and N_2-water in heterogeneous rocks. *Water Resour. Res.* 51, 9464–9489. doi: 10.1002/2015WR018046

Reynolds, C. A., Menke, H., Andrew, M., Blunt, M. J., and Krevor, S. (2017). Dynamic fluid connectivity during steady-state multiphase flow in a sandstone. *Proc. Natl. Acad. Sci. U.S.A.* 114, 8187–8192. doi: 10.1073/pnas.1702834114

Rücker, M., Bartels, W.-B., Singh, K., Brussee, N., Coorn, A., van der Linde, H., et al. (2019). The effect of mixed wettability on pore scale flow regimes based on a flooding experiment in ketton limestone. *Geophys. Res. Lett.* 46, 3225–3234. doi: 10.1029/2018GL081784

Rücker, M., Berg, S., Armstrong, R. T., Georgiadis, A., Ott, H., Schwing, A., et al. (2015b). From connected pathway flow to ganglion dynamics. *Geophys. Res. Lett.* 42, 3888–3894. doi: 10.1002/2015GL064007

Rücker, M., Berg, S., Armstrong, R. T., Georgiadis, A., Ott, H., Simon, L., et al. (2015a). "The fate of oil clusters during fractional flow: trajectories in the saturation-capillary number space," *International Symposium of the Society of Core Analysts held in St. John's Newfoundland and Labrador*.

Schlüter, S., Berg, S., Li, T., Vogel, H.-J., and Wildenschild, D. (2017). Time scales of relaxation dynamics during transient conditions in two-phase flow. *Water Resour. Res.* 53, 7839–7853. doi: 10.1002/2016WR019815

Schneider, M., Köppl, T., Helmig, R., Steinle, R., and Hilfer, R. (2018). Stable propagation of saturation overshoots for two-phase flow in porous media. *Transport Porous Media* 121, 621–641. doi: 10.1007/s11242-017-0977-y

Seth, S., and Morrow, N. R. (2007). Efficiency of the conversion of work of drainage to surface energy for sandstone and carbonate. *SPE Res. Eval. Eng.* 10, 338–347. doi: 10.2118/102490-PA

Simon, C., Hasche, F., and Gasteiger, H. A. (2017). Influence of the gas diffusion layer compression on the oxygen transport in PEM fuel cells at high water saturation levels. *J. Electrochem. Soc*. 164, F591–F599. doi: 10.1149/2.0691706jes

Singh, K., Jung, M., Brinkmann, M., and Seemann, R. (2019). Capillary-dominated fluid displacement in porous media. *Ann. Rev. Fluid Mech.* 51, 429–449. doi: 10.1146/annurev-fluid-010518-040342

Singh, K., Scholl, H., Brinkmann, M., Di Michiel, M., Scheel, M., Herminghaus, S., et al. (2017). The role of local instabilities in fluid invasion into permeable media. *Sci. Rep.* 7:444. doi: 10.1038/s41598-017-00191-y

Sorop, T. G., Masalmeh, S. K., Suijkerbuijk, B. M. J. M., van der Linde, H. A., Mahani, H., Brussee, N. J., et al. (2015). "Relative permeability measurements to quantify the low salinity flooding effect at field scale," in *Abu Dhabi International Petroleum Exhibition and Conference* (Abu Dhabi). doi: 10.2118/177856-MS

Spurin, C., Bultreys, T., Bijeljic, B., Blunt, M. J., and Krevor, S. (2019). Intermittent fluid connectivity during two-phase flow in a heterogeneous carbonate rock. *Phys. Rev. E* 100:043103. doi: 10.1103/PhysRevE.100.043103

Spurin, C., Bultreys, T., Rücker, M., Garfi, G., Schlepütz, C. M., Novak, V., et al. (2020). Real-time imaging reveals distinct pore scale dynamics during transient and equilibrium subsurface multiphase flow. *Water Resour. Res.* 56:e2020WR028287. doi: 10.1029/2020WR028287

Spurin, C., Bultreys, T., Rücker, M., Garfi, G., Schlepütz, C. M., Novak, V., et al. (2021). The development of intermittent multiphase fluid flow pathways through a porous rock. *Adv. Water Resour.* 150:103868. doi: 10.1016/j.advwatres.2021.103868

Strogatz, S. H. (1994). *Nonlinear Dynamics and Chaos*. Reading, MA: Perseus Books.

Tsakiroglou, C. D. (2019). The correlation of the steady-state gas/water relative permeabilities of porous media with gas and water capillary numbers. *Oil Gas Sci. Technol.* 74:45. doi: 10.2516/ogst/2019017

Tuller, M., and Or, D. (2001). Hydraulic conductivity of variably saturated porous media: Film and corner flow in angular pore space. *Water Resour. Res.* 37, 1257–1276. doi: 10.1029/2000WR900328

Unsal, E., Mason, G., Morrow, N. R., and Ruth, D. W. (2007a). Co-current and counter-current imbibition in independent tubes of non-axisymmetric geometry. *J. Colloid Interface Sci.* 306, 105–117. doi: 10.1016/j.jcis.2006.10.042

Unsal, E., Mason, G., Morrow, N. R., and Ruth, D. W. (2009). Bubble snap-off and capillary-back pressure during counter-current spontaneous imbibition into model pores. *Langmuir* 25, 3387–3395. doi: 10.1021/la803568a

Unsal, E., Mason, G., Ruth, D. W., and Morrow, N. R. (2007b). Co-and counter-current spontaneous imbibition into groups of capillary tubes with lateral connections permitting cross-flow. *J. Colloid Interface Sci.* 315, 200–209. doi: 10.1016/j.jcis.2007.06.070

Wang, Y., and Masalmeh, S. K. (2019). Obtaining High Quality SCAL data: combining different measurement techniques, saturation monitoring, numerical interpretation and continuous monitoring of experimental data. *E3S Web Conf.* 89:02007. doi: 10.1051/e3sconf/20198902007

Winkler, M., Gjennestad, M. A., Bedeaux, D., Kjelstrup, S., Cabriolu, R., Hansen, A., et al. (2020). Onsager-symmetry obeyed in athermal mesoscopic systems: two-phase flow in porous media. *Front. Phys.* 8:60. doi: 10.3389/fphy.2020.00060

Xu, L., Ye, W. M., Ye, B., Chen, B., Chen, Y. G., and Cui, Y. J. (2015). Investigation on gas migration in saturated materials with low permeability. *Eng. Geol.* 197, 94–102. doi: 10.1016/j.enggeo.2015.08.019

Yu, F., Jiang, H., Fan, Z., Xu, F., Su, H., and Li, J. (2019). Formation and flow behaviors of *in situ* emulsions in heavy oil reservoirs. *Energy Fuels* 33, 5961–5970. doi: 10.1021/acs.energyfuels.9b00154

Conflict of Interest: AG, NB, HvdL, and SB were employed by the company Shell Global Solutions International B.V.

The remaining authors declare that the research was conducted in the absence of any commercial or financial relationships that could be construed as a potential conflict of interest.

frontiers in Water

ORIGINAL RESEARCH
published: 30 July 2021
doi: 10.3389/frwa.2021.666279

Macroscopic Model for Passive Mass Dispersion in Porous Media Including Knudsen and Diffusive Slip Effects

Francisco J. Valdés-Parada[1]* *and Didier Lasseux*[2]

[1] Departamento de Ingeniería de Procesos e Hidráulica, Universidad Autónoma Metropolitana Iztapalapa, Ciudad de México, Mexico, [2] I2M, UMR 5295, CNRS, Univ. Bordeaux, Cours de la Libération, Talence, France

In this work, a macroscopic model for incompressible and Newtonian gas flow coupled to Fickian and advective transport of a passive solute in rigid and homogeneous porous media is derived. At the pore-scale, both momentum and mass transport phenomena are coupled, not only by the convective mechanism in the mass transport equation, but also in the solid-fluid interfacial boundary condition. This boundary condition is a generalization of the Kramers-Kistemaker slip condition that includes the Knudsen effects. The resulting upscaled model, applicable in the bulk of the porous medium, corresponds to: 1) A Darcy-type model that involves an apparent permeability tensor, complemented by a dispersive term and 2) A macroscopic convection-dispersion equation for the solute, in which both the macroscopic velocity and the total dispersion tensor are influenced by the slip effects taking place at the pore-scale. The use of the model is restricted by the starting assumptions imposed in the governing equations at the pore scale and by the (spatial and temporal) constraints involved in the upscaling process. The different regimes of application of the model, in terms of the Péclet number values, are discussed as well as its extents and limitations. This new model generalizes previous attempts that only include either Knudsen or diffusive slip effects in porous media.

Keywords: dispersion in porous media, Knudsen slip, diffusive slip, volume averaging, Darcy's law

OPEN ACCESS

Edited by:
James E. McClure, Virginia Tech, United States

Reviewed by:
Kalyana Babu Nakshatrala, University of Houston, United States
Peyman Mostaghimi, University of New South Wales, Australia

***Correspondence:**
Francisco J. Valdés-Parada
iqfv@xanum.uam.mx

Specialty section:
This article was submitted to Water and Critical Zone, a section of the journal Frontiers in Water

Received: *10 February 2021*
Accepted: *05 July 2021*
Published: *30 July 2021*

Citation:
Valdés-Parada FJ and Lasseux D (2021) Macroscopic Model for Passive Mass Dispersion in Porous Media Including Knudsen and Diffusive Slip Effects. Front. Water 3:666279. doi: 10.3389/frwa.2021.666279

1. INTRODUCTION

Gas flow in porous media is a relevant topic that has attracted intense research over, at least, the past 50 years (see, for instance, Jackson, 1977; Ho and Webb, 2006). The flow process may be coupled to heat and also to species mass transport, which makes it of major interest in a wide variety of practical situations including: crystal growth from vapor, chemical processes in porous catalysts, material processing using chemical vapor infiltration or deposition, exploitation of natural gas and oil, CO_2 sequestration, micro electro-mechanical systems, shale gas flow in nanoporous media, long-term nuclear waste disposal, contaminant transport in underground formations, gas separation with permeable media, among many others (Rutherford and Do, 1999; Cai et al., 2007; Li et al., 2019; Tian et al., 2019; Barton, 2020; Wang et al., 2020).

Under single-phase and isothermal flow conditions, gas slip may result from either Knudsen effects (also referred to as viscous slip) (Navier, 1823; Einzel et al., 1990) or diffusive slip (Kramers and Kistemaker, 1943; Jackson, 1977; Noever, 1990; Young and Todd, 2005). The first type of slip leads to the Klinkenberg (1941) modification to Darcy's law in porous media (Skjetne and Auriault, 1999; Lasseux et al., 2014, 2016; Woignier et al., 2018) as well as in fractures

(Zaouter et al., 2018) and it is only coupled to mass transport by means of convection (Valdés-Parada et al., 2019). A comprehensive review about modeling gas flow in porous media considering Knudsen slip is available from Lasseux and Valdés-Parada (2017). The second type of slip boundary condition leads to a modification to Darcy's law that involves the macroscopic mass flux, whereas the macroscopic mass equation is more complicated than the classical convection-dispersion model as shown by Altevogt et al. (2003a) for dilute solutions and more recently by Moyne et al. (2020) for multispecies concentrated solutions. Despite these considerable advances, it is possible to encounter in practice situations in which both types of slip effects are present. For example, one may envisage species transport in a porous medium where diffusive slip is relevant and for which the Knudsen number value is not extremely small compared to 1 (i.e., on the order of 0.1) so that viscous slip must also be considered. To the best of our knowledge, modeling of this problem at the different scales of interest has not been addressed so far and the upscaled model corresponding to this situation has not yet been reported in the literature. When both slip effects are considered, the pore-scale model is nonlinear due to the coupling with mass transport at the solid-fluid interface. Hence, the question remains whether the resulting upscaled model is a superposition of the existing ones considering the two slip effects separately.

The rationality of the present work is hence to derive an upscaled model for momentum and total and species mass transport involving both Knudsen and diffusive slip effects at the solid-fluid interface and analyze its correspondence with previous models derived under particular conditions. To this end, the volume averaging method (Whitaker, 1999), enriched with elements from the adjoint homogenization approach to treat the momentum balance equation is employed. It not only provides the means for the derivation of the model, but also allows predicting the effective-medium coefficients involved in the resulting model by means of a closure scheme. To meet this objective, the work is organized as follows. In section 2, the governing equations for mass and momentum transport at the pore-scale are reported together with the corresponding interfacial boundary conditions. The essential elements of the volume averaging method are then briefly provided in section 3. With these elements available, the upscaling process is applied first to the mass conservation equation of the chemical species and second to the total mass conservation equation as detailed in section 4. In order to close the average model for chemical species mass transport, the corresponding boundary-value problem for the concentration deviations is derived, simplified and formally solved in section 5. This step involves the coupling with momentum transport in a periodic unit cell. Hence, the formal solutions are provided not only for the concentration deviations but also for the pressure deviations and pore-scale velocity. Averaging the latter provides the resulting effective-medium equation for momentum transport. For species mass transport, the formal solution of the concentration deviations is substituted into the corresponding filters of information in the macroscale model as reported in section 6. In this way, the corresponding effective-medium coefficients are defined in terms of the ancillary closure variables. The final general macroscopic model is examined in three particular cases depending on the type of interfacial slip under consideration corresponding to different ranges of the Péclet number. As shown in section 7, the model coincides with those previously reported in which either Knudsen slip or diffusive slip is taken into account. Finally, the corresponding conclusions are presented in section 8.

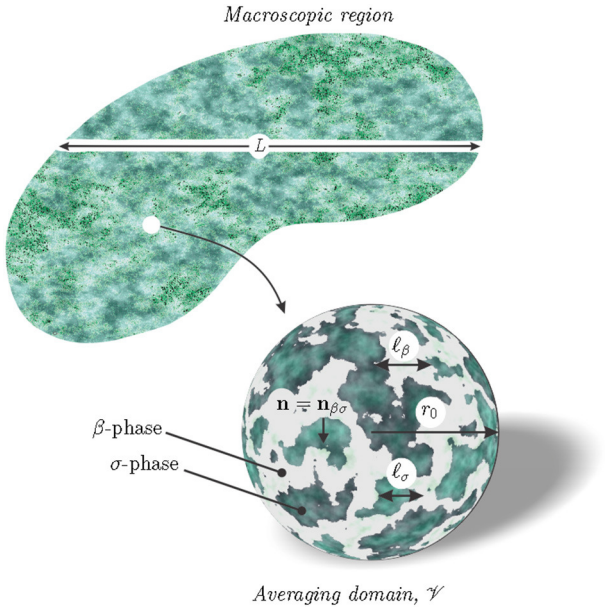

FIGURE 1 | Schematic representation of a porous medium system including the characteristic lengths at the microscale (ℓ_β in the β-phase and ℓ_σ in the σ-phase), and at the macroscale (L) as well as the averaging domain of size r_0.

2. MICROSCALE MODEL

Consider single-phase flow of a Newtonian gas (the β-phase) through a rigid and homogeneous porous medium such as the one sketched in **Figure 1**. A passive solute (species A) forms a dilute solution within the β-phase that is assumed to flow in an incompressible and isothermal regime. The incompressibility assumption indicates that the analysis is restricted to gas flows for which the Mach number is much smaller than unity, so that density variations are completely negligible. For the sake of simplicity, the solid phase (i.e., the σ-phase) is assumed impermeable to mass transport, although interfacial phenomena of adsorption or heterogeneous reaction may certainly be considered (Altevogt et al., 2003a; Valdés-Parada et al., 2019). The only mechanisms considered for mass transport of species A are diffusion and convection. On a molar basis, the governing equation for transport of species A at the pore-scale is

$$\frac{\partial c}{\partial t} + \nabla \cdot (c\mathbf{v}) = \nabla \cdot (\mathscr{D} \nabla c), \quad \text{in the } \beta\text{-phase.} \tag{1a}$$

Here, $\mathscr{D}$ is the molecular diffusivity of species A in the β-phase, c is the pore-scale molar concentration of species A, and $\mathbf{v}$ is

the fluid velocity, which satisfies the total mass conservation and Stokes equations

$$\nabla \cdot \mathbf{v} = 0, \quad \text{in the } \beta\text{-phase}, \tag{1b}$$

$$\mathbf{0} = -\nabla p + \mu \nabla \cdot \left(\nabla \mathbf{v} + (\nabla \mathbf{v})^T \right), \quad \text{in the } \beta\text{-phase}. \tag{1c}$$

In the above equation, p is the pore-scale fluid pressure, μ is the dynamic fluid viscosity, assumed constant, and the body forces due to gravity may be included in the pressure gradient term. Moreover, the term $\nabla \cdot (\nabla \mathbf{v})^T = \nabla(\nabla \cdot \mathbf{v})$ was kept for convenience of the developments that follow, although it does not bring any contribution in the pore-scale momentum balance due to the assumption of incompressible flow. Since the solid surface has been assumed to be impermeable to mass transfer, it is reasonable to impose the following interfacial boundary condition

$$-\mathbf{n} \cdot \mathscr{D} \nabla c = 0, \quad \text{at } \mathscr{A}_{\beta\sigma}. \tag{1d}$$

Here, $\mathbf{n} = \mathbf{n}_{\beta\sigma}$ is the unit normal vector directed from the fluid to the solid phase as shown in **Figure 1**. The tangential component of the fluid velocity vector at the interface can be expressed as the superposition of a first order viscous slip boundary condition (Einzel et al., 1990; Lauga et al., 2007) and a diffusive slip condition (Kramers and Kistemaker, 1943; Altevogt et al., 2003a; Moyne et al., 2020), assuming isothermal conditions for the binary mixture in which species A is sufficiently diluted in order for Fick's law to be applicable. In addition, the gas molecules are conceived as spheres experiencing both specular and diffuse wall collisions. The resulting expression for the boundary condition can be written as follows

$$\mathbf{v} = -\xi \lambda \mathbf{n} \cdot \left(\nabla \mathbf{v} + \nabla \mathbf{v}^T \right) \cdot (\mathbf{I} - \mathbf{nn}) + \frac{\mathscr{D} \nabla c}{c + \alpha} \cdot (\mathbf{I} - \mathbf{nn}), \quad \text{at } \mathscr{A}_{\beta\sigma}. \tag{1e}$$

In this expression, $\mathbf{I}$ is the identity tensor, $\xi = (2 - \sigma_v)/\sigma_v$ (σ_v being the tangential momentum accommodation coefficient representing the fraction of particles experiencing diffuse reflection at $\mathscr{A}_{\beta\sigma}$), λ is the mean free path and α is a coefficient given by

$$\alpha = \frac{\rho}{\sqrt{M_A M_B} - M_A}. \tag{1f}$$

In this relationship, ρ is the fluid density, which is assumed constant, while M_A and M_B are, respectively, the molar mass of species A and of the solvent B. The first term on the right hand side of Equation (1e) accounts for Knudsen effects whereas the second term is due to ordinary diffusion and results from the existence of a concentration gradient in the tangential direction at the solid-fluid interface. It should be noted that the importance of the diffusive slip effect is subject to the value of α. In particular, it is expected to become more significant as the molar mass difference between the solvent and the solute is more pronounced.

The microscale model is completed by the initial condition for c and the boundary conditions at the entrances and exits of the macroscopic domain for the concentration and the pressure or the velocity. However, this information is not required for the derivation of the upscaled model that follows and it is not reported here for the sake of brevity in presentation.

In classical passive dispersion problems, for which there is no impact of the species transport on momentum transport, upscaling of the governing equations for the two processes can be carried out independently from each other (see, for example Chapters 3 and 4 in Whitaker, 1999). In such circumstances, the macroscopic model for momentum transport is usually considered as part of the background knowledge for the development of the macroscopic species transport model (see for instance Valdés-Parada et al., 2019). Here, however, both processes are intimately coupled since the concentration field retroactively impacts the velocity field as can be inferred from the slip boundary condition expressed in Equation (1e). As a result, the derivation of the macroscopic model proposed below requires that the upscaling procedure includes the complete set of equations reported above. In this work, the volume averaging method (Whitaker, 1999) is used to derive the upscaled total and species mass transport equations and, with this in mind, the basic elements of this method are summarized in the next paragraphs. However, for momentum transport a modified version of this method is used, which is consistent with the adjoint homogenization technique proposed by Bottaro (2019).

3. ESSENTIALS OF THE VOLUME AVERAGING METHOD

In order to carry out the upscaling process, it is necessary to define an averaging domain $\mathscr{V}$, of norm V, that contains both solid and fluid phases such as the one sketched in **Figure 1**. In order for this averaging domain to be representative, its characteristic size r_0 must be much larger than the largest pore-scale characteristic size [say $\ell_p = \max(\ell_\beta, \ell_\sigma)$] and, at the same time, it must be much smaller than the smallest characteristic size associated to the macroscale, L. This is

$$\ell_p \ll r_0 \ll L. \tag{2}$$

On this averaging domain, the superficial and intrinsic averaging operators are respectively defined as (Whitaker, 1999)

$$\langle \psi \rangle = \frac{1}{V} \int_{\mathscr{V}_\beta} \psi \, dV, \tag{3a}$$

$$\langle \psi \rangle^\beta = \frac{1}{V_\beta} \int_{\mathscr{V}_\beta} \psi \, dV, \tag{3b}$$

with ψ being a piece-wise smooth function defined in the β-phase. These two averaging operators are related by

$$\langle \psi \rangle = \varepsilon \langle \psi \rangle^\beta, \tag{3c}$$

where $\varepsilon \equiv V_\beta / V$ is the volume fraction of the fluid phase contained in the averaging domain and, in this case, it

corresponds to the porosity. The derivations that follow are constrained to the homogeneous regions of the system, i.e., to the portions of the porous medium located sufficiently far from the macroscopic boundaries where average properties (such as ε) can be treated as constants.

Furthermore, in order to interchange spatial differentiation and integration, the spatial averaging theorem, given by (see, for example, Howes and Whitaker, 1985)

$$\langle \nabla \psi \rangle = \nabla \langle \psi \rangle + \frac{1}{V} \int_{\mathscr{A}_{\beta\sigma}} \mathbf{n} \psi \, dA, \tag{4a}$$

is employed. The use of this theorem requires average quantities to be continuously differentiable, as explained in this reference. Using the relationship given in Equation (3c) and taking into account the assumption that ε can be treated as a constant, the following alternative form, referred to as the *modified averaging theorem* in the rest of the developments, may also be used

$$\langle \nabla \psi \rangle^{\beta} = \nabla \langle \psi \rangle^{\beta} + \frac{1}{V_{\beta}} \int_{\mathscr{A}_{\beta\sigma}} \mathbf{n} \psi \, dA. \tag{4b}$$

In most applications of the volume averaging method, it is necessary to express pore-scale quantities in terms of their intrinsic averages and spatial deviations, $\tilde{\psi}$, as proposed by Gray (1975),

$$\psi = \langle \psi \rangle^{\beta} + \tilde{\psi}, \tag{5}$$

and such a decomposition will be employed in the following. It should be noted that, on the basis of the constraint given in (2), averaged properties can be regarded as constants within the integration domain. A direct corollary of this is the following average constraint for the deviations fields

$$\langle \tilde{\psi} \rangle^{\beta} = 0. \tag{6}$$

With these elements at hand, the derivation of the macroscopic equations can be carried out and this is presented in the section that follows.

4. UPSCALING

4.1. Mass Conservation Equation of Species *A*

Application of the intrinsic averaging operator to Equation (1a) leads to

$$\frac{\partial \langle c \rangle^{\beta}}{\partial t} + \nabla \cdot \langle c \mathbf{v} \rangle^{\beta} = \nabla \cdot \left(\mathscr{D} \langle \nabla c \rangle^{\beta} \right). \tag{7}$$

To obtain the above result, the modified spatial averaging theorem was employed and the interfacial boundary conditions were taken into account together with the assumption that the porous medium structure is rigid and homogeneous. On the basis of the latter assumption, and because the averaging domain is time independent, it follows that $\left\langle \frac{\partial c}{\partial t} \right\rangle^{\beta} = \frac{\partial \langle c \rangle^{\beta}}{\partial t}$. In addition, it was also assumed that $\mathscr{D}$ can be treated as a constant within the averaging domain.

To further develop the convective term, the spatial decomposition given in Equation (5) (for $\psi = c$) can be substituted, and this yields

$$\nabla \cdot \langle c \mathbf{v} \rangle^{\beta} = \nabla \cdot \left(\langle c \rangle^{\beta} \langle \mathbf{v} \rangle^{\beta} \right) + \nabla \cdot \langle \tilde{c} \mathbf{v} \rangle^{\beta}. \tag{8}$$

In addition, a second application of the modified averaging theorem, together with the concentration decomposition, allow expressing the diffusive term as follows

$$\nabla \cdot \left(\mathscr{D} \langle \nabla c \rangle^{\beta} \right) = \nabla \cdot \left[\mathscr{D} \left(\nabla \langle c \rangle^{\beta} + \frac{1}{V_{\beta}} \int_{\mathscr{A}_{\beta\sigma}} \mathbf{n} \tilde{c} \, dA \right) \right]. \tag{9}$$

Here, $\langle c \rangle^{\beta}$ was regarded as constant within the integration domain. This is supported by the combination of Equations (5) and (6), together with the separation of length scales given in (2). In addition, the assumption of spatial homogeneity was used, i.e., $\nabla \varepsilon = -\frac{1}{V} \int_{\mathscr{A}_{\beta\sigma}} \mathbf{n} \, dA = \mathbf{0}$. Substitution of Equations (8) and (9) into Equation (7) leads to

$$\frac{\partial \langle c \rangle^{\beta}}{\partial t} + \nabla \cdot \left(\langle c \rangle^{\beta} \langle \mathbf{v} \rangle^{\beta} \right) + \nabla \cdot \langle \tilde{c} \mathbf{v} \rangle^{\beta} = \nabla \cdot \left[\mathscr{D} \left(\nabla \langle c \rangle^{\beta} + \frac{1}{V_{\beta}} \int_{\mathscr{A}_{\beta\sigma}} \mathbf{n} \tilde{c} \, dA \right) \right]. \tag{10}$$

The above expression is the *unclosed average equation* for species *A* mass transport. The reason for this terminology is due to the fact that it contains integral terms (i.e., filters of information from the pore-scale) involving spatial deviations variables. In order to make further progress, it is necessary to have information about how the concentration deviations, $\tilde{c}$, are related to average fields and this step will be addressed later. At this point, it is pertinent to perform the averaging of the total mass equation.

4.2. Total Mass Conservation Equation

Applying the superficial averaging operator to Equation (1b) and using the averaging theorem in its divergence form, together with the fact that the velocity is tangential at the solid-fluid interface, leads to

$$\nabla \cdot \langle \mathbf{v} \rangle = 0. \tag{11a}$$

Using the relationship given in Equation (3c), the above equation can be written in terms of the intrinsic average of the fluid velocity

$$\nabla \cdot \langle \mathbf{v} \rangle^{\beta} = 0. \tag{11b}$$

Here, again, the assumption of spatial homogeneity, i.e., a constant porosity, was considered. Both versions of the macroscopic total mass conservation equation listed above are closed and do not require further derivations. As a final remark, it is worth noting that Equation (11b) is recovered by making the sum of Equation (10) for all the chemical species involved in the mixture.

5. CLOSURE

As already mentioned, expressions of the deviations in terms of average quantities, a process usually referred to as *closure*, is necessary in order to complete the upscaled model. This is carried out by considering the following steps: (1) Derivation of the governing equations for the deviations as well as the corresponding boundary conditions; (2) Imposition of some reasonable simplifications in order to reduce the complexity of the resulting problem and (3) Formal solution of the problem in order to find the relationships between deviations and average quantities. Usually a set of length-scale constraints and assumptions, which can be regarded as *scaling postulates*, as suggested by Wood and Valdés-Parada (2013), are involved in step 2.

5.1. Conservation Equation for Species *A*

In order to derive the governing equation for $\tilde{c}$, Equation (5) suggests subtracting Equation (10) from the mass balance equation for species A at the pore scale, i.e., Equation (1a). The result is

$$\frac{\partial \tilde{c}}{\partial t} + \nabla \cdot (\langle c \rangle^{\beta} \tilde{\mathbf{v}}) + \nabla \cdot (\tilde{c}\mathbf{v}) - \nabla \cdot \langle \tilde{c}\mathbf{v} \rangle^{\beta} = \nabla \cdot (\mathscr{D} \nabla \tilde{c}) - \nabla \cdot \left(\frac{\mathscr{D}}{V_{\beta}} \int\limits_{\mathscr{A}_{\beta\sigma}} \mathbf{n} \tilde{c} \, dA \right), \quad \text{in the } \beta\text{-phase.} \tag{12}$$

With the intention of simplifying this equation, it may be noticed, on the one hand, that the order of magnitude estimates for the non-local diffusion and convection terms can be expressed as

$$\nabla \cdot \left(\frac{\mathscr{D}}{V_{\beta}} \int\limits_{\mathscr{A}_{\beta\sigma}} \mathbf{n} \tilde{c} \, dA \right) = \mathbf{O}\left(\frac{\mathscr{D}\tilde{c}}{L} \frac{A_{\beta\sigma}}{V_{\beta}} \right), \tag{13a}$$

$$\nabla \cdot \langle \tilde{c}\mathbf{v} \rangle^{\beta} = \mathbf{O}\left(\frac{\tilde{c}v}{L} \right). \tag{13b}$$

Here, $A_{\beta\sigma}$ and v represent the order of magnitude estimates of the measure of $\mathscr{A}_{\beta\sigma}$ and $\mathbf{v}$, respectively. On the other hand, the estimates for the local diffusive and convective terms are given by

$$\nabla \cdot (\mathscr{D} \nabla \tilde{c}) = \mathbf{O}\left(\frac{\mathscr{D}\tilde{c}}{\ell_{\beta}^2} \right), \tag{14a}$$

$$\nabla \cdot (\tilde{c}\mathbf{v}) = \mathbf{O}\left(\frac{\tilde{c}v}{\ell_{\beta}} \right). \tag{14b}$$

Therefore, on the basis of the constraints $\ell_{\beta} \ll L$ and $\frac{A_{\beta\sigma}\ell_{\beta}^2}{V_{\beta}L} \ll 1$, it is reasonable to assume that

$$\nabla \cdot \left(\frac{\mathscr{D}}{V_{\beta}} \int\limits_{\mathscr{A}_{\beta\sigma}} \mathbf{n} \tilde{c} \, dA \right) \ll \nabla \cdot (\mathscr{D} \nabla \tilde{c}), \tag{15a}$$

$$\nabla \cdot \langle \tilde{c}\mathbf{v} \rangle^{\beta} \ll \nabla \cdot (\tilde{c}\mathbf{v}). \tag{15b}$$

Hence, Equation (12) may be simplified to

$$\frac{\partial \tilde{c}}{\partial t} + \tilde{\mathbf{v}} \cdot \nabla \langle c \rangle^{\beta} + \nabla \cdot (\tilde{c}\mathbf{v}) = \nabla \cdot (\mathscr{D} \nabla \tilde{c}), \quad \text{in the } \beta\text{-phase.} \tag{16}$$

It should be noted that, in order to arrive at this last expression, the total mass conservation Equations (1b) and (11b) were employed.

At this point, it is pertinent to estimate the order of magnitude of the accumulation term as follows

$$\frac{\partial \tilde{c}}{\partial t} = \mathbf{O}\left(\frac{\tilde{c}}{t^*} \right), \tag{17}$$

where t^* represents the time scale at which $\tilde{c}$ experiences significant variations. Moreover, from Equations (14), the combined order of magnitude estimates of the local diffusive and convective terms can be shown to be $\mathbf{O}\left(\tilde{c}\mathscr{D}(1+Pe)/\ell_{\beta}^2 \right)$ where the Péclet number, Pe, is defined as

$$Pe = \frac{v\ell_{\beta}}{\mathscr{D}}. \tag{18}$$

Therefore, it is deduced that, when the following time-scale constraint is met

$$\frac{\ell_{\beta}^2}{\mathscr{D}(1+Pe)} \ll t^*, \tag{19}$$

Equation (16) may be considered to be quasi-steady, i.e.,

$$\tilde{\mathbf{v}} \cdot \nabla \langle c \rangle^{\beta} + \mathbf{v} \cdot \nabla \tilde{c} = \nabla \cdot (\mathscr{D} \nabla \tilde{c}), \quad \text{in the } \beta\text{-phase.} \tag{20}$$

This temporal constraint is retained in the remainder of the analysis.

5.2. Momentum Transport Equation

The equation for total mass conservation at the pore-scale given in Equation (1b) is still useful for the closure problem solution in its current form. Nevertheless, it is convenient to spatially decompose the pressure, using Equation (5) with $\psi = p$, in the Stokes equation to obtain

$$\mathbf{0} = -\nabla \tilde{p} + \mu \nabla \cdot \left(\nabla \mathbf{v} + (\nabla \mathbf{v})^T \right) - \nabla \langle p \rangle^{\beta}, \quad \text{in the } \beta\text{-phase.} \tag{21}$$

For the derivations that follow it is not necessary to apply the spatial decomposition for the velocity and therefore no further developments are required in the above equation.

5.3. Interfacial Boundary Conditions

Substituting the spatial decomposition for the species concentration into Equation (1d), leads to

$$-\mathbf{n} \cdot \nabla \tilde{c} = \mathbf{n} \cdot \nabla \langle c \rangle^{\beta}, \quad \text{at } \mathscr{A}_{\beta\sigma}. \tag{22}$$

Before proceeding with the slip condition for the velocity, an order of magnitude analysis can now be performed on this result in order to obtain the following estimate for $\tilde{c}$

$$\tilde{c} = \mathbf{O}\left(\frac{\ell_{\beta}}{L} \langle c \rangle^{\beta} \right). \tag{23}$$

According to the length-scale constraint expressed as $\ell_\beta \ll L$, this leads to the following assumption

$$\tilde{c} \ll \langle c \rangle^\beta. \tag{24}$$

Directing now the attention to the velocity slip boundary condition, let the pore-scale concentration be decomposed into its average and deviations in Equation (1e) in order to obtain

$$\mathbf{v} = -\xi \lambda \mathbf{n} \cdot \left(\nabla \mathbf{v} + \nabla \mathbf{v}^T \right) \cdot (\mathbf{I} - \mathbf{nn}) + \frac{\mathscr{D} \nabla \tilde{c}}{\langle c \rangle^\beta + \alpha} \cdot (\mathbf{I} - \mathbf{nn}) + \frac{\mathscr{D} \nabla \langle c \rangle^\beta}{\langle c \rangle^\beta + \alpha} \cdot (\mathbf{I} - \mathbf{nn}), \quad \text{at } \mathscr{A}_{\beta\sigma}. \tag{25}$$

Note that the assumption given in (24) was used in the terms at the denominator of this last expression. The purpose of such an approximation is to maintain a linear problem for the concentration deviations as it is commonly done in applications of the volume averaging method (see, for example Wood and Whitaker, 1998; Valdés-Parada et al., 2009).

5.4. Local Closure Problem

Since the determination of the deviations fields in the entire macroscopic domain would be, at least, as complicated as solving the original pore-scale equations everywhere, the interest is not to carry out a solution of the closure problem over the entire macroscopic system. Instead, it is more convenient to solve the closure problem within a representative solution domain such as the one sketched in **Figure 2**, which corresponds to a unit cell of the porous medium assimilated to a periodic structure. In this domain, Taylor series expansions for all the average quantities involved in the closure problems can be performed about the centroid of the unit cell located by the position vector denoted by $\mathbf{x}$. On the basis of the separation of length scales, $r_0 \ll L$, these series can be truncated at the zeroth order as explained in Chapter 1 of Whitaker (1999). Under these conditions, the *local closure problem* takes the following form

Total mass transport

$$\nabla \cdot \mathbf{v} = 0, \quad \text{in the } \beta\text{-phase.} \tag{26a}$$

Total momentum transport

$$\mathbf{0} = -\frac{1}{\mu} \nabla \tilde{p} + \nabla \cdot \left(\nabla \mathbf{v} + (\nabla \mathbf{v})^T \right) \underbrace{- \frac{1}{\mu} \nabla \langle p \rangle^\beta \big|_{\mathbf{x}}}_{source}, \quad \text{in the } \beta\text{-phase.} \tag{26b}$$

Species A mass transport

$$\tilde{\mathbf{v}} \cdot \underbrace{\mathbf{f}|_{\mathbf{x}}}_{source} + \mathbf{v} \cdot \nabla \tilde{\chi} = \nabla \cdot (\mathscr{D} \nabla \tilde{\chi}), \quad \text{in the } \beta\text{-phase.} \tag{26c}$$

Interfacial boundary conditions

$$-\mathbf{n} \cdot \nabla \tilde{\chi} = \mathbf{n} \cdot \underbrace{\mathbf{f}|_{\mathbf{x}}}_{source}, \quad \text{at } \mathscr{A}_{\beta\sigma}. \tag{26d}$$

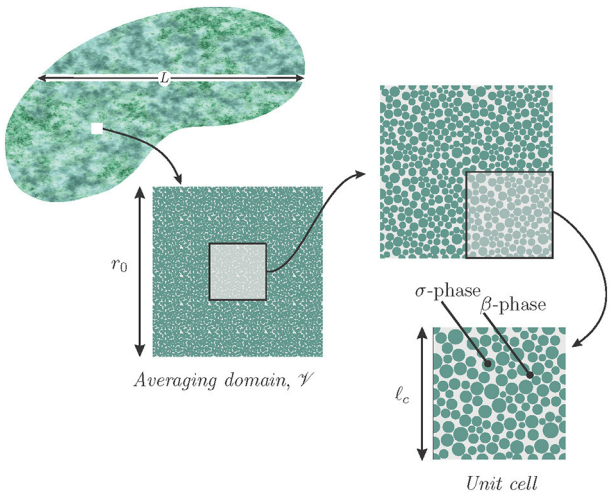

FIGURE 2 | Sketch of a two-dimensional periodic unit cell, of side length ℓ_c, for solving the closure problem.

$$\mathbf{v} = -\xi \lambda \mathbf{n} \cdot \left(\nabla \mathbf{v} + \nabla \mathbf{v}^T \right) \cdot (\mathbf{I} - \mathbf{nn}) + \mathscr{D} \nabla \tilde{\chi} \cdot (\mathbf{I} - \mathbf{nn}) + \mathscr{D} \underbrace{\mathbf{f}|_{\mathbf{x}}}_{source} \cdot (\mathbf{I} - \mathbf{nn}), \quad \text{at } \mathscr{A}_{\beta\sigma}. \tag{26e}$$

Periodicity

$$\mathbf{v}(\mathbf{r}+\mathbf{l}_i) = \mathbf{v}(\mathbf{r}); \quad \tilde{p}(\mathbf{r}+\mathbf{l}_i) = \tilde{p}(\mathbf{r}); \quad \tilde{\chi}(\mathbf{r}+\mathbf{l}_i) = \tilde{\chi}(\mathbf{r}), \quad i = 1, 2, 3. \tag{26f}$$

Average constraints

$$\langle \tilde{p} \rangle^\beta = 0; \quad \langle \tilde{\chi} \rangle^\beta = 0. \tag{26g}$$

For the sake of brevity in writing, the following definitions were used in Equations (26c)–(26g)

$$\tilde{\chi} = \frac{\tilde{c}}{\langle c \rangle^\beta \big|_{\mathbf{x}} + \alpha}; \quad \mathbf{f}|_{\mathbf{x}} = \frac{\nabla \langle c \rangle^\beta \big|_{\mathbf{x}}}{\langle c \rangle^\beta \big|_{\mathbf{x}} + \alpha}. \tag{27}$$

In addition, the fact that $\langle c \rangle^\beta \big|_{\mathbf{x}}$ can be treated as a constant within the unit cell was employed. With the consideration of locality for the closure problem, it becomes clear that the velocity is a variable that does not need to be decomposed according to Equation (5) since $\mathbf{v}$ can be considered as a periodic field at the level of the unit cell.

Note that, due to the convective term in Equation (26c), the problem is non-linear and hence a formal solution is not achievable, in general. To overcome this issue, the velocity in this term might be regarded as a known field, an assumption that is consistent with previous studies of upscaling in porous media involving nonlinear mechanisms (see, for instance, Bottaro, 2019; Lasseux et al., 2019). This allows linearizing the closure problem and integral equations formulations based on Green's functions may then be used, as suggested by Wood and Valdés-Parada (2013) or Bottaro (2019) while employing the adjoint

homogenization method, to obtain the following formal solution for $\mathbf{v}$, $\tilde{p}$ and $\tilde{\chi}$ as linear functions of the sources identified in Equation (26)

$$\mathbf{v} = -\frac{\mathbf{A}}{\mu} \cdot \nabla \langle p \rangle^{\beta} + \mathbf{C} \cdot \mathbf{f}, \tag{28a}$$

$$\tilde{p} = -\mathbf{a} \cdot \nabla \langle p \rangle^{\beta} + \mu \mathbf{c} \cdot \mathbf{f}, \tag{28b}$$

$$\tilde{\chi} = -\frac{\mathbf{d}}{\mu} \cdot \nabla \langle p \rangle^{\beta} + \mathbf{e} \cdot \mathbf{f}. \tag{28c}$$

In these expressions, the closure variables $\mathbf{A}$, $\mathbf{C}$, $\mathbf{a}$, $\mathbf{c}$, $\mathbf{d}$ and $\mathbf{e}$ are integrals of the corresponding Green's functions. In this way, the closure variables may be interpreted as mapping functions of the sources onto $\mathbf{v}$, $\tilde{p}$ and $\tilde{\chi}$, respectively.

Substitution of Equation (28) into Equation (26) and splitting them according to the source gives rise to the following boundary-value problems in terms of the closure variables

Problem-I (source $-\frac{1}{\mu}\nabla\langle p\rangle^{\beta}$*)*

$$\nabla \cdot \mathbf{A} = \mathbf{0}, \quad \text{in the } \beta\text{-phase}, \tag{29a}$$

$$\mathbf{0} = -\nabla \mathbf{a} + \nabla \cdot \left(\nabla \mathbf{A} + (\nabla \mathbf{A})^{T1} \right) + \mathbf{I}, \quad \text{in the } \beta\text{-phase}, \tag{29b}$$

$$\mathbf{v} \cdot \nabla \mathbf{d} = \nabla \cdot (\mathscr{D} \nabla \mathbf{d}), \quad \text{in the } \beta\text{-phase}, \tag{29c}$$

$$-\mathbf{n} \cdot \nabla \mathbf{d} = \mathbf{0}, \quad \text{at } \mathscr{A}_{\beta\sigma}, \tag{29d}$$

$$\mathbf{A} = -\xi\lambda\mathbf{n}\cdot\left(\nabla \mathbf{A} + (\nabla \mathbf{A})^{T1}\right)\cdot(\mathbf{I} - \mathbf{nn}) + \mathscr{D}\nabla\mathbf{d}\cdot(\mathbf{I} - \mathbf{nn}), \quad \text{at } \mathscr{A}_{\beta\sigma}, \tag{29e}$$

$$\psi(\mathbf{r} + \mathbf{l}_i) = \psi(\mathbf{r}), \quad i = 1, 2, 3; \ \psi = \mathbf{A}, \mathbf{a}, \mathbf{d}, \tag{29f}$$

$$\langle \mathbf{a} \rangle^{\beta} = \mathbf{0}; \quad \langle \mathbf{d} \rangle^{\beta} = \mathbf{0}. \tag{29g}$$

Problem-II (source $\mathbf{f}$*)*

$$\nabla \cdot \mathbf{C} = \mathbf{0}, \quad \text{in the } \beta\text{-phase}, \tag{30a}$$

$$\mathbf{0} = -\nabla \mathbf{c} + \nabla \cdot \left(\nabla \mathbf{C} + (\nabla \mathbf{C})^{T1} \right), \quad \text{in the } \beta\text{-phase}, \tag{30b}$$

$$\tilde{\mathbf{v}} + \mathbf{v} \cdot \nabla \mathbf{e} = \nabla \cdot (\mathscr{D} \nabla \mathbf{e}), \quad \text{in the } \beta\text{-phase}, \tag{30c}$$

$$-\mathbf{n} \cdot \nabla \mathbf{e} = \mathbf{n}, \quad \text{at } \mathscr{A}_{\beta\sigma}, \tag{30d}$$

$$\mathbf{C} = -\xi\lambda\mathbf{n} \cdot \left(\nabla \mathbf{C} + (\nabla \mathbf{C})^{T1} \right) \cdot (\mathbf{I} - \mathbf{nn}) + \mathscr{D}\nabla\mathbf{e} \cdot (\mathbf{I} - \mathbf{nn}) + \mathscr{D}(\mathbf{I} - \mathbf{nn}), \quad \text{at } \mathscr{A}_{\beta\sigma}, \tag{30e}$$

$$\psi(\mathbf{r} + \mathbf{l}_i) = \psi(\mathbf{r}), \quad i = 1, 2, 3; \ \psi = \mathbf{c}, \mathbf{C}, \mathbf{e}, \tag{30f}$$

$$\langle \mathbf{c} \rangle^{\beta} = \mathbf{0}; \quad \langle \mathbf{e} \rangle^{\beta} = \mathbf{0}. \tag{30g}$$

In the above equations, the superscript $T1$ was used to denote the transpose, which, for a third order tensor, $\boldsymbol{\kappa}$, permutes the first and second indices, i.e., $\boldsymbol{\kappa}^{T1}_{ijk} = \boldsymbol{\kappa}_{jik}$.

The two closure problems *I* and *II* are coupled both between themselves and also with the macroscale model solution due to the convective terms in Equations (29c) and (30c). This becomes clear when, in these two last equations, the representation given in Equation (28a) is used to express $\tilde{\mathbf{v}}$ and $\mathbf{v}$ in terms of $\nabla\langle p\rangle^{\beta}$ and $\mathbf{f}$. This issue is often encountered while upscaling non-linear processes (see, for instance, Valdés-Parada et al., 2009; Airiau and Bottaro, 2020) and it will be addressed later in section 6.3. At this point, it is pertinent to derive the closed form of the upscaled model.

6. CLOSED MODEL

Now that expressions relating $\mathbf{v}$, $\tilde{p}$ and $\tilde{\chi}$ to average quantities are available, it is of interest to return to the average equations and express them in a closed manner. For total mass transport, the closed equation is given by either one of Equation (11).

6.1. Closed Macroscopic Momentum Equation

For momentum transport, the corresponding equation results from applying the superficial averaging operator to Equation (28a). This leads to

$$\langle \mathbf{v} \rangle = -\frac{\mathbf{K}_s}{\mu} \cdot \nabla \langle p \rangle^{\beta} + \mathbf{D}_c \cdot \frac{\nabla \langle c \rangle^{\beta}}{\langle c \rangle^{\beta} + \alpha}, \tag{31}$$

where the following nomenclature was used

$$\mathbf{K}_s = \langle \mathbf{A} \rangle; \quad \mathbf{D}_c = \langle \mathbf{C} \rangle. \tag{32}$$

Here, $\mathbf{K}_s$ is an apparent permeability tensor that differs from the intrinsic one as it is affected by both the diffusive and viscous slip effects. This tensor reduces to the intrinsic permeability tensor under no-slip conditions. In addition, $\mathbf{D}_c$ is a dispersion tensor, which, for conditions such that Knudsen effects can be disregarded, reduces to the macroscopic slip conductivity introduced by Altevogt et al. (2003a). It should be emphasized that the two effective medium coefficients appearing in Equation (31) depend on the Péclet number defined in Equation (18) and the Knudsen number, *Kn*, given by

$$Kn = \lambda / \ell_{\beta}. \tag{33}$$

The specific nature of this dependency should be extensively studied but the details of this dependency are, however, beyond the scope of this work. Nevertheless, an analysis is presented in section 7 in terms of the Péclet number, allowing to retrieve some transport regimes reported in the literature. The physical meaning of the two terms appearing on the right-hand side of Equation (31) can be understood as follows. The first term is related to momentum transport due to the macroscopic pressure gradient. The second term can be regarded as a correction to momentum transport induced by both slip effects.

6.2. Closed Macroscopic Species Transport Equation

The remaining equation to be closed is the one governing transport of species A. To progress toward this macroscopic equation, the definitions given in Equation (27) can be introduced back into Equation (28c) in order to express the latter as

$$\tilde{c} = -(\langle c\rangle^\beta + \alpha)\frac{\mathbf{d}}{\mu}\cdot\nabla\langle p\rangle^\beta + \mathbf{e}\cdot\nabla\langle c\rangle^\beta. \tag{34}$$

Substituting this result into Equation (10) yields

$$\underbrace{\frac{\partial\langle c\rangle^\beta}{\partial t}}_{\text{mass accumulation}} + \underbrace{\nabla\cdot\left(\langle c\rangle^\beta\langle\mathbf{v}\rangle^\beta\right)}_{\text{convective transport}} + \underbrace{\nabla\cdot\left[(\langle c\rangle^\beta+\alpha)\frac{\mathbf{R}}{\mu}\cdot\nabla\langle p\rangle^\beta\right]}_{\text{slip correction to convective transport}} = \underbrace{\nabla\cdot\left[\mathbf{D}_s\cdot\nabla\langle c\rangle^\beta\right]}_{\substack{\text{mass dispersion including}\\ \text{slip effects}}}, \tag{35}$$

where the physical meaning of each term was identified and the following effective-medium coefficients were introduced

$$\mathbf{R} = -\langle\tilde{\mathbf{v}}\mathbf{d}\rangle^\beta + \frac{\mathscr{D}}{V_\beta}\int\limits_{\mathscr{A}_{\beta\sigma}}\mathbf{n}\mathbf{d}\,dA, \tag{36a}$$

$$\mathbf{D}_s = \mathscr{D}\left(\mathbf{I} + \frac{1}{V_\beta}\int\limits_{\mathscr{A}_{\beta\sigma}}\mathbf{n}\mathbf{e}\,dA - \mathscr{D}^{-1}\langle\tilde{\mathbf{v}}\mathbf{e}\rangle^\beta\right). \tag{36b}$$

Equation (35) differs from the typical convection-dispersion equation as it contains a slip correction to convective transport and it requires the computation of two effective-medium coefficients. The second order tensor, $\mathbf{R}$, has the units of permeability and the product $\frac{\mathbf{R}}{\mu}\cdot\nabla\langle p\rangle^\beta$ may be interpreted as a velocity vector that corrects $\langle\mathbf{v}\rangle^\beta$ in order to account for slip effects. In addition, the dispersion tensor, $\mathbf{D}_s$, given in Equation (36b), is defined in a similar manner as the total dispersion tensor encountered in passive dispersion in porous media (see Chapter 3 in Whitaker, 1999). The main difference with this case lies in the fact that the closure variable, $\mathbf{e}$, depends on both Knudsen and diffusive slip effects as it is evidenced in *Problem-II* (see Equations 30).

6.3. Summary of the Closed Average Model

The closed average model consists of the effective-medium equations given in Equations (11a) or (11b) (total mass conservation), Equation (31) (momentum transport) and Equation (35) (species A mass transport). These three balance equations may be combined to provide an equivalent alternative form of the average model made of two equations on $\nabla\langle p\rangle^\beta$ and $\langle c\rangle^\beta$, respectively. Introducing the expression of the average velocity given in the macroscopic momentum Equation (31) into the averaged total mass conservation Equation (11a) yields

$$\nabla\cdot\left(\frac{\mathbf{K}_s}{\mu}\cdot\nabla\langle p\rangle^\beta - \frac{\mathbf{D}_c}{\langle c\rangle^\beta+\alpha}\cdot\nabla\langle c\rangle^\beta\right) = 0. \tag{37}$$

Similarly, replacing the average velocity in the macroscopic equation for species A mass transport by the modified Darcy Equation (31), and rearranging, leads to

$$\varepsilon\frac{\partial\langle c\rangle^\beta}{\partial t} + \frac{1}{\mu}\nabla\cdot\left[\left(\varepsilon(\langle c\rangle^\beta+\alpha)\mathbf{R} - \langle c\rangle^\beta\mathbf{K}_s\right)\cdot\nabla\langle p\rangle^\beta\right] = \nabla\cdot\left[\left(\varepsilon\mathbf{D}_s - \frac{\langle c\rangle^\beta\mathbf{D}_c}{\langle c\rangle^\beta+\alpha}\right)\cdot\nabla\langle c\rangle^\beta\right]. \tag{38}$$

These two equations clearly show the non-linear coupling between the macroscopic pressure gradient and macroscopic concentration. Once the solutions on $\nabla\langle p\rangle^\beta$ and $\langle c\rangle^\beta$ are achieved, subject to macroscopic boundary and initial conditions, they can be further employed to reconstruct the local velocity field using Equation (28a) over the unit cell. This is necessary to solve the two closure problems *I* and *II* yielding the four effective coefficients. The successive resolution of the macroscopic model and closure problems should be iteratively repeated until convergence is reached. Ultimately, the converged fields of $\nabla\langle p\rangle^\beta$ and $\langle c\rangle^\beta$ can be substituted in Equation (31) to predict the macroscale velocity.

In the following paragraphs, particular forms of the upscaled model are investigated. This analysis is of interest since it shows that the upscaled model derived here is general enough as it allows retrieving the resulting models reported for particular flow and transport conditions. These submodels have been thoroughly analyzed and validated and they hence serve as an indirect validation of the upscaled model derived here.

7. PARTICULAR CASES OF THE UPSCALED MODEL

The upscaled model derived in the previous paragraphs is general in the sense that it is not constrained to a particular range of Péclet or Knudsen numbers values, the latter being non-zero and, at most, $\sim$ 0.1 to be compliant with the slip convective regime. However, it is instructive to analyze how the structure of the model is modified for specific flow and transport conditions (more specifically regarding the momentum transport and species A mass transport equations, the total mass conservation equation remaining unaltered). In essence, the regimes are related to the relative importance of diffusive and convective effects. In the absence of diffusive slip effects, the crossover between the convective and diffusive regimes is characterized by $Pe = 1$ as can be easily inferred from the transport equation for $\tilde{c}$ (see Equation 20). However, a close attention to the right-hand side of the slip boundary condition given in Equation (25), once multiplied by $\ell_\beta/\mathscr{D}$, indicates that the term related to Knudsen slip is $\mathbf{O}(Pe\xi Kn)$ whereas the diffusive slip term is $\mathbf{O}(\ell_\beta/L)$. As a consequence, on the basis of this interfacial boundary condition, the three regimes to be considered here are: (1) the diffusive slip regime for which $Pe \ll \ell_\beta/(L\xi Kn)$; (2) the slip regime containing both slip effects where $Pe = \mathbf{O}(\ell_\beta/(L\xi Kn))$ and finally, (3) the Knudsen slip regime, for which $Pe \gg \ell_\beta/(L\xi Kn)$. In the following paragraphs, some comments about each regime are provided.

7.1. Diffusive Slip Regime $\left(Pe \ll \frac{\ell_\beta}{L\xi Kn}\right)$

In this case, the physical pore-scale model for mass and momentum transport corresponds to the one studied by Altevogt et al. (2003a) under non-adsorption conditions and to the one recently reported by Moyne et al. (2020) under incompressible flow condition and transport of a single chemical species. Furthermore, the interfacial boundary conditions in closure problems *I* and *II* given in Equations (29e) and (30e) reduce to

$$\mathbf{A} = \mathscr{D}\nabla\mathbf{d}\cdot(\mathbf{I}-\mathbf{nn}), \quad \text{at } \mathscr{A}_{\beta\sigma}, \tag{39}$$

$$\mathbf{C} = \mathscr{D}\nabla\mathbf{e}\cdot(\mathbf{I}-\mathbf{nn}) + \mathscr{D}(\mathbf{I}-\mathbf{nn}), \quad \text{at } \mathscr{A}_{\beta\sigma}. \tag{40}$$

The remaining parts of the closure problems are kept unaltered, in general. Consequently, no further simplification to the upscaled model for mass and momentum transport derived here is possible. It is worth pointing out that the mathematical structure of the closure problems in this case is simpler than the one proposed by Altevogt et al. (2003a), since they are not written in an integro-differential form. Nevertheless, the formulations are equivalent.

7.2. Knudsen and Diffusive Slip Regime $\left(Pe = O\left(\frac{\ell_\beta}{L\xi Kn}\right)\right)$

This regime corresponds to the general situation addressed in the previous section of the work and, to the best of our knowledge it has not been studied in the literature. Consequently, the closure problems and the upscaled model need to be solved in a coupled and iterative manner as explained above, a task that is beyond the scope of this work.

7.3. Knudsen Slip Regime $\left(Pe \gg \frac{\ell_\beta}{L\xi Kn}\right)$

In this situation, *Problem-I* can be decoupled into the following two boundary-value problems
Problem-Ia

$$\nabla\cdot\mathbf{A} = \mathbf{0}, \quad \text{in the } \beta\text{-phase}, \tag{41a}$$

$$\mathbf{0} = -\nabla\mathbf{a} + \nabla\cdot\left(\nabla\mathbf{A} + (\nabla\mathbf{A})^{T1}\right) + \mathbf{I}, \quad \text{in the } \beta\text{-phase}, \tag{41b}$$

$$\mathbf{A} = -\xi\lambda\mathbf{n}\cdot\left(\nabla\mathbf{A} + (\nabla\mathbf{A})^{T1}\right)\cdot(\mathbf{I}-\mathbf{nn}), \quad \text{at } \mathscr{A}_{\beta\sigma}, \tag{41c}$$

$$\psi(\mathbf{r}+\mathbf{l}_i) = \psi(\mathbf{r}), \quad i=1,2,3;\ \psi = \mathbf{A},\mathbf{a}, \tag{41d}$$

$$\langle\mathbf{a}\rangle^\beta = \mathbf{0}. \tag{41e}$$

Problem-Ib

$$\mathbf{v}\cdot\nabla\mathbf{d} = \nabla\cdot(\mathscr{D}\nabla\mathbf{d}), \quad \text{in the } \beta\text{-phase}, \tag{42}$$

$$-\mathbf{n}\cdot\nabla\mathbf{d} = \mathbf{0}, \quad \text{at } \mathscr{A}_{\beta\sigma}, \tag{43}$$

$$\mathbf{d}(\mathbf{r}+\mathbf{l}_i) = \mathbf{d}(\mathbf{r}), \quad i=1,2,3, \tag{44}$$

$$\langle\mathbf{d}\rangle^\beta = \mathbf{0}. \tag{45}$$

In addition, a similar decoupling applies for *Problem-II* that gives rise to the following two closure problems
Problem-IIa

$$\nabla\cdot\mathbf{C} = \mathbf{0}, \quad \text{in the } \beta\text{-phase}, \tag{46a}$$

$$\mathbf{0} = -\nabla\mathbf{c} + \nabla\cdot\left(\nabla\mathbf{C} + (\nabla\mathbf{C})^{T1}\right), \quad \text{in the } \beta\text{-phase}, \tag{46b}$$

$$\mathbf{C} = -\xi\lambda\mathbf{n}\cdot\left(\nabla\mathbf{C} + (\nabla\mathbf{C})^{T1}\right)\cdot(\mathbf{I}-\mathbf{nn}), \quad \text{at } \mathscr{A}_{\beta\sigma}, \tag{46c}$$

$$\psi(\mathbf{r}+\mathbf{l}_i) = \psi(\mathbf{r}), \quad i=1,2,3;\ \psi = \mathbf{c},\mathbf{C}, \tag{46d}$$

$$\langle\mathbf{c}\rangle^\beta = \mathbf{0}. \tag{46e}$$

Problem-IIb

$$\tilde{\mathbf{v}} + \mathbf{v}\cdot\nabla\mathbf{e} = \nabla\cdot(\mathscr{D}\nabla\mathbf{e}), \quad \text{in the } \beta\text{-phase}, \tag{46f}$$

$$-\mathbf{n}\cdot\nabla\mathbf{e} = \mathbf{n}, \quad \text{at } \mathscr{A}_{\beta\sigma}, \tag{46g}$$

$$\mathbf{e}(\mathbf{r}+\mathbf{l}_i) = \mathbf{e}(\mathbf{r}), \quad i=1,2,3, \tag{46h}$$

$$\langle\mathbf{e}\rangle^\beta = \mathbf{0}. \tag{46i}$$

Note that the solution of *Problem-Ib* is simply $\mathbf{d} = \mathbf{0}$ and, according to Equation (36a), this leads to $\mathbf{R} = \mathbf{0}$. In a similar way, the solution of *Problem-IIa* is $\mathbf{C} = \mathbf{0}$, thus making $\mathbf{D}_c = \mathbf{0}$ (see the second of Equation 32). In this way, the only remaining non-zero effective-medium coefficients are the apparent permeability tensor $\mathbf{K}_s$ and the dispersion tensor $\mathbf{D}_s$. A detailed analysis of the functionality of $\mathbf{K}_s$ with the geometry and the Knudsen number is available from the works by Lasseux et al. (2014) and Lasseux et al. (2016). Moreover, the disperson coefficient $\mathbf{D}_s$ is still given by Equation (36b) and is influenced by the Knudsen slip effects. The macroscopic mass transport equation for species *A* in the present situation coincides to that explored in detail in the work by Valdés-Parada et al. (2019) when the problem reported in this last reference is conceived without any heterogeneous reaction. This model is the convection-dispersion equation ant it can be written as follows

$$\frac{\partial\langle c\rangle^\beta}{\partial t} + \langle\mathbf{v}\rangle^\beta\cdot\nabla\langle c\rangle^\beta = \nabla\cdot\left(\mathbf{D}_s\cdot\nabla\langle c\rangle^\beta\right). \tag{47}$$

In any of the above three regimes, it is possible to encounter situations for which $Pe \ll 1$. Under this constraint, a reasonable approximation for Equation (29c) is

$$\nabla\cdot(\mathscr{D}\nabla\mathbf{d}) \simeq \mathbf{0}, \quad \text{in the } \beta\text{-phase}. \tag{48}$$

Since $\mathbf{d}$ must satisfy the boundary conditions given in Equations (29d) and (29f), together with the average constraint in the second of Equation (29g), it is deduced that $\mathbf{d} \simeq \mathbf{0}$ in this regime.

The consequence of this is that, as indicated by Equation (36a), $\mathbf{R} \simeq \mathbf{0}$. In addition, from *Problem-II*, under the constraint $Pe \ll 1$, taking into account the estimate $\mathbf{e} = \mathbf{O}(\ell_\beta)$, Equation (30c) can be reasonably reduced to

$$\nabla \cdot (\mathscr{D} \nabla \mathbf{e}) \simeq \mathbf{0}, \quad \text{in the } \beta\text{-phase.} \tag{49}$$

This equation is subject to the boundary conditions given in Equations (30d) and (30f), which, together with the average constraint given in the second of Equation (30g), forms a problem that is decoupled from that on $\mathbf{C}$ and $\mathbf{c}$ and coincides with the closure problem for mass diffusion given in Equations (1.4–58) in Whitaker (1999). Consistently, the dispersion tensor given in Equation (36b) reduces to an *effective diffusion tensor*, $\mathbf{D}_{eff}$ defined as

$$\mathbf{D}_{eff} = \mathscr{D}\left(\mathbf{I} + \frac{1}{V_\beta}\int\limits_{\mathscr{A}_{\beta\sigma}} \mathbf{n}\mathbf{e}\, dA\right). \tag{50}$$

Under these circumstances, the upscaled mass transport equation for species A given in Equation (35) reduces to

$$\frac{\partial \langle c \rangle^\beta}{\partial t} = \nabla \cdot \left(\mathbf{D}_{eff} \cdot \nabla \langle c \rangle^\beta\right), \tag{51}$$

showing, as expected, that the macroscopic species mass transport is purely diffusive when $Pe \ll 1$, whatever the nature of the slip velocity boundary condition. In addition, the upscaled equation for momentum transport given in Equation (31) remains unaltered. However, when the Péclet number value is such that the interfacial and bulk transports are both purely diffusive, i.e., when $Pe \ll \min\left(\ell_\beta/\left(L\xi Kn\right), 1\right)$, the permeability tensor $\mathbf{K}_s$ reduces to the intrinsic permeability tensor.

8. CONCLUSION

In this work, the problem of gas mixture transport in a homogeneous porous medium was addressed with the purpose of deriving an upscaled model. With this aim in mind, the pore-scale problem was formulated in the case of a binary mixture involving a passive solute diluted in a solvent that is transported by advection and diffusion. Slip flow, due to Knudsen effects, as well as diffusive slip are taken into account at the solid-fluid interface following a first-order Navier condition for momentum and a Kramers-Kistemaker condition for species transport. In addition, this interface is considered impervious to mass transfer. Assuming incompressible and isothermal flow, the total and solute species mass conservation equations, together with the momentum balance equation for the fluid mixture associated to the slip boundary condition were upscaled by means of the volume averaging method, complemented with an approach similar to that used in the adjoint homogenization method. The result is a macroscopic model including the corresponding macroscopic balance equations. The macroscopic total mass conservation equation is the classical divergence-free average velocity. The macroscopic momentum balance equation involves a Darcy term but with an apparent permeability tensor that is the intrinsic permeability corrected by both slip effects. An additional term, accounting for momentum induced by the interfacial diffusive slip, is also present that involves a dispersion-like tensor. The macroscale species mass transport is governed by a non-typical convection-dispersion equation, which includes the classical convective transport term corrected by an interfacial diffusive slip-induced convective term involving a tensorial effective coefficient. In addition, the dispersion term involves a tensor that results from the sum of effective diffusion and hydrodynamic dispersion. The four effective tensorial coefficients can be computed from the solution of two coupled closure problems. However, due to the nonlinear nature of the diffusive-slip and to the convective transport term in the species mass conservation equation, the closure problems solution requires an iterative procedure that implies knowledge of the macroscopic pressure gradient as well as of the macroscopic concentration. The model developed in this work is general in the sense that it combines, for the first time, Knudsen and diffusive slip effects and sheds new light on the structure of the upscaled model and the means to predict the involved effective coefficients. Indeed, the use of the macroscale model derived here is restricted by the starting assumptions adopted in the microscale model formulation and also by the spatio-temporal constraints and assumptions involved in the upscaling process. This model was shown to conveniently coincide with those reported in the literature in particular situations corresponding to either diffusive or Knudsen slip conditions only. In these reported studies, predictions of the corresponding effective-medium coefficients were illustrated and, in some cases, validations with experiments (see for instance Altevogt et al., 2003b) and pore-scale simulations were also investigated. This can be considered as a first element of validation of the model reported here. Further investigations in terms of comparisons with experimental data and the consideration of additional mechanisms like heat transfer are certainly part of the perspectives open by the current analysis.

DATA AVAILABILITY STATEMENT

The original contributions presented in the study are included in the article, further inquiries can be directed to the authors.

AUTHOR CONTRIBUTIONS

FV-P and DL worked equally in the manuscript. Both authors contributed to the article and approved the submitted version.

REFERENCES

Airiau, C., and Bottaro, A. (2020). Flow of shear-thinning fluids through porous media. *J. Adv. Water Resour.* 143, 103658. doi: 10.1016/j.advwatres.2020.103658.

Altevogt, A., Rolston, D., and Whitaker, S. (2003a). New equations for binary gas transport in porous media, Part 1: equation development. *J. Adv. Water Resour.* 26, 695–715. doi: 10.1016/S0309-1708(03)00050-2

Altevogt, A., Rolston, D., and Whitaker, S. (2003b). New equations for binary gas transport in porous media, Part 2: experimental validation. *J. Adv. Water Resour.* 26, 717–723. doi: 10.1016/S0309-1708(03)00049-6

Barton, N. (2020). A review of mechanical over-closure and thermal over-closure of rock joints: potential consequences for coupled modelling of nuclear waste disposal and geothermal energy development. *J. Tunnell. Underground Space Technol.* 99, 103379. doi: 10.1016/j.tust.2020.103379

Bottaro, A. (2019). Flow over natural or engineered surfaces: an adjoint homogenization perspective. *J. Fluid Mech.* 877:P1. doi: 10.1017/jfm.2019.607

Cai, C., Sun, Q., and Boyd, I.D. (2007). Gas flows in microchannels and microtubes. *J. Fluid Mech.* 589, 305–314. doi: 10.1017/s0022112007008178.

Einzel, D., Panzer, P., and Liu, M. (1990). Boundary condition for fluid flow: curved or rough surface. *Phys. Rev. Lett.* 64, 2269–2272.

Gray, W. (1975). A derivation of the equations for multiphase transport. *Chem. Eng. Sci.* 30, 229–233.

Ho, C. K., and Webb, S. W. (eds.). (2006). *Gas Transport in Porous Media*. Dordrecht: Springer Netherlands.

Howes, F., and Whitaker, S. (1985). The spatial averaging theorem revisited. *Chem. Eng. Sci.* 40, 1387–1392.

Jackson, R. (1977). Transport in Porous Catalysts. volume Vol. 4, *Chemical Engineering Monographs*. Amsterdam: Elsevier.

Klinkenberg, L. (1941). The permeability of porous media to liquids and gases. *Am. Petrol. Inst.* 2, 200–213. doi: 10.5510/ogp20120200114

Kramers, H., and Kistemaker, J. (1943). On the slip of a diffusing gas mixture along a wall. *Physica* 10, 699–713. doi: 10.1016/s0031-8914(43)80018-5

Lasseux, D., Parada, F. J. V., and Porter, M.L. (2016). An improved macroscale model for gas slip flow in porous media. *J. Fluid Mech.* 805, 118–146. doi: 10.1017/jfm.2016.562

Lasseux, D., Valdés-Parada, F., Ochoa-Tapia, J., and Goyeau, B. (2014). A macroscopic model for slightly compressible gas slip-flow in homogeneous porous media. *Phys. Fluids* 26, 053102. doi: 10.1063/1.4875812

Lasseux, D., Valdés-Parada, F.J., and Bellet, F. (2019). Macroscopic model for unsteady flow in porous media. *J. Fluid Mech.* 862, 283–311. doi: 10.1017/jfm.2018.878

Lasseux, D., and Valdés-Parada, F. J. (2017). On the developments of Darcy's law to include inertial and slip effects. *C. R. Mecan.* 345, 660–669. doi: 10.1016/j.crme.2017.06.005

Lauga, E., Brenner, M. P., and Stone, H. A. (2007). "Microfluidics: the no-slip boundary condition," in Handbook of Experimental Fluid Dynamics. eds J. Foss, C. Tropea, A. Yarin, chapter 19 (New York, NY: Springer), 1219–1240.

Li, L., Zhang, D., and Xie, Y. (2019). Effect of misalignment on the dynamic characteristic of MEMS gas bearing considering rarefaction effect. *Tribol. Int.* 139, 22–35. doi: 10.1016/j.triboint.2019.06.015

Moyne, C., Le, T. D. and Maranzana, G. (2020). Upscaled model for multicomponent gas transport in porous media incorporating slip effect. *Trans. Porous Media* 135, 309–330. doi: 10.1007/s11242-020-01478-x

Navier, C. (1823). Mémoire sur les lois du mouvement des fluides. *Mém. Acad. R. Sci. l'Inst. France* VI, 389–440.

Noever, D. (1990). A note on the no-slip condition applied to diffusing gases. *Phys. Lett. A* 144, 253–255. doi: 10.1016/0375-9601(90)90931-D

Rutherford, S. W., and Do, D. D. (1999). Knudsen, slip, and viscous permeation in a carbonaceous pellet. *Ind. Eng. Chem. Res.* 38, 565–570.

Skjetne, E., and Auriault, J. L. (1999). Homogenization of wall-slip gas flow through porous media. *Trans. Porous Media* 36, 293–306. doi: 10.1023/a:1006572324102

Tian, Y., Yu, X., Li, J., Neeves, K. B., Yin, X., and Wu, Y. S. (2019). Scaling law for slip flow of gases in nanoporous media from nanofluidics, rocks, and pore-scale simulations. *Fuel* 236, 1065–1077. doi: 10.1016/j.fuel.2018.09.036

Valdés-Parada, F., Lasseux, D., and Whitaker, S. (2019). Upscaling reactive transport under hydrodynamic slip conditions in homogeneous porous media. *Water Resour. Res.* 56: e2019WR025954. doi: 10.1029/2019WR025954

Valdés-Parada, F., Porter, M., Narayanaswamt, K., Ford, R., and Wood, B. (2009). Upscaling microbial chemotaxis in porous media. *Adv. Water Resour.* 32, 1413–1428. doi: 10.1016/j.advwatres.2009.06.010

Wang, M., Deng, C., Chen, H., Wang, X., Liu, B., Sun, C., et al. (2020). An analytical investigation on the energy efficiency of integration of natural gas hydrate exploitation with H_2 production (by *in situ* CH_4 reforming) and CO_2 sequestration. *Energy Conver. Manag.* 216:112959. doi: 10.1016/j.enconman.2020.112959

Whitaker, S. (1999). *The Method of Volume Averaging*. Dordrecht: Kluwer Academic Publishers.

Woignier, T., Anez, L., Calas-Etienne, S., and Primera, J. (2018). Gas slippage in fractal porous material. *J. Natural Gas Sci. Eng.* 57, 11–20. doi: 10.1016/j.jngse.2018.06.043

Wood, B., and Valdés-Parada, F. (2013). Volume averaging: Local and nonlocal closures using a Green's function approach. *Adv. Water Resour.* 51, 139–167. doi: 10.1016/j.advwatres.2012.06.008

Wood, B., and Whitaker, S. (1998). Diffusion and reaction in biofilms. *Chem. Eng. Sci.* 52, 397–425. doi: 10.1016/S0009-2509(97)00319-9

Young, J., and Todd, B. (2005). Modelling of multi-component gas flows in capillaries and porous solids. *Int. J. Heat Mass Trans.* 48, 5338–5353. doi: 10.1016/j.ijheatmasstransfer.2005.07.034

Zaouter, T., Lasseux, D., and Prat, M. (2018). Gas slip flow in a fracture: local Reynolds equation and upscaled macroscopic model. *J. Fluid Mech.* 837, 413–442. doi: 10.1017/jfm.2017.868

Conflict of Interest: The authors declare that the research was conducted in the absence of any commercial or financial relationships that could be construed as a potential conflict of interest.

frontiers in Water

ORIGINAL RESEARCH
published: 30 July 2021
doi: 10.3389/frwa.2021.709833

Role of Pore-Size Distribution on Effective Rheology of Two-Phase Flow in Porous Media

Subhadeep Roy[1,2]*, *Santanu Sinha*[2,3] *and Alex Hansen*[2]

[1] PoreLab, Department of Physics, University of Oslo (UiO), Oslo, Norway, [2] PoreLab, Department of Physics, Norwegian University of Science and Technology (NTNU), Trondheim, Norway, [3] Beijing Computational Science Research Center, Beijing, China

Immiscible two-phase flow of Newtonian fluids in porous media exhibits a power law relationship between flow rate and pressure drop when the pressure drop is such that the viscous forces compete with the capillary forces. When the pressure drop is large enough for the viscous forces to dominate, there is a crossover to a linear relation between flow rate and pressure drop. Different values for the exponent relating the flow rate and pressure drop in the regime where the two forces compete have been reported in different experimental and numerical studies. We investigate the power law and its exponent in immiscible steady-state two-phase flow for different pore size distributions. We measure the values of the exponent and the crossover pressure drop for different fluid saturations while changing the shape and the span of the distribution. We consider two approaches, analytical calculations using a capillary bundle model and numerical simulations using dynamic pore-network modeling. In case of the capillary bundle when the pores do not interact to each other, we find that the exponent is always equal to 3/2 irrespective of the distribution type. For the dynamical pore network model on the other hand, the exponent varies continuously within a range when changing the shape of the distribution whereas the width of the distribution controls the crossover point.

Keywords: non-linear fluid flow, two-phase flow, porous media, pore-size distribution, effective rheology

OPEN ACCESS

Edited by:
Charlotte Garing,
University of Georgia, United States

Reviewed by:
Alexandre Puyguiraud,
Instituto de Diagnóstico Ambiental y Estudios del Agua (IDAEA), Spain
Jesse Dickinson,
United States Geological Survey (USGS), United States

***Correspondence:**
Subhadeep Roy
subhadeeproy03@gmail.com

Specialty section:
This article was submitted to Water and Critical Zone, a section of the journal Frontiers in Water

Received: *14 May 2021*
Accepted: *02 July 2021*
Published: *30 July 2021*

Citation:
Roy S, Sinha S and Hansen A (2021) Role of Pore-Size Distribution on Effective Rheology of Two-Phase Flow in Porous Media. Front. Water 3:709833. doi: 10.3389/frwa.2021.709833

1. INTRODUCTION

Multiphase flow is relevant for a wide variety of different applications which deal with the flow of multiple immiscible fluids in single capillaries to more complex porous media (Bear, 1988; Dullien, 1992). The rheology of such flow is guided by a series of parameters: capillary forces at the interfaces, viscosity contrast between the fluids, wettability, and geometry of the system, which collectively make the flow properties different compared to single phase flow. The study of two-phase flow is generally divided in two regimes: (i) the transient regime and (ii) the steady-state flow. In the transient regime, one can obtain different types of flow patterns, namely capillary fingering (Lenormand and Zarcone, 1985), viscous fingering (Chen and Wilkinson, 1985; Måløy et al., 1985), and stable displacement (Lenormand et al., 1988), and models such as diffusion limited aggregation (DLA) (Witten and Sander, 1981) and invasion percolation (Wilkinson and Willemsen, 1983) are used to describe the patterns. When the steady state sets in after the initial instabilities, the flow properties are determined by the global parameters such as global pressure drops, flow rates, saturation, and fractional flow (Valavanides, 2018).

In recent years, many studies on the steady-state two phase flow on Newtonian fluids have revealed a non-trivial rheology, that is, in the regime where capillary forces are comparable to viscous forces, the relation between the total flow rate Q in a sample and the global pressure drop ΔP across it differs from a linear Darcy law (Darcy, 1856; Whitaker, 1986). Instead, Q increases much faster with ΔP, obeying a power law where the power-law exponent β is larger than 1 (Tallakstad et al., 2009a,b; Rassi et al., 2011; Sinha et al., 2017). Furthermore, studies have also shown that it undergoes crossovers to linear regimes at both sides of the non-linear regime, that is, at flow rates below a threshold and at flow rates higher than another larger threshold. Experiments by Tallakstad et al. (2009a,b) for a two-dimensional (2D) Hele-Shaw cell filled with glass beads measured this exponent β as 1.85 ($\approx$ 1/0.54)[1]. For a three-dimensional (3D) porous media, this exponent was observed to vary between 2.2 ($\approx$ 1/0.45) and 3.3 ($\approx$ 1/0.3) (Rassi et al., 2011) depending on the saturation. It was later found to converge to a certain value ≈ 2.17 when a global yield pressure is considered in the system, below which there is no flow (Sinha et al., 2017). By using pore-network modeling with 2D and 3D pore networks, Sinha et al. found the exponent to be close to 2 in the non-linear regime (Sinha and Hansen, 2012; Sinha et al., 2017). They also have reported a crossover to linear Darcy type regime at high capillary number when capillary forces are insignificant. Yiotis et al. (2013) performed Lattice-Boltzmann simulations with stochastically reconstructed porous system and studied the dynamics of fluid blobs in the presence of gravity. In the steady state, they found a non-linear regime with quadratic dependence with an exponent 2, which is bounded by two linear regimes at both the high and low capillary numbers. The blobs were then studied experimentally and the non-linear exponent was found as 1.54 ($\approx$ 1/0.65) (Chevalier et al., 2015). Very recently, Gao et al. (2020) performed experiments of two-phase flow in sandstone samples. They used x-ray micro-tomography measurements and for a fractional flow of 0.5 they found the exponent in the non-linear regime to be equal to 1.67 ($\approx$ 1/0.6). They also reported a regime with linear Darcy type behavior at lower capillary numbers where the conductance does not change significantly. Further experiments by Zhang et al. (2021) explore the dependence of the exponent on fractional flow and reported values in the range of 1.35 ($\approx$ 1/0.74) to 2.27 ($\approx$ 1/0.44). They presented a theory that can predict the boundary between the linear regime and the non-linear intermittent flow regime.

A simple explanation for the observed power law relation between flow rate and pressure drop may be found by following the arguments of Roux and Herrmann (1987), concerning the conductivity of a disordered network of resistors, where each resistor has a threshold voltage to start conducting current. If we compare the voltage across a resistor in this system to the pressure drop over a link in a network of pores, and the threshold voltage to the pressure drop necessary to overcome capillary forces due to the presence of fluid interfaces (Sinha et al., 2013), we may translate the Roux and Herrmann arguments into a language appropriate for porous media. When the pressure drop ΔP across a network of pores containing fluid interfaces is increased by an amount $\mathrm{d}\Delta P$, an additional number of pores ($\mathrm{d}N$) will start contributing to the flow. This leads to an increase in the effective conductivity K of the network as more links are participating to the flow. If correlations between the opened links are ignored, the increase in conductivity $\mathrm{d}K$ will be proportional to the increase in the number of opened links, $\mathrm{d}K \propto \mathrm{d}N$. We integrate to find

$$K(\Delta P') \propto \int_{P_c}^{\Delta P'} \mathrm{d}\Delta P'' = \Delta P' - P_c, \tag{1}$$

where the lower integration limit P_c is the threshold pressure necessary to induce a flow across the network and can be determined from the effective threshold pressure of the first flow path. If the pressure drop ΔP is less than P_c, there will be no flow across the porous media. The flow rate is then given by

$$Q = \int_{P_c}^{\Delta P} K(\Delta P')\mathrm{d}\Delta P' \propto (\Delta P - P_c)^2. \tag{2}$$

Tallakstad et al. (2009a,b) provided another explanation by considering the scaling of clusters that are trapped by capillary forces. They assumed that the flow occurs in channels in between trapped clusters. In a two-dimensional system of length L under a pressure drop ΔP, a cluster will be trapped if the capillary force $p_c > \lambda_\parallel |\Delta P|/L$, where the $\lambda_\parallel$ is the length of such a cluster. The maximum length of a such a trapped cluster is therefore given by $\lambda_\parallel^m = Lp_c/|\Delta P|$. By assuming the distance between the flow channels equal to the typical cluster length, the total number of flow channels will be $n_c = L/\lambda_\parallel^m$. The total flow through all the channels is therefore the number of channels multiplied by the flow rate in each channel, which leads to $Q \propto n_c|\Delta P| \propto |\Delta P|^2$. However, if this formalism is extended to three dimensions, it leads to a cubic relationship, $Q \propto |\Delta P|^3$, which is in contrary to what is observed in experiments and simulations.

Sinha and Hansen (2012) developed a mean-field theory for a disordered network. By analytically calculating the average rheological behavior for such a pore (Sinha et al., 2013) and using Kirkpatrick's self-consistent expression for the equivalent conductivity for a homogeneous network (Kirkpatrick, 1973), they derived the relationship,

$$Q \propto (\Delta P - P_c)^2. \tag{3}$$

Note that the above theoretical approaches find the exponent in the non-linear regime β to be equal to 2, thus hinting at universality.

Recently, Roy et al. (2019) have studied the effect of the threshold distribution on the effective rheology of two Newtonian fluids in a capillary bundle model. The model consists of a bundle of parallel capillary tubes with variable diameters along their lengths which introduce thresholds for each tube (Scheidegger, 1953, 1974). For power-law type distributions of

[1]The values in the brackets are the exponents reported in the literature, the reciprocals of them should be compared here, as we express our results as Q as a power law in ΔP, whereas the cited articles expressed ΔP as a power law in Q, or rather the corresponding capillary number Ca.

the thresholds they find analytically and numerically that the non-linear exponent β can be related to α, the exponent for the power-law distribution, by the relationships $\beta = \alpha + 1$ or $\beta = \alpha + 1/2$ depending on whether the distribution starts from zero or has lower cut off, respectively. This means, for $\alpha = 1$, the uniform threshold distribution, β will be equal to 2 and 3/2, respectively for the two cases. This study clearly hints that the non-linear exponent depends on the distributions related to the system properties. We note that the capillary fiber bundle model in the form studied by Roy et al. only considered variations in the flow thresholds and not directly on the variations in the pore sizes, nor fluctuations in the saturation.

In this article, we present a detailed study on how the distribution of pore sizes controls the effective rheology of the two-phase flow in the steady state. We will first study analytically the capillary bundle model, as it is an analytically tractable model for two-phase flow and provides deeper understanding of the underlying physical mechanism. There we will show that as the applied pressure is increased there exists a transition point below which the relation between flow rate and pressure drop is non-linear. We will investigate how the degree of such non-linearity depends on the shape and width of the distribution of the pore sizes. Above the transition point, we observe that the flow rate increases in a Darcy-like linear manner with the increase in pressure drop and the linearity do not depend on the distribution. We will then move to numerical simulation with dynamic pore-network modeling, where a similar transition is observed. There the variation in exponent in the non-linear regime and the transition point is studied by varying three parameters: the saturation of the wetting fluid, and the span and shape related to the pore-size distribution. Finally, with a two-dimensional plane of the non-linear exponent vs. the transition point, we show how the above three parameters control the effective rheology of two-phase flow.

2. CAPILLARY FIBER BUNDLE MODEL

In this section, we will study the analytically solvable *capillary fiber bundle model* (CFBM) (Scheidegger, 1953, 1974), which can be considered as a prototype for a one-dimensional porous medium. The model was recently studied by the present authors to explore the non-linearity in the effective rheology in two-phase flow in a bundle of capillary tubes (Roy et al., 2019). Here we will analytically derive the relation between average flow rate and pressure drop for this model for different distributions of pore-radii. CFBM is a hydrodynamic analog of the fiber bundle model (Hansen et al., 2015), which is a disordered system driven by threshold activated dynamics and often used as a model system to study mechanical failure under stress.

The model consists of a bundle of N independent parallel tubes each of length L, carrying train of bubbles with different distributions of wetting and non-wetting fluids. A global pressure drop ΔP is applied across the bundle, creating a global flow rate Q. In the steady state, Q is the sum of all the time averaged flow rates $\langle q \rangle$ in each individual tube. The diameter of each tube varies along the length of the tubes which makes the interfacial forces vary as the bubble train moves along the tubes. We assume no film flow so the fluids do not pass each other. The total length of the sections along the tube containing the more wetting fluid (called the wetting fluid) is L_w and the total length of the sections containing the less wetting fluid (called the non-wetting fluid) is L_n. The corresponding volumes are therefore given by $\pi r^2 L_w$ and $\pi r^2 L_n$, where r is the average radius of the capillary tube. The saturations in each tube are then $S_w = L_w/L$ and $S_n = L_n/L$. Each tube making up the bundle contains the same amount of each fluid but with its own division of the fluids into bubbles.

The total volumetric flow rate q in a capillary tube at any instant of time is given by,

$$q = -\frac{\pi r^4}{8\mu_{av}L}\Theta(|\Delta P| - p_c)(|\Delta P| - p_c), \tag{4}$$

where $|\Delta P|$ is the pressure drop across the capillary tube, p_c is the instantaneous capillary pressure given by the sum of all the capillary forces along the capillary tube due to the interfaces and μ_{av} is the effective viscosity given by $\mu_{av} = S_w\mu_w + S_n\mu_n$. Here μ_w and μ_n are the visocities of the wetting and the non-wetting fluids. Here $\Theta(|\Delta P| - p_c)$ is the Heaviside function which is 0 for negative arguments and 1 for positive arguments. When the pressure difference across the tube is kept fixed, the average volumetric flow rate $\langle q \rangle$ in the steady state can be obtained by averaging Equation (4) over a time interval,

$$\langle q \rangle = -\frac{\pi r^4}{8\mu_{av}L}\mathrm{sgn}(\Delta P)\Theta(|\Delta P| - \gamma)\sqrt{|\Delta P|^2 - \gamma^2}, \tag{5}$$

where sgn(ΔP) is the sign of the argument. Here the parameter γ is the effective threshold pressure for the single tube below which there is no flow, and a function of the average pore radii, surface tension, contact angle, and bubble sizes. If the tube is assumed to have a sinusoidal variation in radius with amplitude a about an average radius r and a period of length l, then the exact form of γ is given by,

$$\gamma = \sqrt{\Gamma_s^2 + \Gamma_c^2}, \tag{6}$$

where

$$\Gamma_s = \sum_{j=-K}^{+K} \frac{4\sigma a}{r} \sin\left(\frac{\pi \Delta x_j}{l}\right) \sin\left(\frac{2\pi (x_j - x_0)}{l}\right), \tag{7}$$

and

$$\Gamma_c = \sum_{j=-K}^{+K} \frac{4\sigma a}{r} \sin\left(\frac{\pi \Delta x_j}{l}\right) \cos\left(\frac{2\pi (x_j - x_0)}{l}\right). \tag{8}$$

Here x_j is the position of center of the jth bubble if the tube is filled with $2K + 1$ bubbles. Its width is Δx_j. The surface tension times the cosine of the average contact angle is σ.

We are interested in the effect due to the variation in the pore radii assuming that the average contribution due to the bubble

sizes are the same for all tubes. In such a scenario, γ can be expressed in terms of the link radius r as,

$$\gamma = \frac{k}{r}, \tag{9}$$

where k is a proportionality constant. Equation (9) implies that the larger the radius of a tube, the lower the threshold pressure will be and the fluids will start flowing at a relatively lower value for $|\Delta P|$.

We now consider a bundle of N tubes with average radii drawn from a distribution $\rho(r)$. We assume there is a smallest radius $r_{\min}$ and a largest radius $r_{\max}$, so that $\rho(r) = 0$ for $r < r_{\min}$ and for $r > r_{\max}$. This means that there is a smallest threshold $P_m = k/r_{\max}$ and a largest threshold $P_M = k/r_{\min}$ among the N tubes as $N \to \infty$.

Let us define a radius

$$r_c(|\Delta P|) = \max\left(\frac{k}{|\Delta P|}, r_{\min}\right). \tag{10}$$

The total flow rate is then given by

$$\frac{Q}{N} = \begin{cases} 0 & \text{if } |\Delta P| < P_m, \\ \int_{r_c(|\Delta P|)}^{r_{\max}} q\,\rho(r)\mathrm{d}r & \text{if } |\Delta P| \geq P_m, \end{cases} \tag{11}$$

which combined with Equations (9), (5), and (11) give.

$$\frac{8\mu_{av}LQ}{N\pi} = \begin{cases} 0 & \text{if } |\Delta P| < P_m, \\ -\int_{r_c(|\Delta P|)}^{r_{\max}} r^4\sqrt{|\Delta P|^2 - \left(\frac{k}{r}\right)^2}\,\rho(r)\mathrm{d}r & \text{if } |\Delta P| \geq P_m. \end{cases} \tag{12}$$

2.1. Uniform Distribution

We use a uniform distribution of r between $r_{\min} > 0$ and $r_{\max} > r_{\min}$ as a first illustration. We have that

$$\rho(r) = \begin{cases} 0 & \text{if } r \leq r_{\min}, \\ 1/(r_{\max} - r_{\min}) & \text{if } r_{\min} < r \leq r_{\max}, \\ 0 & \text{if } r > r_{\max}. \end{cases} \tag{13}$$

Equation (12) then gives for $|\Delta P| > k/r_{\max}$

$$Q = -\frac{k^5 N\pi}{120\mu_{av}[r_{\max} - r_c(|\Delta P|)]L} \frac{1}{|\Delta P|^4}\left[(u^2-1)^{3/2}(2+3u^2)\right]_{r_c(|\Delta P|)|\Delta P|/k}^{r_{\max}|\Delta P|/k}. \tag{14}$$

We now have two possibilities, either $|\Delta P| > k/r_{\min}$, making $r_c(|\Delta P|)|\Delta P|/k = r_{\min}|\Delta P|/k$. The other possibility is that $|\Delta P| < k/r_{\min}$ making $r_c(|\Delta P|)|\Delta P|/k = 1$.

We consider the $|\Delta P| > k/r_{\min}$ case first. This is when there is flow in all the fibers. We get

$$Q = -\frac{k^5 N\pi}{120\mu_{av}[r_{\max} - r_{\min}]L} \frac{1}{|\Delta P|^4}\left[(u^2-1)^{3/2}(2+3u^2)\right]_{r_{\min}|\Delta P|/k}^{r_{\max}|\Delta P|/k}. \tag{15}$$

For large pressure drops $|\Delta P| \gg k/r_{\min}$, this expression reduces to

$$Q = -\frac{N\pi[r_{\max}^5 - r_{\min}^5]}{40\mu_{av}[r_{\max} - r_{\min}]L}\,|\Delta P|. \tag{16}$$

We now consider the opposite case, i.e., when $|\Delta P| < k/r_{\min}$. In this case, $r_c(|\Delta P|)|\Delta P|/k = r_{\min}|\Delta P|/k$. The flow rate is then

$$Q = -\frac{k^5 N\pi\left[\left(\frac{r_{\max}|\Delta P|}{k}\right)^2 - 1\right]^{3/2}\left[2 + 3\left(\frac{r_{\max}|\Delta P|}{k}\right)^2\right]}{120\mu_{av}[r_{\max} - k/|\Delta P|]L|\Delta P|^4}. \tag{17}$$

If we now assume that $|\Delta P| - k/r_{\max} = |\Delta P| - P_m \ll P_m$, we may expand this expression in terms of $|\Delta P| - P_m$, finding to lowest order.

$$Q = -\frac{\sqrt{2}\,r_{\max}^{11/2} N\pi}{12\mu_{av}(r_{\max} - r_{\min})k^{1/2}L}\,(|\Delta P| - P_m)^{3/2}. \tag{18}$$

2.2. Power Law Distribution

We now consider a power law distribution where link radii are chosen with different probabilities depending on the slope of the distribution. The expression for $\rho(r)$ we assume to be

$$\rho(r) = \begin{cases} 0 & \text{if } r \leq r_{\min}, \\ \frac{1-\alpha}{r_{\max}^{1-\alpha} - r_{\min}^{1-\alpha}}\,r^{-\alpha} & \text{if } r_{\min} < r \leq r_{\max}, \\ 0 & \text{if } r > r_{\max}. \end{cases} \tag{19}$$

The uniform distribution (Equation 13) illustrated in the previous section is a special case of this distribution with $\alpha = 0$. The global flow rate obtained from Equation (13) is

$$Q = -\frac{k(1-\alpha)N\pi}{8\mu_{av}[r_{\max}^{1-\alpha} - r_{\min}^{1-\alpha}]L}\int_{r_c(|\Delta P|)}^{r_{\max}} r^{4-\alpha}\sqrt{\left(\frac{|\Delta P|}{k}\right)^2 - \left(\frac{1}{r}\right)^2}\mathrm{d}r. \tag{20}$$

As for the uniform distribution, we have two cases to consider: $|\Delta P| > k/r_{\min}$ for which $r_c(|\Delta P|) = r_{\min}$ and $|\Delta P| < k/r_{\min}$ for which $r_c(|\Delta P|) = k/|\Delta P|$.

We consider the case $|\Delta P| > k/r_{\min}$ first. Then, there is flow in all the fibers and we have

$$Q = -\frac{k^{5-\alpha}(1-\alpha)N\pi}{8\mu_{av}[r_{\max}^{1-\alpha} - r_{\min}^{1-\alpha}]L|\Delta P|^{4-\alpha}}\int_{r_{\min}|\Delta P|/k}^{r_{\max}|\Delta P|/k} u^{3-\alpha}\sqrt{u^2-1}\mathrm{d}u. \tag{21}$$

When the pressure drop $|\Delta P|$ becomes very large, i.e., $|\Delta P| \gg k/r_{\min}$, the integral in Equation (21) simplifies by having $\sqrt{u^2-1} \to u$ in the integrand, and we find

$$Q = -\frac{(1-\alpha)[r_{\max}^{5-\alpha} - r_{\min}^{5-\alpha}]N\pi}{8(5-\alpha)\mu_{av}[r_{\max}^{1-\alpha} - r_{\min}^{1-\alpha}]L}\,|\Delta P|. \tag{22}$$

The other case, $|\Delta P| < k/r_{\min}$ leads to $r_c(|\Delta P|) = k/|\Delta P|$ and Equation (20) becomes

$$Q = -\frac{k^{5-\alpha}(1-\alpha)N\pi}{8\mu_{av}[r_{\max}^{1-\alpha} - r_{\min}^{1-\alpha}]L|\Delta P|^{4-\alpha}}\int_{1}^{r_{\max}|\Delta P|/k} u^{3-\alpha}\sqrt{u^2-1}\mathrm{d}u. \tag{23}$$

We now assume that $|\Delta P| - P_m \ll P_m$. We expand the integral in Equation (23) to find

$$\int_1^{1+\Delta} u^{3-\alpha}\sqrt{u^2-1}\mathrm{d}u = \int_0^{\Delta}(1+w)^{3-\alpha}\sqrt{2+w}\sqrt{w}\mathrm{d}w = \frac{2\sqrt{2}}{3}\Delta^{3/2}, \quad (24)$$

to lowest order in Δ. Hence, the total flow rate is to lowest order in $|\Delta P| - P_m$

$$Q = -\frac{\sqrt{2}(1-\alpha)N\pi r_{\max}^{11/2-\alpha}}{12\sqrt{k}\mu_{av}[r_{\max}^{1-\alpha} - r_{\min}^{1-\alpha}]L}(|\Delta P| - P_m)^{3/2}. \quad (25)$$

We see that the exponent α does not affect the exponent β for $|\Delta P|$ larger than but close to P_m. Furthermore, for $\alpha = 0$ we retrieve Equation (18).

Here $P_m = k/r_{\max}$ plays the role of a threshold pressure P_c below which there is no flow, whereas $P_M = k/r_{\min}$ is the crossover pressure drop at which there is flow in all fibers. This pressure (P_M) signals the transition to the Darcy-type flow where Q is proportional to $|\Delta P|$.

In gist, the analytical calculations with the capillary bundle model show that as soon as the pressure drop over the fiber bundle is large enough for flow to start, it enters a non-linear regime where the total flow rate Q is proportional to $(|\Delta P| - P_m)^{3/2}$ irrespective of the exponent α, defined in Equation (19). When the threshold pressure P_M is crossed, the non-linear behavior subsides and we find Darcy-type flow. Mobility is sensitive to the details of the radius distribution for low flow rates and insensitive at higher flow rates. We like to point out here that, unlike the radii distribution, when a distribution of pore thresholds is considered, a quadratic regime with $\beta = 2$ can also obtained for CFBM when the distribution has no lower cutoff (Roy et al., 2019). With any non-zero lower cut-off in the thresholds, β is also 3/2 there. In the present study we considered the distribution of pore radii rather than the thresholds, and for any finite pore radii, there is always a lower cutoff in the thresholds.

3. DYNAMIC PORE NETWORK MODEL (DPNM)

Pore-network modeling is a computational technique to simulate two-phase flow in porous media where the porous matrix is represented by a network of pores with simplified geometries (Joekar-Niasar and Hassanizadeh, 2012). In comparison to other computational methods for simulating two-phase flow in porous media, such as the lattice Boltzmann method (Gunstensen et al., 1991) which solves Boltzmann transport equations at discretized pore space, the pore-network model is a more computationally efficient method when doing simulation with large number of pores. The model is therefore useful to study up-scaled properties of two-phase flow in porous media in the steady state (Sinha et al., 2017) or drainage displacements (Zhao et al., 2019). Here we will use this model to simulate the two-phase flow in the networks with different pore size distributions and will measure total flow rate as a function of the global pressure drop in the steady-state. In this model, one pore is the smallest computational unit and the fluid displacements inside the pores are governed by equations for fully developed flow. We use a dynamic pore-network model where the menisci positions between the fluids track the flow (Aker et al., 1998; Sinha et al., 2021). The network in this model is defined in such a way that total pore space related to both the pore-throat and pore-bodies are represented by *composite links* of varying radii. The nodes of the network therefore only represent the positions of the link intersections and do not contain any volume. We considered a tilted square lattice in two dimensions as a network with coordination number 4. The flow rate in a link in the network is given by (Washburn, 1921),

$$q_j = -\frac{g_j}{l_j\mu_j}\left[\Delta p_j - \sum p_c(x)\right], \quad (26)$$

where Δp_j is the local pressure drop across the jth link. The terms l_j, g_j, and μ_j, respectively define the length, mobility, and effective fluid viscosity related to that link. If μ_w and μ_n are the wetting and non-wetting viscosities, respectively, then $\mu_j = s_{n,j}\mu_n + s_{w,j}\mu_w$, where $s_{n,j}$ and $s_{w,j}$ are wetting and non-wetting saturations inside that link. In this study, we consider links with circular cross sections with radii r_j, for which $g_j = a_j r_j^2/8$ where $a_j = \pi r_j^2$, the cross-sectional area (Langglois, 1964). The interfacial pressure due to surface tension between the fluids is indicated by p_c which is summed over all the interfaces inside the link j, taking into account the direction of the capillary forces. The links here represent the total pore space that consists of a pore throat in between pore bodies and the variation in the link radii along its length is therefore modeled by a sinusoidal periodic shape. The interfacial pressure at a meniscus inside such a pore can be expressed by a modified Young-Laplace equation (Sinha et al., 2013),

$$|p_c(x_k)| = \frac{2\sigma}{r_j}\left[1 - \cos\left(\frac{2\pi x_k}{l_j}\right)\right], \quad (27)$$

where $x \in [0, l_j]$, the position of a meniscus inside the jth link. Here σ is the surface tension times the cosine of the contact angle for the set of fluids and pores which are kept constant throughout the simulations. We considered $\sigma = 0.03$N/m here. We study in-compressible fluids and therefore at every time step Δt we have for each node i from Kirchhoff law, $\sum q_i = 0$, where the sum is over all the links connected to i^{th} link. This, together with Equations (26) and (27), constructs a set of linear equations. We solve these equations by conjugate gradient method (Batrouni and Hansen, 1988) and determine the flow rates q_j in every link. All the menisci in each link are then advanced by an amount $\Delta x_j = q_j \Delta t$. Further technical details related to the menisci displacements can be found in Sinha et al. (2021). We consider periodic boundary conditions that lead the system to evolve to a steady state.

The network we consider in this study consists of 64×64 links in two dimensions (2D) which form a diamond lattice. All the links are therefore at an angle 45° with respect to the overall flow direction. The links have equal lengths, $l_j = 1$mm, and the

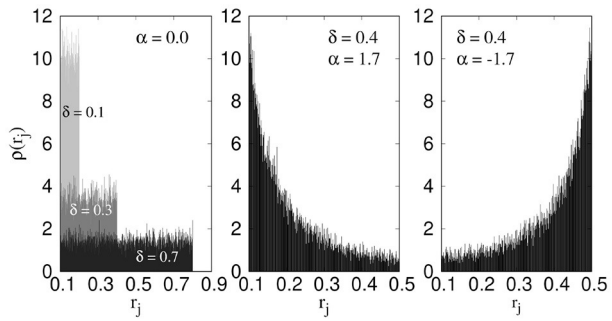

FIGURE 1 | Distributions of link radii r_j for different values of the power α and width δ. For $\alpha = 0$ all the radii within the interval have equal probability whereas for positive and negative values of α there is higher probability to have narrow and wide links, respectively.

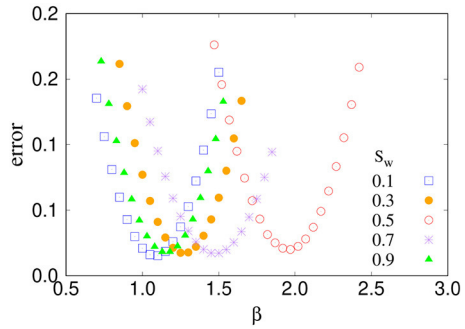

FIGURE 2 | The error associated with least-square fitting of the numerical results to Equation (3) as a function of the trial values of β. Results are shown for five different saturations S_w. The minima of these plots decide the final values of β and P_c.

disorder appears in their radii r_j. We choose the values of r_j from a distribution $\rho(r_j)$ with a power α and in the range $r_{\min}$ to $r_{\max}$ given by the same type of distribution as in Equation (19),

$$\rho(r_j) = \begin{cases} 0 & \text{if } r \le r_{\min}, \\ \frac{1-\alpha}{r_{\max}^{1-\alpha} - r_{\min}^{1-\alpha}} \, r_j^{-\alpha} & \text{if } r_{\min} < r \le r_{\max}, \\ 0 & \text{if } r > r_{\max}. \end{cases} \tag{28}$$

We denote the width of the distribution by $\delta = r_{\max} - r_{\min}$. The power α generates different distribution types, $\alpha = 0$ corresponds to a uniform distribution whereas positive and negative values of α imply higher probability to find narrower and wider links, respectively. **Figure 1** shows $\rho(r_j)$ for $\alpha = 0.0$, 1.7, and -1.7. For $\alpha = 0$, we show the distributions for $\delta = 0.1$, 0.3, and 0.7.

4. NUMERICAL RESULTS FROM DPNM

We perform simulations with constant global pressure drop ΔP and evolve the systems to steady state, where the macroscopic quantities fluctuate around a steady average. In the steady state, we measure the total flow rate Q. Results are averaged over 20 different realizations of the pore network. By fitting the numerical data with Equation (3) for the low capillary number regime, we calculate the exponent β and the threshold pressure P_c. As there are two parameters to determine from each data set, we considered a method of minimizing the error related to the least square fit (Sinha and Hansen, 2012). We illustrate this procedure briefly here. First we choose a trial value of β and perform least square fitting with the data points. This will provide a value of P_c and an error associated with it. We perform this for a set of β values and find the corresponding error values. We then plot the errors as a function of β. This is shown in **Figure 2** for five different saturations where we see non-monotonic behavior of the errors with a minimum. We then consider the value of β that corresponds to the minimum error and use the corresponding value of P_c. When plotting $\log(\Delta P - P_c)$ with $\log Q$, we find the crossover point between a non-linear and a linear regime from eye approximation. From this crossover, we then identify the crossover pressure drop P_t.

In the following we present the results showing how the steady-state rheology depends on the three parameters, (A) the wetting saturation S_w, (B) the power α, and (C) the width δ related to the pore-size distribution. S_w is varied between 0 and 1. We keep $r_{\min} = 0.1$ and vary $r_{\max}$ from 0.2 to 0.8. In case of real a porous media, the pore sizes generally vary over a few orders of magnitude. In the pore-network simulations however, making the pores very small will lead the simulations to reach the steady state in a slower rate and will make the simulations computationally very expensive. Furthermore, as we will see in the following, δ do not affect the value of the exponent β and only controls the crossover point. We therefore considered δ to vary from 0.1 to 0.7 in the present study. The exponent α is varied in the range $-2.0 \le \alpha \le 2.0$. We will focus on the non-linear exponent β and the pressure P_t related to the cross-over from non-linear to linear regime. Then in a P_t vs. β plane we will highlight how the two quantities vary when we change the values of S_w, α and δ.

4.1. Effect of S_w

The variation of the flow rate Q with the pressure drop ΔP is shown in **Figure 3** for three different wetting saturations (**Figure 3A**) 0.1, (**Figure 3B**) 0.5, and (**Figure 3C**) 0.9 where we plotted $\log(Q)$ as a function of $\log(\Delta P - P_c)$. The value of α and δ are kept constant here at 0.0 and 0.3, respectively. The respective threshold pressures (P_c), measured by the minimum error method, are indicated in the plots. All the plots show a non-linear regime at lower pressure drops and then a crossover to a linear regime. However, the slope in the non-linear regime is much higher for $S_w = 0.5$ than 0.1 or 0.9. Similarly, the threshold pressure P_c is also higher for $S_w = 0.5$. This indicates the fact that as $S_w \to 0$ or $S_w \to 1$, the two-phase flow essentially approach to the single phase flow and it should eventually follow the linear Darcy law without any threshold pressure. In order to see the nature of this variation toward the linear regime, we plot in **Figures 3D–F**, the values of β and P_t and P_c as a function of S_w, where S_w is varied from 0.1 to 0.9 with an interval of 0.1. All

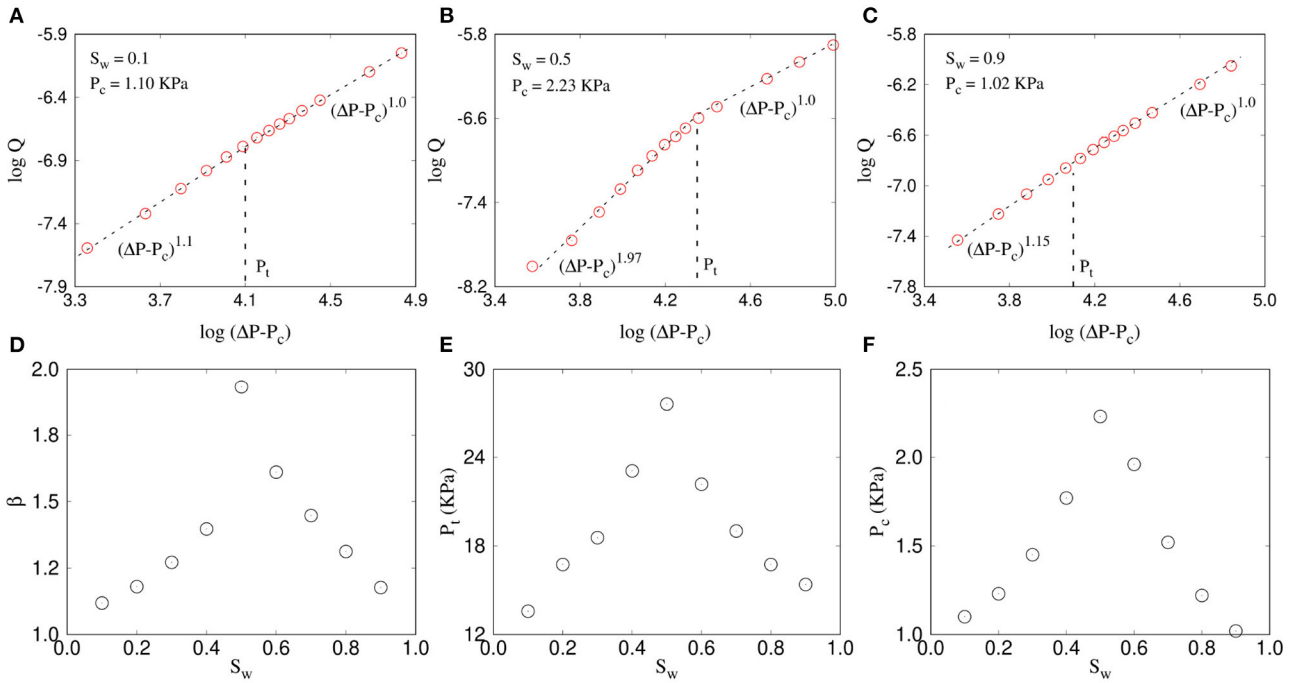

FIGURE 3 | Plot of $\Delta P - P_c$ (Pa) vs. Q (m^3/s) for a network of 64 × 64 links in 2D for three different wetting saturations $S_w = 0.1$, 0.5, and 0.9 are shown in **(A–C)**, respectively. The plots show a non-linear regime at low pressure drop and a liner regime at high pressure drop. The variations of the slopes β in the non-linear regime, the crossover pressure drop P_t (KPa) and the threshold pressure P_c (KPa) as a function of S_w are shown in **(D–F)**, respectively. All the β, P_t, and P_c have a maximum around $S_w = 0.5$ and decreases on either side.

three plots show a peak around $S_w = 0.5$ with $\beta = 1.97$ and then continuously decrease in both sides. The decrease in both β and P_t suggests that not only the non-linearity gradually disappears as S_w deviates from 0.5, but also the linear Darcy regime can be obtained at a relatively lower pressure drop. At the same time, the overall threshold pressure P_c also decreases as the saturation approaches to 0 or 1.

If we consider that the flow occurs in channels with capillary barriers (Roux and Herrmann, 1987), that is, the increase in Q with ΔP is contributed from two factors, the increase in the number of conducting flow paths and the increase in the flow in each path, then that explains the reduction in both β and P_t as $S_w \to 0$ or 1. As the saturation of a certain fluid decreases, either it reduces the number of fluid-fluid interfaces or produces smaller bubbles of one fluid. In both the cases the effective capillary barriers corresponding to any flow path decreases. This results in more flow paths with one fluid or with negligible capillary barriers which will start flowing as soon as any pressure drop is applied, making the β to move toward 1. At the same time, the maximum capillary barrier that the model needs to overcome to make all possible paths flowing also decreases, which moves the non-linear to linear transition point to a lower value of ΔP. Experimental observation of the variation of β with saturation was first reported in Rassi et al. (2011). No threshold pressure was considered in that study while analyzing the results. A recent experimental study (Zhang et al., 2021) explores the variation of β and the crossover point as a function of fractional flow, $F_w = Q_w/Q$. By balancing the surface energy to create fluid meniscus to the injection energy, they developed a theory that can predict the crossover point between the two regimes they have studied. However, they have studied the crossover from the linear regime at very low pressure drop to the non-linear regime at the intermediate pressure drop, whereas our present study addresses the crossover from the non-linear regime at the intermediate pressure drop to the linear regime at high pressure drop.

4.2. Effect of α

The power α related to the pore-size distribution function defined in Equation (28) determines the shape of the distribution and tells us how the probability of having the wider pores are compared to the narrower ones. All the pore radii within the range δ are equally probable for $\alpha = 0$ whereas positive and negative values of α indicate lower or higher probability of having wider pores, respectively (**Figure 1**). As the interfacial pressures are inversely proportional to r_i (Equation 27), the local capillary barriers are larger for $\alpha > 0$ compared to $\alpha < 0$. In **Figure 4**, we plot $\log(\Delta P - P_c)$ with $\log(Q)$ for three different values of α (**Figure 4A**) 0, (**Figure 4B**) 0.5, and (**Figure 4C**) −0.5. The wetting saturation and the distribution width are kept constant here at $S_w = 0.5$ and $\delta = 0.3$, respectively. A few things are to be noticed. The non-linear regime here is highly influenced by the value of α whereas the slope in linear regime remains at ≈ 1 independent of α. The exponent β is maximum for $\alpha = 0$, and then falls to 1.46 and 1.58 at $\alpha = 0.5$ and −0.5,

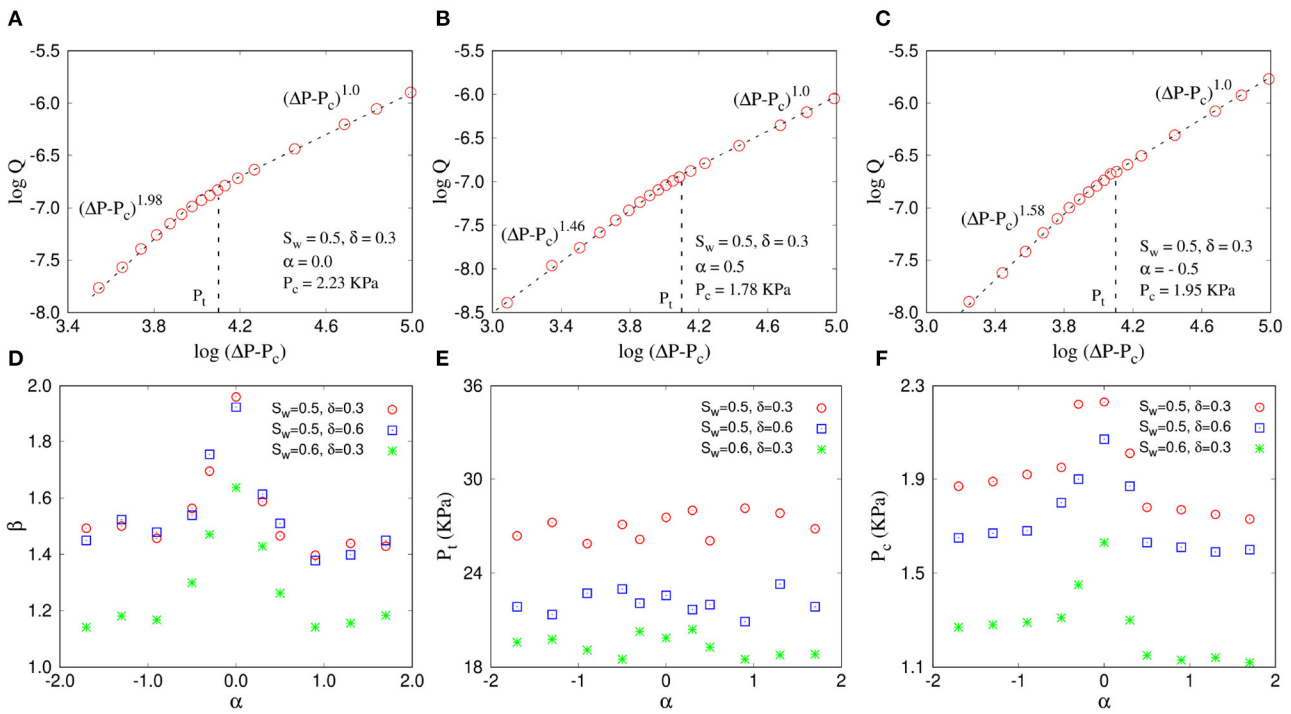

FIGURE 4 | Variation of Q (m^3/s) as a function of $\Delta P - P_c$ (Pa) for a network of 64 × 64 links and for $\alpha = 0$, $+0.5$, and -0.5 are shown in **(A–C)**, respectively. The wetting saturation $S_w = 0.5$ and the distribution width $\delta = 0.3$ here. The variations of the slopes β in the non-linear regime, the crossover pressure drop P_t (KPa) and the threshold pressure P_c (KPa) as a function of S_w are shown in **(D–F)**, respectively where β has a maximum at $\alpha = 0$ whereas P_t does not show any specific dependence on α. P_c has a maximum around $\alpha = 0$ and decreases on either side.

respectively. Moreover, the threshold pressure P_c also decreases with the increase of $|\alpha|$. The decrease in P_c for $\alpha < 0$ is intuitive, since the wider pores are in larger quantity compared to smaller pores, which will cause a less capillary barrier to start the flow. The decrease in P_c for $\alpha > 0$ is rather counter intuitive and may be related to the decrease in slope in the non-linear regime.

In **Figure 4D**, we plot β as a function of α which shows the decreasing trends of β on both sides of $\alpha = 0$ and then becomes constant after it reaches to ≈ 1.5 around $|\alpha| = 1$. This indicates that any change in the fluctuations among the link radii than the uniform distribution causes slower increase in the conductive paths when increasing the ΔP. The crossover pressure drop P_t is plotted in **Figure 4E** which shows that P_t remains constant independent of the value or sign of α. **Figure 4F** shows that P_c shows a maximum at $S_w = 0.5$ and decreases on either side. The decrease of P_c for negative α is understandable as there will more links with larger radius in this case. For positive α we have less links with large radius. P_c is still observed to decrease, most probably because of the nature of the fitting since β decreases here.

Notice that, such a variation in the non-linear exponent β while varying α was not observed in case of CFBM where β has a value of 3/2 irrespective of the radii distribution (Equation 25). This indicates that the mixing of the fluids at the nodes in a pore network has more complex effect than the flow in individual channels in CFBM. The crossover point P_t here is analogous to the maximum threshold P_M in CFBM which do not depend on α in both the models as it only depends on the span of the distribution and not on the shape. Therefore, as we will see in the next section, P_t has a strong dependence on δ, the span of the distribution.

4.3. Effect of δ

We now perform simulations by varying the width of the radii distribution give by, $\delta = r_{\max} - r_{\min} = 0.1, 0.2, 0.3, 0.5$, and 0.7, where $r_{\min}$ was kept constant at 0.1. The wetting saturation and the distribution power are kept constant here at $S_w = 0.5$ and $\alpha = 0$, respectively. The results are illustrated in **Figure 5**. Interestingly, unlike the variation of β with the distribution power α as seen before, here the slopes in the non-linear regime are almost independent of the distribution width δ and remains constant around 2.0 (**Figure 5A**). The crossover pressure drop P_t, on the other hand, decreases with increase in δ, which was almost constant when we varied the distribution power α. We also found that the global threshold pressure P_c gradually decreases with increasing δ, from $P_c \approx 2.5$KPa at $\delta = 0.1$ to ≈ 1.5KPa at $\delta = 0.7$. This is because as we increase δ, $r_{\max}$ also increases and the system contains more pores with larger pore radii. This decreases the capillary barriers and hence reduces the global threshold pressure P_c.

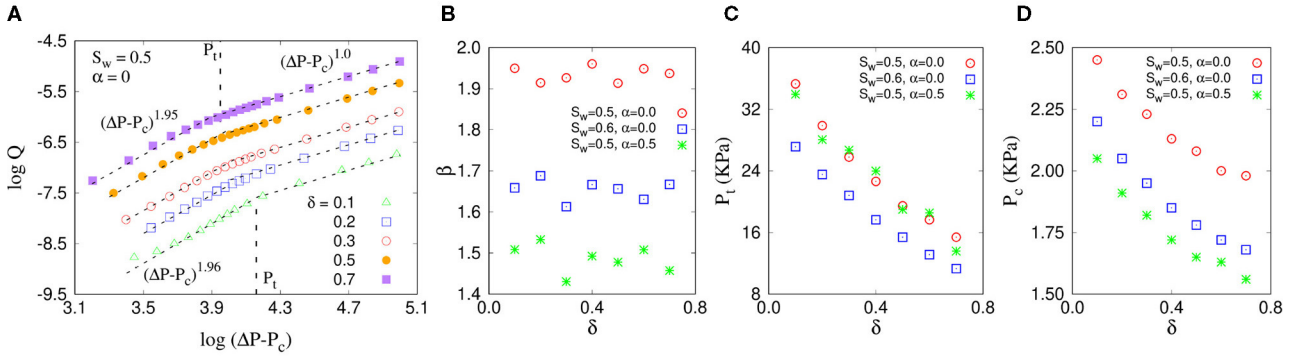

FIGURE 5 | (A) Plot of Q (m^3/s) vs. $\Delta P - P_c$ (Pa) when varying the distribution width δ where the slopes in the non-linear, as well as in the linear regimes do not show any variation with δ. In **(B–D)**, respectively, we show the variation of β, P_t (KPa) and P_c (KPa) with δ.

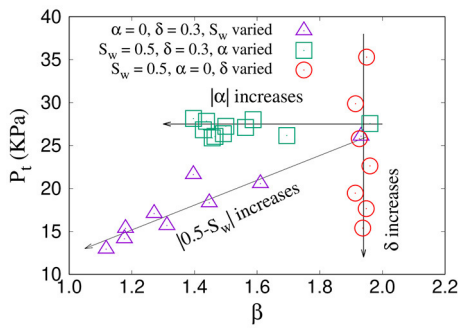

FIGURE 6 | The $P_t - \beta$ plane, which shows the effect of varying S_w, α, and δ on the rheological behavior. As S_w deviates from 0.5 (triangles), both β and P_t decreases. On the other hand, with increasing α (squares) and δ (circles), respectively, either β or P_t decreases keeping the other one constant.

4.4. The P_t vs. β Plane

To illustrate the all variations in the rheological behavior as a function of different parameters, we constructed a $P_t - \beta$ plane. This is shown in **Figure 6**. We indicate all the data points there corresponding to the three sets. The variation in the β and P_t as we increase S_w, α, and δ are indicated by arrows in the plot. They can be summarized as:

Varying α: When α is increased, β decreases keeping P_t constant, and the points moves to left along a horizontal line (green squares).

Varying δ: When δ is increased, P_t decreases keeping β constant, and the points move down along a vertical line (red circles).

Varying S_w: When S_w deviates from 0.5, both β and P_t decreases and the points move to lower values along a diagonal line (purple triangles).

5. DISCUSSION

In this article we explored how the rheological properties two-phase flow in porous media in steady state is affected by the underlying system disorder. We performed analytical calculations with a capillary bundle model and numerical simulations with dynamic pore-network model. We varied the shape and width of the distribution of the pore-radii with two distribution parameters α and δ, respectively, and studied the transition from a non-linear flow regime to a linear Darcy flow. We found that the exponent β related to the non-linearity is equal to 3/2 for the capillary bundle model and do not depend on α. For the pore-network model on the other hand, $\beta \approx 2$ for uniform distribution ($\alpha = 0$) and approaches toward 1.5 as $|\alpha|$ is increased. The width δ of the distribution affects the crossover point P_t in both the models. When δ is increased, the linear regime becomes achievable at a relatively lower pressure drop. Both β and P_t depends on the saturation S_w. As S_w deviates from 0.5, the two-phase flow moves closer to single phase flow and both β and P_t decreases simultaneously making the linear region more and more prominent. These numerical results can be explained qualitatively with the hypothesis that the total flow rate is contributed from the number of conducting paths and the flow in those paths (Roux and Herrmann, 1987), which makes it to increase faster than a linear behavior.

It is worth mentioning here that the single phase flow of Bingham fluid in porous media also shows similar non-linearity with a global yield threshold and a crossover to a linear regime (Roux and Herrmann, 1987; Talon and Bauer, 2013; Chevalier and Talon, 2015). Nash and Rees (2017) has studied Bingham fluid flow in one dimension and obtained different relations between applied pressure drop and Darcy velocity depending on the distribution of channel widths. Talon et al. (2014) have analytically explored the flow of Bingham fluid in 1d channels with aperture variation and observed different scaling between pressure drop and flow rate depending on such variation in apertures. Above studies support the fact that, when up-scaled to a certain pore-network, both Bingham flow and two-phase flow is affected by the pore-size distribution and hence the topology of the network.

The dependency of the effective rheological properties on the pore-size distribution indicates a possibility to predict the transport properties directly from the geometrical properties of the porous media. Puyguiraud et al. (2021) in a recent letter developed a model for single phase flow for the prediction of transport from knowledge of the characteristic pore length and

of the Eulerian velocity distribution. Another approach is based on the Hadwiger theorem stating that any extensive function (such as the free energy) describing the flow may be expressed in terms of the Minkowski functionals describing the geometry of the porous medium. The transport properties may then be found from the free energy (see Khanamiri et al., 2018). Roy et al. (2020) proposed a framework that connects the average seepage velocities to the distribution of local fluid velocities. This means, obtaining the velocity or flow distribution from the distribution of pores is the missing link that would allow the prediction of hydrodynamic transport from geometrical information only. For random bead packs, Coppersmith et al. (1996) showed that the variations of contact angles allow for the relation between distribution of throat radii and the distribution of the flow fractions that depart a pore body. With that, Alim et al. (2017) proposed an approach for single phase flow to predict the flow distribution from the geometrical properties of porous media that is based on Kirchhoff's law for fluid mass conservation coupled with assumptions on the distribution of coordination numbers of pore bodies. There are more studies on the local velocity distribution for single phase flow (Siena et al., 2014; Wu et al., 2016; De Anna et al., 2017; Aramideh et al., 2018; An et al., 2020; Souzy et al., 2020), but detailed study for two-phase flow are lacking. Furthermore, Alim et al. (2017) also emphasized that, in addition to the distribution of pore sizes, the local correlations between adjacent pores are necessary to predict the flow distribution. The observation in our present study, that the non-linear exponent β does not depend on the radii distribution in case of the capillary bundle with disconnected links, whereas it varies continuously with the distribution for the pore-network, also indicates the same, that the network connectivity plays a key role in the transport properties in addition to the pore-size distribution. In our present study we considered a fixed coordination number, and therefore further study is necessary to explore the role of network connectivity on the effective rheology.

DATA AVAILABILITY STATEMENT

The raw data supporting the conclusions of this article will be made available by the authors, without undue reservation.

AUTHOR CONTRIBUTIONS

SR and AH performed all the analytical derivations related to CFBM. The code for DNPM was written by SS. SR performed all numerical simulations and data analysis related to DNPM. The initial draft of the manuscript was written by SR and SS which was then updated by all the authors. All authors contributed to the article and approved the submitted version.

FUNDING

This work was partly supported by the Research Council of Norway through its Centers of Excellence funding scheme, project number 262644. SS was partially supported by the National Natural Science Foundation of China under grant number 11750110430.

REFERENCES

Aker, E., Maloy, K. J., Hansen, A., and Batrouni, G. G. (1998). A two-dimensional network simulator for two-phase flow in porous media. *Transp. Porous Med.* 32:163. doi: 10.1023/A:1006510106194

Alim, K., Parsa, S., Weitz, D. A., and Brenner, M. P. (2017). Local pore size correlations determine flow distributions in porous media. *Phys. Rev. Lett.* 119:144501. doi: 10.1103/physrevlett.119.144501

An, S., Hasan, S., Erfani, H., Babaei, M., and Niasar, V. (2020). Unravelling effects of the pore-size correlation length on the two-phase flow and solute transport properties: GPU-based pore-network modeling. *Water Resour. Res.* 56:e2020WR027403. doi: 10.1029/2020WR027403

Aramideh, S., Vlachos, P. P., and Ardekani, A. M. (2018). Pore-scale statistics of flow and transport through porous media. *Phys. Rev. E* 98:013104. doi: 10.1103/PhysRevE.98.013104

Batrouni, G. G., and Hansen, A. (1988). Fourier acceleration of iterative processes in disordered systems. *J. Stat. Phys.* 52:747. doi: 10.1007/BF01019728

Bear, J. (1988). *Dynamics of Fluids in Porous Media*. Mineola, NY: Dover.

Chen, J. D., and Wilkinson, D. (1985). Pore-scale viscous fingering in porous media. *Phys. Rev. Lett.* 55:1892. doi: 10.1103/PhysRevLett.55.1892

Chevalier, T., Salin, D., Talon, L., and Yiotis, A. G. (2015). History effects on nonwetting fluid residuals during desaturation flow through disorderedporous media. *Phys. Rev. E* 91:043015. doi: 10.1103/PhysRevE.91.043015

Chevalier, T., and Talon, L. (2015). Generalization of Darcys law for Bingham fluids in porous media: from flow-field statistics to the flow-rate regimes. *Phys. Rev. E* 91:023011. doi: 10.1103/PhysRevE.91.023011

Coppersmith, S. N., Liu, C. -H., Majumdar, S., Narayan, O., and Witten, T. A. (1996). Model for force fluctuations in bead packs. *Phys. Rev. E* 53:4673. doi: 10.1103/physreve.53.4673

Darcy, H. (1856). *Les Fontaines Publiques de la Ville de Dijon*. Paris: Victor Dalamont.

De Anna, P., Quaife, B., Biros, G., and Juanes, R. (2017). Prediction of the low-velocity distribution from the pore structure in simple porous media. *Phys. Rev. Fluids* 2:124103. doi: 10.1103/PhysRevFluids.2.124103

Dullien, F. A. L. (1992). *Porous media: Fluid, transport and pore structure*. San Diego, CA: Academic Press.

Gao, Y., Lin, Q., Bijeljic, B., and Blunt, M. J. (2020). Pore-scale dynamics and the multiphase Darcy law. *Phys. Rev. Fluids* 5:013801. doi: 10.1103/PhysRevFluids.5.013801

Gunstensen, A. K., Rothman D. H., Zaleski S., and Zanetti G. (1991). Lattice Boltzmann model of immiscible fluids. *Phys. Rev. A* 43:4320. doi: 10.1103/PhysRevA.43.4320

Hansen, A., Hemmer, P. C., and Pradhan, S. (2015). *The Fiber Bundle Model: Modeling Failure in Materials*. Berlin: Wiley.

Joekar-Niasar, V., and Hassanizadeh S. M. (2012). Analysis of fundamentals of two-phase flow in porous media using dynamic pore-network models: a review. *Crit. Rev. Environ. Sci. Technol.* 42:1895. doi: 10.1080/10643389.2011.574101

Khanamiri, H. H., Berg, C. F., Slotte, P. A., Schlüter, S., and Torsaeter, O. (2018). Description of free energy for immiscible two-fluid flow in porous media by integral geometry and thermodynamics. *Water Resour. Res.* 54, 9045–9059. doi: 10.1029/2018WR023619

Kirkpatrick, S. (1973). Percolation and conduction. *Rev. Mod. Phys.* 45:574. doi: 10.1103/RevModPhys.45.574

Langglois, W. E. (1964). *Slow Viscous Flow*. New York, NY: The Macmillan Company.

Lenormand, R., Touboul, E., and Zarcone, C. (1988). Numerical models and experiments on immiscible displacements in porous media. *J. Fluid Mech.* 189:165. doi: 10.1017/S0022112088000953

Lenormand, R., and Zarcone, C. (1985). Invasion percolation in an etched network: measurement of a fractal dimension. *Phys. Rev. Lett.* 54:2226. doi: 10.1103/PhysRevLett.54.2226

Måløy, K. J., Feder, J., and Jøssang, T. (1985). Viscous fingering fractals in porous media. *Phys. Rev. Lett.* 55:2688. doi: 10.1103/PhysRevLett.55.2688

Nash, S., and Rees, D. A. S. (2017). The effect of microstructure on models for the flow of a Bingham fluid in Porous media: one-dimensional flows. *Transp. Porous Med.* 116:1073. doi: 10.1007/s11242-016-0813-9

Puyguiraud, A., Gouze, P., and Dentz, M. (2021). Pore-scale mixing and the evolution of hydrodynamic dispersion in porous media. *Phys. Rev. Lett.* 126:164501. doi: 10.1103/PhysRevLett.126.164501

Rassi, E. M., Codd, S. L., and Seymour, J. D. (2011). Nuclear magnetic resonance characterization of the stationary dynamics of partially saturated media during steady-state infiltration flow. *New J. Phys.* 13:015007. doi: 10.1088/1367-2630/13/1/015007

Roux, S., and Herrmann, H. J. (1987). Disorder-induced nonlinear conductivity. *Europhys. Lett.* 4:1227. doi: 10.1209/0295-5075/4/11/003

Roy, R., Sinha, S., and Hansen, H. (2020). Flow-area relations in immiscible two-phase flow in porous media. *Front. Phys.* 8:4. doi: 10.3389/fphy.2020.00004

Roy, S., Hansen, A., and Sinha, S. (2019). Effective rheology of two-phase flow in a capillary fiber bundle model. *Front. Phys.* 7:92. doi: 10.3389/fphy.2019.00092

Scheidegger, A. E. (1953). Theoretical models of porous matter. *Producers Monthly* 17:17.

Scheidegger, A. E. (1974). *The Physics of Flow Through Porous Media*. Toronto, ON: University of Toronto Press.

Siena, M., Riva, M., Hyman, J. D., Winter, C. L., and Guadagnini, A. (2014). Relationship between pore size and velocity probability distributions in stochastically generated porous media. *Phys. Rev. E* 89:013018. doi: 10.1103/PhysRevE.89.013018

Sinha, S., Bender, A. T., Danczyk, M., Keepseagle, K., Prather, C. A., Bray, J. M., et al. (2017). Effective rheology of two-phase flow in three-dimensional porous media: experiment and simulation. *Transp. Porous Med.* 119:77. doi: 10.1007/s11242-017-0874-4

Sinha, S., Gjennestad, M. Aa., Vassvik, M., and Hansen, A. (2021). Fluid meniscus algorithms for dynamic pore-network modeling of immiscible two-phase flow in porous media. *Front. Phys.* 8:548497. doi: 10.3389/fphy.2020.548497

Sinha, S., and Hansen, A. (2012). Effective rheology of immiscible two-phase flow in porous media. *Europhys. Lett.* 99:44004. doi: 10.1209/0295-5075/99/44004

Sinha, S., Hansen, A., Bedeaux, D., and Kjelstrup, S. (2013). Effective rheology of bubbles moving in a capillary tube. *Phys. Rev. E* 87:025001. doi: 10.1103/PhysRevE.87.025001

Souzy, M., Lhuissier, H., Meheust, Y., Le Borgne, T. and Metzger, B. (2020). Velocity distributions, dispersion and stretching in three-dimensional porous media. *J. Fluid Mech.* 891:A16. doi: 10.1017/jfm.2020.113

Tallakstad, K. T., Knudsen, H. A., Ramstad, T., Løvoll, G., Måløy, K. J., Toussaint, R., et al. (2009a). Steady-state two-phase flow in porous media: statistics and transport properties. *Phys. Rev. Lett.* 102:074502. doi: 10.1103/PhysRevLett.102.074502

Tallakstad, K. T., Løvoll, G., Knudsen, H. A., Ramstad, T., Flekkøy, E. G., and Måløy, K. J. (2009b) Steady-state, simultaneous two-phase flow in porous media: an experimental study. *Phys. Rev. E* 80:036308. doi: 10.1103/PhysRevE.80.036308

Talon, L., Auradou, H., and Hansen, A. (2014). Effective rheology of Bingham fluids in a rough channel. *Front. Phys.* 2:24. doi: 10.3389/fphy.2014.00024

Talon, L., and Bauer, D. (2013). On the determination of a generalized Darcy equation for yield-stress fluid in porous media using a lattice-Boltzmann TRT scheme. *Eur. Phys. J. E* 36:139. doi: 10.1140/epje/i2013-13139-3

Valavanides, M. (2018). Review of steady-state two-phase flow in porous media: independent variables, universal energy efficiency map, critical flow conditions, effective characterization of flow and pore network. *Transp. Porous Med.* 123:45. doi: 10.1007/s11242-018-1026-1

Washburn, E. W. (1921). The dynamics of capillary flow. *Phys. Rev.* 17:273. doi: 10.1103/PhysRev.17.273

Whitaker, S. (1986). Flow in porous media I: a theoretical derivation of Darcy's law. *Transp. Porous Med.* 1:3. doi: 10.1007/BF01036523

Wilkinson, D., and Willemsen, J. F. (1983). Invasion percolation: a new form of percolation theory. *J. Phys. A* 16:3365. doi: 10.1088/0305-4470/16/14/028

Witten, T. A. Jr., and Sander, L. M. (1981). Diffusion-limited aggregation, a kinetic critical phenomenon, *Phys. Rev. E* 47:1400. doi: 10.1103/PhysRevLett.47.1400

Wu, A., Liu, C., Yin, S., Xue, Z., and Chen, X. (2016). Pore structure and liquid flow velocity distribution in water-saturated porous media probed by MRI. *Trans. Nonferrous Met. Soc. China* 26:1403. doi: 10.1016/S1003-6326(16)64208-5

Yiotis, A. G., Talon, L., and Salin, D. (2013). Blob population dynamics during immiscible two-phase flows in reconstructed porous media. *Phys. Rev. E* 87:033001. doi: 10.1103/PhysRevE.87.033001

Zhang, Y., Bijeljic, B., Gao, Y., Lin, Q., and Blunt, M. J. (2021). Quantification of non-linear multiphase flow in porous media. *Geophys. Res. Lett.* 48:e2020GL090477. doi: 10.1029/2020GL090477

Zhao, B., MacMinn, C. W., Primkulov, B. K., Chen, Y., Valocchi, A. J., Zhao, J., et al. (2019). Comprehensive comparison of pore-scale models for multiphase flow in porous media. *Proc. Natl. Acad. Sci. U.S.A.* 116:13799. doi: 10.1073/pnas.1901619116

Conflict of Interest: The authors declare that the research was conducted in the absence of any commercial or financial relationships that could be construed as a potential conflict of interest.

Publisher's Note: All claims expressed in this article are solely those of the authors and do not necessarily represent those of their affiliated organizations, or those of the publisher, the editors and the reviewers. Any product that may be evaluated in this article, or claim that may be made by its manufacturer, is not guaranteed or endorsed by the publisher.

frontiers in Water

ORIGINAL RESEARCH
published: 16 August 2021
doi: 10.3389/frwa.2021.710370

Pore-Scale Dynamics of Liquid CO_2–Water Displacement in 2D Axisymmetric Porous Micromodels Under Strong Drainage and Weak Imbibition Conditions: High-Speed μPIV Measurements

Yaofa Li[1], Gianluca Blois[2], Farzan Kazemifar[3], Razin S. Molla[1] and Kenneth T. Christensen[2,4]*

[1] Department of Mechanical & Industrial Engineering, Montana State University, Bozeman, MT, United States, [2] Department of Aerospace and Mechanical Engineering, University of Notre Dame, Notre Dame, IN, United States, [3] Department of Mechanical Engineering, San Jose State University, San Jose, CA, United States, [4] Departments of Mechanical, Materials and Aerospace Engineering, Civil, Architectural and Environmental Engineering, Illinois Institute of Technology, Chicago, IL, United States

OPEN ACCESS

Edited by:
James E. McClure, Virginia Tech, United States

Reviewed by:
Apostolos Kantzas, University of Calgary, Canada
Holger Steeb, University of Stuttgart, Germany

****Correspondence:***
Yaofa Li
yaofa.li@montana.edu

Specialty section:
This article was submitted to Water and Critical Zone, a section of the journal Frontiers in Water

Received: *16 May 2021*
Accepted: *22 July 2021*
Published: *16 August 2021*

Citation:
Li Y, Blois G, Kazemifar F, Molla RS and Christensen KT (2021) Pore-Scale Dynamics of Liquid CO_2–Water Displacement in 2D Axisymmetric Porous Micromodels Under Strong Drainage and Weak Imbibition Conditions: High-Speed μPIV Measurements. Front. Water 3:710370. doi: 10.3389/frwa.2021.710370

Resolving pore-scale transient flow dynamics is crucial to understanding the physics underlying multiphase flow in porous media and informing large-scale predictive models. Surface properties of the porous matrix play an important role in controlling such physics, yet interfacial mechanisms remain poorly understood, in part due to a lack of direct observations. This study reports on an experimental investigation of the pore-scale flow dynamics of liquid CO_2 and water in two-dimensional (2D) circular porous micromodels with different surface characteristics employing high-speed microscopic particle image velocimetry (μPIV). The design of the micromodel minimized side boundary effects due to the limited size of the domain. The high-speed μPIV technique resolved the spatial and temporal dynamics of multiphase flow of CO_2 and water under reservoir-relevant conditions, for both drainage and imbibition scenarios. When CO_2 displaced water in a hydrophilic micromodel (i.e., drainage), unstable capillary fingering occurred and the pore flow was dominated by successive pore-scale burst events (i.e., Haines jumps). When the same experiment was repeated in a nearly neutral wetting micromodel (i.e., weak imbibition), flow instability and fluctuations were virtually eliminated, leading to a more compact displacement pattern. Energy balance analysis indicates that the conversion efficiency between surface energy and external work is less than 30%, and that kinetic energy is a disproportionately smaller contributor to the energy budget. This is true even during a Haines jump event, which induces velocities typically two orders of magnitude higher than the bulk velocity. These novel measurements further enabled direct observations of the meniscus displacement, revealing a significant alteration of the pore filling mechanisms during drainage and imbibition. While the former typically featured burst events, which often occur only at one of the several throats connecting a pore, the latter is typically dominated by a cooperative filling mechanism involving

simultaneous invasion of a pore from multiple throats. This cooperative filling mechanism leads to merging of two interfaces and releases surface energy, causing instantaneous high-speed events that are similar, yet fundamentally different from, burst events. Finally, pore-scale velocity fields were statistically analyzed to provide a quantitative measure of the role of capillary effects in these pore flows.

Keywords: porous media, pore scale, micromodel, multiphase flow, particle image velocimetry, drainage, imbibition, wettability

1. INTRODUCTION

Multiphase flow in porous media is ubiquitous in natural systems as well as engineering applications, such as enhanced oil recovery (EOR) (Simjoo et al., 2013), ground water remediation (Dawson and Roberts, 1997), water management in fuel cells (Bazylak, 2009) and carbon capture and storage (CCS) (Huppert and Neufeld, 2014). Notably, the sequestration of carbon dioxide (CO_2) in deep saline aquifers is considered to be a viable technology to reduce carbon emissions into the atmosphere as a means of mitigating green house effect (Koide et al., 1992; Gunter et al., 1997; Bachu, 2000; Pacala and Socolow, 2004; Huppert and Neufeld, 2014). Under typical reservoir conditions (i.e., 2–28 MPa and 20 °C to 100 °C Xu et al., 2015), the injection of CO_2 into saline aquifers often leads to complex and unstable displacement patterns both during and after injection due to the large density and viscosity contrasts between CO_2 and resident brine (Kazemifar and Kyritsis, 2014). These complex processes are crucial to CO_2 injection efficiency as well as storage safety and security, which are key aspects of carbon sequestration planning and operation. It is therefore critical to understand the fundamental mechanisms of immiscible multiphase flow interactions of CO_2 and water in porous media, specifically under reservoir-relevant conditions.

In practical applications, it is desirable to model and predict multiphase flow and transport at the macro/continuum scale (e.g., field) in order to improve system-level performance. However, macroscopic phenomena are governed collectively by various processes at the pore scale, where fundamental flow and transport take place (Sheng and Thompson, 2013; Moebius and Or, 2014; Mehmani and Balhoff, 2015). For instance, a recent study by Ferrari and Lunati (2014) suggested that local instability-induced oscillations of the menisci between the CO_2 and water phases can modify the constitutive relationships adopted in macroscale models, and that pore-scale phenomena should be incorporated in upscaling applications. Therefore, an accurate continuum description of these processes always requires a rigorous understanding of the underlying pore-scale physics (Sheng and Thompson, 2013; Moebius and Or, 2014; Mehmani and Balhoff, 2015).

Over the last few decades, the study of multiphase flow in porous media, specifically at the pore-scale, has received growing attention across the experimental, numerical, and theoretical paradigms. Traditional experimental techniques include the use of x-ray micro-computed tomography (micro-CT) and magnetic resonance imaging (MRI) for visualization of flow patterns in complex 3D geometries (Perrin and Benson, 2010; Song et al., 2013). Direct flow visualization and quantification in specially-designed microfluidic channels incorporating 2D porous structures, hereafter micromodels, have also been accomplished using fluorescent microscopy and microscopic particle-image velocimetry (μPIV) (Lenormand et al., 1988; Zhang et al., 2011a,b; Armstrong and Berg, 2013; Karadimitriou et al., 2014; Blois et al., 2015; Kazemifar et al., 2015, 2016; Roman et al., 2016; Li et al., 2017, 2019). The optical access afforded by micromodels has enabled the application of scientific cameras which overcome the low spatial and temporal resolution limitations typically suffered by the aforementioned 3D approaches. The experimental data generated via micromodel measurements not only allow direct observation of the complex flow dynamics at the pore scale, but also provide a basis to validate numerical and theoretical models with high spatial and temporal resolution. Although extreme care must be taken when extrapolating 2D micromodel results to realistic 3D systems, micromodel experiments have played an important role in visualizing and quantifying pore-scale processes as a means to clarify the underlying flow physics of pore-scale flows in porous media.

Our current understanding of the pore-scale mechanisms of multiphase flow in porous media is based on the notion of two dimensionless numbers: the capillary number, Ca, and the viscosity ratio, M defined as follows Lenormand et al. (1988):

$$Ca = \mu_2 U_{\text{bulk}}/\gamma \tag{1}$$

$$M = \mu_2/\mu_1 \tag{2}$$

Here, μ is the dynamic viscosity, γ is the interfacial tension between the two fluids, and U_{bulk} is the bulk velocity, $U_{\text{bulk}} = Q/(A\varphi)$, where Q is the volumetric flow rate, A is the cross-sectional area of the porous media, and φ is the porosity of the porous media. Indices 1 and 2 refer to the resident and invading phases, respectively (Kazemifar et al., 2016). The capillary number defines the ratio between viscous and capillary forces whereas the viscosity ratio defines the ratio between the dynamic viscosity of the invading fluid and that of the resident fluid. Depending on the balance of viscous and capillary forces, three distinct flow regimes exist: (*i*) stable displacement; (*ii*) viscous fingering; and (*iii*) capillary fingering. These regimes are associated with complex displacement patterns that depend on pore-scale dynamics. For example, during fingering

dominated by capillary forces, the menisci are susceptible to strong instabilities. This behavior can lead to pore-scale burst events, so-called Haines jumps (Haines, 1930), which occur at the time scale of milliseconds and can appreciably affect regions of flow in the domain of up to 30 pore diameters (Armstrong and Berg, 2013; Li et al., 2017). Recent studies have highlighted that these events can greatly accelerate the flow near the fluid–fluid interfaces and render inertial effects as or more important than viscous and capillary ones (Li et al., 2017, 2019). This behavior is quantified by the Reynolds number, $Re = \rho UD/\mu$, which represents the ratio of inertial forces to viscous forces (Here, U is a characteristic velocity and D is a characteristic length scale). Dynamic Haines-jump events yield increases in Re by orders of magnitude to $\mathcal{O}(100)$, indicating that inertial effects may be significant to CO_2 mobility. The intensity and spatiotemporal range of influence of these events illustrate the importance of appropriately defining the elemental volume over which the effects of non-linear (i.e., inertial) mechanisms should be incorporated in subgrid models (Ferrari and Lunati, 2014; Kazemifar et al., 2016).

Despite the progress made by recent work to elucidate the interface dynamics of these flow systems, many fundamental questions remain unanswered. One relevant question concerns the nature of high-speed burst events (hereinafter used interchangeably with the term Haines jumps). The temporal and spatial characteristics of these events have not been experimentally investigated in detail in a quantitative fashion, in part due to their extremely fast dynamics (i.e., a few milliseconds), and in part due to the technical challenges associated with faithfully capturing such events with sufficient temporal and spatial resolution. Armstrong et al. (2014) performed real-time 3D imaging of Haines jumps in a porous medium using a high-speed, synchrotron-based micro-CT with a temporal resolution of 40 ms, which was believed to be sufficient to temporally resolve the burst events. However, this time was much longer than the sub-10 ms time scale suggested by acoustic measurements and optical visualization using a high-speed camera (DiCarlo et al., 2003; Armstrong and Berg, 2013). Moreover, burst events, traditionally referred to as single-pore events (i.e., tens of micrometers in scale), have been recently shown to directly influence much larger regions of the porous media up to a few millimeters (Armstrong and Berg, 2013; Li et al., 2017). These more recent observations highlight the need to revisit the assumptions traditionally made when modeling these highly dynamic systems. Our previous efforts using high-resolution μPIV allowed random capturing of burst events in rectangular micromodels at a single evolutionary stage (Li et al., 2017). However, due to the relatively low imaging rate of the cameras utilized in this past study, it was not possible to record the evolution of these burst events over time which limited our ability to fully elucidate their dynamics.

Another critical parameter in immiscible multiphase flows concerns the surface property of the porous matrix, often defined in terms of wettability. This parameter is extremely difficult to control experimentally and model numerically and poses a further layer of complexity in the study of these dynamic systems (Zhao et al., 2016; Hu et al., 2017). The wettability refers to the "affinity" of a solid surface for one fluid in the presence of one or more other immiscible fluids, and it is often characterized by the contact angle, θ. Fluid–fluid displacement in porous media is classified into drainage and imbibition. Drainage refers to the scenario where the invading fluid is less wetting to the solid surface than the resident fluid (i.e., a non-wetting phase displacing a wetting phase), whereas imbibition refers to the opposite scenario. In practical applications where CO_2 is injected into geological reservoirs (e.g., CCS and EOR), a wide range of wettability conditions can be encountered (Chang et al., 2020). For instance, while deep saline aquifers are typically water-wet to CO_2 injections, depleted hydrocarbon reservoirs can be intermediate-wet or mixed-wet (Salathiel, 1973; Anderson, 1987). Moreover, these conditions may even change over time due to rock reactions modifying surface properties of the porous matrix (Broseta et al., 2012; Seyyedi et al., 2015; Wang and Tokunaga, 2015). Wettability is important as it is well known to dramatically impact the efficiency of the displacement process (Morrow, 1990; Iglauer et al., 2012) and therefore affect the efficiency of oil recovery in EOR and the CO_2 storage capacity in CCS.

From a pore scale perspective, wettability governs the capillary force and directly impacts the interface stability and displacement efficiency (Holtzman and Segre, 2015). A majority of previous studies considering wettability effects on flow behavior in porous media reported that increasing contact angle of the resident wetting phase stabilizes the displacement interface under various flow conditions, leading to more compact displacement patterns and thus increasing the displacement efficiency (Cottin et al., 2011; Holtzman and Segre, 2015; Trojer et al., 2015). Holtzman and Segre (2015) employed a pore-scale model to capture wettability and dynamic effects and showed that increasing the wettability of the invading fluid promotes cooperative pore filling that stabilizes the invasion. Hu et al. (2017) used a high-pressure micromodel-microscopy system to study supercritical CO_2 ($scCO_2$) invasion into brine-saturated water-wet and intermediate-wet micromodels, and observed a smaller number of fingers with larger finger width under intermediate-wet conditions. Zhao et al. (2016) performed a more comprehensive investigation of wettability effects by systematically varying the wettability of the porous flow cell over a wide range of contact angles. They found that increasing the solid matrix affinity to the invading fluid results in more efficient displacement of the resident fluid up to a critical wetting transition, beyond which the trend is reversed. This behavior was attributed to two pore-scale mechanisms: cooperative pore filling (increasing displacement efficiency) and corner flow (decreasing displacement efficiency). These studies have greatly advanced our understanding of pore scale mechanisms controlled by wettability. However, to the best of our knowledge, most, if not all, of the experimental work has been restricted to qualitative visualizations of the interface movement, with little to no quantification of the flow distribution and quantitative reconstruction of the interface dynamics. This missing information limits one's ability to further characterize certain important aspects of pore flow and wettability effects. For instance, without detailed fluid velocity information, it is not possible to perform accurate energy balance analysis (i.e., kinetic energy), or to assess the relative importance of various forces

in the flow (i.e., viscous vs. capillary vs. inertial forces). In that regard, precise wettability control of the solid matrix provides a great opportunity to control the capillary force. For example, by fine-tuning the solid matrix to be neutrally wetting (i.e., $\theta \sim 90^\circ$) to both fluids, it is possible to eliminate the capillary force, whose effect can then be quantitatively evaluated by performing a simple comparison between a neutrally wetting case and a non-neutrally wetting case under otherwise identical conditions.

Additionally, it has been shown that energy balance analyses are particularly insightful in understanding the parameters affecting flow regimes, capillary filling rules and hysteresis (Liu et al., 2011; Berg et al., 2013; Zacharoudiou et al., 2017; Hu et al., 2018). Energy balance analysis is generally performed by breaking down the different energy contributions at each stage of an evolving phenomenon together with computing the total energy. This allows one to track energy fluxes from one component to the other as well as energy dissipation. In addition, the approach may allow one to identify whether a specific component may be disproportionately contributing to dissipation. An important conclusion made by previous studies is that surface energy and external work can only be partially converted to each other or to kinetic energy, with a majority of the energy being dissipated due to the irreversible and non-equilibrium redistribution of the fluids (Morrow, 1970; Ferrari and Lunati, 2014; Zacharoudiou et al., 2017). For example, Berg et al. (2013) performed an energy analysis based on their 3D micro-CT data, and discovered that Haines jumps, typically cascading through 10–20 geometrically defined pores per event, account for 64% of the energy dissipation. Hu et al. (2018) analyzed various energy contributions and conversions in a multiphase flow within a rough fracture and found a fundamental link between regime transition and energy conversion. In the capillary regime, surface energy is partially transformed into external work and about 51–58% is dissipated *via* local rapid, irreversible events, whereas in the capillary-viscous regime, surface energy and external work are partially transformed into kinetic energy and partially dissipated. Unfortunately, despite the importance of energy analysis, little has been done to experimentally quantify the contributions of various forms of energy, especially kinetic energy. For instance, in the energy analysis by Hu et al. (2018), an assumption had to be made to neglect kinetic energy changes during a Haines jump for this analysis, whereas in the work by Berg et al. (2013), it is not clear how kinetic energy or energy dissipation was evaluated. While it is possible to estimate surface energy and external work based on flow visualizations and bulk pressure measurements, it is particularly challenging to quantify the kinetic energy contribution, which requires a comprehensive knowledge of the instantaneous fluid velocity fields.

To this end, the dynamic interactions of water and CO_2 at the pore scale were captured and quantified using high-speed μPIV in 2D circular micromodels meant to mitigate side-wall effects. Particular effort was placed on mimicking realistic conditions. The high-speed μPIV measurements were achieved with the aid of an epi-fluorescence microscope, a high-speed laser and a high-speed camera, allowing for the acquisition of temporally- and spatially-resolved data, which is indispensable to advance our understanding of the flow dynamics at the pore-scale characterized by highly intermittent behaviors as well as to gain further insight into the effects of wettability. The overarching goals of the study include: investigating the transient behavior of Haines jumps to understand how they control the surrounding flow under strong drainage conditions, and evaluating the effect of wettability and capillarity on the pore-scale flow by comparing the former case with a case featuring nearly neutral wettability.

2. MATERIALS AND METHODS

This section provides a brief overview of the experimental methodology, schematically illustrated in **Figure 1**, including the design and fabrication of the micromodels, a description of the high-pressure flow apparatus and an overview of the flow imaging setup and image processing procedures.

2.1. Micromodels

Circular micromodels (see **Figure 1C**) were used in this study as they significantly mitigate side boundary effects which are inevitably present in rectangular micromodels (Fakhari et al., 2018). Each micromodel consisted of a heterogeneous porous region, an inlet, and an outlet, as shown in **Figures 1B,C**. The micromodels were fabricated from silicon and glass using microfabrication techniques (Chomsurin and Werth, 2003; Kazemifar et al., 2015; Ilin et al., 2020), with the porous matrix formed with irregularly patterned 2D poly-disperse cylinders mimicking a natural porous medium, inspired by a previous study (Zhao et al., 2016). The porous pattern was based on an irregular mesh created using the pdemesh tool in MATLAB. The entire porous section had dimensions of $(D, h) = (10, 0.030)$ mm and a porosity of $\varphi = 0.44$. The average equivalent pore diameter was 102 μm and the minimum throat size was 10 μm, yielding an absolute permeability of 624 md based on single-phase flow measurement and Darcy's law for radial flow. A fabrication protocol involving, in sequence, standard photolithography, inductively coupled plasma-deep reactive ion etching (ICP-DRIE) and Piranah cleaning was used to create the heterogeneous structures in the silicon wafer with a nominal depth of 30 μm. It is worth noting that, unlike glass, silicon is naturally hydrophobic, making the Piranah cleaning a critical step in order to render the silicon surface as hydrophilic as the glass wafer, to which the silicon wafer was bonded to form a closed micromodel. Finally, two nanoports (IDEX Health & Science) were attached to the micromodel for fluid delivery (Kazemifar et al., 2015).

The fabrication protocol described above yielded baseline hydrophilic micromodels for drainage experiments. For these micromodels, the static contact angle of water on both surfaces was measured to be $\sim 9 \pm 1^\circ$ using CO_2 as the non-wetting phase under actual experimental conditions. Starting from the baseline hydrophilic micromodels, the wettability was modified by the method of silanization (Trojer et al., 2015; Hu et al., 2017). To this end, both silicon and glass wafers were immersed in a saline solution (2% Dichlorodimethylsilane in hexane) for 20 min and baked at 110 °C for 10 min prior to adhesive bonding. The static contact angle of water on the modified surfaces was measured to be $\sim 120^\circ$. It is

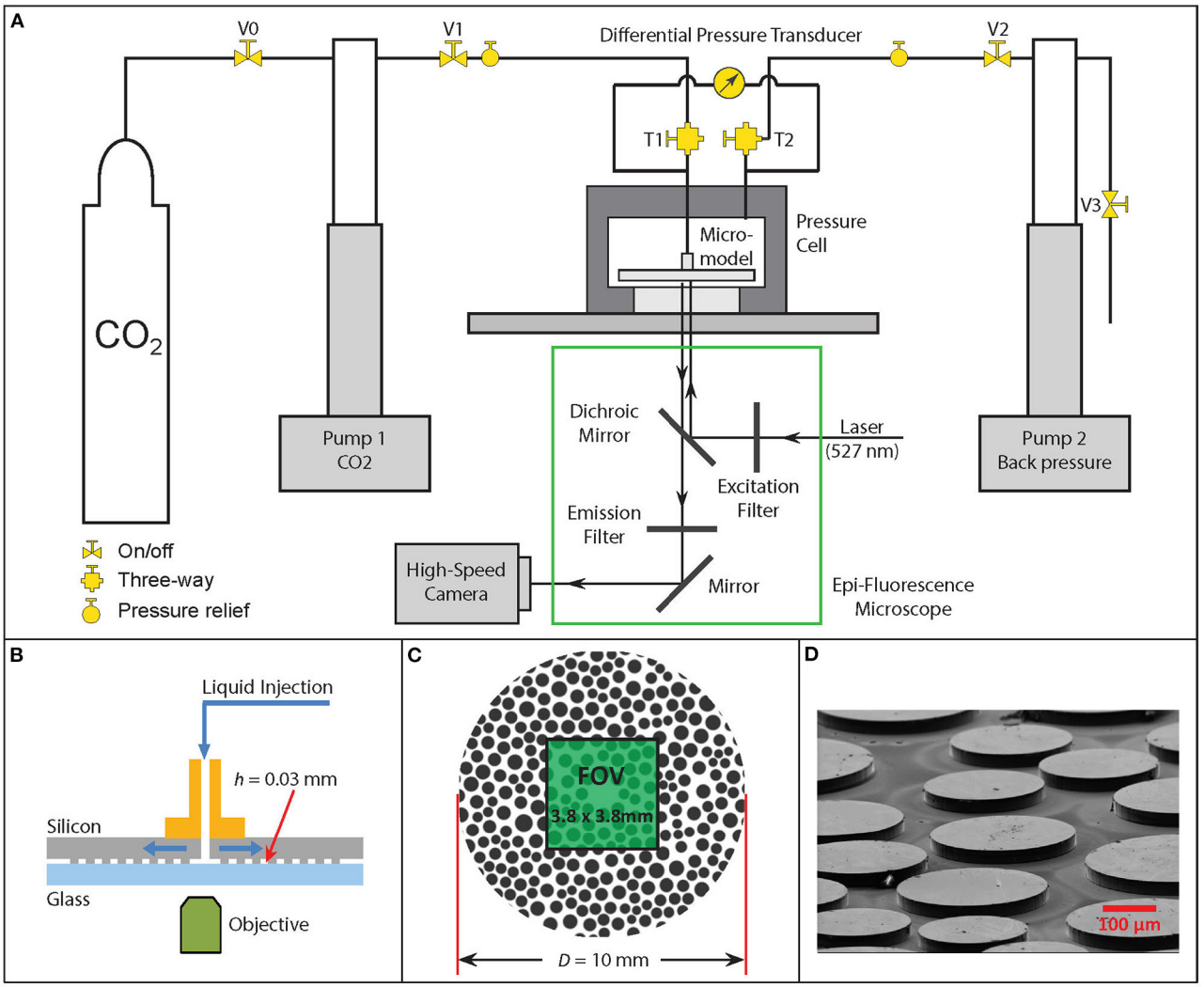

FIGURE 1 | Schematic diagrams depicting **(A)** the experimental apparatus; **(B)** the micromodel in side view showing the flow configuration; and **(C)** the micromodel in top view showing the 2D porous matrix and the imaging field of view (FOV), noted in green; **(D)** an SEM image of part of the porous section within the micromodel.

worth noting that during dynamic flow processes, what is most relevant is the dynamic contact angle (Sedev et al., 1993; Jafari and Jung, 2017). **Figure 2** presents *in-situ* measurements of the contact angles under dynamic flow conditions in a baseline hydrophilic micromodel (**Figure 2A**), and a modified hydrophobic micromodel (**Figure 2B**), confirming that the receding contact angles are $\sim 9^\circ$ and $\sim 98^\circ$ for the former and latter cases, respectively. As mentioned before, the second case was deliberately designed to have a contact angle that is as close as possible to $\sim 90^\circ$ (i.e., neutral wetting), in order to minimize capillary forces in the multiphase flow within such a micromodel.

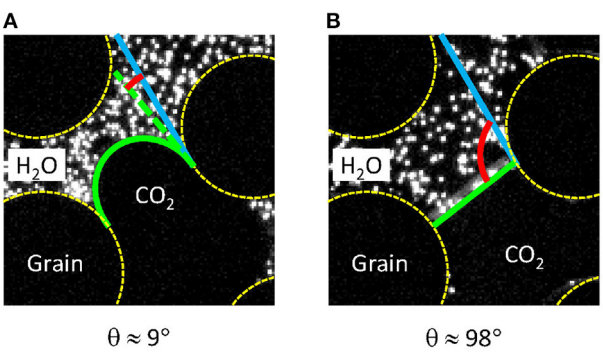

FIGURE 2 | Measurements of receding contact angles of water within a new hydrophilic micromodel **(A)**, and a newly modified micromodel for wettability alteration **(B)** under dynamic flow conditions at 8 MPa, 21 °C. The green and blue lines delineate the fluid–fluid interfaces and the tangent lines of the solid grain, respectively.

2.2. Flow Apparatus and Experimental Procedure

The working fluids used in this study were distilled water and liquid CO_2, which was achieved by maintaining flow conditions at 8 MPa, 21 °C. The physical properties of the working fluids

are reported in **Table 1**. Note that, while the experimental pressure was above the critical pressure of CO_2, the experimental temperature was below its critical temperature. As such, the CO_2 phase herein was therefore in a compressed liquid state (Kazemifar and Kyritsis, 2014). To facilitate μPIV measurement in the water phase, the distilled water was seeded with fluorescent polystyrene particles of 1 μm in diameter (Invitrogen F8819), at a nominal volume fraction of 3×10^{-4}. The volume fraction of the solid particles is low so as to not appreciably change the water properties and their density matched that of water so as to behave in a neutrally buoyant manner. It is also worth noting that tracer particles were only seeded in the water phase. Seeding the CO_2 phase under these operating conditions is extremely challenging owing to its compressibility which makes it impossible to find tracer particles that would consistently behave in a neutrally buoyant manner throughout an experiment. As such, only the water-phase velocity fields were captured by μPIV.

Due to the relatively high operating pressures, the micromodel was encapsulated within an overburden pressure cell designed to protect the micromodel from over-pressurization while still providing optical access (Kazemifar et al., 2015, 2016). The layout of the high-pressure flow apparatus is shown in **Figure 1A**. A brief description of this system, which is slightly modified from our previous work (Kazemifar et al., 2015, 2016; Li et al., 2017, 2019, 2021; Chen et al., 2018; Fakhari et al., 2018), is provided here. For additional technical details on each of the components illustrated in **Figure 1A** the reader is kindly referred to our previous studies (Kazemifar et al., 2015, 2016; Li et al., 2017, 2019, 2021; Chen et al., 2018; Fakhari et al., 2018). As shown schematically in **Figure 1A**, the coupled flow of water and CO_2 through the micromodel was controlled by two high-pressure syringe pumps (Teledyne Isco 100 DM). Pump 1 was used to push the CO_2 into the micromodel through the inlet, while pump 2 was used to withdraw the resident water from the outlet as well as to maintain the back pressure. Prior to each experiment, the CO_2 in Pump 1 was pressurized to 8 MPa and allowed to equilibrate at room temperature for over 2 h. Meanwhile, the micromodel was mounted in the overburden pressure cell with the micromodel center port connected to the pressure cell center port. The pressure cell was then filled with distilled water under ambient conditions. As the outer edge of the micromodel is open, it was partially pre-saturated with distilled water during the pressure cell filling operation. Additionally, $\sim$ 1 mL distilled water seeded with fluorescent tracer particles was injected into the center port of the pressure cell and temporally stored therein. The center and the side ports of the pressure cell were then connected to Pump 1 and Pump 2, respectively, and pressurized to 8 MPa while valve V1 was kept closed. At this high pressure, all air bubbles that may have been trapped in the porous section initially under ambient pressure quickly shrunk and dissolved into the water phase, leading to an initial condition of liquid water only in the micromodel. After the pressures on the water side and CO_2 side both reached equilibrium, valve V1 was opened and the CO_2 and water pumps were simultaneously initiated to run at the desired volumetric flow rates, each with an accuracy of 0.3% of the setpoint.

TABLE 1 | Physical properties of CO_2 and water at reservoir-relevant conditions (8 MPa and 21°C) (Linstrom and Mallard, 2001).

CO_2 density ρ_2 [kg/m^3]	Water density ρ_1 [kg/m^3]	CO_2 viscosity μ_2 [kg/m.s]	Water viscosity μ_1 [kg/m.s]	Interfacial tension γ [kg/s^2]
818.55	1001.6	7.40×10^{-5}	9.75×10^{-4}	0.0294

2.3. Image Acquisition and Processing

A high-speed, dual-head, frequency-doubled Nd:YLF laser (Litron LPY300) with a wavelength of 527 nm was used to excite the fluorescent particles in the water phase. The fluorescence emitted from the tracer particles was passed through a $\lambda = 575 \pm 13$ nm bandpass filter (Semrock BrightLine FF02-575/25-25) and focused by an Olympus IX-73 microscope equipped with an objective lens with 4x magnification and 0.1 numerical aperture (NA), onto the detector of a high-speed scientific CMOS camera (Phantom v641). With this imaging setup, the resultant field of view (FOV) after cropping out the relatively low quality marginal regions was approximately 3.75 $\times$ 3.75 mm, located at the center of the porous section, as indicated by the green region in **Figure 1B**. As the water phase was the only one seeded with tracer particles, this was the only phase in which velocity measurements were conducted.

In order to accurately resolve the instantaneous water velocity fields during a burst, a "frame straddling" scheme was used (Li et al., 2014; Li and Yoda, 2016). In this scheme, the camera recorded pairs of sequential images, frame A and frame B, in each image pair. It is important to note that the images were only exposed during the duration of the laser pulse, which was $\sim$10 ns in these experiments. Such a short exposure provides a snapshot of the distributed tracer particles "frozen" at that time instant of each pulse. The caveat is that the two laser pulses can be conveniently timed to illuminate the particles once in frame A and once in frame B. The time interval between the laser pulses within one frame pair, Δt, can be adjusted for each experiment based on the average particle velocity expected and with the goal to optimize the particle displacement within a 1–15 pixel range. In the experiments reported herein, the Δt was set to be 500 μs for the drainage case and 2 ms for the imbibition case. In addition to the ability of performing frame-straddle imaging, the camera allowed time-resolved acquisitions by acquiring frame pairs at 500 Hz. This frame rate provided sufficient temporal resolution to capture the evolution of dynamic pore-scale phenomena.

The multi-phase nature of the flow requires the identification of the fluid–fluid interfaces in the resulting PIV images and the masking out of unseeded regions prior to image interrogation for quantification of the water velocity distribution. In previous studies (Li and Yoda, 2014; Li et al., 2017), this masking was obtained manually since the datasets were limited to a few images. However, the high-speed imaging used herein yielded 3800 PIV image pairs per experimental run for which the interface must be tracked accurately over its evolution, making manual masking impractical. As such, a novel image

segmentation and interface detection method was developed and tested on samples of particle images experimentally acquired for the present study (Li et al., 2021). As described in Li et al. (2021), the accuracy of this methodology enabled automatic interface detection and tracking in all of the PIV images acquired herein. In particular, this method provided, for each image pair, a digital mask that excluded the CO_2 phase from image interrogation to determine the water velocity field. In this study, for each image pair, a mask based on the segmentation of the first frame was utilized for masking.

For details regarding the image segmentation and image mask creation, the reader is referred to Li et al. (2021). Briefly, for a given image, all tracer particle images seeded in the water phase were detected using a particle tracking algorithm with their coordinates accurately determined, based upon which a triangulation mesh was constructed to link each particle to its nearest neighbors. The regions covered by the mesh were labeled as the water phase, whereas the edges of the mesh were demarcated as interfaces, which were then individually fit to arcs to help clarify interface shapes and locations. This image segmentation process was performed by implementing automatic procedures using an in-house MATLAB code, and the root-mean-square-error (RMSE) of interface detection in experimental images under the current condition was estimated to be ~ 1.5 pixels.

To calculate the water velocity field, both frames in an acquired frame pair were first masked using the mask created in the previous steps and then interrogated in the LaVision DaVis software using a multi-pass, two-frame cross-correlation method (Kazemifar et al., 2015). Unless otherwise stated, the sizes of the initial and final interrogation windows were 128^2 and 16^2 pixels, respectively, both with 50% overlap, which yielded a velocity vector spacing of 20 μm and a spatial resolution of 40 μm. It is worth noting that due to the dynamic nature of these multiphase flows, the fluid–fluid interfaces were continuously deforming and moving throughout an experiment. For instance, during the occurrence of a Haines jump, the meniscus can significantly change in shape and location from the first frame to the second frame of a frame pair. When the tracer particles in the two frame are cross-correlated to compute the velocity vectors, there will be an unavoidable lack of tracer particles in the second frame in the displaced region between the initial and final interfaces, which potentially leads to a loss of velocity vectors in the specific region of the image. And even worse, these lost velocity vectors represent ones of the highest velocities one would expect in the flow. As such, μPIV is likely to underestimate the maximum velocities that exist in the flow, which tend to occur near the displacing menisci. To overcome this challenge and complement our μPIV measurement, we also computed the near meniscus velocities by directly tracking the interface movements during Haines jumps. This approach filled the data gap and produced a more comprehensive set of statistics. This issue will be revisited in § 4.2 in the discussion of flow statistics.

3. RESULTS

The results presented herein consist of sequences of water velocity fields, illustrating some of the dynamic phenomena associated with CO_2 infiltration into a water-saturated micromodel under two different wetting conditions. More specifically, we focus on the migration of the CO_2 front, the evolution of individual menisci, and the growth of dendritic structures (i.e., the fingers) (Lenormand et al., 1988; Kazemifar et al., 2016; Li et al., 2017, 2019). Two wettability cases were considered herein: a hydrophilic case (strong drainage) and a hydrophobic case (weak imbibition), for which the receding contact angles of the micromodel surface with water were $\sim 9^\circ$ and $\sim 98^\circ$, respectively. The bulk flow rate for both cases was the same: 5 μl/min. Based on Equation (1) and the bulk velocity corresponding to the midpoint in the radial direction, the prescribed flow rate corresponds to a capillary number of $\log Ca = -5.7$. Note that the contact angle θ is not included in the definition of Ca (Equation 1) and the calculation of this capillary number in order to provide a meaningful ($Ca > 0$) measure for both drainage (hydrophilic) and imbibition (hydrophobic) cases (Trojer et al., 2015; Hu et al., 2017).

3.1. Prefront Single-Phase Flow

Each experiment involved an initial injection stage in which the micromodel was saturated with water and the CO_2 was being pushed toward the model but had not yet reached the micromodel entrance. This stage is refereed to as prefront single-phase flow. This simple experiment allowed us to test the system and assess potential sources of measurement error that can be useful in interpreting the subsequent and more complex multiphase flow. Before discussing these results, it is useful to clarify aspects of the flow domain. First, the circular micromodel employed has a constant depth. Unlike the rectangular micromodels used in previous studies (Zhang et al., 2011a,b; Blois et al., 2015; Kazemifar et al., 2016; Roman et al., 2016; Li et al., 2017, 2019), the cross-sectional area was not constant, but instead a function of radial position. As such, for the flow rate to remain constant at each radial distance, the velocity must vary inversely with increasing radius, i.e., higher where cross sectional area is smaller (i.e., near the center). The variation in cross sectional area therefore resulted in a strong radial velocity gradient and the dynamic range of the measurements is expected to reflect this gradient along the radius. Other conditions such us fluctuations in the flow rate and transient phenomena further broadened the dynamic range, so variations in accuracy away from this region were expected. With this in mind, **Figure 3a** presents the ensemble-averaged velocity field of the single-phase flow of water obtained from 200 PIV realizations (i.e., 0.4 s), prior to the CO_2 phase entering the porous micromodel. This result primarily quantifies the radial flow of water, which was injected through the center port. As expected from mass conservation for an incompressible flow, **Figure 3a** confirms faster flow near the center and a progressive decrease of velocity as water migrates toward the outer edge of the micromodel. The flow accelerates through the pore throats where the grains are closer together and decelerates within pore spaces, where grains are further apart, all expected based on continuity. Interestingly, **Figure 3a** shows that the water has formed preferential paths of high-momentum that correlate well with the grain distribution.

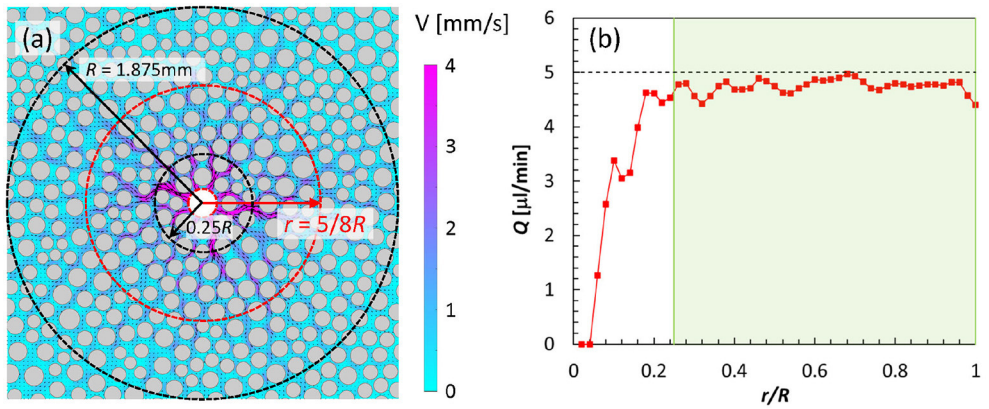

FIGURE 3 | *Pre-drainage* stage: **(a)** Ensemble-averaged water velocity field obtained from 200 PIV realizations depicting water flow prior to the entry of CO_2; contours reflect velocity magnitude and arrows indicate flow directions; gray regions represent solid grains; unless otherwise stated, only every other vector is shown in both the horizontal and vertical directions for clarity. The black dashed lines define the inner and outer edges of the "annulus," which is the region considered for bulk flow analysis; The red dashed at $r = 5/8R$, indicates the location where U_{bulk} was calculated. **(b)** Integrated volumetric flow rate as a function of radial location; the green shading demarcates the region where flow rate measurements accurately reflect conservation of mass. Experimental conditions: 0.005 mL/min, 8 MPa, and 21°C.

The accuracy of these single-phase flow of water results can be assessed as a function of radial position. Since water is incompressible, the concept of continuity means that the volumetric flow rate crossing any circle enclosing the center injection port should be constant and equal to the actual injection rate. This observation offers an opportunity to quantify the fidelity of the measurements presented herein. **Figure 3b** presents volumetric flow rate, obtained by integrating the velocity vectors along a circle of given radius centered at the center of the injection port, as a function of radial location. This result shows that the volumetric flow rate, which is accurately measured for $r/R > 0.25$ (i.e., 5 μl/min), is largely underestimated near the center of the micromodel, $r/R < 0.25$. A less severe underestimation seems to persist also for $r/R > 0.25$, where the measured flow rate oscillates around the value of approximately 4.8 μl/min. This result highlights some of the challenges faced when measuring a flow with a high dynamic range such as that considered herein. The velocity is, in fact, extremely high near the injection port, suggesting that the Δt set for this experiment, which was optimized for the velocities at the middle radius, may have been too long to accurately capture the displacement of the particles near the micromodel entrance. In the region $0.25 < r/R < 1$, the measured flow rate agrees with the prescribed value, with a maximum deviation of $\sim$ 8% with the best agreement in the $0.6 < r/R < 0.7$ region, confirming the high fidelity of our μPIV measurements in this range. The $\sim$ 8% deviation elsewhere does not, however, suggest a low quality measurement. In particular, these small differences could be associated with the high compressibility of the CO_2 that is pushing the water phase through the micromodel. Though the CO_2 has yet to enter the micromodel, its properties are extremely sensitive to small changes in temperature and pressure, particularly under the current experimental conditions (Kazemifar and Kyritsis, 2014), and it represents the driving force behind the water displacement. Similar observations have been reported in previous studies (Kazemifar et al., 2016; Li et al., 2017). As the near-entrance μPIV measurements have relatively low fidelity, in the following statistical and energy analyses, only data within the annulus region of $0.25 < r/R < 1$ are considered.

3.2. Water Velocity Field Evolution During Drainage

In this section, measurements are presented illustrating CO_2 infiltration into the water-saturated micromodel causing dynamic drainage (see **Supplementary Movie 1**). **Figure 4** shows representative snapshots depicting the very first stage of the drainage process featuring resident water being displaced by the arrival of CO_2. Here, $t = 0$ signifies the instant when the CO_2 front crosses the line of $r/R = 0.25$. Results show that at $t = 0$, the water velocities in the entire field are low, even lower than that in the prefront stage, indicating low flow rate in the water phase. This behavior reflects pinning of the CO_2 front at the narrow throats of the porous section where high capillary pressure impedes the flow on both sides of the interface. As the CO_2 pump continuously pushes CO_2 into the micromodel, the pressure behind the interface (i.e., on the CO_2 side) gradually increases to contrast the capillary pressure. Once the capillary pressure is finally exceeded, CO_2 suddenly breaks through into the pore space behind the throat in the form of a burst event (Haines, 1930). The external work due to high pressure is partially converted into kinetic energy and causes high-momentum pathways that propagate at high speed for several pores into the water phase. For instance, the burst event occurring at $t = 4$ ms extends as far as approximately 2 mm away from the pore where it originates, which is $\sim$ 20 times larger than the average pore diameter. Additionally, unlike the single-phase flow whose direction is dictated by the bulk pressure gradient, the local flow produced by a burst does not necessarily follow the radial direction. Instead, it can proceed in any direction, including against the bulk pressure gradient.

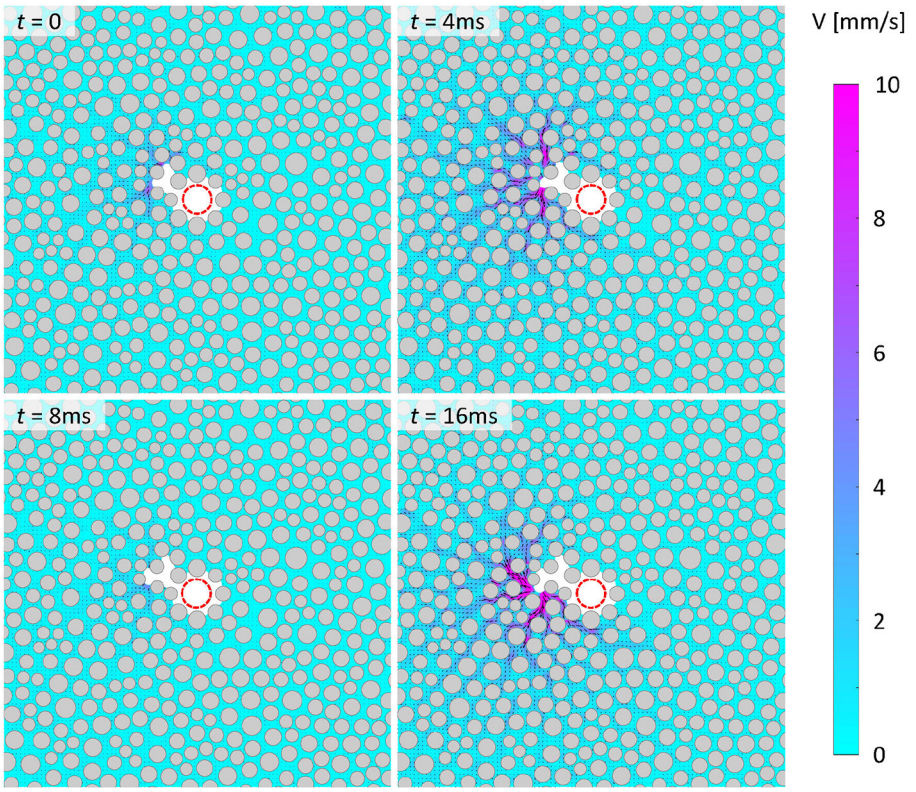

FIGURE 4 | Instantaneous velocity fields depicting water flow owing to displacement by invading CO_2 under *drainage* conditions. Gray and white regions represent solid grains and CO_2 phase, respectively; purple and cyan colors denote high and low velocities, respectively; arrows in the water phase denote flow direction. Experimental conditions: $\log Ca = -5.7$, 8 MPa, 21°C, and $\theta_r \sim 9°$. (For interpretation of the references to contour in the text, the reader is referred to the web version of this article).

This observation is in agreement with previous findings on water drainage in a rectangular micromodel (Kazemifar et al., 2016; Roman et al., 2016; Zhao et al., 2016; Li et al., 2017; Chen et al., 2018), and highlights the critical role of the *local* pressure gradient under the capillary flow regime considered herein. It is also evident that the flow is highly intermittent, meaning that it constantly goes through cycles of deceleration and acceleration associated with compression and expansion of CO_2, respectively. As previously observed, these stages correspond to accumulation followed by release of capillary pressure associated with the occurrences of Haines jumps. When a burst event is occurring, the flow is accelerated in the direction of the local pressure gradient produced by the build up of capillary pressure at the meniscus, and after the energy is released the flow is dramatically decelerated. The typical lifetime of a burst is found to be a few milliseconds in the current experiments. As evident at $t = 8$ ms, the flow quickly subsides following the preceding burst event at $t = 4$ ms. At $t = 16$ ms, a new burst event occurs, bringing the flow into a new cycle, similar to the one before.

The entire drainage process of water is essentially dominated by a succession of local bursts events like the one just described. **Figure 5** presents the occurrences of additional selected burst events later in the drainage process. These events occur at various locations and along various directions, confirming that water can displace along, normal to and even against the bulk pressure gradient in the radial direction. It is worth noting that these burst events do not necessarily occur one after another, but instead they can occur in a cascading manner, meaning that multiple pores can be invaded at once, and that multiple burst events can occur simultaneously at different locations. This is particularly evident from the velocity field at $t = 956$ ms in **Figure 5**. In this particular experiment, this repeated quiescence-burst process continues for over $\sim$ 1 s and can be observed until the CO_2 phase completely breaks through the boundaries of the domain imaged. At $\sim$ 1.8 s the bursting process completely subsides, leaving the remaining water quiescent. From this instant, the CO_2 continues to flow through the region of displaced water, although its dynamics cannot be directly observed due to lack of tracers in the CO_2. These results show that the growth pattern of the CO_2 front is quite irregular and asymmetric about the center, which is indicative of capillary fingering, due to which a large portion of water is left trapped in the porous section behind the CO_2 front.

3.3. Water Velocity Field Evolution During Imbibition

Figures 6, **7** show similar sequences of representative snapshots illustrating the evolution of water flow responding to a condition of *imbibition*, herein experimentally induced by modifying the

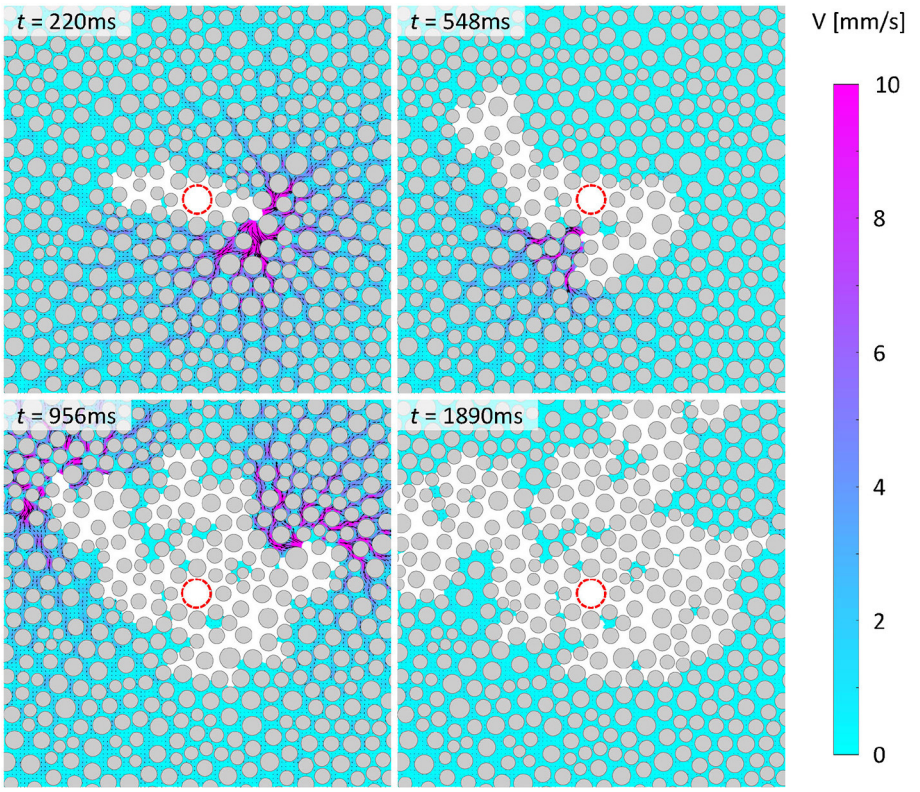

FIGURE 5 | As in **Figure 4**, but showing burst events occurring at different times as CO_2 continuously displaces water under *drainage* conditions. Experimental conditions: $\log Ca = -5.7$, 8 MPa, 21°C, and $\theta_r \sim 9°$.

wettability of the micromodel (see **Supplementary Movie 2**) where the receding contact angle of water, θ_r, was modified to $\sim$ 98°. As expected, the behavior of the water displacement process is fundamentally altered. First, the maximum water flow speed in this imbibition case is much lower than in the drainage case (note the different scale bars used in **Figure 4** compared to **Figure 6**), indicating that the flow discharge is more uniformly distributed across the micromodel, resulting in a more axisymmetric distribution that is reminiscent of the prefront single-phase behavior. While flow continues to be concentrated in high-momentum paths, these paths appear more correlated to the geometry of the porous matrix compared to the drainage burst events whose displacement patterns were not restricted to the radial direction. Under imbibition conditions, flow proceeds more smoothly, which reflects a lack of burst events in this flow scenario. As all other experimental conditions were held constant in this imbibition case compared to the drainage case, these drastically different flow dynamics are entirely due to changes in the wettability of the porous matrix for which the capillary forces in the system have been significantly reduced. Essentially, unlike in the previous case, where the capillary pressure exerted at the CO_2 interface competed against the bulk driving pressure, leading to flow instabilities, in this case the menisci curvatures are inverted, which means that the capillary pressure works to drive the flow forward, significantly mitigating flow instability and burst events. The CO_2 invasion is also much more compact, with very little water phase left behind the radially migrating CO_2 front. These results confirm that modifying the wettability of the porous matrix from a strongly hydrophilic state to one of intermediate wetting dramatically mitigates flow instability and enhances displacement efficiency as reported in with previous studies (Cottin et al., 2011; Holtzman and Segre, 2015; Trojer et al., 2015).

3.4. Pressure Drop and Saturation Curves

The temporal evolution of the bulk flow properties for both drainage and imbibition cases were investigated by quantifying CO_2 saturation from the PIV images and measuring the bulk pressure drop across the micromodel. The CO_2 saturation, defined as the ratio between the volume occupied by CO_2 and the total pore volume within the measurement domain (taken here as the annulus in the range $0.25 < r/R < 1$), was obtained from the segmented particle images. The bulk pressure across the micromodel was measured using a differential pressure transducer (Validyne, P55E-1-N-2-42-S-5-A, 0 – 140 kPa, 0.1% accuracy) between the inlet and outlet (see **Figure 1**). To avoid potential cross interference between tracer particles and the pressure measurement, all pressure measurements were performed in separate experiments but under identical conditions as that in the μPIV measurements,

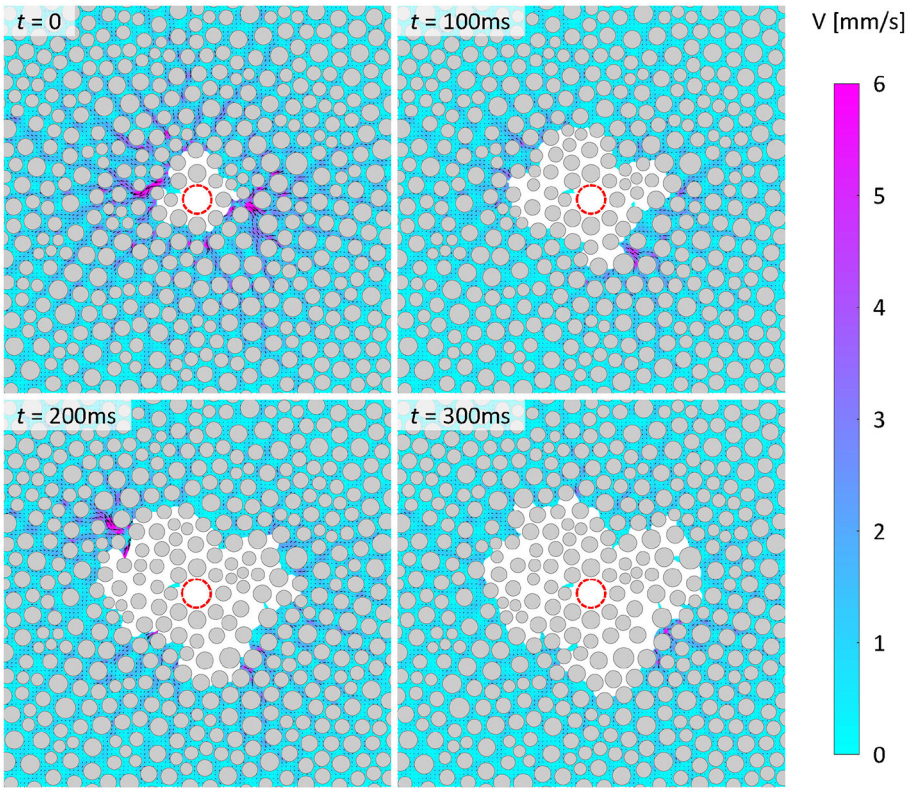

FIGURE 6 | As in **Figure 4**, but showing instantaneous velocity fields depicting water flow as CO_2 continuously displaces water in 2D circular *hydrophobic* micromodels under imbibition conditions. Experimental conditions: $\log Ca = -5.7$, 8 MPa, 21°C, and $\theta_r \sim 98°$.

using a clean micromodel. Likewise, in the actual μPIV measurements the pressure transducer and the tees (i.e., T1 and T2) were not included. Although the pressure drop was measured separately, based on the repeatability of flow patterns and pressure drops, we believe the pressure drop history is a good representation of the actual pressure evolution during a given μPIV experiment. Measurements are presented herein by plotting pressure drops and CO_2 saturation against the number of injected pore volumes, PV. Here, PV is defined as $PV = Q*t/V_{\text{pore}}$, where Q is the volumetric flow rate, t is time and V_{pore} is the total volume of the pore space falling within the annulus region (as indicated in **Figure 3**) and represents a normalized total accumulated volume of CO_2 that was injected into the porous section at any moment. Additionally, simple algebraic manipulation yields that $PV = t/t_c$ as a normalized time, with $t_c = \varphi(r_2 - r_1)/U_{\text{bulk}}$, where r_1 and r_2 are the radii of the inner and outer edges of the annulus, respectively, and U_{bulk} is the bulk velocity corresponding to the midpoint of the annulus in the radial direction. As PV is effectively a normalized time, any PV value corresponding to a moment prior to $t = 0$ (i.e., when the CO_2 front crosses the circle of $r/R = 0.25$) is negative in the reference adopted herein.

Figure 8A presents the variations of the bulk pressure drop as a function of PV for both drainage and imbibition conditions and highlight the distinct behaviors of these two conditions. The initial pressure drop, up to $PV \sim -1.5$, is almost identical between the two conditions and represents the baseline pressure due to viscous forces and is the sum of the pressure required to push water thorough the micromodel and CO_2 through the tubing on its path to the micromodel entrance. The time up to $PV \sim -1.5$ is the time window corresponding to the steady state single-phase flow stage, which is the same for both cases, indicating that the modification of the micromodel surface does not impact its permeability to water. The pressure drops deviate at $PV \sim -1.5$, which corresponds to the moment the CO_2 phase enters the micromodel. At this moment, the wettability begins to impact flow resistance as the onset of capillary forces modify the force balance. In the drainage case, since the micromodel surface is hydrophilic, the capillary pressure across the interface causes pressure to build up in front of the CO_2-water interface, which adds onto the baseline pressure drop, leading to a steep increase in the total pressure drop. As the CO_2 front migrates through the porous section, the pressure drop continues to increase linearly, roughly until $PV \sim 0$, which corresponds to $r/R = 0.25$. After this point, the rate of increase reduces and the pressure drop reaches a maximum at $\Delta P = 3$ kPa, for $PV \sim 1$. After this point, the pressure drop decreases with further increase in PV. In contrast to the drainage case, the pressure drop during the imbibition case remains constant up to $PV \sim 0$. After this point, the bulk pressure drop becomes

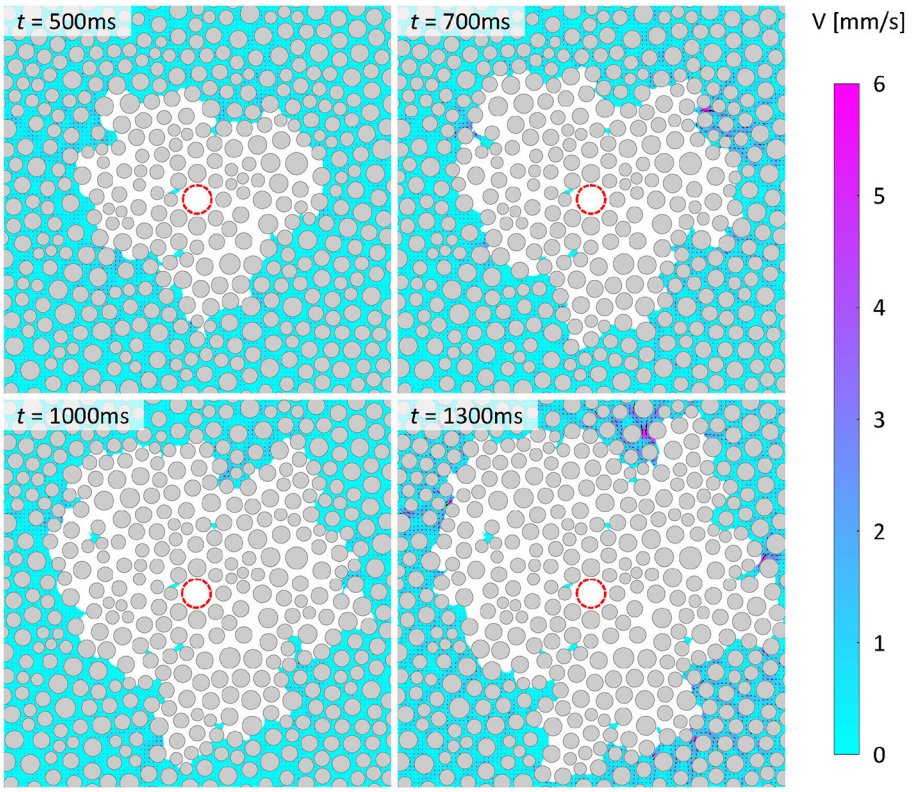

FIGURE 7 | A continuation of **Figure 6**, showing instantaneous velocity fields depicting water flow as CO_2 continuously displaces water in 2D circular *hydrophobic* micromodels under imbibition conditions. Experimental conditions: $\log Ca = -5.7$, 8 MPa, 21°C, and $\theta_r \sim 98°$.

negative and remains nearly constant at $\Delta P = -0.2$ kPa. This negative value of the pressure drop is expected since in this case the micromodel is hydrophobic, causing an inversion of the interfacial curvature, meaning that the capillary pressure induces a higher pressure on the water side, which is high enough to counterbalance the small viscous pressure drop, leading to an overall negative pressure across the micromodel. This behavior also suggests that the external work done by bulk pressure is negative during imbibition, meaning that the system is doing work to the surroundings (i.e., the pumps in the current experimental arrangement) (Hu et al., 2018).

Figure 8B presents the variation of CO_2 saturation within the measurement domain, S_{CO2}, as a function of PV for both drainage and imbibition cases. Note that PV physically represents the total accumulated volume of CO_2 that has been injected into the porous section at any moment, whereas S_{CO2} represents the total volume of CO_2 that is present in the porous section at that moment. As shown in **Figure 8B** for the imbibition case, the saturation curve begins with an approximately linear increase, with PV growing at the same rate as saturation. This behavior supports $PV = S_{CO2}$ which is consistent with conservation of mass for incompressible flow. However, when CO_2 begins to exit from the outer edge of the annulus region, the relation deviates from a linear one, simply because mass storage (S_{CO2}) now is not equal to mass entering the control domain. This simple yet rigorous mass conservation is not, however, satisfied in the drainage case, even for the initial part of the curve (i.e., before CO_2 exits from the outer edge). While the saturation curve initially follows a linear trend, S_{CO2} (i.e., volume stored) is always lower than PV (i.e., volume injected). This is in fact consistent with the expected compression of CO_2 caused by the bulk pressure increase under these conditions. It is important to recall that the CO_2 phase under the experimental conditions herein is in near-critical conditions and, as such, is highly compressible (Kazemifar and Kyritsis, 2014). Given the large volume (compared with the pore volume) contained in the upstream plumbing lines, any small change in pressure could potentially result in an appreciable change in the volume of CO_2 that is contained in the syringe pump and pluming lines. According to **Figure 8A**, the pressure on the CO_2 does increase by $\sim$ 500 Pa during this process. Based on the compressibility of CO_2 (Law and Bachu, 1996) and the cumulative volume of the pluming lines, we estimated that for a pressure change of 500 Pa, a volume change of up to 0.05 μl is possible, which is $\sim$30% of the total pore volume. In this regard, conservation of mass cannot translate to conservation of volume within the system.

Figure 8C presents the variation of CO_2 saturation with the CO_2 leading front position under both drainage and imbibition

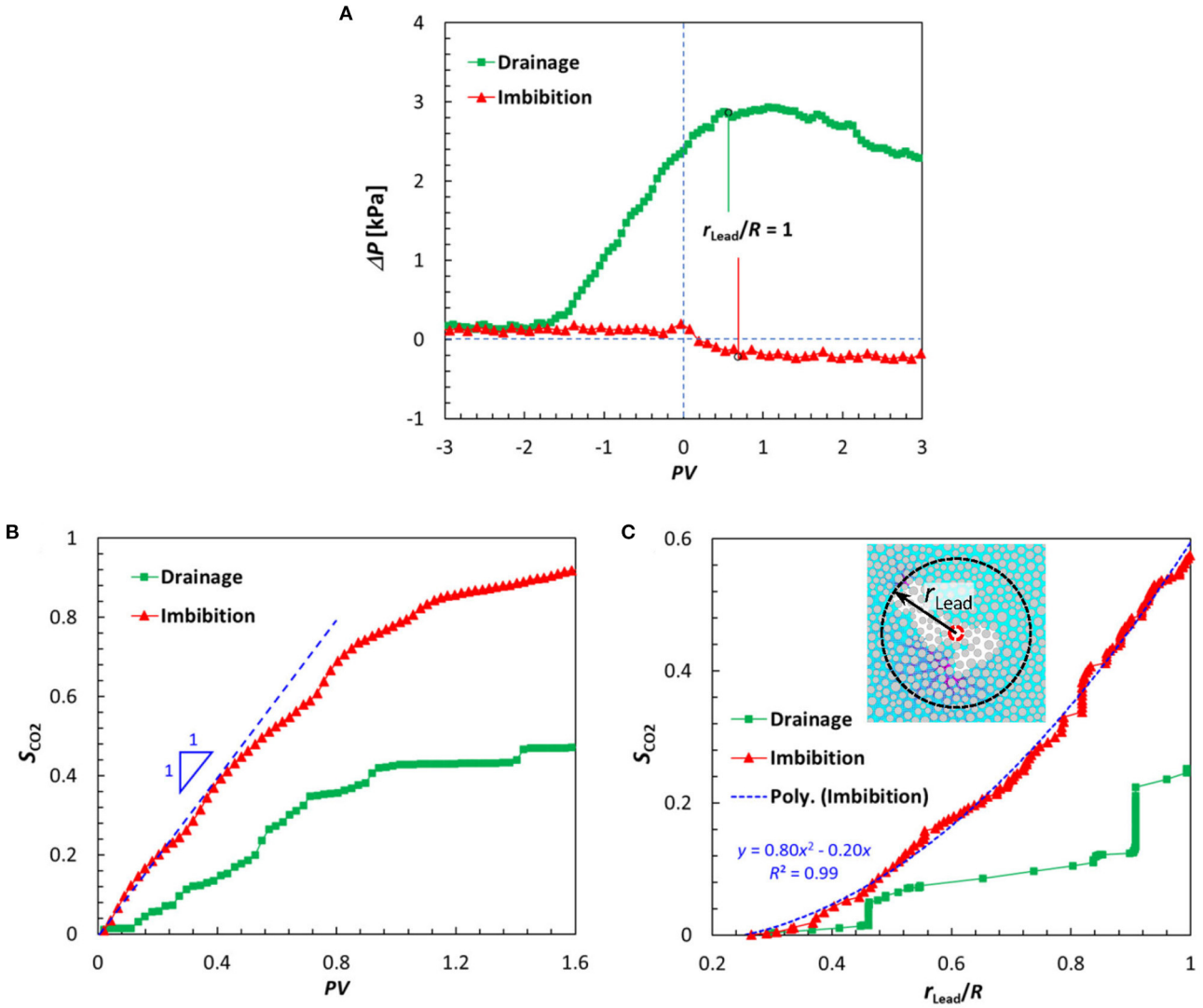

FIGURE 8 | (A) Instantaneous pressure drop across the micromodel measured during drainage and imbibition plotted against the injected pore volume, *PV*. **(B)** Variation of CO_2 saturation, S_{CO2}, vs. injected pore volume, *PV*. Profiles are truncated at $PV = 1.6$ when both cases reach a quasi-steady state. $PV = 0$ signifies when CO_2 first enters the annulus of interest. **(C)** Variation of CO_2 saturation, S_{CO2}, vs. the CO_2 leading front position, r_{Lead}. Here, the CO_2 leading front position is defined as the farthest position of the CO_2 phase in the radial direction at any moment, as illustrated in the inset.

conditions. Here, the leading front position r_{Lead} is defined as the farthest position of the CO_2 phase in the radial direction at any moment, as illustrated by the figure inset. This metric has been used in previous studies to reveal key characteristics of drainage for different flow regimes and the effects of wettability on the displacement process (Tsuji et al., 2016; Hu et al., 2017). As illustrated in **Figure 8C**, in the drainage case, the CO_2 saturation varies in a step-wise manner with the leading front position, revealing that CO_2 saturation continues to increase even when the leading front is pinned at a fixed location. This behavior can be understood by recognizing that capillary fingers can grow in all directions, not just with the radial bulk pressure gradient. Thus, increased CO_2 saturation at constant leading front position is possible due to finger growth in the azimuthal and/or reverse radial directions. Furthermore, this trend implies that the leading edge of the CO_2 front advancing further downstream is not necessarily associated with the same finger, but can instead alternate between fingers at different spatial locations. In contrast, this relationship is much smoother in the imbibition case, with very little stepwise behavior. The relationship also displays a parabolic trend, suggesting that the CO_2 invasion is marked by very compact and axisymmetric displacement, reflecting the flow patterns shown in **Figures 6**, **7**. These results reveal distinct pore-scale invasion mechanisms for drainage and imbibition that are in agreement with previous experimental studies in rectangular micromodels (Li et al., 2019), rough fractures (Chen et al., 2017; Hu et al., 2017) and simulations in 3-D porous rocks (Yamabe et al., 2014; Tsuji et al., 2016).

4. DISCUSSION

The results presented herein are consistent with current knowledge and existing studies, confirming again the validity of these measurements. To gain further insight into the unrevealed pore-scale dynamics and the effects of wettability on the multiphase flow of CO_2 and water in 2D micromodels, the temporal resolution of these measurements is leveraged to investigate unknown aspects of the underlying physics.

4.1. Drainage: Haines Jump

This section focuses on using this data to characterize aspects of the drainage process and the dynamics and nature of Haines jumps. In particular, how large is the region of influence of an individual Haines jump and how long can the perturbation induced by a burst last? As previously mentioned, conflicting results have been reported regarding the temporal and spatial scales of a Haines jump. While acoustic measurements and optical visualizations suggest that Haines jumps occur on a time scale as short as a few milliseconds, and even sub-millisecond (DiCarlo et al., 2003; Armstrong and Berg, 2013), fast micro-CT measurements suggest that the time scale is in the range of $40 - 200$ ms, and the relaxation following a Haines jump can be as long as 2 s (Armstrong et al., 2014). Regarding the spatial size of a Haines jump, at least two different metrics have been proposed. Armstrong et al. (2014) defined the event size as the volume of the wetting phase that is displaced by the non-wetting phase during a certain period of time. They reported that the average volume of the events is approximately two orders of magnitude larger than the average volume of the pores. While this metric properly measures the displacement of the meniscus following a burst, it underestimates its region of influence, which can extend far beyond the new position of the meniscus. On the other hand, Armstrong and Berg (2013) reported that the zone of influence extends at least four pores away from the location where the burst event occurs. Using a similar approach, Li et al. (2017) reported that the zone of influence can extend as far as 30 pore diameters. However, due to the temporally uncorrelated nature of those measurements, it was not possible to determine the temporal duration of these events. Moreover, those observations did not provide conclusive evidence as to the spatial extent of the influence of an individual burst since the possibility of multiple successive jumps acting along the same direction could not be ruled out. Herein, the temporally and spatially resolved water velocity data is leveraged for direct observations of the dynamics of each independent jump along their entire life cycle and to revisit these important questions.

Figure 9 presents selected snapshots illustrating a typical burst event throughout its entire lifetime under drainage conditions. At $t = 0$ s, the CO_2–water interface is pinned at a throat with little flow in the water phase behind the interface. This instant is defined as the temporal origin of the jump for which the meniscus is relatively flat and the water ahead of the meniscus is quiescent. At $t = 2$ ms, the meniscus increases its curvature, thus indicating a build up of capillary pressure. Simultaneously, the interface advances slightly and manages to pass through the narrowest point of the pore throat. This movement results in a slight increase in water velocity, revealing the onset of high-momentum displacement pathways whereby the meniscus is ready to burst into the open pore space. At $t = 4$ ms, the jump of the interface begins, as witnessed by the dramatic acceleration in the water phase, with velocities peaking at $t = 6$ ms. Shortly thereafter, at $t = 8$ ms, the water flow suddenly decelerates returning to the pre-burst state of quiescent water. In this case, two new interfaces form and pin at the new throats. To the best of our knowledge, these results represent the first complete experimental characterization of a pore-scale burst event, reporting detailed velocity information of the surrounding flow from inception to end. These results suggest that the acceleration and deceleration stages have different duration. As shown in **Figure 9**, the acceleration (from quiescence to peak water velocity) of the burst event lasted for ∼6 ms, whereas the relaxation (from peak back to quiescence) period only lasted for ∼2 ms, due presumably to the combined effects of a high viscous dissipation rate in the water phase and the capillary forces induced by the next set of throats.

Figure 9 also reveals the transient behavior of the surrounding water velocity field induced by a burst event with spikes of high momentum flow, followed by quiescent flow, which is consistent with the intermittent behavior noted in **Figures 4**, **5**. This observation enables the identification of Haines jump occurrences in the micromodel based on instantaneous flow rate. **Figure 10A** presents the instantaneous volumetric flow rate by integrating the flow at the outer edge of the annulus ($r/R = 1$)

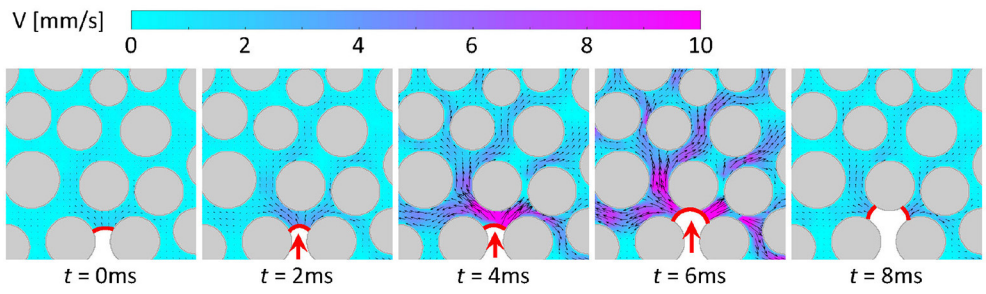

FIGURE 9 | Velocity distribution near a Haines jump revealing the life of an individual burst event. Here, red lines demarcate the interfaces and the red arrows denote the advancing directions of the interfaces.

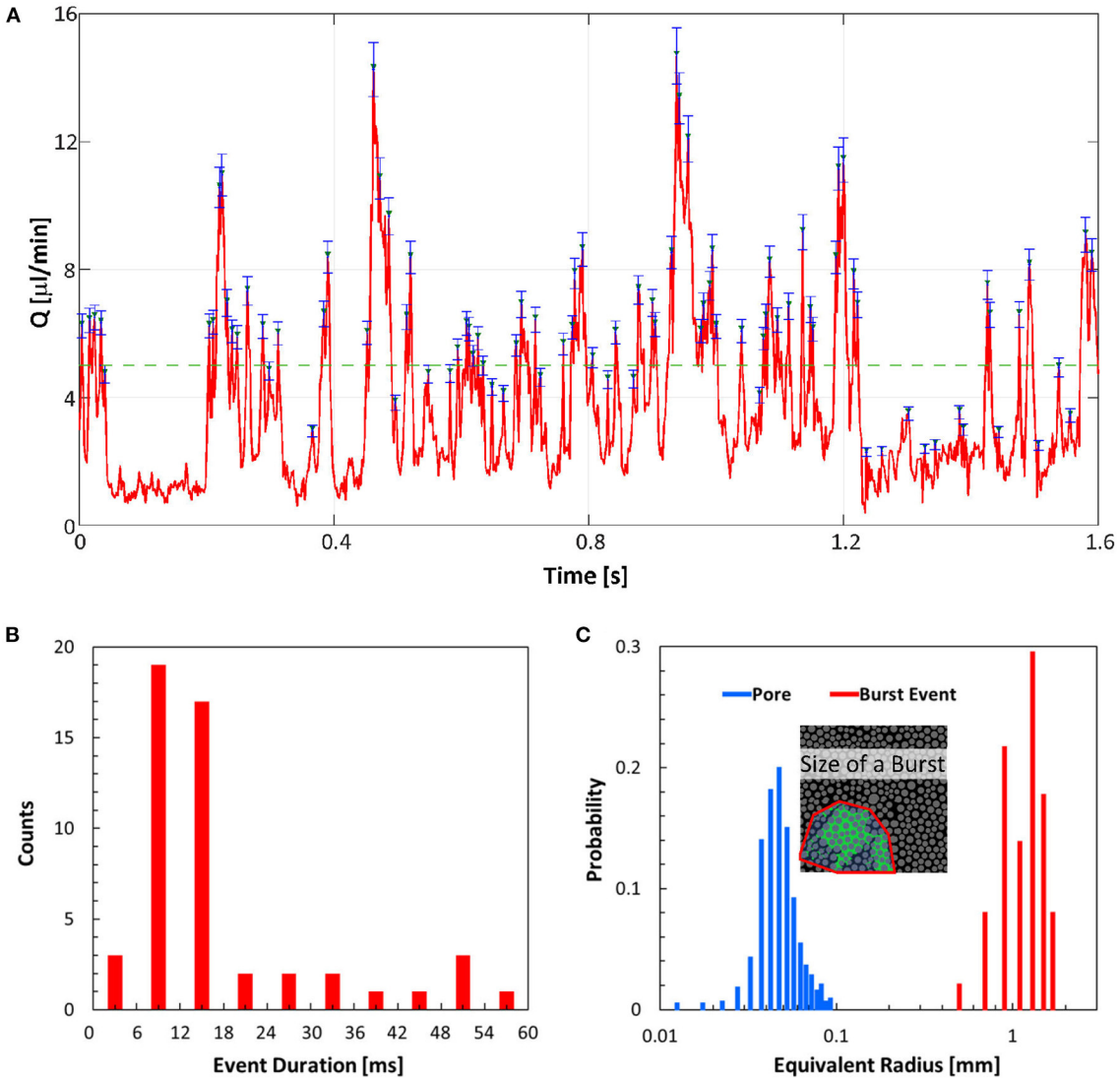

FIGURE 10 | (A) Instantaneous volumetric flow rate exiting the domain of interest. The green triangles denotes the peak locations, indicating the occurrences of Haines jumps, whereas the green dashed line denotes the prescribed flow rate, 5 μl/min. Blue error bars represent 6% of the peak flow rates obtained from the validation experiment. **(B)** Histogram of burst event duration. **(C)** Histograms of burst size and pore size. The inset illustrates how the size of a burst event is calculated.

from $t = 0$ to $t = 1.6$ s. Spikes in flow rate are presumably induced by the occurrences of Haines jumps, while the width of these spikes represent burst durations. The highest instantaneous flow rate noted is 14.7 μL/min, which is three times higher than the prescribed bulk flow rate. Guided by this instantaneous flow rate metric, a total of 51 burst events were visually identified based on the 800 (i.e., 2 ms per field) instantaneous velocity fields during this 1.6 s period. The spatial size and temporal duration of these burst events and their statistical behavior are presented below.

Figure 10B presents a histogram of the event duration, defined as the entire period from quiescence immediately preceding a burst event until a new quiescent state is achieved immediately following the burst event. This metric highlights that burst event duration ranges from 4 ms to approximately 60 ms, with 22 (out of 51) falling within the $0 - 12$ ms range and five falling within the $42 - 60$ ms range. The shortest duration (i.e., 4 ms) most likely corresponds to the occurrences of individual isolated events, whereas the longer duration events correspond to burst events occurring in a cascading manner over multiple pores and throats. Examination of instantaneous water velocity fields indicate that it is possible for one event to cascade through up to 16 throats. Furthermore, our measurement of burst event duration is in good agreement with previous acoustic measurements and optical visualizations (DiCarlo et al., 2003; Armstrong and Berg, 2013), but is not consistent with the micro-CT measurement in 3D porous media (Armstrong et al., 2014). This discrepancy could be in part due to the distinct nature of

2D and 3D flows, and in part due to the fact that micro-CT cannot sufficiently resolve these highly intermittent events. It is worth noting that the total time of all 51 burst events adds up to 0.83 s (out of 1.6 s), corresponding to approximately half of the total time. However, this half of total time is found to be responsible for more than 75% of the total accumulated volume exiting the outer boundary (i.e., water drainage), suggesting that the drainage process is dominated by successive Haines jumps.

Another key property of the burst events is their spatial footprint. While it was traditionally believed that burst events are local, single-pore processes, more recent studies have called this assumption into question. As mentioned previously, Armstrong et al. (2014) reported a two orders of magnitude difference between the average pore volume and the average burst volume, defined as the volume of the fluid that is displaced during a period of time, whereas Armstrong and Berg (2013) reported that the zone of influence in a 2D porous micromodel is at least four pores from the location where the drainage event occurs. Note that, however, the volume of displaced fluid is not a faithful measure of burst event size, as it depends highly on the chosen time interval and does not include the zone of influence. Li et al. (2017) found that the zone of influence can extend as far as 30 pore diameters, which brings the radius of influence close to the Darcy scale (i.e., a few millimeters). The significant data spread in the literature on this topic shows that the distribution of burst event size remains unclear.

Figure 10C shows a histogram of the burst event size along with a histogram of the pore sizes obtained from our measurements. The burst event size was calculated by comparing the instantaneous water velocity field of the corresponding burst event at its peak with the steady-state water velocity field (i.e., **Figure 3A**). For each instantaneous velocity field, any region that displayed a higher velocity than the baseline was considered to be influenced by an ongoing burst event. The total area, A_{event}, was computed through an integration process, as illustrated in the inset of **Figure 10C**. The equivalent radius of the event was then calculated as

$$r_{\text{event}} = \sqrt{A_{\text{event}}/\pi} \tag{3}$$

Similarly, the equivalent pore radius was calculated based on the pore areas, which was in turn determined using the watershed segmentation algorithm (Rabbani et al., 2014). **Figure 10C** clearly shows a large gap between the pore and burst event radii, with the mean pore radius and mean event radius being 0.051 and 1.21 mm, respectively, a difference of $\sim$ 24 fold. The ratio between these radii would presumably translate into a volume difference of $24^3 \sim 14,000$ in a 3D flow (Armstrong et al., 2014). This analysis agrees with the previous estimate based on one single burst event by Li et al. (2017), confirming that burst events are nonlocal and that their influence extends well beyond what is typically considered as Darcy scale. Note that despite the relatively large size of the burst events, they may still, to some extent, be underestimated in this work, due to the finite size of the imaging FOV which could cause an event to be partially cropped at its boundaries (*cf*, inset of **Figure 10C**).

4.2. Effect of Wettability

The impact of wettability on the aforementioned physics and dynamics is now considered by comparing results obtained in the two micromodels with different surface characteristics. Since the micromodel surfaces in the hydrophobic case were modified to be nearly neutral wetting under a weak imbibition condition, capillary forces in this scenario are expected to be largely absent, as confirmed by the bulk pressure measurements shown in **Figure 8A**. Therefore, given that the two cases operated under otherwise identical conditions, any changes in the pore processes and flow pattern can be largely attributed to the effect of capillarity.

The characterization of the fluid–fluid interface is the first focus of this analysis. In multi-phase flow in porous media, many heat, momentum, and mass transfer processes, including shear-induced flow, dissolution, exsolution, and subsequent chemical reactions occur at the fluid–fluid interfaces (Zhang et al., 2011b; Zuo et al., 2013; Liu et al., 2015; Kazemifar et al., 2016; Li et al., 2017), which are strongly affected by wettability. Studying the dynamics of fluid–fluid interfaces is critical for understanding long-term CO_2 solubility and mineral trapping as well as capillary pressure hysteresis (Gray et al., 2019). It is now well accepted that the total fluid–fluid interfaces are due to two distinct contributions: the capillary-associated interfaces and the film-associated interfaces (Porter et al., 2010; Liu et al., 2015; Li et al., 2019), with the former consisting of all non-wetting interfaces in contact with the bulk, mobile wetting phase and wetting phase pendular rings in pore bodies and throats. The latter consist of non-wetting interfaces in contact with the thin wetting films that adhere to the solid grains of pores occupied by the nonwetting phase. For a solid matrix that is highly hydrophilic (i.e., strong drainage), both types of interfaces exist. However, for a neutrally wetting solid matrix (i.e., weak imbibition), only the capillary-associated interfaces are possible (Porter et al., 2010; Kazemifar et al., 2016; Zhao et al., 2016; Li et al., 2017). Additionally, for flow in the 2D micromodels used herein, interfaces are projected to interfacial lines, and interfacial areas become interfacial lengths (Zhang et al., 2011b; Liu et al., 2015).

Figure 11A presents the variations of capillary-associated specific interfacial length, A_{nw}, with CO_2 saturation for both drainage and imbibition. Note that the specific interfacial length, A_{nw} with a unit of mm^{-1}, is simply the interfacial length, a_{nw} with a unit of mm, normalized by the total pore area, in order to account for the finite size of the measurement domain. For the drainage case, the capillary-associated specific interfacial length begins by increasing linearly with CO_2 saturation, up until approximately $S_{CO2} = 0.25$, corresponding to when the CO_2 front arrives at the boundary of the measurement domain (i.e., $r_{\text{Lead}}/R = 1$). This linear behavior is consistent with previous studies and can be understood by considering the following observations. First, for the porous section under study (and this is presumably true for most other porous patterns too), the number of pores within a given sub-domain statistically scales linearly with the number of throats that are associated with the pores in the same sub-domain. Second, for pore invasion during strong drainage, at any moment the majority of the capillary-associated interfaces sits at the throats (as opposed to in the middle of

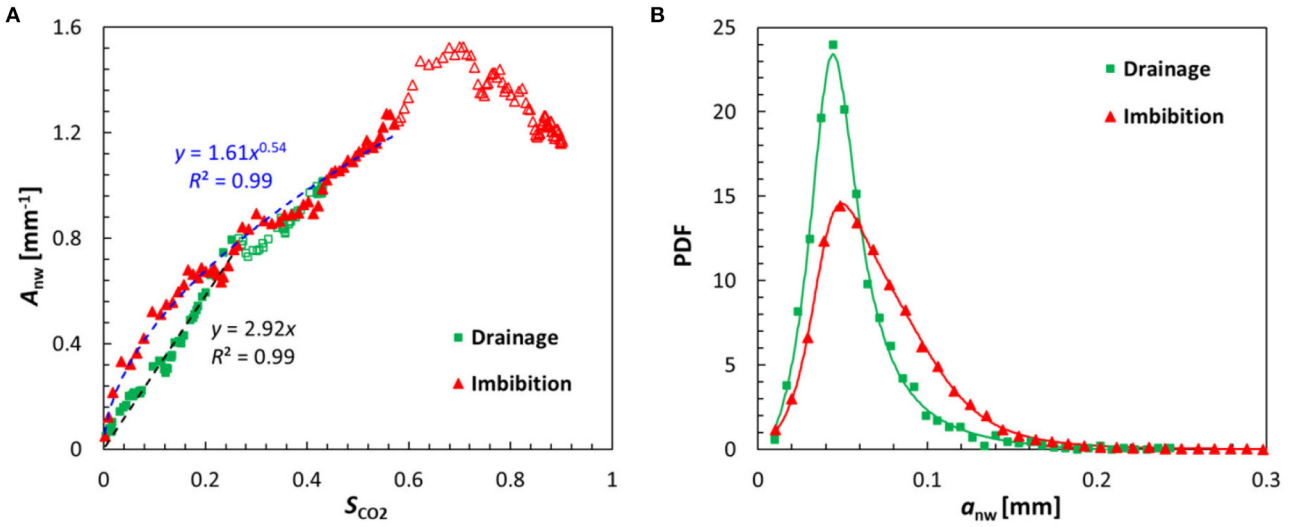

FIGURE 11 | (A) Capillary-associated specific interfacial length functions of CO_2 saturation; dashed lines denote a linear fit to the drainage data and power-law fit to the imbibition data. **(B)** Probability density functions (PDFs) of the individual capillary-associated interfacial lengths under both drainage and imbibition; the symbols represent the original data, whereas the lines are fitted curves using rational polynomial formulas to serve as a visual guide.

the pore spaces). Consequently, for each pore invaded, the number of throats gained is statistically a constant, statistically corresponding to a constant gain of the newly-created interfacial length at those throats. This behavior is further reinforced by capillary fingering during the drainage process, ensuring that the newly created interfaces are separated and sustained by the trapped water ganglia. In fact, as the drainage process continues, the trapped water ganglia slowly drain through wetting films and corner flows, causing the increase of A_{nw} to slow down. This behavior causes the interfacial length growth to depart from a linear relationship, as evident in this result for $S_{CO2} > 0.25$.

This behavior is significantly altered in the weak imbibition case, to yield a relationship $A_{nw} \sim S_{CO2}^{0.54}$, as indicated by the fitted curve. Indeed this nearly 1/2 power law relation is a reflection of the compact displacement pattern during imbibition. The compact and yet relatively axisymmetric pattern caused the fluid–fluid interfaces to form only at the outer rim of the displaced region, with the interior of the region completely occupied by CO_2 (i.e., very few water ganglia). To illustrate this behavior, consider an ideal stable displacement in a circular Hele-Shaw cell, with an injection port in the center similar to our current configuration. The interfacial length is simply the perimeter of the displaced circle, which scales linearly with its radius, whereas the saturation is essentially the area of the same circle, which scales with the square of its radius, leading to a 1/2 power law between interfacial length and saturation. Again, the distinct behaviors of the interfacial length are consistent with the displacement patterns, as illustrated in **Figures 4–7**, and in the imbibition case, is the result of the relative absence of capillarity.

Figure 11B presents the probability density functions (PDFs) of the individual capillary-associated interfacial lengths under both drainage and imbibition conditions. The PDF of the imbibition case is clearly skewed toward larger values compared with the drainage case, indicating that statistically longer interfaces are generated in the former case. As discussed before, fluid interfaces migrated through the porous section via high-speed burst of individual menisci in the drainage case, with a majority of the interfaces remaining static at the throats, which are the narrowest points within the porous section. This leads to a dominance of short interfaces. On the contrary, a majority of interfaces migrated slowly through open pore spaces in the imbibition case, producing long segments of interfaces. Moreover, as shown in **Figure 13**, in the cooperative pore filling process, interfaces merge into longer ones, contributing to the shift of the PDF to larger values.

Besides interfacial length, the flow dynamics are also significantly impacted by the alteration of wettability. **Figures 12A,B** present PDFs of velocity magnitude and direction for single-phase flow and multiphase flows under both drainage and imbibition conditions. The single-phase flow data corresponds to the steady-state water flow prior to the arrival of CO_2 in the porous section, as shown in **Figure 3**, and is presented as a baseline for comparison. As the porous matrix is fully saturated with just one fluid (i.e., no presence of fluid–fluid interfaces) in the single-phase flow, it is unaffected by the wetting conditions of the porous matrix. For multiphase flow, the PDF of velocity magnitude in the drainage case displays a large tail of high velocities, induced by pore-scale burst events, as expected. The highest velocity captured by μPIV in this case is about 50 mm/s, which is almost 50 times larger than U_{bulk} as defined in **Figure 3**. Additionally, the Reynolds number calculated based on this velocity and the average pore diameter is $Re_{water} \sim 5.2$. On the contrary, the PDF of velocity magnitude in the imbibition case resembles the single-phase curve very well, suggesting capillarity and burst events are significantly suppressed, and the statistical behavior of the multiphase flow with little capillarity

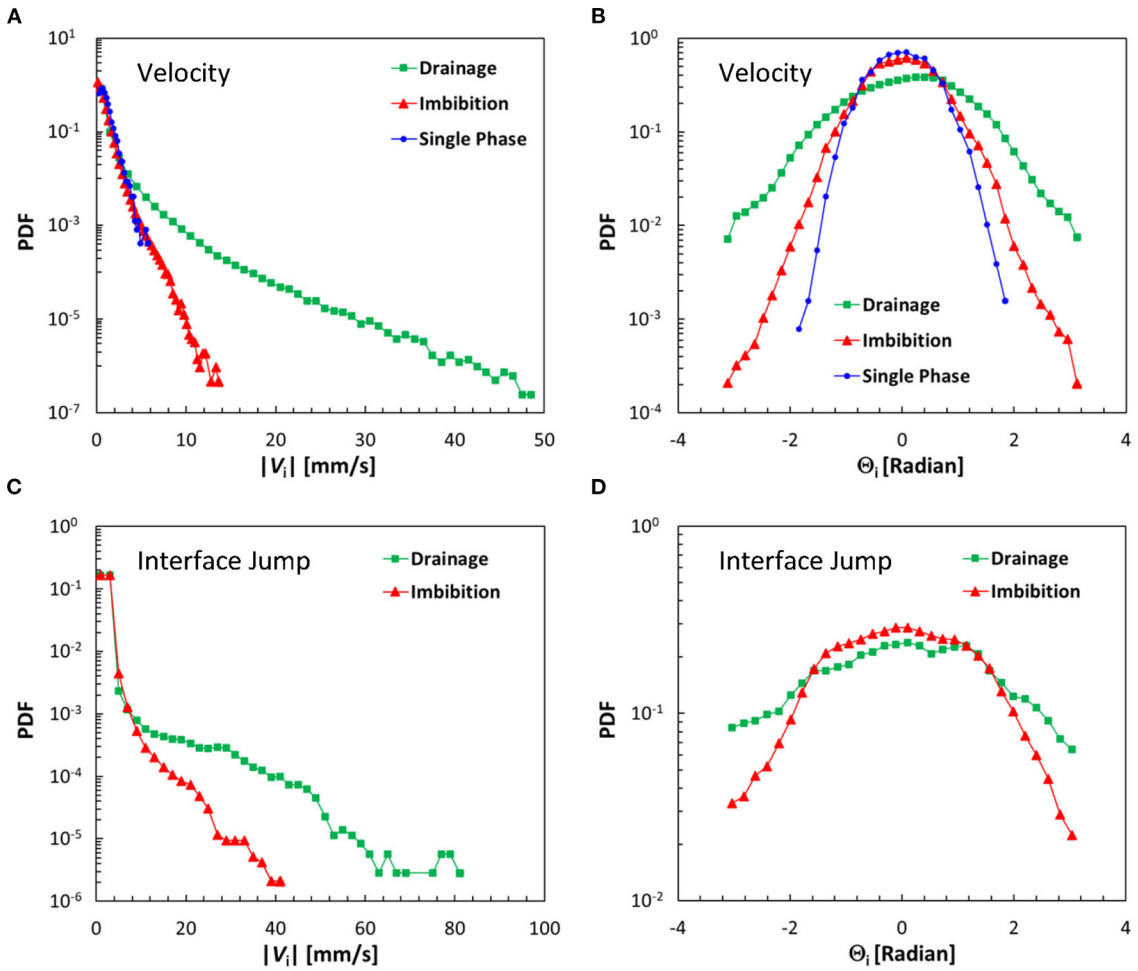

FIGURE 12 | PDFs of velocity **(A)** magnitude and **(B)** direction. The single-phase flow result is based on the data as shown in **Figure 3**, and is presented as a baseline case for comparison purpose. Here, Θ_i is the difference between the polar angle of a velocity vector and the azimuth angle of its corresponding coordinate. PDFs of interface jumps for their **(C)** magnitude and **(D)** direction. Again, Θ_i is the difference between the polar angle of a jump vector and the azimuth angle of its corresponding coordinate.

is quite similar to that of a single-phase flow, as expected. **Figure 12B** presents the PDFs of velocity vector directions for the single-phase flow, drainage and imbibition cases. Here, Θ_i is the difference between the polar angle of a velocity vector and the azimuth angle of its corresponding coordinate. As such, if the flow aligns perfectly with the radial direction, $\Theta_i = 0$. As shown in **Figure 12B**, Θ_i spans over a broad range even for the single-phase flow due to the complex geometry of the porous section where pores and throats are oriented in various directions. Compared with the single-phase flow case, the PDF of the imbibition case is slightly broader, due to the cooperative pore-filling process as will be discussed in relation to **Figure 13**. In cooperative filling, the merging of interfaces induces instantaneous high-speed streams, causing disturbances in the local water flow (note that this is fundamentally different than a burst event during drainage). In fact, this is also the reason why the velocity magnitude PDF of the imbibition case displays a slightly longer tail than the single-phase flow in **Figure 12A**. On the contrary, the PDF of Θ_i in the drainage case is much flatter. This is because the burst events, which can occur in any direction, induce strong disturbance to water flow, causing the velocity vector to deviate even more from the radial direction, and statistically leveling the number of velocity vectors in each direction. These PDFs provide further insight into the drainage processes that are not readily obvious by looking at individual water velocity fields. Moreover, in numerical model validation, it is often difficult to do a pore-by-pore comparison due to random errors and perturbations. As such, statistical comparisons serve as a better option for model validation.

As discussed in § 2.3, there is reason to believe that, occasionally, flow velocities measured herein by μPIV may be underestimated during Haines jumps. In PIV, velocity vectors are determined by tracking the motion of groups of tracer particles between two successive image frames contained in interrogation

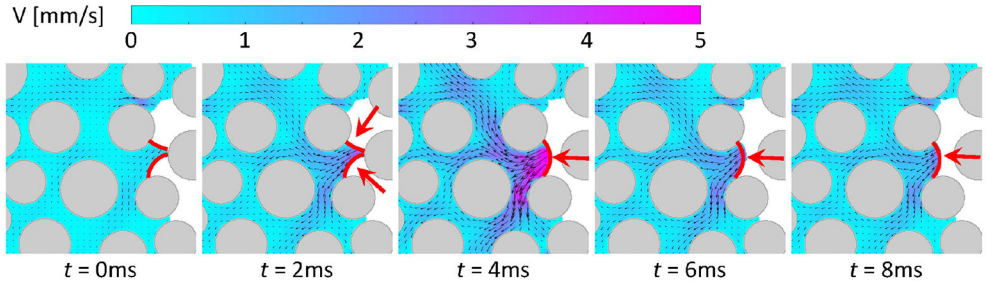

FIGURE 13 | Cooperative filling of a pore during imbibition, with red lines demarcating the interfaces and red arrows denoting the advancing directions of the interfaces.

windows. This approach has limitations near boundaries, particularly moving boundaries. As such, PIV typically fails to correctly evaluate the velocity vectors in the vicinity of morphological change (i.e., moving fluid–fluid interfaces). To partially overcome this limitation and complement the μPIV measurements presented herein, interface movements were also evaluated by directly tracking the interface throughout subsequent image frames (Li et al., 2019). **Figures 12C,D** present PDFs of interface jumps based on their magnitude and jumping direction. Again, Θ_i represents the difference between the polar angle of a jump vector and the azimuth angle of its corresponding coordinate. While the general behavior of these PDFs is very similar to the previous velocity PDFs, a maximum jumping speed of $\sim$ 80 mm/s is observed based on this analysis approach (vs. 50 mm/s based on the μPIV velocity measurements). This new value enables a more accurate estimate of the maximum Reynolds number achieved in these experiments, which is on the CO_2 side of the interface and corresponds to $Re_{CO2} \sim 89$, suggesting the importance of inertial effects during Haines jumps.

As bulk properties and statistical behaviors are rooted in pore-scale processes, the effects of wettability on the pore filling process are assessed, which provides further explanation on why and how bulk flow properties are altered. **Figure 13** presents the invasion of a fixed pore space during imbibition. Unlike what is shown in **Figure 9** under drainage conditions, where pore invasion occurs through one throat at the time, pore invasion under imbibition can simultaneously occur through multiple throats, and is therefore referred to as cooperative filling. At $t = 0$ ms, the two menisci identified migrate from the two sides of a grain and toward the same pore. At $t = 2$ ms, the two menisci begin to touch each other and are ready to merge. At $t = 4$ ms, the two menisci merge into one and cause a release of surface energy, which is partially converted into kinetic energy and significantly accelerates the water behind the newly formed fluid–fluid interface, leading to high-speed water displacement. Note that unlike the drainage case, where the burst of the meniscus is driven by high capillary pressure, here the formation of a new meniscus directly energizes the flow. Once the surface energy release is complete, the water flow quickly diminishes due to high viscous dissipation rate, similar to that in **Figure 9**. This new pore filling mechanism identified herein is caused by the merging of two interfaces. The release of surface energy causes instantaneous high-speed events, that are similar to, yet due to fundamentally different mechanisms, than burst events under drainage conditions. This simple but important mechanism can now be used to explain the observations made in relation to **Figures 11**, **12**. In particular, the interface merging at $t = 4$ ms, is responsible for the PDF shift in **Figure 11**, and the water flow acceleration due to surface energy release at $t = 4$ ms is responsible for the long tail in the PDF of the velocity magnitude during imbibition, compared to the baseline single-phase case, as shown in **Figure 12A**.

4.3. Energy Analysis

As mentioned previously, energy balance analysis can aid the development of predictive models and is particularly insightful for understanding the phenomena impacting capillary filling rules and hysteresis in multiphase flow in porous media. However, kinetic energy is a crucial component of energy balance analysis but has heretofore not been properly evaluated experimentally due to a lack of suitable measurements. Enabled by the spatially and temporally resolved velocity measurements presented herein, a breakdown of the energy budget is presented in order to achieve a better understanding of the importance of each energy contribution and the conversion between them during Haines jumps under drainage conditions as well as interface merging under imbibition conditions.

Following the derivations by Ferrari and Lunati (2014), energy balance in a multiphase flow system in porous media can be described as

$$\frac{\mathrm{d}F}{\mathrm{d}t} + \frac{\mathrm{d}E_\mathrm{k}}{\mathrm{d}t} = P - \Phi, \tag{4}$$

where $F = \int_\Omega \psi \, d\Omega$ is the surface free energy with ψ being the free-energy density, $E_\mathrm{k} = \int_\Omega \frac{1}{2}\rho u^2 \, d\Omega$ is the total kinetic energy, $P = \Delta p Q$ is the work per unit time (i.e., power) done by external forces and Φ is the energy dissipation rate. Herein, E_k can be evaluated based on the instantaneous water velocity field, and $\mathrm{d}F$ can then be calculated according to

$$\mathrm{d}F = \gamma(\mathrm{d}A_\mathrm{nw} + \cos\theta \mathrm{d}A_\mathrm{ns}), \tag{5}$$

where A_nw and A_ns are the fluid–fluid interfacial area and non-wetting-fluid-solid interfacial area, respectively. The power

exerted by external forces can be estimated as

$$P = \Delta pQ = \Delta pV_{\text{pore}}\frac{\mathrm{d}S_{\text{CO2}}}{\mathrm{d}t}. \quad (6)$$

As shown in **Figure 8A**, Δp is positive during drainage but negative during imbibition, meaning that the external work is positive and negative for drainage and imbibition, respectively. According to Equation (5), in the case of drainage, external work is partially converted to kinetic energy and surface energy, with the remainder dissipated by viscosity. On the contrary, in the imbibition case, energy is released from surface energy, which is in turn partially converted to kinetic energy and external work, with the rest dissipated away (Hu et al., 2018). It is worth noting that due to the practical difficulty in measuring pressure in the vicinity of the fluid–fluid interface, Δp here is approximated by the pressure transducer measurements between the inlet and outlet of the micromodel. Because of the small viscous pressure drop in the plumbing lines at such a low flow rate, the pressure transducer offers a good estimate of the actual pressure acting on the interface.

The energy budget for 25 individual burst events was calculated during drainage by excluding the cascaded and overlapped ones from the list created in § 4.1. **Figure 14A** presents surface energy and kinetic energy as a function of external work for these 25 burst events. Both surface energy and kinetic energy vary linearly with external work, with slopes of 0.90 and 0.48 $\times$ 10^{-3}, respectively. These slopes suggest that during burst events, about 90% of the external work is converted to surface energy, and only 0.048% of the external work is converted to kinetic energy. Therefore, although extremely high velocities were observed during burst events, as show by the PDFs in **Figure 12**, the associated kinetic energy is negligibly small. Additionally, this energy balance suggests that about 10% of the external work is dissipated through viscous effects, which is much less than the 64% dissipation observed during drainage in 3D sandstone by Berg et al. (2013). The difference is presumably due to the fact that our 2D micromodel has higher porosity, which reduces the viscous dissipation rate compared with 3D porous media. **Figure 14B** presents a similar energy breakdown for 16 cooperative pore filling events that are similar to what is shown in **Figure 13** during imbibition. Although the different forms of energy are less correlated for this case, presumably due to the relatively high measurement uncertainty, nevertheless, based on order of magnitude, ~20% of the released surface energy is converted into external work, with ~80% of it being dissipated through viscous effects. Again the conversion of kinetic energy from released surface energy is <0.1%. This important finding validates the assumption made by previous studies that the change in kinetic energy of such flow systems is negligible even during Haines jumps and cooperative pore filling events (Berg et al., 2013; Hu et al., 2018).

5. CONCLUSION

In this study, a high-speed μPIV technique was employed that captured spatially and temporally resolved dynamics of multiphase flow of CO_2 and water in 2D microfluidic porous media under reservoir-relevant conditions for both strong drainage and weak imbibition. When CO_2 displaces water in a hydrophilic micromodel (i.e., drainage), unstable capillary fingering occurs along, normal to, and opposing the bulk flow direction. Under these conditions, the pore flow is dominated by successive pore-scale burst events (i.e., Haines jumps), leading to a high degree of fluctuation in the instantaneous water velocity fields. When the micromodel surface was altered to be nearly neutral wetting, consistent with weak imbibition conditions, flow instability and fluctuation were significantly suppressed, leading to more compact and axisymmetric displacement patterns with

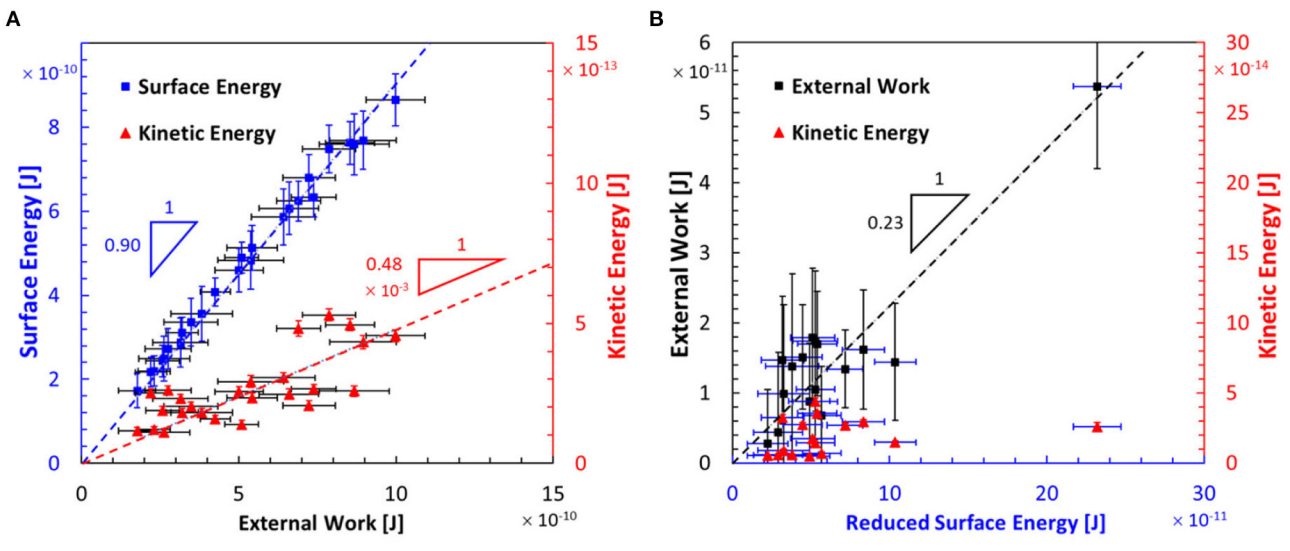

FIGURE 14 | (A) Surface energy and kinetic energy as a function of external work for the largest 25 burst events during the drainage process. **(B)** External energy and kinetic energy as a function of reduced surface energy for 16 selected pore filling events during the imbibition process.

narrower flow velocity distribution, consistent with existing studies.

Leveraging the unique spatially and temporally resolved datasets, detailed analyses were performed on the pore-scale flow dynamics, flow statistics, the effects of capillarity, and flow energy balance, which has revealed valuable insights, including:

1. The drainage process is dominated by a succession of Haines jumps, which cause extremely high velocities, typically two orders of magnitude higher than the bulk velocity, resulting in $Re_{CO2} \sim \mathcal{O}(100)$, confirming the importance of inertial effects.
2. Haines jump duration ranges from 4 ms to approximately 60 ms in the current micromodels, with the shortest burst events corresponding to individual isolated events and the longer duration events corresponding to burst events occurring in a cascading manner over multiple pores and throats. The instantaneous water velocity fields indicate that it is possible for one event to cascade over 16 throats.
3. The radius of influence of Haines jumps is estimated to be as large as 1.21 mm, a $\sim$ 24 fold increase over the mean pore radius, 0.051 mm, suggesting that burst events are highly nonlocal and their influence extends up to and perhaps beyond what is typically considered as Darcy scale in these applications.
4. Modifying the wettability of the porous matrix, from being strongly hydrophilic to intermediate wetting, fundamentally and dramatically changes the behavior of the displacement process. In particular, doing so mitigates the flow instability and enhances displacement efficiency. Due to a reduction of capillarity and thus instability, the maximum flow speed in the imbibition case is much lower.
5. Direct observation of the pore filling behavior on an individual pore basis reveals a significant alteration of the pore filling mechanisms during drainage and imbibition. While the former typically features a burst event, which occurs only at one of the several throats connecting a pore, the latter is typically dominated by a cooperative filling mechanism, which involves simultaneous invasion of a pore from multiple throats. This mechanism leads to merging of two interfaces and a subsequent release of the surface energy, inducing instantaneous high-momentum flow events that appear similar, but are fundamentally different from, a burst event.
6. Energy balance analyses indicate that the conversion efficiency between surface energy and external work is as high as 90%, with the remaining energy dissipated instantaneously. Moreover, kinetic energy is disproportionately smaller than surface energy and external work (by more than three orders of magnitude), despite the extremely high flow velocities that occur during flow drainage. This finding validates the assumption made in previous studies that the change in kinetic energy is negligible during Haines jumps and cooperative pore filling events.

To our knowledge, the observations reported herein and afforded by the innovative experimental protocol used represent the first of their kind. They have advanced our fundamental understanding of these flow processes and will hopefully contribute to the next generation of pore-scale model development and validation.

DATA AVAILABILITY STATEMENT

The original contributions presented in the study are included in the article/**Supplementary Material**, further inquiries can be directed to the corresponding author/s.

AUTHOR CONTRIBUTIONS

KTC, GB, and YL conceived and planned the experiments. YL and FK built the apparatus and carried out the experiments. YL, GB, FK, RSM, and KTC contributed to the data processing, analysis and interpretation of the results. RSM contributed to literature review, micromodel characterization and revision of the manuscript. YL took the lead in writing the manuscript. All authors provided critical feedback and helped shape the research, analysis and manuscript.

FUNDING

This work was jointly funded by the U.S. Department of Energy, Office of Science, BES under award SC0C12504, the International Institute for Carbon-Neutral Energy Research (WPI-I2CNER) sponsored by the Japanese Ministry of Education, Culture, Sports, Science and Technology, and the Faculty Excellence Grants at Montana State University. This work was performed in part at the Montana Nanotechnology Facility, an NNCI facility supported by NSF Grant ECCS-1542210, and with support by the Murdock Charitable Trust.

ACKNOWLEDGMENTS

YL thanks the Faculty Excellence Grants and the Norm Asbjornson College of Engineering at Montana State University for their support.

SUPPLEMENTARY MATERIAL

The Supplementary Material for this article can be found online at: https://www.frontiersin.org/articles/10.3389/frwa.2021.710370/full#supplementary-material

REFERENCES

Anderson, W. G. (1987). Wettability literature survey-part 6: the effects of wettability on waterflooding. *J. Petrol. Technol.* 39, 1–605. doi: 10.2118/16471-PA

Armstrong, R. T., and Berg, S. (2013). Interfacial velocities and capillary pressure gradients during Haines jumps. *Phys. Rev. E* 88, 043010. doi: 10.1103/PhysRevE.88.043010

Armstrong, R. T., Ott, H., Georgiadis, A., Rücker, M., Schwing, A., and Berg, S. (2014). Subsecond pore-scale displacement processes and

relaxation dynamics in multiphase flow. *Water Resour. Res.* 50, 9162–9176. doi: 10.1002/2014WR015858

Bachu, S. (2000). Sequestration of CO_2 in geological media: Criteria and approach for site selection in response to climate change. *Energy Conversion Manag.* 41, 953–970. doi: 10.1016/S0196-8904(99)00149-1

Bazylak, A. (2009). Liquid water visualization in PEM fuel cells: a review. *Int. J. Hydrogen Energy* 34, 3845–3857. doi: 10.1016/j.ijhydene.2009.02.084

Berg, S., Ott, H., Klapp, S. A., Schwing, A., Neiteler, R., Brussee, N., et al. (2013). Real-time 3D imaging of haines jumps in porous media flow. *Proc. Natl. Acad. Sci. U.S.A.* 110, 3755–3759. doi: 10.1073/pnas.1221373110

Blois, G., Barros, J. M., and Christensen, K. T. (2015). A microscopic particle image velocimetry method for studying the dynamics of immiscible liquid-liquid interactions in a porous micromodel. *Microfluid Nanofluidics* 18, 1391–1406. doi: 10.1007/s10404-014-1537-1

Broseta, D., Tonnet, N., and Shah, V. (2012). Are rocks still water-wet in the presence of dense CO_2 or H_2S? *Geofluids* 12, 280–294. doi: 10.1111/j.1468-8123.2012.00369.x

Chang, C., Kneafsey, T. J., Wan, J., Tokunaga, T. K., and Nakagawa, S. (2020). Impacts of mixed-wettability on brine drainage and supercritical CO_2 storage efficiency in a 2.5-d heterogeneous micromodel. *Water Resour. Res.* 56:e2019WR026789. doi: 10.1029/2019WR026789

Chen, Y., Li, Y., Valocchi, A. J., and Christensen, K. T. (2018). Lattice Boltzmann simulations of liquid CO_2 displacing water in a 2D heterogeneous micromodel at reservoir pressure conditions. *J. Contam Hydrol.* 212:14–27. doi: 10.1016/j.jconhyd.2017.09.005

Chen, Y.-F., Fang, S., Wu, D.-S., and Hu, R. (2017). Visualizing and quantifying the crossover from capillary fingering to viscous fingering in a rough fracture. *Water Resour. Res.* 53, 7756–7772. doi: 10.1002/2017WR021051

Chomsurin, C., and Werth, C. J. (2003). Analysis of pore-scale nonaqueous phase liquid dissolution in etched silicon pore networks. *Water Resour. Res.* 39. doi: 10.1029/2002WR001643

Cottin, C., Bodiguel, H., and Colin, A. (2011). Influence of wetting conditions on drainage in porous media: a microfluidic study. *Phys. Rev. E* 84:026311. doi: 10.1103/PhysRevE.84.026311

Dawson, H. E., and Roberts, P. V. (1997). Influence of viscous, gravitational, and capillary forces on DNAPL saturation. *Groundwater* 35, 261–269. doi: 10.1111/j.1745-6584.1997.tb00083.x

DiCarlo, D. A., Cidoncha, J. I., and Hickey, C. (2003). Acoustic measurements of pore-scale displacements. *Geophys. Res. Lett.* 30. doi: 10.1029/2003GL017811

Fakhari, A., Li, Y., Bolster, D., and Christensen, K. T. (2018). A phase-field lattice Boltzmann model for simulating multiphase flows in porous media: application and comparison to experiments of CO_2 sequestration at pore scale. *Adv. Water Resour.* 114, 119–134. doi: 10.1016/j.advwatres.2018.02.005

Ferrari, A., and Lunati, I. (2014). Inertial effects during irreversible meniscus reconfiguration in angular pores. *Adv.Water Resour.* 74, 1–13. doi: 10.1016/j.advwatres.2014.07.009

Gray, W. G., Bruning, K., and Miller, C. T. (2019). Non-hysteretic functional form of capillary pressure in porous media. *J. Hydraulic Res.* 57, 747–759. doi: 10.1080/00221686.2019.1671520

Gunter, W., Wiwehar, B., and Perkins, E. (1997). Aquifer disposal of CO_2-rich greenhouse gases: extension of the time scale of experiment for CO_2-sequestering reactions by geochemical modelling. *Mineral. Petrol.* 59, 121–140. doi: 10.1007/BF01163065

Haines, W. B. (1930). Studies on the physical properties of soil. V. The hysteresis effect in capillary properties, and the modes of moisture distribution associated therewith. *J. Agric. Sci.* 20, 97–116. doi: 10.1017/S002185960008864X

Holtzman, R., and Segre, E. (2015). Wettability stabilizes fluid invasion into porous media via nonlocal, cooperative pore filling. *Phys. Rev. Lett.* 115, 164501. doi: 10.1103/PhysRevLett.115.164501

Hu, R., Wan, J., Kim, Y., and Tokunaga, T. K. (2017). Wettability effects on supercritical CO_2-brine immiscible displacement during drainage: Pore-scale observation and 3d simulation. *Int. J. Greenhouse Gas Control* 60, 129–139. doi: 10.1016/j.ijggc.2017.03.011

Hu, R., Wu, D.-S., Yang, Z., and Chen, Y.-F. (2018). Energy conversion reveals regime transition of imbibition in a rough fracture. *Geophys. Res. Lett.* 45, 8993–9002. doi: 10.1029/2018GL079302

Huppert, H. E., and Neufeld, J. A. (2014). The fluid mechanics of carbon dioxide sequestration. *Annu. Rev. Fluid Mech.* 46, 255–272. doi: 10.1146/annurev-fluid-011212-140627

Iglauer, S., Fernø, M., Shearing, P., and Blunt, M. (2012). Comparison of residual oil cluster size distribution, morphology and saturation in oil-wet and water-wet sandstone. *J. Colloid Interface Sci.* 375, 187–192. doi: 10.1016/j.jcis.2012.02.025

Ilin, E., Li, Y., Colla, E. V., Christensen, K. T., Sahimi, M., Marchevsky, M., et al. (2020). Nanoscale detection of metastable states in porous and granular media. *J. Appl. Phys.* 127, 024901. doi: 10.1063/1.5135321

Jafari, M., and Jung, J. (2017). Direct measurement of static and dynamic contact angles using a random micromodel considering geological CO_2 sequestration. *Sustainability* 9, 2352. doi: 10.3390/su9122352

Karadimitriou, N., Hassanizadeh, S., Joekar-Niasar, V., and Kleingeld, P. (2014). Micromodel study of two-phase flow under transient conditions: quantifying effects of specific interfacial area. *Water Resour. Res.* 50, 8125–8140. doi: 10.1002/2014WR015388

Kazemifar, F., Blois, G., Kyritsis, D. C., and Christensen, K. T. (2015). A methodology for velocity field measurement in multiphase high-pressure flow of CO_2 and water in micromodels. *Water Resour. Res.* 51, 3017–3029. doi: 10.1002/2014WR016787

Kazemifar, F., Blois, G., Kyritsis, D. C., and Christensen, K. T. (2016). Quantifying the flow dynamics of supercritical CO_2-water displacement in a 2D porous micromodel using fluorescent microscopy and microscopic PIV. *Adv. Water Resour.* 95, 352–368. doi: 10.1016/j.advwatres.2015.05.011

Kazemifar, F., and Kyritsis, D. C. (2014). Experimental investigation of near-critical CO_2 tube-flow and Joule-Thompson throttling for carbon capture and sequestration. *Exp. Therm. Fluid Sci.* 53, 161–170. doi: 10.1016/j.expthermflusci.2013.11.026

Koide, H., Tazaki, Y., Noguchi, Y., Nakayama, S., Iijima, M., Ito, K., et al. (1992). Subterranean containment and long-term storage of carbon dioxide in unused aquifers and in depleted natural gas reservoirs. *Energy Conversion Manag.* 33, 619–626. doi: 10.1016/0196-8904(92)90064-4

Law, D. H.-S., and Bachu, S. (1996). Hydrogeological and numerical analysis of co2 disposal in deep aquifers in the alberta sedimentary basin. *Energy Conversion Manag.* 37, 1167–1174. doi: 10.1016/0196-8904(95)00315-0

Lenormand, R., Touboul, E., and Zarcone, S. (1988). Numerical models and experiments on immiscible displacements in porous media. *J. Fluid Mech.* 189:165–187. doi: 10.1017/S0022112088000953

Li, Y., Blois, G., Kazemifar, F., and Christensen, K. T. (2019). High-speed quantification of pore-scale multiphase flow of water and supercritical CO_2 in 2-D heterogeneous porous micromodels: flow regimes and interface dynamics. *Water Resour. Res.* 55, 3758–3779. doi: 10.1029/2018WR024635

Li, Y., Blois, G., Kazemifar, F., and Christensen, K. T. (2021). A particle-based image segmentation method for phase separation and interface detection in piv images of immiscible multiphase flow. *Meas. Sci. Technol.* 32, 095208. doi: 10.1088/1361-6501/abf0dc

Li, Y., Grigoriev, R., and Yoda, M. (2014). Experimental study of the effect of noncondensables on buoyancy-thermocapillary convection in a volatile low-viscosity silicone oil. *Phys. Fluids* 26, 122112. doi: 10.1063/1.4904870

Li, Y., Kazemifar, F., Blois, G., and Christensen, K. T. (2017). Micro-PIV measurements of multiphase flow of water and liquid CO_2 in 2-D heterogeneous porous micromodels. *Water Resour. Res.* 53, 6178–6196. doi: 10.1002/2017WR020850

Li, Y., and Yoda, M. (2014). Convection driven by a horizontal temperature gradient in a confined aqueous surfactant solution: the effect of noncondensables. *Exp. Fluids* 55, 1–11. doi: 10.1007/s00348-013-1663-7

Li, Y., and Yoda, M. (2016). An experimental study of buoyancy-marangoni convection in confined and volatile binary fluids. *Int. J. Heat Mass. Transf.* 102, 369–380. doi: 10.1016/j.ijheatmasstransfer.2016.06.004

Linstrom, P. J., and Mallard, W. G. (2001). The NIST chemistry webbook: a chemcial data resource on the internet. *J. Chem. Eng. Data* 46, 1059–1063. doi: 10.1021/je000236i

Liu, H., Zhang, Y., and Valocchi, A. J. (2015). Lattice boltzmann simulation of immiscible fluid displacement in porous media: Homogeneous versus heterogeneous pore network. *Phys. Fluids* 27, 052103. doi: 10.1063/1.4921611

Liu, Y., Nolte, D., and Pyrak-Nolte, L. (2011). Hysteresis and interfacial energies in smooth-walled microfluidic channels. *Water Resour. Res*. 47. doi: 10.1029/2010WR009541

Mehmani, Y., and Balhoff, M. T. (2015). Mesoscale and hybrid models of fluid flow and solute transport. *Rev. Mineral. Geochem*. 80, 433–459. doi: 10.2138/rmg.2015.80.13

Moebius, F., and Or, D. (2014). Inertial forces affect fluid front displacement dynamics in a pore-throat network model. *Phys. Rev. E* 90:023019. doi: 10.1103/PhysRevE.90.023019

Morrow, N. R. (1970). Physics and thermodynamics of capillary action in porous media. *Ind. Eng. Chem*. 62, 32–56. doi: 10.1021/ie50726a006

Morrow, N. R. (1990). Wettability and its effect on oil recovery. *J. Petrol. Technol*. 42, 1–476. doi: 10.2118/21621-PA

Pacala, S., and Socolow, R. (2004). Stabilization wedges: Solving the climate problem for the next 50 years with current technologies. *Science* 305, 968–972. doi: 10.1126/science.1100103

Perrin, J.-C., and Benson, S. (2010). An experimental study on the influence of sub-core scale heterogeneities on CO_2 distribution in reservoir rocks. *Transp. Porous Media* 82, 93–109. doi: 10.1007/s11242-009-9426-x

Porter, M. L., Wildenschild, D., Grant, G., and Gerhard, J. I. (2010). Measurement and prediction of the relationship between capillary pressure, saturation, and interfacial area in a napl-water-glass bead system. *Water Resour. Res*. 46. doi: 10.1029/2009WR007786

Rabbani, A., Jamshidi, S., and Salehi, S. (2014). An automated simple algorithm for realistic pore network extraction from micro-tomography images. *J. Petrol. Sci. Eng*. 123, 164–171. doi: 10.1016/j.petrol.2014.08.020

Roman, S., Soulaine, C., AlSaud, M. A., Kovscek, A., and Tchelepi, H. (2016). Particle velocimetry analysis of immiscible two-phase flow in micromodels. *Adv. Water Res*. 95, 199–211. doi: 10.1016/j.advwatres.2015.08.015

Salathiel, R. (1973). Oil recovery by surface film drainage in mixed-wettability rocks. *J. Petrol. Technol*. 25, 1–216. doi: 10.2118/4104-PA

Sedev, R., Budziak, C., Petrov, J., and Neumann, A. (1993). Dynamic contact angles at low velocities. *J. Colloid Interface Sci*. 159, 392–399. doi: 10.1006/jcis.1993.1338

Seyyedi, M., Sohrabi, M., and Farzaneh, A. (2015). Investigation of rock wettability alteration by carbonated water through contact angle measurements. *Energy Fuels* 29, 5544–5553. doi: 10.1021/acs.energyfuels.5b01069

Sheng, Q., and Thompson, K. (2013). Dynamic coupling of pore-scale and reservoir-scale models for multiphase flow. *Water Resour. Res*. 49, 5973–5988. doi: 10.1002/wrcr.20430

Simjoo, M., Dong, Y., Andrianov, A., Talanana, M., and Zitha, P. (2013). CT scan study of immiscible foam flow in porous media for enhancing oil recovery. *Ind. Eng. Chem. Res*. 52, 6221–6233. doi: 10.1021/ie300603v

Song, Y., Zhu, N., Zhao, Y., Liu, Y., Jiang, L., and Wang, T. (2013). Magnetic resonance imaging study on near miscible supercritical CO_2 flooding in porous media. *Phys. Fluids* 25, 053301. doi: 10.1063/1.4803663

Trojer, M., Szulczewski, M. L., and Juanes, R. (2015). Stabilizing fluid-fluid displacements in porous media through wettability alteration. *Phys. Rev. Appl*. 3:054008. doi: 10.1103/PhysRevApplied.3.054008

Tsuji, T., Jiang, F., and Christensen, K. T. (2016). Characterization of immiscible fluid displacement processes with various capillary numbers and viscosity ratios in 3d natural sandstone. *Adv. Water Resour*. 95, 3–15. doi: 10.1016/j.advwatres.2016.03.005

Wang, S., and Tokunaga, T. K. (2015). Capillary pressure-saturation relations for supercritical CO_2 and brine in limestone/dolomite sands: implications for geologic carbon sequestration in carbonate reservoirs. *Environ. Sci. Technol*. 49, 7208–7217. doi: 10.1021/acs.est.5b00826

Xu, R., Li, R., Ma, J., and Jiang, P. (2015). CO_2 exsolution from CO_2 saturated water: Core-scale experiments and focus on impacts of pressure variations. *Environ. Sci. Technol*. 49, 14696–14703. doi: 10.1021/acs.est.5b03826

Yamabe, H., Tsuji, T., Liang, Y., and Matsuoka, T. (2014). Lattice Boltzmann simulations of supercritical CO_2-water drainage displacement in porous media: CO_2 saturation and displacement mechanism. *Environ. Sci. Technol*. 49, 537–543. doi: 10.1021/es504510y

Zacharoudiou, I., Chapman, E. M., Boek, E. S., and Crawshaw, J. P. (2017). Pore-filling events in single junction micro-models with corresponding lattice boltzmann simulations. *J. Fluid Mech*. 824, 550–573. doi: 10.1017/jfm.2017.363

Zhang, C., Oostrom, M., Grate, J. W., Wietsma, T. W., and Warner, M. G. (2011a). Liquid CO_2 displacement of water in a dual-permeability pore network micromodel. *Environ. Sci. Technol*. 45, 7581–7588. doi: 10.1021/es201858r

Zhang, C., Oostrom, M., Wietsma, T. W., Grate, J. W., and Warner, M. G. (2011b). Influence of viscous and capillary forces on immiscible fluid displacement: pore-scale experimental study in a water-wet micromodel demonstrating viscous and capillary fingering. *Energy Fuels* 25, 3493–3505. doi: 10.1021/ef101732k

Zhao, B., MacMinn, C. W., and Juanes, R. (2016). Wettability control on multiphase flow in patterned microfluidics. *Proc. Natl. Acad. Sci. U.S.A*. 13, 10251–10256. doi: 10.1073/pnas.1603387113

Zuo, L., Zhang, C., Falta, R. W., and Benson, S. M. (2013). Micromodel investigations of CO_2 exsolution from carbonated water in sedimentary rocks. *Adv. Water Resour*. 53, 188–197. doi: 10.1016/j.advwatres.2012.11.004

Conflict of Interest: The authors declare that the research was conducted in the absence of any commercial or financial relationships that could be construed as a potential conflict of interest.

Publisher's Note: All claims expressed in this article are solely those of the authors and do not necessarily represent those of their affiliated organizations, or those of the publisher, the editors and the reviewers. Any product that may be evaluated in this article, or claim that may be made by its manufacturer, is not guaranteed or endorsed by the publisher.

frontiers in Water

ORIGINAL RESEARCH
published: 19 November 2021
doi: 10.3389/frwa.2021.766338

Modeling Longitudinal Dispersion in Variable Porosity Porous Media: Control of Velocity Distribution and Microstructures

Philippe Gouze[1]*, *Alexandre Puyguiraud*[2], *Thierry Porcher*[1] and *Marco Dentz*[2]

[1] Geoscience Montpellier, CNRS, Université de Montpellier, Montpellier, France, [2] Spanish National Research Council, Institute of Environmental Assessment and Water Research (IDAEA-CSIC), Barcelona, Spain

Hydrodynamic dispersion process in relation with the geometrical properties of the porous media are studied in two sets of 6 porous media samples of porosity θ ranging from 0.1 to 0.25. These two sets of samples display distinctly different evolutions of the microstructures with porosity but share the same permeability trend with porosity. The methodology combines three approaches. First, numerical experiments are performed to measure pre-asymptotic to asymptotic dispersion from diffusion-controlled to advection-controlled regime using Time-Domain Random Walk solute transport simulations. Second, a porosity-equivalent network of bonds is extracted in order to measure the geometrical properties of the samples. Third, the results of the direct numerical simulations are interpreted as a Continuous Time Random Walk (CTRW) process controlled by the flow speed distribution and correlation. These complementary modeling approaches allow evaluating the relation between the parameters of the conceptual transport process embedded in the CTRW model, the flow field properties and the pore-scale geometrical properties. The results of the direct numerical simulations for all the 12 samples show the same scaling properties of the mean flow distribution, the first passage time distribution and the asymptotic dispersion vs. the Péclet number than those predicted by the CTRW model. It allows predicting the asymptotic dispersion coefficient D^* from $Pe = 1$ to the largest values of Pe expected for laminar flow in natural environments ($Pe \approx 4{,}000$). $D^* \propto Pe^{2-\alpha}$ for $Pe \geq Pe^{crit}$, where α can be inferred from the Eulerian flow distribution and Pe^{crit} depends on porosity. The Eulerian flow distribution is controlled by the distribution of fractions of fluid flowing at each of the pore network nodes and thus is determined mainly by the distribution of the throat radius and the coordination number. The later scales with the number of throats per unit volume independently on the porosity. The asymptotic dispersion coefficient D^* decreases when porosity increases for all Péclet values larger than 1 due to the increase with porosity of both α and the flow speed decorrelation length.

Keywords: dispersion, continuous time random walk, microstructure, velocity distribution, pore network

OPEN ACCESS

Edited by:
Carl Fredrik Berg, Norwegian University of Science and Technology, Norway

Reviewed by:
Kalyana Babu Nakshatrala, University of Houston, United States
Giuseppe Francesco Cesare Lama, University of Naples Federico II, Italy

***Correspondence:**
Philippe Gouze
Philippe.Gouze@Umontpellier.fr

Specialty section:
This article was submitted to Water and Critical Zone, a section of the journal Frontiers in Water

Received: *28 August 2021*
Accepted: *22 October 2021*
Published: *19 November 2021*

Citation:
Gouze P, Puyguiraud A, Porcher T and Dentz M (2021) Modeling Longitudinal Dispersion in Variable Porosity Porous Media: Control of Velocity Distribution and Microstructures. Front. Water 3:766338. doi: 10.3389/frwa.2021.766338

1. INTRODUCTION

Modeling transport of solute in porous media is a prerequisite for many environmental and engineering applications, ranging from aquifers contaminant risk assessment to industrial reactors, filters and batteries design. The solutes can be pollutants, reactants and products involved in solute-solute or solute-mineral reactions, but also (bio-)nanoparticles or nutriments involved in the growth of bio-mass. The mechanism under consideration is the spatial dispersion which leads to the spreading and the mixing of dissolved chemicals, thus controlling the potential reactions in the flowing fluid and between the fluid and the porous media (Bear, 1972; Brenner and Edwards, 1993; Dentz et al., 2011). The dispersion process has been, and still is, a largely studied topic in the field of geosciences because rocks at depth are, as a general rule, porous media saturated with fluid(s) that move due to natural or artificial pressure gradients, and display a large spectrum of heterogeneities. In all these domains, reliable predictive models that can be parameterized by direct measurements are necessary, for example, to monitor and assess risks linked to the use of underground water resources, or in the course of industrial operations, such as hydrocarbon exploitation and CO_2 or underground nuclear waste storage.

Hydrodynamic dispersion is the macroscopic result of the mass transfers by diffusion and advection that occurs at the pore scale (Whitaker, 1967; Sahimi, 2011; De Anna et al., 2013). Together, diffusion and advection of solute produce a large spectrum of dispersion features because (natural) porous media display complex structures inducing a large diversity of velocity fields, and thus distinctly different speed distributions and spatial correlations. Probably the most obvious behavior that illustrates the complexity of dispersion mechanisms in porous media is the variably-lasting pre-asymptotic dispersion regime that cannot be modeled by a single Fickian dispersion coefficient. Pre-asymptotic, or non-Fickian, dispersion is commonly observed in laboratory experiments (Moroni and Cushman, 2001; Levy and Berkowitz, 2003; Seymour et al., 2004; Morales et al., 2017; Carrel et al., 2018; Souzy et al., 2020), and numerical simulations (Bijeljic et al., 2011, 2013; De Anna et al., 2013; Icardi et al., 2014; Kang et al., 2014; Li et al., 2018; Puyguiraud et al., 2019c). It is characterized by heavy-tailed arrival time distributions $f_t(t)$ and super-diffusive growth of the longitudinal displacement variance $\sigma^2(t)$. For a given porous medium, the duration of the non-Fickian regime is controlled by solute particles that move the slowest, which emphasizes the determinant role of both the regions where the velocity is low and the tortuosity of the flow paths. Asymptotically, dispersion converges toward Fickian behavior, characterized by the constant longitudinal dispersion coefficient D^* (Bear, 1972; Brenner and Edwards, 1993).

Evaluating the longitudinal asymptotic dispersion coefficient D^* is a fundamental issue, because most operational modeling tools have been constructed around the Fickian advection-dispersion equation that reads for transport in the direction of the mean flow, here the z-direction (Bear, 1972):

$$\frac{\partial \theta c(z,t)}{\partial t} - \frac{\partial}{\partial z}\left[\theta D^* \frac{\partial c(z,t)}{\partial z} + u_z(z) c(z,t)\right] = 0, \qquad (1)$$

where c is the solute concentration, θ is the connected porosity, $u_z = \theta\langle \mathrm{v_z}\rangle$ denotes Darcy's velocity, with $\langle \mathrm{v_z}\rangle$ being the mean pore velocity.

Many experimental studies and mathematical developments on dispersion using mainly simple porous media have been performed since the pioneering works of Danckwerts (1953). The reader will find an exhaustive review of the different results and models of both longitudinal and transverse dispersion in Delgado (2006). A main well-observed feature of longitudinal dispersion D^* is its non-linear increase with the mean flow velocity. It is recognized since the pioneering works of Saffman (1959) and then Bear (1972). It is generally expressed in terms of D^*/d_m vs. the Péclet number $Pe = \langle v_e\rangle \ell/d_m$, where ℓ is a characteristic length, d_m is the molecular diffusion coefficient and $\langle v_e\rangle$ is the mean Eulerian flow speed ($v_e = \sqrt{\mathrm{v_x^2} + \mathrm{v_y^2} + \mathrm{v_z^2}}$, with v_i denoting the flow velocity component i, see section 2.2). Simulations in networks of constant velocity tubes (Sahimi and Imdakm, 1988) of radius r following distributions such as $P(r) \propto re^{-r^2}$ (Chatzis and Dullien, 1985) indicated a relation of the form

$$D^*/d_m \propto Pe^{\beta}, \qquad (2)$$

with $\beta = 1.2 \mp 0.1$ (Sahimi, 2011), while for instance $\beta = 2$ in a single tube (Taylor, 1953). For infinite Pe, experimental particle tracking results (e.g, Souzy et al., 2020) give the relation $D^*/d_m \approx Pe$, where the characteristic length ℓ is of the order of the pore length. However, it is worth noticing that in Souzy et al. (2020)'s experiments the lowest velocities cannot be measured because they use finite-size particles that cannot access to the vicinity of the solid. Interestingly, the behavior (Equation 2) with $\beta \simeq 1.2$ was cited in numerous studies concerning bead-packs and homogeneous sand-packs for intermediate Péclet numbers (Pfannkuch, 1963; Han et al., 1985; Sahimi et al., 1986; Seymour and Callaghan, 1997; Bijeljic et al., 2004). For instance, particle tracking simulations in pore-networks reported in Bijeljic and Blunt (2006) gave $\beta = 1.2$, for $Pe < 400$ and $\beta = 1$, for $Pe > 400$. Conversely, similar numerical simulations (using random walk particle tracking) performed by Puyguiraud et al. (2021) using digitized images of consolidated sandstone, gave a value of $\beta = 1.65$ for $10 \leq Pe \leq 10^5$. The few experimental data on rocks (obviously more heterogeneous than bead-packs) displayed a broader range of behaviors; for example Kinzel and Hill (1989) reported $1.30 \leq \beta \leq 1.33$. However, it is worth noticing that evaluating dispersion in rocks, for a large range of Pe values, either at laboratory or field scale from tracer tests is challenging. For instance, controlling the boundary conditions and verifying that the tracer is conservative are some of the known issues that may introduce errors in the estimation. Yet, the main issue is probably linked to the fact that, by definition, the experimental results are interpreted using the Fickian model, whereas it is difficult to prove that dispersion is asymptotic without being able

to measure the tracer breakthrough curves over several orders of magnitude in order to capture the low speed fraction of the solute transport (Gouze et al., 2008). We will show in section 3.4 that measuring asymptotic dispersion for large values of *Pe* in natural porous media is in fact virtually impossible using cm- or even meter-scale experiments.

While measuring dispersion experimentally is burdensome, modeling approaches are now mature to perform numerical experiments. Direct numerical simulations (DNS) are unique tools for investigating both the pre-asymptotic and the asymptotic behavior in a common frame. They can be used to accurately measure D^*, but also to study the mechanisms that produce dispersion in relation with the measurable (average) properties of the material, and to test upscaling theories. Recent works (Bijeljic and Blunt, 2006, 2007; De Anna et al., 2013; Puyguiraud et al., 2020, 2021) showed that hydrodynamic transport in porous media can be adequately conceptualized and modeled by a continuous time random walk (CTRW) that models streamwise transport through particle transitions over fixed spatial distance with a transition time given by the local flow speed and diffusion. The spatial distance at which particles speed changes corresponds to the decorrelation distance ℓ_c of the mean flow speed. The CTRW integrates in a statistical framework parameters that are similar to the classical representation of porous media as a network of throats and pores. As such one can be tempted to investigate how ℓ_c, which is a major ingredient of the CTRW model, is related to the topological and geometrical properties of the real 3-dimensional pore network. Moreover, the CTRW model predicts that asymptotic dispersion is controlled by the dispersion evolution during the pre-asymptotic regime which itself is controlled by the flow speed distribution. How the later is related to the properties of the pore network is a further issue that requires investigation.

The main objective of the present study, is to investigate the relation between the longitudinal dispersion D^* (and its evolution with the mean flow rate) and the porous media microstructural properties in the frame of the theory proposed by Puyguiraud et al. (2021) which gives a generalized explanation of longitudinal dispersion (from pre-asymptotic to asymptotic regimes) and a formal relation between dispersion and the properties of the flow field (velocity distribution, velocity spatial decorrelation and flow path tortuosity).

The core of this study is a set of about 150 numerical experiments designed to measure pre-asymptotic to asymptotic dispersion from diffusion-controlled to advection-controlled regime in 12 sandstone-like samples of porosity ranging from 10 to 25%. For that, one first computes the steady-state Stokes flow field from which, the flow speed distribution and the decorrelation distance as well as advective tortuosity are derived. Then, the direct numerical simulation (DNS) of solute transport at pore scale, involving diffusion and advection, are performed using Time-Domain Random Walk (TDRW). The dispersion mechanisms are characterized from the time-resolved particles displacement variance and the first passage time distribution (FPT) given as outputs of the TDRW simulations. In parallel, the geometrical properties of the porous samples are evaluated from the computation of the bonds network model (BNM) for each of the samples, that is obtained from the medial axis transform, or squeletonization, of the connected porosity. This gives us the unique opportunity to characterize the topology of the connected porosity including the number of throats (bonds) and pores (network nodes) and the coordination (number of throats per pore), as well as the throat radius and length. Then, the results of the direct numerical simulations are analyzed in the light of the CTRW theory proposed by Puyguiraud et al. (2021) which provides quantitative links between the tail behaviors of the FPT distribution $f_t(t)$, the distribution of flow speeds v_e, the particles displacement variance $\sigma^2(t)$ and the asymptotic dispersion coefficient D^* scaling with the *Pe* value.

The methodology, including the conceptual and numerical tools used in this study are detailed in section 2. The geometrical and topological characteristics of the samples and the flow field properties are presented in section 3. The results of the direct numerical simulation of solute transport and the calculation of the dispersion coefficient for a large range of values of *Pe* are discussed in section 3.4. The conclusions of this study are exposed in section 4.

2. METHODOLOGY

2.1. Porous Media Samples

The porous media are binary images made of 480^3 regular voxels (cubes) that are either void or solid. The first set of 6 samples, noted *FSxx*, were *xx* is replaced by the porosity value expressed in percent (ex: *FS*13 for the sample with $\theta = 0.13$) was downloaded from the Digital Rocks Portal (Berg, 2016a). They were generated with the commercial software e-Core following a methodology described in Oren (2002), in order to mimic Fontainebleau sandstone at different porosity (Berg, 2016b). The op. cit. author indicated that they use identically parameterized silica grain sedimentation and compaction processes typical for Fontainebleau sandstones, the different porosity values (0.10, 0.13, 0.15, 0.21, and 0.25) being obtained by varying the amount of silica cement. As such, this process mimics the progressive diagenetic cementation by silica precipitation (from *FS*25 to *FS*10) of an initially poorly cemented sandstone. Conversely, we made the second set of samples by step-by-step homogeneous erosion of the solid phase starting from *FS*10. By removing 1 to 6 layers of solid at the solid-void interface we obtain 6 samples, denoted *FSDxx* of porosity 0.12, 0.15, 0.17, 0.20, 0.23, and 0.25. This process mimics homogeneous dissolution of the silica material. The top panel in **Figure 1** displays the three-dimensional structure of the lowest porosity sample *FS*10, and the highest porosity samples *FS*25 and *FSD*25. It can be qualitatively appraised that the cement precipitation model used to construct *FS*25 increases the number of pores compared *FS*10, while the pore size is kept roughly similar. In contrast, the dissolution process producing *FS*25 from *FS*10 acts as increasing strongly the pore size, while the number of pores remains roughly unchanged. This set of sample is viewed as ideal for investigating dispersion of end-members of natural sandstones.

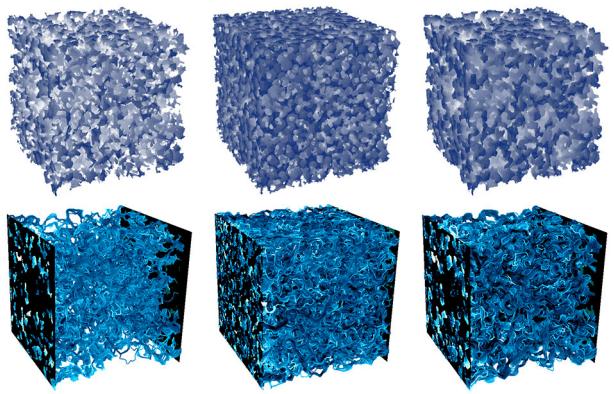

FIGURE 1 | Three-dimensional structure of *FS*10 **(left)**, *FS*25 **(middle)**, *FSD*25 **(right)** samples. The top row displays the void space. The lines in the bottom panel show particle paths, the color scheme indicating the particle speed from white ($u/\langle u\rangle \leq 7 \times 10^{-4}$) to dark blue ($u/\langle u\rangle = 10$).

2.2. Flow

Flow simulations are performed on the three-dimensional binary images. The mesh used for solving the flow is obtained by dividing each of the image voxels by 2 in each of the directions so that 1 voxel of the raw image is represented by 8 cubic cells of size $\Delta x = \Delta y = \Delta z = 2.85 \times 10^{-6}$ m. This procedure is applied for improving the resolution of the flow field in the smallest throats (Gjetvaj et al., 2015). The resulting discretization for the regular grid consists of 960^3 cubic cells. We are considering steady-state flow of an non-compressible Newtonian fluid at low Reynolds number so that the pore-scale flow velocity $\mathbf{v}(\mathbf{x})$ is given by the Stokes equation

$$\mu \nabla^2 \mathbf{v}(\mathbf{x}) - \nabla p(\mathbf{x}) = 0, \tag{3}$$

where $p(\mathbf{x})$ is the fluid pressure. Stokes flow is solved using the finite volume SIMPLE (SemiImplicit Method for Pressure Linked Equations algorithm) scheme implemented in the SIMPLEFOAM solver of the OpenFOAM platform (Weller et al., 1998). Twenty layers are added at the inlet and outlet in order to minimize boundary effects (Guibert et al., 2016). The main flow direction is considered in the z-direction all over this study. We prescribe (1) a macroscopic pressure gradient $\nabla^* p$ between the inlet ($z = 0$) and the outlet ($z = Lz$) boundary conditions such that the Reynolds number Re is smaller than 10^{-6}, i.e., laminar flow and (2) no-slip conditions at the void-solid interfaces and at the remaining boundaries of the sample. After convergence, that is, once the normalized residual of the pressure and velocity components is below 10^{-5} between two consecutive steps, we extract the components of the velocity at the voxel interfaces ($\mathrm{v}_x, \mathrm{v}_y, \mathrm{v}_z$). The results of the flow simulations allow us to extract the three properties that control dispersion according to Puyguiraud et al. (2019b): (1) the Eulerian speed distribution $p_e(v)$ (2) the decorrelation distance ℓ_c and (3) the advective tortuosity χ_a. These fundamental flow properties are respectively displayed in **Figures 5–7**, and discussed in section 3.

2.3. Solute Transport

Pore-scale hydrodynamic transport is classically modeled by the advection-diffusion equation

$$\frac{\partial c(\mathbf{x},t)}{\partial t} - \nabla \cdot \left[d_m \nabla + \mathbf{v}(\mathbf{x}) \right] c(\mathbf{x},t) = 0, \tag{4}$$

where $c(\mathbf{x},t)$ is the solute concentration at position $\mathbf{x}$ and time t, d_m is the molecular diffusion coefficient which is set equal to $d_m = 10^{-9}$ m^2/s, and $\mathbf{v}(\mathbf{x})$ is the flow velocity at position $\mathbf{x}$ which is obtained by solving the Stokes problem (see section 2.2). Here we use the time domain random walk (TDRW) method that is based on a finite volume discretization of Equation (4) (Delay et al., 2005). A detailed description of the TDRW method, its derivation and implementation using voxelized binary images can be found in Dentz (2012) and Russian et al. (2016); the main features of the method are given below. A study of the performance and accuracy of the TDRW method for a large range of values of the Péclet number can be found in Gouze et al. (2021). The domain discretization used for transport is that used for computing the flow, i.e., 960^3 cubic voxels .

The TDRW method is a grid-based method that models the displacement of particles in space and time according to the master equation that results from a finite volume discretization of the advection-diffusion equation. The ensemble average of the particle displacement gives the solution of the transport equation. A particle transition corresponds to a single transition of a constant length $\xi = \Delta x$ from the center of a voxel j to the center of one of the 6 face-neighboring voxels i. The direction and the transition duration are random variables ruled by the local values of the fluid velocity at the voxel interface embedded into the local coefficients b_{ij} (Russian et al., 2016).

$$b_{ij} = \frac{d_m}{\xi^2} + \frac{|\mathrm{v}_{ij}|}{2\xi}\left(\frac{\mathrm{v}_{ij}}{|\mathrm{v}_{ij}|} + 1\right), \tag{5}$$

where v_{ij} is the velocity component of $\mathbf{v}_j$ in the direction of voxel i, $\mathrm{v}_{ij} = \mathbf{v}_j \cdot \boldsymbol{\xi}_{ij}$. Voxel i is downstream from voxel j if $\mathrm{v}_{ij} > 0$, as a convention. The velocity at the solid-void interface is zero and $d_m = 0$ if voxel i is a solid voxel. The recursive relations that describe the random walk from position $\mathbf{x}_j$ to position $\mathbf{x}_i$ of a given particle transition n are

$$\mathbf{x}_i(n+1) = \mathbf{x}_j(n) + \boldsymbol{\xi}, \quad t(n+1) = t(n) + \tau_j. \tag{6}$$

The probability p_{ij} for a transition of length ξ from voxel j to voxel i is

$$p_{ij} = \frac{b_{ij}}{\sum_{[jk]} b_{kj}}, \tag{7}$$

where $\sum_{[jk]}$ denotes the summation over the nearest neighbors of voxel j. The transition time τ_j is independent on the transition direction and is exponentially distributed $\psi_{\tau_j}(t) = \overline{\tau}_j \exp(-t/\overline{\tau}_j)$ with $\overline{\tau}_j$ the mean transition time from voxel j;

$$\overline{\tau}_j = \frac{1}{\sum_{[jk]} b_{kj}}. \tag{8}$$

The algorithm consists in computing once the probability p_{ij} (Equation 7) and the mean transition time $\overline{\tau}_j$ (Equation 8) for each of the voxels belonging to the pore space and then solving the random walk (Equation 6) in which the direction for each particle transition is drawn from the p_{ij} vector and the transition time is drawn from the exponential distribution of mean $\overline{\tau}_j$.

2.3.1. Simulation Setup

For each sample, we performed simulations for different values of the Péclet number. The Péclet number is defined as $Pe = \langle v_e \rangle \lambda / d_m$ where λ is the mean throat length that is displayed for the 12 samples in **Figure 2** and ranges from 6.5×10^{-5}m to 8.8×10^{-5}m. The different flow fields used for the TDRW simulations at different Péclet numbers are obtained by multiplying the raw flow field resulting from the Stokes simulation by a constant.

A *pulse* of constant concentration at the sample inlet ($z = 0$) is applied at $t = 0$ by locating particles in a flux weighted injection mode. Note that the *pulse* is formally an exponential distribution function of characteristic time $\tau_j|_{z=0}$ whose mean value is negligible compared to the mean time required for the particles to move through the sample (Russian et al., 2016). Flux weighted injection means that the number of particles injected at a location is proportional to the local velocity. This corresponds to a constant concentration Dirichlet boundary condition. Particles that reach the sample outlet with a speed v_{out} are reinjected randomly at the inlet plane at a position $\mathbf{x}$ satisfying the condition $|v_{\mathbf{x}} - v_{out}| \ll \langle v \rangle$.

The distribution (PDF) of first passage times at a given distance Z from the injection location, that denotes the solute breakthrough curve (BTC) usually measured in laboratory or field tracer tests, is noted $f_t(t)$ (**Figure 8**). The apparent longitudinal dispersion coefficient $D(t)$ is evaluated from the displacement variance $\sigma_z^2(t)$ of the particles (Fischer, 1966):

$$D(t) = \frac{1}{2} \frac{d\sigma_z^2(t)}{dt}, \tag{9}$$

with $\sigma_z^2(t) = \langle (z(t) - \langle z \rangle)^2 \rangle - \langle z(t) - \langle z \rangle \rangle^2$. The asymptotic longitudinal dispersion coefficient $D^* = \sigma_z^2(t)/2t$ is obtained for $t > t^*$, where t^* is the time required for all the particles to sample the entire heterogeneity, i.e., when $\sigma_z^2(t) \sim t$ (see for example **Figure 10**).

2.4. The Equivalent Bond Network Model

We compute the bond network model (BNM) for each of the *FS* and *FSD* samples in order to extract the geometrical and topological characteristics of the connected porosity. The methodology to obtain the network representation of the connected porosity of the sample includes two main steps. The first one is the extraction of the void space skeleton which is the one-dimensional continuous object centrally located (and spatially referenced) inside the pore space. The skeleton can be computed using different approaches; here we used a thinning algorithm inspirited from the works of Lee et al. (1994) that provides the local medial-axis. The coordinate of the skeleton is known with a spatial resolution equivalent to that of the original 3D-image and associated with the local hydraulic radius r_l normal to the local medial axis that is evaluated using a pondered 45 degree multi-ray method. Thus, the skeleton keeps the relevant geometrical and topological features of the pore space (Siddiqi and Pizer, 2008). The second step consists in transforming the skeleton into a network of bonds and nodes that connect three or more bonds. This yields an irregular lattice. The length λ of a given bond is the sum of the length of the skeleton components used to built this bond, so that the local tortuosity of the skeleton is embedded into λ. For each bond, the radius r_h is obtained from the harmonic means (noted $\langle \rangle_H$) of the local conductance, so that $r_h = (\langle r_l \rangle_H)^{1/4}$. The algorithm is non-parametric; there is no assumption on any of the characteristics of the obtained lattice.

2.5. Upscaled CTRW Model

Puyguiraud et al. (2021) proposed a continuous time random walk (CTRW) model that describes transport through particle transitions over the length ℓ_c with a transition time that is given by the local flow speed and diffusion. The central assumption of this model is that transition times at subsequent CTRW steps are independent identically distributed random variables. Furthermore, it is assumed that particles move at the mean pore velocity, that is, it is assumed that during a transition particles are able to diffusively sample the velocities across pore conducts. The scale ℓ_c is set equal to the decorrelation distance of particle speeds so that subsequent particle speeds can be considered statistically independent. The distribution of the Eulerian mean flow speeds $p_m(v)$ is obtained from the Eulerian speed PDF as

$$p_m(v) = -2v \frac{dp_e(2v)}{dv}. \tag{10}$$

As particles move at equidistant spatial steps, they sample flow speeds in a flux-weighted manner. This is due to the fact that particles are distributed at pore intersections according to the relative downstream fluxes. Thus, the distribution $p_v(v)$ of subsequent particle speeds are related to the distribution of Eulerian mean flow speeds through flux-weighting as (Puyguiraud et al., 2021).

$$p_v(v) = \frac{v p_m(v)}{\langle v_m \rangle}. \tag{11}$$

At each turning point of the CTRW, particles are assigned a random speed from $p_v(v)$. The particle transition time distribution $\psi(t)$ reflects both advection and diffusion. It is cut-off at times larger than $\tau_D = \ell_c^2/d_m$, the diffusion time over the decorrelation distance. For times small compared to the cut-off time, $\psi(t)$ can be approximated by

$$\psi(t) = \frac{\ell_c^2}{t^3 \langle v_m \rangle} p_m(\ell_c/t). \tag{12}$$

At times larger than τ_D it is cut-off exponentially fast.

The flow speed distribution is at the center of the transport process. In porous media, such as rocks, the mean flow speed can often be approximated by a Gamma-type distribution (Dentz et al., 2018; Puyguiraud et al., 2019b; Souzy et al., 2020) and

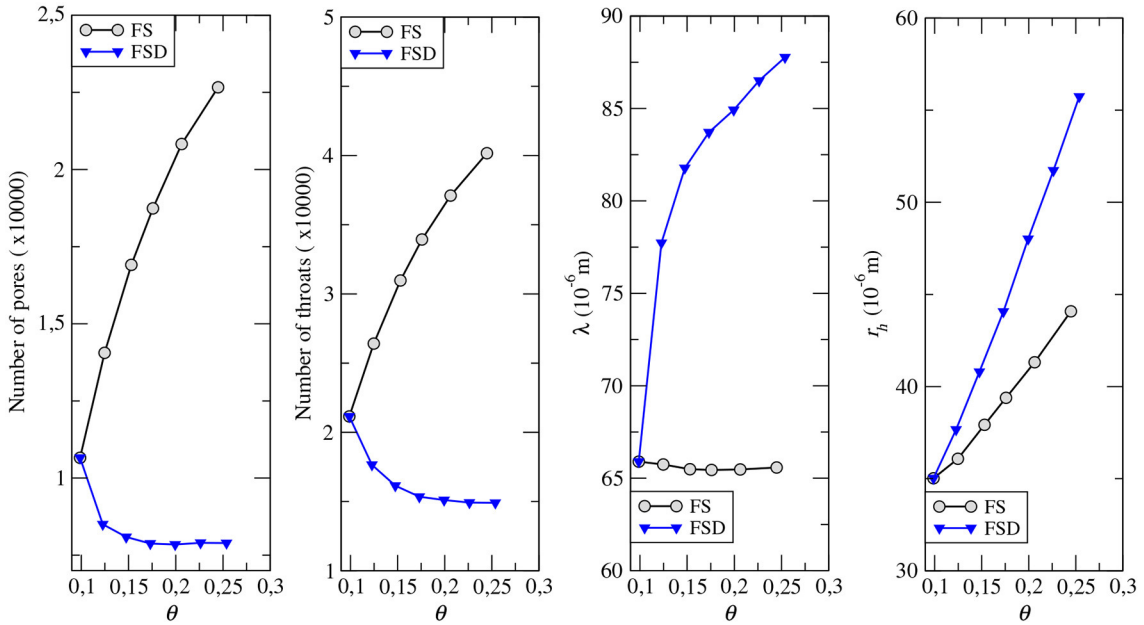

FIGURE 2 | From **left** to **right**: number of pores; number of throats; mean throat length λ; mean throat radius r_h vs. porosity θ for the *FS* and *FSD* samples.

displays a power-law scaling $p_e(v) \sim v^{\alpha-1}$ for $v < \langle v_m \rangle$. For sphere packs and simple structures such as sand-pack the linear flow profile close to the grains (due to the no-slip boundary condition) implies that $p_e(v)$ is flat at low velocities, so that $\alpha \simeq 1$ (Dentz et al., 2018). In more heterogeneous porous media, other values of α are expected. For example, Puyguiraud et al. (2021) found $\alpha \approx 0.35$ for a Berea sandstone sample. For such Gamma-type distributions, $p_e(v) \sim v^{\alpha-1}$ at small flow speeds, $\psi(t)$ behaves for high Péclet numbers as $\psi(t) \sim t^{-2-\alpha}$ before the exponential cut-off at times larger than τ_D. The tortuosity of particle trajectories in this framework is given by the ratio of the mean asymptotic particle speed $\ell_c/\langle\tau\rangle \equiv \langle v_e \rangle$ (where $\langle\tau\rangle$ denotes the particle mean travel time) and the mean streamwise flow velocity $\langle v_z \rangle$. Furthermore, for this type of flow speed distributions, the CTRW approach predicts some further interesting scaling laws that can be verified from direct numerical simulations. The behavior of particle breakthrough curves $f(t, Z)$ at a control plane located at the streamwise location Z is analogous to the behavior of $\psi(t)$. They show a power-law dependence as $f(t, Z) \sim t^{-2-\alpha}$ if $Z/v_z \ll \tau_D$ (i.e., the peak time is much smaller than the cut-off time), and exponential decay for times larger than the cut-off time τ_D. The predicted dependence of the asymptotic longitudinal dispersion coefficients on the Péclet number is for $Pe \gg 1$

$$\frac{D^*}{d_m} \sim Pe^{2-\alpha} \tag{13}$$

for $0 < \alpha < 1$ and

$$\frac{D^*}{d_m} \sim Pe \ln Pe \tag{14}$$

for $\alpha = 1$, see also Saffman (1959) and Koch and Brady (1985).

To sum-up, this upscaled model, constructed on the representation of the hydrodynamic transport as a CTRW process in a 1-dimensional network of bonds, is fully constrained, for any values of $Pe > 1$ by the knowledge of the distribution of Eulerian flow speeds $p_e(v)$ and the decorrelation distance ℓ_c of particle speeds.

From here one can recognize on one hand the complementarity of the BNM and the DNS to explore the relation between the dispersion and the pore network characteristics, and on the other hand the conceptual framework that links the CTRW model and the BNM representation of the porous medium. This emphasizes the possibility of (1) relating the distribution of the Eulerian flow speed to the large scale transport behavior and (2) characterizing dispersion for different porous media based on the knowledge of the flow speed distribution. Indeed, the BNM gives us the information on the real topology of the pore network as well as the distribution and the average of bond properties (radius and length), while the DNS provides the information on the flow field (speed distribution and decorrelation distance as well as the advective tortuosity).

3. PORE NETWORK PROPERTIES, FLOW FIELDS, AND DISPERSION

The top row in **Figure 1** illustrates the 3-dimensional structure of sample *FS*10 ($\theta = 0.1$) and of both *FS*25 and *FSD*25 sharing the same porosity $\theta = 0.25$. The bottom row in **Figure 1** displays flow lines (and the local velocity) within the connected porosity for these three samples and gives a qualitative appraisal

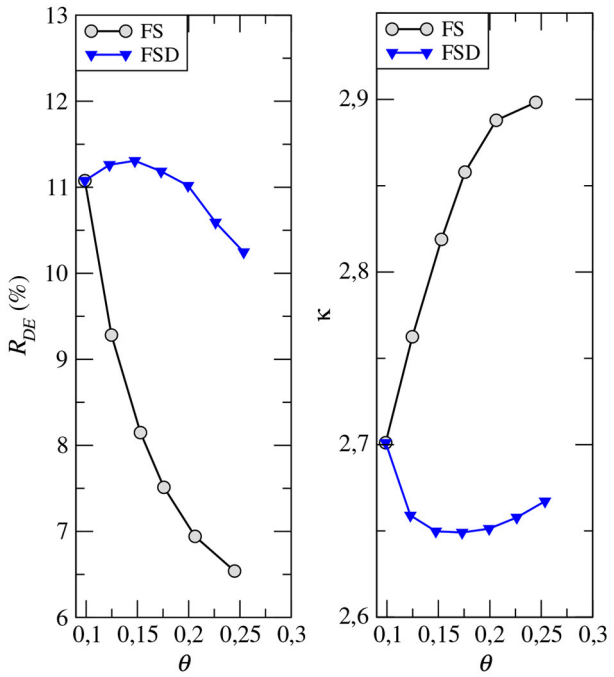

FIGURE 3 | Left: Ratio (in %) of the number of dead-ends to the number of throats. **Right**: Mean number of throats per pore κ vs. porosity θ for the *FS* and *FSD* samples.

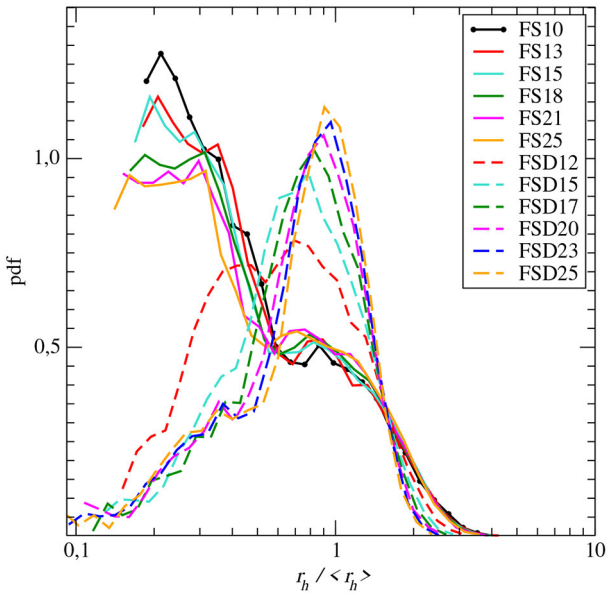

FIGURE 4 | Normalized distribution of r_h for the *FS* and *FSD* samples.

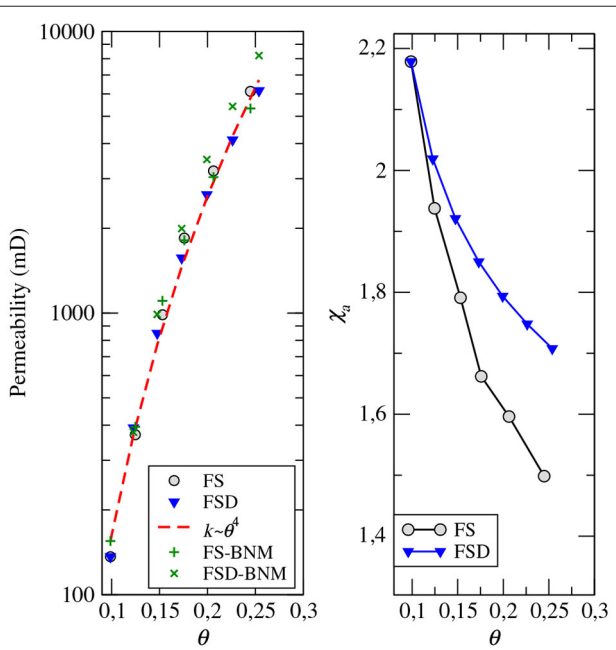

FIGURE 5 | Permeability **(left)** and advective tortuosity χ_a **(right)** vs. porosity θ for the *FS* and *FSD* samples.

of the dissimilarities between the lowest porosity and the highest porosity samples on one hand, and on the other hand those occurring between the highest porosity sample of each of the two sets in relation with the pore network structures. In the following we will quantify these differences and their implications on dispersion.

3.1. Connected Porosity Geometrical Properties Retrieved From the BNM

As explained in section 2.1, we computed the Bond Network Model (BNM) for each of the 12 samples, in order to evaluated the topology and the geometry of the connected porosity and specifically how these characteristics change with the sample porosity for the *FS* and the *FSD* sets of samples. The main properties vs. porosity are summarized in **Figures 2**, **3**. The topology of the connected porosity is characterized by the number of throats (network bonds) and pores (network nodes) per volume of rock (here the reference is the sample volume) as well as the coordination number κ that denotes the mean number of throats connected to a given pore. The bonds are characterized by the mean of the radius r_h and length λ and by the radius r_h distribution displayed in **Figure 4**.

For the *FS* set, decreasing porosity from the highest to the lowest porosity values is obtained by allocating increasing amounts of cement into localized clusters that acts as increasingly closing connections and thus decreasing the number of pores and throats and the coordination number. The fixed distribution of the cement clusters determines the length of the bonds independently of the porosity ($\lambda \approx 65\mu m$), but volume conservation imposes that the hydraulic radius r_h increases with porosity. The distribution of $r_h/\langle r_h \rangle$ is wide, decreases almost monotonically from small to high r_h and does not depends on porosity.

For the *FSD* set, increasing porosity from the lowest to the highest is obtained by homogeneous erosion of the solid phase,

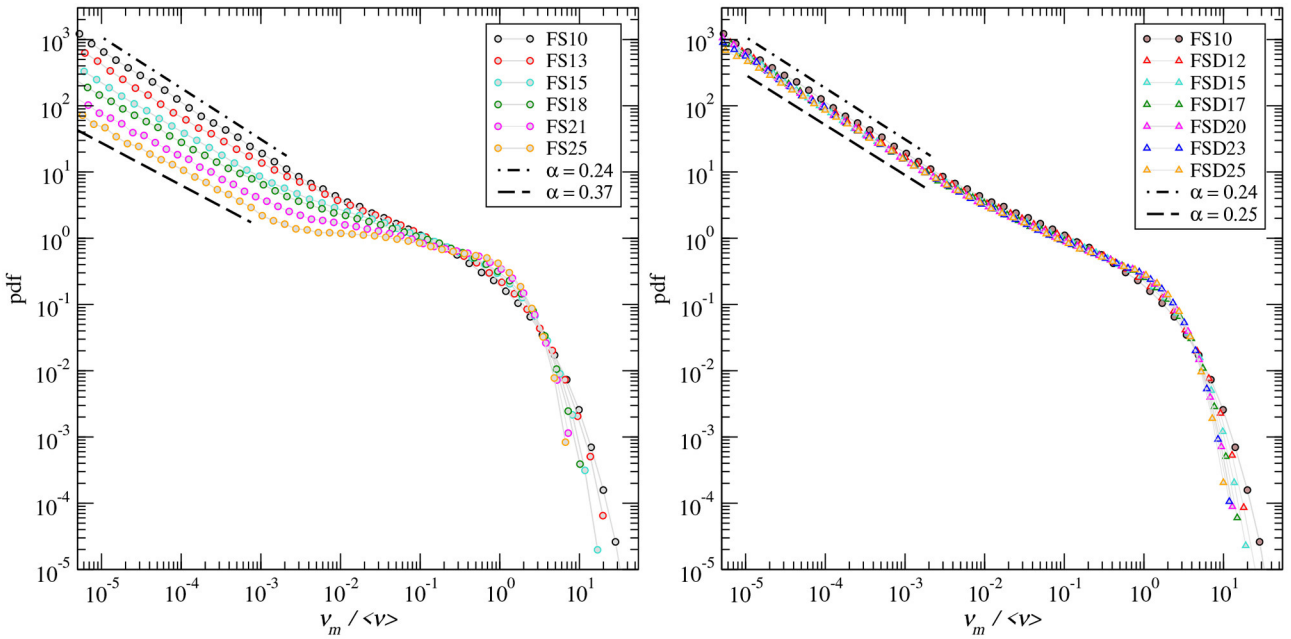

FIGURE 6 | Distribution of the Eulerian mean speeds $p_m(v)$ normalized to its mean, for the *FS* **(left)** and the *FSD* **(right)** samples.

i.e., both the grains and the cement. The number of pores and throats as well as κ first decreases for $\theta \leq 0.15$ caused by merging of adjacent throats following a process which is roughly the opposite of that described for the *FS* set of samples. Then, the number of pores and throats stays almost constant for $\theta > 0.15$. As a result, the increase of porosity is mainly due to the increase of the throat length λ and radius r_h. The distribution of $r_h/\langle r_h \rangle$ is almost Gaussian around the mean value, and independent of the porosity for $\theta > 0.15$. The transition from the original sample *FS*10 to the *FSD*12 and then *FSD*15 is well visible the r_h distribution. Note that, as soon as the throats are widely distributed like for the *FS* set of samples, κ is an indicator of the potential local flow rate disorder at the network nodes because the probability of having upstream and downstream bonds of distinctly different flow rates is high.

Altogether, these results show that the two sets of samples are very different in terms of (1) the topology of the network; for the *FSD* set, the topology is almost similar for all the porosity range, while it is increasingly complex (with increasing tortuosity, see discussion below) as porosity decreases for the *FS* set of samples, and (2) the characteristic size of the throats which is almost independent of the porosity for the *FD* set whereas it increases with porosity for the *FSD* set.

3.2. Permeability and Flow Field Properties

Permeability values k for the 12 samples computed using Darcy's law ($k = \bar{v}_z \mu / \nabla^* p$) are plotted in the left panel of **Figure 5**. Permeability increases from 1.4×10^{-13}m^2 for sample *SF*10 to 6.04×10^{-12}m^2 (6.08×10^{-12}m^2) for sample *SF*25 (*SFD*25) and are all aligned with the relation $k \sim \theta^4$ independently on geometrical characteristics of the pore space. The permeability computed on the BNM (solving a Kirchhoff problem) is also reported **Figure 5** in order to evaluate the accuracy of the BNM.

The right panel of **Figure 5** displays the advective tortuosity χ_a, i.e., the mean tortuosity of the flow lines. The advective tortuosity is obtained from the ratio of the mean Eulerian speed v_e to the mean velocity in the direction of the flow v_z (Koponen et al., 1996; Ghanbarian et al., 2014; Puyguiraud et al., 2019c): $\chi_a = \langle v_e \rangle / \langle v_z \rangle$. For both the sets of samples, χ_a decreases when porosity increases, but it is more pronounced for the *FS* set of samples. These trends seem to be mainly controlled by the increase of the throat radius as porosity increases, while the topological characteristic of the network plays a minor role which is probably resulting from a complex coupling of the geometrical and topologically parameters discussed above. This makes the advective tortuosity, which is one of the three parameters of the CTRW model proposed by Puyguiraud et al. (2021), an intrinsic characteristic of the hydrodynamic system that is essentially porosity-dependant.

The distributions of the Eulerian mean speed for the 12 samples are plotted in **Figure 6**. The dissimilarity of the $p_m(v)$ curves between the *FS* and the *FSD* sets is clearly visible. The *FSD* samples are displaying almost the same mean speed distributions with power-law trend $p_m(v) \sim v^{\alpha-1}$ for $v < \langle v_m \rangle$ with $\alpha = 0.245 \pm 0.05$. For the *FS* set, the evolution of $p_m(v)$ with porosity includes two features. First, $p_m(v)$ gradually diverges from a Gamma distribution as porosity increases, with the occurrence of increasingly marked transition between the values of speed larger than the mean ($v > \langle v_m \rangle$) and the power-law slope for the slower speed values. Second, the power-law slope for $v \ll \langle v_m \rangle$ increases when porosity decreases, ranging from $\beta = \alpha - 1 = 1.63$ for $\theta = 0.25$ to $\beta = 1.75$ for $\theta = 0.10$.

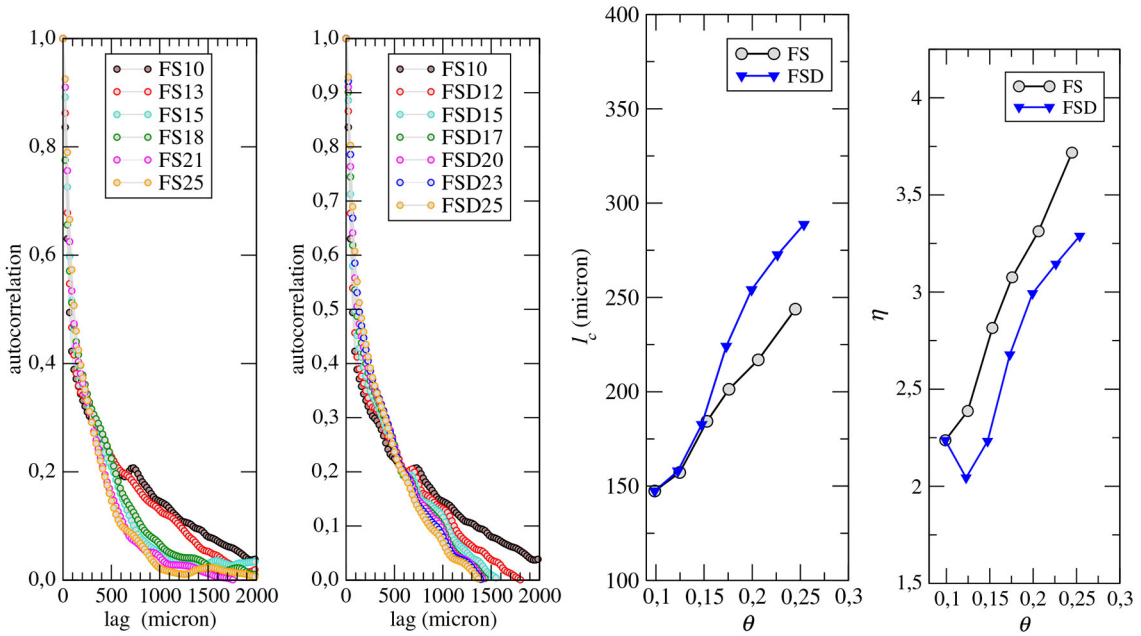

FIGURE 7 | Flux weighted Langrangian speed auto-correlation function $\Upsilon_{v_l}(l)$ for the *FS* **(left)** and the *FSD* **(middle-left)** samples. The **middle-right** panel displays the decorrelation length ℓ_c and the **right** panel displays the ratio $\eta = \ell_c/\lambda$ vs. porosity.

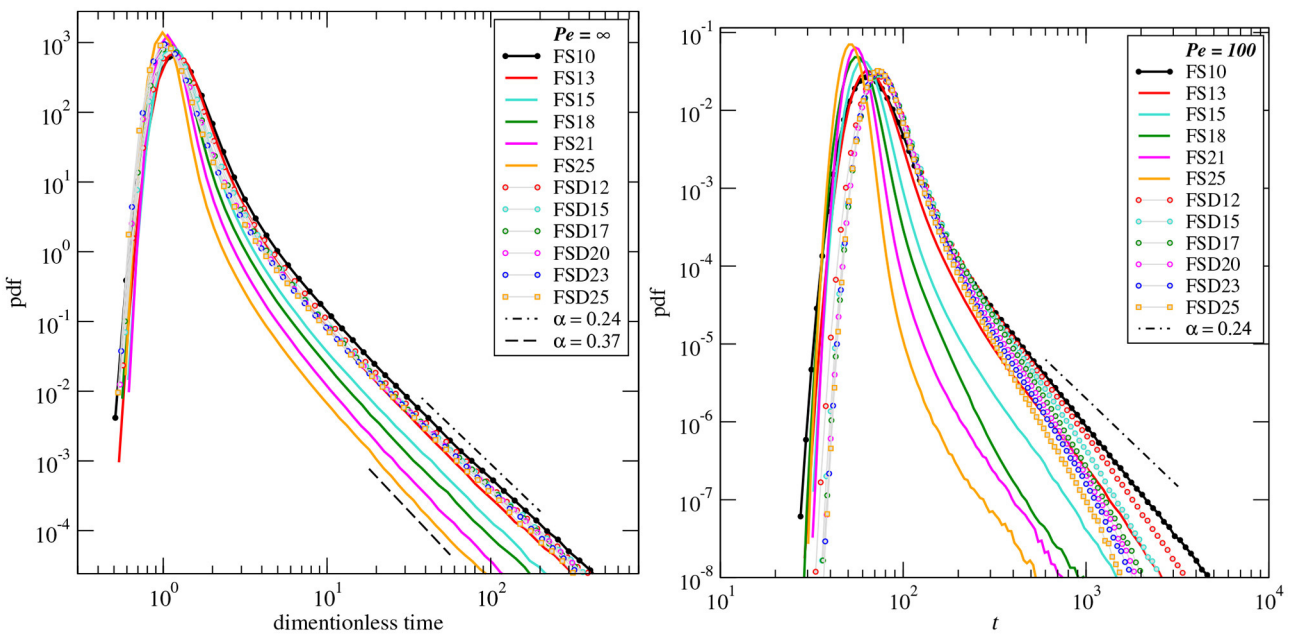

FIGURE 8 | First passage time PDF f_t at $Z = 5.47\times10^{-2}$m from the inlet. **Left**: results for infinite *Pe* vs. dimensionless time Z/v. **Right**: results for $Pe = 100$ vs. time.

These values are in agreement with the value of 1.65 found by Puyguiraud et al. (2021) for the Beara sandstone. As far as we know, they have been very few studies of the correlation between the flow speed distribution and the properties of the pore space microstructures (Siena et al., 2014; Matyka et al., 2016; Alim et al., 2017). For instance, Alim et al. (2017) investigated this issue using numerical simulations in 2-dimensional simple artificial porous media made of circular or elliptical discs placed on a square or triangular lattices with increasing disorder. By extracting and analyzing the corresponding network of tubes, following a procedure quite similar to that implemented for extracting the BNM (section 2.4), they concluded that the flow

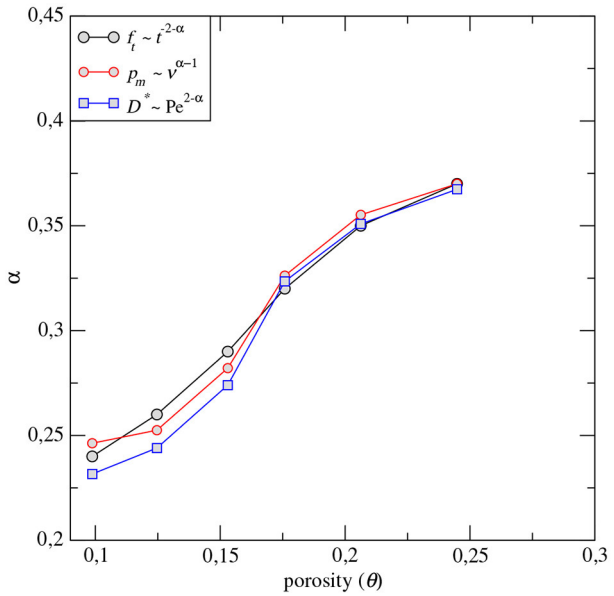

FIGURE 9 | Comparison of the value of α for the *FS* samples evaluated from (1) the slope of the first passage time plotted in the left panel, (2) the slope of the mean speed PDF plotted in **Figure 6** and (3) the slope of the D^*/d_m vs. *Pe* plotted in **Figure 11**.

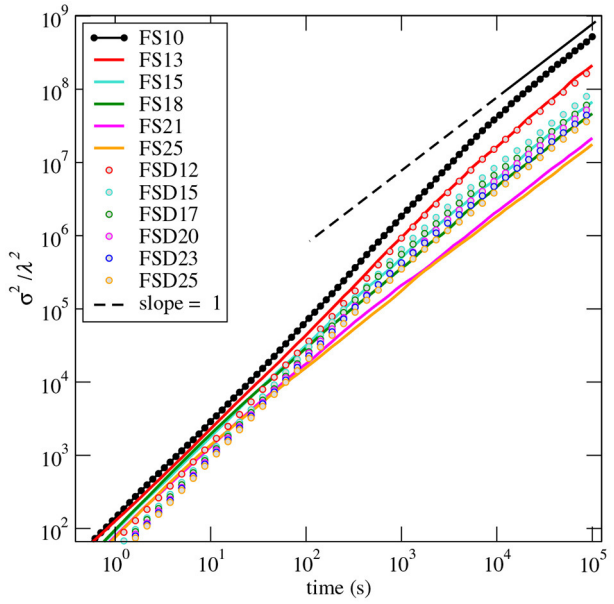

FIGURE 10 | Normalized *z*-direction displacement variance vs. time for $Pe = 100$.

distribution is mainly determined by the distribution of fractions of fluid flowing at each of the network node and not by the overall tube size distribution. Our results lead us to a similar conclusion for the complex 3-dimensional porous media studied here. The evolution of the mean flow speed with porosity for the *FS* set in comparison with the weak evolution of the mean flow speed with porosity for the *FSD* set appears to be correlated to the noticeable increase with porosity of the number of throats as well as the mean number of throats per pore κ (**Figure 3**) measured for the *FS* set, whereas both the number of throats and κ are almost constant for the *FSD* set of samples.

3.3. Speed Decorrelation Distance Length

The decorrelation distance ℓ_c is evaluated from the Lagrangian flux weighted speed autocorrelation function $\Upsilon_{vv}(l) = \langle (v_v(s) - \langle v_v \rangle)(v_v(s+l) - \langle v_v \rangle) \rangle / \sigma^2_{v_v}$, where l denotes the lag. The decorrelation distance ℓ_c is given by the value of the lag corresponding to $\Upsilon_{vv}(l) = 1/e$. The two panels at left of **Figure 7** display the Lagrangian flux weighted speed autocorrelation function $\Upsilon_{vv}(l)$ for the two set of samples. The corresponding values of the decorrelation distance ℓ_c vs. porosity are given in the third panel of **Figure 7**, and the ratio of the decorrelation distance to the mean throat length $\eta = \ell_c/\lambda$ vs. porosity is given in the right panel.

For both the sample sets, the decorrelation distance ℓ_c increases with porosity from about 150 μm at $\theta = 0.1$ to about 240 μm for *FS* and 290 μm for *FSD*. The slight increase of ℓ_c for the *FSD* set for $\theta > 0.15$ compared to the *FS* set is caused by the increase of the throat radius and the decrease of tortuosity with porosity that are more important for *FSD* than for *FS*. The ratio η also displays an increase with porosity following a similar trend for both the *FS* and the *FSD* set of samples, the values for *FSD* being smaller of ~ 0.5 unit than for *FS*. Thus, in average, the number of bond lengths traveled before losing the memory of the initial speed ranges from about 2 to 4. These values are in good agreement with the value of 4 obtained by Puyguiraud et al. (2021) by fitting DNS and CTRW for Berea sandstone of porosity 0.18.

3.4. Dispersion

In this section, we are presenting the results of the transport DNS, discussing them in the frame of the scaling properties derived from the CTRW model proposed by Puyguiraud et al. (2021) and of the properties retrieved from the BNM (section 3.1).

The first passage time distributions $f_t(t)$ (or breakthrough curves) at a distance of 20 times the sample size are given in **Figure 8** for $Pe = 100$ and also for purely advective transport ($d_m = 0$; $Pe = \infty$). For the latter, all the curves display the power-law tailing that characterize pre-asymptotic (non-Fickian) regime over 3 to 4 orders of magnitude. The scaling $f_t(t) \sim t^{-2-\alpha}$ predicted by Puyguiraud et al. (2021) with the values of α corresponding to those measured on the mean speed distribution is confirmed for all the samples. The comparison of the value of α ($0.24 \leq \alpha \leq 0.37$) for the *FS* set of samples is given in **Figure 9**. For $Pe = 100$, even if it can be considered a quite large value for natural porous media, diffusion acts as increasing the rate at which $f_t(t)$ decreases with time and the α-dependent power-law trend is not present. Note that the beginning of the exponential decrease is visible for *FSD*25 at $t \approx 5\tau_D$, where $\tau_D = \ell_c^2/d_m \approx 80s$.

We now focus on determining the asymptotic dispersion coefficient D^* from the asymptotic regime of the displacement

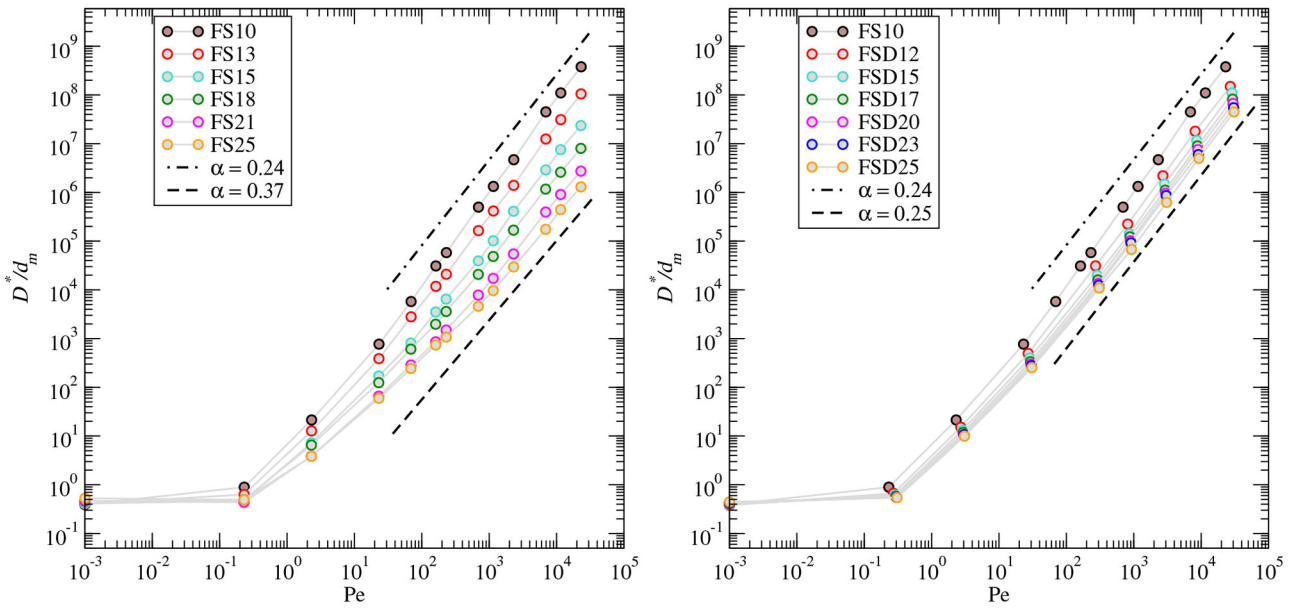

FIGURE 11 | Asymptotic dispersion coefficient vs. *Pe* for the *FS* and *FSD* samples.

variance. **Figure 10** displays, as an example, the displacement variance normalized to the throat length (σ^2/λ^2) for the 12 samples in the case $Pe = 100$, but the following comments apply for all values of *Pe* larger than 1. All curves converge to the asymptotic regime ($\sigma^2/\lambda^2 \sim t$) for time $t \geq t_a$, where t_a is independent of the value of *Pe* but depends on porosity; $t_a \approx 10^3$s for $\theta = 0.1$ and $t_a \approx 10^4$s for $\theta = 0.25$, i.e., about 40 and 120 times τ_D, respectively. This point is important regarding the possibilities of measuring the asymptotic dispersion from laboratory experiments, deriving D^* from the breakthrough curves, for instance. For $Pe = 100$, that corresponds to a mean flow speed of 1.5×10^{-3} m/s for *FS*10, a sample of about 1.5 m long displaying the same properties of the mm-scale sample would be necessary to measure D^*; a distance of 60 m would be necessary for $Pe = 4{,}000$. This indicates that experimental measurement of D^* can be performed only for low values of *Pe*, typically of the order $Pe \leq 10$. However, for such low values of *Pe* it is not possible to measure α and thus determine the trend $D^*(Pe)$.

Conversely, the DNS allows us to perform numerical experiments over large range of *Pe* values; **Figure 11** displays the value of D^* vs. *Pe* for the 12 samples from diffusion-dominant regime ($Pe = 10^{-3}$) to advection-dominant ($Pe = 2 \times 10^4$). These curves can be commented in terms of their slope and of their scaling with porosity, for $Pe \gg 1$. Note that for $Pe \to 0$ the ratio D^*/d_m is equal to the inverse of the diffusive tortuosity ($D^*/d_m = \chi_d^{-1}$). For both the *FS* and *FSD* sets of samples, the relation $D^*/d_m \propto Pe^{2-\alpha}$ predicted by the CTRW model for $Pe \gg 1$ is observed. The values of α compared to those measured using the speed distribution and the tailing of $f_t(t)$ are given in **Figure 9**. The minimum value Pe_c at which $D^*/d_m \propto Pe^{2-\alpha}$ is effectively observed, is correlated with the shape of the mean speed distribution (**Figure 6**). For *FS*10, the trend $p_m(v) \sim v^{\alpha-1}$ with $\alpha = 0.24$ extends up to $5 \times 10^{-3} v/\langle v_m \rangle$, while for *FS*25 the trend $\alpha = 0.37$ extends up to $3 \times 10^{-4} v/\langle v_m \rangle$ only. This gives values of Pe_c ranging from 1,000 for *FS*10 to 50 for *FS*25. The same trend is observed for the *FSD* set of samples. These results demonstrate the clear control of the particle mean speed distribution on the evolution of D^* with the Péclet number. However, both the two sets of samples display a scaling of D^* with porosity, independently of the slope determined for $Pe \geq Pe_c$. The expected decrease of D^* for all values of $Pe > 1$ when porosity increases, corresponding to a decrease of the slope of $p_m(v)$ for $v \ll \langle v_m \rangle$ is clearly visible for the *FS* set of samples. But, the results for the *FSD* set, that share the same mean speed distribution (**Figure 6**), show also a clear decrease of D^* as porosity increases, which indicates that the dispersion scaling with porosity is not solely controlled by $p_m(v)$ for $v \ll \langle v_m \rangle$. Indeed, the increase of D^* with porosity is also related to the increase of the speed decorrelation distance ℓ_c with porosity. In the frame of the CTRW model l_c denotes the length at which a new velocity is drawn from the mean speed distribution, and as such ℓ_c determines the rate at which the speed changes.

Furthermore, we observe in **Figure 11** that D^* shows different power-law behaviors for $Pe < Pe_c$ that can be related to the scaling behavior of the distribution of mean flow speeds and the transition time distribution. In the limit of infinite *Pe*, the transition time distribution is given by (Equation 12). For finite *Pe*, it is cut-off at the diffusion time τ_D. The log-slope of $\psi(t)$ at the cut-off time depends on the average flow speed $\langle v_m \rangle$. This is shown in **Figure 12**, which displays the distribution of purely advective transition times rescaled by $\tau_v = \ell_c/\langle v_m \rangle$ for *FS*10 and *FS*25. The behavior of D^* for $Pe < Pe_c$ corresponds to the power-law scaling of $\psi(t)$ at dimensionless times equal to *Pe*. The slope

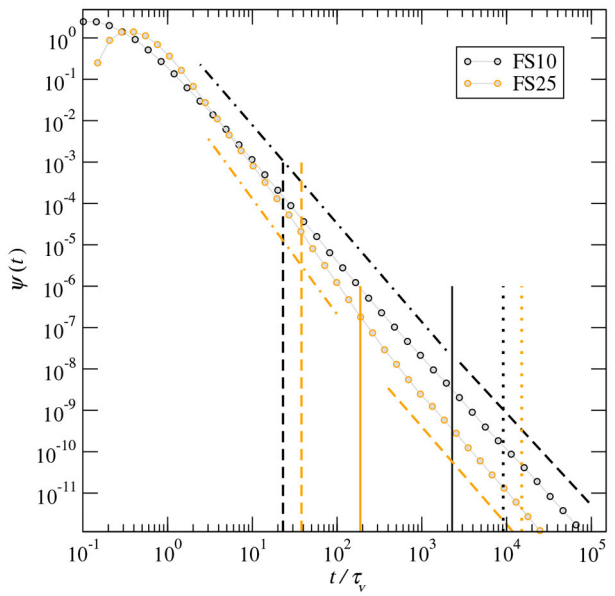

FIGURE 12 | Distribution of advective transition times rescaled by τ_v for *FS*10 and *FS*25. The dimensionless cut-off time is $Pe = \tau_D/\tau_v$. The vertical lines denote $Pe = 10$ (dashed lines), $Pe = Pe_c$ (solid lines) and $Pe = 4{,}000$ (dot line). The sloped lines denote the power-law behaviors $t^{-2-\alpha'}$ for $Pe < Pe_c$ with $\alpha' = 0.38$ and 0.79 for *FS*10 and *FS*25, respectively, and $t^{-2-\alpha}$ for $Pe \geq Pe_c$ with $\alpha = 0.23$ and 0.37 for *FS*10 and *FS*25, respectively.

of the $\psi(t)$ curves display the power-law behaviors $t^{-2-\alpha'}$ for $Pe < Pe_c$ with $\alpha' = 0.38$ and 0.79 for *FS*10 and *FS*25, respectively. For $Pe \geq Pe_c$ the values of α are similar to those reported in **Figure 9** for $f_t(t)$, $p_m(v)$ and $D^*(Pe)$, i.e., $\alpha = 0.23$ and 0.37 for *FS*10 and *FS*25, respectively.

4. SUMMARY AND CONCLUSIONS

We performed numerical experiments of passive solute transport for two sets of porous media mimicking a large range of porosity and microstructures expected in sandstones. The aim was to test the validity of the CTRW model, to explore how the flow field characteristics are linked to the porous media geometrical properties and to determine the scaling of asymptotic dispersion coefficient D^* with the Péclet number. The two sets of six samples share similar porosity, ranging from 0.1 to 0.25, and the same permeability-porosity trend $k(\theta)$ but displays distinctly different microstructures and thus dispersion evolution.

The conceptual CTRW model of solute transport in porous media, as the one proposed by Puyguiraud et al. (2021), infers that solute spreading along particle paths is controlled by the transition time of the solute particles which is determined by the distribution of solute particle mean speeds $p_m(v)$, the velocity decorrelation distance ℓ_c and diffusion. The effective tortuosity factor that depends on Pe and on the advective tortuosity χ_a (that can be also easily evaluated form the flow field) allows mapping dispersion in the streamwise direction which is aligned with the mean pressure gradient. With decreasing Pe, the effective tortuosity of the solute particles increases and the control of $p_m(v)$ on dispersion decreases but remains important up to high values of Pe because of the wide distribution of the particles speeds toward low speed values. This means that for heterogeneous media, such as sandstones, the pre-asymptotic (non-Fickian) dispersion regime is likely to persist over long time scales.

We found that the scaling properties, measured by the coefficient α, predicted by Puyguiraud et al. (2021)'s model are effectively measurable for all the 12 studied samples. For instance, results shows that at high Pe, the tail of the breakthrough curves, that is controlled by the low flow speeds, scales as $f_t(t) \sim t^{-2-\alpha}$ where α is given by the slope of the mean speed distribution $p_m(v) \sim v^{\alpha-1}$, for $v < \langle v_m \rangle$. As Pe decreases, diffusion eventually dominates over low flow speeds, thus cuts off the power-law tail of the breakthrough curves and leads to Fickian behavior from which the asymptotic dispersion coefficient D^* can be theoretically evaluated (Van Genuchten and Wierenga, 1986). However, the analysis of the displacement variance $\sigma^2(t)$ indicates that D^* cannot be measured experimentally at laboratory scale, for high values of Pe, because the distance required for reaching the asymptotic regime is orders of magnitude larger than what is workable at laboratory scale. Thus, measuring experimentally the value of α, for determining how D^* scales with Pe seems difficult.

The asymptotic dispersion coefficient D^* was computed up to the largest values of Pe expected for laminar flow in natural environments. Results show that $D^*/d_m \propto Pe^{2-\alpha}$ from Pe_c up to the highest value of Pe ($Pe = 4{,}000$). Note that for the values of α expected for such heterogeneous rock samples, neither the trend $D^* \sim Pe\ln(Pe)$ (Saffman, 1959; Koch and Brady, 1985) assuming that the distribution of flow speeds is flat ($\alpha = 1$), nor the trend $D^* \sim Pe$ expected for $\alpha > 1$ at high Pe are expected. For $1 < Pe < Pe_c$, $D^*/d_m \propto Pe^{2-\alpha'}$ where $\alpha' > \alpha$ depends on the mean speed distribution and the speed decorrelation distance ℓ_c that are the parameters that determine the advective particle transition distribution and subsequently the value of Pe_c. The mean particle speed remains correlated for longer distances in porous media with straighter and larger bonds (throats). As such ℓ_c is a good indicator of the complexity of flow field, because it encompasses the effect of tortuosity that ubiquitously decreases with increasing porosity and the effect of the mean throat radius that ubiquitously increases with porosity, while the other structural parameters are distinctly different for the two sets of samples. Yet, when reported in term of number of bonds length traveled before speed decorrelates, it is observed that *FS* and *FSD* sets behave quite similarly; the equivalent number of pores (intersection nodes) crossed before losing the memory of the initial speed equals $\eta - 1$ and ranges from about 1 for $\theta = 0.1$ to about 3 for $\theta = 0.25$. We conjecture that the increase of the number nodes crossed before speed decorrelates is linked to the speed changes caused by the splitting of the flow at the network node and thus to both the mean radius of the bonds and the coordination number κ. Similar conjecture can be done for the distribution of the solute mean

speed $p_m(v)$ which should be controlled by the speed changes caused by splitting of the flow where throats are connected, as it was anticipated by Alim et al. (2017) in numerical simulations in 2-dimensional simple artificial networks. The structural and hydrodynamic mechanisms that determine the flow distribution in 3-dimensional porous media, focusing on the impact pore size distribution, coordination number and local correlations on the speed distributions will be discussed in a forthcoming paper. Yet, from the results presented in this paper, one can conclude that the flow distribution, and thus the mean speed, are controlled by the distribution of fractions of fluid flowing at each of the network nodes which in turn is determined by the distribution of the throat radius (and not the mean) and the coordination number. At given porosity and mean bond radius the latter is controlled by the number of throats per unit volume that increases with porosity for the *FS* set and decrease with porosity for the *FSD* set of samples. We believe that these results give a first insight into both the mechanisms and the microstructural parameters that control dispersion in porous media.

DATA AVAILABILITY STATEMENT

The original contributions presented in the study are included in the article/supplementary material, further inquiries can be directed to the corresponding author/s.

AUTHOR CONTRIBUTIONS

All authors contribute to all the aspects of the presented work.

ACKNOWLEDGMENTS

The authors gratefully acknowledge the support of the CNRS-PICS project CROSSCALE (Project No. 280090). A. P. and M. D. gratefully acknowledge the support of the Spanish Ministry of Science and Innovation through the project HydroPore (PID2019Ű106887 GB-C31). Computations have been realized with the support of MESOLR, the Center of Competence in High-Performance Computing from the Languedoc-Roussillon region, France.

REFERENCES

Alim, K., Parsa, S., Weitz, D. A., and Brenner, M. P. (2017). Local pore size correlations determine flow distributions in porous media. *Phys. Rev. Lett.* 119:144501. doi: 10.1103/PhysRevLett.119.144501

Bear, J. (1972). *Dynamics of Fluids in Porous Media*. New York, NY: American Elsevier.

Berg, C. F. (2016a). *Fontainebleau 3d Models*. Available online at: http://www.digitalrocksportal.org/projects/57

Berg, C. F. (2016b). Fundamental transport property relations in porous media incorporating detailed pore structure description. *Transport Porous Media* 112, 467–487. doi: 10.1007/s11242-016-0661-7

Bijeljic, B., and Blunt, M. J. (2006). Pore-scale modeling and continuous time random walk analysis of dispersion in porous media. *Water Resour. Res.* 42:W01202. doi: 10.1029/2005WR004578

Bijeljic, B., and Blunt, M. J. (2007). Pore-scale modeling of transverse dispersion in porous media. *Water Resour. Res.* 43:W12S11. doi: 10.1029/2006WR005700

Bijeljic, B., Mostaghimi, P., and Blunt, M. J. (2011). Signature of non-Fickian solute transport in complex heterogeneous porous media. *Phys. Rev. Lett.* 107:204502. doi: 10.1103/PhysRevLett.107.204502

Bijeljic, B., Muggeridge, A. H., and Blunt, M. J. (2004). Pore-scale modeling of longitudinal dispersion. *Water Resour. Res.* 40:W11501. doi: 10.1029/2004WR003567

Bijeljic, B., Raeini, A., Mostaghimi, P., and Blunt, M. J. (2013). Predictions of non-fickian solute transport in different classes of porous media using direct simulation on pore-scale images. *Phys. Rev. E* 87:013011. doi: 10.1103/PhysRevE.87.013011

Brenner, H., and Edwards, D. (1993). *Macrotransport Processes*. Boston: Butterworth-Heinemann, MA.

Carrel, M., Morales, V. L., Dentz, M., Derlon, N., Morgenroth, E., and Holzner, M. (2018). Pore-scale hydrodynamics in a progressively bioclogged three-dimensional porous medium: 3-d particle tracking experiments and stochastic transport modeling. *Water Resour. Res.* 54, 2183–2198. doi: 10.1002/2017WR021726

Chatzis, I., and Dullien, F. A. (1985). The modeling of mercury porosimetry and the relative permeability of mercury in sandstones using percolation theory. *Int. Chem. Eng.* 25:1.

Danckwerts, P. (1953). Continuous flow systems: distribution of residence times. *Chem. Eng. Sci.* 2, 1–13. doi: 10.1016/0009-2509(53)80001-1

De Anna, P., Le Borgne, T., Dentz, M., Tartakovsky, A. M., Bolster, D., and Davy, P. (2013). Flow intermittency, dispersion, and correlated continuous time random walks in porous media. *Phys. Rev. Lett.* 110:184502. doi: 10.1103/PhysRevLett.110.184502

Delay, F., Ackerer, P., and Danquigny, C. (2005). Simulating solute transport in porous or fractured formations using random walk particle tracking. *Vadose Zone J.* 4, 360–379. doi: 10.2136/vzj2004.0125

Delgado, J. M. P. Q. (2006). A critical review of dispersion in packed beds. *Heat Mass Transfer* 42, 279–310. doi: 10.1007/s00231-005-0019-0

Dentz, M. (2012). Concentration statistics for transport in heterogeneous media due to stochastic fluctuations of the center of mass velocity. *Adv. Water Resour.* 36, 11–22. doi: 10.1016/j.advwatres.2011.04.005

Dentz, M., Borgne, T. L., Englert, A., and Bijeljic, B. (2011). Mixing, spreading and reaction in heterogeneous media: a brief review. *J. Contaminant Hydrol.* 120–121:1–17. doi: 10.1016/j.jconhyd.2010.05.002

Dentz, M., Icardi, M., and Hidalgo, J. J. (2018). Mechanisms of dispersion in a porous medium. *J. Fluid Mech.* 841, 851–882. doi: 10.1017/jfm.2018.120

Fischer, H. B. (1966). *Longitudinal Dispersion in Laboratory and Natural Streams*. Technical report, California Inst. of Technology.

Ghanbarian, B., Hunt, A. G., Ewing, R. P., and Skinner, T. E. (2014). Universal scaling of the formation factor in porous media derived by combining percolation and effective medium theories. *Geophys. Res. Lett.* 41, 3884–3890. doi: 10.1002/2014GL060180

Gjetvaj, F., Russian, A., Gouze, P., and Dentz, M. (2015). Dual control of flow field heterogeneity and immobile porosity on non-Fickian transport in Berea sandstone. *Water Resour. Res.* 51, 8273–8293. doi: 10.1002/2015WR017645

Gouze, P., Borgne, T. L., Leprovost, R., Lods, G., Poidras, T., and Pezard, P. (2008). Non-fickian dispersion in porous media: 1. Multiscale measurements using single-well injection withdrawal tracer tests. *Water Resour. Res.* 44:W06426. doi: 10.1029/2007WR006278

Gouze, P., Puyguiraud, A., Roubinet, D., and Dentz, M. (2021). Pore-scale transport in rocks of different complexity modeled by random walk methods. *Transport Porous Media* 1573–1634. doi: 10.1007/s11242-021-01675-2

Guibert, R., Horgue, P., Debenest, G., and Quintard, M. (2016). A comparison of various methods for the numerical evaluation of porous media permeability tensors from pore-scale geometry. *Math. Geosci.* 48, 329–347. doi: 10.1007/s11004-015-9587-9

Han, N.-W., Bhakta, J., and Carbonell, R. G. (1985). Longitudinal and lateral dispersion in packed beds: effect of column length and particle size distribution. *AIChE J.* 31, 277–288. doi: 10.1002/aic.690310215

Icardi, M., Boccardo, G., Marchisio, D. L., Tosco, T., and Sethi, R. (2014). Pore-scale simulation of fluid flow and solute dispersion in three-dimensional porous media. *Phys. Rev. E* 90:013032. doi: 10.1103/PhysRevE.90.013032

Kang, P. K., de Anna, P., Nunes, J. P., Bijeljic, B., Blunt, M. J., and Juanes, R. (2014). Pore-scale intermittent velocity structure underpinning anomalous transport through 3-d porous media. *Geophys. Res. Lett.* 41, 6184–6190. doi: 10.1002/2014GL061475

Kinzel, D. L., and Hill, G. A. (1989). Experimental study of dispersion in a consolidated sandstone. *Can. J. Chem. Eng.* 67, 39–44. doi: 10.1002/cjce.5450670107

Koch, D. L., and Brady, J. F. (1985). Dispersion in fixed beds. *J. Fluid Mech.* 154, 399–427. doi: 10.1017/S0022112085001598

Koponen, A., Kataja, M., and Timonen, J. (1996). Tortuous flow in porous media. *Phys. Rev. E* 54:406. doi: 10.1103/PhysRevE.54.406

Lee, T., Kashyap, R., and Chu, C. (1994). Building skeleton models via 3-d medial surface axis thinning algorithms. *CVGIP Graph. Models Image Process.* 56, 462–478. doi: 10.1006/cgip.1994.1042

Levy, M., and Berkowitz, B. (2003). Measurement and analysis of non-Fickian dispersion in heterogeneous porous media. *J. Contaminant Hydrol.* 64, 203–226. doi: 10.1016/S0169-7722(02)00204-8

Li, M., Qi, T., Bernabé, Y., Zhao, J., Wang, Y., Wang, D., et al. (2018). Simulation of solute transport through heterogeneous networks: analysis using the method of moments and the statistics of local transport characteristics. *Sci. Rep.* 8:3780. doi: 10.1038/s41598-018-22224-w

Matyka, M., Gołembiewski, J., and Koza, Z. (2016). Power-exponential velocity distributions in disordered porous media. *Phys. Rev. E* 93:013110. doi: 10.1103/PhysRevE.93.013110

Morales, V. L., Dentz, M., Willmann, M., and Holzner, M. (2017). Stochastic dynamics of intermittent pore-scale particle motion in three-dimensional porous media: experiments and theory. *Geophys. Res. Lett.* 44, 9361–9371. doi: 10.1002/2017GL074326

Moroni, M., and Cushman, J. H. (2001). Statistical mechanics with three-dimensional particle tracking velocimetry experiments in the study of anomalous dispersion. II. Experiments. *Phys. Fluids* 13, 81–91. doi: 10.1063/1.1328076

Oren, P.-E. (2002). Process based reconstruction of sandstones and prediction of transport properties. *Transport Porous Media* 46, 311–343. doi: 10.1023/A:1015031122338

Pfannkuch, H. O. (1963). Contribution a l'étude des déplacements de fluides miscibles dans un milieux poreux. *Rev. Inst. Fr. Petr.* 18, 215–270.

Puyguiraud, A., Gouze, P., and Dentz, M. (2019b). Stochastic dynamics of lagrangian pore-scale velocities in three-dimensional porous media. *Water Resour. Res.* 55:1196–1217. doi: 10.1029/2018WR023702

Puyguiraud, A., Gouze, P., and Dentz, M. (2019c). Upscaling of anomalous pore-scale dispersion. *Transport Porous Media* 128, 837–855. doi: 10.1007/s11242-019-01273-3

Puyguiraud, A., Gouze, P., and Dentz, M. (2020). Is there a representative elementary volume for anomalous dispersion? *Transport Porous Media* 131, 767–778. doi: 10.1007/s11242-019-01366-z

Puyguiraud, A., Gouze, P., and Dentz, M. (2021). Pore-scale mixing and the evolution of hydrodynamic dispersion in porous media. *Phys. Rev. Lett.* 126:164501. doi: 10.1103/PhysRevLett.126.164501

Russian, A., Dentz, M., and Gouze, P. (2016). Time domain random walks for hydrodynamic transport in heterogeneous media. *Water Resour. Res.* 52, 3309–3323. doi: 10.1002/2015WR018511

Saffman, P. G. (1959). A theory of dispersion in a porous medium. *J. Fluid Mech.* 6, 321–349. doi: 10.1017/S0022112059000672

Sahimi, M. (2011). *Flow and Transport in Porous Media and Fractured Rock: From Classical Methods to Modern Approaches*. John Wiley & Sons. doi: 10.1002/9783527636693

Sahimi, M., Hughes, B. D., Scriven, L., and Davis, H. T. (1986). Dispersion in flow through porous media–i. one-phase flow. *Chem. Eng. Sci.* 41, 2103–2122. doi: 10.1016/0009-2509(86)87128-7

Sahimi, M., and Imdakm, A. (1988). The effect of morphological disorder on hydrodynamic dispersion in flow through porous media. *J. Phys. A* 21, 3833–3870. doi: 10.1088/0305-4470/21/19/019

Seymour, J. D., and Callaghan, P. T. (1997). Generalized approach to NMR analysis of flow and dispersion in porous media. *AIChE J.* 43, 2096–2111. doi: 10.1002/aic.690430817

Seymour, J. D., Gage, J. P., Codd, S. L., and Gerlach, R. (2004). Anomalous fluid transport in porous media induced by biofilm growth. *Phys. Rev. Lett.* 93:198103. doi: 10.1103/PhysRevLett.93.198103

Siddiqi, K., and Pizer, S. (2008). *Medial Representations: Mathematics, Algorithms and Applications, 1st Edn*. Springer Publishing Company. doi: 10.1007/978-1-4020-8658-8

Siena, M., Riva, M., Hyman, J. D., Winter, C. L., and Guadagnini, A. (2014). Relationship between pore size and velocity probability distributions in stochastically generated porous media. *Phys. Rev. E* 89:013018. doi: 10.1103/PhysRevE.89.013018

Souzy, M., Lhuissier, H., Méheust, Y., Borgne, T. L., and Metzger, B. (2020). Velocity distributions, dispersion and stretching in three-dimensional porous media. *J. Fluid Mech.* 891:A16. doi: 10.1017/jfm.2020.113

Taylor, G. (1953). Dispersion of soluble matter in solvent flowing slowly through a tube. *Proc. R. S. Lond. A Math. Phys. Eng. Sci.* 219, 186–203. doi: 10.1098/rspa.1953.0139

Van Genuchten, M. T., and Wierenga, P. J. (1986). *Solute Dispersion Coefficients and Retardation Factors*. Madison: John Wiley & Sons, Ltd. doi: 10.2136/sssabookser5.1.2ed.c44

Weller, H. G., Tabor, G., Jasak, H., and Fureby, C. (1998). A tensorial approach to computational continuum mechanics using object-oriented techniques. *Comput. Phys.* 12, 620–631. doi: 10.1063/1.168744

Whitaker, S. (1967). Diffusion and dispersion in porous media. *AIChE J.* 13, 420–427. doi: 10.1002/aic.690130308

Conflict of Interest: The authors declare that the research was conducted in the absence of any commercial or financial relationships that could be construed as a potential conflict of interest.

frontiers in Water

ORIGINAL RESEARCH
published: 04 January 2022
doi: 10.3389/frwa.2021.710160

Using Direct Numerical Simulation of Pore-Level Events to Improve Pore-Network Models for Prediction of Residual Trapping of CO_2

Amir H. Kohanpur[1]*, *Yu Chen*[2] *and Albert J. Valocchi*[1]*

[1] Department of Civil and Environmental Engineering, University of Illinois at Urbana-Champaign, Champaign, IL, United States, [2] Los Alamos National Laboratory (DOE), Los Alamos, NM, United States

Direct numerical simulation and pore-network modeling are common approaches to study the physics of two-phase flow through natural rocks. For assessment of the long-term performance of geological sequestration of CO_2, it is important to model the full drainage-imbibition cycle to provide an accurate estimate of the trapped CO_2. While direct numerical simulation using pore geometry from micro-CT rock images accurately models two-phase flow physics, it is computationally prohibitive for large rock volumes. On the other hand, pore-network modeling on networks extracted from micro-CT rock images is computationally efficient but utilizes simplified physics in idealized geometric pore elements. This study uses the lattice-Boltzmann method for direct numerical simulation of CO_2-brine flow in idealized pore elements to develop a new set of pore-level flow models for the pore-body filling and snap-off events in pore-network modeling of imbibition. Lattice-Boltzmann simulations are conducted on typical idealized pore-network configurations, and the interface evolution and local capillary pressure are evaluated to develop modified equations of local threshold capillary pressure of pore elements as a function of shape factor and other geometrical parameters. The modified equations are then incorporated into a quasi-static pore-network flow solver. The modified model is applied on extracted pore-network of sandstone samples, and saturation of residual trapped CO_2 is computed for a drainage-imbibition cycle. The modified model yields different statistics of pore-level events compared with the original model; in particular, the occurrence of snap-off in pore-throats is reduced resulting in a more frontal displacement pattern along the main injection direction. Compared to the original model, the modified model is in closer agreement with the residual trapped CO_2 obtained from core flow experiments and direct numerical simulation.

Keywords: pore-network (PN) modeling, lattice-boltzmann, residual trapping, CO_2 storage and sequestration, pore-scale modeling

OPEN ACCESS

Edited by:
Anna L. Herring,
The Australian National University, Australia

Reviewed by:
Zhe Li,
Australian National University, Australia
Marcio Carvalho,
Pontifical Catholic University of Rio de Janeiro, Brazil
Nicole Vorhauer-Huget,
Otto von Guericke University Magdeburg, Germany

***Correspondence:**
Amir H. Kohanpur
kohanpu2@illinois.edu
Albert J. Valocchi
valocchi@illinois.edu

Specialty section:
This article was submitted to Water and Critical Zone, a section of the journal Frontiers in Water

Received: *15 May 2021*
Accepted: *07 December 2021*
Published: *04 January 2022*

Citation:
Kohanpur AH, Chen Y and Valocchi AJ (2022) Using Direct Numerical Simulation of Pore-Level Events to Improve Pore-Network Models for Prediction of Residual Trapping of CO_2. Front. Water 3:710160. doi: 10.3389/frwa.2021.710160

1. INTRODUCTION

Physics of two-phase flows in natural rocks plays an important role in addressing many current issues in subsurface water and energy resource assessment. In particular, capture and geological storage of carbon dioxide (CO_2) in deep saline reservoirs is being studied as a potential technology to reduce emission of greenhouse gases from industrial sources including conventional power

plants. Pore-scale modeling is necessary to understand fundamental behavior of CO_2-brine flow and obtain macroscopic flow properties needed for field-scale studies using reservoir simulation. Direct numerical simulation (DNS) methods and pore-network (PN) modeling are common approaches to study such flow systems in natural rocks because experimental methodologies are difficult to implement, time-consuming, and expensive. On one hand, DNS solves directly the Navier-Stokes equations from detailed 3D images of rock. Recent advances in X-ray computed tomography (CT) scanning has provided high resolution images needed to reconstruct the 3D pore structure of rock. This non-destructive technology is now able to produce images of pore space and fluids in real rocks at micron resolution for larger rock samples compared to its early days (Andrä et al., 2013; Blunt et al., 2013; Wildenschild and Sheppard, 2013; Schlüter et al., 2014; Bultreys et al., 2016; Balcewicz et al., 2021). On the other hand, PN modeling extracts a simplified network of pore elements from the real geometry of pore spaces and solves the Navier-Stokes equations in the simplified geometry.

Although PN modeling is more computationally efficient compared with DNS due to simplifications of the pore structure and governing flow equations, conventional PN models have some challenges in simulation of imbibition and residual trapping of CO_2 where pore filling processes are important (Blunt, 2017). Estimation of residual trapped CO_2 is important for assessing the long-term storage capacity and safety of geological sequestration since it impacts the predicted fate and distribution of the CO_2 plume in the reservoir. Theoretical and numerical studies in addition to experimental observations have shown that capillary trapping plays a key role in CO_2 plume migration (Juanes et al., 2010; MacMinn et al., 2010; Pentland et al., 2011; Krevor et al., 2015; Rasmusson et al., 2018).

CO_2-brine flow is usually considered to be capillary-dominated in real-world applications. Therefore, capillary forces determine the interface movement, flow, and trapping throughout the pore space, and hence so-called quasi-static PN models that neglect viscous forces are suitable. In general, if the viscous forces are comparable with the capillary forces, then a dynamic PN model is needed that includes more physics with the added expense of model complexity and computational costs (Joekar-Niasar and Hassanizadeh, 2012). However, quasi-static PN is more computationally efficient and describes pore-level events through the local threshold capillary pressure of pore elements. The competition among these events in CO_2-brine flow determines the invasion pattern and saturation of phases. Thus, the accuracy of calculated residual trapping is dependent on the accuracy of the defined pore-level flow models and pre-solved equations of local threshold capillary pressure of events in pore elements.

There are several PN modeling studies on real rock samples that focus on the physics of CO_2 and brine flow and residual trapping of CO_2. Mahabadi et al. (2020) studied immiscible displacement patterns during drainage with a dynamic PN model by varying capillary number (Ca) and viscosity ratio (M). They also examined the effect of pore-throat size distribution and PN connectivity on a sandy sediment for different sets of Ca and M. Matching their findings with properties of a typical CO_2-brine flow system ($Ca \simeq 10^{-5}$ and $M \simeq 10 - 15$), the dominant displacement pattern is capillary fingering and CO_2 saturation at the end of drainage is roughly $0.50 - 0.60$, an important quantity since it is the starting point for simulation of imbibition. Rasmusson et al. (2018) used a quasi-static PN model of CO_2-brine flow on Heletz sandstone to investigate the sensitivity of residual trapping of CO_2 to several parameters such as advancing contact angle and average connection number (number of pore-throats connected to a pore-body). They found that PNs with higher average connection number, higher advancing contact angle, and lower aspect ratio have smaller amount of trapped CO_2. They also obtained the initial-residual saturation curves of CO_2 for different drainage-imbibition scenarios. In addition, Hefny et al. (2020) applied quasi-static PN modeling on a highly permeable sandstone from a depleted oil field to study residual trapping of CO_2 and obtain characteristic curves during drainage-imbibition cycle. They investigated the effect of initial brine saturation at the reversal point from drainage to imbibition on residual trapping and relative permeabilities. They also found that smaller contact angle values (more brine-wet rock) lead to higher trapped amount of CO_2 at the end of imbibition process. These PN modeling studies have mainly used existing pore-level models in conventional PN flow solvers to study residual trapping of CO_2. An in-depth investigation of pore-level events in PN modeling of CO_2-brine flow can shed light on the physics and prediction of residual trapping of CO_2.

Ever since the early generation of two-phase flow PN models, there have been attempts to improve pore-level flow models during drainage and imbibition processes for better understanding of pore-scale displacement and prediction of core-scale properties of interest. Lenormand et al. (1983) first described pore-scale displacement mechanisms during drainage and imbibition from a 2D micromodel experiment. These mechanisms, namely, piston-type, snap-off, and pore-body filling, are widely used in PN flow solvers. For example, Raeini et al. (2018) developed a capillary-dominated PN flow solver that includes the concept of half-throats, several corners in pore elements, and new formulations of pore-level events. The solver was verified experimentally by Bultreys et al. (2020) using measured contact angle and based on the evolution of fluid distributions and flow paths during imbibition.

There are several studies that focus on pore-level events of PN modeling and using DNS for improvement, such as proposing new cross sections of pore elements, flow properties in pore-throats, local capillary pressure relations, corner flow behavior, and so on. Xie et al. (2017) used the lattice-Boltzmann (LB) method, a well-known and widely applied DNS approach, to simulate individual pores with triangular cross section to develop empirical terms to describe viscous coupling in oil-water flow. They incorporated these terms into a quasi-static PN solver that provided a more accurate prediction of relative permeability curves. In another study, Zhao et al. (2020) applied LB for real pore-throat cross sections to modify conductance and local threshold capillary pressure terms in a conventional PN model. Then, they simulated drainage through sandstones using quasi-static PN model to compute flow properties, namely, macroscopic capillary pressure curve, absolute permeability, and

relative permeability. Suh et al. (2017) used a morphological analysis technique along with LB simulation on different irregular pore-throat cross sections to establish a correlation between effective shape factor and local capillary pressure. They validated their method by comparing macroscopic capillary pressure with experimental data for the water retention curve. Ruspini et al. (2017) also investigated geometrical features of the pore elements, and introduced a new model of pore-body filling to investigate capillary trapping of non-wetting phase in water-wet rocks. The model incorporated geometrical characteristics of the pore-body, spatial location of connecting filled pore-throats, and wetting properties. They studied residual trapping, imbibition relative permeability, and capillary pressure curves from PN modeling of different sandstone samples.

Other DNS approaches have also been applied on pore elements to improve conventional PN models. Miao et al. (2017) proposed a new description of pore elements to avoid geometry simplifications of conventional PN models by using circularity, convexity, and elongation of voxelized pores. They carried out finite element simulations to obtain single-phase flow conductance and approximate the relationship between pore shape parameters and hydraulic conductance. Shams et al. (2018) incorporated viscous coupling effects into flow conductance of triangular tubes for different wettability conditions with the aid of finite volume simulation. They investigated the flow in the center and corners of a capillary tube and related pore geometry, viscosity ratio, wetting phase saturation, and wettability to the flow conductance term. Tang et al. (2018) carried out volume-of-fluid two-phase flow simulations using the commercial Fluent software on various tube cross sections to investigate the effect of contact angle on meniscus behavior and local capillary pressure in individual pores based on Young-Laplace equation. Thus, DNS methods are capable of improving pore-level events of PN modeling, and can be used in pore-scale modeling of residual trapping of CO_2.

In this work, we apply LB simulation as a DNS method on various geometric PN configurations that encompass a small collection of connected pore-bodies and pore-throats, in order to evaluate local threshold capillary pressure during the imbibition process. Then, we propose a modified model of imbibition events. The modified model is then incorporated into a quasi-static PN flow solver that can be applied on extracted PNs from natural rocks (Dong and Blunt, 2009; Raeini et al., 2018) or on larger PNs from upscaling approaches (Aghaei and Piri, 2015; Kohanpur and Valocchi, 2020), thereby resulting in more realistic macroscopic characteristic curves. We apply the modified PN model for two sandstones to evaluate residual trapping in a drainage-imbibition cycle of CO_2-brine flow, and compare the results with experimental and DNS data. The goal is to take advantage of the relative strengths of both modeling approaches and combine them into a new set of equations for incorporation into conventional PN models that can provide more physically-based estimates of residual trapping, as well as other continuum properties.

The organization of the rest of this paper is as follows. Section 2 explains the physics of two-phase flow processes for pore-level events in PN modeling. Section 3 discusses the defined PN configurations and the LB and PN simulation methods. In section 4, the main results from LB simulations of pore-body filling and snap-off are discussed (section 4.1). Then, the modified model is presented and incorporated into the quasi-static PN flow model, and applied on real rock samples (section 4.2). Finally, the conclusions are summarized in section 5.

2. PORE-NETWORK PROCESSES

2.1. Drainage and Imbibition

In geological storage of CO_2, the pore space of a saline aquifer is initially filled with brine as the wetting phase. Injection of CO_2, as the non-wetting phase into the pore space is a drainage process where the macroscopic capillary pressure and overall saturation of CO_2 increases. As the macroscopic capillary pressure drops, brine fills the pore space gradually during the imbibition process. Due to wettability, the entire CO_2 will not be displaced by the brine and some gets trapped across the pore space at the end of imbibition. This phenomenon is called residual trapping of CO_2, which is favorable for long-term CO_2 sequestration. In a field-scale CO_2 injection operation, the flow rates will decrease away from injection well, and therefore, one can assume capillary forces dominate and drive the flow (Kopp et al., 2009).

In quasi-static PN modeling of drainage and imbibition processes, the macroscopic capillary pressure is gradually changed to control the direction of invasion. On one hand, capillary pressure is increasing incrementally during drainage process which allows non-wetting CO_2 to displace the brine in the center of pores through piston-type displacement while brine resides in the corners and crevices. Based on Young-Laplace equation, wider pore-throats are invaded first in drainage followed by invasion of narrower pore-throats.

On the other hand, the imbibition process occurs after the drainage process, which has left residual brine in the corners of pore-bodies and throats due to wettability. Macroscopic capillary pressure decreases incrementally by increasing brine pressure which allows brine to displace CO_2 through different displacement events, namely, piston-type displacement, pore-body filling, and snap-off (Lenormand et al., 1983). The occurrence and frequency of these events generally depend on the local capillary pressure in a pore element, the topology of brine and CO_2 (connection number and filling), wettability (contact angle), pore irregularity (shape factor), and relative size of pore-body with respect to neighboring pore-throats (aspect ratio).

In the low capillary number condition of CO_2-brine flow, the assumption of local capillary equilibrium is valid which relates the curvature of interface in any pore at any time to the local capillary pressure based on the Young-Laplace equation. This assumption is the basis of quantifying the local threshold capillary pressure of different displacement events through the shape of interface in pore elements.

2.2. Pore-Level Events

Piston-type displacement is a common event in both drainage and imbibition processes. In this event, the invading phase displaces the defending phase from the center of pore element. In drainage, if CO_2 pressure is high enough (i.e., local capillary

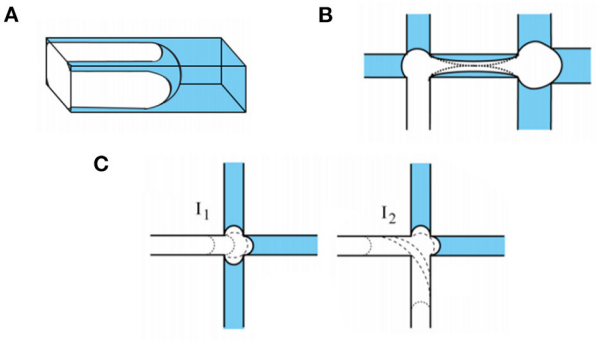

FIGURE 1 | Schematic representation of **(A)** piston-type displacement during drainage process in a rectangular tube, **(B)** snap-off in pore-throat during imbibition process, and **(C)** pore-body filling, I_1 and I_2 events, during imbibition process. CO_2 is shown in white and brine is shown in blue (Images from Rasmusson et al., 2018).

pressure passes the threshold) in the pore element, it displaces brine through its terminal meniscus from the center of pore element. **Figure 1A** shows schematically how CO_2 (in white) is advancing through the center of a rectangular tube and pushing brine (in blue). The threshold capillary pressure depends on the wettability and geometry of the pore element through the Young-Laplace equation, which for a circular tube pore element is:

$$P_c = \frac{2\sigma\cos\theta}{r} \tag{1}$$

In Equation (1), P_c is the local threshold capillary pressure, σ is interfacial tension, θ is contact angle between phases, and r is the radius of the cross section of the tube. In imbibition, brine displaces CO_2 from the center of tube when capillary pressure falls below the threshold. Related equations for rectangular and triangular cross sections are more complex than Equation (1) and can be found in Valvatne (2004).

Snap-off is an important pore-level event that usually causes trapping of non-wetting phase. The injected CO_2 occupies the center of pore elements at the end of drainage process while brine resides in the corners as connected layers throughout the PN. As the brine pressure increases and the imbibition process starts, these layers swell and increase the CO_2 saturation gradually. If the brine layer is not connected to any adjacent brine-filled elements and swelling continues, at some point brine layers from corners meet and create an unstable state. This leads to snap-off where brine spontaneously fills the center of pore element. Snap-off in a pore-throat that does not have adjacent brine-filled elements disconnects CO_2 in adjacent pore-bodies which translates into either partial filling or trapping in the following states of the PN, and impacts the distribution of CO_2 throughout the PN. **Figure 1B** shows schematically how the progress of brine layer swelling in a pore-throat can lead to snap-off and cause trapping in the pore-body on the right.

Pore-body filling is another type of imbibition event that occurs in different orders based on connectivity of the non-wetting phase. When the capillary pressure decreases during imbibition, the invading brine starts with filling narrower pore-throats and displacing CO_2 to the available adjacent elements, which are pore-bodies filled with CO_2. Depending on the connection number of the pore-body and number of CO_2-filled adjacent pore-throats, different scenarios of pore-body filling can occur. **Figure 1C** shows a schematic representation of two scenarios (I_1 and I_2 events) for a pore-body with connection number of 4. I_n refers to a pore-body filling where there are n connected pore-throats filled with CO_2 that allows an escape path during the invasion of brine into the pore-body. For a pore-body with connection number of z_{cn}, n can be between 0 and $z_{cn} - 1$.

The important feature of I_n events is that their local threshold capillary pressure can be different depending on the filling scenario, since the interface curvature during invasion is different. For example in **Figure 1C**, the I_1 event has smaller radius of curvature (i.e., higher capillary pressure) than I_2 based on the drawn dash lines referring to the next pore-level steps.

If only a single connected pore-throat is filled with CO_2 (I_1 event), the displacement process will be similar to piston-type displacement. The complexity of modeling is for higher order events (I_n, n from 2 to $z_{cn} - 1$) where the exact location and curvature of the interface in the pore-body is not clear. There are several studies in the literature proposing different parametric models by taking into account geometry-based and statistics-based parameters in the model (Blunt, 1998; Hughes and Blunt, 2000). For example, Blunt (1998) proposed a model based on the generic form of P_c in piston-type displacement and modified it with a parametric term to describe P_c of higher order I_n events:

$$P_c = \frac{2\sigma\cos\theta}{r_p} - \sigma\sum_{i=1}^{n} A_i x_i \tag{2}$$

In Equation (2), A_i is the model parameter chosen correlated with the inverse of absolute permeability of the PN, and x_i is a random number between zero and one. More details on pore-level events during drainage and imbibition processes can be found in Valvatne and Blunt (2004), Blunt et al. (2013), and Blunt (2017).

2.3. Competition of Events

The imbibition process in a PN flow model consists of a series of pore-level events in pore elements based on their local threshold capillary pressure that controls the timing and location of events. These events compete with one another in determining the invasion pattern and distribution of phases during imbibition. Therefore, the prediction of CO_2 distribution and trapping is highly dependent on the specific occurrences of these events. A change in the local threshold capillary pressure causes change in the order of displacement events which leads to a different pattern of phases, relative permeability, and residual trapping.

The topology of the brine phase also matters to determine the type of event during imbibition. If the adjacent element has brine at its center, the piston-type or pore-body filling would occur if the local threshold capillary pressure is already reached. Snap-off, however, does not require adjacent filled elements since it starts with swelling of brine in corners which is assumed present throughout the PN.

Geometrical and topological parameters of a PN play an important role in the equations of local threshold capillary pressure, and hence, competition of pore-level events during imbibition and residual trapping of CO_2. Some of these key PN parameters are as following:

- **Shape factor:** This summarizes the irregularities of the pores into one parameter in pore elements. The half-angle values of a triangular pore element can be obtained based on the shape factor (Patzek and Silin, 2000). These half-angle values are involved in the local threshold capillary pressure (P_c) relations of different pore events. In this study, different defined shape factors of the cross section are considered to evaluate the effect of shape factor on imbibition pore-level events.
- **Aspect ratio:** The aspect ratio of a pore-body is the ratio of its radius to the radius of its connected pore-throats ($a = r_p/r_t$). This parameter can also be expressed using average radius of multiple connected pore-throats to a pore-body. The competition of threshold P_c of pore-body filling and snap-off events is correlated with aspect ratio. This competition can be quantified by the ratio of their threshold P_c (Blunt, 2017). Generally, higher aspect ratio values results in more snap-off events compared with pore-body filling events. In this study, typical aspect ratio values from extracted PNs of natural rocks are used to define PN configurations.
- **Connection number:** The number of connected pore-throats to a pore-body is its connection number. It can be averaged across all pore-bodies of the PN as the average connection number of network that represents the connectivity of porous medium. Although connection number is not explicitly used in threshold P_c relations, it is also correlated with trapping of CO_2. Higher connectivity generally implies more potential pore-throats for the CO_2 to escape from the invaded pore-bodies during imbibition process.

3. METHODOLOGY

3.1. Pore-Network Configurations

We aim to apply DNS of two-phase flow using the LB code developed by Chen et al. (2018) on pore elements of PNs extracted from natural rocks to assess the physical assumptions used for pore-level events during imbibition. Therefore, the geometry of simulations consists of typical pore-bodies and pore-throats of extracted PNs with sufficient grid resolution to capture the interface and corner flow. We define a PN configuration as a small number of interconnected pore-throats and pore-bodies that is designed for investigation of pore-level events in the pore element of interest. We limit this study to two common types of PN configurations due to computational costs of LB simulations:

- **PTP configuration:** This refers to a pore-throat connecting two adjacent pore-bodies. The pore-throat is the focus of this configuration to investigate corner flow, piston-type displacement, or snap-off. The pore-bodies can be connected to inlet and outlet reservoirs of non-wetting and wetting fluids or additional pore elements. We study the PTP configuration to capture the interface in the cross section of the pore-throat and find the threshold P_c right before snap-off occurs.
- **TPT configuration:** This refers to a pore-body defined between two or more connecting pore-throats. The pore-throats can be directly connected to the inlet and outlet reservoirs or other pore-bodies. The pore-body is the focus of this configuration to investigate the filling process via different number of pore-throats and simulate pore-body filling during imbibition.

Conventional quasi-static PN models can use pore elements with different cross sections; triangle, square, circle are considered here as they are commonly used. The shape factor (G) is a dimensionless geometrical parameter that is used in assigning familiar geometries to the cross section of a tube-shape pore element (Patzek and Silin, 2000). It is defined as:

$$G = \frac{VL}{A^2} \tag{3}$$

In Equation (3), A is the cross-sectional area, V is the volume, and L is the length of the tube-shape pore element with an arbitrary cross section. Our experience from studying extracted PNs of various sandstone cores shows that the triangular cross section comprises the majority of pore elements of PNs. Shape factor of triangular elements can vary in a range from 0 (slit-shape) to 0.0481 (equilateral).

In this study, we select three shape factor values equal to 0.020, 0.030, 0.040 for the designed PN configurations to represent a reasonable range, while limiting the number of required LB simulations. These three shape factor values represent three different triangular cross sections which are characterized by their corner half-angles ($\beta_1, \beta_2, \beta_3$). We use an algorithm introduced by Patzek and Silin (2000) to determine three corner half-angles of each shape factor G to define triangular cross sections of pore elements. The resulting β's (with the convention of $\beta_1 < \beta_2 < \beta_3$) for each shape factor are as following:

- $G = 0.020$: $\beta_1 = 6.20^\circ$, $\beta_2 = 19.7^\circ$, and $\beta_3 = 64.1^\circ$.
- $G = 0.030$: $\beta_1 = 9.60^\circ$, $\beta_2 = 35.6^\circ$, and $\beta_3 = 44.8^\circ$.
- $G = 0.040$: $\beta_1 = 18.0^\circ$, $\beta_2 = 23.7^\circ$, and $\beta_3 = 48.3^\circ$.

As discussed in section 2.2, pore-body filling event can occur in different scenarios depending on the number of adjacent CO_2-filled pore elements. These scenarios can be defined with different TPT configurations based on the number of connecting pore-throats to the pore-body of configuration, which will be addressed in section 4.1.1.

3.2. Lattice-Boltzmann Method

The lattice-Boltzmann (LB) method is used for DNS for the idealized pore element geometry noted above. Use of LB for DNS on voxelized pore geometry is now well established, and its popularity is due to its favorable computational features (Ahrenholz et al., 2008; Chen et al., 2019). The LB is a so-called mesoscopic method that can simulate fluid mass and momentum balance. The fluid is represented by particles with probability of moving in different directions along a predefined lattice. The LB method is based on streaming and collision of a set of

fluid particle distribution functions (PDF) on a lattice. The no-slip boundary conditions on solid surfaces are implemented by simply switching the directions of the particles on the surface nodes, the so-called bounce-back scheme. Among several LB schemes for simulating multiphase flows, the color-fluid model (Gunstensen et al., 1991; Grunau et al., 1993) is capable of producing a relatively sharp interface between immiscible phases and capturing their interface evolution. The color-fluid model is also able to incorporate high viscosity ratios due to its independent control of the surface tension and viscosity which makes it quite relevant to CO_2-brine flow system where viscosity ratio is about 10–15. On the other hand, it has limitations on the density ratio and a large absolute value of color gradient may produce numerical instabilities (Ramstad et al., 2019).

We use a variant of the multiple relaxation time (MRT) color-fluid LB simulator (Tölke, 2002; Tölke et al., 2006; Chen et al., 2018). In this model, each phase has its own set of PDFs and the discrete Boltzmann equation is solved for each phase. We consider two sets of the D3Q19 PDFs, i.e., a 3D model with 19 velocities, representing the two fluid phases, referred to as the fluids r (CO_2) and b (brine), which follow the collision-streaming procedure for the PDF:

$$f_i^s\left(x+e_i\Delta t, t+\Delta t\right) = f_i^s\left(x,t\right) + \Omega_i^{s(3)}\left\{\Omega_i^{s(1)} + \Omega_i^{s(2)}\right\}, s = r, b \tag{4}$$

In Equation (4), $\Omega_i^{s(1)}$ is the standard LB collision operator, $\Omega_i^{s(2)}$ is the perturbation step that generates the surface tension effect, and $\Omega_i^{s(3)}$ is the recoloring step that separates the two fluids. The collision operators $\Omega_i^{s(1)}$ and $\Omega_i^{s(2)}$ are constructed under the MRT framework that increases stability and accuracy of the model (d'Humieres, 2002; Tölke et al., 2006). The macroscopic quantities of flow, such as fluid velocity and pressure, are computed by calculating the moments of the PDFs. More details of our in-house code are given by Chen et al. (2018).

In the present work, we carry out LB simulations of CO_2-brine flow system on idealized PN configurations. The fluid properties and flow conditions are listed in **Table 1**, which are realistic for CO_2-brine flow and similar parameters used in Kohanpur et al. (2020), except for the contact angle which comes from an experimental study by Dalton et al. (2018). We simulate the drainage process followed by the imbibition process with inlet velocity and outlet pressure boundary conditions. More details on implementation of boundary conditions can be found in Chen et al. (2019).

Th capillary number is defined as the ratio of viscous forces over capillary forces ($Ca = \frac{\mu_{nw} V}{\sigma}$) where μ_{nw} is dynamic viscosity of CO_2, V is the average inlet velocity, and σ is the interfacial tension between CO_2 and brine. For the LB simulations, capillary number equal to 5×10^{-5} is used, which is relatively small to guarantee a capillary-dominated flow consistent with field injection conditions and the assumptions of the quasi-static PN model. Unfortunately, even smaller values of capillary number can be computationally expensive to reach steady-state with potential numerical instabilities and spurious velocities in LB simulation.

TABLE 1 | Properties of CO_2-brine flow system.

Properties	Value
Contact angle (°)	56 (brine-wet)
Interfacial tension (mN/m)	30.0
Brine density (Kg/m^3)	1,100
CO_2 density (Kg/m^3)	1,100
Brine kin. viscosity (m^2/s)	1×10^{-6}
CO_2 kin. viscosity (m^2/s)	1×10^{-7}
Capillary number	5×10^{-5}
Viscosity ratio	10

3.3. Quasi-Static Pore-Network Model

The quasi-static PN flow simulation is an efficient tool to characterize CO_2-brine flow properties. As noted previously, for field-scale carbon capture and storage (CCS), the velocity is low (with the exception of a local region near the injection well) and hence the capillary number is relatively small, justifying the assumption of capillary-dominated flow and use of a quasi-static PN model. In this work, we conduct drainage and imbibition simulations using the publicly available PN flow codes of Valvatne and Blunt (2004) and Raeini et al. (2018). We incorporate modified equations for imbibition pore-level events (which are presented in sections 4.1.1 and 4.1.2) into the PN flow solver of Raeini et al. (2018), which is then applied to extracted PNs from real rock images to obtain residual trapping of CO_2 and other quantities of interest during the drainage-imbibition process. The detailed procedure of the PN flow solver is described in Valvatne (2004) and Raeini (2013).

4. RESULTS

4.1. Lattice-Boltzmann Simulation

The PN configuration types listed in section 3.1 are used as the geometry of LB simulations where each voxel of the image is converted to a lattice unit. It is standard practice in LB simulation to use dimensionless parameters normalized with lattice units and then convert to physical units when needed. A lattice unit can be either pore (0-value) or wall (1-value), and the set of PDFs of each phase is computed. At each stage of the LB drainage and imbibition simulations, the fluid-fluid interface location and the local capillary pressure need to be computed. The interface location can be distinguished with the order parameter (ϕ) in the color-fluid LB model:

$$\phi = \frac{\rho_r - \rho_b}{\rho_r + \rho_b} \tag{5}$$

In Equation (5), ρ_r and ρ_b are fluid densities of red and blue fluids in lattice unit, respectively. The density of each phase is computed by the zeroth moment of the respective PDFs. Therefore, $\phi \approx 1$ refers to the presence of red fluid (CO_2) while $\phi \approx -1$ represents the presence of blue fluid (brine) (Chen et al., 2018). The location of interface is where $\phi \approx 0$. in the color-fluid LB model the fluid interface is diffuse and spread over several lattice units, but if fine

grids are used then a relatively sharp interface results. In practice, we use the cut-off of 5% for ϕ to specify the location of each fluid.

In order to evaluate local capillary pressure in pore elements, one should compute average pressure of each phase in the pore volume. In the color-fluid LB method, the ideal gas equation-of-state is assumed which allows calculation of fluid pressure from the density. The order parameter is used to detect the location of phases and the interface. To compute the pressure of the pure red and blue fluid phases, lattice points should be far enough away from where the order parameter is close to zero. The pressure of red and blue fluids can be averaged based on the total density of the respective fluid of a calculation volume (e.g., pore-body).

$$\bar{P}_r = \frac{\sum 1/3\rho_{r_i}}{n_r} \tag{6}$$

$$\bar{P}_b = \frac{\sum 1/3\rho_{b_i}}{n_b} \tag{7}$$

In Equations 6 and 7, the summation is over the lattice points of a defined calculation volume with n_r and n_b lattice units of red and blue fluids, respectively. Thus, the local capillary pressure (P_c) in the calculation volume can be obtained using the difference in the average pressure of fluids.

$$P_c = \bar{P}_r - \bar{P}_b \tag{8}$$

In Equation (8), P_c is the calculated average local capillary pressure within the calculation volume of interest.

This procedure to calculate the local capillary pressure is validated on a simple piston-type displacement in a cylindrical tube, as illustrated in **Figure 2A**, where boundary conditions of velocity (inlet) and constant pressure (outlet) are implemented, and CO_2 (shown in red) moves upward and displaces brine (transparent) in the tube. We use the resulting density of fluids to obtain the pressure distribution in each fluid to calculate the local capillary pressure during the filling process. The calculation volume is marked with two green planes. **Figure 2B** shows a cross-sectional view through the center of the tube. The radius of interface (r') can be captured and used in the Young-Laplace equation to evaluate local capillary pressure, which is denoted the cross-sectional approach. This approach can be utilized in simple geometries and is preferred wherever the radius of interface can be captured. However, this is not always the case for 3D LB simulations on more complex PN configurations such as for pore-body filling events in triangular elements where the interface can have a 3D complex shape. In such cases, the LB density-based approach can be used to evaluate P_c.

In **Figure 2C**, the resulting P_c from LB simulation of the simple piston-type displacement in a cylindrical tube is calculated and compared with the theoretical values based on Young-Laplace equation for different radii ($r = 5$, $r = 15$, $r = 20$ in lattice units). The results show a good agreement (less than 10% error), thereby giving us confidence in the procedure for calculation of P_c based on the order parameter and densities in lattice unit is feasible in 3D LB simulations.

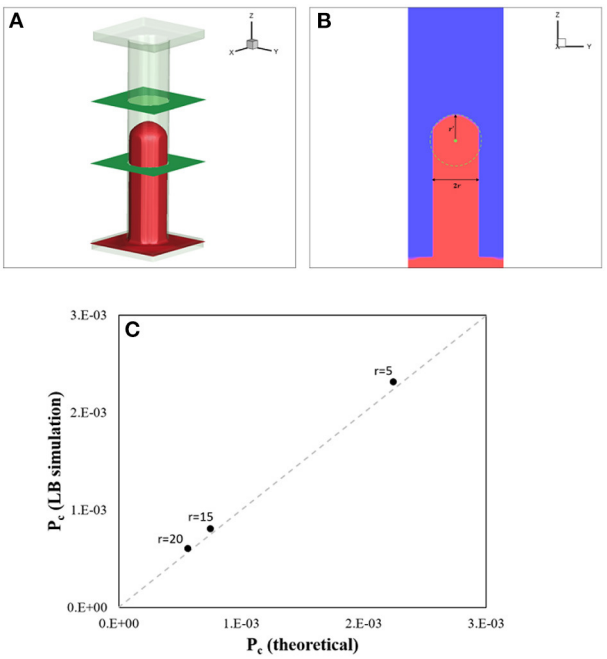

FIGURE 2 | A validation of LB simulation on a simple piston-type displacement in a cylindrical tube for calculation of local capillary pressure: **(A)** CO_2 is in red, brine is transparent, and the green planes define the bounds of calculation volume. **(B)** Cross-sectional view parallel to yz-plane through the center of tube to capture the radius of interface. **(C)** Comparison of calculated P_c from LB simulation and theoretical P_c from Young-Laplace equation on different radii of a cylindrical tube.

In following sections 4.1.1 and 4.1.2, we present the LB simulation results on PN configurations plus the modified models of pore-body filling and snap-off events during imbibition process that will be incorporated in quasi-static PN flow solver.

4.1.1. Simulation of Pore-Body Filling

Three different TPT configurations with different shape factors but equal radius of inscribed circle and connection number of 4, shown in **Figure 3**, are studied to model the I_1, I_2, and I_3 pore-body filling events during imbibition. Based on our experience, the average connection number of PNs from various rock samples is usually within the range of 3–5. Therefore, the choice of connection number of 4 is reasonable. In addition, having 4 connecting pore-throats allows us to include pore-body filling events up to order 3. As explained in section 2.2, lower orders of pore-body filling have higher threshold P_c and are hence more favorable than higher order pore-body filling (I_{4+}) during imbibition. The higher orders of pore-body filling usually have a small number of occurrences and are hence less important with respect to trapping of non-wetting phase. Thus, we focus on lower orders of pore-body filling in the LB simulations and investigate key factors in the filling process such as shape factor and corner half-angles.

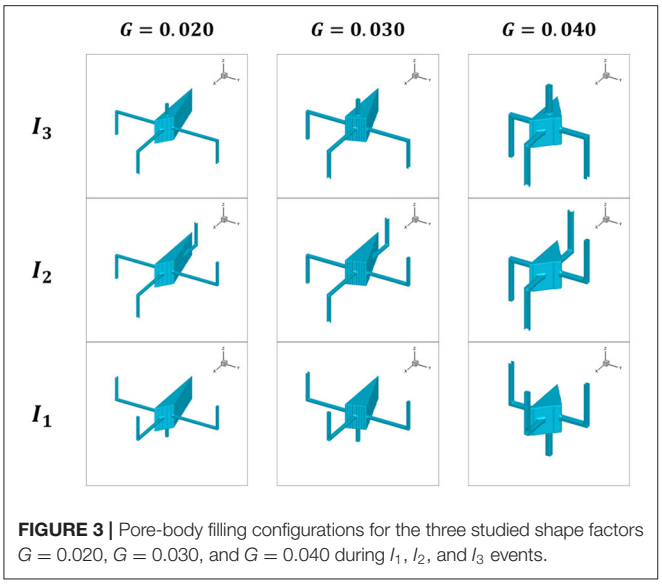

FIGURE 3 | Pore-body filling configurations for the three studied shape factors $G = 0.020$, $G = 0.030$, and $G = 0.040$ during I_1, I_2, and I_3 events.

The cross section of the pore-body is defined as a triangle with three different shape factors with their corresponding corner half-angles. The cross section of pore-throats in all cases is square to reduce the complexity and ensure a simultaneous invasion from different connecting pore-throats across different configurations. This is achieved by designing configurations in a way that all pore-throats have the same cross section and path length from the inlet or outlet reservoirs to the pore-body, as depicted in **Figure 3**. An example of such a configuration is illustrated from different views in **Figure 4A**, which is designed for modeling I_1 event with $G = 0.040$ for the pore-body. The inscribed radii of all pore-throats are equal and the geometric aspect ratio between pore-body and pore-throat is 5 in all configurations.

In LB flow simulation of these configurations, the inlet reservoir is connected to bottom pore-throats and the outlet reservoir is connected to top pore-throats, and the flow is always in +z (upward) direction. Initially, drainage is simulated which results in CO_2 occupying the center of pore elements until steady-state saturation. Then, brine is injected from the same inlet reservoir to displace the CO_2 from the pore-body. The boundary conditions in both drainage and imbibition are prescribed velocity at the inlet and fixed pressure for the outlet. **Figure 4B** shows an example of LB simulation of pore-body filling during drainage and imbibition processes on a triangular TPT configuration, shown in **Figure 4A**, with the shape factor of $G = 0.040$ during I_1 event.

Since the pore-body filling event is a dynamic process, we can track the saturation of CO_2 in the pore-body in order to specify the relevant time step for the evaluation of threshold P_c. We choose the saturation of 0.50, when half of the CO_2 is displaced, as the time step to calculate the threshold P_c, using the procedure described earlier. The procedure is applied on all configuration of **Figure 3** and the corresponding P_c is computed. The normalized capillary pressure in a pore-body ($\hat{P}_c$) is defined as:

$$\hat{P}_c = P_c \frac{r_p}{\sigma} \tag{9}$$

In Equation (9), r_p is the inscribed radius of pore-body and σ is the surface tension. This definition makes the analysis more straightforward since the conversion from lattice unit to physical unit is not necessary.

Based upon the LB simulations, we propose modifying the conventional models (e.g., Valvatne and Blunt, 2004) for the local threshold capillary pressure of pore-body filling event with some new parameters as:

$$\hat{P}_{c_i} = 2cos(\theta) - \left(\frac{r_p}{G\bar{r}_t} \times a'_i \times C_{f_i}\right) \tag{10}$$

In Equation (10), the subscript i refers to the order of pore-body filling event. C_{f_i} is defined as the filling factor that comes from the analysis of LB simulations of PN configurations. a'_i is defined as effective aspect ratio of the pore-body which is similar to the classic definition of geometric aspect ratio but it considers just the invading pore-throats rather than all connecting ones. Therefore, a'_i can be a function of the filling event and it involves the radius of invading pore-throat during the pore-body filling event. The second term on the right hand side of Equation (10) is the main difference between our proposed model and conventional model. For example, Valvatne and Blunt (2004) chose a term proportional to $K^{-1/2}$ where K is the absolute permeability of PN. We consider the effective aspect ratio and shape factor to include the effect of the order of pore-body filling event and pore-body shape factor on local threshold capillary pressure, which will result in a different filling factor.

In order to use this modified model, one needs to know C_{f_i} for different orders of filling events for different pore-body shape factors. We consider $C_{f_1} = 0$ the same as in conventional models. In order to evaluate C_{f_2} and C_{f_3}, we define the ratio of $\hat{P}_{c_i}$ of events with respect to $\hat{P}_{c1}$ as:

$$f_{21} = \frac{\hat{P}_{c_2}}{\hat{P}_{c_1}} \tag{11}$$

$$f_{31} = \frac{\hat{P}_{c_3}}{\hat{P}_{c_1}} \tag{12}$$

If we combine Equations (10–12), the filling factors can be described as:

$$C_{f_2} = \frac{2G\bar{r}_t cos(\theta)(1 - f_{21})}{r_p a'_2} \tag{13}$$

$$C_{f_3} = \frac{2G\bar{r}_t cos(\theta)(1 - f_{31})}{r_p a'_3} \tag{14}$$

Therefore, by having $\hat{P}_{c_i}$ of different events from LB simulation, one can compute the corresponding f_{i1} and use Equations (13) and (14) to obtain the filling factors of the modified model.

Table 2 presents the resulting normalized local capillary pressure of pore-body filling events (I_1, I_2, I_3) for the studied

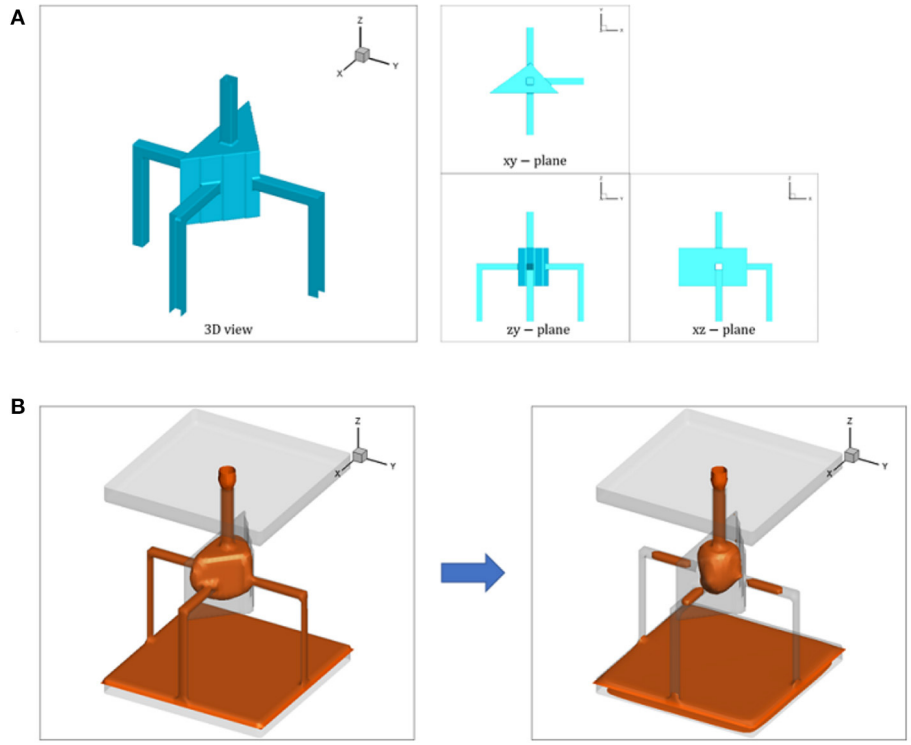

FIGURE 4 | Pore-body filling configuration for the shape factor of $G = 0.040$ designed for modeling I_1 event: **(A)** The equal length and cross section of pore-throats provide the desired simultaneous invasion. **(B)** LB simulation of pore-body filling during drainage (left) and imbibition (right) processes. CO_2 is shown in red and brine is transparent.

TABLE 2 | The resulting normalized local capillary pressure ($\hat{P_{c_i}}$) and filling capillary pressure ratios (f_{i1}) defined in the modified pore-body filling model from LB simulations on PN configurations.

G	$\hat{P_{c_1}}$	$\hat{P_{c_2}}$	$\hat{P_{c_3}}$	f_{21}	f_{31}
0.020	2.020	1.514	0.984	0.750	0.487
0.030	1.884	1.362	0.859	0.723	0.456
0.040	1.433	0.994	0.614	0.694	0.428
Conventional				0.676	0.412

shape factors. The $\hat{P_{c_i}}$ is used to calculate the capillary pressure ratio (f_{i1}) and the filling factor (C_{f_i}), as listed in **Table 2** as well. The resulting f_{i1} from the modified model is slightly higher than conventional model which translates into higher local threshold capillary pressure that makes pore-body filling event more favorable during imbibition process.

The results in **Table 2** are used to describe the filling factor as a function of shape factor and incorporate it into a quasi-static PN flow solver where pore-body filling events of I_2 and I_3 are modified with Equation (10), accordingly.

4.1.2. Simulation of Snap-Off

Three different shape factors, $G = 0.020$, $G = 0.030$, $G = 0.040$, with triangular cross sections in a PTP configuration, as shown in **Figure 5A**, are studied to investigate the threshold P_c during snap-off events. In each configuration, ratios involvolving the diameter and length of pore-body and pore-throat are defined as $l_t/2r_t = 10$ and $r_p/r_t = 5$. The focus is the cross section of the center of the pore-throat. We first perform a drainage simulation with receding contact angle (10°) followed by imbibition with advancing contact angle (60°). These values are based on Morrow's contact angle hysteresis model (Morrow, 1975) for intrinsic contact angle of 56° that comes from an experimental CO_2-brine flow study by Dalton et al. (2018) on a Berea sandstone sample. The model relates the intrinsic contact angle to receding and advancing ones. The boundaries are connected to bounding pore-bodies and a pressure-driven flow is implemented in the LB simulation.

We use the local threshold capillary pressure of a snap-off event in a similar format to conventional snap-off models, but with a new correction factor:

$$\hat{P}_c = cos(\theta) - C_i sin(\theta) \tag{15}$$

In Equation (15), C_i is defined as the snap-off factor and $\hat{P}_c$ is defined similar to Equation (9) (r_p replaced with r_t). In conventional models (Valvatne and Blunt, 2004), C_i can be described in terms corner half-angles:

$$C_i = \frac{2}{cot(\beta_1) + cot(\beta_2)} \tag{16}$$

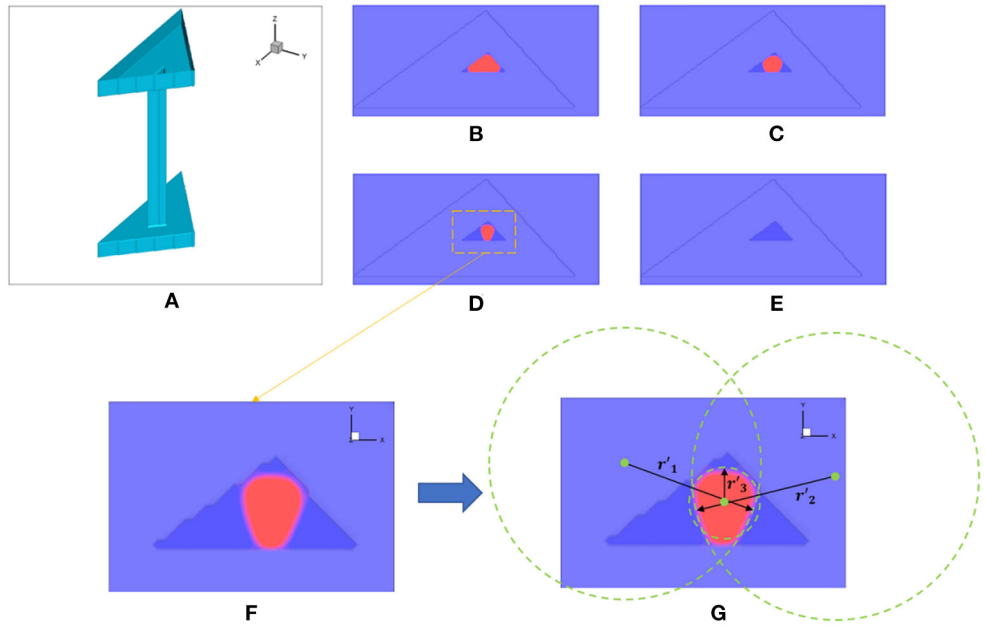

FIGURE 5 | (A) PTP configuration with $G = 0.040$ defined for assessing the snap-off event in pore-throat. Evolution of cross section of a pore-throat with $G = 0.040$ from LB simulation during snap-off event: **(B)** beginning of imbibition, **(C)** moving the interface toward the center, **(D)** before snap-off, **(E)** and after snap-off. **(F)** Higher resolution of pore-throat cross section before snap-off. **(G)** Cross-sectional approach in evaluation of capillary pressure based on the radius of curvature of three corners.

In Equation (16), β_1 and β_2 are defined as the two smaller corner half-angles of a triangular cross section (Patzek and Silin, 2000).

However, we carry out LB simulation for different shape factors to find C_i as a function of G. The drainage invasion of CO_2 into the PTP configurations is implemented first. Then, the gradual imbibition of brine is implemented via an incremental increase of brine pressure. This allows the brine in corners to expand gradually prior to snap-off in the pore-throat, as shown in the pore-throat cross section in **Figures 5B–E**.

A cross-sectional analysis is applied on the results from LB simulation to obtain the radius of curvature in each corner, as illustrated in **Figures 5F,G**, during the snap-off event. The minimum radius among the three is substituted into the Young-Laplace equation ($P_c = 2\sigma cos(\theta)/r'$) to evaluate the local threshold capillary pressure of the pore-throat:

$$r' = min\left\{r'_1, r'_2, r'_3\right\} \tag{17}$$

In Equation (17), r'_i refers to the calculated radius of curvature in each corner of the pore-throat, as shown in **Figure 5G**. On the other hand, by defining the local capillary pressure of snap-off in the form of Equation (15), one can relate the correction factor of C_i to the radius of curvature r' from LB simulation results:

$$C_i = \frac{1 - 2r_t/r'}{tan(\theta)} \tag{18}$$

In Equation (18), r_t refers to the inscribed radius of the pore-throat (a purely geometrical parameter) while r' refers to the minimum radius of curvature of the interface right before the snap-off event in the pore-throat (determined from LB simulation results).

TABLE 3 | The resulting snap-off factor (C_i) as a function of shape factor from LB simulations on PTP configurations compared with the conventional model.

G	Conventional model	Modified model
0.020	$C_i = 0.167$	$C_i = 0.163$
0.030	$C_i = 0.274$	$C_i = 0.213$
0.040	$C_i = 0.373$	$C_i = 0.337$

Table 3 presents the resulting snap-off factors from LB simulation on PTP configurations for the three studied shape factors. The snap-off factors from modified model are slightly smaller than factors from conventional model for all studied shape factors. This results in higher local threshold capillary pressure for snap-off events in the modified model as well. Although only three shape factors are considered, covering a range from 0.020 to 0.040 with linear interpolation used to fill in, based on our experience with different types of rock samples, this range of shape factor is sufficient to include the majority of both pore-bodies and pore-throats across various PNs of different samples.

4.2. Modified Pore-Network Modeling Results

4.2.1. Rock Sample and Extracted Pore-Network

In this section, two natural rock samples of Berea sandstone and Mt. Simon sandstone are selected to investigate residual

TABLE 4 | Selected samples for pore-network modeling of CO_2-brine flow after a drainage-imbibition cycle.

Sample	Porosity	Res. (μm)	Size (mm^3)	Study
Berea sandstone	0.202	2.36	$1.89 \times 1.89 \times 1.42$	Dalton et al., 2018
Mt. Simon sandstone	0.263	2.80	$1.40 \times 1.40 \times 1.40$	Kohanpur et al., 2020

trapping of CO_2 after a drainage-imbibition cycle. The former sample was the focus of an experimental study of measurement of contact angle between CO_2 and brine by Dalton et al. (2018). The latter sample was the focus of a rock characterization study and CO_2-brine flow simulation with different modeling approaches by Kohanpur et al. (2020). The core plugs of both samples were scanned at the micro-CT imaging facility at the National Energy Technology Laboratory (NETL) which produced a series of grayscale scans. These scans are processed through several steps of image processing in Fiji (Schindelin et al., 2012) to filter and smooth images in order to distinguish existing image phases (solid, pores, CO_2, brine) from each other via thresholding algorithms. **Table 4** presents relevant information for the studied sandstone samples. We report flow simulation results from the Berea sandstone sample, shown in **Figure 6A**, in detail here. For brevity, the results from the Mt. Simon sandstone sample are presented in the **Supplementary Material**.

Dalton et al. (2018) used a fractional flow experimental apparatus to perform a drainage-imbibition cycle of CO_2-brine flow on the Berea sandstone sample. They scanned post-imbibition micro-CT images to measure residual CO_2. **Figure 6B** shows an example of post-imbibition grayscale image and its corresponding segmented image which consists of three phases: solid in white, CO_2 in black, brine in gray. This is obtained by a ternary segmentation implemented in Fiji, which entails two sequential binary segmentation on dry scans and post-imbibition scans, respectively, in order to obtain their differences and extract the distribution of CO_2.

Figure 6C shows the 3D representation of the pore structure, and **Figure 6D** shows the residual trapped CO_2 after imbibition in the Berea sandstone sample. Saturation of residual of trapped CO_2 is equal to the ratio of the number of CO_2 voxels in **Figure 6D** to the number of pore voxels in **Figure 6C**. The resulting experimental residual CO_2 saturation after imbibition is 0.331 for the Berea sandstone sample based on this processing of the micro-CT images.

Dalton et al. (2018) also provided the distribution of contact angle by using measurements on the captured interface from 2D micro-CT images. The contact angle average (55.9°) and standard deviation (15.5°) come from measurement on 40 different 2D micro-CT images located in different parts of the core. More details can be found in Dalton et al. (2018). The average value of 55.9° is used as the contact angle in our LB and PN simulations.

We use the PN extraction code based on Maximal Ball (MB) algorithm from Dong and Blunt (2009) and Raeini et al. (2017) to obtain corresponding PNs of the rock images. The algorithm was originally introduced by Silin and Patzek (2006) where the entire 3D voxelized pore space is searched to find

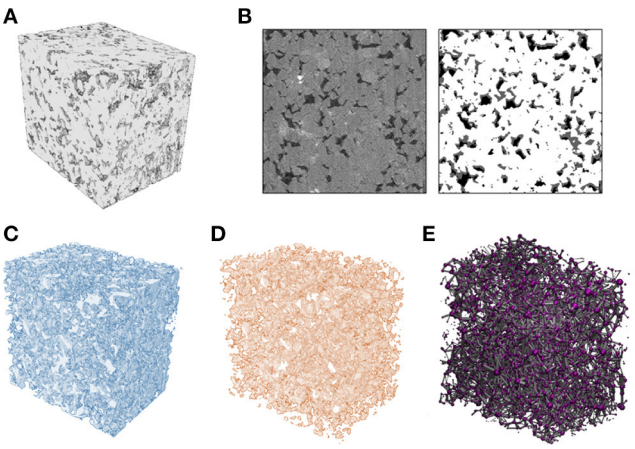

FIGURE 6 | (A) 3D representation of the Berea sandstone sample. **(B)** A slice of micro-CT images: left image is the raw grayscale slice and right image is the ternary segmented slice where solid part is in white, CO_2 is in black, and brine is in gray. **(C)** 3D representation of the pore structure. **(D)** 3D representation of residual trapped CO_2 after imbibition process. **(E)** Extracted pore-network of the Berea sandstone sample from maximal-ball algorithm.

the largest possible voxelized spheres, known as MBs. This PN extraction tool can provide the inherent randomness of pore structure in real rocks with a wide range of connection numbers for pore-bodies. More details of this PN extraction tool can be found in Dong and Blunt (2009). The output of this code is geometrical and topological information of pore-bodies and pore-throats including the location, radius, volume, length, total length, and shape factor. **Figure 6E** shows extracted PN of the Berea sandstone sample. This PN has 6207 pore-bodies and 10160 pore-throats with the average connection number of 3.18. The computed absolute permeability of the PN is 455 mD using the Valvatne and Blunt (2004) PN flow solver.

As mentioned earlier, the shape factor (Equation 3) in PN models is a metric of irregularities of the pore space of pore elements. **Figure 7** shows the shape factor distribution of pore-bodies (left plot) and pore-throats (right plot) in the extracted PN of the Berea sandstone sample. The distribution in both follows approximately a normal distribution with the average of 0.0298 and 0.0312 and standard deviation of 0.0078 and 0.0064 for pore-bodies and pore-throats, respectively. Therefore, these distributions justify the selected values of shape factors in PN configurations studied in section 3.1.

Next, we present detailed results from the CO_2-brine flow simulation with properties listed in **Table 1**. We use a modified PN flow solver that is based on Raeini et al. (2018) but with its

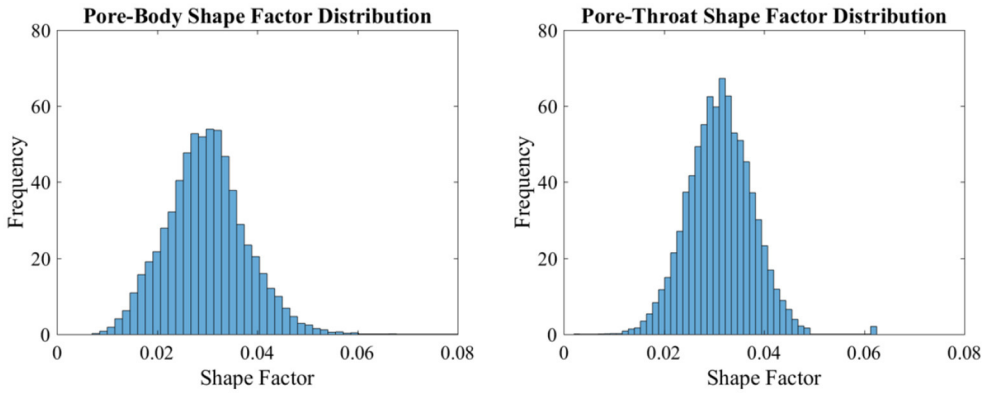

FIGURE 7 | Shape factor distribution of pore elements in the extracted pore-network of Berea sandstone sample: (left) pore-body shape factor distribution, (right) pore-throat shape factor distribution.

imbibition threshold P_c equations of pore-body filling and snap-off events replaced with the new pore-level models described in sections 4.1.1 and 4.1.2. Then, the outputs from the modified PN flow solver are compared with those from the original PN flow solver that uses conventional models, and the predicted residual trapped CO_2 are compared with the experimental value from Dalton et al. (2018). Results for residual trapping of CO_2 after a drainage-imbibition cycle are discussed in section 4.2.2, and the statistics of pore-level events during imbibition are investigated in section 4.2.3.

4.2.2. Residual Trapping

In quasi-static PN flow simulation, the saturation at the end point of the drainage process is needed as the start point of the imbibition process. The resulting saturation of trapped non-wetting phase at the end of imbibition follows a hysteretic behavior that depends on the initial saturation in the imbibition process. Therefore, the PN flow solver can be used to compute a so-called trapping curve that gives residual trapped CO_2 as a function of the initial CO_2 saturation at the start of imbibition; this is similar to Land's initial-residual trapping model (Land, 1968).

In **Figure 8**, the residual trapping curve of CO_2-brine flow for the Berea sandstone sample is compared between the original and modified PN models. When the initial CO_2 saturation is higher, the resulting residual saturation of CO_2 is about 0.48 for the original PN model and 0.44 for the modified PN model. However, this difference is negligible when the initial CO_2 saturation is smaller. In both models, a full drainage process leaves a relatively small saturation of brine (i.e., more CO_2) in the PN, mainly in corners and small or isolated pore elements. **Figure 8** shows that a full drainage process is followed by an imbibition process with more trapped CO_2. On the other hand, for smaller values of initial CO_2 saturation, the resulting residual saturation of CO_2 decreases i.e., less trapping of CO_2 which is consistent with experimental observations (Niu et al., 2015).

Unfortunately the experimental study of Dalton et al. (2018) did not report the saturation at the drainage end point. Therefore,

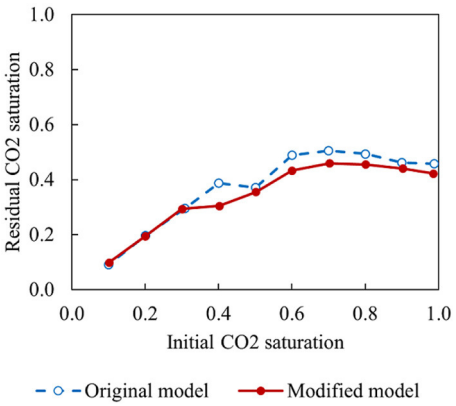

FIGURE 8 | Residual trapping curve from pore-network modeling of CO_2-brine flow on the Berea sandstone sample.

in order to choose a proper drainage end point for the Berea sandstone sample, we perform LB simulation of drainage on the full rock image. In addition, imbibition is also simulated to obtain a DNS prediction of residual trapped CO_2 for comparison with the experimental value and prediction from PN flow simulation.

The LB simulations of drainage and imbibition on the 3D rock images were conducted with contact angle of 55.9° and capillary number of 5×10^{-6} to obtain the saturation at the end of drainage and residual trapped CO_2 at the end of imbibition. **Figure 9** shows the resulting distribution of CO_2 at the end of drainage and imbibition processes. The corresponding CO_2 saturation at the end of these processes are $S_{nw}^{drain.} = 0.434$ and $S_{nw}^{imbib.} = 0.289$, respectively. We therefore use $S_{nw}^{drain.} = 0.434$ as the end point of drainage in the PN flow solver. Then, we simulate imbibition to estimate residual CO_2 saturation from PN and compare the result with the LB result: $S_{nw}^{imbib.} = 0.289$.

The resulting residual trapping of CO_2 after imbibition is presented in **Table 5** where the modified PN model is

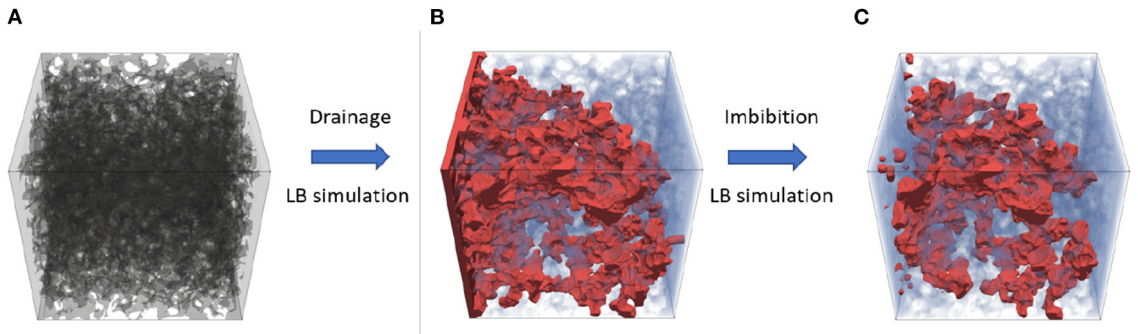

FIGURE 9 | LB simulations of drainage and imbibition processes on the Berea sandstone sample to obtain end point saturations. **(A)** pore space of the sample **(B)** end of drainage process **(C)** end of imbibition process. CO_2 is shown in red. Brine is not rendered.

TABLE 5 | Comparison of the original and modified pore-network flow models on the Berea sandstone sample based on predicted saturation of residual trapping of CO_2 after a drainage-imbibition cycle.

Method	Saturation of residual trapped CO_2
Original PN model	0.422
Modified PN model	0.328
LB simulation	0.289
Experimental	0.331

compared with the original PN model. The residual saturation of CO_2 is also compared with an experimental value based on analysis of volume ratio of CO_2 in micro-CT images rendered in **Figure 6D**. The modified model predicts residual saturation of trapped CO_2 in excellent agreement with the experimental value while the error from the original model is about 27%.

4.2.3. Statistics of Pore-Level Events

In each step of imbibition process, piston-type displacement, pore-body filling, and snap-off occur in pore elements of the PN. These pore-level events determine the invasion pattern and residual trapping during imbibition. The saturation of residual trapped CO_2 is the summation of trapped CO_2 saturation in all pore elements of PN. One approach to study the effect of changes in the model is to track the frequency and statistics of pore-level events on the same PN. The cumulative statistics of these events for the original and modified PN model during imbibition steps on the Berea sandstone sample are presented in **Figure 10**. As seen from the results, the modified model predicts higher number of pore-body filling events (14.8% more) and piston-type displacement in pore-throats (17.2% more). On the hand, it predicts a smaller number of snap-off events compare to the original model (9.6% less). Snap-off event is the mechanism that contributes the most to trapping since it disconnects CO_2 in adjacent pore-bodies and leads to isolated trapped CO_2 bubbles in the PN. Thus, the decrease in number of snap-off events in the modified model for this sample is expected to result in less trapping of CO_2 and smaller saturation of residual trapped CO_2.

In terms of invasion pattern, this can translate into a more frontal pattern due to more piston-type displacements in the modified model, which implies less chance of trapping CO_2. This is also in agreement with reported residual saturation in **Table 5**. Thus, the modified model outperforms the original model and predicts residual trapping in better agreement with the experimental and LB simulation predictions.

In the Mt. Simon sandstone sample (see **Supplementary Material**), the modified model also predicts that the residual trapped CO_2 is closer to the reference value, which is from LB simulation, than the original model. However, the discrepancy between PN modeling and LB predictions are about 20%. This can be due to higher heterogeneity of pore structure in the Mt. Simon sandstone sample compare to the Berea sandstone sample.

It is worth mentioning that different statistics of pore-level events results in a different invasion pattern that corresponds to different average flow rates across the PN. This means that the modified PN solver gives different relative permeability values at each saturation point. The relative permeability curves of CO_2-brine flow on the studied Berea sandstone sample are reported in details in Kohanpur (2020). Therefore, use of the modified PN method would yield different relative permeability curves for CO_2 and brine in a field-scale simulator which would lead to different long-term movement and storage of CO_2 in a reservoir.

5. SUMMARY AND CONCLUSIONS

The pore-scale physics of CO_2-brine flow plays a key role for predicting the amount and fate of residual trapped CO_2 in geological storage of CO_2 in deep saline reservoirs. The description of this flow system in the form of pore-level flow models through pore-bodies and pore-throats of an extracted PN from micro-CT images of real rock is a practical approach to obtain important pore-scale properties during a drainage-imbibition cycle. However, this description can be improved by more specific and accurate relations for CO_2-brine flow that can

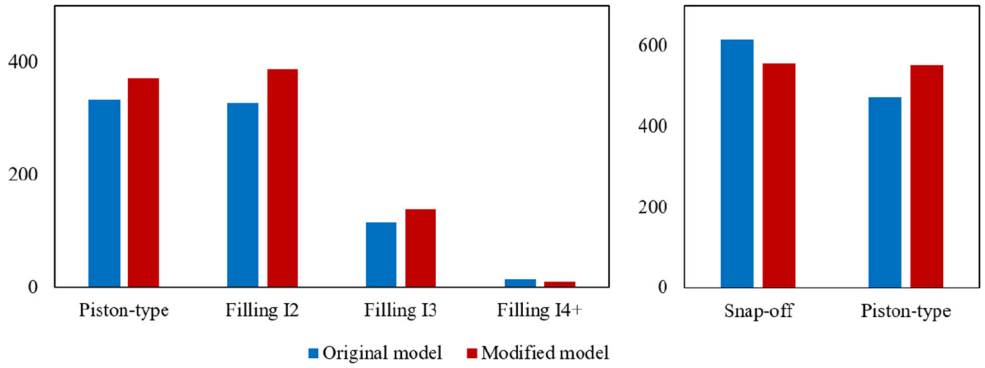

FIGURE 10 | Statistics of number of pore-level events during imbibition process in pore-bodies (left) pore-throats (right) of the Berea sandstone sample.

be derived from DNS methods. This study presented a new set of pore-level flow models during pore-body filling and snap-off events of the imbibition process in PN modeling of CO_2-brine flow. LB simulations were carried out on several typical idealized PN configurations and the local capillary pressure was evaluated to develop modified equations for local threshold capillary pressure of pore elements as a function of shape factor. We also defined effective aspect ratio of pore-body filling as a new parameter in the modified model, which was not proposed in other models in the literature.

The modified equations of local threshold capillary pressure were incorporated into a widely available quasi-static PN flow solver. This modified model resulted a new pattern of invasion during imbibition due to a different order of competing pore-level events compare to the original model. We applied the modified model on extracted PNs of Berea and Mt. Simon sandstone samples to obtain saturation of residual trapped CO_2 after a drainage-imbibition cycle. The statistics of pore-level imbibition events changed by replacing the original model with the modified model. The occurrence of snap-off in pore-throats was reduced which means a more frontal displacement pattern across the sample. As a result, our modified model was in closer agreement than the original model based on the comparison of the residual trapped CO_2 with reference data from experimental and LB simulation approaches.

Additional future work could include comparing predicted residual trapping of CO_2 with other experimental data or high resolution DNS methods. Also, the effect of lattice resolution and capillary number in LB simulations of PN configurations requires further study. This may lead to some changes in the proposed modified model such as new values for factors reported in **Tables 2**, **3**. A preliminary study is discussed in Kohanpur (2020) on one shape factor and can be extended to more shape factors and other PN configurations.

Finally, we note that the core idea of this study was to combine DNS with PN to improve the physical representation of key pore-level events, while preserving the computational efficient of quasi-static PN. In this work, we focused on pore-body filling and snap-off events which have an important impact on residual trapping of CO_2. This framework can be applied to improve estimation of other quantities of interest such as relative permeability and effective diffusion.

DATA AVAILABILITY STATEMENT

The raw data supporting the conclusions of this article will be made available by the authors, without undue reservation.

AUTHOR CONTRIBUTIONS

All authors listed have made a substantial, direct, and intellectual contribution to the work and approved it for publication.

FUNDING

This work was supported by the Center for Geologic Storage of CO_2, an Energy Frontier Research Center funded by the U.S. Department of Energy (DOE), Office of Science, Basic Energy Sciences (BES), under Award # DE-SC0C12504. Simulations for this research are part of the Blue Waters sustained-petascale computing project, which is supported by the National Science Foundation (awards OCI-0725070 and ACI-1238993) the State of Illinois, and as of December 2019, the National Geospatial-Intelligence Agency. Blue Waters is a joint effort of the University of Illinois at Urbana-Champaign and its National Center for Supercomputing Applications.

SUPPLEMENTARY MATERIAL

The Supplementary Material for this article can be found online at: https://www.frontiersin.org/articles/10.3389/frwa.2021.710160/full#supplementary-material

REFERENCES

Aghaei, A., and Piri, M. (2015). Direct pore-to-core up-scaling of displacement processes: dynamic pore network modeling and experimentation. *J. Hydrol.* 522, 488–509. doi: 10.1016/j.jhydrol.2015.01.004

Ahrenholz, B., Tölke, J., Lehmann, P., Peters, A., Kaestner, A., Krafczyk, M., et al. (2008). Prediction of capillary hysteresis in a porous material using lattice-boltzmann methods and comparison to experimental data and a morphological pore network model. *Adv. Water Resour.* 31, 1151–1173. doi: 10.1016/j.advwatres.2008.03.009

Andrä, H., Combaret, N., Dvorkin, J., Glatt, E., Han, J., Kabel, M., et al. (2013). Digital rock physics benchmarks–part i: Imaging and segmentation. *Comput. Geosci.* 50, 25–32. doi: 10.1016/j.cageo.2012.09.005

Balcewicz, M., Siegert, M., Gurris, M., Ruf, M., Krach, D., Steeb, H., et al. (2021). Digital rock physics: a geological driven workflow for the segmentation of anisotropic ruhr sandstone. *Front. Earth Sci.* 9:493. doi: 10.3389/feart.2021.673753

Blunt, M. J. (1998). Physically-based network modeling of multiphase flow in intermediate-wet porous media. *J. Petrol. Sci. Eng.* 20, 117–125. doi: 10.1016/S0920-4105(98)00010-2

Blunt, M. J. (2017). *Multiphase Flow in Permeable Media: A Pore-Scale Perspective*. Cambridge, MA: Cambridge University Press.

Blunt, M. J., Bijeljic, B., Dong, H., Gharbi, O., Iglauer, S., Mostaghimi, P., et al. (2013). Pore-scale imaging and modelling. *Adv. Water Resour.* 51, 197–216. doi: 10.1016/j.advwatres.2012.03.003

Bultreys, T., De Boever, W., and Cnudde, V. (2016). Imaging and image-based fluid transport modeling at the pore scale in geological materials: a practical introduction to the current state-of-the-art. *Earth Sci. Rev.* 155, 93–128. doi: 10.1016/j.earscirev.2016.02.001

Bultreys, T., Singh, K., Raeini, A. Q., Ruspini, L. C., Øren, P.-E., Berg, S., et al. (2020). Verifying pore network models of imbibition in rocks using time-resolved synchrotron imaging. *Water Resour. Res.* 56, e2019WR026587. doi: 10.1029/2019WR026587

Chen, Y., Li, Y., Valocchi, A. J., and Christensen, K. T. (2018). Lattice boltzmann simulations of liquid CO_2 displacing water in a 2D heterogeneous micromodel at reservoir pressure conditions. *J. Contam. Hydrol.* 212, 14–27. doi: 10.1016/j.jconhyd.2017.09.005

Chen, Y., Valocchi, A. J., Kang, Q., and Viswanathan, H. S. (2019). Inertial effects during the process of supercritical CO_2 displacing brine in a sandstone: lattice boltzmann simulations based on the continuum-surface-force and geometrical wetting models. *Water Resour. Res.* 55, 11144–11165. doi: 10.1029/2019WR025746

Dalton, L. E., Klise, K. A., Fuchs, S., Crandall, D., and Goodman, A. (2018). Methods to measure contact angles in scco2-brine-sandstone systems. *Adv Water Resour.* 122, 278–290. doi: 10.1016/j.advwatres.2018.10.020

d'Humieres, D. (2002). Multiple-relaxation-time lattice boltzmann models in three dimensions. *Philos. Trans. R. Soc. Lond. A* 360, 437–451. doi: 10.1098/rsta.2001.0955

Dong, H., and Blunt, M. J. (2009). Pore-network extraction from micro-computerized-tomography images. *Phys. Rev. E* 80, 036307. doi: 10.1103/PhysRevE.80.036307

Grunau, D., Chen, S., and Eggert, K. (1993). A lattice boltzmann model for multiphase fluid flows. *Phys. Fluids A* 5, 2557–2562. doi: 10.1063/1.858769

Gunstensen, A. K., Rothman, D. H., Zaleski, S., and Zanetti, G. (1991). Lattice boltzmann model of immiscible fluids. *Phys. Rev. A* 43, 4320. doi: 10.1103/PhysRevA.43.4320

Hefny, M., Qin, C., Saar, M. O., and Ebigbo, A. (2020). Synchrotron-based pore-network modeling of two-phase flow in nubian sandstone and implications for capillary trapping of carbon dioxide. *arXiv preprint* arXiv:2004.06792. doi: 10.1016/j.ijggc.2020.103164

Hughes, R. G., and Blunt, M. J. (2000). Pore scale modeling of rate effects in imbibition. *Trans. Porous Media* 40, 295–322. doi: 10.1023/A:1006629019153

Joekar-Niasar, V., and Hassanizadeh, S. (2012). Analysis of fundamentals of two-phase flow in porous media using dynamic pore-network models: a review. *Crit. Rev. Environ. Sci. Technol.* 42, 1895–1976. doi: 10.1080/10643389.2011.574101

Juanes, R., MacMinn, C. W., and Szulczewski, M. L. (2010). The footprint of the CO_2 plume during carbon dioxide storage in saline aquifers: storage efficiency for capillary trapping at the basin scale. *Trans. Porous Media* 82, 19–30. doi: 10.1007/s11242-009-9420-3

Kohanpur, A. H. (2020). *Improving capabilities of pore-scale modeling of multiphase flow for geological storage of $_2$* (Ph.D. thesis). University of Illinois at Urbana-Champaign.

Kohanpur, A. H., Rahromostaqim, M., Valocchi, A. J., and Sahimi, M. (2020). Two-phase flow of CO_2-brine in a heterogeneous sandstone: characterization of the rock and comparison of the lattice-boltzmann, pore-network, and direct numerical simulation methods. *Adv. Water Resour.* 135, 103469. doi: 10.1016/j.advwatres.2019.103469

Kohanpur, A. H., and Valocchi, A. J. (2020). Pore-network stitching method: a pore-to-core upscaling approach for multiphase flow. *Trans. Porous Media* 135, 659–685. doi: 10.1007/s11242-020-01491-0

Kopp, A., Class, H., and Helmig, R. (2009). Investigations on co2 storage capacity in saline aquifers: Part 1. dimensional analysis of flow processes and reservoir characteristics. *Int.J. Greenhouse Gas Control* 3, 263–276. doi: 10.1016/j.ijggc.2008.10.002

Krevor, S., Blunt, M. J., Benson, S. M., Pentland, C. H., Reynolds, C., Al-Menhali, A., et al. (2015). Capillary trapping for geologic carbon dioxide storage-from pore scale physics to field scale implications. *Int. J. Greenhouse Gas Control* 40, 221–237. doi: 10.1016/j.ijggc.2015.04.006

Land, C. S. (1968). Calculation of imbibition relative permeability for two- and three-phase flow from rock properties. *Soc. Petrol. Eng. J.* 8, 149–156. doi: 10.2118/1942-PA

Lenormand, R., Zarcone, C., and Sarr, A. (1983). Mechanisms of the displacement of one fluid by another in a network of capillary ducts. *J. Fluid Mech.* 135, 337–353. doi: 10.1017/S0022112083003110

MacMinn, C. W., Szulczewski, M. L., and Juanes, R. (2010). Co2 migration in saline aquifers. part 1. capillary trapping under slope and groundwater flow. *J. Fluid Mech.* 662, 329-351. doi: 10.1017/S0022112010003319

Mahabadi, N., van Paassen, L., Battiato, I., Yun, T. S., Choo, H., and Jang, J. (2020). Impact of pore-scale characteristics on immiscible fluid displacement. *Geofluids* 2020:5759023. doi: 10.1155/2020/5759023

Miao, X., Gerke, K. M., and Sizonenko, T. O. (2017). A new way to parameterize hydraulic conductances of pore elements: a step towards creating pore-networks without pore shape simplifications. *Adv. Water Resour.* 105, 162–172. doi: 10.1016/j.advwatres.2017.04.021

Morrow, N. R. (1975). The effects of surface roughness on contact: angle with special reference to petroleum recovery. *J. Can. Petrol. Technol.* 14, 42–53. doi: 10.2118/75-04-04

Niu, B., Al-Menhali, A., and Krevor, S. C. (2015). The impact of reservoir conditions on the residual trapping of carbon dioxide in berea sandstone. *Water Resour. Res.* 51, 2009–2029. doi: 10.1002/2014WR016441

Patzek, T. W., and Silin, D. B. (2000). Shape factor and hydraulic conductance in noncircular capillaries. i. one-phase creeping flow. *J. Colloid Interface Sci.* 236, 295–304. doi: 10.1006/jcis.2000.7413

Pentland, C. H., El-Maghraby, R., Iglauer, S., and Blunt, M. J. (2011). Measurements of the capillary trapping of super-critical carbon dioxide in berea sandstone. *Geophys. Res. Lett.* 38:L06401. doi: 10.1029/2011GL046683

Raeini, A. Q. (2013). *Modelling multiphase flow through micro-CT images of the pore space* (Ph.D. thesis). Imperial College London.

Raeini, A. Q., Bijeljic, B., and Blunt, M. J. (2017). Generalized network modeling: network extraction as a coarse-scale discretization of the void space of porous media. *Phys. Rev. E* 96, 013312. doi: 10.1103/PhysRevE.96.013312

Raeini, A. Q., Bijeljic, B., and Blunt, M. J. (2018). Generalized network modeling of capillary-dominated two-phase flow. *Phys. Rev. E* 97, 023308. doi: 10.1103/PhysRevE.97.023308

Ramstad, T., Berg, C. F., and Thompson, K. (2019). Pore-scale simulations of single-and two-phase flow in porous media: approaches and applications. *Trans. Porous Media* 130, 77–104. doi: 10.1007/s11242-019-01289-9

Rasmusson, K., Rasmusson, M., Tsang, Y., Benson, S., Hingerl, F., Fagerlund, F., et al. (2018). Residual trapping of carbon dioxide during geological storage–insight gained through a pore-network modeling approach. *Int. J. Greenhouse Gas Control* 74, 62–78. doi: 10.1016/j.ijggc.2018.04.021

Ruspini, L., Farokhpoor, R., and Øren, P. (2017). Pore-scale modeling of capillary trapping in water-wet porous media: a new cooperative pore-body filling model. *Adv. Water Resour.* 108, 1–14. doi: 10.1016/j.advwatres.2017.07.008

Schindelin, J., Arganda-Carreras, I., Frise, E., Kaynig, V., Longair, M., Pietzsch, T., et al. (2012). Fiji: an open-source platform for biological-image analysis. *Nat. Methods* 9, 676–682. doi: 10.1038/nmeth.2019

Schlüter, S., Sheppard, A., Brown, K., and Wildenschild, D. (2014). Image processing of multiphase images obtained via x-ray microtomography: a review. *Water Resour. Res.* 50, 3615–3639. doi: 10.1002/2014WR015256

Shams, M., Raeini, A. Q., Blunt, M. J., and Bijeljic, B. (2018). A study to investigate viscous coupling effects on the hydraulic conductance of fluid layers in two-phase flow at the pore level. *J. Colloid Interface Sci.* 522, 299–310. doi: 10.1016/j.jcis.2018.03.028

Silin, D., and Patzek, T. (2006). Pore space morphology analysis using maximal inscribed spheres. *Physica A* 371, 336–360. doi: 10.1016/j.physa.2006.04.048

Suh, H. S., Kang, D. H., Jang, J., Kim, K. Y., and Yun, T. S. (2017). Capillary pressure at irregularly shaped pore throats: Implications for water retention characteristics. *Adv. Water Resour.* 110, 51–58. doi: 10.1016/j.advwatres.2017.09.025

Tang, Y., Min, J., Zhang, X., and Liu, G. (2018). Meniscus behaviors and capillary pressures in capillary channels having various cross-sectional geometries. *Chin. J. Chem. Eng.* 26, 2014–2022. doi: 10.1016/j.cjche.2018.04.031

Tölke, J. (2002). Lattice boltzmann simulations of binary fluid flow through porous media. *Philos. Trans. R. Soc. Lond. A* 360, 535–545. doi: 10.1098/rsta.2001.0944

Tölke, J., Freudiger, S., and Krafczyk, M. (2006). An adaptive scheme using hierarchical grids for lattice boltzmann multi-phase flow simulations. *Comput. Fluids* 35, 820–830. doi: 10.1016/j.compfluid.2005.08.010

Valvatne, P. H. (2004). *Predictive pore-scale modelling of multiphase flow* (Ph.D. thesis). Department of Earth Science and Engineering, Imperial College London London.

Valvatne, P. H., and Blunt, M. J. (2004). Predictive pore-scale modeling of two-phase flow in mixed wet media. *Water Resou.r Res.* 40:W07406. doi: 10.1029/2003WR002627

Wildenschild, D., and Sheppard, A. P. (2013). X-ray imaging and analysis techniques for quantifying pore-scale structure and processes in subsurface porous medium systems. *Adv. Water Resour.* 51, 217–246. doi: 10.1016/j.advwatres.2012.07.018

Xie, C., Raeini, A. Q., Wang, Y., Blunt, M. J., and Wang, M. (2017). An improved pore-network model including viscous coupling effects using direct simulation by the lattice boltzmann method. *Adv. Water Resour.* 100, 26–34. doi: 10.1016/j.advwatres.2016.11.017

Zhao, J., Qin, F., Derome, D., and Carmeliet, J. (2020). Simulation of quasi-static drainage displacement in porous media on pore-scale: coupling lattice boltzmann method and pore network model. *J. Hydrol.* 588:125080. doi: 10.1016/j.jhydrol.2020.125080

Conflict of Interest: The authors declare that the research was conducted in the absence of any commercial or financial relationships that could be construed as a potential conflict of interest.

Publisher's Note: All claims expressed in this article are solely those of the authors and do not necessarily represent those of their affiliated organizations, or those of the publisher, the editors and the reviewers. Any product that may be evaluated in this article, or claim that may be made by its manufacturer, is not guaranteed or endorsed by the publisher.

frontiers in Water

ORIGINAL RESEARCH
published: 14 January 2022
doi: 10.3389/frwa.2021.800944

Pore-Scale Modeling of Mineral Growth and Nucleation in Reactive Flow

*Vitalii Starchenko**

Chemical Sciences Division, Oak Ridge National Laboratory, Oak Ridge, TN, United States

A fundamental understanding of mineral precipitation kinetics relies largely on microscopic observations of the dynamics of mineral surfaces exposed to supersaturated solutions. Deconvolution of tightly bound transport, surface reaction, and crystal nucleation phenomena still remains one of the main challenges. Particularly, the influence of these processes on texture and morphology of mineral precipitate remains unclear. This study presents a coupling of pore-scale reactive transport modeling with the Arbitrary Lagrangian-Eulerian approach for tracking evolution of explicit solid interface during mineral precipitation. It incorporates a heterogeneous nucleation mechanism according to Classical Nucleation Theory which can be turned "on" or "off." This approach allows us to demonstrate the role of nucleation on precipitate texture with a focus at micrometer scale. In this work precipitate formation is modeled on a 10 micrometer radius particle in reactive flow. The evolution of explicit interface accounts for the surface curvature which is crucial at this scale in the regime of emerging instabilities. The results illustrate how the surface reaction and reactive fluid flow affect the shape of precipitate on a solid particle. It is shown that nucleation promotes the formation of irregularly shaped precipitate and diminishes the effect of the flow on the asymmetry of precipitation around the particle. The observed differences in precipitate structure are expected to be an important benchmark for reaction-driven precipitation in natural environments.

Keywords: mineral precipitation, pore-scale modeling, crystal nucleation, interface motion, reactive transport modeling, Mullins–Sekerka instability, Pèclet–Damköhler diagram

OPEN ACCESS

Edited by:
James E. McClure,
Virginia Tech, United States

Reviewed by:
Peter Kang,
University of Minnesota Twin Cities, United States
Francesco Costanzo,
The Pennsylvania State University (PSU), United States

***Correspondence:**
Vitalii Starchenko
starchenkov@ornl.gov

Specialty section:
This article was submitted to Water and Critical Zone, a section of the journal Frontiers in Water

Received: *24 October 2021*
Accepted: *30 November 2021*
Published: *14 January 2022*

Citation:
Starchenko V (2022) Pore-Scale Modeling of Mineral Growth and Nucleation in Reactive Flow. Front. Water 3:800944. doi: 10.3389/frwa.2021.800944

1. INTRODUCTION

Recent advances in studies of natural minerals and chemical processes occurring in the subsurface have significantly improved understanding of reaction kinetics at mineral-water interfaces (Brantley et al., 2008; Putnis and Ruiz-Agudo, 2013; Beckingham et al., 2016; Yuan et al., 2019; Noiriel et al., 2020). However, there is still a gap in understanding how to derive the kinetic coefficients or order of reactive rate from the fundamental physical or chemical parameters of the system. Some studies approach this problem from the atomic scale using advanced molecular dynamics techniques to calculate transition-state theory rate constant (Raiteri et al., 2010; Stack et al., 2012). Furthermore, different upscaling techniques connect local molecular scale processes obtained from Atomic Force Microscopy data to overall reactivity (Teng et al., 2000; Yoreo et al., 2009; Bracco et al., 2013). In these studies the rate of crystal growth is linked to the surface features and their dynamics such as velocity of step propagation (Bosbach et al., 1996), kink cite

density (Higgins et al., 2000), presence of impurity ions (Weber et al., 2018), and two dimensional nucleation (Pina et al., 1998).

At the same time, modern computational techniques and synchrotron-based sources allowed us to investigate mineral reactivity at meso- and pore-scale using reactive transport modeling and X-ray tomography (Godinho et al., 2016; Noiriel et al., 2019). These methods provide an opportunity to incorporate flow in porous media (Molins et al., 2014) and resolve the interface between solid and fluid (Dutka et al., 2020).

The most used reaction rates for minerals are empirically derived from batch-type reaction experiments, in which the ideal mixing condition is expected, mineral particles are assumed to be impermeable, and the reactive surface of particles is determined by the methods such as BET (Plummer and Busenberg, 1982; Zhen-Wu et al., 2016). Such methods give a good estimate rate law that allow calculating reaction kinetics for a particular mineral. Moreover, the general expressions have been developed to describe difference between nucleation-dominated and growth-dominated regimes. For instance, the precipitation mechanism of barite mineral is described as a spiral hillock growth at low degrees of supersaturation and two-dimensional nucleation-dominated growth at high degrees of supersaturation (Bosbach, 2002). The transition from one to another is estimated to be at about $\Omega = 50$ which corresponds to the saturation index $SI \approx 1.699$. The growth rate follows the second order

$$R = k(\Omega - 1)^n \tag{1}$$

where k is the reaction rate constant, Ω is the saturation state in the solution, and n is the reaction order.

However, there is still a lack of theoretical tools which can be used to derive the transition between different precipitation regimes or predict the structure and texture of precipitate under conditions at which the transport phenomena has a major impact (Molins et al., 2017). Moreover, vast majority of the modeling tools neglect the nucleation process during mineral precipitation. It is particularly important in case the nucleation defines the reactive surface area and local distribution of the sites at which growth reaction can occur.

Although incorporation of nucleation process into the pore-scale reactive modeling has been done in several previous works, it still remains a challenging problem which require novel approaches to be developed. The reason for that is mostly related to approximations which are needed for connecting the scales between several nanometers (approximate size of a nucleus) and several micrometers (typical size of a pore in pore-scale reactive modeling). Additionally, the lack of information regarding surface properties of a particular material, such as heterogeneity in the interfacial energy between solid substrate and reactive liquid, and general debates regarding nucleation mechanisms (Gebauer et al., 2008; De Yoreo et al., 2015; Weber et al., 2021) make determination or estimation of nucleation rates particularly challenging. The importance of incorporating nucleation process into the reactive transport modeling emerged when only growth processes failed to match experimental results. For instance, simulation of CO_2 deteriorated cement could not reproduce experimental results using only growth kinetics (Li et al., 2017). After implementing nucleation mechanism based on Classical Nucleation Theory (CNT) into 1D reactive transport model the authors successfully matched the experiments. Prasianakis et al. introduced cross scale modeling concept into 2D Lattice Boltzmann approach for reactive transport which was applied to realistic 2D geometry of porous media (Prasianakis et al., 2017). In their approach authors linked CNT and growth of nuclei at atomic level represented as a parameter in particular cell of the simulation lattice. The nucleation rate was calculated based on local concentration in the cell and the surface area and growth rate of spherical nuclei was traced through the simulation. This approach provides a powerful tool to compare effect of homogeneous and heterogeneous nucleation, however the necessity to link the nucleation to a volume of Lattice-Boltzmann grid may introduce artifacts in case of high concentration gradients near interfaces. Another way to model nucleation process is calculation of the induction time or the time of the first stable crystals appearance. To implement randomness of spatial distribution of nuclei, Fazeli et al. (2020) introduced a normal distribution for probabilistic induction times. The authors coupled the probabilistic induction times to the 2D Lattice Boltzmann approach for reactive transport, which allowed them to connect the local induction time to the local concentration and vary reactive fluid saturation, mineral growth rate, and flow rates.

The novelty of the method developed in the current study consists in: (a) the implementation of nucleation on an explicit surface mesh (body fitted grids) which locally takes into account area of each face of the mesh, (b) ability to calculate normal and surface curvature using points which belong to the surface mesh (inset in the **Figure 1C**) (c) continuous motion of surface mesh points along the normal vector proportionally to the local reaction rate, (d) utilization of unstructured and non-uniform grids for volume mesh (**Figures 1B–D**), and (f) use of heterogeneous nucleation rate (expressed in number of nuclei per area per time) directly for calculating the probability of nucleation at each time step proportional to the local face area of the surface mesh.

Precise control of interface dynamics has substantial implications in geological and environmental systems as it is described in recent comprehensive review by Noiriel and Soulaine (2021). The review is focused on recent advances in X-ray computed tomography (Noiriel and Daval, 2017; Yuan et al., 2021) and development of pore-scale reactive transport models (Molins et al., 2012; Prasianakis et al., 2020; Soulaine et al., 2021; Yang et al., 2021). In both, experimental and numerical studies it is emphasized that the accurate capture of the fluid-solid interface is extremely important (Hunter et al., 2020; Khatoonabadi et al., 2021; Noiriel et al., 2021; Qin and Beckingham, 2021).

The two specific knowledge gaps this study is focused on are (a) the dynamics of fluid-solid interface and instability phenomena in wide range of reaction and flow rates including high concentration gradients near the surface (**Supplementary Figure 2**), and (b) interconnection between heterogeneous reaction, nucleation, and transport phenomena

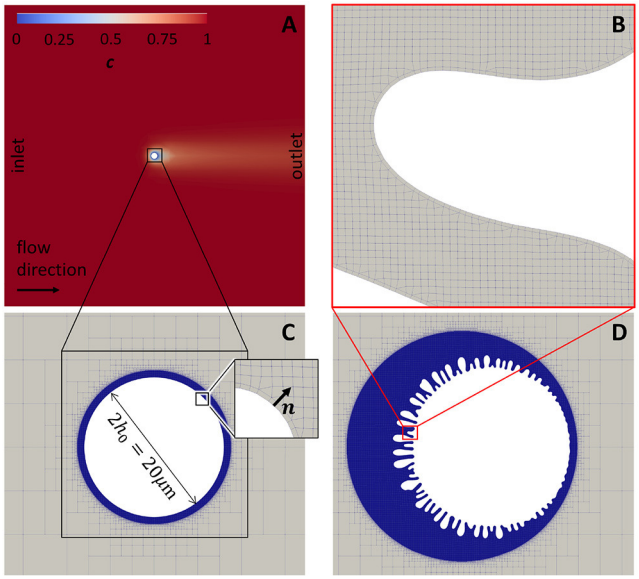

FIGURE 1 | The geometry and initial concentration distribution in the flow around a particle in two dimensional simulation domain. **(A)** Concentration distribution in a whole 2D simulation domain of 1 × 1 mm with a particle of radius 10 μm at the center of the domain. **(B)** Mesh at the boundary between the meshed fluid domain and solid. **(C)** Meshed domain around the particle before precipitation (initial geometry). **(D)** Meshed domain around the particle after precipitation.

(both convective and diffusive) and their influence on evolution of the precipitate texture.

This manuscript is organized as follows. First, the governing equations for the model are introduced in the section 2. Also, in this section the implementation of nucleation procedure on the liquid-solid interface is described using the Classical Nucleation Theory. The results of precipitate growth simulations are presented in section 3 in which the importance of nucleation and its effect on precipitate texture is discussed. In the section 4, the dynamics of surface roughness and surface velocity propagation are analyzed. The results summary and direction of the future studies are discussed in the section 5.

2. MODEL

Here, the pore-scale modeling approach is used in which the interface between solid and fluid is explicitly introduced via fitting boundary of the simulation domain to the shape of a solid (body fitted grid). As it is typical for geochemical systems, fluid is considered to be incompressible. The heterogeneous reaction is modeled at the boundary and results in precipitation of a solid phase. The displacement of the surface mesh is modeled using Arbitrary Eulerian-Lagrangian (ALE) approach (Hirt et al., 1997).

2.1. Governing Equations

The fluid motion is described by incompressible Navier-Stokes equations

$$\nabla \cdot \boldsymbol{u} = 0, \tag{2}$$

$$\frac{\partial \boldsymbol{u}}{\partial t} + \nabla \cdot (\boldsymbol{u}\boldsymbol{u}) + \nabla p = \nu \nabla^2 \boldsymbol{u}, \tag{2}$$

where $\boldsymbol{u}$ is the fluid velocity, p is the pressure normalized by the fluid density, ν is the kinematic viscosity. The transport of reactant is described by a convection-diffusion equation

$$\frac{\partial c}{\partial t} + \nabla \cdot (\boldsymbol{u}c) = \nabla \cdot (D \nabla c) \tag{3}$$

where c is the reactant concentration, D is the molecular diffusion coefficient.

The heterogeneous precipitation reaction is implemented as a boundary condition applied to the reactive surface. In this simplified model for mineral precipitation a binary reaction is considered, in which the concentrations of anions, A, and cations, B, in the solution define the saturation state of the solution in respect to a mineral AB. Schematically it can be represented as

$$\mathrm{A}^- + \mathrm{B}^+ \longrightarrow \mathrm{AB} \downarrow \tag{4}$$

It is assumed that the species A and B have equal concentrations and are well mixed at the inlet. Also, it is assumed that the diffusion of ions is similar, and the activity coefficient for both type of ions is equal to 1. The Onsager correction to the diffusive transport, which has been shown having significant impact in case of mineral dissolution (Dutka et al., 2020) in comparison to lesser effect during precipitation (Yang et al., 2021), is not considered in this work. Thus, the Equation (3) can be solved for only one type of species and the saturation state, Ω, can be expressed as

$$\Omega = \frac{c^2}{c_{eq}^2}, \tag{5}$$

where c_{eq} is the equilibrium ion concentrations for a specific mineral.

Therefore, the surface reaction rate and Equation (1) can be rewritten in terms of local concentration

$$R = k\left(\frac{c^2}{c_{eq}^2} - 1\right) \tag{6}$$

To model the surface motion it is imposed that the flux of mineral ions to the surface during precipitation must match the reaction rate $R(c)$ (Szymczak and Ladd, 2012).

$$D\boldsymbol{n} \cdot \nabla c = R(c), \tag{7}$$

where $\boldsymbol{n}$ is the normal to the surface (inset in the **Figure 1C**). During precipitation process a solid-fluid interface, Γ, is propagated. The interface is modeled by a boundary mesh that confines the simulation domain and represents the reactive surface. The points of the surface mesh are propagating with velocity $\boldsymbol{u}_\Gamma$

$$\nu_m^{-1} \boldsymbol{u}_\Gamma = R(c)\boldsymbol{n}, \tag{8}$$

where ν_m is the molar volume of the mineral.

2.2. Dimensionless Equations

For the convenience, the governing equations can be scaled using the unit of time, t_d, and the unit of length, h_0,

$$\hat{t} = \frac{t}{t_d}; \qquad \hat{\boldsymbol{r}} = \frac{\boldsymbol{r}}{h_0}; \qquad \hat{\boldsymbol{\nabla}} = h_0 \boldsymbol{\nabla}, \tag{9}$$

where hat above a symbol indicates that the quantity is dimensionless. In this study the equations are scaled using $t_d = 0.01$ s and $h_0 = 10\mu$m (see **Table 2**).

Correspondingly, pressure, viscosity, and molecular diffusion coefficient are scaled as

$$\hat{p} = \frac{t_d^2}{h_0^2} p; \qquad \hat{\nu} = \frac{t_d}{h_0^2} \nu; \qquad \hat{D} = \frac{t_d}{h_0^2} D. \tag{10}$$

In order to make transport equation dimensionless the concentration of reactant is scaled by the concentration at the inlet $\hat{c} = c/c_{in}$. Then, the dimensionless governing Equations (2) and (3) can be rewritten as

$$\frac{\partial \hat{\boldsymbol{u}}}{\partial \hat{t}} + \hat{\nabla} \cdot (\hat{\boldsymbol{u}}\hat{\boldsymbol{u}}) + \hat{\nabla}\hat{p} = \hat{\nu}\hat{\nabla}^2 \hat{\boldsymbol{u}} \tag{11}$$

$$\frac{\partial \hat{c}}{\partial \hat{t}} + \hat{\nabla} \cdot (\hat{\boldsymbol{u}}\hat{c}) = \hat{\nabla} \cdot (\hat{D}\hat{\nabla}\hat{c}) \tag{12}$$

By scaling reaction rate as $\hat{R} = R/k$ the Equation (7) can be rewritten as

$$\hat{R} = l_R \boldsymbol{n} \cdot \hat{\nabla}\hat{c}, \tag{13}$$

where $l_R = \frac{Dc_{in}}{kh_0}$.

Typically, to analyze dynamic processes that are governed by flow conditions and reaction rates a set of dimensionless numbers is defined (Soulaine et al., 2017; Starchenko and Ladd, 2018; Xu et al., 2020). This study is relevant to the case in which the flow rates are relatively low and the work is focused on competition between reaction and transport. Thus, the most interesting dimensionless numbers are the Pèclet number (Pe) and the second Damköhler number (Da_{II}), which represent ratio of flow rate to diffusive rate and reaction rate to diffusive rate

$$Pe = \frac{u_{in} h_0}{D}; \qquad Da_{\mathrm{II}} = \frac{h_0 \nu_m R(c_{in})}{D}, \tag{14}$$

where u_{in} is the flow velocity at the inlet, and $R(c_{in})$ is the reaction rate which corresponds to the inlet concentration. Following the dimensional scaling, the Equation (8) for the interface motion can be written as

$$\nu_m^{-1} \frac{h_0}{t_d} \hat{\boldsymbol{u}}_\Gamma = k\hat{R}\boldsymbol{n} \tag{15}$$

Replacing $\hat{R}$ using the Equation (13) the interface motion velocity can be expressed as

$$\hat{\boldsymbol{u}}_\Gamma = \gamma_\Gamma (\boldsymbol{n} \cdot \hat{\nabla}\hat{c})\boldsymbol{n}, \tag{16}$$

where $\gamma_\Gamma = \hat{D}\nu_m c_{in}$.

By scaling the reactant concentration with c_{in} and defining $\theta = c_{in}/c_{eq}$ the reaction rate Equation (6) can be rewritten as,

$$\hat{R} = \left(\theta^2 \hat{c}^2 - 1\right) \tag{17}$$

2.3. Surface Energy

Analysis of Mullins–Sekerka instability (Mullins and Sekerka, 2004) shows that fast growing interfaces generate perturbations with wavelength which is not bound by lower limit. To stabilize the growth, the Gibbs-Thomson relation (Landau and Lifshitz, 1980) was included into the model. It implies that interfaces with higher curvature will require more energy to form. Therefore, the effective equilibrium concentration, $\tilde{c}_{eq}$, becomes higher and suppresses the short-wavelength perturbations. The stabilizing mechanism corresponds to the additional term for the equilibrium concentration at the solid-fluid interface where the curvature is large. Therefore, the concentration gradient gets smaller and regulates the growth of the interface by removing indefinitely small wavelength of the perturbations. In general, the expression for curvature-dependent equilibrium concentration according to Gibbs-Thomson relation can be described (Rigos and Deutch, 1986) as follows

$$\tilde{c}_{eq}(\boldsymbol{r}) = c_{eq} \exp\left[\frac{\gamma \nu_m \kappa(\boldsymbol{r})}{RT}\right] \tag{18}$$

where γ is the interfacial free energy of material, $\kappa(\boldsymbol{r})$ is the curvature of the surface at a particular location, R is the gas constant, and T is temperature. The expression can be simplified using simple expansion

$$\tilde{c}_{eq}(\boldsymbol{r}) = c_{eq}\left(1 + \frac{d_0}{h_0}\hat{\kappa}(\boldsymbol{r})\right), \tag{19}$$

where $d_0 = (\gamma \nu_m)/(RT)$ is the capillary constant, and $\hat{\kappa} = h_0\kappa$ is the dimensionless curvature.

2.4. Nucleation Model

Nucleation during mineral precipitation can follow either classical or non-classical pathways. The non-classical pathway includes such processes as pre-nucleation cluster formation, particle aggregation, transition between mineral polymorphs, etc. (De Yoreo et al., 2015), which is not considered in this work. The Classical Nucleation Theory states that to form a stable nucleus the particle has to exceed a certain size to overcome an energy barrier which arises from the balance between penalty on the formation of new surface and the total crystal lattice volume energy of a particle. This work is focused on heterogeneous nucleation which means the mineral precipitates on the surface and not in the solution. Based on CNT, nucleation rate defines number of particles which can nucleate on a particular surface area at a certain period. The heterogeneous nucleation rate, J_s, is a function of the free energy change, ΔG, during the nucleation of a new phase (Fernandez-Martinez et al., 2013; Li et al., 2014) on the fluid-solid interface

$$J_s = A \exp\left[-\frac{\Delta G}{k_B T}\right] \tag{20}$$

where A is a prefactor. The ΔG is a function of interfacial free energy, γ, and the supersaturation, $\ln \Omega$:

$$\Delta G = \frac{\beta (v_m/N_A)^2 \gamma^3}{(k_B T \ln \Omega)^2}, \tag{21}$$

where $\beta = 16\pi/3$ is the geometric factor, N_A is the Avogadro number.

To introduce nucleation in the model it is assumed that a single nucleus can not be resolved. Therefore, each face of the volume mesh, which defines the interface between fluid and solid, is marked as non-reactive until a nucleation event occurs. The probability of a stochastic event (which obeys a rate law J) in time t can be expressed as an exponential probability distribution function: $J \exp(-Jt)$. The cumulative distribution function over period of time, Δt, is an integral of probability distribution

$$P = 1 - \exp(-J\Delta t). \tag{22}$$

The Equation (22) defines the nucleation probability on a particular face of the area A_f, where $J = A_f J_s$. Once the condition for nucleation is reached, the face is marked as a reactive one and the boundary condition (13) is applied. The current model does not resolve a single nucleus growth. Since a single nucleus does not cover the face completely, the surface coverage parameter, χ, is introduced, which indicates a ratio between the covered area and total area of each cell. It is assumed that a single nucleation event generates a hemisphere that covers an area of 5 nm^2. Assuming that the nucleation adds much less precipitate than mineral growth, the increment for the surface coverage parameter was derived from the growth of a hemisphere with a growth rate corresponding to Equation (17). Therefore, the change in surface coverage in a particular cell each time step can be defined as

$$\Delta\chi = \pi(\Delta\hat{r})^2 + \sqrt{\pi \hat{A}_s \chi}\,\Delta\hat{r}, \tag{23}$$

where $\Delta\hat{r}$ is a dimensionless increment of the hemisphere radius at a particular growth rate $\hat{R}(c)$

$$\Delta\hat{r} = \frac{v_m k t_d}{h_0}\hat{R}\Delta\hat{t}. \tag{24}$$

This model is a rough estimation of real processes and does not capture multiple nucleation events, crystal surface energy anisotropy which defines shape of crystalline particles, nuclei impingement, etc. However, it allows smoothing out transition from non-reactive surface to a reactive one when the resolution of a single nucleus is not possible. Surface coverage for a particular face is changing within the range $0 \leq \chi \leq 1$. The reaction rate on the partially covered face is scaled proportionally to the surface coverage $\hat{R}_{part} = \chi\hat{R}$. This results in an inert surface at $\chi = 0$ and fully reactive surface at $\chi = 1$. The detailed future studies are needed to make current nucleation model applicable to specific materials or minerals. The nucleation rate is controlled by changing the prefactor A in Equation (20).

2.5. Implementation

Fluid flow and transport equations were solved using an open-source Computational Fluid Dynamics package OpenFOAM®. OpenFOAM® is based on the finite volume discretization. The details of numerical implementation of the OpenFOAM® software can be found elsewhere (Jasak, 1996; Weller et al., 1998). The PISO algorithm used for solving the equations is described in detail in a recent book (Moukalled et al., 2016). The interface motion was implemented using earlier development of the simplified Arbitrary-Lagrangian-Eulerian (ALE) method in `dissolFoam` solver (Starchenko et al., 2016) which is also described in a recent review paper (Molins et al., 2021).

Briefly, the method implemented in this work combines the `pisoFoam` solver from OpenFOAM for transient incompressible flow (based on the PISO algorithm), the transient convection-diffusion equation, dynamic volume meshes (implemented in OpenFOAM) and boundary mesh motion/relaxation implemented in `dissolFoam` solver.

Since the shape of the growing features in some cases is highly irregular, the topological changes to an initial mesh are necessary. In current implementation, remeshing procedure using OpenFOAM meshing tool `snappyHexMesh` was performed with different intervals through the simulation depending on how unstable the growth is and how rough the surface becomes. The higher the curvature of the growing dendrites the faster the mesh will become significantly distorted. In average for all simulations the criterion for remeshing was set to 1000 time steps. The time integration scheme used in the simulations is Euler implicit scheme which is first order accurate. The spatial discretization is a second-order accurate (Jasak, 1996; Tuković and Jasak, 2012). To perform the simulations, the CADES high performance computing cluster at Oak Ridge National Laboratory was used.

2.6. Geometry, Initial, and Boundary Conditions

The geometry used in this study represents a spherical particle in a flow (**Figure 1A**). To simplify the visualization, accelerate calculations, and capture the interface growth, 2D simulations are performed in this study. It is important to note that current implementation is capable to model 3D geometry with no additional changes, however, at higher computational cost. A particle at the center of the domain is a cylinder which is confined between two parallel planes with `empty` boundary conditions. The boundaries in the direction perpendicular to the flow (top and bottom of the **Figure 1A**) are implemented as the `symmetry` boundary condition. The flow was defined by the constant flow rate condition. Fluid velocity was set to u_{in} value at the inlet (left side of the **Figure 1A**) and `pressureInletVelocity` boundary condition at the outlet. At the solid surface of a particle a no-slip boundary condition was applied.

For the concentration field and transport Equation (3) a custom boundary condition was implemented at the reactive surface. It follows the balance equation (13), reaction rate equation (17), and implements a curvature correction to the

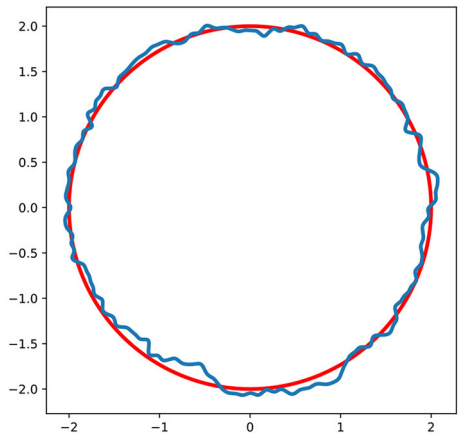

FIGURE 2 | Surface roughness generation. Red line is an initial surface of the particle. Blue line is a surface of a particle with generated roughness.

equilibrium concentration according to the Equation (19). Additionally, in case of enabled nucleation, the rate is scaled proportionally to the parameter χ. The concentration field is scaled by the reactant concentration at the inlet, c_{in}, (see section 2.2), therefore a Dirichlet boundary condition for $\hat{c}$ is applied at the inlet and always $\hat{c} = 1$. The details of implementation of custom Robin boundary condition for concentration at reactive surface can be found in Starchenko et al. (2016). Also, the details were added to **Supplementary Material** for convenience. At the outlet a `zeroGradient` Newman boundary condition is applied.

A starting point for all simulations (time 0) is a steady state solution for the flow and reactant concentration. During simulation the transient Equations (2) and (3) are solved and combined with dynamic mesh motion until the mesh becomes highly distorted and required remeshing (described in section 2.5). After remeshing, the volume fields are mapped from the old to the new mesh using OpenFOAM's field mapping tool `mapFieldsPar` with the mapping method option `correctedCellVolumeWeight`. It implements the cell-volume-weighted mesh-to-mesh based interpolation. After the volume fields are mapped to the new mesh, the simulation (transient equations with dynamic mesh) is restarted.

Radius of a particle in the flow is 10 μm and the total dimensions of a domain is 1 × 1 mm. To accelerate calculations, the non-uniform meshes were used in this study. **Figure 1C** shows the magnified area near the particle to demonstrate the refinement of the mesh near the surface. **Figure 1D** shows the same area after surface was moved as a result of the precipitation. It demonstrates the need of refinement near the interface in order to resolve features that occur due to the instability growth. **Figure 1B** shows magnified area around one of the surface features that demonstrates the finest cells. All meshes were generated using `snappyHexMesh` tool. Briefly, the 2D simulation domain was divided into 320 × 320 cells followed by 6× refinement around the particle surface. Total number of cells is not fixed in the simulation due to the nature of the method and meshing procedures. Average number of cells at the beginning of the simulation did not exceed one million cells. Due to the growth of rough surfaces during precipitation (**Figure 1D**), the number of cells was continuously increasing during simulation after each remeshing procedure. To maintain the stability of the fluid flow solver the timestep, δt, was chosen to satisfy condition $Co = \delta t|\hat{\boldsymbol{u}}_i|/\delta x_i < 1$, where Co is a Courant number, $|\hat{\boldsymbol{u}}_i|$ is the magnitude of the velocity in the cell i, and δx_i is the size of the cell i in the direction of the velocity.

In order to overcome the effect of initial instability generation, which is usually related either to mesh symmetry or floating point numerical error, roughness was introduced on the surface of the initial particle (**Figure 2**). The algorithm is similar to the generation of roughness on surface of the fracture described in Starchenko et al. (2016). Briefly, the displacements were generated on the surface of a spherical particle using Fourier synthesis (Peitgen, 1988). The standard deviation in the displacement was set to $0.003h_0$. In case of fracture dissolution, it has been shown that the evolving dissolution patterns in fractures is insensitive to the amplitude and correlation length which characterizes the roughness of the initial fracture surface (Upadhyay et al., 2015). Nevertheless, it is still debated how much surface roughness affects mineral precipitation, which is a topic of the future studies. In case of nucleation, the simulation starts from the smooth surface, since the randomness of the initial growing points is guaranteed by the implemented nucleation algorithm.

To calculate mean local curvature scalar of the surface mesh, the functionality of `finiteArea` method implemented in OpenFOAM® is used. The implementation details can be found in work of Tuković and Jasak (Tuković and Jasak, 2012).

3. RESULTS

Calcite mineral ($CaCO_3$) has been chosen as a reference material for the precipitation. Calcite precipitation is a complex process that depends on many parameters such as CO_2 pressure, pH of the solution, etc. Moreover, $CaCO_3$ precipitation can result in a variety of polymorphs (including amorphous calcium carbonate). To focus on the implementation of the pore-scale reactive transport model coupled with heterogeneous reactions and dynamic interface, the simplest surface reaction model has been chosen. The concentrations of counterions

TABLE 1 | Parameters for the calcite mineral precipitation.

Parameter	Symbol	Value
Diffusion coefficient	D	$1.4 \cdot 10^{-5}$ cm^2/s
Molar mass	M	100.09 g/mol
Molar volume	v_m	37 cm^3/mol
Equilibrium concentration	c_s	$0.58 \cdot 10^{-4}$ mol/L
Interfacial free energy	γ_{ca}	35 mJ/m^2
Capillarity	d_0	$5 \cdot 10^{-6}$ cm

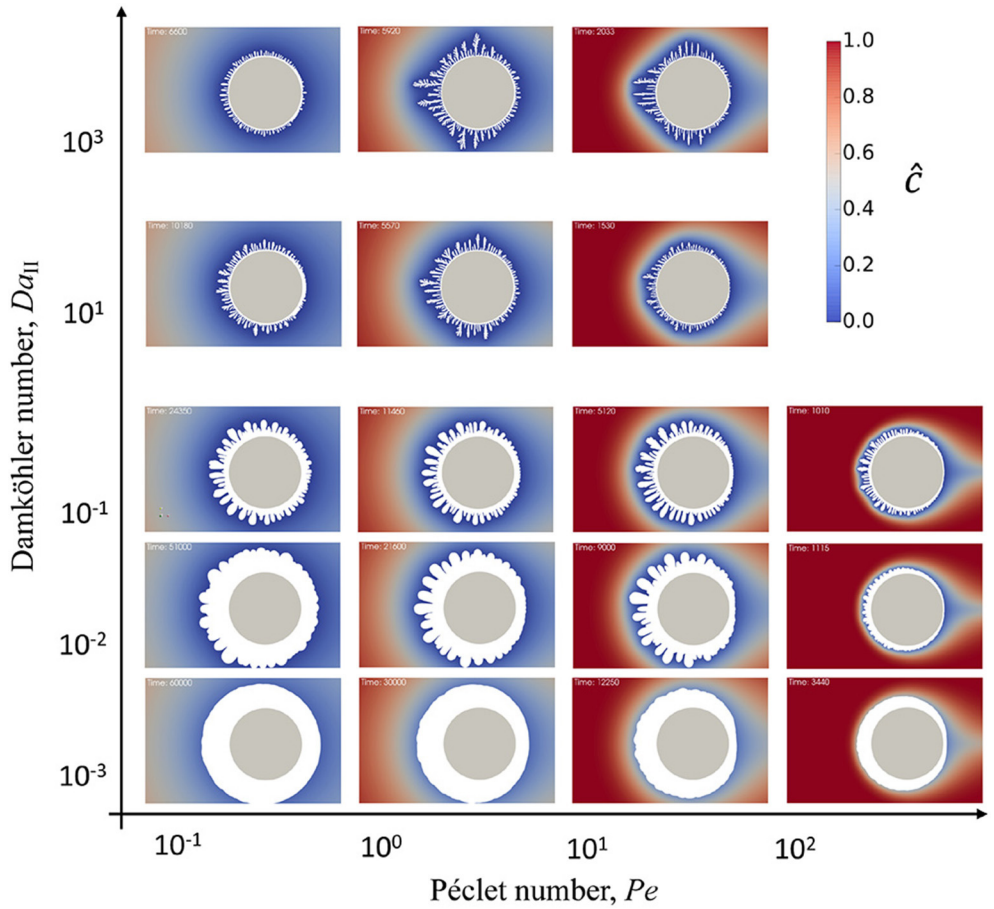

FIGURE 3 | Second Damköhler number, Da_{II}, vs. Péclet number, Pe, phase diagram of precipitation patterns on a particle in reactive flow. The initial particle is shown in gray, precipitate is shown in white, and blue-to-red color scheme shows distribution of reactive species in solution around the particle and solid precipitate.

Ca^{2+} and CO_3^{2-} are defined by the equation (3) and the precipitation rate equation (6). **Table 1** contains parameters for calcite precipitation. Equilibrium concentration for calcite was estimated as the square root of the equilibrium constant published by Plummer and Busenberg (Plummer and Busenberg, 1982). Additionally, the capillary length in the Equation (19) is assumed to be $d_0 = 5 \cdot 10^{-6}$ cm. It is clear that the mentioned above assumptions and simplifications, such as Equation (6), result in a system which do not reflect fully the actual conditions for calcite mineral precipitation. The parameters used in this work needed to be reasonable and close enough to a realistic system. However, to model precipitation of a specific mineral, parameters such as reaction rate constants need to be carefully reviewed and, perhaps, corrections such as ion activities need to be used instead of concentrations to calculate species diffusivity and local saturation states.

3.1. Precipitate Growth

In the parametric study, a Pèclet–Damköhler diagram demonstrates that both reaction and flow rate define regime of mineral precipitation (**Figure 3**). Namely, the rates control the instability emergence during the evolution of the reactive surface. To effectively change Da_{II} and Pe numbers, the reaction rate constant k and flow velocity at the inlet u_{in} are varied. In most of the simulations the inlet concentration is assumed to be $c_{in} = 6.6 \cdot 10^{-3}$ mol/L. Although the reaction rate constant for calcite precipitation is $k_{calcite} = 3.81 \cdot 10^{-11}$ mol/cm^2/s (Nilsson and Sternbeck, 1999), for the parametric study k was varied in the range between 10^{-4} and 10^{-10} mol/cm^2/s; and u_{in} was varied in the range between 0.01 and 10 cm/s. All other parameters used in simulations are summarized in **Table 2**.

TABLE 2 | Constant parameters used in simulations.

Parameter	Symbol	Value
Unit time	t_d	0.01 s
Unit length	h_0	0.001 cm
Kinematic viscosity	ν	0.008926 cm^2/s
Temperature	T	298.15 K
Solvent density	ρ	0.997 g/cm^3

The diagram in **Figure 3** shows the result of precipitation at different flow rate and reaction rate conditions. The simulation images in the diagram were taken at different simulation times and scaled to the same size for comparison. The particle in the center of each snapshot in **Figure 3** is shown to demonstrate the scale. At very high *Pe* numbers the criteria dictated by *Co* number makes the timestep very small. For instance, at $Pe = 7.14 \cdot 10^2$, which is the last row in **Figure 3**, the corresponding $\delta t = 10^{-4} t_d$. This requires significantly longer simulation times, however, the snapshots included into the diagram demonstrate the general tendency. Although a generation of the short wave instabilities is limited by the Gibbs-Thomson effect, the diagram shows that the number of growing features increases and the size of the instability decreases with increasing Da_{II} and *Pe* numbers. This remains consistent with early works on Mullins–Sekerka instability (Langer, 1980) reflecting that the faster the surface growth the more unstable it becomes. The diagram demonstrates that this effect can be achieved by either enhancing the reaction itself by increasing the rate constant or by increasing transport of reactant to the solid surface (in this case, increasing flow velocity). Moreover, the higher the reaction rate—the higher the curvature of the growing features which start to grow as very thin dendrites with many branches.

In general, by moving from low to high *Pe* numbers the diffusive layer around the reactive particle becomes smaller. This results in enhanced transport of reactant to the particle interface and, therefore, smaller wavelength of the instability that corresponds to higher reaction rate. Additionally, for all *Da* numbers the increase in fluid flow velocity introduces anisotropy into the amount of precipitate. The precipitate growth faster on the front side of the particle exposed to the flow. The amount of reactant that reaches the back side of the particle is smaller since it is consumed during the precipitation. Therefore, the overall reaction rate is reduced.

It can be seen in the diagram in **Figure 3** that a primary dense precipitate layer growth around the initial particle which then branches into the dendrites. However, the thickness of the primary layer depends on the reaction and flow rates. The primary layer thickens at low Da_{II} and *Pe*. In real systems it can probably be controlled by the surface roughness or surface defects as well. The growth of the primary layer slows down as dendrites start to grow and at a particular time it is terminated completely. Eventually, the porous secondary precipitate layer is formed out of the growing dendrites which screen the primary layer by consuming all the reactant from the solution.

3.2. Nucleation

To test the coupling of surface growth with nucleation a comparison between the evolution of precipitate on the surface of a particle in flow with nucleation "on" and "off" (**Figure 4**) was done at different reaction rates. The nucleation switch set to "on" in the solver modifies the boundary condition on the particle in the flow so that initially the surface is inert (i.e., reaction rate is set to zero) and after nucleation it is proportional to the surface coverage (Equation 23) as it is described in the section 2.4. **Figures 4A,C** correspond to the nucleation switch set to "on." **Figures 4B,D** correspond to the case in which nucleation is "off" and the rest of the parameters are the same. The concentration at the inlet was set to $c_{in} = 2.1 \cdot 10^{-2}$ mol/L, the equilibrium concentration was set to $c_{eq} = 1.84 \cdot 10^{-4}$ mol/L, and the flow rate was such that $Pe = 0.71$. **Figures 4A,B** correspond to the reaction rate constant $k = 10^{-8}$ mol/cm^2/s and **Figures 4C,D** correspond to $k = 10^{-6}$ mol/cm^2/s. It is important to note that the parameter l_R from the Equation (13) depends on c_{in}. Therefore, the effect of diffusional hindrance on the reaction rate is different from **Figure 3** and the resulting growth of precipitate will be different as well. In simple geometries such as channel flow it is possible to estimate an effective reaction rate which includes diffusional hindrance (Szymczak and Ladd, 2012). However, in case of more complex geometries like mineral grain in flow (Dutka et al., 2020) the correction is only an approximation. Although such detailed analysis of diffusional hindrance in the interfacial layer is not included in current manuscript, it is an interesting topic for future studies, especially in case of charged surfaces.

Since in case of nucleation "on" initial surface is inert, the concentration around the particle in the beginning becomes equal to the concentration at the inlet. After nucleation event occurs the faces of the surface mesh become reactive and the nucleation sites consume reactant locally as it can be seen at time $300 t_d$ (**Figure 4**). At both low and high reaction rates nucleation affects distribution of the precipitate and eventually accelerates instabilities in surface growth. The effect is more significant in case of higher reaction rate case (**Figure 4C**). It is interesting to note that although nucleation accelerates growth of particular sites resulting in irregular shape of the precipitate, the growth without nucleation (**Figure 4D**, time $5600 t_d$) creates porous precipitate with smaller dendrite features. This indicates that nucleation promotes formation of less porous however non-uniformly distributed precipitate.

As it was shown above in **Figure 3**, the higher flow rate effectively increases the reaction rate at the surface and reduces the width of the dendrites. **Figure 5** demonstrates the influence of nucleation rate on precipitate shape at different flow rates. The snapshots were taken at different simulation times chosen so that the total amount of precipitate in all 6 cases was the same. Comparison between low flow rate at $Pe = 0.714$ (**Figure 5A**) and high flow rate at $Pe = 71.4$ (**Figure 5B**) demonstrates that at all modeled nucleation rate values the width of the growing features slightly decreases for smaller flow rates as expected. It is interesting to note that decreasing nucleation rate results in reduced asymmetry of the precipitate caused by the flow direction. In fact, in **Figure 5** at $\ln(A) = 15$ demonstrates that the flow direction almost does not affect whether there is more precipitate on the front or back side of the particle, whereas this effect can be seen at lower nucleation rate [$\ln(A) = 20$] or in case without nucleation.

4. DISCUSSION

Since precipitate shape is anisotropic due to the flow direction (in case nucleation is "off"), a plausible way to present the data is in form of angular distribution. **Figure 6** shows dependence of surface velocity magnitude, $|\hat{\boldsymbol{u}}_\Gamma|$, and surface curvature, $\hat{\kappa}$,

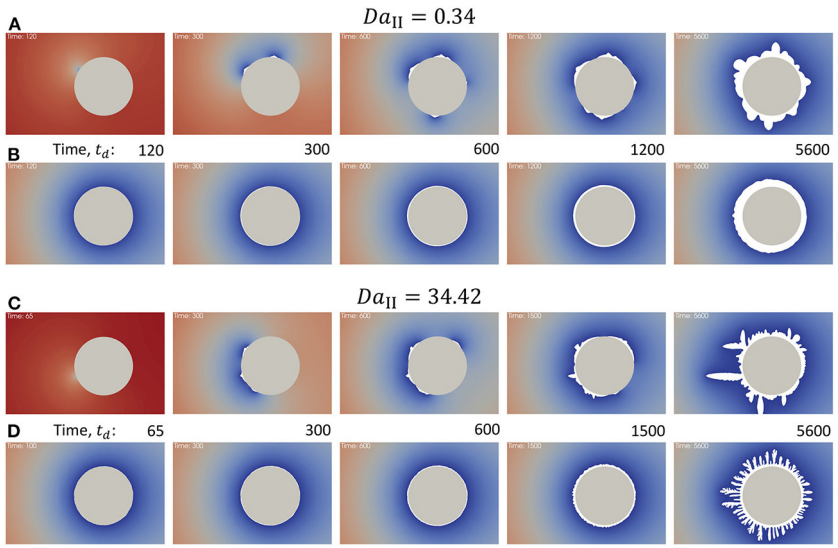

FIGURE 4 | Precipitation on a particle in flow, $Pe = 0.71$. Time when the snapshots were taken is shown in time units, t_d. **(A)** $Da_{II} = 0.34$ and nucleation is "on," initial surface is inert. **(B)** $Da_{II} = 0.34$ and nucleation is "off," initial surface is reactive. **(C)** $Da_{II} = 34.42$ and nucleation is "on." **(D)** $Da_{II} = 34.42$ and nucleation is "off."

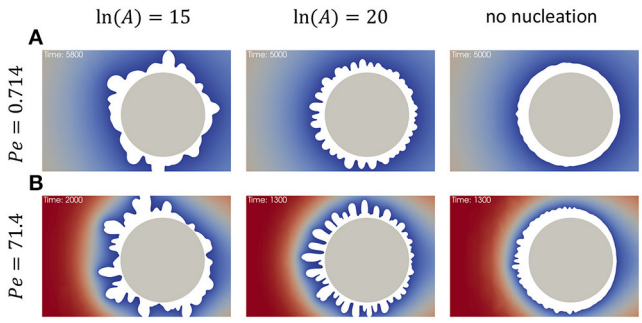

FIGURE 5 | Effect of nucleation rate on the precipitation on a particle in reactive flow at $Da_{II} = 0.34$. **(A)** $Pe = 0.714$, **(B)** $Pe = 71.4$. The snapshots in the left column correspond to nucleation rate prefactor $\ln(A) = 15$, in the middle column $\ln(A) = 20$, and in the right column the nucleation is "off" (all surface is reactive from the beginning).

as function of angular coordinate φ. The angular coordinate is defined to be $\varphi = 0 = 2\pi$ in the back side of the particle and $\varphi = \pi$ in the front side of the particle which faces the flow (**Figure 6A**). Both max and min functions of $|\hat{\boldsymbol{u}}_\Gamma|$ and $\hat{\kappa}$ were applied to the groups of points on the interface which were gathered within ranges $4^\circ(i-1) < \varphi \leq 4^\circ i$, where $i = 0, 1, 2, .., 90$. In other words, the full range of angular coordinate $[0, 2\pi)$ is divided into 90 bins and then the max and min functions were applied to the points that correspond to each bin.

Figures 6B,C show the change in surface velocity of growing precipitate. Initially, the profiles of $\max|\hat{\boldsymbol{u}}_\Gamma|$ and $\min|\hat{\boldsymbol{u}}_\Gamma|$ are similar with total maximum located at the front side of the particle at $\varphi = \pi$ and total minimum located at the back side of the particle. At later stages, the $\min|\hat{\boldsymbol{u}}_\Gamma|$ drops to zero in range $0.5\pi < \varphi \leq 1.5\pi$ at time $5000t_d$ and almost all around the particle at time $11500t_d$. This behavior corresponds to the formation of the primary dense layer around the particle and complete termination of its growth at later stages due to the screening from reactant by growing dendrites. **Figure 6C** indicates that the growth termination occurs earlier at the front side.

To investigate the evolution of surface the curvature at high ($Da_{II} = 3,442$) and low ($Da_{II} = 0.34$) reaction rates at different stages of precipitation is compared. Negative curvature corresponds to the concave area of the precipitate surface in respect to the solution. **Figures 6E,H** demonstrate similar structure of precipitate at early stages. Naturally, at later stages of precipitation, growth of dendrites generates highly curved surfaces. Both, concave and convex areas become more curved. As it was discussed above, higher reaction rate promotes shorter wavelength instabilities. Accordingly, the curvature of growing features is smaller at lower reaction rates (orange curves in **Figures 6F,G,I,J**). However, the curvature of concave areas remains in the same range for both high and low reaction rates (blue curves in **Figures 6F,G,I,J**). It can be interpreted that the average distance between dendrites is much less affected by the reaction rate than the width of the growing dendrites.

Figure 7 shows the flow velocity maps which correspond to the data presented in **Figure 6**. The color map is scaled to $|\hat{\boldsymbol{u}}|_{max} = 0.001$ in order to focus on the area of growing dendrites. The value of absolute maximum velocity in whole domain was registered between 1.2 and 1.25 depending on the case and simulation time. **Figure 7A** corresponds to the **Figures 6B–G** and **Figure 7B** corresponds to the **Figures 6H–J**. At early simulation stages both velocity maps develop similarly mostly defined by the shape of the initial particle. At later stages, lower reaction rate results in wider dendrites as it can be seen in **Figure 7A** at time $11500t_d$ in comparison

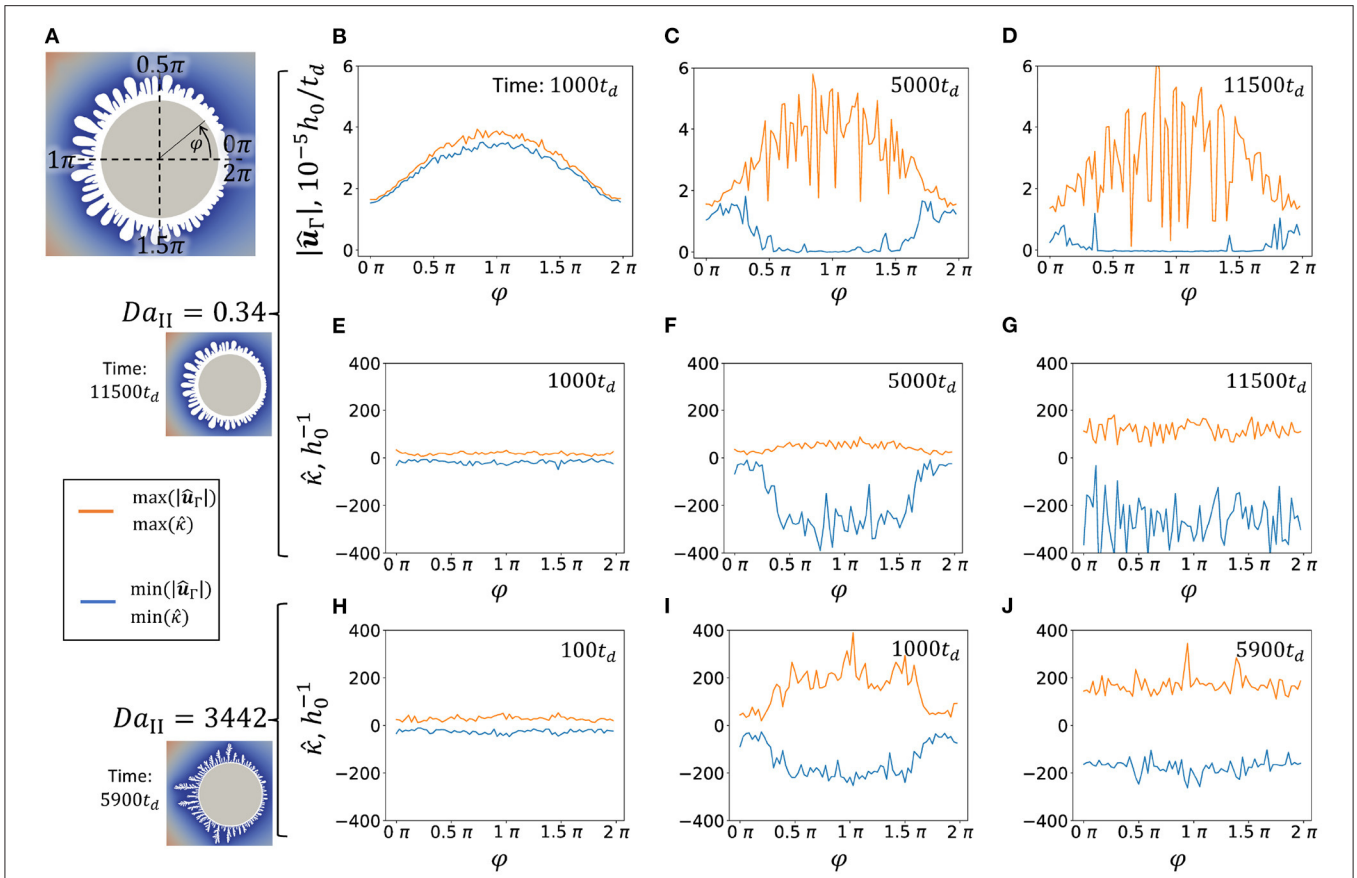

FIGURE 6 | Maximum and minimum of surface velocity magnitude, $|\hat{u}_\Gamma|$, and surface curvature, $\hat{\kappa}$, distribution along angular coordinate φ at flow rate $Pe = 7.14$. **(A)** Schematics of angular coordinate φ definition. **(B–D)** $\max(|\hat{u}_\Gamma|)$ and $\min(|\hat{u}_\Gamma|)$ at different simulation times ($Da_{II} = 0.34$). **(E–G)** $\max(\hat{\kappa})$ and $\min(\hat{\kappa})$ at different simulation times ($Da_{II} = 0.34$). **(H–J)** $\max(\hat{\kappa})$ and $\min(\hat{\kappa})$ at different simulation times ($Da_{II} = 3442$). Little snapshots on the right demonstrate the shape of precipitate at corresponding Da_{II} at the later simulation times.

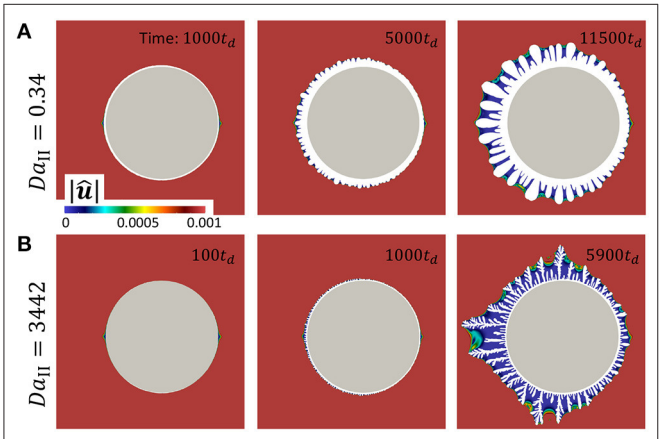

FIGURE 7 | Flow velocity map and precipitate shape which correspond to the data in **Figure 6**. **(A)** $Da_{II} = 0.34$. **(B)** $Da_{II} = 3442$. The color map is scaled to $|\hat{u}|_{max} = 0.001$. The snapshots were taken at the simulation times which correspond to the data in **Figure 6**.

to **Figure 7B** at time $5900t_d$. However, in both cases fluid velocity drops almost to zero between the dendrites, which means that convective transport of reactive ions in channels between dendrites is absent. Therefore, one can hypothesize that the diffusive nature of reactive species in channels between dendrite branches controls the channel width. To test this hypothesis in future studies one should carefully consider both diffusive transport of reactive species into the channel and reactive flux balance at the fluid-solid interface controlled by the Equation 7.

In this study only a 2D geometry is considered. Therefore, the amount of precipitated material proportional to the mass of the mineral can be estimated as the area of precipitate (**Figure 8**). First two figures (**Figures 8A,B**) show the amount of precipitate in time at different values of Da_{II} and Pe without nucleation. **Figure 8A** demonstrates that only at lowest $Da_{II} = 3.41 \cdot 10^{-3}$ the curve differs from the rest of the cases. This means that mostly the simulations are performed in transport limited regime. It is also confirmed by the **Figure 8B**, which demonstrates a significant influence of flow rate (or Pe) on the accumulation of precipitate.

Interestingly, comparison of the amount of precipitate in case of nucleation "on" and "off" shows that at high nucleation rates ($\ln A = 20$) the curves almost overlap (blue and orange

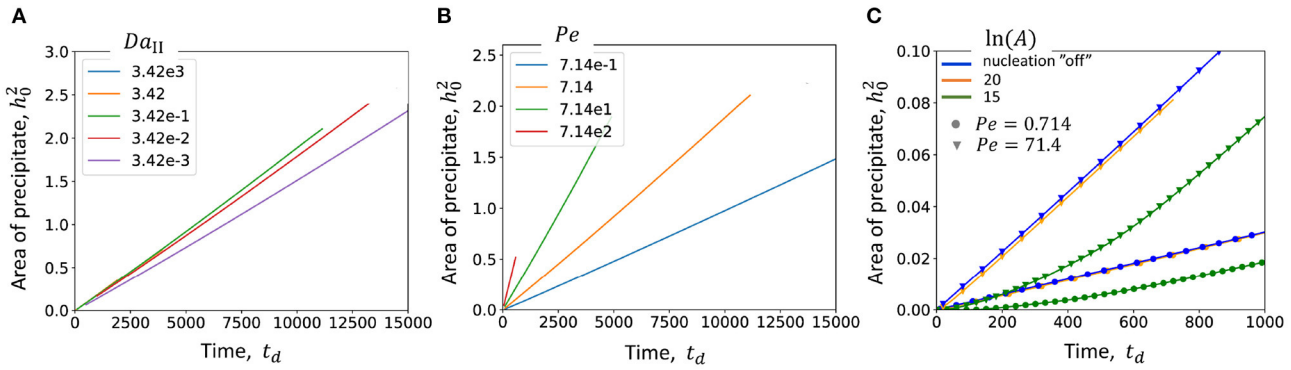

FIGURE 8 | Amount of precipitate vs. simulation time. **(A)** At different Da_{II} numbers; **(B)** At different *Pe* numbers; **(C)** in case of nucleation is "off" (blue) and "on" at $\ln A = 20$ (orange) and 15 (green) the dependencies are presented at $Pe = 0.714$ and $Pe = 71.4$, which corresponds to the data presented in **Figure 8**.

curves in **Figure 8C**). Only at lower nucleation rates (green curve) the growth of precipitate is delayed at earlier times. However, nucleation does not affect the slope of the curve at later times. Similar behavior is observed at low and high flow rates ($Pe = 0.714$ and $Pe = 7.14$). This might indicate that although nucleation affects the shape of precipitate as it was demonstrated in **Figure 8**, it does not change the overall kinetics in case of limited available reactive surfaces, such as a surface of a particle in flow in this study.

5. CONCLUSIONS

In this paper a model that couples pore-scale reactive transport with the Arbitrary Lagrangian-Eulerian approach to simulate interface motion during mineral precipitation has been described. Additionally, the heterogeneous nucleation based on CNT was integrated into the model. The ALE approach allows us to stabilize the short wavelength instabilities by including surface curvature dependent equilibrium concentration. To demonstrate the interplay between reactive transport, chemical reaction, and nucleation phenomena the precipitate formation on a single particle in reactive flow has been modeled.

In the first part of the study (nucleation is turned "off"), Pèclet–Damköhler diagram demonstrates the influence of reaction and flow rate on the shape of the precipitate. The emergence of Mullins–Sekerka instability on growing surfaces becomes more pronounced at higher Da_{II} and *Pe* numbers. All simulation cases show an appearance of a primary dense precipitate layer around the particle and a secondary porous precipitate layer formed by the instabilities. It is shown that the growth of the dense layer is completely terminated at later times due to the inability of reactant to penetrate into pores. Although the absolute thickness of the primary layer most likely depends on the condition of initial surface in real systems (such as defects, roughness, chemical heterogeneity), the presented model shows that at equal initial conditions the thickness decreases at higher reaction and higher flow rates.

In the second part of the study (nucleation is turned "on"), it is demonstrated that nucleation promotes formation of irregularly shaped precipitate by enhancing instabilities in surface growth. Additionally, it is shown that low nucleation rate reduces the impact of flow direction on the asymmetry of formed precipitate around the particle. Although the shape of precipitate is irregular [**Figure 5** at $\ln(A) = 15$], there is no distinct asymmetry (front vs. back of the particle) which is present at larger nucleation rates and when all surface is reactive from the beginning of the simulation. Nevertheless, it is expected that the limit exists at which nucleation is also affected by the flow direction. This requires rigorous studies which perhaps can capture nucleation at mesoscale when single nucleation events can be distinguished.

The presented model provides the capability to simulate complex fluid-solid interfaces and their dynamics. It captures highly irregular surfaces with great precision, utilizes non-uniform meshes for efficient computation and resolution of high concentration gradients, and allows us to introduce required surface properties (e.g., surface coverage). Although this study presents results of two dimensional simulations, the implementation is not limited to 2D. It does not require additional changes to the solver (except of generating different simulation domain). The full 3D simulations are necessary to model a realistic system, since surface instabilities might be suppressed by 2D. Also, it is necessary to simulate a 3D flow in porous systems with significantly more complex pore geometries, since the flow patterns even in 2D can have significantly different properties depending on solid fraction, pore distribution and pore texture (Ramanuj et al., 2020). Naturally, the presented work does not cover all aspects of mineral precipitation process. The number of assumptions and approximations which were discussed in the paper require a careful revision. Directions for the future development should take into account phenomena that become important at the mesoscale, for instance: crystal surface energy anisotropy that defines mineral crystal facets, transport in confinement or near charged interfaces at scales just slightly larger than Debye length, collective growth of individually resolved nuclei.

DATA AVAILABILITY STATEMENT

The raw data supporting the conclusions of this article will be made available by the authors, without undue reservation.

AUTHOR CONTRIBUTIONS

VS wrote the solver, performed the simulations and analysis, and prepared the manuscript.

FUNDING

This work was supported by the U.S. Department of Energy, Office of Science, Office of Basic Energy Sciences, Chemical Sciences, Geosciences, and Biosciences Division. This research used resources of the Compute and Data Environment for Science (CADES) at the Oak Ridge National Laboratory, which was supported by the Office of Science of the U.S. Department of Energy under Contract No. DE-AC05-00OR22725.

ACKNOWLEDGMENTS

VS would like to acknowledge helpful discussions with Anthony J. C. Ladd (University of Florida) and Piotr Szymczak (University of Warsaw).

SUPPLEMENTARY MATERIAL

The Supplementary Material for this article can be found online at: https://www.frontiersin.org/articles/10.3389/frwa.2021.800944/full#supplementary-material

REFERENCES

Beckingham, L. E., Mitnick, E. H., Steefel, C. I., Zhang, S., Voltolini, M., Swift, A. M., et al. (2016). Evaluation of mineral reactive surface area estimates for prediction of reactivity of a multi-mineral sediment. *Geochim. Cosmochim. Acta* 188, 310–329. doi: 10.1016/j.gca.2016.05.040

Bosbach, D. (2002). "Water-rock interactions, ore deposits, and environmental geochemistry a tribute to David A. Crerar," in *The Geochemical Society, Special Publication Number 7, Vol.5*, eds R. Hellmann and S. A. Wood (McLean, VA: The Canadian Mineralogist), 97–110.

Bosbach, D., Junta-Rosso, J. L., Becker, U., and Hochella, M. F. (1996). Gypsum growth in the presence of background electrolytes studied by Scanning Force Microscopy. *Geochim. Cosmochim. Acta* 60, 3295–3304. doi: 10.1016/0016-7037(96)00147-0

Bracco, J. N., Stack, A. G., and Steefel, C. I. (2013). Upscaling calcite growth rates from the mesoscale to the macroscale. *Environ. Sci. Technol.* 47, 7555–7562. doi: 10.1021/es400687r

Brantley, S. L., White, A. F., and Kubicki, J. D. (2008). *Kinetics of Water-Rock Interaction*. New York, NY: Springer. doi: 10.1007/978-0-387-73563-4

De Yoreo, J. J., Gilbert, P. U. P. A., Sommerdijk, N. A. J. M., Penn, R. L., Whitelam, S., Joester, D., et al. (2015). Crystallization by particle attachment in synthetic, biogenic, and geologic environments. *Science* 349:6247. doi: 10.1126/science.aaa6760

Dutka, F., Starchenko, V., Osselin, F., Magni, S., Szymczak, P., and Ladd, A. J. (2020). Time-dependent shapes of a dissolving mineral grain: comparisons of simulations with microfluidic experiments. *Chem. Geol.* 540:119459. doi: 10.1016/j.chemgeo.2019.119459

Fazeli, H., Masoudi, M., Patel, R. A., Aagaard, P., and Hellevang, H. (2020). Pore-scale modeling of nucleation and growth in porous media. *ACS Earth Space Chem.* 4, 249–260. doi: 10.1021/acsearthspacechem.9b00290

Fernandez-Martinez, A., Hu, Y., Lee, B., Jun, Y.-S., and Waychunas, G. A. (2013). *In situ* determination of interfacial energies between heterogeneously nucleated CaCO 3 and quartz substrates: thermodynamics of CO2 mineral trapping. *Environ. Sci. Technol.* 47, 102–109. doi: 10.1021/es3014826

Gebauer, D., Volkel, A., and Colfen, H. (2008). Stable prenucleation calcium carbonate clusters. *Science* 322, 1819–1822. doi: 10.1126/science.1164271

Godinho, J. R. A., Gerke, K. M., Stack, A. G., and Lee, P. D. (2016). The dynamic nature of crystal growth in pores. *Sci. Rep.* 6:33086. doi: 10.1038/srep33086

Higgins, S. R., Bosbach, D., Eggleston, C. M., and Knauss, K. G. (2000). Kink dynamics and step growth on barium sulfate (001): a hydrothermal scanning probe microscopy study. *J. Phys. Chem. B* 104, 6978–6982. doi: 10.1021/jp0001135

Hirt, C., Amsden, A., and Cook, J. (1997). An arbitrary Lagrangian-Eulerian computing method for all flow speeds. *J. Comput. Phys.* 135, 203–216. doi: 10.1006/jcph.1997.5702

Hunter, H. A., Ling, F. T., and Peters, C. A. (2020). Metals coprecipitation with barite: nano-XRF observation of enhanced strontium incorporation. *Environ. Eng. Sci.* 37, 235–245. doi: 10.1089/ees.2019.0447

Jasak, H. (1996). *Error analysis and estimation in the finite volume method with applications to fluid flows* (Ph.D. thesis). University of London, London, United Kingdom.

Khatoonabadi, M., Prasianakis, N. I., and Mantzaras, J. (2021). Lattice Boltzmann model with generalized wall boundary conditions for arbitrary catalytic reactivity. *Phys. Rev. E* 103:063303. doi: 10.1103/PhysRevE.103.063303

Landau, L., and Lifshitz, E. (eds.). (1980). "Surfaces," in *Statistical Physics* (Elsevier), 517–537. doi: 10.1016/C2009-0-24487-4

Langer, J. S. (1980). Instabilities and pattern formation in crystal growth. *Rev. Modern Phys.* 52:1. doi: 10.1103/RevModPhys.52.1

Li, Q., Fernandez-Martinez, A., Lee, B., Waychunas, G. A., and Jun, Y. S. (2014). Interfacial energies for heterogeneous nucleation of calcium carbonate on mica and quartz. *Environ. Sci. Technol.* 48, 5745–5753. doi: 10.1021/es405141j

Li, Q., Steefel, C. I., and Jun, Y.-S. (2017). Incorporating nanoscale effects into a continuum-scale reactive transport model for CO2-deteriorated cement. *Environ. Sci. Technol.* 51, 10861–10871. doi: 10.1021/acs.est.7b00594

Molins, S., Soulaine, C., Prasianakis, N. I., Abbasi, A., Poncet, P., Ladd, A. J. C., et al. (2021). Simulation of mineral dissolution at the pore scale with evolving fluid-solid interfaces: review of approaches and benchmark problem set. *Comput. Geosci.* 25, 1285–1318. doi: 10.1007/s10596-019-09903-x

Molins, S., Trebotich, D., Miller, G. H., and Steefel, C. I. (2017). Mineralogical and transport controls on the evolution of porous media texture using direct numerical simulation. *Water Resour. Res.* 53, 3645–3661. doi: 10.1002/2016WR020323

Molins, S., Trebotich, D., Steefel, C. I., and Shen, C. (2012). An investigation of the effect of pore scale flow on average geochemical reaction rates using direct numerical simulation. *Water Resour. Res.* 48:W03527. doi: 10.1029/2011WR011404

Molins, S., Trebotich, D., Yang, L., Ajo-Franklin, J. B., Ligocki, T. J., Shen, C., et al. (2014). Pore-scale controls on calcite dissolution rates from flow-through laboratory and numerical experiments. *Environ. Sci. Technol.* 48, 7453–7460. doi: 10.1021/es5013438

Moukalled, F., Mangani, L., and Darwish, M. (2016). *The Finite Volume Method in Computational Fluid Dynamics*. Cham: Springer International Publishing. doi: 10.1007/978-3-319-16874-6

Mullins, W. W., and Sekerka, R. F. (2004). Stability of a planar interface during solidification of a dilute binary alloy. *J. Appl. Phys.* 35:444. doi: 10.1063/1.1713333

Nilsson, Ö., and Sternbeck, J. (1999). A mechanistic model for calcite crystal growth using surface speciation. *Geochim. Cosmochim. Acta* 63, 217–225. doi: 10.1016/S0016-7037(99)00026-5

Noiriel, C., and Daval, D. (2017). Pore-scale geochemical reactivity associated with CO2 storage: new frontiers at the fluid-solid interface. *Acc. Chem. Res*. 50, 759–768. doi: 10.1021/acs.accounts.7b00019

Noiriel, C., Oursin, M., and Daval, D. (2020). Examination of crystal dissolution in 3D: a way to reconcile dissolution rates in the laboratory? *Geochim. Cosmochim. Acta* 273, 1–25. doi: 10.1016/j.gca.2020.01.003

Noiriel, C., Oursin, M., Saldi, G., and Haberthür, D. (2019). Direct determination of dissolution rates at crystal surfaces using 3D X-ray microtomography. *ACS Earth Space Chem*. 3, 100–108. doi: 10.1021/acsearthspacechem.8b00143

Noiriel, C., Seigneur, N., Le Guern, P., and Lagneau, V. (2021). Geometry and mineral heterogeneity controls on precipitation in fractures: an X-ray micro-tomography and reactive transport modeling study. *Adv. Water Resour*. 152:103916. doi: 10.1016/j.advwatres.2021.103916

Noiriel, C., and Soulaine, C. (2021). Pore-scale imaging and modelling of reactive flow in evolving porous media: tracking the dynamics of the fluid-rock interface. *Transport Porous Media* 140, 181–213. doi: 10.1007/s11242-021-01613-2

Peitgen, H.-O. (1988). *The Science of Fractal Images*. New York, NY: Springer-Verlag.

Pina, C. M., Becker, U., Risthaus, P., Bosbach, D., and Putnis, A. (1998). Molecular-scale mechanisms of crystal growth in barite. *Nature* 395, 483–486. doi: 10.1038/26718

Plummer, L. N., and Busenberg, E. (1982). The solubilities of calcite, aragonite and vaterite in CO2-H2O solutions between 0 and 90°C, and an evaluation of the aqueous model for the system CaCO3-CO2-H2O. *Geochim. Cosmochim. Acta* 46, 1011–1040. doi: 10.1016/0016-7037(82)90056-4

Prasianakis, N. I., Curti, E., Kosakowski, G., Poonoosamy, J., and Churakov, S. V. (2017). Deciphering pore-level precipitation mechanisms. *Sci. Rep*. 7:13765. doi: 10.1038/s41598-017-14142-0

Prasianakis, N. I., Haller, R., Mahrous, M., Poonoosamy, J., Pfingsten, W., and Churakov, S. V. (2020). Neural network based process coupling and parameter upscaling in reactive transport simulations. *Geochim. Cosmochim. Acta* 291, 126–143. doi: 10.1016/j.gca.2020.07.019

Putnis, C. V., and Ruiz-Agudo, E. (2013). The mineral-water interface: where minerals react with the environment. *Elements* 9, 177–182. doi: 10.2113/gselements.9.3.177

Qin, F., and Beckingham, L. E. (2021). The impact of mineral reactive surface area variation on simulated mineral reactions and reaction rates. *Appl. Geochem*. 124:104852. doi: 10.1016/j.apgeochem.2020.104852

Raiteri, P., Gale, J. D., Quigley, D., and Rodger, P. M. (2010). Derivation of an accurate force-field for simulating the growth of calcium carbonate from aqueous solution: a new model for the calcite?water interface. *J. Phys. Chem. C* 114, 5997–6010. doi: 10.1021/jp910977a

Ramanuj, V., Starchenko, V., Sankaran, R., and Kidder, M. K. (2020). Characteristics of flow through randomly packed impermeable and permeable particles using pore resolved simulations. *Chem. Eng. Sci*. 228:115969. doi: 10.1016/j.ces.2020.115969

Rigos, A. A., and Deutch, J. M. (1986). Concentration effects on the Mullins-Sekerka instability. *J. Chem. Phys*. 86, 7119–7125. doi: 10.1063/1.452361

Soulaine, C., Pavuluri, S., Claret, F., and Tournassat, C. (2021). porousMedia4Foam: Multi-SCALE open-source platform for hydro-geochemical simulations with OpenFOAM®. Environ. Modell. Softw. 145:105199. doi: 10.1016/j.envsoft.2021.105199

Soulaine, C., Roman, S., Kovscek, A., and Tchelepi, H. A. (2017). Mineral dissolution and wormholing from a pore-scale perspective. *J. Fluid Mech*. 827, 457–483. doi: 10.1017/jfm.2017.499

Stack, A. G., Raiteri, P., and Gale, J. D. (2012). Accurate rates of the complex mechanisms for growth and dissolution of minerals using a combination of rare-event theories. *J. Am. Chem. Soc*. 134, 11–14. doi: 10.1021/ja204714k

Starchenko, V., and Ladd, A. J. C. (2018). The development of wormholes in laboratory-scale fractures: perspectives from three-dimensional simulations. *Water Resour. Res*. 54, 7946–7959. doi: 10.1029/2018WR022948

Starchenko, V., Marra, C. J., and Ladd, A. J. C. (2016). Three-dimensional simulations of fracture dissolution. *J. Geophys. Res. Solid Earth* 121, 6421–6444. doi: 10.1002/2016JB013321

Szymczak, P., and Ladd, A. J. C. (2012). Reactive-infiltration instabilities in rocks. Fracture dissolution. *J. Fluid Mech*. 702, 239–264. doi: 10.1017/jfm.2012.174

Teng, H. H., Dove, P. M., and De Yoreo, J. J. (2000). Kinetics of calcite growth: Surface processes and relationships to macroscopic rate laws. *Geochim. Cosmochim. Acta* 64, 2255–2266. doi: 10.1016/S0016-7037(00)00341-0

Tuković, Ž., and Jasak, H. (2012). A moving mesh finite volume interface tracking method for surface tension dominated interfacial fluid flow. *Comput. Fluids* 55, 70–84. doi: 10.1016/j.compfluid.2011.11.003

Upadhyay, V. K., Szymczak, P., and Ladd, A. J. C. (2015). Initial conditions or emergence: what determines dissolution patterns in rough fractures? *J. Geophys. Res. B Solid Earth* 120, 6102–6121. doi: 10.1002/2015JB012233

Weber, J., Bracco, J. J. N., Poplawsky, J. D. J., Ievlev, A. V. A., More, K. K. L., Lorenz, M., et al. (2018). Unraveling the effects of strontium incorporation on barite growth–*in situ* and *ex situ* observations using multiscale chemical imaging. *Crystal Growth Design* 18, 5521–5533.

Weber, J., Bracco, J. N., Yuan, K., Starchenko, V., and Stack, A. G. (2021). Studies of mineral nucleation and growth across multiple scales: review of the current state of research using the example of barite (BaSO 4). *ACS Earth Space Chem*. 5, 3338–3361. doi: 10.1021/acsearthspacechem.1c00055

Weller, H. G., Tabor, G., Jasak, H., and Fureby, C. (1998). A tensorial approach to computational continuum mechanics using object-oriented techniques. *Comput. Phys*. 12:620. doi: 10.1063/1.168744

Xu, L., Szymczak, P., Toussaint, R., Flekkøy, E. G., and Måløy, K. J. (2020). Dissolution phase diagram in radial geometry. *Front. Phys*. 8:369. doi: 10.3389/fphy.2020.00369

Yang, F., Stack, A. G., and Starchenko, V. (2021). Micro-continuum approach for mineral precipitation. *Sci. Rep*. 11:3495. doi: 10.1038/s41598-021-82807-y

Yoreo, J. J. D., Zepeda-Ruiz, L. A., Friddle, R. W., Qiu, S. R., Wasylenki, L. E., Chernov, A. A., et al. (2009). Rethinking classical crystal growth models through molecular scale insights: consequences of kink-limited kinetics. *Crystal Growth Design* 9, 5135–5144. doi: 10.1021/cg900543g

Yuan, K., Starchenko, V., Lee, S. S., De Andrade, V., Gursoy, D., Sturchio, N. C., et al. (2019). Mapping three-dimensional dissolution rates of calcite microcrystals: effects of surface curvature and dissolved metal ions. *ACS Earth Space Chem*. 3, 833–843. doi: 10.1021/acsearthspacechem.9b00003

Yuan, K., Starchenko, V., Rampal, N., Yang, F., Yang, X., Xiao, X., et al. (2021). Opposing effects of impurity ion Sr 2+ on the heterogeneous nucleation and growth of barite (BaSO 4). *Crystal Growth Design* 21, 5828–5839. doi: 10.1021/acs.cgd.1c00715

Zhen-Wu, B., Dideriksen, K., Olsson, J., Raahauge, P., Stipp, S., and Oelkers, E. (2016). Experimental determination of barite dissolution and precipitation rates as a function of temperature and aqueous fluid composition. *Geochim. Cosmochim. Acta* 194, 193–210. doi: 10.1016/j.gca.2016.08.041

Conflict of Interest: The author declares that the research was conducted in the absence of any commercial or financial relationships that could be construed as a potential conflict of interest.

frontiers in Water

ORIGINAL RESEARCH
published: 25 January 2022
doi: 10.3389/frwa.2021.800369

Comparative Study of Traditional and Deep-Learning Denoising Approaches for Image-Based Petrophysical Characterization of Porous Media

Miral S. Tawfik[1], Amogh Subbakrishna Adishesha[2], Yuhan Hsi[2], Prakash Purswani[3], Russell T. Johns[3,4], Parisa Shokouhi[5], Xiaolei Huang[2] and Zuleima T. Karpyn[3,4]*

[1] Reservoir Engineering and Simulation, Chevron Technical Center, Houston, TX, United States, [2] Information Science and Technology, The Pennsylvania State University, University Park, PA, United States, [3] The Energy Institute, The Pennsylvania State University, University Park, PA, United States, [4] John and Willie Leone Family Department of Energy and Mineral Engineering, The Pennsylvania State University, University Park, PA, United States, [5] Department of Engineering Science and Mechanics, The Pennsylvania State University, University Park, PA, United States

OPEN ACCESS

Edited by:
James E. McClure, Virginia Tech, United States

Reviewed by:
Tim Scheibe, Pacific Northwest National Laboratory (DOE), United States
Xiaofan Yang, Beijing Normal University, China

***Correspondence:**
Miral S. Tawfik
mtawfik@alumni.psu.edu

Specialty section:
This article was submitted to Water and Critical Zone, a section of the journal Frontiers in Water

Received: *23 October 2021*
Accepted: *10 December 2021*
Published: *25 January 2022*

Citation:
Tawfik MS, Adishesha AS, Hsi Y, Purswani P, Johns RT, Shokouhi P, Huang X and Karpyn ZT (2022) Comparative Study of Traditional and Deep-Learning Denoising Approaches for Image-Based Petrophysical Characterization of Porous Media. Front. Water 3:800369. doi: 10.3389/frwa.2021.800369

Digital rock physics has seen significant advances owing to improvements in micro-computed tomography (MCT) imaging techniques and computing power. These advances allow for the visualization and accurate characterization of multiphase transport in porous media. Despite such advancements, image processing and particularly the task of denoising MCT images remains less explored. As such, selection of proper denoising method is a challenging optimization exercise of balancing the tradeoffs between minimizing noise and preserving original features. Despite its importance, there are no comparative studies in the geoscience domain that assess the performance of different denoising approaches, and their effect on image-based rock and fluid property estimates. Further, the application of machine learning and deep learning-based (DL) denoising models remains under-explored. In this research, we evaluate the performance of six commonly used denoising filters and compare them to five DL-based denoising protocols, namely, noise-to-clean (N2C), residual dense network (RDN), and cycle consistent generative adversarial network (CCGAN)—which require a clean reference (ground truth), as well as noise-to-noise (N2N) and noise-to-void (N2V)—which do not require a clean reference. We also propose hybrid or semi-supervised DL denoising models which only require a fraction of clean reference images. Using these models, we investigate the optimal number of high-exposure reference images that balances data acquisition cost and accurate petrophysical characterization. The performance of each denoising approach is evaluated using two sets of metrics: (1) standard denoising evaluation metrics, including peak signal-to-noise ratio (PSNR) and contrast-to-noise ratio (CNR), and (2) the resulting image-based petrophysical properties such as porosity, saturation, pore size distribution, phase connectivity, and specific surface area (SSA). Petrophysical estimates show that most traditional filters perform well when estimating bulk properties but show large errors for pore-scale properties like phase connectivity. Meanwhile, DL-based models give mixed outcomes, where supervised

methods like N2C show the best performance, and an unsupervised model like N2V shows the worst performance. N2N75, which is a newly proposed semi-supervised variation of the N2N model, where 75% of the clean reference data is used for training, shows very promising outcomes for both traditional denoising performance metrics and petrophysical properties including both bulk and pore-scale measures. Lastly, N2C is found to be the most computationally efficient, while CCGAN is found to be the least, among the DL-based models considered in this study. Overall, this investigation shows that application of sophisticated supervised and semi-supervised DL-based denoising models can significantly reduce petrophysical characterization errors introduced during the denoising step. Furthermore, with the advancement of semi-supervised DL-based models, requirement of clean reference or ground truth images for training can be reduced and deployment of fast X-ray scanning can be made possible.

Keywords: image processing, micro-computed tomography, deep learning, denoising, image enhancement, digital rock physics, carbon capture utilization and storage (CCUS), enhanced oil recovery

BACKGROUND AND INTRODUCTION

Micro-computed tomography (MCT) is a non-destructive technique used to visualize the internal structure of objects in a variety of disciplines including medicine, dentistry, tissue engineering, aerospace engineering, geology, and material and civil engineering (Orhan, 2020). The physical principle behind this technique is that X-rays attenuate differently as they penetrate through different materials depending on their density and atomic mass (Knoll, 2000; Attix, 2004; Ritman, 2004; Hsieh, 2015). This makes MCT an ideal tool for characterizing multiphase materials such as rocks with fluid phases of different densities.

The use of MCT imaging is becoming increasingly indispensable in several disciplines, including geotechnical and petrophysical characterization and understanding multiphase flow in porous media. Wang et al. (1984) first adopted medical CT imaging to monitor the injectant front to understand the effect of pore structure heterogeneity on oil recovery and interactions between oil and injected fluid in a Berea sandstone. However, medical CT imaging soon proved inadequate in describing the underlying pore-scale phenomena responsible for multiphase flow behavior in porous media (Cromwell et al., 1984). Therefore, high-resolution MCT imaging was used to obtain quantitative pore-scale information about structure–function relationships (Jasti et al., 1993). They characterized the 3D pore structure in a glass bead pack and three Berea sandstone samples to determine whether topological properties such as pore connectivity and phase features of individual fluid phases such as saturation can be resolved. Micro-computed tomography has since been successfully used for quantifying a wide range of petrophysical properties such as volume fraction for porosity and saturation quantification, specific surface area (SSA), pore- and blob-size distributions, *in-situ* contact angles, interface curvatures for local capillary pressures, grain sphericity, angularity, roughness as well as phase connectivity (Sharma and Yortsos, 1987; Prodanović and Bryant, 2006; Karpyn et al., 2010; Herring et al., 2013; Landry et al., 2014; Larpudomlert et al., 2014; Berg et al., 2016; Klise et al., 2016; Scanziani et al., 2017; Chen et al., 2018; Tawfik et al., 2019; McClure et al., 2020). The accuracy with which we can estimate these pore-scale properties affect our ability to explain and predict multiphase fluid flow in porous media. For example, pore-network modeling, which is used in a variety of digital rock studies to explain and predict macroscopic transport properties such as absolute permeability, relative permeability, and capillary pressure, uses simplified pore structures composed of a network of pores and throats, which can be directly extracted from the MCT images (Valvatne and Blunt, 2004; Jia et al., 2007; Dong et al., 2009; Mostaghimi et al., 2013; Berg et al., 2016; Zahaf et al., 2017; Raeini et al., 2019). Similarly, Lattice Boltzmann simulation of multiphase flow is used to estimate the same transport properties but on real pore structures by directly using the binarized MCT images as input (Grader et al., 2010; Andrä et al., 2013; Landry et al., 2014; Liu et al., 2014; Armstrong et al., 2016; Kakouei et al., 2017; Li et al., 2018). The accuracy of the model predictions thus depends on the accuracy of processing the images that feed into these models.

Despite the fast-paced advances in MCT imaging, there are several factors that introduce noise to MCT images limiting the image quality and feature detectability. Those limitations can hinder our ability to accurately identify structure-function relationships and predict fluid flow behavior, which is essential in several applications including CO_2 storage, aquifer remediation, and hydrocarbon recovery. Some of the inherent limitations of MCT imaging include photon statistics, balance between representative elementary volume and resolution or feature detection, and partial volume consideration (Van Stappen, 2018). Apart from image resolution, there are numerous artifacts that arise during image acquisition. The prominent ones include photon starvation, detector saturation also known as ghosting, central rotation artifact, cone-beam effect, metal artifact, cupping artifact, streaks and dark bands, under-sampling, poor contrast, beam hardening, scatter, and ring artifacts (Boas and Fleischmann, 2012). These imaging artifacts result in different forms of noise in a CT image. Though noise in MCT has not been fully profiled, many studies including Diwakar and Kumar

(2018) and Lee et al. (2018) have attempted to profile the noise distributions through known statistical distributions. The most prevalent noise forms follow Poisson and Gaussian distributions. There are several other forms of noise including fractal noises like Perlin noise, periodic noise from helical sampling and finally random noise that may occur due to the change in X-ray quanta for multiple subject densities. Gaussian and Poisson noise are the most common types of noise observed in MCT images. Gaussian noise is additive and signal independent. Poisson noise is a consequence of low photon count, and results in random thin bright and dark streaks that appear preferentially along the direction of greatest attenuation (Boas and Fleischmann, 2012). The low photon count coupled with the error in quantization of the received photons leads to a mixture noise-model, which is a combination of Poisson and Gaussian distributions. Perlin noise is a pseudo-random texture gradient noise which is generated using octaves of noise flow vectors along with frequency and amplitude parameters to simulate spatially interpolated textures (Perlin, 1985). The granularity and texture of the noise profile in low quality (LQ) CT images can be captured by Perlin noise. Bae et al. (2018) showed that using Perlin noise profile to augment a lung CT dataset resulted in higher classification accuracy indicating that the features extracted from Perlin noise augmented images matched those of certain low-dose CT scans with lung conditions.

Mathematically, denoising is an inverse ill-posed problem where noisy data is a sparse representation of the real data and a unique solution for its restoration does not necessarily exist (Fan et al., 2019). For an exact solution to the problem, a priori knowledge of the types of noise, variance of noise within an image and along the image stack would be required. This information is usually not readily available. The basic principle behind most of the traditional spatial domain denoising filters is noise removal based on spatial correlation between an input pixel gray value and its neighboring pixels. Those filters can be classified into linear and non-linear filters. Linear filters are spatially invariant filters that output pixel values as a linear combination of the input pixel value and its neighborhood. Examples of linear filters include Gaussian and mean filters, which are optimal for Gaussian noise. However, linear filters tend to blur edges and blur small features. Conversely, non-linear filters can be spatially invariant like the median filter, or spatially variant like the anisotropic diffusion (AD) filter (Huang et al., 1979; Perona and Malik, 1990). Another approach to denoise MCT images involves machine-learning-based models. As such, the objective is to find the parameters that act on the sparse noisy data to obtain the closest representation of the clean signal. Several works in literature have approached this parameter estimation through the use of classic machine learning and modern neural network-based models (Tian et al., 2020). Improvements in the DL denoising field result from a clearer understanding of the specific noise forms and improvements in the architecture of neural networks. The literature points to three specific architectures, namely U-Nets, Residual Networks, and Generative Adversarial Networks (GANs), that have been established for addressing common noise forms including Poisson, Gaussian, and their mixtures which are predominant in CT images (Kulathilake et al., 2021).

Deep learning (DL) powered computer vision has seen phenomenal improvement since the introduction of AlexNet in 2012 (Krizhevsky et al., 2017). However, adaptation of imaging techniques for porous media is still work in progress. Kamrava et al. (2019) trained a 20-layer feedforward neural network using synthetic data generated by the stochastic cross-correlation-based simulation (CCSIM) algorithm and found that neural networks perform better compared to bi-cubic interpolation for image super-resolution while the synthetic data further improved the model's generalizability. Sidorenko et al. (2021) implemented an encoder-decoder network for denoising MCT images obtained from tight sandstone samples. The authors compared the effect of different loss functions and found that the least absolute deviation (L1) loss gave a better result in terms of peak signal to noise ratio (PSNR) and structural similarity index measure (SSIM) when compared to the least square errors (L2) loss, SSIM loss, and Visual Geometry Group (VGG) perceptual loss. Recently, Alsamadony et al. (2021) acquired low-exposure and high-exposure CT scans on the same carbonate sample and compared denoising performance using a pre-trained very deep super resolution (VDSR) network against a shallow U-Net. They demonstrated that DL-based image processing can improve image quality; and that pre-trained VDSR network with fine-tuning tends to out-perform VDSR trained from scratch. Wang et al. (2021) reviewed various DL applications in pore-scale imaging and modeling, including image segmentation, image super-resolution, petrophysical property prediction, flow simulation, as well as common convolutional neural network (CNN) architectures and various types of GANs for image generation. However, the discussion on image denoising was brief. A summary of findings from select literature on image denoising with applications in digital rock physics is provided in **Table 1**.

The literature survey reveals a need for a comprehensive comparison of denoising approaches for petrophysical applications. Existing studies mostly utilize non-learnable filters and rely on visual inspection to evaluate the effect of image denoising. The lack of quantitative metrics, both standard and physics-based, cause errors during this critical image processing step to remain largely unquantified. Finally, none of the reported studies consider the impact of denoising techniques on downstream tasks such as image segmentation and petrophysical property estimation, which is often the ultimate goal of quantitative imaging.

In this paper, we address these research gaps and compare the performance of traditional (user-based) denoising methods against more sophisticated DL-based denoising methods. Four types of models are considered in this study: (a) commonly used filters such as the Gaussian, non-local means (NLM), Median etc., (b) fully supervised models including the noise-to-clean (N2C), residual dense network (RDN), and cycle consistent generative adversarial network (CCGAN), (c) semi-supervised models that use a portion of clean reference images for learning, and (d) completely unsupervised techniques like the noise-to-noise (N2N) and noise-to-void (N2V). We evaluate the performance of the different denoising models using both qualitative and quantitative analyses against an independent ground truth.

TABLE 1 | A summary of selected publications that report on MCT imaging in the digital rock physics domain, highlighting the commonly used denoising methods.

References	Porous medium	Resolution, microns	Denoising protocol(s)	Denoising evaluation	Image-based petrophysical analyses
Culligan et al., 2004	Glass beadpack	18	Median	–	Saturation, interfacial area
Porter and Wildenschild, 2010	Beadpack	11.8, 5.9	Anisotropic diffusion, Median	Qualitative	Interfacial area
Landry et al., 2011	Acrylic Beadpack	25.9	Median	–	Surface and interfacial area
Iglauer et al., 2012	Clashach Sandstone	9	Anisotropic regularization	–	Porosity, residual oil saturation, residual oil cluster distribution
Brown et al., 2014	SiO_2 Beadpack	10.6, 5.3	Median, total variation, majority	Qualitative	Saturation, interfacial area, mean interface curvature
Andrew et al., 2014	Bentheimer SS Doddington SS Ketton LS Mount Gambier LS Estaillades LS	6.16 5.39 4.60 4.44 3.93	Non-local means	–	Pore size distribution, trapped residual $scCO_2$ saturation, trapped $scCO_2$ ganglia size distribution
Alyafei et al., 2015	Berea SS Doddington SS Ketton LS Estaillades LS	2.7, 5.4, 10.8, 21.6	Wavelet-Fourier filter, anisotropic regularization	–	Porosity, pore size distribution, permeability
Freire-Gormaly et al., 2015	Indiana Limestone Pink Dolomite	7.5, 8.3, 11.07	Median	–	Porosity, pore size distribution, pore and throat radius, coordination number, pore-to-pore distance, capillary pressure
Menke et al., 2016	Estaillades LS Portland Base bed LS	4.76	Non-local means	–	Porosity, permeability, specific surface area
Al-Menhali et al., 2016	Estaillades LS	4.9	Non-local means	–	CO_2 and N_2 saturation, ganglia morphology, and distribution, *in-situ* contact angles
Berg et al., 2016	Gildehauser SS	2.2	Non-local means	–	Porosity, saturation, permeability, relative permeability
AlRatrout et al., 2017	Ketton Limestone	3.28	Non-local means	–	*In-situ* contact angles
Verri et al., 2017	Tight rock 1 Tight rock 2 Sandstone 1 Sandstone 2	2.175 2.73 2.13 2.05	Bilateral, non-local means	Qualitative	Porosity, specific surface area, equivalent pore diameter, permeability, tortuosity
Singh et al., 2017	Ketton LS	3.28	Non-local means	SNR	Local capillary pressure, oil saturation
Gao et al., 2017	Bentheimer SS	6	Non-local means	–	Saturation, relative permeability
Lin et al., 2018	Bentheimer SS	3.58	Non-local means	SNR, Average phase boundary sharpness	Interfacial curvature, local capillary pressure
Rücker et al., 2019	Ketton LS	3.28	Non-local means	–	*In-situ* contact angles, fluid distribution as a function of pore size
Tawfik, 2020	Indiana LS	2.6	Anisotropic diffusion	Qualitative	*In-situ* contact angles
Purswani et al., 2020	Sintered glass frit	6, 18	Non-local means	–	Porosity, saturation, interfacial area, connectivity
Sidorenko et al., 2021	Tight SS	1.2	Residual encoder-decoder network (RedNet)	SSIM, L1, L2, VGG-perceptual	–
Niu, 2021	Sintered glass frit	15	Non-local means	Qualitative	Porosity, saturation, *in-situ* contact angles
Alsamadony et al., 2021	Carbonate rock	14	Pre-trained very deep SR (VDSR), U-Net	SSIM, L2	–

LS, limestone; SS, sandstone.

TABLE 2 | Properties of the porous core sample (Niu, 2021).

Diameter, in	0.5
Length, in	2.0
Porosity, %	∼14.7
Absolute permeability, mD	630.4
Pore size distribution, μm	250–500
Inner surface (BET), m^2/g	∼0.015

TABLE 3 | MCT scanning parameters.

	HQ	LQ
Resolution, μm	15	
Voltage, kV	200	
Current, μA	70	
Magnification	13.5X	
Scanning time, min	90	12

We also compare computational resource requirements and ease of implementation of the different methods and provide recommendations. From quantitative comparison, we show the utility of physics-informed evaluation based on petrophysical property estimation. From this exercise, we address the following research questions: can sophisticated denoising protocols yield a reasonable characterization of a saturated porous medium using fast X-ray scanning with low-exposure time? Can we use a reduced number of, or no clean reference images and still yield accurate petrophysical characterization estimates using low-exposure MCT images?

METHODOLOGY

Image Acquisition

In this section, we briefly describe the experiment conducted by Niu (2021) to generate the datasets used in this study. The MCT images used in this study are of a fritted Robu-type glass (borosilicate) filter procured from Adam & Chittenden Scientific Glass Cooperation. This porous medium was selected as a proxy for real rocks to minimize changes that typically take place in real rock samples when fluids are injected, such as dissolution, which can alter the results of the study. The core sample properties are given in **Table 2**.

The experimental procedure consisted of wrapping the core sample in a heat shrink jacket and placing it in an X-ray transparent Core Lab biaxial FCH series core holder (CoreLab, 2021; https://www.corelab.com/cli/core-holders/x-ray-core-holder-fch-series). This core holder is made of an aluminum body wrapped in carbon fiber composite, which reduces the holder's X-ray absorption capacity during scanning. The porous medium is saturated with high salinity brine that has a composition representative of a saline aquifer (Tawfik et al., 2019). Brine was pre-equilibrated with CO_2 at 1,500 psi and 45°C before being used to saturate the core. The core sample was then flooded with supercritical CO_2 ($scCO_2$) at a pore pressure of 1,180 psi and temperature of 41.7 ± 0.2°C (107.06 ± 0.36°F), as well as confining pressure of 1,430 ± 50 psi. The confining pressure was applied by injecting deionized water into the annular space of the core holder. The high pore pressure and temperature enabled the maintenance of $scCO_2$ conditions.

The MCT images were acquired using a GE v|tome|x L300 multi-scale nano/microCT system, using the 300 kV X-ray tube. Two datasets were acquired at the same voxel resolution of 15 μm: a high-quality (HQ) scan, where more exposure time was allowed to reduce noise. The second dataset was a low-quality (LQ) scan which was under the same experimental conditions, using the same scanning parameters except for exposure time, where less scanning time (∼7.5 times less) was needed to produce a noisier version of the HQ dataset. The HQ dataset is used in this study as a ground truth to evaluate the different denoising methods and compare the petrophysical properties computed using the different denoised datasets. The HQ dataset is also used as a clean reference dataset to train the model for some of the DL denoising algorithms, which are discussed later in this section. The scanning details for both datasets are presented in **Table 3**. The sinograms generated during image acquisition were reconstructed using GE's proprietary GPU-based reconstruction software *datos|x 2 reconstruction*.

Selection and Implementation of Denoising Methods

The datasets obtained from the scans contain 2,024 32-bit images. Pre-processing of the datasets involved extracting a cylindrical sub-volume to eliminate the core holder and heat shrink jacket. Additionally, the top 103 and bottom 490 slices were removed to eliminate the cone-beam effect, which is typically observed at the top and bottom of the scan volume.

Non-learnable, Traditional Denoising Filters

Numerous filtering algorithms have been developed for reducing image noise to make the gray-scale CT images ready for the image segmentation step, after which feature extraction and quantitative analysis is carried out. In this study, we focus on the errors incurred particularly during the denoising step. Denoising may take place before image reconstruction by taking advantage of existing statistical models of noise, derived from an understanding of its physical origin. However, due to missing visual perception, operations performed on a sinogram might have unpredictable effects on real features post reconstruction (Matrecano et al., 2010). On the other hand, post-reconstruction filters are pixel-to-pixel transformations of an image. This transformation is based on the gray-scale intensity of each pixel and its neighboring pixels (Machado et al., 2013). They can be classified as low-pass or high-pass filters; a low-pass filter is used for image smoothing, whereas a high-pass filter is typically used for image sharpening. Some of the most commonly used filters include Gaussian filter, median filter, NLM, and AD filter.

The Gaussian filter is a low-pass filter that uses a Gaussian function. Applying this filter involves convolving an image with a Gaussian function, which may result in a blurrier image. A

median filter is also a low-pass smoothening filter. It replaces the gray-scale value of each pixel with the median of its neighborhood. The neighborhood is pre-specified by the user as 6 faces, 18 edges, or 26 vertices. The process may be repeated to further smooth the image. The median Filter usually works well when images contain non-Gaussian noise and/or very small artifacts. The NLM filter first proposed by Buades et al. (2005) assumes the noise to be white noise. The value specified for the target voxel is a weighted-average of neighboring voxels within a user-specified search window. The weights are determined by applying a Gaussian kernel based on the similarity between the neighborhoods. The AD filter (Weickert, 1996) also known as the Perona-Malik diffusion, aims to reduce image noise within each phase while preserving edges and boundaries between phases. Typically, a diffusion stop criterion that exceeds the variation within a given phase is set to identify when diffusion should no longer take place to terminate diffusion and preserve edges. If this stop criterion is set to the maximum difference between voxel intensity values, diffusion never stops and the AD filter converges to a simple isotropic Gaussian filter. Some of the other used filters applied include Bilateral, SNN, Total variance, Nagao, Kuwahara, BM3D, Minimum, and Maximum filters.

The image processing software Avizo (v2020) was used to implement the simple filters, including the Gaussian, median, NLM, AD, bilateral, and SNN filters. For the Gaussian filter, the standard deviation was set to two voxels, and the kernel size was set to nine voxels in each direction. The median filter neighborhood was set to 26 (vertex neighborhood), and a total of three iterations are performed. The NLM filter was implemented using the adaptive-manifolds-based approach (Gastal and Oliveira, 2012). The search window was specified to be 500 voxels, and the local neighborhood was set to four. A large enough search window is selected to increase the chances of finding similar structures and phases. The local neighborhood value was determined such that it is similar in size to the fine structures that can be found in the image. Spatial standard deviation (which determines the relationship between how fast the similarity value decreases as distance between the target and neighboring voxel increases), was set to five. Similarly, the intensity standard deviation (which determines the relationship between how fast the similarity value decreases based on voxel intensities) was set to 0.2. For the AD filter, a total of five smoothing iterations per image is performed, with the diffusion stop threshold set to 0.048. That is, if the difference between the target voxel value and the value of its neighboring six voxels exceeds this stop threshold value, diffusion will not occur, hence preserving and enhancing phase interfaces. The bilateral filter parameters were kernel size $= 3$ and similarity $= 20$. Finally, for the SNN filter a kernel size of 3 was used. It is evident that these simple filters rely heavily on the user and their experience which lend themselves to likely bias. As such, there is a need for non-user-based denoising protocols.

Deep Learning Denoising Methods

A few notable DL-based denoising algorithms have been selected based on their architecture and input requirements. The most common architectures for encoder-decoder based denoising are U-Nets, GANs and RDNs. U-Nets are a sequence of contracting and expanding convolution blocks (forming a "U" shape) originally proposed by Ronneberger et al. (2015) for the purpose of biomedical image segmentation. U-Nets have the ability to accumulate hierarchical features at multiple resolutions and maintain sharpness throughout the decoding process (Diwakar and Kumar, 2018). Residual dense networks, on the other hand, are inspired by the neural connections present in a human brain. Here, output of a convolution block is combined with its input to help train deeper neural networks and maintain a version of the original input features. Residual dense networks have lately shown that accumulating features through local and global residual learning can significantly improve image restoration (Zhang et al., 2021). Finally, GANs, are a recent addition to the neural network family which are designed to generate data in a semi-supervised setting. The primary reason for the success of GANs, however, is its robust loss function which inherently accommodates several noise removal objectives like L1 distance, distribution matching etc. (Yang et al., 2018). This advantage proves essential in denoising tasks where noisy inputs have to be mapped to clean outputs.

In each of the above architectures, a state-of-the-art model has been identified and used for comparison against the traditional filter-based denoising techniques. Noise-to-clean is a U-Net proposed by Lehtinen et al. (2018) which learns to minimize a mean absolute error (MAE) distance between the denoised image and its corresponding clean reference. Similarly, residual dense network by Zhang et al. (2021) is a residual network aimed at improving fine-grained features in the restoration of noisy images. Cycle Consistent Generative Adversarial Denoising Network (CCGAN) by Kang et al. (2019) is multi-stage GAN network originally designed to denoise coronary CT images. The three models mentioned above use a supervised approach where they extract the 1:1 mapping between noisy and clean pixel intensities. However, in practice, clean reference MCT images are costly and hard to obtain, since this equates to higher X-ray exposure, longer scan durations and other noise prevention techniques which may not be cost- and/or time-efficient. For this reason, an evaluation involving unsupervised machine learning approaches is essential for practical purposes. In this direction, noise-to-noise by Lehtinen et al. (2018) is a reference-less approach based on a U-Net architecture and used for removing common noise forms present in images. Similarly, N2V is another unsupervised technique introduced by Krull et al. (2019), which uses pixel manipulations to infer the presence and removal of noise. Noise-to-noise ratio is a unique model which tries to estimate the unvarying signal behind varying noise realizations. This is intuitively similar to removing moving tourists in an unchanging scenic photo. The training for N2N requires the addition of a synthetic noise profile which matches low dose signal. For our purpose, we use a mixture of Poisson-Gaussian along with Perlin noise textures to simulate random noise. For the Poisson-Gaussian mixture, we first simulate the Poisson process using the pixel intensities as the mean (λ). We then scale this value with a Gaussian factor using mean (μ) of 0 and standard deviation (σ) that is randomly picked between 0 and 0.005. For the Perlin noise, we use a simplex model with

scale set to 5, octaves to 6, persistence to 0.5, and lacunarity to 2.0 which showed the best match for the texture. Such profiles have been shown to emulate low-exposure noise in CT images (Lee et al., 2018). The model then learns to estimate the mean of the signal through several iterations. For test purposes, we do not add any noise and since the model is already accustomed to removing similar noise profiles, the denoising is successful.

Fully supervised and fully unsupervised DL models account for the best and worst-case scenarios of data availability, respectively. In this study, we propose new semi-supervised denoising models, where we use limited number of HQ high-exposure images to denoise a larger LQ low-exposure dataset. This can be applicable in several scenarios, including: (1) when the full length of a core sample needs to be scanned at a high resolution, yet resources in terms of time, availability, and money, are limited, and (2) when the processes or state of the core sample we are interested in visualizing changes quickly, and a fast, low exposure scan is deemed necessary (Gao et al., 2017), and (3) to avoid or minimize drift errors resulting from increased temperature of the experimental setup during longer scans, which leads to deviation of a feature from its original location due to mechanical and thermal stresses (Probst et al., 2016). Therefore, we extend the use of the N2N model to accommodate three HQ to LQ ratios where N2N25 is the scenario where 25% of the LQ data has a corresponding HQ reference image while 75% has no clean reference. Similarly, N2N50 and N2N75 indicate scenarios with a higher percentage of clean reference images. In the literature, fully supervised models use MAE between pixel intensities (L1 loss) to learn the mapping, whereas models like N2N and N2V, utilize a mean squared distance error (L2 loss). We propose a combination of the losses to reflect our semi-supervised task in training. For N2N25, we scale the L1 loss with a 0.25 weight and the L2 loss with a 0.75 weight. Similarly, for N2N50 and N2N75, we modify the weights to reflect the percentage of clean references. Using either L1 or L2 only yielded lower PSNR and SSIM values. **Table 4** details the models and their specifications.

For the DL models, we split the training and testing data using a 80–20% non-overlapping split where 286 slices are randomly sampled from each of the LQ and HQ datasets and reserved for testing and validation, while the remaining 1,140 slices are used for training. The slices are reshaped to 512 × 512-pixel resolution using bicubic interpolation (Keys, 1981) in order to accommodate GPU memory limitations. After the model has been trained and evaluated, the original 800 × 800 resolution is obtained through similar bicubic interpolation. All the models are trained in accordance with their original implementation. Some hyperparameters are optimized to obtain the best possible performance from the model. Further details about the architecture, input requirements and choice of hyper-parameters like batch sizes, learning rate and number of epochs are provided in **Table 4**. We perform training over 200 epochs and use the ADAM optimization algorithm for all the models. We pick the epoch with the lowest validation PSNR in order to perform testing. Upon the completion of training, the evaluation is performed on the held out 286 slices from the test set. For all the models, ADAM optimization was used (Kingma and Ba, 2015).

Standard Quantitative Denoising Evaluation Metrics

Traditionally, image degradations that take place during acquisition, reconstruction, processing, and storage have been evaluated qualitatively by visual inspection and subjective assessment based on the assumption that human visual perception is highly adapted to extract structural information (Wang et al., 2004). However, as more data is being generated and more complex structures are being studied, it becomes increasingly difficult to rely on just human inspection. Thus, efforts to automate image quality assessment have been undertaken since 1972, when Budrikis developed one of the first quantitative measures to predict perceived image quality (Budrikis, 1972). These metrics have since evolved to match modern imaging and perceptual standards.

Peak Signal to Noise Ratio (PSNR)

Peak signal to noise ratio is a comparative metric widely used to determine noise degradation in an image with respect to a clean reference. Peak signal to noise ratio is an expression for the ratio between the maximum possible value (power) of a signal and the power of distorting noise that affects the quality of its representation. It is measured in decibels (dB) and the higher the PSNR, the better the image. Theoretically, PSNR for the HQ image is not defined and so it is manually set to 100 dB. In our setting, we calculate the PSNR on the test set which has not been used for training the models. The PSNR value reported for a model is averaged over the previously 286 held-out slices from the test set. The PSNR of the LQ slices act as a baseline for comparison.

Structural Similarity Index Measure (SSIM)

Unlike PSNR, SSIM is a perceptual metric which is not based on pixel intensities but rather on structural similarity between the denoised and the clean reference images (Wang et al., 2004). This is especially important when trying to evaluate fine-grained details and edges. It ranges from 0 to 1, where higher SSIM indicates a cleaner image. Similar to PSNR each of the SSIM values are calculated and averaged. The equation for the SSIM calculation is detailed in the **Appendix** in Supplementary Material.

Blurring Index

Many denoising algorithms focus on removing high-frequency components which correspond to noise. However, this leads to blurry images with fuzzy edges and high smoothness. Blurring index penalizes such images with a lower blurring index score. Occasionally, some DL models, smoothen regions based on expected intensity values leading to the removal of sharp high frequency noise elements. Though this is beneficial, the models obtain lower blurring index (BI) scores. The implementation of BI is detailed in the **Appendix** in Supplementary Material.

Contrast to Noise Ratio (CNR)

In grayscale images, a vital requirement of restoration models is the ability to separate foreground region intensities from the background noise. Contrast-to-noise ratio (CNR) is a reference-less metric which yields a higher value for higher

TABLE 4 | Parameters selected for the DL-based denoising algorithms used in this study.

Model	Architecture	Input Requirement	Selected Epoch*	Batch Size	Initial Learning Rate	Learning Rate Algorithm	Loss Function
CCGAN	GAN	LQ, HQ	198	4 slices	0.001	Plateau	$L_{Adv} + L_{Cyc} + L_{Iden}$
RDN	Dense residual network		136		0.0001	Step	L1 (MAE)
N2C	U-Net		167	8 slices	0.001	Exponential	
N2N-75%		LQ, 75% HQ	177				(0.75*L1) + (0.25*L2)
N2N-50%		LQ, 50% HQ	172				(0.50*L1) + (0.50*L2)
N2N-25%		LQ, 25% HQ	138				(0.25*L1) + (0.75*L2)
N2N		LQ	195				L2 (MSE)
N2V			171	32 (128 × 128) patches		Linear	

**Selected epoch is based on the lowest validation PSNR.*

contrasts and lower values for indistinguishable foreground and background regions. The higher the CNR, the cleaner the image, which makes it easier to segment the different phases. Our implementation follows Shahmoradi et al. (2016), where we identify six key regions of interest (ROI) including a background region from 10 random slices in the denoised test set. A detailed explanation of the CNR formula is provided in the **Appendix** in Supplementary Material.

Blind/Reference-Less Image Spatial Quality Evaluator (BRISQUE)

Blind/reference-less image spatial quality evaluator (BRISQUE) helps understand the presence of noise in an image without the use of a reference (Mittal et al., 2011). It relies on spatial statistics of the natural scene (NSS) model of locally normalized luminance coefficients in the spatial domain, as well as the model for pairwise products of these coefficients in order to extract spatially dense variances which occur in noisy images. We use the publicly available PyBRISQUE-1.0 software package (2020) for the implementation of this metric (https://pypi.org/project/pybrisque/).

Naturalness Image Quality Evaluator (NIQE)

Naturalness image quality evaluator (NIQE) unlike BRISQUE computes distortion specific features such as ringing, blur, and blocking to quantify possible losses of "naturalness" in the image due to the presence of distortions, thereby leading to a holistic measure of quality (Mittal et al., 2013). For this, we use the skvideo.measure.niqe package from the Scikit-Video library version 1.1.11 (Skvideo, 2013; http://www.scikit-video.org/stable/modules/generated /skvideo.measure.niqe.html). Each of the 286 slices are individually passed through the function and the scores are averaged for each model.

Physics-Informed Quantitative Denoising Evaluation Metrics: Petrophysical Characterization

Physics-informed denoising evaluation is performed through the estimation of petrophysical properties extracted from image data. To estimate these petrophysical properties, the denoised images need to be segmented to extract phase labels. In order to highlight the effect of different denoising approaches, and their effect on image-based rock and fluid property estimates, we used the same segmentation method on all denoised data. The segmentation method used was Ilastik[1], a supervised machine-learning based segmentation tool that is built using a fast random forest algorithm (Sommer et al., 2011). The user manually provides a limited number of voxel labels for training. We maintain the same features among the different denoised datasets (**Table 5**). An almost equal number of marker voxels were selected for each of the three phases (solid/glass, brine, and $scCO_2$). Also, the number of markers was kept to a minimum (∼0.005% of sample voxels) to avoid overfitting. The same number of marker voxels per slice is maintained across all the datasets to minimize bias.

TABLE 5 | Features selected for segmentation for the different datasets using ilastik.

	σ0	σ1	σ2	σ3	σ4
Feature	**0.3**	**0.7**	**1**	**1.6**	**3.5**
Color/Intensity					
Gaussian smoothing	✓	✓	✓	✓	✓
Edge					
Laplacian of Gaussian	✓	✓	✓	✓	✓
Gaussian gradient magnitude	✓	✓	✓	✓	✓
Difference of Gaussians	✓	✓	✓	✓	✓
Texture					
Structure tensor eigenvalues	✓	✓	✓	✓	✓
Hessian of Gaussian eigenvalues	✓	✓	✓	✓	✓

The use of quantitative denoising evaluation metrics is a good practice over qualitative and subjective assessment of image quality. However, a HQ image as determined by standard denoising evaluation metrics may not necessarily render the most accurate estimate of petrophysical properties,

[1]Ilastik (2021). Available online at: https://www.ilastik.org/ (accessed January 4, 2021).

either due to insufficient noise removal, or excessive filtering which results in information loss. Therefore, we evaluate the implemented denoising algorithms based on how various calculated petrophysical properties compare to those calculated using the HQ benchmark dataset. To achieve this, a toolbox was developed in Matlab R2019a to calculate different petrophysical properties, including (1) porosity, (2) saturation, (3) phase connectivity, which is represented by phase specific Euler number (phase Euler number divided by the phase volume), (4) phase SSA, which is calculated as the area of a given phase divided by its volume, (5) fluid-fluid interfacial area, (6) mean pore size, and (7) mean $scCO_2$ blob volume. We also calculate phase fractions per slice along the length of the core.

RESULTS AND DISCUSSION

In this section, we first describe the denoising results qualitatively by visual comparison of denoised datasets to the HQ ground truth images. Next, we present quantitative comparison results. The first set of quantitative comparison include standard metrics. Finally, we compare the quantitative petrophysical results of the denoised images post segmentation against the ground truth HQ segmented images.

Qualitative Evaluation of Denoising Methods

Figure 1 shows top view cross-sections from the HQ and the LQ data sets. The LQ image is evidently noisier than the HQ image. We have also marked regions to highlight spatial feature differences between the HQ and LQ images and associated implications for petrophysical property estimation. The red region shows that some small solid features can be inaccurately characterized as fluid, resulting in porosity estimation errors, while the green region demonstrates a blurry fluid-fluid interface in the LQ image, which can lead to errors in estimating fluid saturation and petrophysical properties pertaining to fluid–fluid interfaces. Similarly, the blue region shows an example where the solid phase can be falsely characterized as connected in the LQ image, while the HQ image shows some disconnection of the solid phase. This could result in errors in topological characterization, such as Euler number calculations for the solid phase.

A cross-sectional image for each of the HQ dataset, LQ dataset and the denoised datasets are shown in **Figure 2**. Visually, the NLM filter results in an overall smoother image with significantly less variation within each phase (solid, brine, and $scCO_2$), as it replaces the value of each voxel with the mean of similar voxels within the search window. The median and SNN filters also visually exhibit smoother phases, compared to the AD and bilateral filters. Conversely, the Gaussian filter expectedly results in image blurring, which can highly affect the accuracy of calculated interfacial petrophysical properties, such as interfacial area and mean interface curvature. The reference-based DL methods qualitatively show good performance compared to traditional filters. Noise-to-clean and CCGAN show a superior performance over RDN, with smoother phases and sharper edges. However, comparing the two models (N2C and CCGAN) with the HQ reference image, CCGAN resembles the reference image more closely in some features (highlighted in the blue circles), while N2C resembles the reference image more closely in other features (highlighted in the green circles). This exemplifies that qualitative or visual evaluation of denoising models is not a sufficient means of evaluation when deciding on the best denoising model to use. Reference-less DL methods (N2V and N2N) show little improvement compared to the LQ dataset. Finally, the semi-supervised DL methods show visually promising results, where the N2N-75% and N2N-50% show significant improvement compared to LQ.

The histogram representing the distribution of gray-scale intensities within a dataset can be used to qualitatively assess image quality. In our dataset, where we expect to see three phases—solid glass, brine, and $scCO_2$, an ideal histogram would have three well-defined peaks with varying maximum voxel count, depending on the abundance of the phase represented by that peak in the imaged sample. The more distinguishable those peaks are, the sharper the phase boundaries and interfaces, and the easier the segmentation. Also, the smaller the spread of each peak, the smoother the bulk phase is (i.e., the phase is represented by less gray-scale values indicating a more homogeneous or smooth bulk phase). In **Figure 3**, we show the histograms of the HQ, LQ, and denoised datasets. The solid glass peak has the highest voxel count in all datasets, as expected, being the most abundant phase in our sample. We also observe a clear difference between the HQ and LQ datasets, where we can see three peaks in 3a, but only one visible peak in 3b, which makes the differentiation between $scCO_2$ and brine more difficult. From the denoised dataset histograms, the supervised and semi-supervised DL denoising models perform better than traditional and un-supervised DL denoising methods. Also, we observe that the issue of fluid-fluid differentiation (where we can't see all three peaks) persists when using the bilateral, N2V, N2N25, and N2N denoising methods. We also observe that some denoising models possibly outperformed the HQ dataset where the three peaks are even more distinguishable, including N2C, RDN, CCGAN, and N2N75. Additionally, upon comparing 3i and 3k with 3j, we can see results consistent with our observations from **Figure 2**, where N2C and CCGAN have more well-defined and narrower peaks compared to RDN. Despite the additional insight obtained from inspecting the gray-scale intensity histograms, histograms alone cannot be used to infer image quality. The histogram indicates the distribution of pixel intensities but not their location. This calls for a more localized inspection of the images to assess how voxel spatial distribution impacts the accuracy of petrophysical property estimates.

Quantitative Evaluation of Denoising Methods

Figure 4 demonstrates a more quantitative method for evaluating the performance of the different denoising models using an intensity profile along a line A–A′. Here, we use N2C as an example. From this profile, we can obtain insights on the (1) smoothing effect within each phase by comparing the plateau

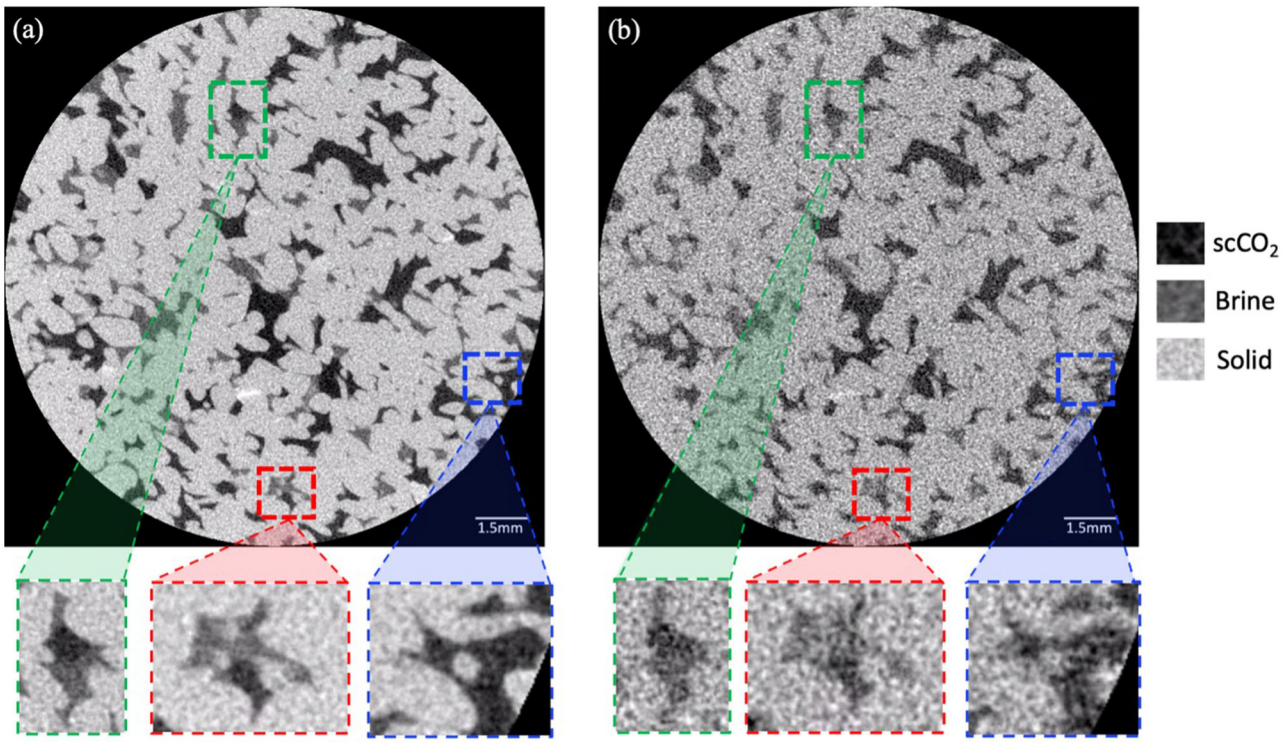

FIGURE 1 | (a) Sample cross-sectional slice from the HQ dataset, **(b)** Sample cross-sectional slice from the LQ dataset. Dashed boxes represent spatial features that demonstrate differences between the two datasets. The red box represents an example region which can cause deviation in calculated porosity. The blue box represents an example region which can cause deviation in calculated connectivity. The green box represents an example region which can cause deviation in calculated saturation.

of the noisy LQ dataset to that of the HQ and denoised dataset, and (2) contrast enhancement, which can be assessed by comparing the difference in intensities between the different phases. A larger difference implies an improvement in contrast, and finally (3) we can also assess phase boundary sharpness by calculating the steepness of the slope at each phase boundary. A steeper slope indicates a sharper boundary, which makes it more easily identifiable during image segmentation and petrophysical characterization. In **Figure 4**, we observe that the HQ profile exhibits oscillations within each phase, which shows that noise still exists in the HQ data, but the amplitude of those oscillations is smaller, which implies less noise and more homogeneous phases. We also observe slightly higher average intensity for the solid and brine phases in the HQ profile compared to the LQ profile. Additionally, we observe that N2C has improved the image quality on all three aspects: smoothing bulk phases, improving contrast between phases, and improving boundary sharpness. The $scCO_2$-solid phase boundary has the most improvement in boundary sharpness with ∼28% increase in slope.

Example regions are highlighted in **Figure 5a**, following the workflow proposed by Shahmoradi et al. (2016) to assess local image quality using CNR. ROI-0 corresponds to the background which is used to calculate the CNR of other regions. ROI-1 corresponds to brine with no interfaces, while ROI-2 corresponds to the $scCO_2$ phase, and ROI-3 corresponds to the solid phase. In addition, two interface regions, ROI-4, an interface between solid and brine and ROI-5, an interface between solid and $scCO_2$ are also considered. We pick a random slice and indentify ROIs 1–5 in the next 22 consecutive slices. **Figures 5b,c** show localized average CNR values within bulk phases and at solid-fluid interfaces, respectively. We see that all denoising models, except for N2V, result in an improved CNR both in bulk phases and at interfaces. Supervised DL denoising models result in the largest CNR improvement, with N2C being a top performer. The N2N75 model also yields similar results as fully supervised denoising models, which is promising for cases where not all the HQ data is available. We also observe that the N2N25 model results in lower average CNR compared to N2N, which can be counter intuitive. However, this could be due to the inherent training objective of the model. The base N2N model estimates the mean of the signal and uses multiple noisy versions of the same signal to do so. However, when a small number of clean samples are provided, the network's estimate of the mean diverges from the expected value, which negatively affects learning. When provided with enough clean samples (50% or greater), the model converges to the mean more accurately compared to the base N2N or N2N25 versions. Comparing the improvement within bulk phases and at phase boundaries,

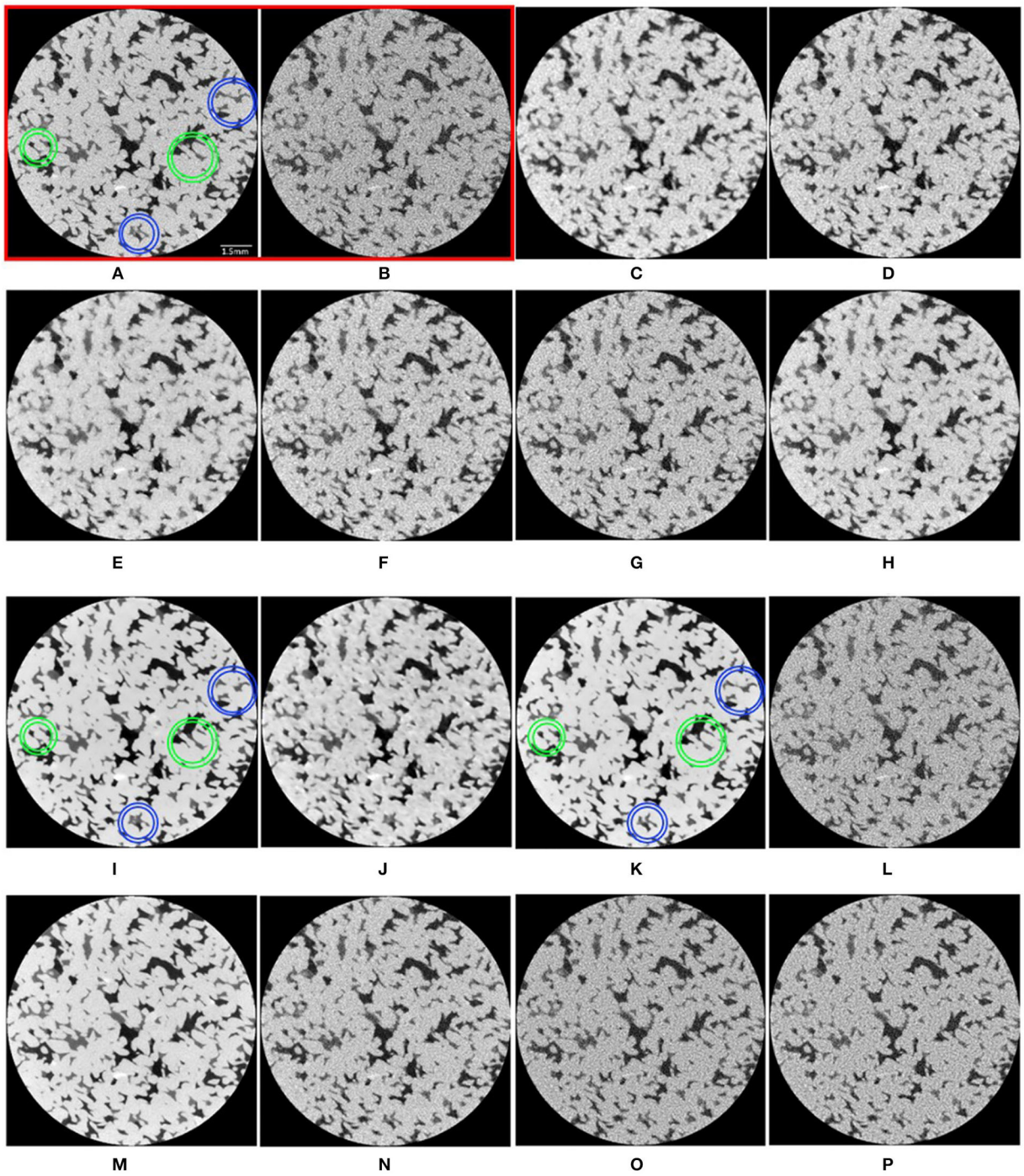

FIGURE 2 | Qualitative comparison of the performance of the different denoising methods through example cross-sectional slices. **(A)**, HQ reference; **(B)**, LQ; **(C)**,Gaussian; **(D)**, Median; **(E)**, Non-local means; **(F)**, Anisotropic diffusion; **(G)**, Bilateral; **(H)**, Symmetric nearest neighbor; **(I)**, Noise-to-clean; **(J)**, Residual dense network; **(K)**, Cycle consistent generative adversarial network; **(L)**, Noise-to-void; **(M)**, Noise-to-noise (75%); **(N)**, Noise-to-noise (50%); **(O)**, Noise-to-noise (25%); **(P)**,Noise-to-noise.

we do not see a significant difference, indicating that all denoising methods improve contrast homogeneously throughout the image. Although quantitative, one limitation of the type of analysis performed in **Figures 4**, **5** is that they evaluate the performance of the denoising models locally, which requires manual selection of specific sites. A comprehensive denoising

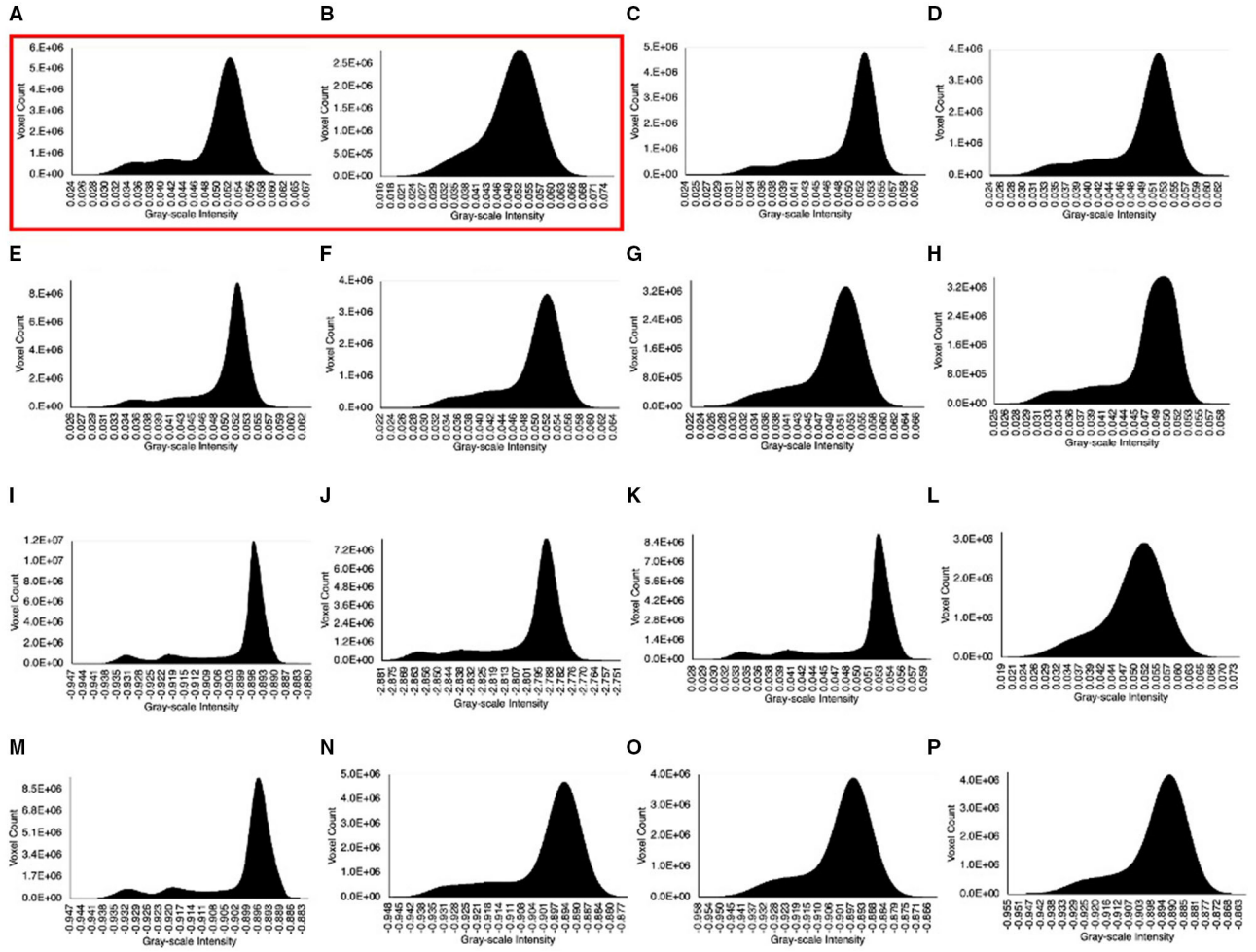

FIGURE 3 | Qualitative comparison of the performance of the different denoising methods through gray-scale histograms.

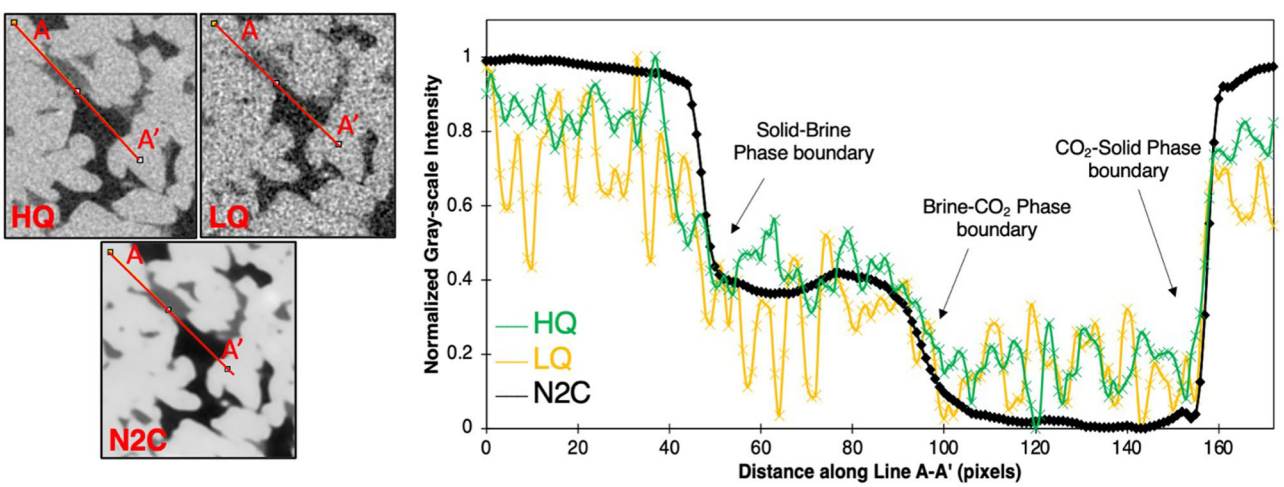

FIGURE 4 | (Left) Example cross-sections through the high quality (HQ), low quality (LQ) and Noise-to-Clean (N2C) datasets. **(Right)** Normalized gray-scale values along a line (A-A′) passing through the solid, brine, and $scCO_2$ phases in the example cross sections. Slopes at the phase boundaries are indicative of phase boundary sharpness for the HQ, LQ, and N2C profiles.

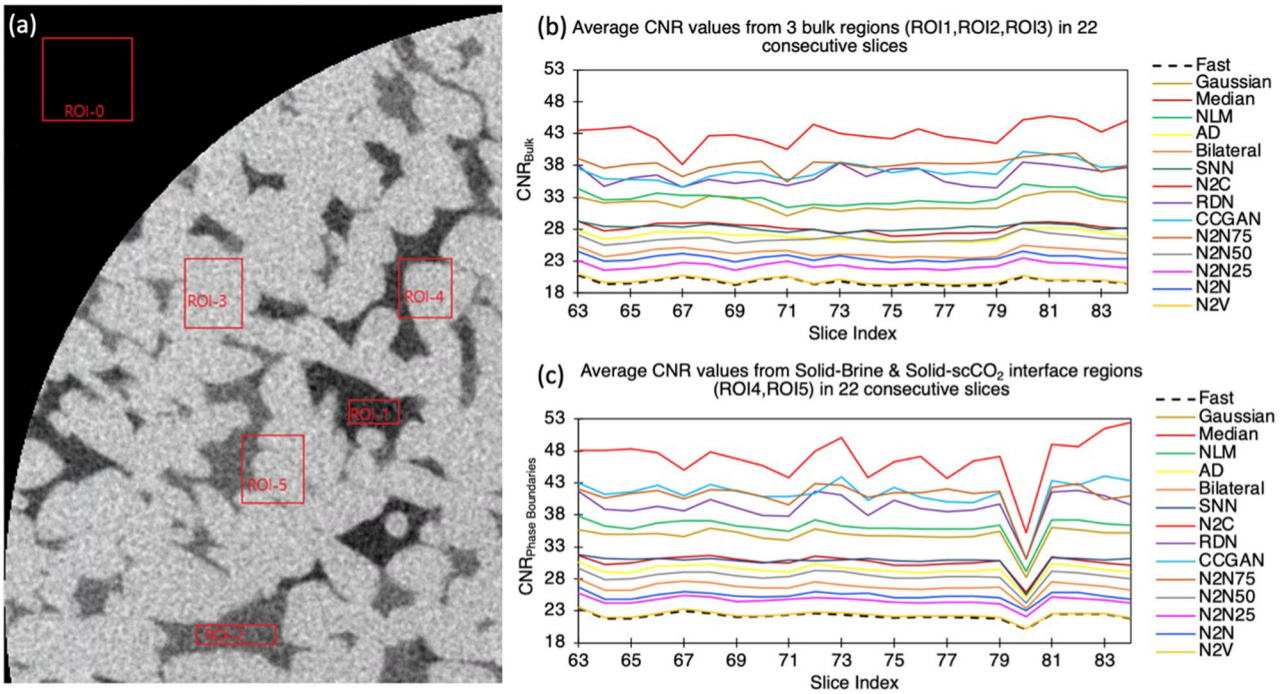

FIGURE 5 | Comparison of contrast-to-noise (CNR) ratio for denoised datasets against noisy LQ dataset. **(a)** Example regions of interest (ROI 1–5) considered for bulk and edge CNR calculations are shown in red boxes. ROI 0 represents the background ROI against which contrast is calculated. **(b)** Average CNR of bulk phases (solid, brine, $scCO_2$) in 22 slices, and **(c)** Average CNR of phase boundaries (solid-brine and solid-$scCO_2$) in 22 slices.

TABLE 6 | Quantitative comparison of denoising algorithms using standard denoising evaluation metrics.

	Models	PSNR	SSIM	Blur index	CNR	BRISQUE	NIQE
	HQ Images (Reference)	100*	1*	0.724	19.233	118.183	26.645
	LQ Images	18.224	0.507	0.634	21.472	106.619	25.517
Traditional filters	Gaussian	23.378	0.769	0.783	34.584	116.833	26.875
	Median	24.593	0.716	0.753	30.504	118.237	27.173
	NLM	25.396	0.760	0.715	36.018	116.948	26.900
	AD	25.019	0.700	0.735	29.326	118.336	27.287
	Bilateral	24.271	0.652	0.706	26.384	117.239	27.164
	SNN	22.354	0.677	**0.789**	30.139	118.065	26.713
Fully supervised DL models	N2C	24.702	0.798	0.752	**46.517**	116.387	26.874
	RDN	**25.397**	0.785	0.730	40.313	116.443	26.902
	CCGAN	24.716	0.795	0.728	39.702	116.536	26.875
Semi-supervised DL models	N2N-75%	25.332	**0.800**	0.726	40.413	116.774	26.884
	N2N-50%	24.518	0.716	0.711	28.356	**118.799**	**27.325**
	N2N-25%	23.084	0.636	0.687	24.019	117.427	26.860
Un-supervised DL models	N2N	23.339	0.650	0.718	25.099	117.707	26.981
	N2V	20.607	0.546	0.662	21.569	112.048	26.356

Good Performance

Poor Performance

Colors represent how well a model performs compared to the rest of the models for a given denoising evaluation metric.
**PSNR and SSIM are calculated with respect to HQ reference and thus are set to 100 and 1 for HQ inputs, respectively.*

model performance evaluation is quantified using standard evaluation metrics detailed in **Table 6**.

The CNR value reported here represents the average of the five individual CNR regions detailed earlier (**Figure 5**). Of the six metrics measured, the DL models performed the best in five of them. With Blur Index however, the metric measures the presence of sharpness which can be spiked by high frequency noise. The traditional filters failing to remove such

noise achieve a misleading high blur-index score. Though the unsupervised models performed poorly, they were comparable to the traditional filter-based methods. Noise-to-noise ratio had the lowest values across all the metrics. It is also observed that PSNR values are generally low across all denoising methods. However, PSNR uses pixel distance and may incorrectly favor models that have higher resemblance to the HQ images rather than actual signal accuracy. The DL models tend to produce images that appear cleaner than the HQ image but score lower PSNR due to this reason. Residual dense network had the highest PSNR gain with an average increase of 7.173 dB. Though it might be possible for an image to obtain a high PSNR, SSIM penalizes structural anamolies like blurring, noise contamination, wavelet ringing, and blocking (caused by image compressions like JPEG) leading to lower SSIM scores.

Each evaluation metric points to unique capabilities of the models. For example, a high CNR obtained for N2C makes it ideal for segmentation tasks while a high SSIM obtained through N2N-75% model makes it favorable for CT image artifact removal task. The differences observed, however, between supervised DL-based models and N2N-75% in terms of SSIM are not statistically significant, meaning that they all perform equally well for this metric. N2N-50% produced the most natural looking images (NIQE) and can be used to generate additional synthetic clean samples when only 50% of clean data is available.

We also evaluated the denoising methods using physics-based metrics, or more specifically—petrophysical properties. To perform the petrophysical characterization, we first segmented the datasets. **Figure 6** shows example segmented cross sections from the HQ and LQ datasets. It also shows a difference image, where the segmented LQ image was subtracted from the segmented HQ image. The percent mislabeling for each phase pair: brine-solid, $scCO_2$-brine, and $scCO_2$-solid is 2.46, 0.37, 1.57%, respectively. Based on the percent mislabeling of the denoised images, we see minor improvement compared to the LQ image. Similarly, image subtraction was performed between each of the denoised images and the HQ image. Noise-to-clean and N2N75 showed the most improvement especially in CO_2-solid and brine-solid phase mislabeling. The differences are presumed to be mainly due to the difference in the amount of noise in each image since the user interference was kept to a minimum in the segmentation step. Further, the differences within this single image might seem subtle, but it has a significant effect on petrophysical characterization performed using the entire image stack. The full petrophysical characterization and error quantification against the ground truth is presented in **Figure 7** and **Table 7**.

For petrophysical property estimations, we first consider bulk measures of phase fractions and saturations along the length of the core sample. **Figure 7** shows the percent errors in porosity, $scCO_2$ saturation, and brine fraction (measured as brine volume divided by the bulk volume for the sample space considered) profiles along the length of the sample for the different denoising methods post segmentation. The performance of denoising methods, namely, traditional methods, supervised, unsupervised, and semi-supervised DL-based methods are compared against the HQ dataset. Generally, most of the traditional and semi-supervised DL-based methods show closer results to the ground truth (**Figure 7A**). Out of the traditional filters, the median filter seems to have the closest porosity profile to the ground truth HQ dataset, followed by the AD and bilateral filters. Conversely, the Gaussian filter performed poorly, consistently underestimating porosity. Similarly, NLM, which is one of the most commonly used filters in the digital rock physics literature, underestimates porosity throughout the length of the core and has the second worst performance. Unlike their performance in terms of standard evaluation metrics (**Table 6**), supervised methods show poor performance, consistently underestimating porosity along the entire length of the sample. Additionally, the error is increasing toward the bottom of the sample in most denoising methods, especially Gaussian, RDN, and N2V methods. Upon inspecting the root cause of this, the original LQ dataset was noisier toward the bottom of the sample as evidenced by lower PSNR (**Supplementary Figure 1A**). This is mainly due to the aluminum container, covering the bottom half of the sample, used to fix the coreholder in place during the scan and avoid wobbling which can result in image blurring (**Supplementary Figure 1B**). The Gaussian filter, which is a linear spatially invariant filter, cannot resolve the noise variation along the sample. Residual dense network, a very deep network, could be overfitting the data and therefore less able to adjust to the varying noise along the sample, compared to other supervised models (N2C and CCGAN).

When comparing the CO_2 saturation error profiles (**Figure 7B**), it is observed that traditional methods show close results, while most of the DL-based methods show poor performance when compared to the ground truth. Out of the traditional filters, SNN followed by median filters showed the most deviation from the ground truth. The Gaussian filter, on the other hand, had the closest results out of all the denoising models. Residual dense network and N2N significantly overestimate CO_2 saturation. The supervised DL-based methods, except for N2C, show weak performance while the semi-supervised DL-based methods show slightly better performance. Noise-to-noise ratio, as an exception, shows the second-best performance of all methods, while RDN significantly underestimates $scCO_2$ saturation. Larger error is seen at the top of the sample for all denoising methods except N2C and N2N75.

As the intermediate phase, brine fraction error profile is presented as opposed to brine saturation to account for errors that may result from misclassification of brine as solid or CO_2 post-denoising (**Figure 7C**). Noise-to-clean, followed by NLM show the least deviation compared to the ground truth, whereas RDN, CCGAN, and N2N show a significant deviation. Noise-to-noise ratio also shows a surprisingly close match to the ground truth brine fraction profile. Overall, these results demonstrate that even within bulk property estimates, since differences occur at fluid-fluid and fluid-solid interfaces, consideration of both porosity and saturation errors is critical. Again, here we see that N2C and N2N75 are robust enough to maintain consistent performance throughout the sample even though the dataset has a spatially varying noise profile.

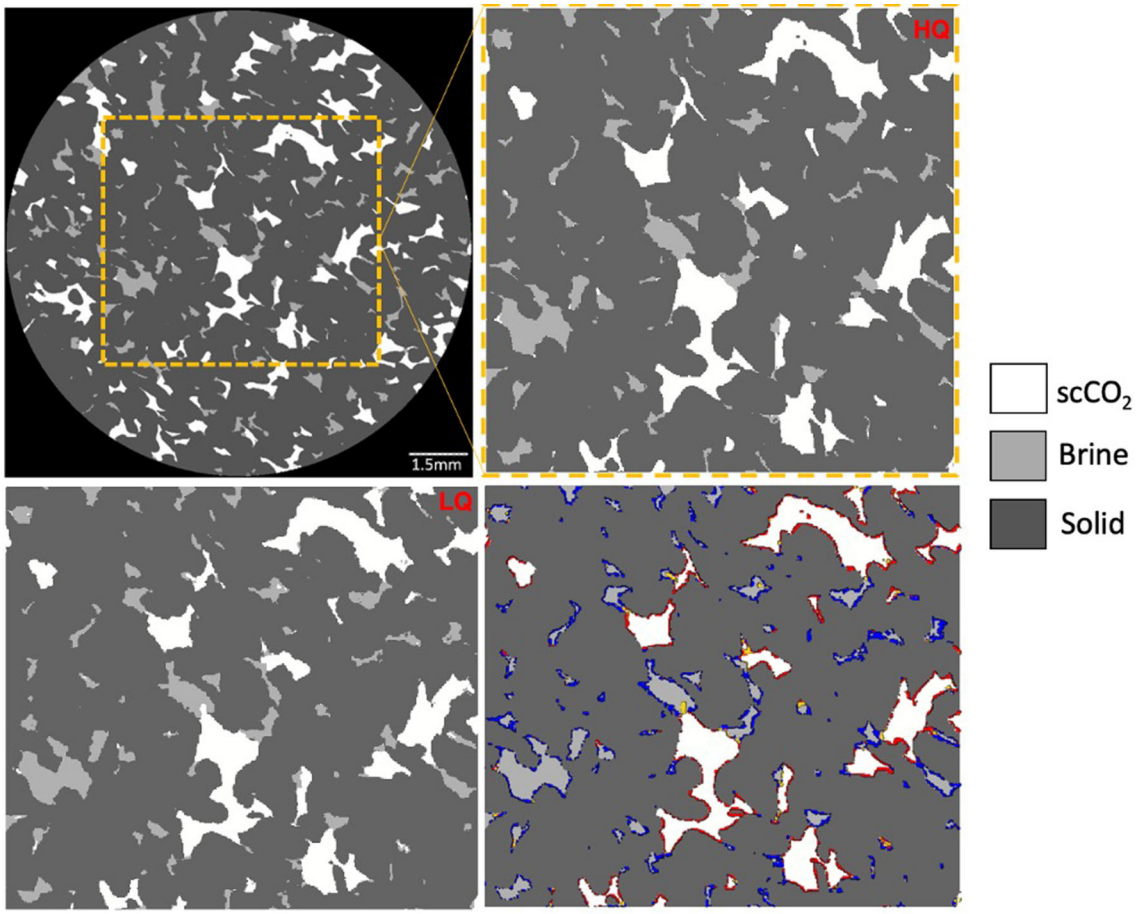

FIGURE 6 | Example segmented HQ image using ilastik, and difference image |HQ–LQ| showing the mislabeling in LQ compared to the HQ image. Red, $scCO_2$-solid mislabeling; Blue, brine-solid mislabeling; yellow, $scCO_2$-brine mislabeling.

Table 7 summarizes the % errors associated with the estimates of bulk petrophysical properties, namely porosity and $scCO_2$ saturation, as well as pore-scale properties including, specific Euler number, SSAs, interfacial area, average pore size and average $scCO_2$ blob volume. These errors are quantified relative to the ground truth HQ images. The actual property estimates for the ground truth HQ images are presented in the first row of **Table 7**. Traditional filters like the median, AD and bilateral filters show an improved porosity estimate compared to the original LQ images, but the Gaussian filter results in the highest error for porosity (13.9%). This can be explained by the blurring caused by the Gaussian filter at phase interfaces, making it more difficult to locate boundaries, especially where the gray-scale intensities are less distinguishable like at the solid-brine interfaces. However, the Gaussian filter shows the best performance in terms of $scCO_2$ saturation, which may be due to a larger surface area of the $scCO_2$ phase being in contact with the solid phase rather than the brine phase, hence, enabling us to distinguish between the two phases more easily in terms of gray-scale intensity and labeling. The median filter on the other hand shows an opposite result where it exhibits better performance when estimating porosity and poorer performance in estimating $scCO_2$ saturation. This can be explained by how a median filter works, where it involves replacing the gray-scale values of voxels within a user-specified window by their median value. This means that the small $scCO_2$ blobs observed in the dataset in the bulk brine phase will be replaced with gray-scale values that resemble brine, leading to a lower $scCO_2$ saturation (compared to HQ), but not affecting porosity as much. In general, most traditional filters perform better for bulk estimates of porosity and phase saturation, compared to DL-based methods.

For the pore-scale properties, we observe that supervised and semi-supervised methods show a better performance overall, except for $scCO_2$ SSA and average pore size, where bilateral and SNN filters, respectively, show better performance. This can be attributed to the edge preserving nature of both the bilateral and SNN filters. For the $scCO_2$ SSA, this allows fine-scale details like small $scCO_2$ blobs observed in our dataset to be preserved, leading to a more accurate representation of phase boundaries and surfaces. Noise-to-clean and N2N75 perform well for most of the properties with ∼10% error or less. Other methods like RDN and N2N25 perform poorly with errors as large as 348.28%.

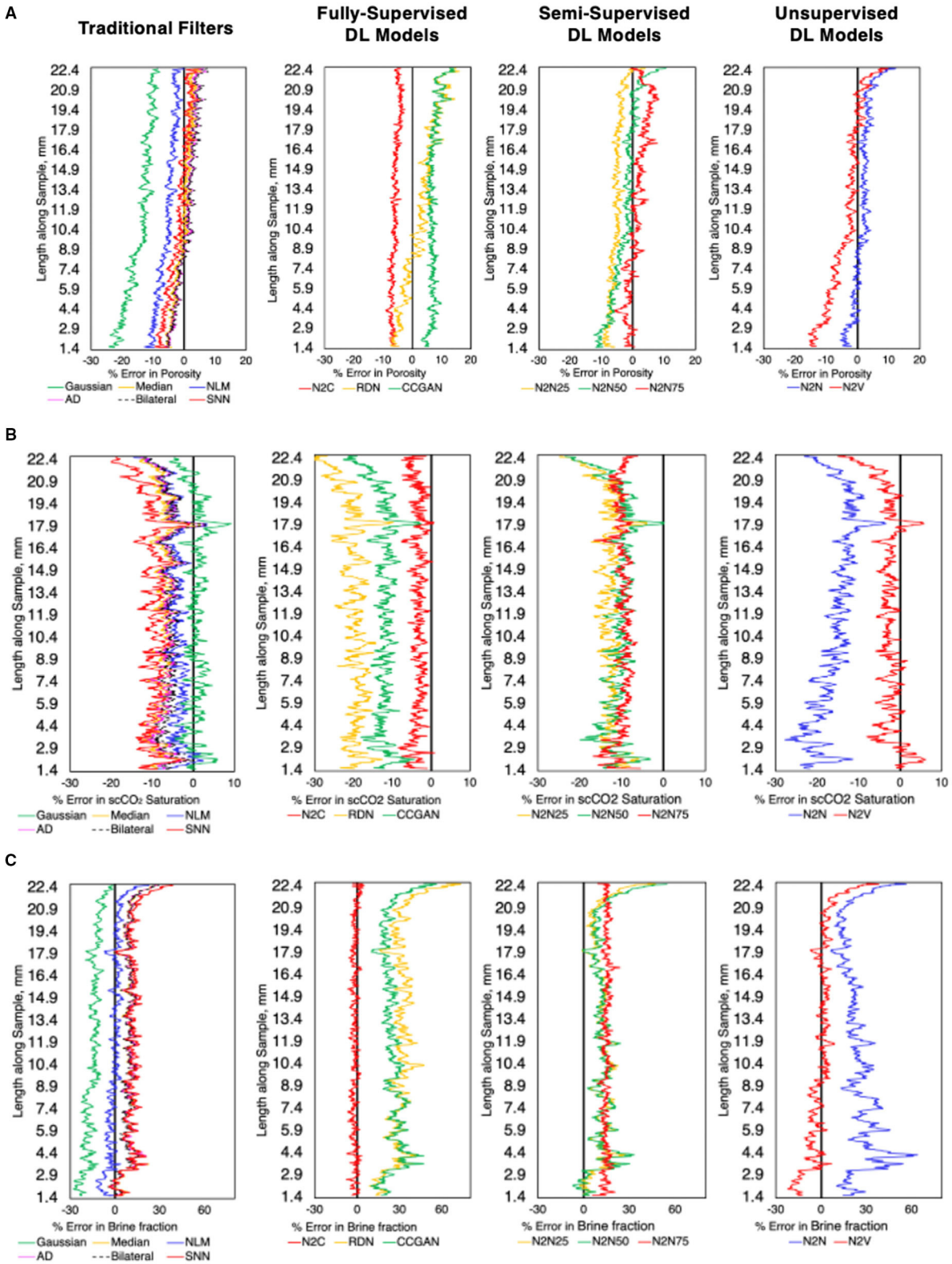

FIGURE 7 | (A) Porosity, **(B)** $scCO_2$ saturation, and **(C)** brine phase fraction percent error (relative to HQ) along the length of the core for the different denoising methods.

TABLE 7 | Physics-based comparison of denoising algorithms using bulk and pore-scale petrophysical properties.

		Porosity, %	$scCO_2$ saturation, %	SEN (solid), mm^{-3}	SEN (pore), mm^{-3}	SEN (Brine), mm^{-3}	SEN ($scCO_2$), mm^{-3}	SSA (Solid), mm^{-1}	SSA (Brine), mm^{-1}	SSA ($scCO_2$), mm^{-1}	Interfacial area, mm^{-1}	Avg. pore size, microns	Avg. $scCO_2$ blob volume, mm^3
	HQ	14.940	56.750	−8.709	−67.164	909.459	809.306	4.469	32.115	21.593	24.619	35.778	0.002
	LQ	1.14%	7.75%	17.53%	169.22%	70.12%	71.34%	0.51%	12.81%	7.36%	11.63%	13.52%	118.32%
Traditional filters	Gaussian	13.92%	**0.44%**	95.60%	180.03%	34.86%	90.46%	20.64%	2.45%	4.94%	1.89%	27.04%	438.94%
	Median	**0.07%**	7.31%	56.79%	52.58%	22.59%	88.73%	3.17%	8.30%	1.55%	5.02%	6.73%	520.31%
	NLM	5.42%	4.21%	48.45%	97.74%	11.18%	96.78%	9.85%	3.69%	3.31%	2.97%	21.17%	795.99%
	AD	0.80%	6.63%	13.92%	143.82%	4.32%	86.44%	2.22%	10.31%	2.68%	8.10%	9.86%	314.17%
	Bilateral	1.00%	5.92%	5.59%	118.58%	11.30%	81.05%	2.05%	8.97%	**0.46%**	6.24%	5.79%	297.10%
	SNN	1.67%	10.20%	62.59%	123.40%	20.61%	105.95%	5.63%	1.09%	4.53%	0.77%	**0.28%**	1256.85%
Fully supervised DL models	N2C	5.89%	3.47%	6.39%	**7.92%**	11.93%	57.78%	7.39%	1.73%	2.77%	**0.76%**	24.55%	56.40%
	RDN	3.01%	20.28%	12.40%	194.80%	53.78%	54.32%	2.63%	**0.87%**	4.69%	1.73%	57.89%	163.94%
	CCGAN	7.16%	12.25%	2.49%	41.32%	49.34%	64.49%	2.62%	11.35%	12.16%	12.50%	59.07%	55.36%
Semi-supervised DL models	N2N75	1.47%	9.96%	**1.37%**	65.06%	**2.78%**	**47.54%**	**0.32%**	4.25%	10.40%	1.76%	8.77%	**7.15%**
	N2N50	2.54%	10.96%	91.08%	108.44%	10.42%	90.26%	15.29%	8.10%	3.06%	8.01%	116.57%	569.64%
	N2N25	5.29%	13.02%	108.40%	143.58%	86.10%	74.32%	15.87%	16.29%	7.60%	15.40%	68.18%	348.28%
Un-supervised DL models	N2N	1.61%	15.75%	96.86%	128.31%	3.31%	93.10%	10.92%	14.85%	2.06%	11.58%	71.72%	549.56%
	N2V	3.61%	2.85%	93.15%	161.36%	117.84%	93.12%	16.64%	10.92%	2.87%	9.89%	35.40%	345.72%

Good Performance

Poor Performance

Values represent the absolute % error in the estimate of each petrophysical property compared to the ground truth (HQ images), except for the first row, which represents the actual property values for the segmented HQ images. The best denoising model for each property is highlighted with bold borders. SEN, specific Euler number; SSA, specific surface area.

N2N75 also shows a more superior performance over N2C in terms of pore-scale estimates, which might not be expected due to the availability of more clean reference data to train the model for N2C, and the better overall standard metrics performance of N2C as shown in **Table 6**. However, it should be noted that the higher performance of N2N75 observed in **Table 7** can be attributed to being a closer representation of the HQ data, which in our study is used as a ground truth. The HQ data is not an idealistic ground truth data, it has its own noise associated with it. Therefore, the comparison between N2C and N2N75 is limited by the amount of noise that is present in the HQ data which is the reference of comparison. We also observe one exception where RDN performs better than N2C and N2N75 in terms of brine SSA. This can be attributed to the ability of the RDN model to preserve high frequency details, which translates to a better ability to preserve high contrast phase boundaries and surfaces where SSA is calculated (Zhang et al., 2021).

Unsupervised DL-based methods (N2N and N2V) generally exhibit poor performance for most properties compared to other denoising methods including some of the traditional filters. This is in line with previous observations made during the analysis of the standard metrics in **Table 6**. Semi-supervised models, as expected, are performing better than unsupervised models. Counter-intuitively, adding additional information in low quantities (e.g., N2N25) can sometimes affect the model's capability to converge, leading to larger errors, as seen when we compare N2N and N2N25 errors for most properties. As we continue to add further information, the model manages to converge at the best possible parameters, which can also be seen for most properties when we compare N2N25, N2N50 and N2N75. We believe this is possible only after an optimum threshold percentage of clean reference images are provided.

To decide which denoising methods perform better in terms of bulk properties (porosity and $scCO_2$ saturation) and pore-scale properties (SEN, SSA, interfacial area, average pore size and average blob volume), we sum up the absolute errors for each of the denoising methods for those two groups of properties. We also sum up all errors in **Table 7** to identify the overall accuracy of each denoising method in terms of combined petrophysical characterization. Additionally, an aggregated standard evaluation metric is calculated by summing up the values in **Table 6** for each method. The four aggregate metrics are presented in **Supplementary Table 1**. It is clear from **Supplementary Table 1** that the denoising method selection should be highly dependent on the type of analysis of interest. For example, a denoising method that can offer accurate bulk properties might not be able to provide accurate pore-scale properties and vice versa. Aggregating the error percentages point out that N2N75 has the most consistent performance with the lowest overall error across both bulk and pore-scale properties while SNN has the highest error in estimating pore-scale properties and combined petrophysical properties. Noise-to-clean comes in a close second, however, it requires the complete HQ reference dataset. Among the traditional filters, the bilateral filter was the best performer across all aggregated metrics.

Computational Requirements of DL-Based Denoising Methods

Another important factor to consider when selecting a DL-based denoising model is computational requirements. **Figure 8** shows the comparison of computational expenditure for the different DL-based models. Specifically, we compare the time required to process a single image slice of 800 × 800 pixels and the memory requirement which is computed from the parameters required for training. The system hardware available for implementing all models was the same (two Nvidia Quadro RTX 6000 GPU systems). Here, the comparison is presented against the traditional metric of PSNR to show how the models perform with the use of the required computational resources. We find that the supervised models, which show higher performance for PSNR, have substantially different computational needs, where RDN and CCGAN are approximately 5.6 and 8.6 times slower than N2C. Similarly, CCGAN is also found to be the most memory intensive primarily due to the training requirements of four individual networks while all other models share similar memory requirements ($\sim 1/6^{th}$ that of CCGAN). When comparing the semi-supervised models, all three models (N2N25, N2N50, and N2N75) require the exact same computational resources both in terms of processing time and memory requirements. Finally, the unsupervised models (N2V and N2N) require similar memory requirements, but N2V is approximately four times slower than N2N. This could be attributed to the original PIP[2] based implementation of the model. Overall, CCGAN is found to be the least computationally efficient, whereas N2C, N2N%, and N2N are the most efficient.

Denoising Method Recommendation

Denoising is a mainstay pre-processing step performed to improve our ability to detect features and perform more accurate quantitative analyses using CT images. Comparing denoising methods through standard metrics and petrophysical property estimates helps us understand the use-cases in which certain models perform better. For example, despite performing well in terms of standard evaluation metrics, supervised DL models like N2C and RDN rely upon the availability of clean HQ data and such models cannot be used when such reference data is scarce or not available. Similarly, downstream tasks also determine the choice of denoising model. N2N50 can be recommended for generative tasks where additional synthetic data is required while N2C can be used if image segmentation is the proceeding step. Additionally, another important consideration is the availability of computational resources. Deep learning-based models require GPU-based systems to perform the training efficiently while traditional filters only require basic computational resources.

Based on the results we find that there is no one denoising method that ultimately performs better in all cases. Micro-computed tomography users are encouraged to adopt a similar evaluation workflow to derive an optimum denoising method that works best for their dataset(s) and use case. However, we present a high-level denoising model recommendation

[2]PIP (2021). Available online at: https://pip.pypa.io/en/stable/ (accessed January 4, 2021).

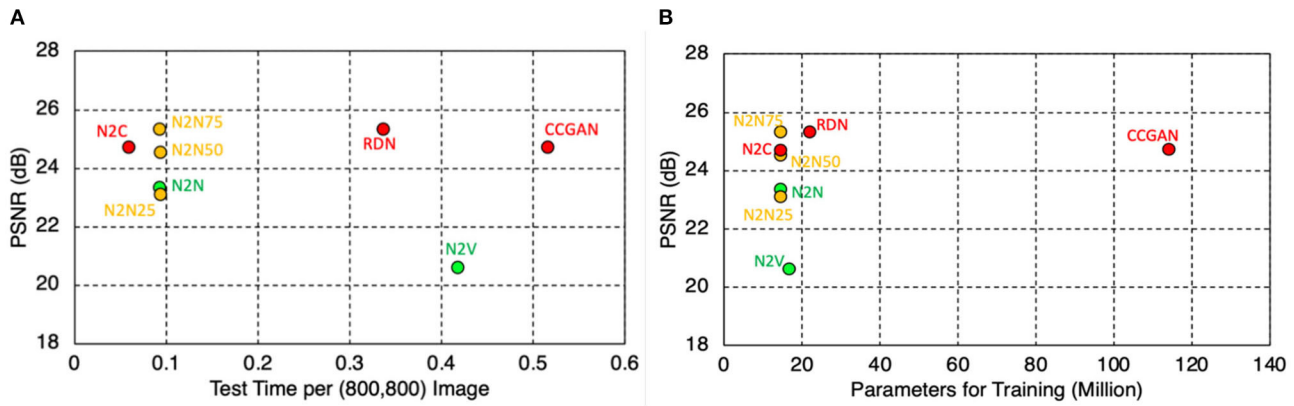

FIGURE 8 | Comparison of computational requirement for the different DL-based denoising algorithms on 2 Nvidia Quadro RTX 6000 GPU systems, in terms of **(A)** computation time per (800,800) image, and **(B)** memory requirements as represented by parameters required for training. Red, fully supervised DL denoising models; yellow, semi-supervised DL denoising models; green, un-supervised DL denoising models.

in **Supplementary Table 2**, based upon the different factors analyzed in this study. Though these factors influence the choice of a model individually, we list combinations of those factors to offer model recommendations for different scenarios. We derive the recommendations from **Supplementary Table 1** and **Figure 8** where we illustrate the superiority of some algorithms over others.

CONCLUSIONS AND FUTURE WORK

Micro-computed tomography image artifacts and alterations resulting from using a non-tailored denoising protocol can result in inaccurate image-based characterization of porous media. In this paper, we present a comprehensive comparison of the performance of various image denoising methods which are broadly categorized as traditional (user-based) non-learnable denoising filters and DL-based methods. The DL-based methods are further sub-categorized depending on their reliance on reference data for the training process. Common architectures are used for supervised and unsupervised methods. We also proposed new semi-supervised denoising models (N2N75, N2N50, and N2N25) to assess the value of information and explore whether faster, lower exposure MCT images can partially substitute high-exposure datasets, which can be costly and can also hinder our ability to capture phenomena that occur at smaller time scales. The datasets used are those of a porous sintered glass core that has been saturated with brine and $scCO_2$. We use both qualitative and quantitative evaluations to compare the performance of different denoising methods. For the latter, we consider standard denoising evaluation metrics, as well as physics-based petrophysical property estimates. The following conclusions are derived based on the analysis of our results,

- Commonly used denoising filters in the digital rock physics literature, namely NLM and AD, show reasonable performance in terms of traditional denoising metrics like PSNR and SSIM. These methods also show reasonable estimates for the bulk petrophysical properties. However, when estimating pore-scale properties like phase connectivity, these methods could result in significant errors. NLM and SNN filters were found to perform least favorably in terms of pore-scale petrophysical estimates.
- Qualitative evaluation is usually used in the digital rock physics literature. However, we show that visual image quality is not sufficient to select an appropriate denoising algorithm.
- The selection of an optimum denoising model cannot solely depend on the visual quality of the denoised image, or even on the standard denoising evaluation metrics. Several factors need to be considered, including the availability of computational resources, and the post-processing analysis of interest. Physics-based petrophysical evaluation metrics are key in selecting a fit-for-purpose denoising method since a superior performance based on standard evaluation metrics may not necessarily indicate a superior performance in terms of petrophysical characterization accuracy. Additionally, there is no single best denoising algorithm across all petrophysical properties.
- The performance of the newly proposed semi-supervised methods, especially N2N75, is very promising considering that less high-exposure data can be used to achieve accurate petrophysical characterization, while significantly reducing scanning time and cost. This can also be useful in cases where the phenomenon being investigated has a short time-scale like chemical processes and pore-scale flow events. It can also help minimize rotational drift errors during scans.
- The unsupervised DL models, in general, showed the weakest performance both on standard and petrophysical evaluation metrics, with N2V giving the least favorable outcomes across most properties of interest.
- N2C (fully supervised) and N2N75 (semi-supervised with 75% HQ data) overall showed the most favorable outcomes.

However, other supervised models like RDN and CCGAN and semi-supervised models like N2N50 and N2N25 showed weaknesses either on traditional metrics, petrophysical estimates, or computational requirements.

This study laid the groundwork for comparing and screening denoising methods for different use-cases within the digital rock physics domain. The following tasks are to be addressed in future work.

- Compare the performance of the different denoising methods using more complex petrophysical properties like surface roughness, tortuosity, interfacial curvature, *in-situ* contact angles, as well as fluid flow parameters such as absolute permeability, relative permeability, and capillary pressure. This comparison can enable optimum image processing workflow selection for creating accurate digital rocks that can be used for multiphase flow prediction and explanation.
- Optimize different denoising methods to accommodate different types of datasets. For that, we would need to first investigate the effect of porous medium structure complexity and image resolution on the performance of the different denoising methods.
- Use idealized simulated or synthetic ground truth reference images and test the effect of different types and levels of noise on the performance of each of the denoising methods, as well as combinations of the denoising methods.
- To identify the effect of noise in the HQ ground truth images on the conclusions drawn in this study, the same study can be conducted while using HQ datasets of varying exposure time.
- Optimize the newly proposed semi-supervised denoising models to determine the optimum threshold percentage of HQ high-exposure images that are needed while maintaining high accuracy of petrophysical analysis.
- Test the hypothesis of whether the sequential use of N2N25 can improve image quality to a point where accurate results are achievable.
- Explore the merits and drawbacks of sequential vs. co-learning in DL-based image processing, including reconstruction, denoising, and segmentation steps.
- Explore more novel unsupervised denoising methods to remove dependency upon HQ, high-exposure images and make use of less time and cost intensive scans for accurate petrophysical characterization.
- Compare the performance of denoising methods pre-reconstruction vs. post-reconstruction.

DATA AVAILABILITY STATEMENT

The datasets generated and analyzed for this study can be found here: Tawfik, M., Karpyn, Z., and Huang, S. X. (2022). scCO2-Brine-Glass Dataset for Comparing Image Denoising Algorithms [Data set]. Digital Rocks Portal. https://doi.org/10.17612/A1QA-2A25.

AUTHOR CONTRIBUTIONS

MT, AA, XH, and ZK: study conception and design. MT, ZK, and PP: data collection. MT, AA, YH, and PP: analysis and interpretation of results. MT, AA, YH, PP, RJ, PS, XH, and ZK: draft manuscript preparation. All authors reviewed the results and approved the final version of the manuscript.

ACKNOWLEDGMENTS

The authors thank the financial support of the National Energy Technology Laboratory's ongoing research under the RSS contract number 89243318CFE000003.

SUPPLEMENTARY MATERIAL

The Supplementary Material for this article can be found online at: https://www.frontiersin.org/articles/10.3389/frwa.2021.800369/full#supplementary-material

REFERENCES

Al-Menhali, A. S., Menke, H. P., Blunt, M. J., and Krevor, S. C. (2016). Pore Scale observations of trapped CO_2 in mixed-wet carbonate rock: applications to storage in oil fields. *Environ. Sci. Technol.* 50, 10282–10290. doi: 10.1021/acs.est.6b03111

AlRatrout, A., Raeini, A. Q., Bijeljic, B., and Blunt, M. J. (2017). Automatic measurement of contact angle in pore-space images. *Adv. Water Resour.* 109, 158–169. doi: 10.1016/j.advwatres.2017.07.018

Alsamadony, K. L., Yildirim, E. U., Glatz, G., Bin, W. U., and Hanafy, S. M. (2021). Deep learning driven noise reduction for reduced flux computed tomography. *Sensors* 21, 1–17. doi: 10.3390/s21051921

Alyafei, N., Raeini, A. Q., Paluszny, A., and Blunt, M. J. (2015). A sensitivity study of the effect of image resolution on predicted petrophysical properties. *Transp. Porous Media*. 110, 157–169. doi: 10.1007/s11242-015-0563-0

Andrä, H., Combaret, N., Dvorkin, J., Glatt E., Han, J., Kabel, M., et al. (2013). Digital rock physics benchmarks-part II: computing effective properties. *Comput. Geosci.* 50, 33–43. doi: 10.1016/j.cageo.2012.09.008

Andrew, M., Bijeljic, B., and Blunt, M. J. (2014). Pore-scale imaging of trapped supercritical carbon dioxide in sandstones and carbonates. *Int. J. Greenh. Gas Control*. 22, 1–14. doi: 10.1016/j.ijggc.2013.12.018

Armstrong, R. T., McClure, J. E., Berrill, M. A., Rücker, M., Schlüter, S., and Berg, S. (2016). Beyond Darcy's law: the role of phase topology and ganglion dynamics for two-fluid flow. *Phys Rev E.* 94, 1–10. doi: 10.1103/PhysRevE.94.043113

Attix, F. H. (2004). *Introduction to Radiological Physics and Radiation Dosimetry*. Weinheim: WILEY-VCH Verlag GmbH & Co. KGaA.

Bae, H.-J., Kim, C.-W., Kim, N., Park, B. H., Kim, N., Seo, J. B., et al. (2018). A perlin noise-based augmentation strategy for deep learning with small data samples of HRCT images. *Sci. Rep.* 8, 1–7. doi: 10.1038/s41598-018-36047-2

Berg, S., Rücker, M., Ott, H., Georgiadisa, A., van der Lindea, H., Enzmannb, F., et al. (2016). Connected pathway relative permeability from pore-scale imaging of imbibition. *Adv. Water Resour.* 90, 24–35. doi: 10.1016/j.advwatres.2016.01.010

Boas, F. E., Fleischmann, D. (2012). CT artifacts: causes and reduction techniques. *Imaging Med.* 4, 229–240. doi: 10.2217/iim.12.13

Brown, K., Schluter, S., Sheppard, A., and Wildenschild, D. (2014). On the challenges of measuring interfacial characteristics of three-phase fluid flow with x-ray microtomography. *J. Microsc.* 253, 171–182. doi: 10.1111/jmi.12106

Buades, A., Coll, B., and Morel, J. M. (2005). "A non-local algorithm for image denoising," in *2005 IEEE Computer Society Conference on Computer Vision and Pattern Recognition (CVPR'05)* (San Diego, CA), 60–65. doi: 10.1109/CVPR.2005.38

Budrikis, Z. L. (1972). Visual fidelity criterion and modeling. *Proc. IEEE* 60, 771–779. doi: 10.1109/PROC.1972.8776

Chen, X., Verma, R., Espinoza, D. N., and Prodanović, M. (2018). Pore-scale determination of gas relative permeability in hydrate-bearing sediments using, x-ray computed micro-tomography and lattice boltzmann method. *Water Resour. Res*. 54, 600–608. doi: 10.1002/2017WR021851

CoreLab (2021). *X-ray Transparent CoreLab Biaxial FCH Series Coreholder*. Available online at: https://www.corelab.com/cli/core-holders/x-ray-core-holder-fch-series (accessed January 9, 2021).

Cromwell, V., Kortum, D. J., and Bradley, D. J. (1984). "The use of a medical computer tomography (CT) system to observe multiphase flow in porous media," in *Proceedings of the SPE Annual Technical Conference and Exhibition* (Houston, TX), 1–4. doi: 10.2523/13098-ms

Culligan, K. A., Wildenschild, D., Christensen, B. S. B., Gray, W. G., Rivers, M. L., and Tompson, A. F. B. (2004). Interfacial area measurements for unsaturated flow through a porous medium. *Water Resour. Res*. 40, 1–12. doi: 10.1029/2004WR003278

Diwakar, M., and Kumar, M. (2018). A review on CT image noise and its denoising. *Biomed. Signal Process Control*. 42, 73–88. doi: 10.1016/j.bspc.2018.01.010

Dong, H., Blunt, M. J., (2009). Pore-network extraction from micro-computerized-tomography images. *Phys. Rev. E Stat. Nonlinear Soft Matter Phys*. 80, 1–11. doi: 10.1103/PhysRevE.80.036307

Fan, L., Zhang, F., Fan, H., and Zhang, C. (2019). Brief review of image denoising techniques. *Vis. Comput. Ind. Biomed. Art*. 2:7. doi: 10.1186/s42492-019-0016-7

Freire-Gormaly, M., Ellis, J. S., MacLean, H. L., and Bazylak, A. (2015). Pore structure characterization of Indiana limestone and pink dolomite from pore network reconstructions. *Oil Gas Sci. Technol*. 71:33. doi: 10.2516/ogst/2015004

Gao, Y., Lin, Q., Bijeljic, B., and Blunt, M. J. (2017). X-ray microtomography of intermittency in multiphase flow at steady state using a differential imaging method. *Water Resour. Res*. 53, 10274–10292. doi: 10.1002/2017WR021736

Gastal, E. S. L., and Oliveira, M. M. (2012). Adaptive manifolds for real-time high-dimensional filtering. *ACM Trans. Graph*. 31, 33:1–33:13. doi: 10.1145/2185520.2185529

Grader, A., Mu, Y., Toelke, J., Baldwin, C., Fang, Q., Carpio, G., et al. (2010). "SPE 138591. Estimation of relative permeability using the lattice boltzmann method for fluid flows in a cretaceous formation, Abu Dhabi," in Paper presented at the Abu Dhabi International Petroleum Exhibition and Conference (Abu Dhabi).

Herring, A. L., Harper, E. J., Andersson, L., Sheppard, A., Bay, B. K., and Wildenschild, D. (2013). Effect of fluid topology on residual nonwetting phase trapping: implications for geologic CO_2 sequestration. *Adv Water Resour*. 62, 47–58. doi: 10.1016/j.advwatres.2013.09.015

Hsieh, J. (2015). *Computed Tomography: Principles, Design, Artifacts, and Recent Advances, 3rd Edn*. Bellingham WA: SPIE.

Huang, T. S., Yang, G. J., and Tang, G. Y. (1979). A fast two-dimensional median filtering algorithm. *IEEE Trans. Acoust*. 27, 13–18. doi: 10.1109/TASSP.1979.1163188

Iglauer, S., Fernø, M. A., Shearing, P., and Blunt, M. J. (2012). Comparison of residual oil cluster size distribution, morphology and saturation in oil-wet and water-wet sandstone. *J. Colloid Interface Sci*. 375, 187–192. doi: 10.1016/j.jcis.2012.02.025

Jasti, J. K., Jesion, G., and Feldkamp, L. (1993). Microscopic imaging of porous media with X-ray computer tomography. *SPE Form. Eval*. 8, 189–193. doi: 10.2118/20495-PA

Jia, L., Ross, C. M., and Kovscek, A. R. (2007). A pore-network-modeling approach to predict petrophysical properties of diatomaceous reservoir rock. *SPE Reserv. Eval. Eng*. 10, 597–608. doi: 10.2118/93806-pa

Kakouei, A., Vatani, A., Rasaei, M. R., Sedaee Sola, B., and Moqtaderi, H. (2017). Cessation of Darcy regime in gas flow through porous media using LBM: comparison of pressure gradient approaches,. *J. Nat. Gas Sci. Eng*. 45, 693–705. doi: 10.1016/j.jngse.2017.06.018

Kamrava, S., Tahmasebi, P., and Sahimi, M. (2019). Enhancing images of shale formations by a hybrid stochastic and deep learning algorithm. *Neural Netw*. 118, 310–320. doi: 10.1016/j.neunet.2019.07.009

Kang, E., Koo, H. J., Yang, D. H., Seo, J. B., and Ye, J. C. (2019). Cycle-consistent adversarial denoising network for multiphase coronary CT angiography. *Med. Phys*. 46, 550–562. doi: 10.1002/mp.13284

Karpyn, Z. T., Piri, M., and Singh, G. (2010). Experimental investigation of trapped oil clusters in a water-wet bead pack using X-ray microtomography. *Water Resour. Res*. 46, 1–25. doi: 10.1029/2008WR007539

Keys, R. G. (1981). Cubic convolution interpolation for digital image processing. *IEEE Trans. Acoust. Speech Signal Process*. 29, 1153. doi: 10.1093/nq/s10-III.69.308-b

Kingma, D. P., and Ba, J. L. (2015). "Adam: a method for stochastic optimization," in *3rd International Conference on Learning Representations, ICLR 2015* (San Diego, CA), 1–15.

Klise, K. A., Moriarty, D., Yoon, H., and Karpyn, Z. (2016). Automated contact angle estimation for three-dimensional X-ray microtomography data. *Adv. Water Resour*. 95, 152–160. doi: 10.1016/j.advwatres.2015.11.006

Knoll, G. F. (2000). *Radiation Detection and Measurement, 3rd Edn*. New York, NY: Wiley. doi: 10.1002/hep.22108

Krizhevsky, B. A., Sutskever, I., and Hinton, G. E. (2017). ImageNet classification with deep convolutional neural networks. *ACM Commun.* 60, 84–90. doi: 10.1145/3065386

Krull, A., Buchholz, T. O., and Jug, F. (2019). "Noise2void-learning denoising from single noisy images," in *2019 IEEE/CVF Conference on Computer Vision and Pattern Recognition (CVPR)* (Long Beach, CA), 2124–2132. doi: 10.1109/CVPR.2019.00223

Kulathilake, K. A. S. H., Abdullah, N. A., Sabri, A. Q. M., and Lai, K. W. (2021). *A Review on Deep Learning Approaches for Low-Dose Computed Tomography Restoration*. Kuala Lumpur: Springer International Publishing. doi: 10.1007/s40747-021-00405-x

Landry, C. J., Karpyn, Z. T., and Piri, M. (2011). Pore-scale analysis of trapped immiscible fluid structures and fluid interfacial areas in oil-wet and water-wet bead packs. *Geofluids* 11, 209–227. doi: 10.1111/j.1468-8123.2011.00333.x

Landry, J. C., Karpyn, Z. T., Ayala, O., (2014). Relative permeability of homogenous-wet and mixed-wet porous media as determined by pore-scale lattice Boltzmann modeling. *Water Resour. Res.* 50, 3672–3689. doi: 10.1002/2013WR014979.Reply

Larpudomlert, R., Torrealba, V. A., Karpyn, Z. T., and Halleck, P. (2014). Experimental investigation of residual saturation in mixed-wet porous media using a pore-scale approach. *J. Pet. Explor. Prod. Technol*. 4, 175–187. doi: 10.1007/s13202-013-0076-8

Lee, S., Lee, M. S., and Kang, M. G. (2018). Poisson-gaussian noise analysis and estimation for low-dose X-ray images in the NSCT domain. *Sensors (Switzerland)*. 18, 1–22. doi: 10.3390/s18041019

Lehtinen, J., Munkberg, J., Hasselgren, J., Laine, S., Karras, T., Aittala, M., et al. (2018). "Noise2Noise: learning image restoration without clean data," in *Proceedings of the 35th International Conference on Machine Learning,* Vol. 7, (Stockholm), 4620–4631.

Li, Z., Galindo-Torres, S., Yan, G., Scheuermann, A., and Li, L. (2018). A lattice Boltzmann investigation of steady-state fluid distribution, capillary pressure and relative permeability of a porous medium: effects of fluid and geometrical properties. *Adv. Water Resour*. 116, 153–166. doi: 10.1016/j.advwatres.2018.04.009

Lin, Q., Bijeljic, B., Pini, R., Blunt, M. J., and Krevor, S. (2018). Imaging and measurement of pore-scale interfacial curvature to determine capillary pressure simultaneously with relative permeability. *Water Resour Res*. 54, 7046–7060. doi: 10.1029/2018WR023214

Liu, H., Valocchi, A. J., Werth, C., Kang, Q., and Oostrom, M., (2014). Pore-scale simulation of liquid CO_2 displacement of water using a two-phase lattice Boltzmann model. *Adv. Water Resour*. 73, 144–158. doi: 10.1016/j.advwatres.2014.07.010

Machado, A. C. S., Machado, A. C. S., and Lopes, R. T. (2013). "Influence of mathematical filters in the volume measurement of a travertine sample using high resolution x-ray microtomography," in *2013 International Nuclear Atlantic Conference - INAC 2013* (Recife, PE).

Matrecano, M., Poderico, M., Poggi, G., Romano, M., and Cesarelli, M. (2010). "Application of denoising techniques to micro-tomographic images," in *Proceedings of the 10th IEEE International Conference on Information Technology and Applications in Biomedicine* (Corfu), 1–4. doi: 10.1109/ITAB.2010.5687713

McClure, J. E., Ramstad, T., Li, Z., Armstrong, R. T., and Berg, S. (2020). Modeling geometric state for fluids in porous media: evolution of the euler characteristic. *Transp. Porous Media* 133, 229–250. doi: 10.1007/s11242-020-01420-1

Menke, H. P., Andrew, M. G., Blunt, M. J., and Bijeljic, B. (2016). Reservoir condition imaging of reactive transport in heterogeneous carbonates using fast synchrotron tomography - effect of initial pore structure and flow conditions. *Chem. Geol*. 428, 15–26. doi: 10.1016/j.chemgeo.2016.02.030

Mittal, A., Moorthy, A. K., and Bovik, A. C. (2011). "Blind/referenceless image spatial quality evaluator," in *2011 Conference Record of the Forty Fifth Asilomar Conference on Signals, Systems and Computers (ASILOMAR)* (Pacific Grove, CA).

Mittal, A., Soundararajan, R., and Bovik, A. C. (2013). Making a "completely blind" image quality analyzer. *IEEE Signal Process. Lett.* 20, 209–212. doi: 10.1109/LSP.2012.2227726

Mostaghimi, P., Blunt, M. J., and Bijeljic, B. (2013). Computations of absolute permeability on micro-CT images. *Math. Geosci.* 45, 103–125. doi: 10.1007/s11004-012-9431-4

Niu, F. (2021). *Experimental Investigation of Pressure Dependence of Contact Angle in CO_2-Brine Systems*. Master Thesis, Pennsylvania State University.

Orhan, K. (2020). *Micro-Computed Tomography (Micro-CT) in Medicine and Engineering*. Cham: Springer. doi: 10.1007/978-3-030-16641-0

Perlin, K. (1985). An image synthesizer. *Comput Graph.* 19, 287–296. doi: 10.1145/325165.325247

Perona, P., and Malik, J. (1990). Scale-space and edge detection using anisotropic diffusion. *IEEE Trans. Pattern Anal. Mach. Intell.* 12, 629–639.

Porter, M. L., and Wildenschild, D. (2010). Image analysis algorithms for estimating porous media multiphase flow variables from computed microtomography data: a validation study. *Comput. Geosci.* 14, 15–30. doi: 10.1007/s10596-009-9130-5

Probst, G., Boeckmans, B., Kruth, J.-P., and Dewulf, W. (2016). "Compensation of drift in an industrial computed tomography system," *6th Conference on Industrial Computed Tomography* (Wels), 1–6.

Prodanović, M., and Bryant, S. L. (2006). A level set method for determining critical curvatures for drainage and imbibition. *J Colloid Interface Sci.* 304, 442–458. doi: 10.1016/j.jcis.2006.08.048

Purswani, P., Karpyn, Z. T., Enab, K., Xue, Y., and Huang, X. (2020). Evaluation of image segmentation techniques for image-based rock property estimation. *J. Pet. Sci. Eng.* 195, 107890. doi: 10.1016/j.petrol.2020.107890

PyBRISQUE-1.0 software package (2020). Available online at: https://pypi.org/project/pybrisque/ (accessed January 4, 2021).

Raeini, A. Q., Yang, J., Bondino, I., Bultreys, T., Blunt, M. J., and Bijeljic, B., (2019). Validating the generalized pore network model using micro-CT Images of two-phase flow. *Transp. Porous Media.* 130, 405–424. doi: 10.1007/s11242-019-01317-8

Ritman, E. L. (2004). Micro-computed tomography—current status and developments. *Annu. Rev. Biomed. Eng.* 6, 185–208. doi: 10.1146/annurev.bioeng.6.040803.140130

Ronneberger, O., Fischer, P., and Brox, T. (2015). U-Net: convolutional networks for biomedical image segmentation. *IEEE Access.* 9, 16591–16603. doi: 10.1109/ACCESS.2021.3053408

Rücker, M., Bartels, W. B., Singh, K., Brussee, N., Coorn, A., van der Linde, H. A., et al. (2019). The effect of mixed wettability on pore-scale flow regimes based on a flooding experiment in ketton limestone. *Geophys. Res. Lett.* 46, 3225–3234. doi: 10.1029/2018GL081784

Scanziani, A., Singh, K., Blunt, M. J., and Guadagnini, A. (2017). Automatic method for estimation of *in situ* effective contact angle from X-ray micro tomography images of two-phase flow in porous media. *J. Colloid. Interface Sci.* 496, 51–59. doi: 10.1016/j.jcis.2017.02.005

Shahmoradi, M., Lashgari, M., Rabbani, H., Qin, J., and Swain, M. (2016). A comparative study of new and current methods for dental micro-CT image denoising. *Dentomaxillofacial Radiol.* 45, 20150302. doi: 10.1259/dmfr.20150302

Sharma, M. M., and Yortsos, Y. C. (1987). Fines migration in porous media. *AIChE J.* 33, 1654–1662. doi: 10.1002/aic.690331009

Sidorenko, M., Orlov, D., Ebadi, M., and Koroteev, D. (2021). Deep learning in denoising of micro-computed tomography images of rock samples. *Comput. Geosci.* 151:104716. doi: 10.1016/j.cageo.2021.104716

Singh, K., Menke, H., Andrew, M., Lin, Q., Rau, C., Blunt, M. J., et al. (2017). Dynamics of snap-off and pore-filling events during two-phase fluid flow in permeable media. *Sci. Rep.* 7, 5192. doi: 10.1038/s41598-017-05204-4

Skvideo (2013). *Skvideo.measure.niqe Package*. Available online at: http://www.scikit-video.org/stable/modules/generated /skvideo.measure.niqe.html. (accessed January 4, 2021).

Sommer, C., Straehle, C., Kothe, U., and Hamprecht, F. A. (2011). Ilastik: interactive learning and segmentation toolkit. *Proc. Int. Symp. Biomed. Imaging.* 2011, 230–233. doi: 10.1109/ISBI.2011.5872394

Tawfik, M. S. (2020). *Multi-Scale Investigation of Wettability Alteration via Chemically-tuned Waterflooding in Carbonate Rocks: Understanding the Effect of Oil Chemistry*. Dissertation, Pennsylvania State University.

Tawfik, M. S., Karpyn, Z., and Johns, R. (2019). "Multiscale study of chemically-tuned waterflooding in carbonate rocks using micro-computed tomography," in *IOR 2019 - 20th Eur Symp Improv Oil Recover* (Pau). doi: 10.3997/2214-4609.201900074

Tian, C., Fei, L., Zheng, W., Xu, Y., Zuo, W., and Lin, C. W. (2020). Deep learning on image denoising: an overview. *Neural Networks.* 131, 251–275. doi: 10.1016/j.neunet.2020.07.025

Valvatne, P. H., and Blunt, M. J. (2004). Predictive pore-scale modeling of two-phase flow in mixed wet media. *Water Resour. Res.* 40, 1–21. doi: 10.1029/2003WR002627

Van Stappen, J. (2018). *A Micro-CT investigation into pore-Scale CO_2 Sequestration Processes in Fratured Reservoir Rocks*. Thesis, PhD. in Geology, Ghent University.

Verri, I., Della Torre, A., Montenegro, G., Onoratia, A., Ducab S., Morab, C. A et al., (2017). Development of a digital rock physics workflow for the analysis of sandstones and tight rocks. *J. Pet. Sci. Eng.* 156, 790–800. doi: 10.1016/j.petrol.2017.06.053

Wang, S. Y., Ayral, S., and Gryte, C. C. (1984). Computer-assisted tomography for the observation of oil displacement in porous media. *Soc Pet Eng, J.* 24, 53–55. doi: 10.2118/11758-PA

Wang, Y. D., Blunt, M. J., Armstrong, R. T., and Mostaghimi, P. (2021). Deep learning in pore scale imaging and modeling. *Earth Sci. Rev.* 215:103555. doi: 10.1016/j.earscirev.2021.103555

Wang, Z., Bovik, A. C., Sheikh, H. R., Simoncelli, E. P. (2004). Image quality assessment: from error visibility to structural similarity. *IEEE Trans. Image Process.* 13, 600–612. doi: 10.1109/TIP.2003.819861

Weickert, J. (1996). *Anisotropic Diffusion in Image Processing*. Stuttgart: B.G. Teubner. Available online at: https://www.mia.uni-saarland.de/weickert/Papers/book.pdf

Yang, Q., Yan, P., Zhang, Y., Yu, H., Shi, Y., Mou, X., et al. (2018). Low-dose CT image denoising using a generative adversarial network with wasserstein distance and perceptual loss. *IEEE Trans. Med. Imaging.* 37, 1348–1357. doi: 10.1109/TMI.2018.2827462

Zahaf, K., Lecoq, T. F., Badi, B. S. A. L., Roth, S., Dong, H., Blunt, M. J. (2017). "Prediction of relative permeability and capillary pressure using digital rock physics : case study on two giant middle eastern carbonate reservoirs," in *International Symposium of the Society of Core Analysts* (Vienna), 1–9.

Zhang, Y., Tian, Y., Kong, Y., Zhong, B., and Fu, Y. (2021). Residual dense network for image restoration. *IEEE Trans. Pattern Anal. Mach. Intell.* 43, 2480–2495. doi: 10.1109/TPAMI.2020.2968521

Conflict of Interest: The authors declare that the research was conducted in the absence of any commercial or financial relationships that could be construed as a potential conflict of interest.

Publisher's Note: All claims expressed in this article are solely those of the authors and do not necessarily represent those of their affiliated organizations, or those of the publisher, the editors and the reviewers. Any product that may be evaluated in this article, or claim that may be made by its manufacturer, is not guaranteed or endorsed by the publisher.

NOMENCLATURE

AD	Anisotropic diffusion
BET	Brunauer, Emmett and Teller
BI	Blurring index
BM3D	Block-matching and 3D filtering
BRISQUE	Blind/reference-less image spatial quality evaluator
CCGAN	Cycle consistent generative adversarial network
CCSIM	Cross-correlation-based simulation
CCUS	Carbon capture, utilization, and storage
CNN	Convolutional neural network
CNR	Contrast-to-noise ratio
dB	Decibels
DL	Deep learning
GANs	Generative adversarial networks
GPU	Graphics processing unit
HQ	High quality
L1	loss Least absolute deviations loss function
L2	loss Least square errors loss function
LQ	low quality
LS	Limestone
MAE	Mean absolute error
MCT	Micro-computed tomography
N2C	Noise-to-clean
N2N	Noise-to-noise with no reference ground truth images
N2N25	Noise-to-noise with 25% of the dataset having reference ground truth images
N2N50	Noise-to-noise with 50% of the dataset having reference ground truth images
N2N75	Noise-to-noise with 75% of the dataset having reference ground truth images
N2V	Noise-to-void
NIQE	Naturalness image quality evaluator
NLM	Non-local means
PSNR	Peak signal-to-noise ratio
RDN	Residual dense network
ROI	Region of interest
$scCO_2$	Supercritical carbon dioxide
SEN	Specific Euler number
SNN	Symmetric nearest neighbor
SS	Sandstone
SSA	Specific surface area
SSIM	Structural similarity index
VDSR	Very deep super resolution
VGG	Visual Geometry Group
λ	Poisson process mean
μ	Gaussian distribution mean
σ	Gaussian distribution standard deviation

Advantages of publishing in Frontiers

OPEN ACCESS
Articles are free to read for greatest visibility and readership

FAST PUBLICATION
Around 90 days from submission to decision

HIGH QUALITY PEER-REVIEW
Rigorous, collaborative, and constructive peer-review

TRANSPARENT PEER-REVIEW
Editors and reviewers acknowledged by name on published articles

Frontiers
Avenue du Tribunal-Fédéral 34
1005 Lausanne | Switzerland

Visit us: www.frontiersin.org
Contact us: frontiersin.org/about/contact

REPRODUCIBILITY OF RESEARCH
Support open data and methods to enhance research reproducibility

DIGITAL PUBLISHING
Articles designed for optimal readership across devices

FOLLOW US
@frontiersin

IMPACT METRICS
Advanced article metrics track visibility across digital media

EXTENSIVE PROMOTION
Marketing and promotion of impactful research

LOOP RESEARCH NETWORK
Our network increases your article's readership